JAERI-Review
2005-034

研究炉利用における研究成果集

（平成15年度）

2005年9月

（編）研究炉利用課

日本原子力研究所
Japan Atomic Energy Research Institute

本レポートは，日本原子力研究所が不定期に公刊している研究報告書です。
入手の問合わせは，日本原子力研究所研究情報部研究情報課（〒319-1195　茨城県那珂郡東海村）あて，お申し越しください。なお，このほかに財団法人原子力弘済会資料センター（〒319-1195　茨城県那珂郡東海村日本原子力研究所内）で複写による実費頒布をおこなっております。

This report is issued irregularly.
Inquiries about availability of the reports should be addressed to Research Information Division, Department of Intellectual Resources, Japan Atomic Energy Research Institute, Tokai-mura, Naka-gun, Ibaraki-ken, 319-1195, Japan.

編集兼発行　　日本原子力研究所

研究炉利用における研究成果集（平成１５年度）

日本原子力研究所東海研究所研究炉部
（編）研究炉利用課

（2005年7月25日受理）

平成15年度、東海研究所研究炉においてはJRR-3の8サイクルとJRR-4の42サイクルの共同利用運転が行われた。

研究炉は、中性子散乱、即発ガンマ線分析、中性子ラジオグラフィ、医療照射（ＢＮＣＴ）などの実験利用及び、各種試料の放射化分析、原子炉材料の照射試験、フィッションートラックの照射利用など、様々な目的に利用されている。

本報告書は、研究炉の利用者（原研外を含む）から成果の提出246件を受け、中性子散乱（９分野）、中性子ラジオグラフィ、即発ガンマ線分析、放射化分析、RIの製造、原子炉材料照射試験、その他の分野別に取りまとめたものである。

東海研究所：〒319-1195　茨城県那珂郡東海村白方白根2-4

JAERI-Review 2005-034

Activity Report on the Utilization of Research Reactors (Japanese Fiscal Year, 2003)

(Ed.) Research Reactor Utilization Division

Department of Research Reactor
Tokai Research Establishment
Japan Atomic Energy Research Institute
Tokai-mura, Naka-gun, Ibaraki-ken

(Received July25, 2005)

During the fiscal year 2003, the Tokai Research Establishment research reactors carried out 8 cycles of joint use reactor operation at JRR-3 and 42 cycles at JRR-4.
The research reactors are being utilized for various purposes including experimental studies such as neutron scattering, prompt gamma analysis, neutron radiography and medical irradiation (BNCT), and irradiation utilization such as neutron activation analysis of various samples, Irradiation Test of Reactor Materials and fission track.
This volume contains 246 activity reports, which are categorized into the fields of neutron scattering (9 subcategories), neutron radiography, neutron activation analysis, reactor materials, prompt gamma analysis, and others, submitted by the users in JAERI and from other organizations.

Keywords: JRR-3, JRR-4, Research Reactor, Neutron Scattering, Neutron Radiography, Neutron Activation Analysis, Neutron Beam, Irradiation

目　次

Contents

はじめに

平成１５年度には、ＪＲＲ－３において８サイクルの共同利用運転、ＪＲＲ－４において４２サイクルの共同利用運転が行なわれ、これに伴いさまざまな利用が行われた。

本報告書は、利用者（原研外利用者を含む）から当該利用の成果の提出を受け、取りまとめたものである。

提出して頂いた成果の件数は、中性子散乱１９３件、中性子ラジオグラフィ１４件、即発ガンマ線分析９件、放射化分析２２件、RIの製造１件、原子炉材料照射試験２件、その他５件で合計２４６件であった。なお、本報告書の一部は下記報告書の中から転載させて頂いた。

最後に、原稿を提出して頂いた利用者の皆様のご協力に感謝するとともに、今後も研究炉が有効に利用され、種々の研究がさらに進展されることを期待します。

研究炉利用課長
楠　剛

---

1)標　　題　：ACTIVITY REPORT ON NEUTRON SCATTERING RESEARCH issued by ISSP-NSL,University of Tokyo
（東京大学物性研究所発行）
レポート番号：Vol.11（第１１巻）
編　　者　：東京大学物性研究所
発 行 年　：２００４年

2)標　　題　：原研施設利用共同研究成果報告書（平成１５年度）
レポート番号：UTRCN-G-33
編　　者　：東京大学原子力研究総合センター
発 行 年　：２００４年

This is a blank page.

研 究 成 果 一 覧

Research Reports

This is a blank page.

1. 中性子散乱 1)構造・励磁

1. Neutron Scattering 1) Structure・Excitation

This is a blank page.

研究テーマ：高効率熱電材料スクッテルダイトの格子振動
表　題：高効率熱電材料スクッテルダイトの格子振動

1-1-1

Phonon study on high performance thermoelectric material "skutterudite"

C. H. Lee, M. Matsuda[1] and H. Sugawara[2]

National Institute of Advanced Industrial Science and Technology, 1-1-1 Umezono, Tsukuba, Ibaraki 305-8568, Japan
[1] *Advanced Science Research Center, Japan Atomic Energy Research Institute, Tokai, Ibaraki 319-1195, Japan*
[2] *Graduate School of Science, Tokyo Metropolitan University, Minami-Ohsawa, Hachioji, Tokyo 192-0397, Japan*

Filled skutterudite compounds RM_4X_{12} (R = rare-earth; M = Fe, Ru or Os; X = P, As or Sb) have attracted great attention due to their potential as thermoelectric devices. In particular, their low lattice thermal conductivity is advantageous to achieve high thermoelectric performance. For further improvement in their performance, the origin of their low lattice thermal conductivity needs to be investigated. Previous studies suggest that the suppression of thermal conductivity is a consequence of free vibration of rare-earth atoms in a large lattice cage, which is so called rattling effect[1]. To confirm the hypothesis, phonon behavior should be studied. In this work, we have studied phonon of $CeRu_4Sb_{12}$ by neutron scattering using single crystal samples. Note that all previous neutron scattering studies of phonons were restricted to powder samples and this is the first report on a phonon study using single crystals.

The measurements were conducted using the 3-axis spectrometer, TAS-1, at JRR-3M reactor of Japan Atomic Energy Research Institute in Tokai. The incident (final) neutron energy was fixed at E_i (E_f) = 14.7 meV or 13.7 meV using the (002) reflection of a pyrolytic graphite monochromator and an analyzer. In order to increase the sample volume, five single crystals were assembled and mounted in an Al container filled with He thermal exchange gas. Total volume of the samples is about 0.2 cc.

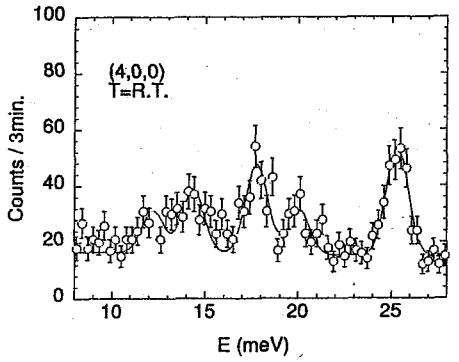

Figure 1: Energy spectrum of phonons at (4,0,0) for $CeRu_4Sb_{12}$.

Figures 1 and 2 depict energy spectra of phonon at Γ point in the energy range of 8meV $\leq E \leq$ 50 meV at room temperature. Solid lines depict a fit using gaussian function. Many branches are observed in the measurements. According to V. Keppens *et al.*[1], there is a broad peak around E = 15 meV for $LaFe_4Sb_{12}$ measured by inelastic powder neutron technique. They discussed that the broadening is an effect of hybridization with accoustic phonons. The present results, however, indicate that their observation of broad peak is not due to such hybridization but rather due to the emergence of many phonon branches. Feldman *et al.* has calculated phonon energies of $LaFe_4Sb_{12}$ and show that their maximum energy is E = 32 meV[2]. Although sample composition is different, our observation of phonons around E = 40 meV, higher than the prediction, requires recalculating using more suitable parameters. Further studies should be carried out to clarify the rattling effect.

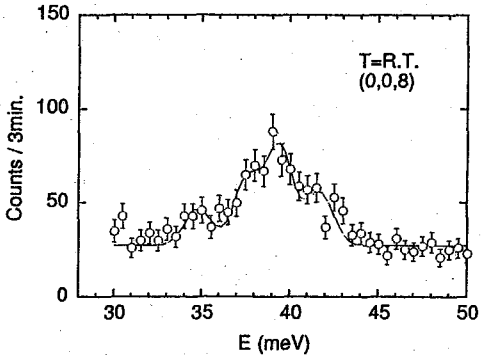

Figure 2: Energy spectrum of phonons at (0,0,8) for $CeRu_4Sb_{12}$.

References

1) V. Keppens *et al.* : Nature 395, 876 (1998).
2) J. L. Feldman *et al.* : Phys. Rev. B 68, 94301 (2003).

原子炉：JRR-3　　装置：TAS-1(2G)　　分野：中性子散乱（構造）

研究テーマ:Liドープしランタンチタン酸塩の相転移機構およびLiイオンのディスオーダーと伝導経路
表題:Li添加ランタンチタン酸塩ペロブスカイト $La_{2/3-x}Li_{3x}TiO_3$ の構造変化

1-1-2

Structural change of the Li-doped lanthanum titanate perovskite $La_{2/3-x}Li_{3x}TiO_3$

Wataru Nakamura,[a] Masatomo Yashima,[a,*] Daiju Ishimura,[a] Syuuhei Kobayashi,[a] Kenjiro Oh-uchi,[a] Mitsuru Itoh,[b] Kenji Ohoyama[c]

[a]Department of Materials Science and Engineering, Interdisciplinary Graduate School of Science and Engineering, Tokyo Institute of Technology, 4259 Nagatsuta-cho, Midori-ku, Yokohama, 226-8502, Japan
[b]Materials and Structures Laboratory, Tokyo Institute of Technology, 4259 Nagatsuta-cho, Midori-ku, Yokohama, 226-8503, Japan
[c]Institute for Materials Research, Tohoku University, Katahira 2-1-1, Aoba-ku, Sendai, 980-8577, Japan
* (yashima@materia.titech.ac.jp).

Li-doped lanthanum titanate perovskites $La_{2/3-x}Li_{3x}TiO_3$ have high Li ion conductivity ($10^{-3}Scm^{-1}$ at room temperature) and A-site deficient layered perovskite-type structure with the ordered distribution of La ions on the A-sites along the *c*-axis. But the detailed crystal structure and the phase transition of $La_{2/3-x}Li_{3x}TiO_3$ have not been reported yet. In this work, we have chosen the composition $La_{0.52}Li_{0.32}TiO_{2.94}$, because it has highest Li-ion conductivity in $La_{2/3-x}Li_{3x}TiO_3$ ($0 \le x \le 0.15$). The tilt of the TiO_6 octahedron in layered perovskite is the key to understand the crystal structure [1]. However, the tilt angle has not been known in $La_{0.52}Li_{0.32}TiO_{2.94}$. The purpose of this study is to investigate the crystal structure and phase transition in $La_{0.52}Li_{0.32}TiO_{2.94}$.

$La_{0.52}Li_{0.32}TiO_{2.94}$ compound was studied by high-temperature neutron diffraction technique. Neutron-diffraction data were collected in the temperature range from room temperature to 1268K, using the multi-detector system HERMES [2] and an electric furnace to heat the sample [3]. Crystal structure of $La_{0.52}Li_{0.32}TiO_{2.94}$ was refined by Rietveld analysis of diffraction data using a computer program RIETAN-2000 [4].

In the literature the $La_{0.52}Li_{0.32}TiO_{2.94}$ has been assumed to belong to the space group *P4/mmm* at room temperature. However, the *P4/mmm* could not explain the observed 113, 133, 115, 315, 533, 117, and 355 reflection peaks where the *hkl* was indexed based on the basic perovskite lattice. On the other hand, the space group *Cmmm* yielded these reflection peaks (Fig.1). The lattice parameter increased continuously with temperature as shown in Fig.2. The low-temperature orthorhombic phase has tilt of TiO_6 octahedron along *b* axis. The tilt angle decreased with temperature and became 0 at 1098±59K (Fig.3). We found that the tetragonal-to-orthorhombic (*P4/mmm-Cmmm*) transition is induced by the tilt of the TiO_6 octahedron (Fig.4). Similar *P4/mmm-Cmmm* phase transition was reported for $La_{0.64}(Ti_{0.92}Nb_{0.08})O_3$ [1] and $La_{0.6}Sr_{0.1}TiO_3$ [5].

References

1 Yashima, M., Mori, M., Kamiyama, T., Oikawa, K., Hoshikawa, A., Saitoh, K. and Tsuda, K. (2003) *Chem. Phys. Lett.* **375**, 240.
2 Ohoyama, K., (1998) *Jpn. J. Appl. Phys.* **37**, 3319
3 Yashima, M. *J. Am. Ceram. Soc.* (2002) **85**, 2925.
4 Izumi, F. and Ikeda, T., (2000) *Mater. Sci. Forum* **321-324**, 198.
5 Howard, C. J. and Zhang, Z., (2003) *J. Phys. Cond. Matt.* **15**, 4543.

使用施設:JRR-3M, 装置:HERMES(T1-3), 分野:1. Structures & Excitations

研究テーマ:Liドープしランタンチタン酸塩の相転移機構およびLiイオンのディスオーダーと伝導経路
表題:Li添加ランタンチタン酸塩ペロブスカイト $La_{2/3-x}Li_{3x}TiO_3$ の構造変化

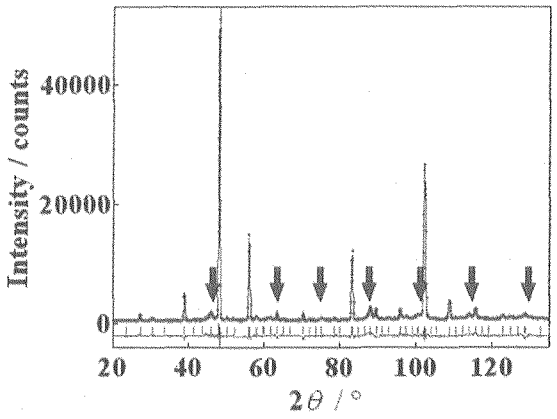

Fig.1 Rietveld fitting pattern of $La_{0.52}Li_{0.32}TiO_{2.94}$ measured at 299K. Peaks with arrows correspond to reflections that could not be explained by the *P4/mmm* structure but by the *Cmmm* space group.

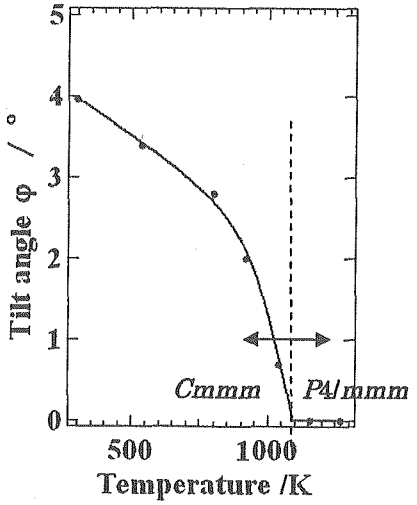

Fig.3 Temperature dependence of tilt angle of $La_{0.52}Li_{0.32}TiO_{2.94}$.

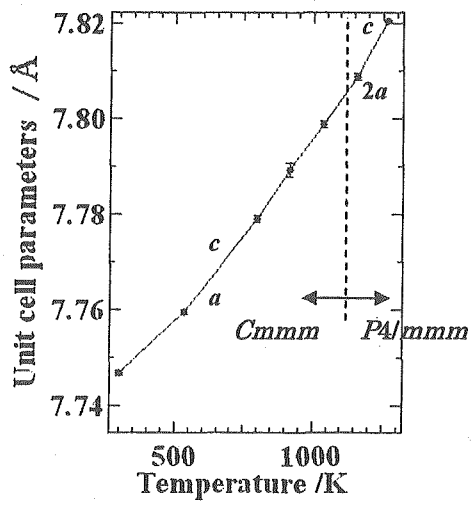

Fig.2 Temperature dependence of unit cell parameters of $La_{0.52}Li_{0.32}TiO_{2.94}$.

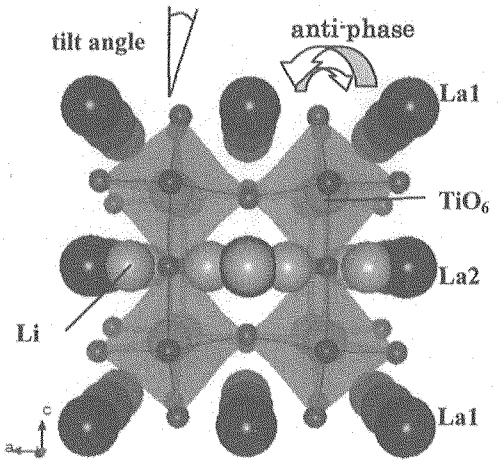

Fig.4 Crystal structure of $La_{0.52}Li_{0.32}TiO_{2.94}$ depicted with the refined crystal parameters (299K).

使用施設:JRR-3M, 装置:HERMES(T1-3), 分野:1. Structures & Excitations

研究テーマ：アミド類からラクタム環の形成における水素移動反応の機構解明
表　題：中性子回折による有機固相反応中の水素移動の直接観察

1-1-3

DIRECT OBSERVATION OF THE HYDROGEN TRANSFER IN THE SOLID-STATE ORGANIC PHOTOREACTION BY NEUTRON DIFFRACTION METHOD

T. Hosoya, H. Uekusa, T. Ozeki, Y. Ohashi, T. Ohhara[1], I. Tanaka[1] and N. Niimura[2]

Department of Chemistry and Materials Science, Tokyo Institute of Technology, Tokyo 152-8550
[1]Institute of Materials Structure Science, HEARO (KEK), Tsukuba, Ibaraki 305-0801
[2]Department of System Engineering, Ibaraki University, Hitachi, Ibaraki 316-8511

Hydrogen/proton transfer is one of the most elemental chemical reaction, and often observed in many organic and enzymatic reactions. In many cases, the hydrogen/proton transfer is key point of reaction process. Though many spectroscopic methods, e.g., ^{1}H-NMR, FT-IR, and theoretical calculations have been carried out to track the hydrogen/proton, more accurate and direct positional information is needed in order to clarify transfer process by using neutron diffraction method.

Light-induced reversible color change of substances is known as photochromism and has attracted attention due to their potential applications such as optical data storage etc. Salicylideneaniline derivatives show photochromism or thermochromism, which is reversible color change with variation of temperature. The color change from stable yellow to unstable red is brought about by the change of molecular conformation. This reaction involves a proton transfer in the keto-enol tautomerization. Previously, photo-irradiated trans-keto form of N-3,5-di-tert-butylsalicylidene-3-nitroaniline **1b** were observed by X-rays (Fig. , R=NO_2)[1].

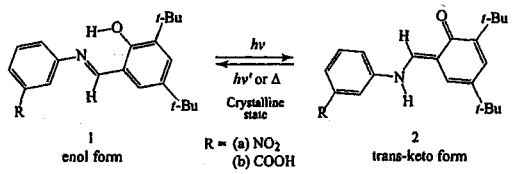

Scheme

Photoirradiation was carried out with two photon absorption method by laser, and the population of trans-keto **1b** form was about 10%. Therefore, the transferred proton was not observed. We try to observe the transferred proton of trans-keto form with neutron diffraction method. Crystals of **1a** and N-3,5-di-tert-butylsalicylidene-3-carboxyaniline **1b** were prepared and photo-irradiated with ultra high pressure Hg lamp.

Trans-keto form of **1a** has long lifetime enough for neutron diffraction measurement at room temperature (~ 4 days), but population of trans-keto form was only 10% with laser. On the other hand, corresponding form of **1b** has short lifetime at room temperature (~ 1 hour), but population of trans-keto form was more than 15% with Hg lamp. So the diffraction measurement of **1b** was carried out at 173 K.

Soon after the irradiation with Hg lamp (410 nm) for 2 hours from four direction, crystals were mounted on the BIX-III (1G) neutron imaging plate diffractometer set up at the JRR-3M reactor in JAERI. Neutron diffraction data were collected for total 5 days at 173 K (**1b**) and 293 K (**1a**) and peak integration by *DENZO* created a *SHELX*-format *hkl* file.

Table 1: Experimental/Refinement details

	m-COOH	*m*-NO_2
Crystal system	Monoclinic	Triclinic
Space group	$P2_1/n$	P-1
a /Å	14.734(2)	6.02(3)
b /Å	6.004(2)	10.31(4)
c /Å	21.997(3)	16.75(5)
α /°	-	101.19(5)
β /°	91.26(1)	92.12(7)
γ /°	-	101.50(8)
V /Å^3	1945.4(7)	996(7)
Z	4	4
θ range /°	7.89–70.39	9.76–70.73
Temp. /K	173	173
Refs. collected / unique	864 / 864	246 / 246
Completeness to θ /%	21.3	6.1
R_{int}	0.0482	0.0603
R_1, wR(F^2)	0.262, 0.594	0.298, 0.610
Goodness-of-Fit	3.26	5.64
Data / params.	846 / 112	246 / 33

After structure analysis, enol form were clearly observed both **1a** and **1b**. However, the reactions were not proceeded. 410 nm light did not reach inside the thick crystals (but 0.3 mm is too thin for single-crystal neutron diffraction measurement) because the light-induced trans-keto form highly absorbs this light. Initial structures was well refined in spite of small number of reflections (**1a**: 246, **1b**: 864). So it is practical to carry out this measurement using thin crystal if more diffraction data are collected for longer exposure time.And further refinement of light-irradiation condition will be needed in order to increase the population of trans-keto form in a crystal.

References

1) Harada, J., Uekusa, H., and Ohashi, Y., *J. Am. Chem. Soc.*, **121**, 5809 (1999).

原子炉：JRR-3　　装置：BIX-3M(1GB)　　分野：中性子散乱（構造）

研究テーマ：$CH_3NH_3PbI_3$の無秩序配向と原子変位の相関
表題：中性子単結晶回折法による$CH_3NH_3PbBr_3$のメチルアンモニウムの立方晶無秩序配向

1-1-4 Determination of Disordered Configuration of Methylammonium in the Cubic Phase of $CH_3NH_3PbBr_3$ by a Single Crystal Neutron Diffraction Method

H. Mashiyama, H. Kasano, T. Asahi, Y. Noda* and H. Kimura*

Faculty of Science, Yamaguchi University, Yamaguchi 753-8512, Japan;
**Institute of Multidisciplinary Research for Advanced Materials, Tohoku University, Sendai 980-8577, Japan*

$CH_3NH_3PbX_3$ (X=Cl, Br, I) crystals take perovskite-type cubic structure with space group $Pm3m$ in the highest temperature phase, where methylammonium (MA) ion is necessarily disordered because C_{3v} symmetry of the ion is incongruent with the site symmetry O_h. Phase sequences of the three compounds are somewhat different to each other, but successive ordering of MA ion plays an important role any way. Yamamuro *et al.*[1] proposed three types of models on the basis of specific heat measurements; MA ion points <100>, <110> or <111> direction in the cubic phase. In our previous works[2] by the methods of single crystal X-ray diffraction and neutron powder diffraction, <110> model was preferred but not concluded definitely. Thus, we planned the present experiment.

Although room temperature tetragonal phase of $MAPbI_3$ was the initial target of our experiment, single crystals of good quality could not be prepared. Instead, the cubic phase of $MAPbBr_3$ was measured at room temperature. Neutron diffraction intensity was collected by the use of four-circle diffractometer, FONDER, installed by Tohoku University at a beam line T2-2, JRR3M in JAERI (Tokai). The incident wavelength 1.2402Å (Ge 311 monochrometer); the measured range $2\theta<160$deg; the size of specimen ca. 12 mm^3. Intensity data of 494 reflections in one eighth of the reciprocal space were measured. After applying absorption and extinction corrections, we averaged equivalent reflections with $F>3\sigma$ to obtain 98 independent reflections.

Least squares refinement of the crystal structure, with thermal parameters anisotropic for Br and isotropic for other atoms, converged to R=0.077, 0.065 and 0.086 for <100>, <110> and <111> model, respectively. As was expected, <110> model was the best one. In <110> model, isotropic thermal parameters of C and N atoms were so large that we tried two further calculations; one with anisotropic thermal parameters and the other by split atom model. They converged to R=0.045 and 0.046, respectively, and gave the same set of signs for structure factors. We performed MEM analysis with PRIMA developed by Izumi and Dilanian. Figure 1 shows nuclear density images thus obtained; four-leaved negative density due to H atoms in Fig.1(a) and elongated distribution due to N and C atoms disordered along <110> in Fig.1(b) should be noted.[3]

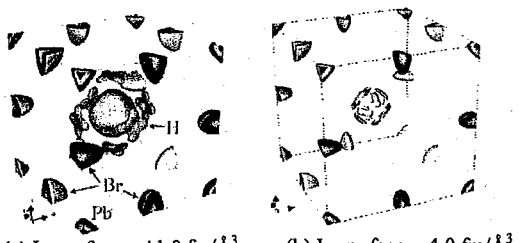

(a) Isosurface = ±1.0 fm/Å^3 (b) Isosurface = 4.0 fm/Å^3

Figure 1: Nuclear density images of $MAPbBr_3$.

References

[1] N. O. Yamamuro *et al.*, J. Phys. Chem. Solids **51** (1990) 6373. [2] Y. Kawamura *et al.*, J. Phys. Soc. Jpn. **71** (2002) 1694; H. Mashiyama *et al.*, J. Korean Phys. Soc. **42** (2003) S1026. [3] H. Mashiyama *et al.*, Meeting Abstracts of the of the Phys. Soc. Jpn. **59**(Issue 1, Pt.4) (2004) 946.

使用施設：JRR-3M, 装置：FONDER(T2-2), 分野 Structures & Excitations

研究テーマ：名包接水和物の動的特性の研究
表　題：メタンハイドレートの低エネルギーモードの運動量依存性

1-1-5

Momentum Dependence of Low Energy Modes of Methane Hydrate

T. Kamiyama, S. Ohonuma, D. Nio, Y. Kiyanagi, T. Uchida[1], T. Ebinuma[1], H. Narita[1], N. Igawa[2], Y. Ishii[2]

Graduate School of Engineering, Hokkaido University, Sapporo 060-8628
[1]*Institute for Energy Utilization, National Institute of Advanced Industrial Science and Technology, Sapporo 062-8517*
[2]*Advanced Science Research Center, JAERI, Tokai, Ibaraki 319-1195*

Clathrate hydrates have many properties that are interesting not only for scientific reasons but also in the fields of geology and nuclear engineering. Gas clathrate hydrates are a non-stoichiometric inclusion of elements or molecules within a host framework or "cage" composed of water molecules. There are many elements and molecules that are able to act as guest molecules, including: Ar, O_2, N_2, CH_4, and CO_2, but in this study we are specifically interested in methane hydrate (MH).

There has recently been a surge of interest in MH due to its potential use as an energy source, and for geo-scientific or environmental reasons. However, our interest is in its potential use as a moderator on a pulsed neutron source. A good moderator material should have a high hydrogen density and a large density-of-states in and around the thermal region (1-100meV) in order to produce a well-defined Maxwellian. Pure solid methane is already used in various pulsed sources around the world and is excellent for producing a high flux of cold neutrons. In contrast water ice lacks low energy vibrational modes and is much better at producing thermal neutrons. Because of its high content of methane, MH potentially combines the properties of ice and methane to produce a moderator with a high performance over a wide energy range.

Until now the several inelastic neutron scattering measurements of MH have already been undertaken by our group. For lower energy (E) and momentum (Q) transfer region, we have measured the dynamical structure factor S(Q,E) map and found the discrete feature of the dispersive peak which is in proportion to Q^2. The main discrete peaks can be explained as the rotational peaks of methane free-rotation, but there still remain the excess intensities of the cross-section around 4.5 meV and over 7 meV (figure 1). It is said that in the low E-Q region there exist the translational modes of methane in the water cage [1]. In this study we have measured these unknown peaks in detail and made clear the features of them.

Figure 2 shows the E-constant spectra of S(Q,E) around E = 6.5 meV and 8 meV, respectively. The points with error bars correspond to the data taken by MARI at ISIS, UK. The TAS-1 data show good agreements with the MARI data on tendencies. The TAS-1 data, which have better statistics and wider Q region, can be recognized the peak shapes and positions. Now we are trying to subtract the influences of rotational peaks from the S(Q,E) and analysing the excess intensities on the S(Q,E). Next, we will discuss about the origin of them.

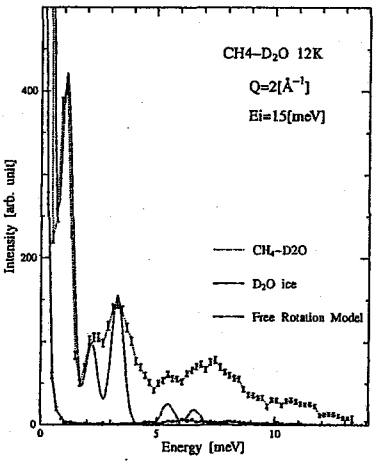

Figure 1: Comparison between experimental S(Q,E) of methane hydrate (MARI at ISIS) and methane free rotation model at 12 K.

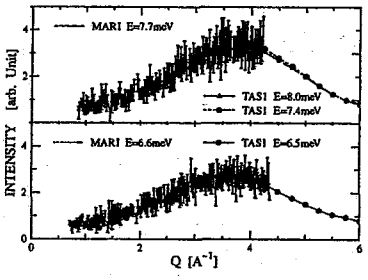

Figure 2: Constant energy spectra of methane hydrate.

References

1) J. S. Tse, C. I. Ratcliffe, B. M. Powell, V. F. Sears and Y. P. Handa, J. Phys. Chem. A, 101 (1997) 4491.

原子炉：JRR-3　　装置：TAS-1(2G)　　分野：中性子散乱（構造）

研究テーマ:ランダム交替鎖系$(CH_3)_2CHNH_3Cu(Cl_xBr_{1-x})_3$のギャップレス相における磁気構造
表題:Random alternating Heisenberg 鎖物質 IPACu$(Cl_xBr_{1-x})_3$の中性子線回折実験

1-1-6

Neutron diffraction Study on $(CH_3)_2CHNH_3Cu(Cl_xBr_{1-x})_3$

H. Manaka, M. Watanabe[1], Y. Noda[1], and I. Yamada[2]

Graduate School of Science and Engineering, Kagoshima University, Korimoto, Kagoshima 890-0065; [1]Institute of Multidisciplinary Research for Advanced Materials, Tohoku University, Sendai 980-8577; [2]Department of Physics, Faculty of Science, Chiba University, 1-7-1 Inageku, Chiba 263-8522

The compounds $(CH_3)_2CHNH_3CuCl_3$ (abbreviated as IPACuCl$_3$) and IPACuBr$_3$ are known as the materials that exhibit the Haldane state and the singlet dimer state at low temperature, respectively. Therefore, a mixed crystal of these compounds, IPACu$(Cl_xBr_{1-x})_3$ has attracted much interest in terms of the effect of randomness in magnetic bond. Indeed, in the intermediate region of $0.44 < x < 0.87$, appearance of a gapless phase has been reported.[1]

As the first step to reveal the magnetic structure of IPACu$(Cl_xBr_{1-x})_3$, we carried out a single crystal neutron diffraction experiment at room temperature by using FONDER, the 4-circled diffract meter at T2-2 in JRR-3M as the PAC No. **2725**. We prepared six single crystals expected to be IPACu$(Cl_{0.65}Br_{0.35})_3$ for this experiment and chose the sample that exhibited the most intensive Bragg reflection among them. The size of the sample was about 5 x 2 x 2 mm^3. To avoid deliquescence of the sample, the sample was setted in the vacuum sheloud of cryo-cooler and evaporated by a vacuum pump during the experiment. The neutron of λ=1.5668 Å was used as an incident beam monochromatized by Si422 monochrometor. At first, the lattice parameters were determined using 13 Bragg reflections (2θ<32°). The resulted lattice parameters were a=17.69(2) Å, b=7.351(5) Å, c=6.43(2) Å, $\alpha=\beta=\gamma$=90°(0.3°), V=418(1) Å^3.

Next, for crystal structure analysis, we collected intensities of 437 Bragg reflections (2θ<90°). Among them, only 270 reflections (including 93 crystallographic unique reflections) have significant intensities. The initial structural parameters for refinements were taken from the structure of IPACuCl$_3$ and that of IPACuBr$_3$.[2,3] In the case of IPACuCl$_3$, the system belongs to orthorhombic *Pcan* (an axial transform of *Pbcn*) at room temperature as same as our present lattice. On the other hand, in the case of IPACuBr$_3$, the space group is triclinic $P\bar{1}$. The mixed crystal was expected to be triclinic. In spite of them, our present lattice seems to belong to orthorhombic *Pcan*. Therefore, we tested the orthorhombic case (total number of refined parameters is 46.) as well as the triclinic case. Occupancies of the halogen atoms were also refined. However, in both case, the structural refinements were unsuccessful. It may be because of insufficient number of significant reflections. For example, even the most intensive Bragg reflection (1 0 0) was less than 200 cps at maximum as shown in Fig. 1. Better sample quality is desired in further study.

References

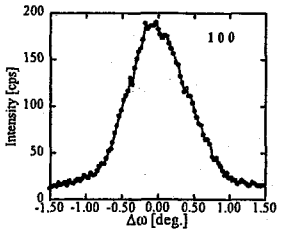

Fig. 1 Peak profile of the Bragg reflection (1 0 0).

[1] H. Manaka et al., Phys. Rev. B **63** (2001) 104408.
[2] D. R. Bloomquist et al., J. Am. Chem. Soc. **103** (1981) 2615.
[3] S. A. Robert et al., J. Am. Chem. Soc. **103** (1981) 2603.

使用施設:JRR-3M, 装置:FONDER(T2-2), 分野 Structure & Excitations

研究テーマ：中性子小角散乱によるナノヘテロ構造を有する実用金属材料の微細構造の解明
表　題：中性子小角散乱による 6000 系 Al 合金の微細組織の研究

1-1-7

Small-angle neutron scattering study on the precipitation of 6000 Al alloys

M. Ohnuma, J. Suzuki[1], T. Honma[2] and K. Hono

National Institute for Materials Science, Tsukuba, Ibaraki 305-0047
[1]Advanced Science Research Center, JAERI, Tokai, Ibaraki 319-1195
[2]University of Tsukuba, Tsukuba, Ibaraki 305-0047

Because of the strong demand on weight reduction of automotive bodies for better fuel efficiency and lower exhaust emission, there is a strong drive to replace the current steel sheet to aluminum alloy sheet for automotive body applications. Due to its excellnet formability and mediam stregth after age hardening, Al-Mg-Si based 6000 series alloys are considered to be the best candicate for automotive body sheet material. In addition, the alloys can be strengthened during an automotive paint bake cycle, i.e. aging treatment at 170-175C for approximately 20 - 30 min. This bake hardening (BH) effect is known to be degraded by aging at room temperature (RT). For preventing this problem, alloys are heated to 250C which is called reversion treatment, before BH heat treatment. It is also known that the Cu addition to Al-Mg-Si based 6000 alloys can help reversion treatment. Although the microstructure of the alloy are extensively studied by transmission electron microscope (TEM), positron annihilation lifetime (PAL) and three dimensional atom probe (3DAP)[1)], the relation between the mechanical properties and the microstructure and the effect of Cu addition are not clear yet. Most important information at this stage is an average information of the precipitats, i.e. the size and volume fraction of the precipitates. A small-angle scattering is most suitable technique for this purpose, however, because of the small difference of electron density among these three constituent elements, small-angle X-ray scatting can not be applied for this alloy. Thus, small-angle neutron scatting (SANS) is only the way to get average information of precipitates. In this paper, we studied SANS for Al-0.7Mg-1.0Si and Al-0.6Mg-1.0Si-0.3Cu (at%) alloys with different annealing processes.

Figure 1 shows the SANS profiles of the Al-0.7Mg-1.0Si and Al-0.6Mg-1.0Si-0.3Cu alloys before and after BH treatment accompanied with aging at RT. No detectable deference between the alloys with and without BH treatment in both alloys indicating no additional precipitates form by BH treatment. Consequently, no strengthening occurs by this process. In contrast, the SANS profiles of these alloys before and after BH treatment accompanied with reversion treatment after aging at RT show some difference in high-q region as shown in Fig.2. The excess scattering corresponds to the formation of β" phase. The differ-

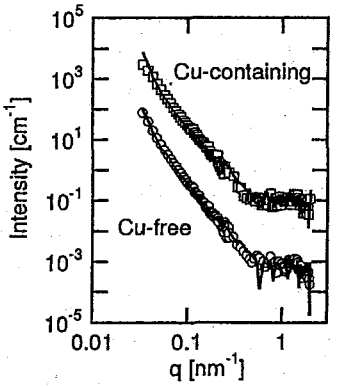

Figure 1: SANS profiles of the alloy aged at RT. Markers and lines are the profiles before and after BH treatments, respectively. The profiles of Cu containing alloys are shifted by factor of 100.

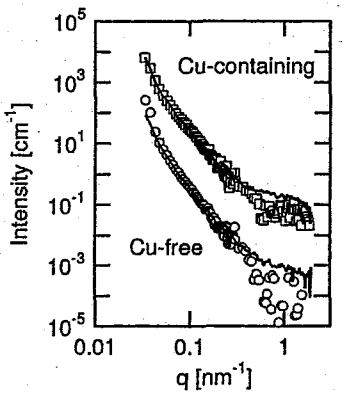

Figure 2: SANS profiles of the alloy after reversion treatment. Markers and lines are the profiles before and after BH treatments, respectively. The profiles of Cu containing alloys are shifted by factor of 100.

原子炉：JRR-3　　装置：SANS-J(C3-2)　　分野：中性子散乱（構造）

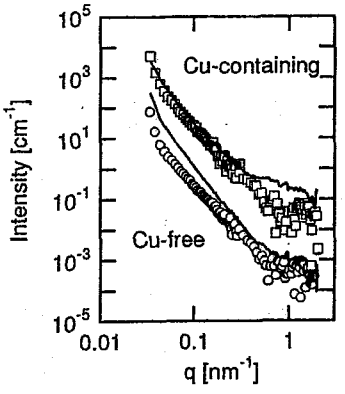

Figure 3: SANS profiles of the as-queched alloy. Markers and lines are the profiles before and after BH treatments, respectively. The profiles of Cu containing alloys are shifted by factor of 100.

ence before and after BH treatment is larger in the alloy with Cu than the one in Cu-free alloys, suggesting that the addition of Cu increase the volume fraction of β" phase. For confirming the enhancement of β" formation by adding Cu, SANS profiles of the sample without room temperature aging were also observed and show in Fig.3. Again, the profile of Cu-containing alloy shows excess scattering due to the formation of beta" phase in high-q region. In contrast, the difference in this q-region is not clear in the profiles for Cu-free alloy before and after BH treatment, suggesting that the amount of β" precipitate is relatively small. Instead, there is clear difference in low-q region which indicates the change in larger scale unit ($\geq$100 nm) is prominent in Cu-free alloy. It is known that 6000-alloys include a certain amount of large precipitates ($\geq$100 nm) which are believed to give no effects to mechanical properties. The change in low-q region seems to be attributed to the contrast change between large precipitate and matrix due to the formation of GP zone. Unfortunately, the formation of GP zone cannot be detected by SANS because of the small difference in concentration. However combined with TEM and 3DAP results[2], we can summarize the relation between mechanical property and precipitation as follows. In as-quenched state from solid solution treatment, solute elements are in highly super saturated state. Therefore, GP zones are formed by RT aging and Vickers hardness increase from about 60Hv in as-quenched state up to about 90Hv after RT aging. Because the formation of GP zone consume solute element, driving force for the formation of beta" which can occur at 170C, decrease prominently. Thus the amounts of beta" precipitates is less than the detectable level by SANS (Fig.1) and no clear difference in Vicikers hardness value in the alloy aged at RT and then BH. Since the GP zone formed during RT aging is resolved by reversion treatment (at 250C), the driving force for formation of β" is high after reversion treatment. Therefore, the β" can be obtained by BH treatment after reversion if the formation of GP zone during BH treatment can be suppressed. This condition is actually obtained in Cu-containing alloy and clear contribution from beta" phase is observed in SANS (Fig.2) . TEM results also shows no indication of GP zone formation. The hardness increase from 70Hv to 97Hv due which is attributed to the β" precipitates. In the Cu-free alloy, however, the formation of GP zone occurs together with β" formation. Therefore the scattering from beta" in SANS profiles is weaker than that of Cu-containing alloy(Fig.2). The hardness increase from 66 to 93Hv which is higher than the value of the alloy aged at RT (85Hv) indicating some contribution of β" precipitates. The effect of Cu is much clearer in the alloy without aging at RT (Fig.3). Because highly saturated solute elements is used for the formation of beta" phase efficiently in Cu-containing alloy, the amount of β" reach maximum value among the measured alloys and the hardness also reach maximum value, 117Hv. In contrast, high super saturation of solute element is mostly consumed for the formation of GP zone in Cu-free alloy. Therefore, the amount of β" is very small after BH treatment and increment of Hv is same value with the one after RT aging which can be explained by the formation of GP zone. Because of the concentration change in matrix due to the formation of the large amount of GP zone, the scattering contrast between large precipitate and matrix become large and cause the increasing of scattering in low-q region. Instead, the scattering from β" is unclear due to the their small volume(Fig.3). As summary, the relation of mechanical property and microstructure in 6000 alloy become clear using SANS. Especially, it is confirmed that addition of Cu suppress or delay the GP zone formation at 170C and enhance the formation of β".

References

1) Y.Nagai, M. Murayama, Z. Tang, T. Nonaka, K. Hono and M.Hasegawa, Acta mater. 49(2001), 913-920.
2) T.Honma,K.Matsumoto, K.Hono, Y. Nagai, and M. Hasegawa, to be published.

研究テーマ:セリア固溶体における酸化物イオンのディスオーダーと伝導経路
表題:1497℃までの酸化セリウム CeO_2 の高温中性子粉末回折による研究

1-1-8

High-Temperature Neutron Powder Diffraction Study of Cerium Dioxide CeO_2 up to 1497℃

S. Kobayashi, M. Yashima[+], D. Ishimura, K. Oh-uchi, W. Nakamura, K. Ohoyama[*], K. Kawachi[**], and T. Yasui[**]

Department of Materials Science and Engineering, Interdisciplinary Graduate School of Science and Engineering, Tokyo Institute of Technology, 4259 Nagatsuta-cho, Midori-ku, Yokohama, 226-8502, Japan; [*]Institute for Materials Research, Tohoku University, Katahira 2-1-1, Aoba-ku, Sendai, 980-8577, Japan; [**]Daiichi Kigenso Kagaku Kogyo, Hirabayashi-Minami 1-6-38, Sumie-ku, Osaka 559-0025, Japan.

([+]yashima@materia.titech.ac.jp)

Here we report the disorder of oxygen ions in ceria (cerium dioxide, CeO_2) from 1005 to 1497 ℃ studied by neutron powder diffraction and the Rietveld method [1].

High-purity ceria powders were pressed into pellets, and they were sintered at 1500 °C for 5 h. The cylindrical product of 16 mm in diameter and of 410 mm in height was obtained after the sintering. Neutron-diffraction measurements were performed in air with HERMES, [2] installed at the JRR-3M reactor in Japan Atomic Energy Research Institute, Tokai, Japan. Neutron wavelength was 1.8207 Å. Diffraction data were collected in the 2θ range from 20° to 150° in the step interval of 0.1°, between 1005 and 1497 °C. A furnace with $MoSi_2$ heaters was placed on the sample table [3] and used for measurements at high temperatures. Sample temperature was kept constant within ± 1.5 °C during each data collection. The experimental data were analyzed by a combination technique of Rietveld analysis using a computer program RIETAN-2000 [4] and the maximum-entropy method (MEM)-based pattern fitting. The powder pattern indicated a single phase with the fluorite-type structure (Fig1).

First, Rietveld analysis was done assuming a split-atom model where the O atoms were distributed at 4*c* 1/4,1/4,1/4 and at 32*f* *x*, *x*, *x* positions (x=1/4+δ). The

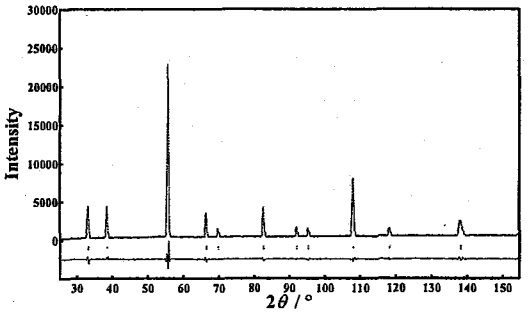

Fig.1 Rietveld fitting pattern of CeO_2 measured at 1497℃.

isotropic harmonic model was used for all the atomic displacement parameters. We used the split-atom model, because the Rietveld analysis with this model yielded a better fit. The calculated profile with the split-atom model agreed well with the observed one (Fig.1). The atomic displacement parameters of oxygen atoms were larger than that of Ce atom, suggesting the conduction of oxygen ions.

Second, the MEM analysis was done using the structural factors obtained by the Rietveld analysis with the split-atom model. The MEM calculations were done using a computer program PRIMA [5]. The nuclear distribution was plotted by a computer program VENUS [5]. MEM map provided information on the disorder of oxygen ions (Figs. 2 and 3). To visualize the structural disorder at 1005 and 1497 °C, nuclear density distribution maps on the (110) plane are shown in Fig. 3.

使用施設:JRR-3M, 装置:HERMES(T1-3), 分野:1. Structures & Excitations

(a) (b)

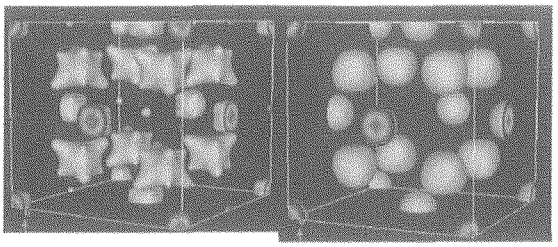

FIG. 2. Equicontour surface of the scattering amplitude distribution at 0.7 fm/Å^3 with scattering amplitude distribution on the (100) plane of CeO_2 obtained by Rietveld refinement and the MEM-based pattern fitting of data measured (a) at 1497 and (b) 1005 °C.

The results reveal that the oxygen ions in the CeO_2 have a complicated disorder and spread over a wide area, compared with Ce ions. Bulges in the <111> directions are clearly seen at 1497 °C in Figs. 2 and 3, comparing with those at 1005°C. The direction of bulges of oxygen ions is opposite side of the Ce ion and the oxygen ions shift to the position of the cavity at 1/2,1/2,1/2 position. The bulges indicate a possible diffusion mechanism where the oxygen ions move through a face of the surrounding Ce tetrahedron to the octahedral cavity and then re-entering a neighboring anion site. In fact, there is a small but significant maximum at the 1/2,1/2,1/2 position of the nuclear density distribution at 1497 °C as shown in Figs. 2 and 3. This mechanism was also suggested in other materials with the fluorite-type structure. The bulges in the <111> directions also suggest another diffusion path where the oxygen ions move in the <100> directions along the *c* axis. These features were also confirmed in the MEM analysis of the same sample measured at different temperatures 1100, 1200, 1300, and 1400 °C. The earlier complicated disorder of oxygen ions would be responsible for the ionic conduction. Two possible diffusion paths in the <111> and <100> directions were confirmed in CeO_2.

These results were published in ref. [1].

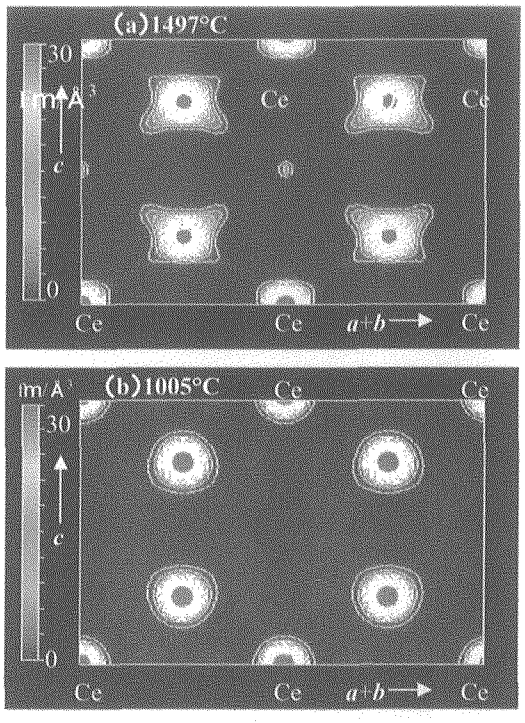

FIG. 3. Scattering amplitude distribution on (110) plane of CeO_2 at (a) 1497°C and at (b) 1005°C with white contours in the range from at 0.7 to 30 fm/Å^3 (1fm/Å^3 step). Oxygen ions have a disorder along [111] directions, while the possible conducting paths of the oxygen ion are seen along <1 1 1> and <1 0 0> directions.

Reference

[1] M. Yashima and S. Kobayashi, *Appl. Phys. Lett.*, **84**, 526 (2004).

[2] K. Ohoyama, T. Kanouchi, K. Nemoto, M, Ohashi, T.Kajitani and Y. Yamaguchi, *Jpn. J. Appl. Phys*, **37**, 3319-3326 (1998).

[3] M. Yashima, *J. Cryst. Soc. Jpn.*, **44**, 121-126, (2002)

[4] F. Izumi and T. Ikeda, *Mater. Sci. Forum*, **321-324**, 198-204, (2000).

[5] F. Izumi, and R.A. Dilanian, *Recent Research Developments in Physics,* Vol. 3, Part II, TransWorld Research Network, Trivandrum, p.699 (2002).

研究テーマ：先端偏極中性子散乱によるスピン一格子物性の研究
表　題：S=1/2 量子反強磁性体 NH_4CuCl_3 の粉末中性子回折

1-1-9

Neutron Powder Diffraction Study for S = 1/2 Quantum Antiferromagnet NH_4CuCl_3

M. Fujisawa, A. Oosawa[1], Y. Ishii[1], H. Tanaka[2] and K. Kakurai[1]

Department of Physics, Tokyo Institute of Technology, Meguro, Tokyo 152-8551
[1]Advanced Science Research Center, JAERI, Tokai, Ibaraki 319-1195
[2]Low Temperature Center, Tokyo Institute of Technology, Tokyo 152-8551

The space group of NH_4CuCl_3 has been reported to be $P2_1/c$ at room temperature [1], which is isomorphous to the related antiferromagnetic dimer systems $TlCuCl_3$ and $KCuCl_3$ which have a gapped singlet ground state. NH_4CuCl_3 has a magnetic ground state with no gap and shows magnetization plateaus at 1/4 and 3/4 of the saturation magnetization [2]. The origin of the 1/4 and 3/4 plateaus is still unclear. In order to understand the unusual magnetic properties in NH_4CuCl_3, it may be important to consider the freezing process of the reorientational dynamics of the NH_4^+ ions at low temperature. For instance, Matsumoto recently suggested that the inequivalent dimer model, in which the ground state consists of the inequivalent three Cu^{2+} dimers, can explain the 1/4 and 3/4 plateaus [3]. The inequivalent dimer sites may be induced by the freezing of the dynamics of the NH_4^+ ions, of course, by the structural phase transition to lower symmetries at low temperature. In order to investigate the freezing process of NH_4^+ ions or the existence of the structural phase transition at low temperature, it is important to determine precise crystal structures, so that we performed a neutron diffraction investigation in fully deuterated ND_4CuCl_3 at low temperature.

Powder neutron diffraction measurements were carried out using a high resolution powder diffractometer (HRPD) at T = 296 K, 48 K and 2.8 K in JAERI, Tokai, Japan. The wavelength of neutrons is 1.823 Å. Rietveld refinements of the neutron diffraction data were carried out by using the RIETAN-2000 program [4]. It is noted that we have already confirmed that ND_4CuCl_3 has the same magnetic properties as NH_4CuCl_3.

The experimental results are shown in Fig.1. No remarkable changes of the diffraction pattern between 296 K, and low temperatures 48 K and 2.8 K can be seen. Namely, no super lattice reflections appear and only the peak position of the reflections, as denoted by the arrows in Fig.1 (b), has a slight shift for 48 K and 2.8 K. This means that we could observe no structural phase transntions and only the changes of the lattice parameters to lower temperature in the present measurements. We also analyzed this diffraction pattern in the viewpoints of the freezing of the reorientation of NH_4^+ ions, however we could not obtain the good fitting results.

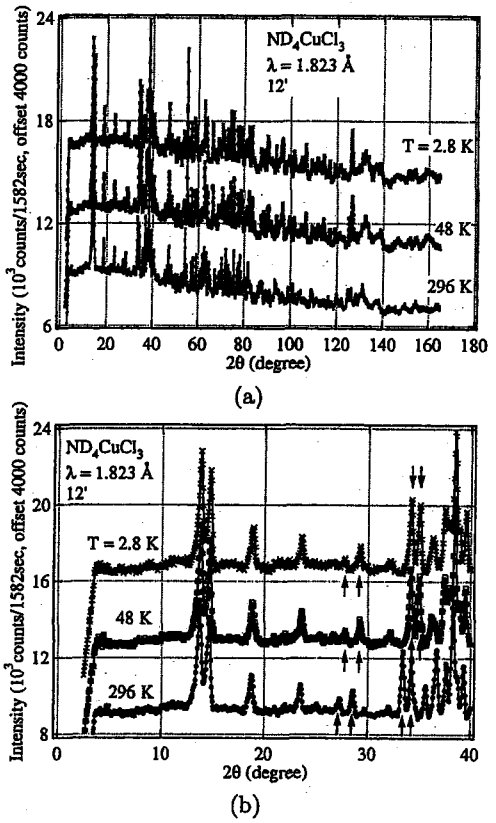

Figure 1: Neutron powder diffraction patterns of ND_4CuCl_3 at T = 296 K, 48 K and 2.8 K obtained on HRPD ((a) for all 2θ and (b) for low 2θ).

In the present analysis, we assumed that no ND_4^+ tetrahedrons are distorted. We will try to reanalyze the diffraction data in consideration of the distorted those for the future.

References

1) R. D. Willett *et al.*: J. Chem. Phys. **38** (1963) 2429.
2) W. Shiramura *et al.*: J. Phys. Soc. Jpn. **67** (1998) 1548.
3) M. Matsumoto: Phys. Rev. B **68** (2003) 180403.
4) F. Izumi and T. Ikeda: Mater. Sci. Forum **321-324** (2000) 198.

原子炉：JRR-3　　装置：HRPD(1G)　　分野：中性子散乱（構造）

1-1-10

研究テーマ：孤立水素結合型物質 BrHPLN($C_{13}O_2H_7Br$) の水素結合のX線と中性子による研究
表題： 室温及び低温における h-BrHPLN の中性子構造解析

Neutron Structure Analysis of h-BrHPLN at Room temperature and Low Temperature

R. Kiyanagi, H. Kimura, M. Watanabe, Y. Noda, T. Sugawara[1] and T. Mochida[2]
Institute of Multidisciplinary Research for Advanced Materials, Tohoku University, 2-1-1 Katahira, Aoba-ku, Sendai 980-8577
[1] *Department of Basic Science, Graduate School of Arts and Science, The University of Tokyo 3-8-1 komaba, meguro-ku 153-8902*
[2] *Department of Chemistry, Faculty of Science, Toho University 2-2-1 miyama, funabashi 273-8510*

Some ferro/antiferroelectric materials containing hydrogen-bonds show various physical property. In particular, when the hydrogen atom in the hydrogen-bond is replaced with a deuterium atom, they show drastic changes of the ferro/antiferroelectric phase transition temperature.

5-Bromo-9-hydroxyphenalenon($C_{13}H_7O_2Br$, BrHPLN) is an antiferroelectric material with an intra-molecular hydrogen-bond. The material does not show any phase transitions if a hydrogen atom is participating in the hydrogen-bond(h-BrHPLN). On the other hand, if a deuterium atom is in the hydrogen-bond(d-BrHPLN), the material undergoes 2 successive phase transitions via an incommensurate phase. The point is considered to be the behavior of the hydrogen atom in the hydrogen-bond at low temperature and the relation between the hydrogen atom and the phase transition. We carried out neutron structure analyses of h-BrHPLN at 300 K and 10 K and revealed the feature of the hydrogen atom in the hydrogen-bond.

The experiments were performed with the four circle neutron diffractometer FONDER installed at T2-2 beam port at JRR-3M in JAERI(Tokai). The single crystals of h-BrHPLN was prepared with the dimension of 1.0 × 0.9 × 8.5 mm^3 for the experiment at 300 K and 0.75 × 0.75 × 9.0 mm^3 for the experiment at 10 K. Total numbers of the collected data at 300 K and 10 K were 630 and 583, respectively.

After applying absorption corrections, least-square fitting analyses and Maximum Entropy Method analyses were carried out to refine the parameters and to calculate the nuclear density distribution, respectively. It is found that the hydrogen atom in the hydrogen-bond region is in a disordered state at both temperatures, as well as 5-methyl-9-hydroxyphenalenon in the room temperature phase[1, 2]. The nuclear density distribution around the hydrogen-bond region at 300 K and 10 K is shown in Fig. 1. At 300 K, though the hydrogen atom actually occupies two equivalent sites around the center of the hydrogen-bond according to the least-square fitting analysis, the hydrogen atom seems to be located at the center of the hydrogen-bond due to the large thermal vibration. At 10 K, we can see the clear splitting of the hydrogen atom, as the thermal vibration is sufficiently suppressed. The disordered feature of the hydrogen atom at 10 K implies the tunneling motion of the hydrogen atom, which is a controversial issue on the hydrogen-isotope effect.

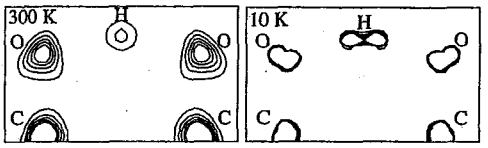

Fig. 1. The nuclear distribution around the hydrogen-bond at 300 K (left panel) and at 10 K (right panel).

References

[1] Y. Noda *et al.*: Ferroelectrics **269** (2002)327.
[2] R. Kiyanagi *et al.*: J. Phys. Soc. Jpn. **72** (2003)2816.

使用施設：JRR-3M, 装置： T2-2 (FONDER) , 分野： 1, Structure & Excitations (x)

研究テーマ：$PbTiO_3$ のフォノン分散関係
表　題：$PbTiO_3$ の格子力学
1-1-11

Lattice dynamics of $PbTiO_3$

I. Tomeno, Y. Ishii[1] Y. Tsunoda[2] K. Oka[3] and H. Unoki[3]

Faculty of Education and Human Studies, Akita University, Akita 010-8502
[1]*Neutron Science Research Center, JAERI, Tokai, Ibaraki 319-1195*
[2]*School of Science and Engineering, Waseda University, Shinjuku-ku, Tokyo 169-8555*
[3]*Nanoelectronics Research Institute, AIST, Tsukuba, Ibaraki 305-8568*

$PbTiO_3$ has attracted much attention from the scientific and engineering viewpoints. Unlike $BaTiO_3$, $PbTiO_3$ undergoes only a single phase transition from a cubic to tetragonal phase at T_c=763 K. $PbTiO_3$ is also the end member of relaxor ferroelectrics (1-x)$Pb(Zn_{1/3}Nb_{2/3})O_3$-x $PbTiO_3$ (PZN-PT). The inelastic neutron-scattering experiments were carried out using the triple-axis spectrometer, TAS-1 at JRR-3M.

The TA phonon dispersion relations for tetragonal $PbTiO_3$ are compared in Fig.1 with those for tetragonal $KNbO_3$, [1] tetragonal $BaTiO_3$ [2] and cubic PZN. [3] Both $PbTiO_3$ and PZN possess two common features. First, the ZB TA phonon energies for Pb-based crystals are considerably lower than those for the other perovskites. The ZB TA phonon energies for cubic PZN are lower than the corresponding energies for tetragonal $PbTiO_3$. The mass and charge randomness at the B site appears to weaken the effective force-constants in PZN. Second, the TA phonon dispersion relations are isotropic with respect to the high-symmetry directions. The isotropic TA phonon dispersion relations are also found for tetragonal $BaTiO_3$. [2] The ZB TA phonon energies for $PbTiO_3$ are approximately half of those for $BaTiO_3$. [2] The Pb atom plays a major role in the ZB acoustic phonons. In contrast, the extremely anisotropic TA phonon curves are found for tetragonal $KNbO_3$. [1]

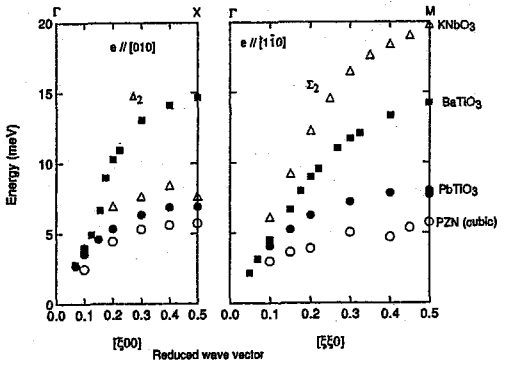

Figure 1: The TA phonon dispersion relations for typical perovskites.

Figure 2 depicts the temperature dependence of phonon dispersion relations along the [110] and [001] directions. The energy of the zone-center TO-A_1 mode is significantly higher than that for the TO-E mode at room temperature. In view of the LST relationship, the dielectric-constant relation $\epsilon_{11} > \epsilon_{33}$ mainly originates from the fact that the low-lying zone-center TO-A_1 mode is well stiffened at room temperature.

The energy of the zone-center TO-A_1 mode decreases to 12.7 meV at 643 K ($0.84T_c$). On the other hand, the energy of the zone-center TO-E mode practically remains constant up to 643 K. The softening of the TO-A_1 mode up to 643 K is rather moderate compared to the behavior of the TO-F_{1u} mode in the cubic phase. [4] The distinctive behavior of the TO modes in both sides is consistent with the fact that the temperature dependence of ϵ_{33} is characterized by a first-order phase transition.

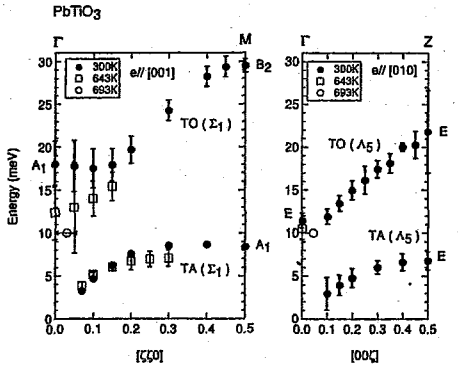

Figure 2: Temperature dependence of phonon dispersion relations for $PbTiO_3$.

References

1) M. D. Fontana, G. Dolling, G. E. Kugel, and C. Carabatos, Phys. Rev. B20 (1979) 3850.
2) G. Shirane, J. D. Axe, J. Harada, and A. Linz, Phys. Rev. B2 (1970) 3651.
3) I. Tomeno, S. Shimanuki, Y. Tsunoda, and Y. Ishii, J. Phys. Soc. Jpn. **70** (2001) 1444.
4) G. Shirane, J. D. Axe, J. Harada and J. P. Remeika : Phys. Rev.B2 (1970) 155.

原子炉：JRR-3　　装置：TAS-1(2G)　　分野：中性子散乱（構造）

研究テーマ：充填スクッテルダイトの磁気構造

表題：充填スクッテルダイト $TbRu_4P_{12}$ の磁気構造

1-1-12 Magnetic Structure of Filled Skutterudite $TbRu_4P_{12}$

K. Kihou[1], C. H. Lee[2], C. Sekine[1], H. Kitô[2] and I. Shirotani[1]

[1] *Muroran Institute of Technology,27-1 Mizumoto-cho, Muroran 050-8585, Japan*

[2] *AIST, 1-1-1 Umezono, Tsukuba, Ibaraki 305-8568, Japan*

Filled skutterudite compounds RM_4X_{12} (R = rare-earth, M = Fe, Ru or Os; X = P, As or Sb) have attracted a great deal of interest due to a wide variety of physical properties such as superconductivity, metal-insulator transition and magnetic ordering. It is believed that their properties are originated from f electron instability and/or the nesting of the Fermi surface. Although intensive studies on filled skutterudites have been carried out, there is only a few study on magnetic structure analysis. In this work, we have performed powder neutron scattering measurements using $TbRu_4P_{12}$ samples and have analyzed their magnetic structure.

Powder samples of $TbRu_4P_{12}$ were synthesized by a high-pressure cell under high temperature using a wedge-type cubic-anvil high-pressure apparatus. Magnetic susceptibility measurements reveal the presence of magnetic phase transitions at $T_1 = 20$ K and $T_2 = 10$ K. To clarify the magnetic structure at low temperature phases, we performed powder neutron scattering measurements using the powder diffractometer HERMES in JRR-3M of JAERI at Tokai. The incident neutron wave length was 1.82035 Å. The powder samples were inserted in a 5 ϕ vanadium cylinder and mounted in an Al container filled with He thermal exchange gas.

Fig. 1 shows neutron diffraction pattern at $T = 30$ K and $T = 13$ K. The pattern at $T = 30$ K is well defined by the crystal structure with space group $Im\bar{3}$. At low temperature, new peaks appear, indicating the presence of an antiferro - magnetic ordering below T_1. The data can be well explained assuming that spins on Tb atoms at corner and center of unit cell are oriented in the opposite direction. Magnetic moment on Tb atoms is estimated to be 8.8 μ_B/Tb, which is comparable to the value of free ions (9 μ_B/Tb).

Fig. 2 show the temperature dependence of the magnetic peak intensity at (1,0,0) below $T = 25$ K. As shown, the intensity decreases with increasing temperature and disappears above $T = T_1$. This suggests that T_1 is a Néel temperature. At $T = T_2$, however, there is no anomaly. Further studies is required to clarify the transition at T_2.

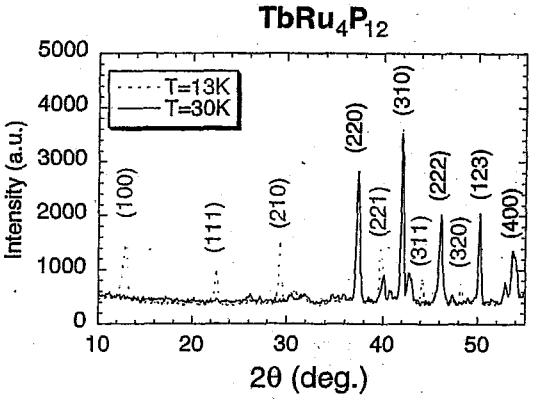

Fig. 1. Powder neutron diffraction patterns of $TbRu_4P_{12}$ at $T = 30$ K and 13 K.

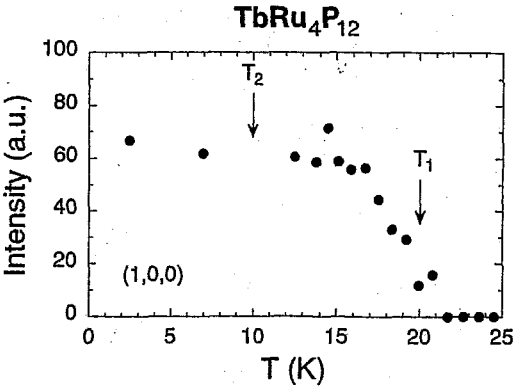

Fig. 2. Temperature dependence of magnetic intensity at (1,0,0) below $T = 25$ K.

使用施設：JRR-3, 装置：T1-3(HERMES), 分野：1. Structure and Excitations

研究テーマ：半磁性電気伝導体の磁性と化学構造、II
表　題：Bi で部分置換したミスフィット型層状酸化物 $[Ca_2CoO_3]_pCoO_2$ の変調構造
1-1-13

Modulated Structure of Bi-substituted Misfit Layered Cobaltite $[Ca_2CoO_3]_pCoO_2$

Y. MIYAZAKI, Y. SUZUKI, M. ONODA[1], N. IGAWA[2], Y. ISHII[2], Y. MORII[2] and T. KAJITANI

Department of Applied Physics, Tohoku University, Sendai 980-8579
[1]*Advanced Materials Laboratory, NIMS, Tsukuba, Ibaraki 305-0044*
[2]*Neutron Science Research Center, JAERI, Tokai, Ibaraki 319-1195*

Misfit-layered cobalt oxides have recently attracted much attention as potential candidates for thermoelectric (TE) materials. Among the compounds, partly Bi-substituted $[Ca_2CoO_3]_pCoO_2$ samples are known to exhibit excellent TE properties at higher temperatures. We have employed a high-resolution neutron powder diffraction technique to investigate the modulated crystal structure of the Bi-substituted compound, in particular the site preference of Bi and the substitution effect on the positional modulation of atomic sites.

Neutron powder diffraction (ND) data were collected at 293 K by means of HRPD diffractometer installed at the JRR-3M reactor in JAERI. The ND data were analyzed using a Rietveld refinement program PREMOS 91. The superspace group of $C2/m(1\ p\ 0)s0$ was appropriately adopted.

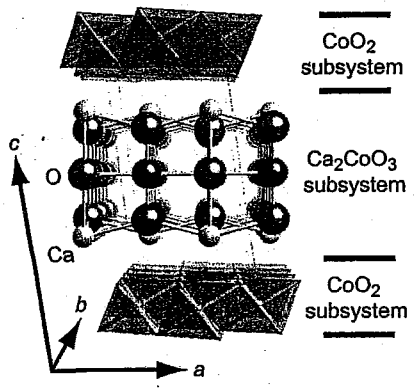

Figure 1: Fundamental crystal structure of $[Ca_2CoO_3]_pCoO_2$.

Figure 1 shows the fundamental structure viewed in perspective from the b-axis. The structure consists of a CoO_2 sheet and an ordered three-layered rock salt (RS)-type Ca_2CoO_3 block, stacked parallel to the c-axis. The CoO_2 sheet is composed of a triangular lattice as seen in the CdI_2-type structure. Bismuth atoms are found to substitute both for Ca and Co atoms in the RS-type $[Ca_2CoO_3]$ subsystem. The resulting structural formula is expressed as $[(Ca_{0.90}Bi_{0.10})_2(Co_{0.95}Bi_{0.05})O_3]_{0.6183}CoO_2$. Upon Bi-substitution, the a- and c-axis lengths markedly increased while the b_{CoO_2}- and b_{RS}-axes showed only slight expansion. The variation of the atomic positional modulation can be further understood by plotting against t', a complementary coordinate in the (3+1)-dimensional superspace. Figure 2 shows the Co-O distances of Bi-free (a) and Bi-substituted (b) samples. The upper left panel shows the Co2-O distances in the RS-type subsystem of Bi-free $[Ca_2CoO_3]_pCoO_2$ sample, plotted against t'. The Co2-O distances are periodically altered with the interval of $t' = 0.6181$. A Co atom at $z = 1/2$ has six oxygen neighbors, with four equatorial O2 and two apical O3 atoms. Among these bonds, two apical bonds (iii and v) are fairly shorter than the other four equatorial bonds.

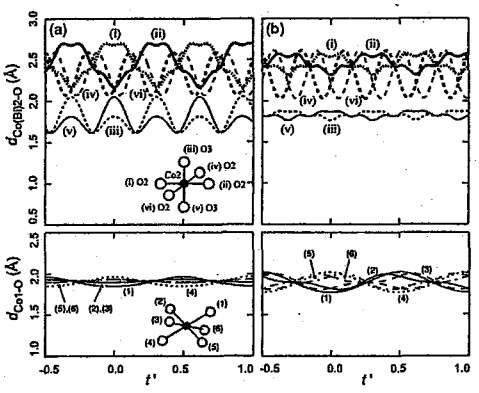

Figure 2: Co-O distances plotted against a complementary coordinate, t', for (a) the Bi-free and (b) Bi-substituted samples.

When a small amount (5%) of Bi is substituted for the Co2 site, the modulation amplitudes of the two apical Co(Bi)2-O3 bonds (iii and v) are remarkably reduced as illustrated in the upper right panel. In contrast to the Co(Bi)2-O bonds, the six Co1-O1 bonds illustrated in the lower panels show an opposite substitution effect. The Co1-O1 bonds of the Bi-free phase (lower left panel) show small modulation amplitudes from 1.8 to 1.95 Å, relative to the Bi-substituted phase of 1.75 to 2.0 Å.

The observed increase in Seebeck coefficient and electrical resistivity of the Bi-substituted phase can be explained in terms of the decrease of hole concentration in the CoO_2 sheets, as well as the significant modulation of the conduction paths.

原子炉：JRR-3　装置：HRPD(1G)　分野：中性子散乱（構造）

研究テーマ： 重い電子系超伝導体 $PrOs_4Sb_{12}$ の結晶構造異常
表題： $PrOs_4Sb_{12}$ における Pr イオンの異常に大きな Debye-Waller 因子

1-1-14 Anomalously Large Debye-Waller Factor of Pr ions in $PrOs_4Sb_{12}$

K. Iwasa[1], M. Kohgi[2], H. Sugawara[3], and H. Sato[2]
[1] *Dept. of Physics, Tohoku University, Sendai 980-8578*
[2] *Dept. of Physics, Tokyo Metropolitan University, Hachioji, Tokyo 192-0397*
[3] *Dept. of Mathematical and Natural Sciences, Tokushima University, Tokushima 770-8502*

One of recent topics in the field of strongly correlated electron systems is the various physical properties and phase transitions of the filled skutterudite compounds (RT_4X_{12}, R = lanthanide and actinide elements, T = transition metal, X = pnictogen) crystallizing in the common body centered cubic structure (space symmetry $Im\bar{3}$) as shown in Fig. 1.

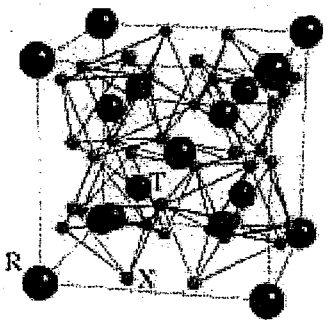

Fig. 1. Crystal stricture of filled skutteridite.

In addition to the electronic phenomena, there is an interesting property of the crystal lattice [1]. The R ions are located at a rather large space between the rigid cages formed by T and P atoms. Thus, the Pr ions are expected to be loosely.bounded in the crystal lattice and to exhibit local anharmonic vibration with an anomalously large amplitude, which is called as "rattling". Such local mode was suggested to be a key for a good thermoelectric property, since it reduces thermal conductivity due to propagating phonons. In order to investigate a temperature variation of the Debye-Waller factor, we performed X-ray and neutron diffraction measurements of crystal structure of $PrOs_4Sb_{12}$ between room temperature and 7 K. The former was at the conventional X-ray diffractometer, and the latter at powder neutron diffractometer HERMES (T1-3) in JRR-3M reactor, JAERI.

The observed Bragg reflection patterns at room temperature in the both X-ray and neutron diffraction experiments are consistent with the previously determined isotropic B factors for the Debye-Waller factor of 3.009 at Pr, 0.1980 at Os and 0.3350 at Sb sites [2]. It is noticeable that the B value of Pr ions is ten times larger than those of Os and Sb. The temperature variation of B factors are depicted in Fig. 2. The B values of Os and Sb becomes almost zero below around 170 K. On the other hand, that of Pr keeps the large value down to 20 K. This result supports the rattling mode of Pr-ion which survives down to low temperature.

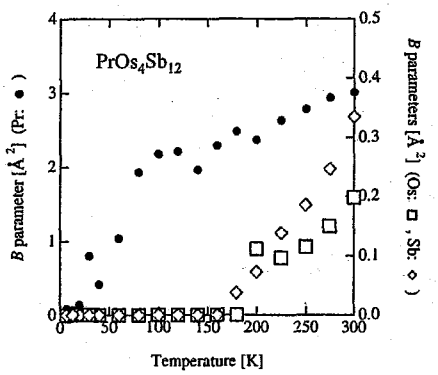

Fig. 2. Experimentally determined B values for the Debye-Waller factors.

This work was supported by Prof. K. Ohoyama, IMR, Tohoku University.

References

[1] B. C. Sales, *Handbook of Physics and Chemistry of Rare Earths Vol . 33* (Elsevier Science B. V., Amsterdam, 2003) p.1.
[2] K. Oikawa *et al.*, private communication.

使用施設：JRR-3M, 装置： T1-3 (HERMES) , 分野： 1. Structure & Excitations (x)

研究テーマ：多重極限環境下における中性子散乱実験法の研究
表　題：希土類十二ホウ化物 RB_{12} の粉末中性子回折
1-1-15

Neutron powder diffraction study of RB_{12}

T. Osakabe, F. Iga[1]

Advanced Science Research Center, JAERI, Tokai, Ibaraki 319-1195
[1] *Graduate School of Advanced Sciences of Matter, Hiroshima Univ., Higashi-Hiroshima, Hiroshima 739-8530*

Rare-eath dodecaborides RB_{12} (R=Tb, Dy, Ho, Er, Tm, Yb, Lu) series has NaCl-type crystal structures consisting of R and B_{12} cubooctahedrons. It has shown clearly from the recent single-crystal neutron diffraction experiments on R = Ho, Er, and Tm that these compounds show the same antipahse domain type antiferromagnetic structures with the propgation vector $\mathbf{Q} = (1/2-\delta, 1/2-\delta, 1/2-\delta)$, $\delta \approx 1/26$ [1]. On the other hand, R=Yb is well known as a mixed-valence compound and a Kondo-semiconductor with the gap of about 200 K at Fermi level. The gap develops below about 100 K. A lot of studies on this compound has been done in order to solve the mechanism of the gap formation. Recently, Iga *et al.* carried out neutron inelastic scattering experiments on this compound using the single crystal sample [2]. They found that, although the compound did not undergo the long-range magnetic order, the compound showed the (1/2, 1/2, 1/2) antiferromagnetic correlation in the excitation energy of about 160 K at low temperature. They claimed the correspondence between the magnetic behavior of YbB_{12} and that of the other compounds which show the long-range magnetic order. In this report, we show a part of the result of the neutron powder diffraction study on $R^{11}B_{12}$ series. The purpose of the study is investigating the relation between the magnetic behavior and the crystal parameter of these compouds.

The crystal lattices of these compouds are very hard, bacause the lattice constant changes only 0.1 % or less by changing the temperature from 300 K to 4 K. Fortunatery, neutrons are not absorbed so strongly by ^{11}B atoms and have almost same sensitiviy to ^{11}B atoms as those of other elements. Thus, we could detect the temperature dependence of the atomic positions of ^{11}B atoms of these compounds, although the errors were large. Figure 1(a) and (b) show the temperature dependence of the lattice constant and interatomic distance of YbB_{12} obtained by the Rietveld analysis (RIETAN-2000). With decreasing temperature, the lattice constant stops decreasing at about 100 K, at which the gap starts to develop. Furthermore, as clearly shown in Fig. 1(b), the size of the B_{12} cluster enlarges and consequently interatomic distance between Yb atom and B atom rapidly decreases. On the other hand, in HoB_{12} which shows the long-range antiferromagnetic order, B_{12} cluster suddenly diminishes at magnetically ordering temperature,T_N=7.2 K and consequently the Ho-B distance is lengthened. These results indicate that the gap formation or the long-range magnetic order of RB_{12} are closely connected with the interatomic distance between rare-earth atom and boron atom.

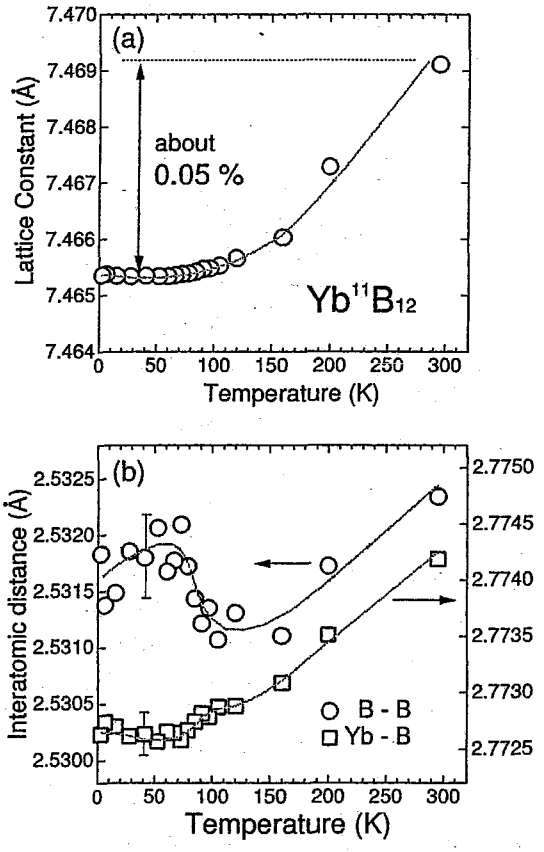

Figure 1: (a) Temperature dependence of the lattice constant and (b) temperature dependence of the interatomic distance of YbB_{12} obtained by RIETAN-2000 analysis.

References

1) T. Osakabe *et al.*: to be published.
2) F. Iga, T. Takabatake, J.-M. Mignot, P. A. Alekseev, L.-P. Regnault: JPSJ meeting, 2003 autumn, 20pPSA-40

原子炉：JRR-3　　装置：HRPD(1G)　　分野：中性子散乱（構造）

研究テーマ：欠陥エンジニアリングを利用した蛍光体材料の構造解析
表題：中性子回折を用いた $Ca_{0.5}Sr_{1.5}Al_2SiO_7:Ce^{3+}$の構造解析

1-1-16 Crystal Structure determination of $Ca_{0.5}Sr_{1.5}Al_2SiO_7:Ce^{3+}$ by Neutron Diffraction

Y. Ito, K. Uematsu*, K. Toda and M. Sato *

*Graduate School of Science and Technology, *Department of Chemistry and Chemical Engineering, Niigata University, Ikarashi 2-nocho 8050, Niigata 950-2181, Japan*

N. Kodama et al have observed the long-persistent phosphorescence of Ce^{3+} in $Ca_2Al_2SiO_7$ [1], [2]. We observed white afterglow in Tb and Ce co-doped $Ca_{0.5}Sr_{1.5}Al_2SiO_7$ quite recently [3]. These melilite-type compounds are promising candidate for new phosphors. Therefore, the crystal structure was refined by the Rietveld method with neutron diffraction pattern in order to clarify the atomic positions and surrounding environment of Ce^{3+} in $Ca_{0.5}Sr_{1.5}Al_2SiO_7$.

Powder neutron diffraction pattern for refinement was obtained with the powder diffractmeter for high efficiency high resolution measurements (HERMES) of Institute for Materials Research (IMR), Tohoku University, installed at JRR-3M reactor [4]. An incident neutron wavelength of $\lambda = 0.182035$ nm was obtained from a Ge(311) monochromater. The powder sample was enclosed in a cylindrical vanadium vessel and mounted on a double-axis diffractmeter.

The measured pattern was analyzed by a program RIETAN [5], assuming the space symmetry P4-2_1m (No.113) and Ce^{3+} substituted for Ca/Sr site [6]. Figure 1 shows observed and calculated diffraction patterns for $Ca_{0.5}Sr_{1.5}Al_2SiO_7:Ce^{3+}$. The crystal structure was determined to be the tetragonal structure with the space group of P4-2_1m (a = 0.78050(2) nm, b = 0.78050(2) nm, c = 0.52262(2) nm). A satisfactory good fit was achieved and the final *R*wp factor was 4.38 %.

The brilliant luminescent properties of Tb and Ce co-doped $Ca_{0.5}Sr_{1.5}Al_2SiO_7$ are closely related to its layered structure.

Reference

[1] N. Kodama, Y. Tanii, M. Yamaga, *Appl. Phys. Lett.*, **75** (1999) 1715-1717.
[2] N. Kodama, T. Takahashi, M. Yamaga, Y. Tanii, Qiu, K. Hirao, *J. Lumi*, **87-89** (2000) 1076-1078.
[3] Y. Ito, K.Uematsu, K. Toda, M.Sato, *Rare earthes*, **44** (2004) 146-147
[4] K.Ohyama, T. Kanouchi, K.Nemoto, M. Ohashi, T. Kajitani, Y. Yamaguchi, *Jpn. J.Appl. Phys.*, **37**(1998),3319-3326
[5] F. Izumi and T. Ikeda, *Mater. Sci. Forum*, **198** (2000) 321-324.
[6] M. Kimata, *Zeitschrift fuer Kristallographie*, **167** (1984) 103-116

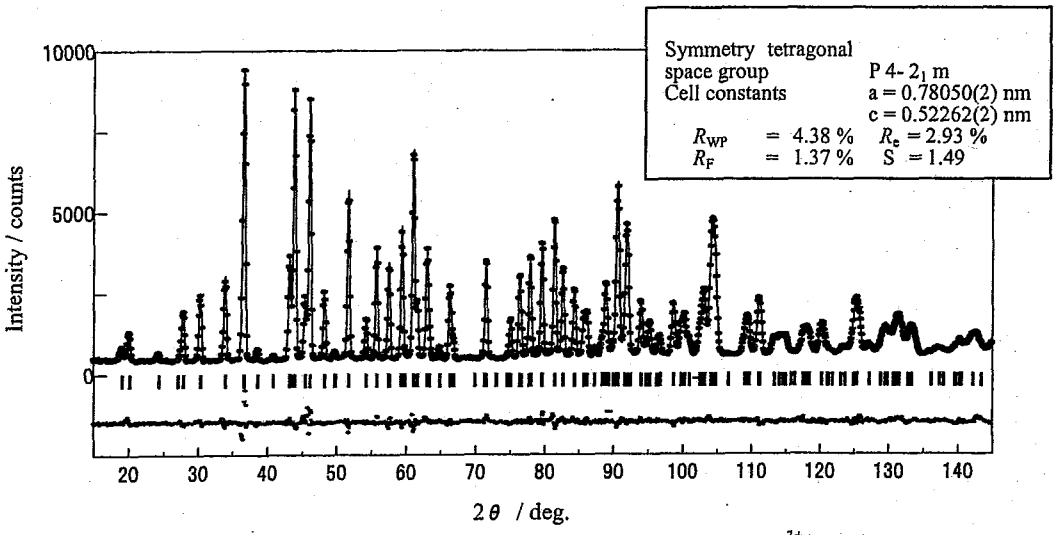

Fig.1 Neutron Rietveld refinement patterns of $Ca_{0.5}Sr_{1.5}Al_2SiO_7:Ce^{3+}$(3 mol%).

使用施設：JRR-3M，装置：HERMES，分野 Structure & Excitation

研究テーマ：$Sr_3Ru_2O_7$ のナノスケール構造歪みとメタ磁性転移の関係
表　題：$Ca_3Ru_2O_7$ の粉末中性子回折による構造解析
1-1-17

Structural study of $Ca_3Ru_2O_7$ by powder neutron diffraction

Y. Yoshida, S. I. Ikeda, N. Shirakawa, N. Aso[1], M. Nishi[1], Y. Uwatoko[1] and S. Katano[2]

Nanoelectronics Research Institute, AIST, Tsukuba, Ibaraki 305-8568
[1]*ISSP, the university of Tokyo, Kashiwa, Chiba 277-8581*
[2]*Advanced Science Research Center, JAERI, Tokai, Ibaraki 319-1195*

The Ruddlesden-Popper (R-P) type ruthenates $(Sr, Ca)_{n+1}Ru_nO_{3n+1}$ attract many researchers since the discovery of the spin-triplet superconductor, Sr_2RuO_4 (n=1).[1)] The double-layered $Sr_3Ru_2O_7$ (n=2) shows the Fermi-liquid behavior and ferromagnetic instability in the ground state, which has been lately discussed a quantum criticality tuned by a magnetic field. [2,3)] The recent report revealed that substantial ferromagnetic ordering emerged under the uniaxial pressure up to 1 GPa.[5)] The crystal structure is a distorted R-P type structure with the orthorhombic space group *Bbcb* [4)], which have rotations of RuO_6 octahedra around *c*-axis. Such a distortion may play an important role in magnetic properties of $Sr_3Ru_2O_7$. It is interesting to investigate how the structural distortion relates to the physical properties.

$Ca_3Ru_2O_7$ has a more distorted crystal structure than $Sr_3Ru_2O_7$ owing to the smaller ionic radius of Ca^{2+} than of Sr^{2+}. The crystal structure shows the orthorhombic symmetry with $Bb2_1m$ space group, accompanying both the rotation and tilting of RuO_6 octahedra.[6)] $Ca_3Ru_2O_7$ shows a quasi-two-dimensional metallic ground state with antiferromagnetic ordering (T_N = 56 K) and have a first-order metal-to-nonmetal transition at T_{MI} = 48 K.[7,8)] Recently, the jump of the lattice parameters was observed at the first-order transition temperature from x-ray diffraction and a thermal contraction measurement.[9,10)] To clarify the temperature dependence of the structural parameters, we carried out neutron powder diffraction measurements for $Ca_3Ru_2O_7$.

Powdered sample was prepared from crushed single crystals of $Ca_3Ru_2O_7$ grown by a floating zone method. Neutron-diffraction measurements were performed at the JRR-3M reactor, Tokai, JAERI. The powder diffractometer HRPD was used in the measurements from 10 K to room temperature (*RT*).

Nuclear structure refinements were made for $Ca_3Ru_2O_7$ measured at 10 K and *RT* using a Rietveld refinement program RIETAN.[11)] In the nuclear structure refinements, the obtained *R* values for each temperatures are in the range from 7.56 to 9.86%. The final structural parameters at *RT* are consistent with those in the previous report.[6)] From the result of Rietveld analysis, the temperature dependences of the structural parameters are obtained. For example,

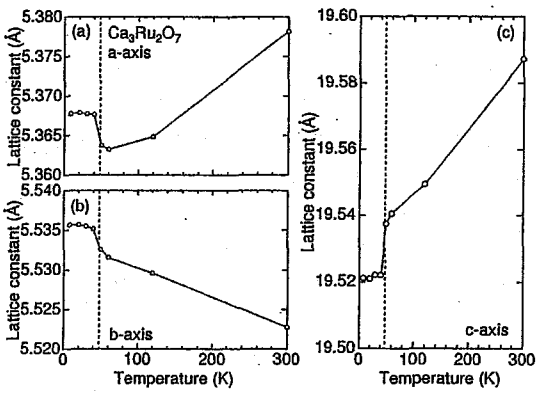

Figure 1: Temperature dependences of lattice constants (a) a, (b) b and (c) c.

Figs. 1(a), (b) and (c) show the temperature dependences of the lattice constants *a*, *b* and *c* of $Ca_3Ru_2O_7$, respectively. The lattice constants *a* and *c* shorten on cooling from *RT*, while *b* elongates with decreasing temperature. As mentioned in the previous report, the lattice parameters jump at the first-order transition temperature, denoted as broken lines in the figure, where *c* shortens about 0.1%, while *a* and *b* lengthen both about 0.07%. The lattice volume increases at this transition.

On cooling below T_N, an additional reflection emerges and can be observed at 10 K, which can be indexed in the $Bb2_1m$ lattice with (100). This peak corresponds to an antiferromagnetic ordering. To discuss magnetic structure, it needs further neutron-diffraction study using single crystals.

References

1) Y. Maeno *et al.*, *Physics Today* **54**, (2001) 42.
2) S. I. Ikeda *et al.*, Phys. Rev. B **62**,(2000) R6089.
3) S. A. Grigera *et al.*, *Science* **294**, (2001) 329.
4) H. Shaked *et al.*, J. Solid State Chem. **154**, (2000) 361.
5) S. I. Ikeda *et al.*, J. Phys. Soc. Jpn. **73**, (2004) 1322.
6) G. Cao *et al.*, Phys. Rev. B **62**,(2000) 998.
7) G. Cao *et al.*, Phys.Rev.Lett. **78**, (1997) 1751.
8) Y. Yoshida *et al.*, Phys. Rev. B **69**,(20004) 220411.
9) G. Cao *et al.*, Phys. Rev. B **67**,(2003) 184405.
10) E. Ohmichi *et al.*, to be published in Phys. Rev. B.
11) F. Izumi and T. Ikeda, Mater. Sci. Forum, **321-324** (2000) 198.

原子炉：JRR-3　　装置：HRPD(1G)　　分野：中性子散乱（構造）

研究テーマ：リチウム二次電池用正極活物質 $LiMn_{2-x}M_xO_{4-\delta}$の熱力学安定性および結晶構造と電池特性の Li 量依存
表題：リチウム二次電池正極活物質 $Li_xMn_{2-y}M_yO_4$ の熱力学安定性，結晶構造と電極特性の Li 量依存

1-1-18

Li Content Dependence of Thermodynamic Stability, Crystal Structure and Electrode Performance of $Li_xMn_{2-y}M_yO_4$ as a Cathode Active Material for the Lithium Secondary Battery

Y. Idemoto, K. Horiko, H. Sekine and N. Koura

Faculty of Science and Technology, Tokyo University of Science,

2641 Yamazaki, Noda-shi, Chiba 278-8510, Japan

1. Li content dependence of thermo-dynamic stability, crystal structure and electronic structure for chemical delithiation of $Li_xMn_{2-y}M_yO_4$(M=Mg, Al, Cr, Mn, Co, Zn, Ni) as a cathode active material for Li secondary battery

We investigated the relation between the thermodynamic stability and crystal structure dependence of Li content for the chemical delithiated spinel, $Li_xMn_{2-y}M_yO_4$ (M=Mg, Al, Cr, Mn). The enthalpy change per mole of atoms for the formation reaction, ΔH_R, were calculated from the heat of dissolution. ΔH_R increased with the decreasing Li content. ΔH_R of the all amounts of Li content for $Li_xMn_{2-y}M_yO_4$ (M=Mg, Al, Cr, Mn) decreased compared to those of $Li_xMn_2O_4$. The crystal structure analysis by powder neutron diffraction [HERMES, JRR3M in JAERI (Tokai)] was examined for $Li_xMn_{2-y}M_yO_4$ (M= Mg, Al, Cr, Mn). The Madelung energy for $Li_xMn_{2-y}M_yO_4$ (M= Mg, Al) decreases with decreasing Li content, and it was associated with the thermodynamic data. From these results, the host structure is structurally and thermodynamically stable of the all amounts of Li content with the substitution of M for $Li_xMn_{2-y}M_yO_4$.

Next, we investigated the crystal structure, electronic structure and nuclear state of chemical delithiated spinel $Li_xMn_{2-y}M_yO_4$ (M=Mg, Al, Cr, Mn, Co, Zn, Ni) dependence Li content, x. We obtained the electronic and nuclear density distributions of the samples from XRD and neutron diffraction data using the maximum entropy method. Li content of $Li_xMn_{2-y}M_yO_4$ was controlled by changing concentration of H_2SO_4-H_2O aqueous solution. Mn valence increased and lattice parameter, *a*, decreased with the decreasing Li content. The electron of $Li_{0.095}Mn_2O_4$ was delocalization from the results of electronic density distribution. The amount of change of covalent bonding of (Mn, M)-O for $Li_xMn_{2-y}M_yO_4$ (M= Mg, Al, Cr, Co, Zn, Ni) decreased in comparison with that of $Li_xMn_2O_4$ when Li content change. From the results, the host structure is stable with the substitution of M for $Li_xMn_{2-y}M_yO_4$.

2. Crystal structure, physical property and electrode performance depend on synthetic condition and crystal structural change during charge-discharge process of $LiMn_{1.5}Ni_{0.5}O_4$ as cathode materials for 5V class lithium secondary battery

We investigated the physical property, crystal structure and electrode performance of $LiMn_{1.5}Ni_{0.5}O_4$ as a 5V class cathode active material, which was prepared by changing the calcination temperature with the sol-gel method. Cycle performance is different from the calcination temperature. $LiMn_{1.5}Ni_{0.5}O_4$, which calcined at 700℃, showed a good cycle performance with the maximum discharge capacity of 125.3mAh/g, and the capacity after 100

使用施設：JRR-3M, **装置**：HERMES(T1-3), **分野** Structure & Excitations(x)

cycles was 95.1% of the maximum capacity. The crystal structure was determined by Rietveld analysis using powder neutron diffraction[HERMES, JRR3M in JAERI (Tokai)]. From a result, $LiMn_{1.5}Ni_{0.5}O_4$, which calcined at 650℃, composed of mixing two space group $P4_332$ phases. It is suggested that the oxidation states of Ni change in the sample, as these phases are different from each lattice parameter. Ni valence of sub-phase for $LiMn_{1.5}Ni_{0.5}O_4$ calcined at 650℃, which was calculated from Bond Valence Sum, increase. Moreover, we investigated, the distortion and the stability of crystal structure by the bond length and the Madelung energy, nuclear and electron densities by MEM method with neutron diffraction and X-ray diffraction.[1]

Next, we investigated the relation between the cycle performance and crystal structural change during the charge-discharge process of $LiMn_{1.5}Ni_{0.5}O_4$ as a 5V class cathode active material, which was prepared by changing the calcination temperature using the sol-gel method. The lithium content of $Li_{1-x}Mn_{1.5}Ni_{0.5}O_4$ (x=0.5, 0.7, 1.0) was controlled by electrochemical lithium extraction. The crystal structure was determined by Rietveld analysis using powder neutron diffraction. As a result, all samples consisted of three phases (space group: $P4_332$) of different lattice constants and Ni valences. The main phase, which has the maximum percentage, was shifted to a phase with a lower lattice constant with the decreasing lithium content, and then finally $Li_{1-x}Mn_{1.5}Ni_{0.5}O_4$ (x=1.0) was almost oxidized to Ni^{4+} by a charging process. Furthermore, $LiMn_{1.5}Ni_{0.5}O_4$, by changing the synthesis temperature, was different for a few oxidation processes; the structure of the phase at Ni^{3+} was not stable based on the distortion of the each phase and the Madelung energy. It was suggested that these factors should provide an effective cycle performance.[2]

References

[1] Y. Idemoto, et al., Electrochemistry, in printing.
[2] Y. Idemoto, et al. Electrochemistry, **71**, 1142 (2003).

研究テーマ：酸素過剰パイロクロア酸化物 $Zr_2Ce_2O_{7+x}$ の構造解析
表　題：中性子粉末回折を用いて明らかにされた酸素過剰パイロクロア型 $Ce_2Zr_2O_8$ の欠陥構造
1-1-19

Defect structure of oxygen-excess pyrochlore-type $Ce_2Zr_2O_8$ elucidated using neutron powder diffraction

H. Otobe, N. Igawa[1], Y. Ishii[1]

Department of Material Science, JAERI, Tokai, Ibaraki 319-1195
[1]Neutron Science Research Center, JAERI, Tokai, Ibaraki 319-1195

The neutron diffraction studies have been performed on oxygen-excess pyrochlore-type (P-type) $Ce_2Zr_2O_8$ in order to elucidate the defect structure of this material.

P-type $An_2Zr_2O_{7+x}$ (An = Pu, Am, Cm etc.) has attracted significant research interest as radioactive waste-forms and targets for actinide transmutation in nuclear engineering field.[1,2] It is important to clarify the thermodynamic and defect properties of these systems for such applications. However, it is difficult to handle the transuranium materials for their high radiotoxicity. It is convenient to study the thermodynamic and defect properties of P-type $Ce_2Zr_2O_{7+x}$, a rare earth analogue of P-type $An_2Zr_2O_{7+x}$ (An = Pu, Am, Cm etc.) and apply the study to that of transuranium materials.

Thomson *et al.* studied the structure of P-type $Ce_2Zr_2O_{7.97}$ by neutron and X-ray powder diffraction methods.[3] P-type $Ce_2Zr_2O_8$ is the first example of oxygen-excess pyrochlores with fluorite-dioxide composition (O/M=2) among a variety of pyrochlores already synthesized. Their neutron diffraction data were different from that of stoichiometric fluorite dioxide and P-type $Ce_2Zr_2O_7$. The peaks seen over 2.1 < *d*-spacing < 2.6 Å could not be attributed to those of the stoichiometric materials. They proposed a defect model that excess oxygen sites are composed of two types: One is a tetrahedrally coordinated anion site as in the fluorite-type zirconia, the other is a trigonal anion site surrounded by three cerium ions, although the cations are ordered in the usual pyrochlore arrangements. Their data and model are very impressive, but their samples had the impurities as written in their papers. Therefore, we have prepared the P-type $Ce_2Zr_2O_8$ sample without impurities.

Figure 1 shows the neutron diffraction pattern of pyrochlore $Ce_2Zr_2O_8$ obtained by using HRPD (λ=1.823 Å). This pattern exhibited the same peaks as those of Thomson *et al.* The result indicates the peaks over $40° < 2\theta < 50°$ are intrinsic to P-type $Ce_2Zr_2O_8$, oxygen-excess pyrochlore. Figure 1 also shows the calculated pattern of stoichiometric P-type $Ce_2Zr_2O_7$ by a program RIETAN-2000.[4] The Rietveld analysis is in progress.

References

1) 1. W.L. Gong, W. Lutze, R.C. Ewing; J.Nucl. Mater.277, 239 (2000).
2) P.E. Raison, R.G. Haire, T. Sato and T. Ogawa; Mat. Res. Soc. Symp. Proc, Materials Research Society 556, 1 (1999).
3) J. B. Thomson, A. R. Armstrong, P. G. Bruce; J. Solid State Chem.148, 56 (1999).
4) F. Izumi and T. Ikeda; Mater. Sci. Forum 321-324, 198 (2000).

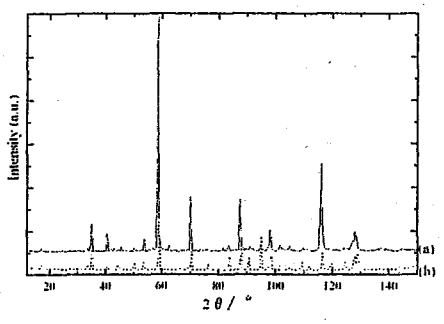

Figure 1: (a) the observed pattern of P-type $Ce_2Zr_2O_8$.
(b) the calculated pattern of stoichiomeric P-type $Ce_2Zr_2O_7$.

原子炉：JRR-3　　装置：HRPD (1G)　　分野：中性子散乱（構造）

1-1-20

研究テーマ： 圧力誘起強磁性体$Sr_3Ru_2O_7$の一軸圧力下での結晶構造解析
表題： 中性子回折用一軸圧力セルの開発と圧力誘起強磁性体$Sr_3Ru_2O_7$の研究

Development of the Uniaxial Pressure Cell for Neutron Diffraction and its Study on Pressure Induced Ferromagnet $Sr_3Ru_2O_7$

N Aso[1], H. Kimura[2], Y. Noda[2], Y. Uwatoko[3], Y. Yoshida[4], S-I Ikeda[3], and S. Katano[5]
[1]*Neutron Sci. Lab., ISSP, Univ. of Tokyo, Tokai, Ibaraki 319-1106,* [2]*Inst. Multidisciplinary Res. Adv. Mater., Tohoku Univ., Sendai 980-8577* [3]*Institute for Solid State Phys., Univ. of Tokyo Kashiwa 277-8581* [4]*Nanoelectronics Res. Inst. AIST, Tsukuba, Ibaraki 305-8568*
[5]*ASRC, Japan Atomic Energy Research Institute, Tokai, Ibaraki 319-1195.*

The bilayered perovskite $Sr_3Ru_2O_7$ show a crossover from paramagnetism to ferromagnetism (FM) under not only applied pressure[1, 2] but also magnetic field[3]. The interaction between the rotation of RuO_6 octahedra around c-axis and the FM, often discussed in connection with FM correlations in the spin-triplet superconductor Sr_2RuO_4, and the FM in the $SrRuO_3$, attracts much attention in recent years.

To clarify the above magnetism, we have developed uniaxial pressure cells for neutron diffraction. Four-circle neutron diffraction experiments on $Sr_3Ru_2O_7$ under uniaxial pressure along c-axis has been performed at the FONDER in the research reactor JRR-3M, JAERI, to examine both the neutron absorption effect of cells themselves and lattice parameters of as a function of uniaxial pressure and temperature. It turned out to be that the cells are good enough for the four-circle neutron diffraction technique and the crystals do not break at pressures up to about 4 kbar.

Figure 1 shows temperature dependence of lattice parameters of $< a >$ (Top) and c (bottom) under both ambient pressure and uni-axial pressure at 4 kbar along c-axis in $Sr_3Ru_2O_7$. At room temperature, the lattice parameter c shirinks by ~ 0.3 % and $< a >$ expands by ~ 0.2 % increasing the uni-axial pressure up to ~ 4 kbar along c-axis. It also cleary shows the similar temperature behavior to those under ambient pressure, implying the existence of the rotation of RuO_6 octahedra around c-axis even under uni-axial pressure at 4 kbar along c-axis.

Our crystal structure analysis of the study under uni-axial pressure is now under way.

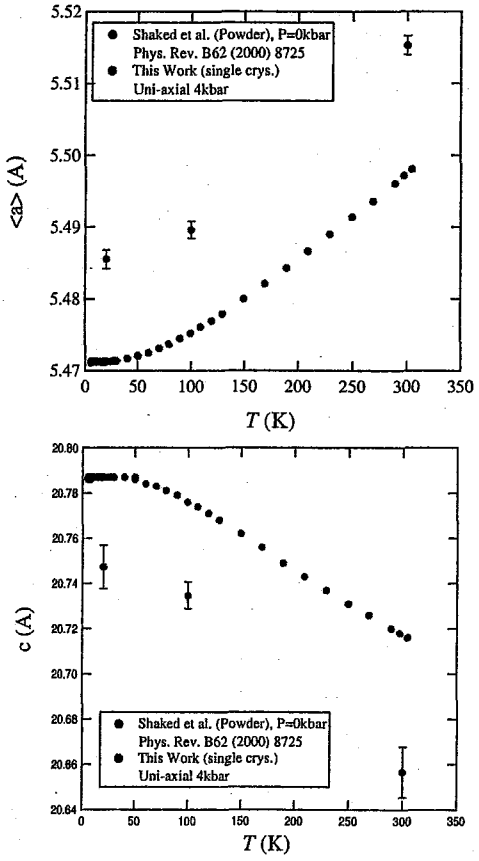

Fig. 1. Temperature dependence of lattice parameters of $< a >$ (Top) and c (bottom) under ambient pressure and uni-axial pressure at 4 kbar along c-axis in $Sr_3Ru_2O_7$.

References

[1] S.-I. Ikeda et al., Phys. Rev. **B62** (2000) R6089.
[2] S.-I. Ikeda et al., J. Phys. Soc. Jpn **73** (2004) 1322.
[3] S. A. Grigera et al., Science **294** (2001) 329.

使用施設：JRR-3M，装置： T2-2 (FONDER)，分野： 1. Structure & Excitations

研究テーマ：ヌクレオチド水和物結晶における水素結合網の動的挙動の解析
表題：中性子回折法によるイノシン5'-リン酸二ナトリウム水和物（高湿度領域安定相）における水素結合網の解析

1-1-21 Neutron Diffraction Analysis of Hydrogen Bonding Networks of Inosine 5'-Monophosphate Hydrate Stable in the High-Humidity Range

S. Yamamura, Y. Sugawara, H. Kimura*, and Y. Noda*

*School of Science, Kitasato University, 1-15-1 Kitasato, Sagamihara, Kanagawa 228-8555, Japan; *Institute of Multidisciplinary Research for Advanced Materials, Tohoku University, 2-1-1 Katahira, Aoba-ku, Sendai 980-8577, Japan*

Humidity-induced phase transitions of nucleotide hydrates proceed accompanying reconstruction of hydrogen-bonding net-works. To establish the hydrogen-bonding scheme, neutron diffraction analysis was started. Succeeding to disodium ionsine 5'-phophate heptahydrate (Na_2IMP $7H_2O$: the dry form),[1] neutron diffraction analysis of the octahydrate (the wet form) was carried out.

Using an as-grown crystal with approximate dimensions 10 x 8 x 1 mm^3 sealed in a quartz capillary tube, data collection was carried out by a four-circle diffractometer, FONDER, at T2-2 of JRR3M in JAERI (Tokai). At room temperature 3878 neutron intensity data up to 0.88 Å were collected with the neutron wavelength of 1.24 Å. Crystal data are shown in Table 1. All hydrogen atoms of the IMP molecules and 34 hydrogen sites of 21 crystal water sites in an asymmetric unit were determined by iteration of difference Fourier syntheses and full-matrix least squares refinement cycles starting from the coordinates of non-hydrogen atoms of the IMP molecule determined by X-ray analysis. The final R factor is 0.07 for 2719 observed reflections ($|F_o|>4\sigma(F_o)$).

In the wet form, one sodium ion and five water molecules are disordered and grouped into two, the occupancy factors of which were determined to be 0.6 and 0.4, respectively (dark gray circles and light gray circles in Figure 1). Sodium coordination and hydrogen-bonding networks for each group were confirmed. The environment of 12 crystal water sites in the wet form and in the dry form is highly similar judging from the hydrogen bonding and sodium coordination schemes.

References

[1] Y. Sugawara et al., *ISSP Activity Report on Neutron Scattering Research*, **10**, 86-87 (2003).

Table 1: Crystal data

Chemical formula	$Na_2C_{10}H_{11}N_4O_8P.8.2H_2O$
Crystal system	monoclinic
Space group	$P2_1$
a/Å	8.723(13)
b/Å	22.395(16)
c/Å	12.299(8)
β/deg	109.62(8)
Z	4

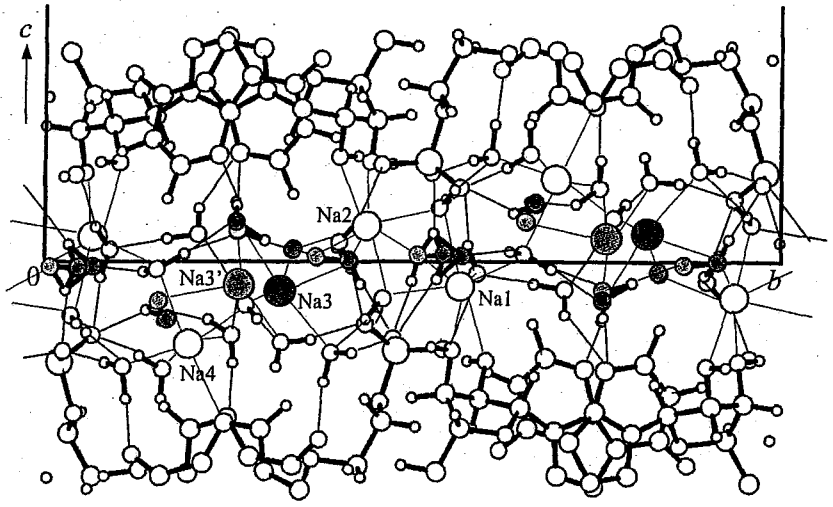

Figure 1: Crystal water region of the wet form viewed along the *a* axis.

使用施設：JRR-3M，装置：FONDER(T2-2)，分野：Structure & Excitations

研究テーマ：臨界組成をもつ量子常誘電体におけるＴＡフォノンとＴＡフォノンの挙動
表題：臨界組成をもつ量子常誘電体におけるＴＡフォノンとＴＡフォノンの挙動

1-1-22

Impurity-induced Ferroelectric Phase Transition in a Quantum Paraelectric $KTaO_3$

Yasusada YAMADA, Takamitsu KOMAKI, Shutaro ASANUMA and Yoshiaki UESU

Advanced Research Institute for Science and Engineering, Waseda University 3-4-1, Okubo, Shinjuku-ku, Tokyo 169-0072

Quantum paraelectricity is one of the characteristic features exhibited by several anharmonic optical phonon systems. Due to the anharmonic self energy, the frequency of the lowest lying optical mode becomes strongly temperature dependent with general tendency that the frequency becomes remarkably reduced as $T \to 0$, which is called the 'soft optic mode'. Actually, however, at low temperatures the quantum fluctuations (zero point vibration) start to play a role to tend to suppress the transition. Such a system is called quantum paraelectric.

$KTaO_3$ is known to be one of the representatives of quantum paraelectrics. By introduction of Li impurity at K-site by a few percent, the system induces ferroelectric phase transition at sufficiently high temperature. At x=0.05, KTO:Li-x becomes ferroelectric. For x >0.05, the phase boundary between ferro-para transition is well defined.

The observed dielectric constant of the sample of x =0.03 exhibits sharp peak at the transition temperature, 50K. If we assume the 'soft mode' mechanism similar to the case of pure KTO system holds, we expect sharp decrease (complete softening) of the $\hat{\omega}_{TO}$ in x=0.03 system in a narrow temperature range around 50K.

We have carried out neutron inelastic scattering experiments on pure KTO and KTO:Li-0.03 crystal in order to investigate the behavior of the lowest-lying optical mode at low temperatures. Inelastic neutron scattering experiments were performed using a triple-axis spectrometer T1-1HQR installed in JRR-3M in Japan Atomic Energy Research Institute with the incident energy of neutron beams of 13.60 meV (λ = 2.459 Å).

The results are summarized in Fig. 1. The data on pure KTO are consistent with the previous observation of the dispersion curves by Axe et al. taken at T = 90K, and 6K.

The most remarkable point of the present results is that the curve of $\hbar\hat{\omega}_{TO}(T)$ of KTO:Li-0.03 lies consistently higher by about 1 meV above that of pure KTO throughout the observed temperature range. This is in complete disagreement with the expected curve if the critical softening of the optical mode is assumed to be the driving mechanism of the phase transition.

We have also carried out X-ray diffraction experiments to observe the lattice constants to elucidate the structural characteristic of the 'glassy' state. It turns out that the glassy state is characterized by the semimacroscopic random coexistence of paraelectric and ferroelectric phases. Those results seem to suggest strongly that in a narrow concentration range $0.02 \le x \le 0.03$, the observed specimens are in a state of the two-phase (paraelectric and ferroelectric)

使用施設：ＪＲＲ－３Ｍ，装置：HQR (T1-1) GPTAS (4G) ，分野：1. Structures and Excitations

coexistence. This situation probably would correspond to the `glassy' state where the macroscopic symmetry can not be unambiguously defined.

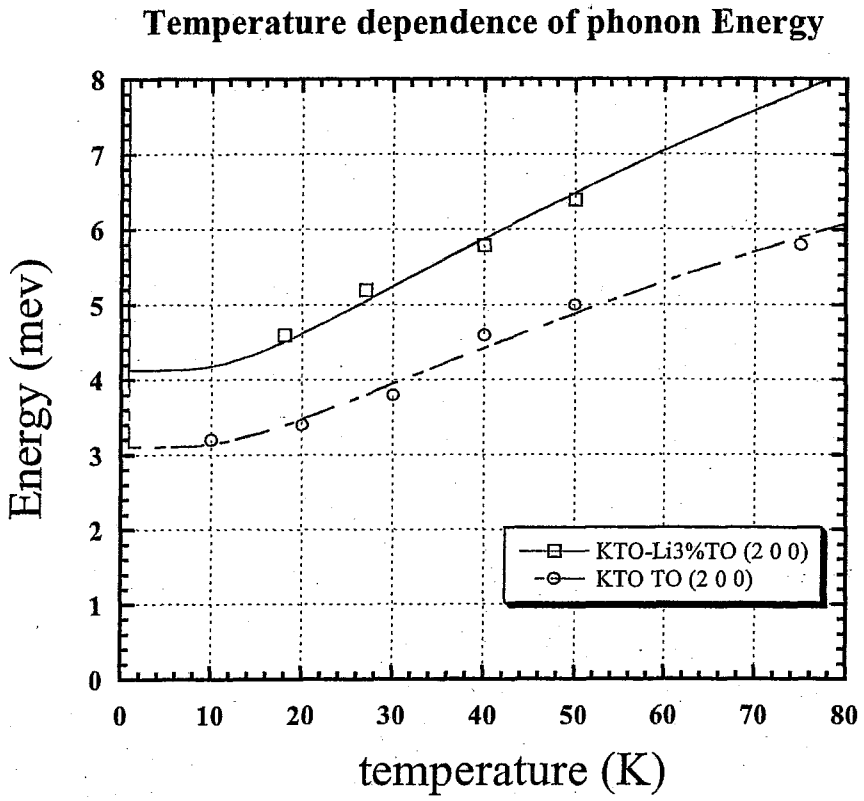

Fig. 1. The observed temperature dependences of the soft mode energies for pure KTO (open circle) and KTO:Li-0.03 (open rectangular). The solid and dash-dot curves are the calculated curves using the Barette formula. The parameter values are commonly taken as T_1=44.98K and T_0=1.45K for both cases.

研究テーマ：新規合成法によるリチウムイオン二次電池用正極材料の開発
表題：中性子回折によるリチウム挿入 β-$Fe_2(SO_4)_3$ 正極材料の構造解析

1-1-23

Structure Determination of Lithium-inserted $Fe_2(SO_4)_3$ Cathode Materials with β-$Fe_2(SO_4)_3$ Type by Neutron Diffraction

M. Sato, Y. Katayama, S. Tajimi, K. Uematsu, and K. Toda

Department of Chemistry and Chemical Engineering,Faculty of Engineering, Niigata University, 8050 Ikarashi 2-nocho, Niigata 950-2181, Japan

NASICON-related compounds have been known as not only good ionic conductors but also good cathode materials for lithium ion batteries, because of giving open space for the conduction of mobile ions. $Fe_2(SO_4)_3$ has two forms: a hexagonal (rhombohedral) NASICON structure and a related monoclinic form known as β-$Fe_2(SO_4)_3$ type. Both the monoclinic and rhombohedral modifications gave an essentially flat open-circuit voltage of 3.6 vs. Li/Li^+ over a wide range of lithium solubility and a reversible capacity of about 1.8 lithium atoms per formula unit. Such a high voltage is the most highest among iron-related cathode materials, making these iron sulfates the most attractive candidates for materials for lithium ion batteries. In this study, we have determined the location of lithium ions inserted into the monoclinic $Fe_2(SO_4)_3$ phase.

A homogenous precipitation of monoclinic $Fe_2(SO_4)_3$ samples was obtained by refluxing of an $Fe_2(SO_4)_3 \cdot 7H_2O$ solution in concentrated sulfuric acid for about 2-4 h. For the preparation of lithium-inserted $Fe_2(SO_4)_3$ samples, n-butyllithium (n-BuLi) in n-hexane solution was added as reducing reagent for $Fe_2(SO_4)_3$ powder dispersed in n-hexane at 25°C under an argon atmosphere. The amount of the inserted lithium was determined by flame spectrochemical analysis. Powder neutron diffraction patterns were recorded using the HERMES(T1-3) diffractometer installed at JRR-3M Guide Hall in the Japan Atomic Energy Research Institute (TAERI). The data were collected on thoroughly ground powders by a multi-scanning mode in the 2θ range from 5 to 155° with a step width of 0.05° and a monitoring time of 16 min. The powder patterns obtained were analyzed using the RIETAN2000 profile refinement program.

The crystal structure of the $Li_xFe_2(SO_4)_3$ with x=0, 0.5, and 1.5 could be successfully analyzed; R_{wp}=2.92%, 2.67%, and 5.30%, respectively. The cell volumes refined for the samples are 823.93(4)Å^3, 824.31(5)Å^3, and 825.34(15)Å^3, respectively for x=0.0, 0.5, and 1.5. This result indicates a strong repulsive interaction between the inserted lithium ions and the framework of $Fe_2(SO_4)_3$. With reference to the structure of $Li_3Sc_2(PO_4)_3$ having a β-$Fe_2(SO_4)_3$ type, the inserted lithium ions into $Fe_2(SO_4)_3$ should be located on either three sites as shown in Fig.1. These sites are located almost within the ac plane with y～1/4 and 3/4. The neutron diffraction study clearly indicates that, in the samples with x=0.5, the inserted lithium ions are preferentially located only on Li3 site with almost full occupancy, while those are distributed on both Li1 and Li3 sites with almost half and almost full occupancies, respectively, in the sample with x=1:5. Such an escalated insertion step found should be responsible for the flat discharge behavior, typically found in two-phase discharge processes.

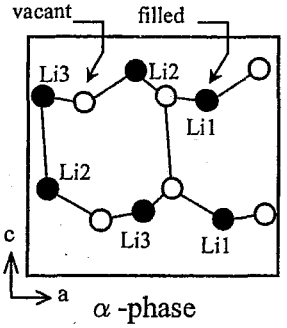

Fig.1 Lithium ion sites in β- $Fe_2(SO_4)_3$

使用施設：JRR-3M，装置：HERMES(T1-3)，分野 Structure and Excitations

研究テーマ：新規合成法によるリチウムイオン二次電池用正極材料の開発
表題：中性子回折によるリチウムイオン伝導体 Li_4GeSe_4 の構造解析

1-1-24

Structure Determination of Lithium Ion Conductor Li_4GeSe_4 with Thio-LISICON Related Structure by Neutron Diffraction

M. Sato, T. Makita, K. Uematsu, and K. Toda

Department of Chemistry and Chemical Engineering,Faculty of Engineering, Niigata University, 8050 Ikarashi 2-nocho, Niigata 950-2181, Japan

All-solid state lithium batteries are of particular interest as future rechargeable lithium batteries because they may solve the safety problems of conventional batteries using non-aqueous liquid electrolytes. In order to develop all-solid lithium batteries, lithium ion conductors for the electrolyte must have a high ionic conductivity. Recently, a new lithium ion conducting family, named as thi-LISICON, based on germanium and silicon sulfides, is synthesized by Kano et al.[1]. The highest conductivity of $2.2x10^{-3}$ Scm^{-1} was achieved among this family. Generally, increase in polarization of anions in the lithium ion conductors enhances its ionic conductivity. This fact prompts us to synthesize a thio-LISICON related selenides. In this study, we have determined the structure of Li_4GeSe_4 by neutron diffraction.

Powder neutron diffraction patterns were recorded using the HERMES(T1-3) diffractometer installed at JRR-3M Guide Hall in the Japan Atomic Energy Research Institute (TAERI). The data were collected on thoroughly ground powders by a multi-scanning mode in the 2θ range from 5 to 155° with a step width of 0.1° and a monitoring time of 16 min. The powder patterns obtained were analyzed using the RIETAN2000 profile refinement program.

The X-ray diffraction pattern of Li_4GeSe_4 was successfully indexed as an orthorhombic cell and similar to that of the corresponding sulfide, Li_4GeS_4[1]. The structure Li_4GeSe_4 of was refined using the structural model of Li_4GeS_4 with space group Pnma. Finally refined structure parameters were listed in Table 1. Fig.1 illustrates the fitted profile and difference patterns for Li_4GeSe_4. The structure of Li_4GeSe_4 is exactly the same as that of Li_4GeS_4[1]. It is composed of hexagonal close-packed selenide ion arrays, and the lithium and germanium ions are distributed over the tetrahedral and octahedral sites. The distances between lithium ions and anions in $LiSe_4$ tetrahedron are much difference in these two compounds: the average distance in Li_4GeSe_4, 2.588Å, is much greater than that of Li_4GeS_4, 2.473Å. This fact seems to be favorable for lithium ionic conduction in Li_4GeSe_4.

Table 1. Neutron Rietveld refinement results of Li_4GeSe_4

Atom	Site	x	y	z	B(Å^2)
Li1	4c	0.421(4)	0.75	0.370(7)	4.1(1)
Li2	8d	0.172(2)	0.011(4)	0.316(4)	2.8(6)
Li3	4b	0.0	0.0	0.5	6.3(4)
Ge	4c	0.4118(7)	0.25	0.351(1)	1.9(2)
Se1	8d	0.3426(4)	0.0137(7)	0.231(1)	1.7(2)
Se2	4c	0.0899(6)	0.75	0.214(1)	1.9(2)
Se3	4c	0.0626(6)	0.25	0.262(2)	2.6(3)

Pnma, a=14.636(1)Å, b= 8.2339(7)Å, c= 6.4956(6) Å, R_{wp}=5.66%, R_P=4.30%, R_R=19.66%, R_e=2.02%, R_I=6.68%, R_F=3.22%, S= 2.80.

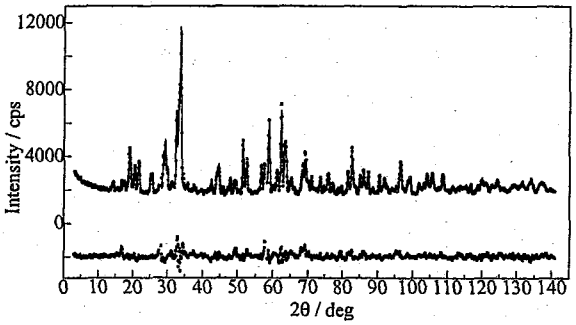

Fig.2. Neutron Rietveld refinement pattern of Li_4GeSe_4.

References

[1] M. Murayama et al., Solid State Ionics, **154-155** (2002)789.

使用施設：JRR-3M，装置：HERMES(T1-3)，分野 Structure & Excitations

研究テーマ:KTa1-xNbxO3 のフォノン
表題:KTa1-xNbxO3 の格子力学
1-1-25

Lattice dynamics of $KTa_{1-x}Nb_xO_3$

I. Tomeno, M. Nishi[1], Y. Tsunoda[2], K. Oka[3], and H. Unoki[3]

Faculty of Education and Human Studies, Akita University, Akita 010-8502, Japan
[1]Institute for Solid State Physics, The University of Tokyo, Tokai 319-1106, Japan
[2]School of Science and Engineering, Waseda University, Tokyo 169-8555 , Japan
[3]National Institute of Advanced Industrial Science and Technology, Tsukuba, 319-1195, Japan

The mixed perovskite system $KTa_{1-x}Nb_xO_3$ (KTN) has been studied extensively from the scientific and engineering viewpoints. The end member $KTaO_3$ is an incipient ferroelectric, whereas the other end $KNbO_3$ is a proper ferroelectric. The nominal charge at the B site remains at 5+ in the KTN system. In this study, we investigated the lattice dynamics of $KTa_{1-x}Nb_xO_3$ with x=0.1. The ferroelectric transition temperature T_c is approximately 100 K for KTN with x=0.1. A single crystal was grown by a flux method. The inelastic scattering experiments were performed using the triple-axis spectrometer HQR(T1-1) installed at a thermal guide of JRR-3M, JAERI, Tokai.

Figure 1 shows the temperature dependence of the TA and TO phonon dispersion relation along the [ζ00] direction for KTN with x=0.1. The zone-boundary TA phonon energy decreases with decreasing temperature. Similar behavior is found for $KTaO_3$.[1] The TA mode at the X point for $KTaO_3$ is dominated by the Ta atom vibration.[2] The substitution of 10% Nb, however, appears to have little influence on the softening of the TA mode.

The softening of the TO mode at the Γ point is significantly affected by the Nb substitution. For pure $KTaO_3$, the energy of the zone-center TO phonon is lowered to 3meV at 20 K. The soft TO mode for $KTaO_3$ is well-defined in a wide temperature range.[1-2] For KTN with x=0.1, the energy of the zone-center TO phonon is approximately 7.5 meV at 120 K. In addition, the line width for the TO phonon peak is broadened near T_c. The Nb substitution disturbs the well-defined soft mode behavior. Since the softening of the TO mode is incomplete even near T_c, the interaction between TA and TO phonons seems absent in the small q region for KTN. In contrast, the coupling of TO and TA phonon branches exists in the typical relaxor $Pb(Zn_{1/3}Nb_{2/3})O_3$ (PZN).

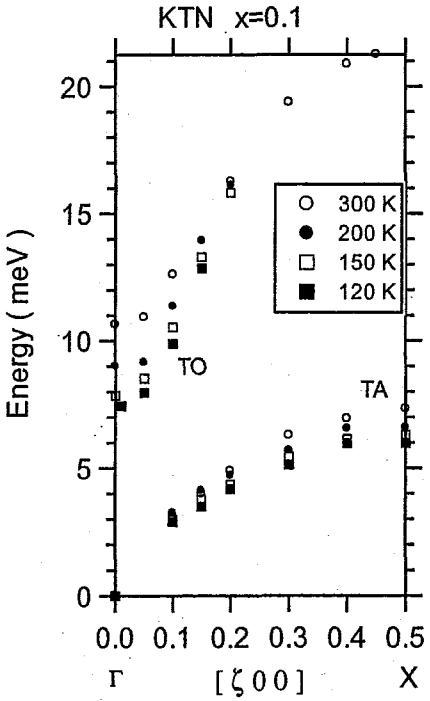

Fig.1 The temperature dependence of phonon dispersion relations for KTN with x=0.1

References

[1] R. Comès and G. Shirane, Phys. Rev. B **5** (1972) 1886.
[2] C. H. Perry et al., Phys. Rev. B **39** (1989) 8666.

使用施設:JRR-3M, 装置:HQR(T1-1), 分野 Structures & Excitations

研究テーマ： Sn の $\beta - -\alpha$ 構造相転移の研究
表題： β-Sn における異方的熱散漫散乱

1-1-26 Anisotropic Diffuse Scattering in β- Tin

M. Takahashi[1], K. Ohshima[1] and Y. Noda[2]
[1] *Institute of Materials Science, University of Tsukuba, Tsukuba 305-8573*
[2] *Institute of Multidisciplinary Research for Advanced Materials, Tohoku University, Sendai 980-8577*

The rod-like diffuse scattering in Sn was studied extensively by x-ray scattering for more than fifteen years ago.[1], [?]. The diffuse intensity decreases with decreasing temperature and thus it has been considered as a temperature diffuse scattering (TDS). However, detailed study has not been done since 1960' and its origin is still not clear. Recently, we have studied the diffuse scattering by a single crystal diffractometer FOX at KENS and found that it is not a simple rod but has a wavy distribution along [110]. To study its detailed structure in a reciprocal space, we have measured three-dimensional intensity distribution by using four-circle single crystal diffractometer FONDER at the thermal guide at the JRR-3M. Fig. 1 shows intensity contour map around 002 on the scattering plane of *hhl* (upper) and *hk*2 (lower) measured at R.T.. The diffuse intensity shows maximum at 002 where reflection is forbidden in the β-Sn structure. With decreasing temperature, the diffuse intensity decreases while the maximum at 002 becomes strong. The result indicates that the diffuse intensity concentrates to 002 maximum with decreasing temperature. In TDS theory, one-phonon scattering explains diffuse maximum around zone center and two-phonons scattering explains that around zone boundary. Thus, diffuse maximum around the zone center of forbidden reflection can not be explained by either 1st or 2nd TDS. Considering that the packing of β-Sn structure is rather low, its origin should be related to a defect structure. The temperature dependence of diffuse scattering indicates a strong coupling between the defect and phonons. Diffuse scattering at higher **Q** and inelastic scattering measurement is necessary to understand origin of the anisotropic distribution of the diffuse scattering.

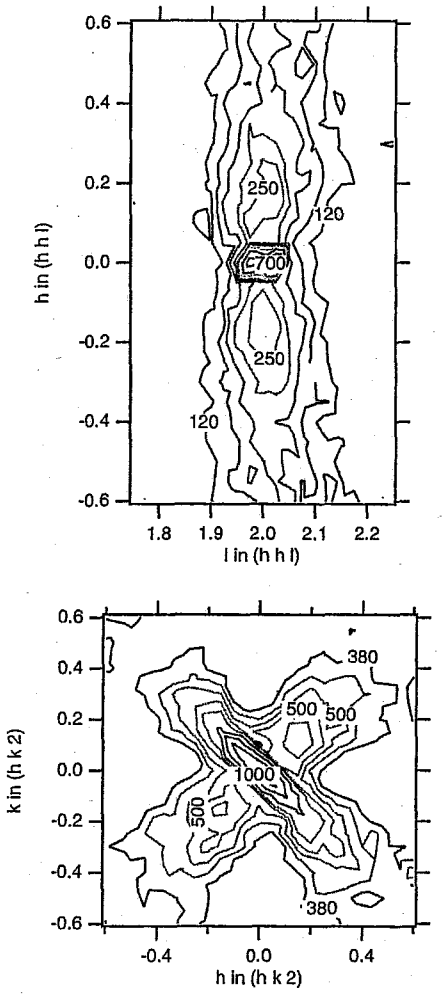

Fig. 1. Intensity contour map around 002 on the scattering plane of *hhl* (upper) and *hk*2 (lower) at R.T..

References

[1] J. Bouman *et al.*: Physica XII (1946)23.
[2] S. C. Prasad *et al.*:Acta Cryst. **9** (1956)35.

使用施設：JRR-3M, 装置： T2-2 (FONDER) , 分野： 1. Structural and Excitations

研究テーマ：$(K_{1-x}Rb_x)_2SeO_4$の仮想転移に寄与するソフトモードの振る舞い
表題：$(K_{1-x}Rb_x)_2SeO_4$の仮想転移に寄与するΣ_2-Σ_3フォノン分枝の振る舞い
1-1-27

Behavior of Σ_2-Σ_3 Phonon Branches that contribute to the hypothetical phase transition in $(K_{1-x}Rb_x)_2SeO_4$

H. Shigematsu and Y. Akishige

Department of Physics, Faculty of Education, Shimane University, Matsue 690-8504, Japan

Among a lot of A_2BO_4-type ferroelectrics with β-K_2SO_4 type structure (space group *Pnam*), a typical soft phonon-mode was observed in K_2SeO_4 both above and below the normal-incommensurate (N-INC) phase transition point by neutron scattering measurement. However, such N-INC transitions were not observed in most of the A_2BO_4-type ferroelectrics like K_2SO_4, Rb_2SeO_4 and Cs_2SeO_4. Contrastively, the results of molecular-dynamics simulation revealed that the static and dynamic features of the calculated dispersion-curves of Rb_2SeO_4 and K_2CrO_4 are similar to those of prototypical incommensurate materials like K_2SeO_4. Indeed, a partial softening of the Σ_2 phonon branch was observed in Rb_2SeO_4 [1].

We have studied in order to clarify the mechanism of low-temperature incommensurate phase transition and hypothetical one in A_2BO_4-type ferroelectrics. In order to obtain an additional information about the behavior of the low-energy Σ_2-Σ_3 phonon branches in $(K_{1-x}Rb_x)_2SeO_4$, we performed inelastic neutron scattering experiments by use of the triple-axis spectrometers (4G, T1-1 and C1-1) at JRR-3M of JAERI.

Two modes, which anticrossed each other at around (~ 0.7 0 0), were observed in all $(K_{1-x}Rb_x)_2SeO_4$ crystals. One of them is the lowest Σ_2-Σ_3 phonon branch. Figure 1 shows the phonon dispersion curves of the lowest Σ_2-Σ_3 phonon branches along the (ξ 0 0) line below room temperature. In a case of K_2SeO_4, the prolongation of the acoustic branch has its minimum around 0.7 a^* and the crystal transforms into an incommensurate phase at 131 K [2]. On the other hand, in $(K_{1-x}Rb_x)_2SeO_4$ (x = 0.1, 0.2 and 0.3), N-INC phase transitions were observed about 100 K (x = 0.1, q ~ 5/18 a^*), 80 K (x = 0.2, q ~ 4/17 a^*) and 5 K (x = 0.3, q ~ 1/6 a^*). According to the clear softening of the Σ_2-Σ_3 phonon branches around a^* for x > 0.3, existence of the hypothetical phase transition was confirmed.

In consequence the present work confirms that the clear softening of the Σ_2 branch and the existence of the hypothetical phase transition originate in the anticrossing of the acoustic with the optical branch.

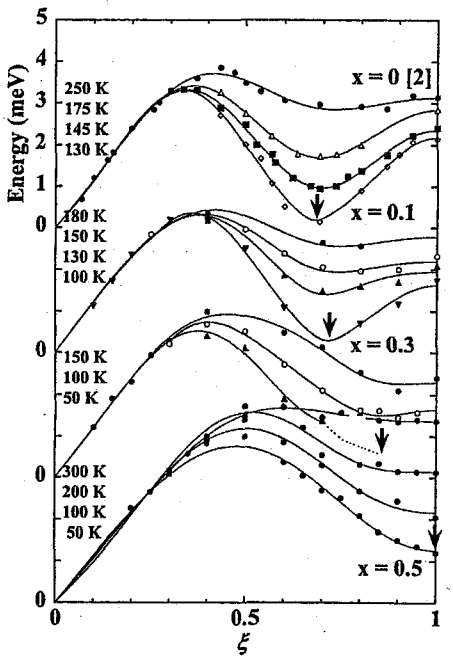

Figure 1: Phonon dispersion curves in an extended-zone scheme on the (ξ 0 0) for $(K_{1-x}Rb_x)_2SeO_4$. The minimum position of the Σ_2 branches are indicated by arrows.

References

[1] H. Shigematsu *et al.*, to be published in J. Korean Phys. Soc. (2004).
[2] M. Iizumi, J. D. Axe, G. Shirane and K. Shimaoka, Phys, Rev. B **15** (1977) 4392.

使用施設：JRR-3M, 装置： GPTAS(4G), HQR(T1-1) and HER(C1-1), 分野 Structure&Excitations

研究テーマ：元素置換した γ-Na_xCoO_2 の熱電特性と結晶構造
表題：γ-$Na_{0.70}Ca_{0.07}CoO_2$ の相転移

1-1-28

Phase Transition of γ-$Na_{0.70}Ca_{0.07}CoO_2$

Y.Ono[1], T.Motohashi[2], H.Yamauchi[2] and T.Kajitani[1]

[1] *Department of Applied Physics, Tohoku University, Sendai, Japan*
[2] *Materials and Structures Laboratory, Tokyo Institute of Technology, Yokohama, Japan*

A promising oxide thermoelectric material, γ-$Na_{0.75}CoO_2$, undergoes a phase transition near room temperature [1]. No magnetic anomaly has been associated at the transition temperature. Although the details of this phase transition are not clarified, one possibility is some kind of ordering in Na layer, i.e., a structural phase transition. Recently, we found that Ca can be introduced into the Na layer of γ-$Na_{0.70}CoO_2$ without changing the initial Na content [2]. In this study, we report the differential scanning calorimetry and structure analyses of γ-$Na_{0.75}CoO_2$ and γ-$Na_{0.70}Ca_{0.07}CoO_{2-\delta}$.

Polycrystalline samples of γ-$Na_{0.70}CoO_{2-\delta}$ were prepared from Na_2CO_3 (99.5%) and Co_3O_4 (99.9%) by a conventional solid-state reaction, as described in the previous report [3]. The Ca-doped sample, γ-$Na_{0.70}Ca_{0.07}CoO_{2-\delta}$, was prepared by the following two-step sintering procedure [2]. The starting materials, γ-$Na_{0.70}CoO_{2-\delta}$ and $Ca(NO_3)_2{\cdot}4H_2O$ (99.9%), were thoroughly mixed with an appropriate molar ratio, sintered at 873 K for 12 h in air and subsequently homogenized at 1123 K for 12 h in air with an intermediate grinding. Sample compositions were determined to be $Na_{0.67}CoO_{2-\delta}$ and $Na_{0.64}Ca_{0.07}CoO_{2-\delta}$ by the inductively coupled plasma (ICP) analysis [2]. Oxygen deficiency, δ, was evaluated to be negligibly small (less than 0.03) by a standard iodometric titration technique [2]. The differential scanning calorimetry (DSC) was performed using a Parkin Elmer Pyris Diamond DSC with heating and cooling rates of 20 K/min in the temperature range from 100 K to 523 K. Neutron diffraction measurements were carried out between 10 K and 290 K using HERMES (λ=1.82032 Å), installed at JRR-3M in JAERI (Tokai). The measured intensities were analyzed by a program, RIETAN 2000 [4], assuming the space symmetry $P6_3/mmc$ (No.194). Na and Ca contents were constrained to be those of the ICP results during the analysis.

A specific heat anomaly for γ-$Na_{0.70}CoO_{2-\delta}$ was observed at 288.4 K on cooling (exothermic) and at 300.5 K on heating (endothermic), while, for γ-$Na_{0.70}Ca_{0.07}CoO_{2-\delta}$, at 257.3 K on cooling and at 275.6 K on heating. The transition temperatures are considerably lowered by the Ca doping.

Figure 1 shows lattice parameters vs. temperature on heating. Both the lattice parameters of γ-$Na_{0.70}Ca_{0.07}CoO_{2-\delta}$, ***a*** and ***c***, show small discontinuity between 270 K and 280 K, which is consistent with the DSC results. However, we could not find clear difference in the atomic arrangement in the Na layer above and below 275 K.

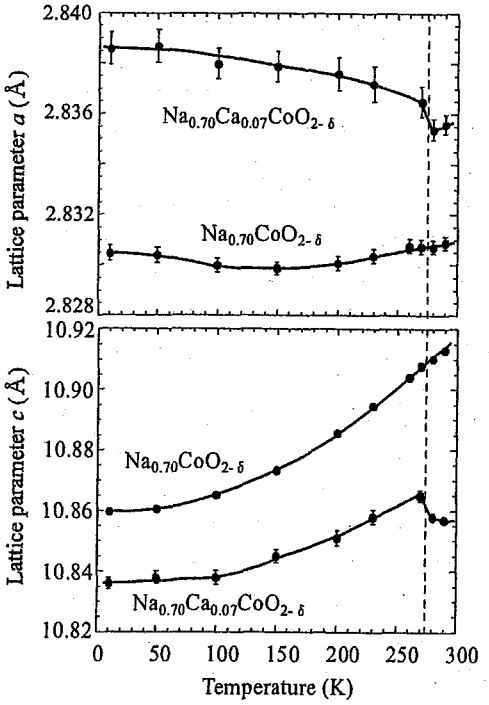

Figure 1: Lattice parameters vs. temperature on heating.

References

[1] T.Tojo et al., Phys. Rev. B **65** (2002) 052105.
[2] Y.Ono et al., J. Ceram.Soc.Jpn., Suppl., **112-1** (2004) S626.
[3] Y,Ono et al., J.Phys.Soc.Jpn.,Suppl., **39** (2002) 5867.
[4] F. Izumi and T.Ikeda, J. Crystallogr. Soc. Jpn., **42**(2000)1127.

使用施設：JRR-3M, 装置：HERMES(T1-3), 分野 Structure & Excitation

研究テーマ：ペロブスカイト型ジルコン酸塩の構造変化
表題：ペロブスカイト型ジルコン酸カルシウムの高温中性子粉末回折による研究

1-1-29 High-temperature Neutron Powder Diffraction Study of the $CaZrO_3$ Perovskite

K. Oh-uchi, M. Yashima, D. Ishimura, S. Kobayashi, W. Nakamura, and K. Ohoyama*

Department of Materials Science and Engineering, Interdisciplinary Graduate School of Science and Engineering, Tokyo Institute of Technology, 4259 Nagatsuta-cho, Midori-ku, Yokohama, 226-8502, Japan
**Institute for Materials Research, Tohoku University, Katahira, Aoba, Sendai, 980-8577, Japan*

Perovskite-structured oxides have received recent attention as high-temperature proton conductors with potential applications as fuel cells and hydrogen sensors. For example, a commercial sensor using doped $CaZrO_3$ as a proton conducting electrolyte has been developed. Doping of $CaZrO_3$ with some trivalent cations such as In^{3+}, Ga^{3+} and Sc^{3+} modifies its electrical properties, and then calcium zirconate possess appreciable levels of protonic conductivity in hydrogen-containing atmosphere. In order to understand the electrical properties of these materials, it is necessary to investigate the precise crystal structure of $CaZrO_3$. In this study, we have used neutron powder diffraction technique to investigate the crystal structure of $CaZrO_3$ at high temperature.

Neutron-diffraction measurements were performed in air with a 150-detector system, HERMES, installed at the JRR-3M reactor in JAERI [1]. The neutron wavelength was 1.82035(7) Å and the diffraction data were collected in the 2θ range from 20° to 153° in step interval of 0.1°, in the temperature range from 23°C to 1388°C. A furnace with $MoSi_2$ heaters was placed on the sample table [2], and used for neutron-diffraction measurements at high temperatures. The temperature was kept constant within ± 1.5°C during each data collection. The neutron-diffraction data were analyzed using the Rietveld program RIETAN-2000 [3].

Rietveld analyses of neutron powder diffraction data of $CaZrO_3$ measured in the whole temperature range were performed assuming an orthorhombic *Pnma* structure. Figure 1 shows Rietveld analysis pattern of neutron diffraction of $CaZrO_3$ measured at 1388°C. The reliability factors were R_{wp} = 4.47%, R_I = 1.14% and R_F = 0.63%. Goodness of fit was 2.05. Refined unit-cell parameters were a_o = 5.7892(2) Å, b_o = 8.1323(3) Å and c_o = 5.6997(2) Å.

Figure 2 shows the temperature dependence of the normalized unit-cell parameters of $CaZrO_3$. The unit-cell parameters increase continuously with increasing temperature. No phase transitions were observed and the *Pnma* structure is kept in the temperature range from room temperature to 1388°C.

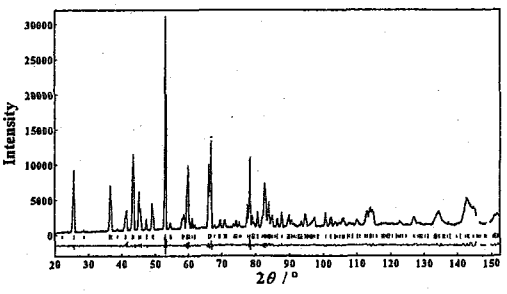

Figure 1: Neutron powder pattern of $CaZrO_3$ measured at 1388°C. Red crosses and green solid curve are observed and calculated intensity data.

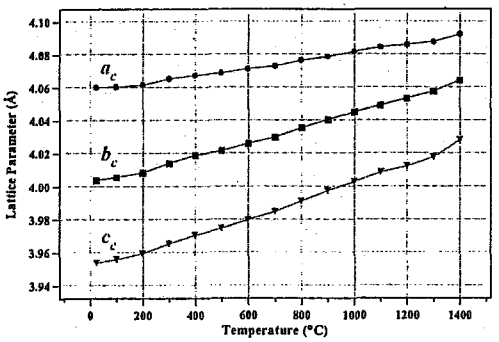

Figure 2: Temperature dependence of the normalized lattice parameters for $CaZrO_3$, where a_c, b_c and c_c are the pseudocubic cell parameters. Each data was collected keeping the sample temperature after heating.

References

[1] K. Ohoyama *et al.*, Jpn. J. Appl. Phys. **37** (1998) 3319-3326.
[2] M. Yashima, J. Cryst. Soc. Jpn. **44** (2002) 121-126.
[3] F. Izumi and T. Ikeda, Materia. Sci. Forum. **321-324** (2000) 198-204.

使用施設：JRR-3M，装置：HERMES(T1-3)，分野：1. Structures & Excitations

1-1-30
研究テーマ:$LaGaO_3$系ペロブスカイト型酸化物イオン導電体の高温中性子回折、
表題:$LaGaO_3$系ペロブスカイト型化合物の酸化物イオン伝導経路の可視化

Visualization of oxide-ion conduction path in $LaGaO_3$-based perovskites

K. Nomura, M. Yashima [1], H. Kageyama, Y. Miyazaki,
N. Chitose [2], K. Adachi [2], and K. Ohoyama [3]

Research Institute for Ubiquitous Energy Devices, National Institute of Advanced Industrial Science and Technology – Kansai, 1-8-31 Midorigaoka, Ikeda, Osaka 563-8577, Japan
[1]Department of Materials Science and Engineering, Interdisciplinary Graduate School of Science and Engineering, Tokyo Institute of Technology, 4259 Nagatsuta-cho, Midori, Yokohama, Kanagawa, 226-8502, Japan
[2]Central Research Institute Naka Research Center, Mitsubishi Materials Corporation, 1002-14 Mukohyama, Naka-machi, Naka-gun, Ibaraki, 311-0102, Japan
[3]Institute for Materials Research, Tohoku University, 2-1-1 Katahira, Aoba, Sendai, 980-8577, Japan

Recently, $LaGaO_3$-based perovskite-type oxides have been investigated as electrolyte materials of solid oxide fuel cells (SOFCs), because of the high oxide-ion conductivity. Of these, Sr-, Mg-, and Co-doped oxide, $(La_{0.8}Sr_{0.2})(Ga_{0.8}Mg_{0.15}Co_{0.05})O_{3-\delta}$ (LSGMC) is one of the best oxide-ion conductors [1]. In this study, we analyzed the nuclear density distributions in the LSGMC, to elucidate the oxide-ion conduction pathway in $LaGaO_3$-based perovskites.

High purity LSGMC sinter was prepared by using a solid-state reaction method. La_2O_3 (4N), $SrCO_3$ (3N), Ga_2O_3 (4N), MgO (4N), and CoO (99.5%) were used as starting materials. Neutron diffraction data were collected in the temperature range from 26 to 1392°C in air, using an electric furnace with $MoSi_2$ heaters [2] and a diffractometer HERMES installed at JRR-3M in JAERI (Tokai) [3]. The diffraction data obtained were analyzed by the combination technique of Rietveld analysis using a computer program RIETAN-2000 [4] and a maximum-entropy method (MEM)-based pattern fitting. MEM calculation was carried out using a computer program PRIMA [5].

Figure 1 shows the scattering amplitude distributions on the (100) planes and equicontour surfaces of scattering amplitude (0.05fm/Å) in the cubic ($Pm\bar{3}m$) perovskite LSGMC at 1392°C [6]. The conduction path of oxide-ions was not along the edges of BO_6 octahedra (shown as dotted line in Fig. 1), but showed an arc shape away from the B-site cations ($Ga_{0.8}Mg_{0.15}Co_{0.05}$) between adjacent two oxygen positions (O1 and O2). This result was consistent with the oxide-ion conduction pathway so far predicted from the molecular dynamics (MD) calculation [7].

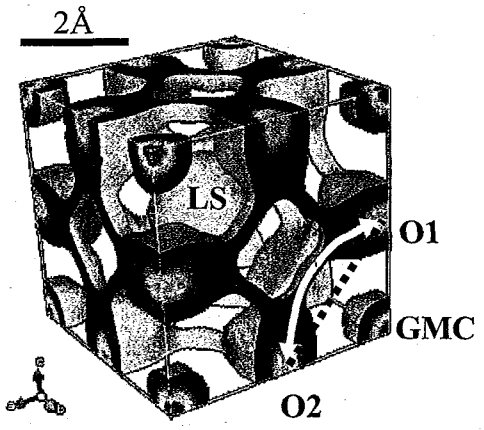

Fig. 1. Scattering amplitude distributions on the (100) planes and equicontour surfaces of scattering amplitude (0.05fm/Å) in the cubic perovskite $(La_{0.8}Sr_{0.2})(Ga_{0.8}Mg_{0.15}Co_{0.05})O_{3-\delta}$ at 1392°C. LS and GMC refer to the A-site cation ($La_{0.8}Sr_{0.2}$) and B-site one ($Ga_{0.8}Mg_{0.15}Co_{0.05}$), respectively. The conduction path of oxide-ions between two stable positions (O1, O2) is depicted as a curved solid arrow.

使用施設:JRR-3M, 装置:HERMES(T1-3), 分野 Structure & Excitations

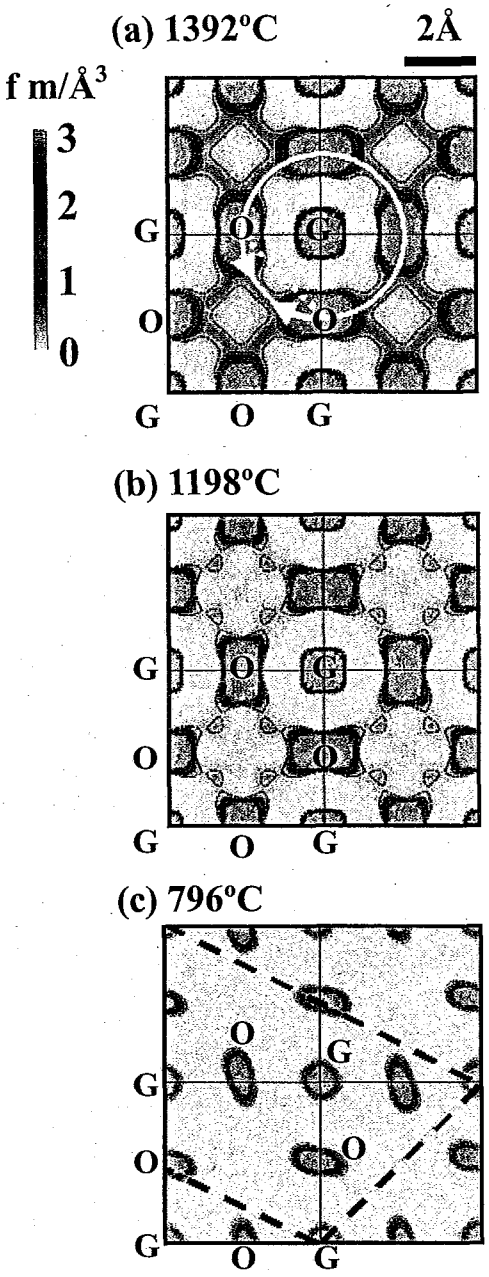

Fig. 2. Scattering amplitude distributions on the (100) plane of cubic ($Pm\bar{3}m$) $(La_{0.8}Sr_{0.2})(Ga_{0.8}Mg_{0.15}Co_{0.05})O_{3-\delta}$ at 1392°C and (b) 1198°C, and on the (012) plane of rhombohedral ($R\bar{3}c$) $(La_{0.8}Sr_{0.2})(Ga_{0.8}Mg_{0.15}Co_{0.05})O_{3-\delta}$ at 796°C, with contours in the range from 0.3 to 4.0 fm/Å^3 (0.3fm/Å step). G and O refer to the B-site cation ($Ga_{0.8}Mg_{0.15}Co_{0.05}$) and oxide ion, respectively.

Figure 2 depicts the temperature dependence of the scattering amplitude distributions on the (100) plane of cubic ($Pm\bar{3}m$) LSGMC at (a) 1392°C and (b) 1198°C, and on the (012) plane of rhombohedral ($R\bar{3}c$) LSGMC at 796°C [6]. The nuclear density on conduction path was higher at 1392°C (Fig. 2a) than at 1198°C (Fig.2b), which is consistent with an increase in oxide-ion conductivity of LSGMC with increasing temperature [1]. It is further noticed from Fig. 2 that the oxide ions are localized near equilibrium positions in the rhombohedral ($R\bar{3}c$) phase at 796°C (Fig.2c). With increasing temperature, the oxide ions spread over a wide area between the ideal positions (Figs. 2a and 2b), which suggests the lower activation energy for the migration of oxide ions at high temperature cubic ($Pm\bar{3}m$) phase.

References

[1] T. Ishihara, T. Akbay, H. Furutani and Y. Takita, *Solid State Ionics*, **113-115**, 585 (1998).
[2] T. Yashima, *J. Am. Ceram. Soc.*, **85**, 2925 (2002).
[3] K. Ohoyama, T. Kanouchi, K. Nemoto, M. Ohashi, T. Kajitani and Y. Yamaguchi, *Jpn. J. Appl. Phys.*, **37**, 3319 (1998).
[4] F. Izumi and T. Ikeda, *Mater. Sci. Forum*, **321-324**, 198 (2000).
[5] F. Izumi and R.A. Dilanian, in: Recent Research Developments in Physics, vol.3, Transworld Research Network, Trivandrum, 2002, p.699.
[6] M. Yashima, K. Nomura, H. Kageyama, Y. Miyazaki, N. Chitose, and K. Adachi, *Chem. Phys. Lett.*, **380**, 391 (2003).
[7] M.S. Islam, *J. Mater. Chem.*, **10**, 1027 (2000).

1. 中性子散乱 2) 磁　性

1. Neutron Scattering　2) Magnetism

This is a blank page.

研究テーマ：先端偏極中性子散乱によるスピン－格子物性の研究
表　題：スピンギャップ系 $TlCuCl_3$ におけるフォノン測定

1-2-1

Phonon Measurements in the Spin Gap System $TlCuCl_3$

A. Oosawa, K. Kakurai and H. Tanaka[1]

Advanced Science Research Center, JAERI, Tokai, Ibaraki 319-1195
[1]*Res. Cent. for Low Temperature Physics, Tokyo Institute of Technology, Oh-okayama, Meguro-ku, Tokyo 152-8551*

$TlCuCl_3$ is a spin gap system with the excitation gap $\Delta = 7.5$ K. This system shows the various quantum phase transitions, such as field-induced, impurity-induced and pressure-induced magnetic orderings, so that has been attracting considerable attentions both theoretically and experimentally. Besides, the importance of the spin-phonon coupling has been suggested from some experiments in this system recently. For instance, in the polarized neutron scattering study under the high-pressure, the pressure-induced successive magnetic phase transitions indicative of the reorientation of the ordered moments were observed and discussed in terms of the spin-phonon coupling [1]. From the NMR [2] and sound attenuation [3] studies in the field-induced magnetic ordering, the hysterisis behavior of the phase transition indicative of the weakly first order was observed. Also, the unusual temperature dependence of the broadened two-magnon continuum and Fano lines have been observed in the Raman scattering study [4]. In order to investigate the lattice properties in this system, we carried out the phonon measurements in $TlCuCl_3$ by means of the neutron inelastic scattering experiments.

The preparation of the single crystal of $TlCuCl_3$ has been reported in ref. 5. Neutron inelastic scattering measurements were performed using the JAERI-TAS1. The constant-$\boldsymbol{k}_f$ mode was taken with a fixed final neutron energy E_f of 14.7 meV and collimations were set as open-80'-80'-80'. Sapphire and pyrolytic graphite filters were placed to suppress the background by high energy neutrons and higher order contaminations, respectively. We used a sample with a volume of approximately 2.5 cm^3. The sample was mounted in the cryostat with its a^*- and c^*-axes in the scattering plane. The crystallographic parameters were determined as $a^* = 1.5885$ $Å^{-1}$, $c^* = 0.71195$ $Å^{-1}$ and $\cos\beta^* = 0.1106$ at room temperature.

First, we measured the constant-$\boldsymbol{Q}$ energy scan profile in $TlCuCl_3$ for $T = 297$ K and observed six phonon excitations up to E=20 meV. From the dispersion relations of the six excitations, it was found that one of these excitations is the acoustic mode, while the other modes are the optic modes, in which the excitation energys of the five optic modes are 1.7, 4.3, 7.5, 11.1 and 15.0 meV at the zone center, respectively. The result, in which five optic modes exist, is consistent with that obtained from the Raman scattering experiments [4].

Figure 1 shows the temperature dependence of integrated intensity I and the excitation energy E of the acoustic mode at $\boldsymbol{Q} = (2.4, 0, 0)$ in $TlCuCl_3$. The temperature dependence of the integrated intensities can be well described by the phonon temperature factor,

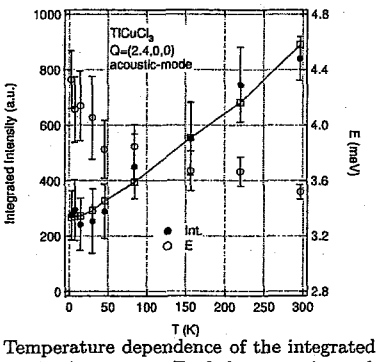

Figure 1: Temperature dependence of the integrated intensity I and the excitation energy E of the acoustic mode at $\boldsymbol{Q} = (2.4, 0, 0)$ in $TlCuCl_3$. The solid line with open squares denote the fitting result of temperature dependence of the integrated intensity by eq. (1).

$$I \propto \frac{1}{E} \times \left(\frac{1}{\exp\left(\frac{E}{k_B T}\right) - 1} + 1 \right) \qquad (1)$$

as shown in the solid line with open squares of Fig. 1. As shown in Fig. 1, the temperature dependence of the excitation energy E looks unusual. Namely, with decreasing temperature from $T = 300$ K, the excitation energy E gradually increases, and then shows a rapid increase below $T = 50$ K. From the magnetic susceptibility measurements [5], it has been found that the magnetic susceptibility has a broad maximum at $T = 38$ K, and then decreases steeply toward zero with decreasing temperature to $T = 0$ K. This results obtained from the magnetic susceptibility measurements indicate that the antiferromagnetic short range correlations begin to develop below $T = 38$ K. Hence, we infer that the rapid phonon energy increase below $T = 50$ K obtained from the present measurements is related to the development of the antiferromagnetic short range correlations, namely the formation of the spin singlet.

References

1) A. Oosawa *et al.*: J. Phys. Soc. Jpn. **73** (2004) 1446.
2) O. Vyaselev *et al.*: Phys. Rev. Lett. **92** (2004) 207202.
3) E. Ya. Sherman *et al.*: Phys. Rev. Lett. **91** (2003) 057201.
4) K.-Y. Choi *et al.*: Phys. Rev. B **68** (2003) 174412.
5) A. Oosawa *et al.*: J. Phys.:Condens.Matter **11** (1999) 265.

原子炉：JRR-3　　装置：TAS-1(2G)　　分野：中性子散乱（磁性）

研究テーマ： CeGaにおける圧力誘起磁気相転移
表題： 圧力下におけるCeGaの中性子回折実験

1-2-2 Neutron Diffraction Study on CeGa under High Pressure

S. Koiwai[1], M. Kosaka[1], M. Nishi[2] and N. Môri[1]

[1] *Department of Physics, Faculty of Science, Saitama University, Saitama, 338-8570, Japan*
[2] *Neutron Science Laboratory, ISSP, University of Tokyo, Takai, 319-1106, Japan*

The binary intermetallic compound CeGa of orthorhombic CrB type structure with space group *Cmcm* shows antiferromagnetic order below $T_N = 6.0$ K [1],[2],[3]. We determined the magnetic structure of CeGa with the propagation vector k = [1 0 0.3] at ambient pressure.

The new anomaly was observed in magnetic and electrical resistivity measurements above 0.8GPa. We have carried out the neutron experiments to determine the magnetic structure under high pressure.

Single crystalline samples (approximately $4 \times 4 \times 0.5$ mm^3) were prepared by a flux-growth technique. The lattice parameters of CeGa are estimated to be $a = 4.49$ Å, $b = 11.47$ Å and $c = 4.23$ Å at room temperature. Neutron diffraction measurements were performed in the reciprocal $a^* - c^*$ plane using the HQR spectrometer of JRR-3M in JAERI. A hydrostatic pressure was applied to CeGa using the McWhann type pressure cell. To reinforce the intensity of Bragg reflections in the pressure cell, we piled eleven single crystalline samples which are cleaved along the a-c plane and fixed them by Al_2O_3 adhesive as shown in Fig. 1. The intensity of the nuclear reflection from (0 0 2) has increased by four times larger than that of the one piece.

Fig.2 shows the schematic representation of the nuclear and magnetic peak positions in the reciprocal $a^* - c^*$ plane with the pressure of 0.2 GPa and 1.8 GPa at 4 K. The lattice parameters change abruptly from a =4.45 Å and c =4.16 Å to a =4.77 Å and c =3.96 Å accompanied by a structural phase transition. The values of $\Delta a/a$ and $\Delta c/c$ are 7.2 % and -4.8 %, respectively. It seems that the extinction rule is unchanged both before and after the structural phase transition. In this work, no magnetic reflections are found at 1.8GPa in the reciprocal $a^* - c^*$ plane.

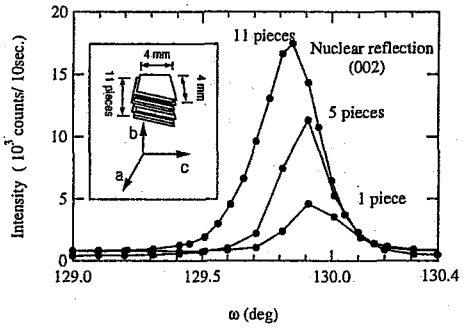

Fig. 1. The intensity of nuclear reflection from (0 0 2) without the pressure cell. The intensity is increased by the pile of single crystalline samples with an accuracy of 0.2 degree.

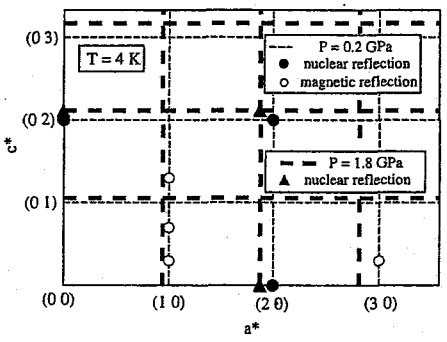

Fig. 2. Schematic representation of the nuclear and magnetic peak positions in the reciprocal $a^* - c^*$ plane with the pressure of 0.2GPa and 1.8GPa at 4K.

References

[1] E.Matsuoka et al.: Physica B **259-261** (1999) 112-113.
[2] S.Koiwai et al.: Physica B **312-313** (2002) 478-479.
[3] S.Koiwai et al.: Physica B **329-333** (2003) 643-644.

使用施設：JRR-3M, 装置： HQR(T1-1) , 分野： Magnetism

研究テーマ：先端偏極中性子散乱によるスピン-格子物性の研究
表　題：直鎖トライマー系 $A_3Cu_3(PO_4)_4$ (A=Ca, Sr, Pb) の磁気励起

1-2-3

Magnetic Excitations from the Linear Heisenberg Antiferromagnetic Spin Trimer System $A_3Cu_3(PO_4)_4$ with A=Ca, Sr, and Pb

M. Matsuda, K. Kakurai, A. A. Belik[1], M. Azuma[1], M. Takano[1], and M. Fujita[2]

Advanced Science Research Center, JAERI, Tokai, Ibaraki 319-1195
[1]*Institute for Chemical Research, Kyoto University, Gokasho, Uji 610-0011*
[2]*Institute for Materials Research, Tohoku University, Katahira, Sendai 980-8577*

$A_3Cu_3(PO_4)_4$ (A=Ca, Sr, and Pb) is an candidate to study the spin trimer antiferromagnetism. [1-5] A schematic view of the magnetic interactions in the copper chains is shown in Fig. 1. In the isolated Heisenberg antiferromagnetic $S = \frac{1}{2}$ trimer in a line the energy level scheme is described as follows. The ground state is a doublet with $E(0)=-J_1$ and $S_T = \frac{1}{2}$, where J_1 is the intra-trimer interaction and S_T is the total spins of a trimer. The first and second excited states are a doublet with $E(1)=0$ and $S_T = \frac{1}{2}$ and a quartet with $E(2)=\frac{1}{2}J_1$ and $S_T = \frac{3}{2}$, respectively. The neutron scattering technique is an ideal tool to directly investigate the energy level scheme of the spin trimer system as mentioned above. We have performed inelastic neutron scattering experiments on the polycrystalline samples of $A_3Cu_3(PO_4)_4$ (A=Ca, Sr, and Pb) on TAS2.

Temperature dependence of the inelastic neutron spectra in constant-Q scans in $Pb_3Cu_3(PO_4)_4$ is shown in Fig. 2(a). Figure 2(b) shows the Q-dependence of the peak intensities at 9 meV and 13.5 meV measured at 8 K. Since a cluster of the linear spin trimer is well isolated, almost dispersionless and sharp excitation peaks are observed even in the powder measurements. With increasing temperature intensities at 9.00 meV and 13.69 meV decrease, whereas a new excitation peak develops at 4.9 meV. The excitation energies of 4.9 meV, 9.00 meV, and 13.69 meV correspond to $E(2)-E(1)$, $E(1)-E(0)$, and $E(2)-E(0)$, respectively. Our analysis of the temperature and Q dependencies on the scattering intensities indicates that $Pb_3Cu_3(PO_4)_4$ is well described by the isolated Heisenberg antiferromagnetic spin trimer model without any adjustable parameters except the overall scale factor. This result indicates that the anisotropy in the exchange interaction is considered to be very small in this compound.

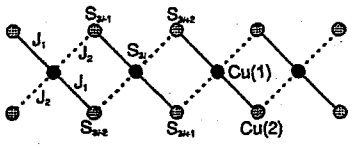

Figure 1: Schematic view of the major magnetic interactions J_1 and J_2 in the one-dimensional array of copper spin trimers.

We also performed inelastic neutron scattering experiments on the polycrystalline samples of $Sr_3Cu_3(PO_4)_4$ and $Ca_3Cu_3(PO_4)_4$ and obtained the results similar to those in $Pb_3Cu_3(PO_4)_4$. Only the exchange parameters are slightly changed. In this study the intra-trimer coupling contants are determined to be 9.45(3), 10.04(3), and 9.13(2) meV for $A_3Cu_3(PO_4)_4$ with A=Ca, Sr, and Pb, respectively.

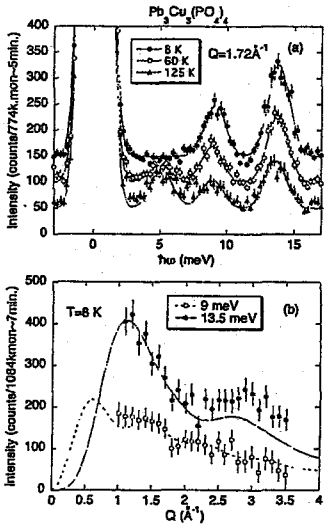

Figure 2: (a) Constant-Q scans at various temperatures in $Pb_3Cu_3(PO_4)_4$. 50 counts are added at each successive temperature so that the scans are compared on one graph. (b) Q dependence of neutron scattering intensity at 9 meV and 13.5 meV. Background intensity measured at a different energy is subtracted from the raw data.

References

1) J. B. Anderson, E. Kostiner and F. A. Ruszala: J. Solid State Chem. **39** (1981) 29.
2) M. Drillon, E. Coronado, M. Belaiche and R. L. Carlin: J. Appl. Phys. **63** (1988) 3551.
3) H. Effenberger: J. Solid State Chem. **142** (1999) 6.
4) A. A. Belik, A. P. Malakho, B. I. Lazoryak and S. S. Khasanov: J. Solid State Chem. **163** (2002) 121.
5) Y. Ajiro, T. Asano, K. Nakaya, M. Mekata, K. Ohyama, Y. Yamaguchi, Y. Koike, Y. Morii, K. Kamishima, H. Aruga-Katori and T. Goto: J. Phys. Soc. Jpn. **70** Suppl. A (2001) 186.

原子炉：JRR-3　　装置：TAS-2(T2-4)　　分野：中性子散乱（磁性）

研究テーマ;強磁性と反強磁性スピン相関が競合する系の磁性
表題:PtFe 合金のマグノン分散関係

1-2-4

Magnon dispersion relations in PtFe alloy

Hiroyuki Kobayashi and Yorihiko Tsunoda

Dept. Appl. Physics, Waseda University, 3-4-1, Ohkubo, Shinjuku, Tokyo 169-8555 Japan

An $L1_0$(CuAu) type PtFe alloy is an excellent candidate for the high density perpendicular magnetic recording media due to large magnetic anisotropy energy and saturation magnetization. The fundamentals of the magnetism are, however, not so well understood. Magnetic structure of PtFe alloy is reported to be a ferrimagnetic one with ferromagnetic coupling in the c-plane and anti-parallel coupling between Fe and Pt planes. The magnetic moments are parallel to the c-axis and Fe and Pt carry the magnetic moments of 3.01 μ_B and 0.38 μ_B, respectively. The exchange coupling constants are ,however, not determined yet. To study the exchange coupling constants between spins, we measured the magnon dispersion relations of the system using inelastic scattering of neutrons.

PtFe alloy single crystal with volume of about 1cc was grown by the Bridgmann method. Neutron scattering measurements were performed at 5G (PONTA) spectrometer. All of the data were taken at room temperature.

Experimental data of magnon dispersion relation curves for the [0 0 1] and [1 0 0] directions were analyzed using a ferrimagnetic Hamiltonian with two magnetic sites. In this calculation, exchange parameters J_1(Fe-Fe,1st n), J_2(Fe-Fe,2nd n), J_3(Pt-Fe,1st n) and anisotropy energies on Fe and Pt sublattices were used as fitting parameters. Experimental magnon dispersion relations for the [001] and [100] directions and calculated best fitting curves using the values of J_1= −2.3 meV, J_2 = −1.1meV, J_3 = 0.5 meV, H_{Fe} = 15.1 meV and H_{Pt} = 5.6meV are given in Fig.1 and Fig. 2, respectively.

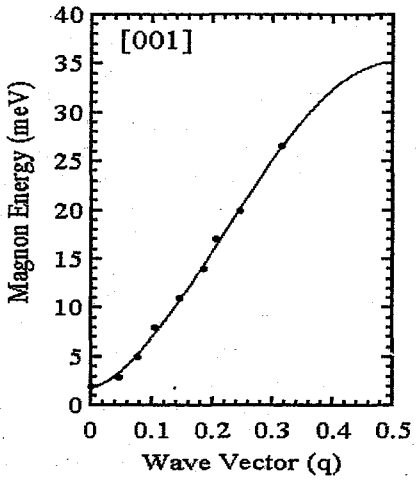

Fig.1

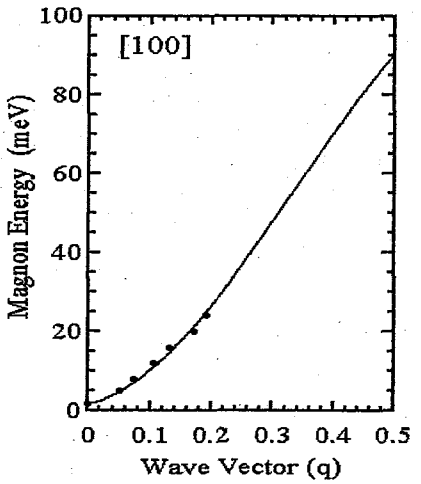

Fig.2

使用施設:JRR-3M, 装置:5G (PONTA), 分野:Magnetism

研究テーマ：$RBaCo_2O_{5.5}$(R=Tb, Ho, Y) の逐次相転移
表　題：$NdBaCo_2O_5$ における２つの磁気転移

1-2-5

Two Magnetic Transitions of $NdBaCo_2O_5$

M. Soda, Y. Yasui, M. Ito, S. Iikubo, M. Sato and K. Kakurai[1]

Department of Physics, Nagoya University, Chikusa-ku, Nagoya 464-8602
[1]*Advanced Science Research Center, JAERI, Tokai, Ibaraki 319-1195*

Co-oxides often exhibit spin state change, which bring about a variety of physical behaviors.[1,2] $RCoO_3$ (R=Y and rare earth elements) and $RBaCo_2O_{5+\delta}$ are examples of such systems. The latter systems are called oxygen deficient perovskites: $RBaCo_2O_5$ have the linkage of corner-sharing CoO_5 pyramids, while $RBaCo_2O_{5.5}$ have the linkage of alternating CoO_6 octahedra and CoO_5 pyramids. For these systems, various kinds of magnetic states and charge-ordered states have been reported.[3,4]

In the present work, neutron scattering studies have been carried out on a single crystal of $NdBaCo_2O_5$ to collect information on the spin state of Co ions in relation to the local structures. The average valence of Co ions is +2.5.

Neutron measurements were carried out by using the triple axis spectrometer TAS-2 installed at the thermal guide of JRR-3 of JAERI in Tokai. The crystal was first oriented with the [010] (or [100]) axis vertical, where both $(h,0,l)$ and $(0,k,l)$ points in the reciprocal space could be reached due to the coexistence of the a^*- and b^*-domains. Measurements were also carried out for the crystal orientation with the [110] axis vertical.

Integrated reflection intensities have been measured at various reciprocal points in the temperature (T) range of 7-370 K. (We use here the unit cell with the size of $\sim a_p \times 2a_p \times 2a_p$, where a_p is the lattice parameter of the cubic perovskite cell.) With decreasing T, the superlattice peaks appear at $T_N \sim$360 K at $Q=(k'/2,k'/2,l)$ (k':odd), which corresponds to the antiferromagnetic order. With further decreasing T, another set of superlattice peaks at $Q=(k'/2,0,l)$ (k':odd) appears at $T_{CO} \sim$250 K. Detailed structure analyses have revealed that the set of superlattice peaks stems from the existence of two distinct Co-sites with different valences and different magnetic moments, indicating that the charge ordering exists below T_{CO}. When the temperature of the system is lowered through T_{CO}, the profile widths of all reflections which exist above T_{CO}, begin to increase at $\sim T_{CO}$ and the peak intensities are reduced with the integrated intensities being kept unchanged. We think that large local lattice distortions caused by the charge ordering are the origin of the significant broadening of the reflections.

The magnetic structures have been determined at T=300 K (antiferromagnetic phase) and T=7 K (antiferromagnetic and charge ordered one). The magnetic structures at both temperatures have been found to be so-called G-type antiferromagnetic one (or NaCl-type). At 300 K, the aligned moments μ of Co ions, all of which have the average valence of +2.5, is 2.14±0.09 μ_B.

By analyzing the data at 7 K, we have found that all the apical oxygens of the pyramids and on the O-Co-O chains along the a-axis, are shifted in the way that the volumes of the pyramids expand or contract alternatingly from the positions above T_{CO}, which confirms that the charge ordering really takes place at T_{CO}. The magnitudes μ of the aligned moments of two crystallographically distinct Co sites are 2.68±0.04 μ_B and 2.46±0.04 μ_B at 7 K. (The moment directions are parallel or anti-parallel to [100].) Because the magnetic reflection intensities do not exhibit anomalous T dependence, we think that Co ions are in the high spin state over the whole temperature range studied here ($T < T_N \sim$360 K). The difference between the aligned moments of two Co sites is significantly smaller than that reported to be the ordering of Co^{3+} and Co^{2+}. The presently observed small difference of the moments between the crystallographically distinct sites indicates that the real charge difference between the sites may not be unity, that is, the time- or spatially-averaged valences of Co ions in the distinct sites cannot be considered to be +3 and +2.

References

1) H. Masuda *et al.*: J. Phys. Soc. Jpn. **72** (2003) 873.
2) T. Fujita *et al.*: J. Phys. Soc. Jpn. **73** (2004) No. 7
3) D. Akahoshi and Y. Ueda: J. Solid State Chem. **156** (2001) 355.
4) M. Soda *et al.*: J. Phys. Soc. Jpn. **72** (2003) 1729.

原子炉：JRR-3　　装置：TAS-2(T2-4)　　分野：中性子散乱（磁性）

研究テーマ:強誘電体 RMn_2O_5 (R=希土類)における長周期磁気構造
表題:強誘電体 $ErMn_2O_5$における逐次磁気相転移

1-2-6 Successive magnetic phase transitions associated with ferroelectricity in $ErMn_2O_5$

S. Kobayashi, T. Osawa, H. Kimura, Y. Noda, I. Kagomiya*, and K. Kohn*

*Institute of Multidisciplinary Research for Advanced Materials, Tohoku University, Sendai 980-8577; *Department of Physics, Waseda University, Shinjuku-ku, Tokyo 169-8555*

Rare-earth manganese oxides RMn_2O_5 (R= Nd-Lu,Y,Bi) belonging to the space group of *Pbam*, show ferroelectricity below T_{C1} = 32-39 K close to the Neel temperature of T_{N1}= 39-45 K. Previously, we studied YMn_2O_5 by neutron diffraction[1] and reported that the ferroelectric transition at T_{C1} = 39 K is associated with a magnetic phase transition from a two-dimensionally modulated incommensurate magnetic (2D-ICM) phase with the propagation vector $q_M=(q_x,0,q_z)$ to a lock-in commensurate magnetic (CM) one with q_M=(1/2,0,1/4). This result indicates strong coupling between ferroelectricity and magnetic ordering in YMn_2O_5. Nevertheless, the mechanism that both magnetic and ferroelectric phase transitions occur simultaneously is unclear and systematic investigation of magnetic ordering of RMn_2O_5 with changing R^{3+} ion is required.

Neutron diffraction measurements have been performed on $ErMn_2O_5$, using a four-circle neutron diffractometer (FONDER), installed at guidehall of JRR-3M. Figures 1(a)-1(c) show the temperature dependence of q_x, q_z and dielectric constant along the *b* axis (polarization axis), respectively[2]. Below T_{N1}, $ErMn_2O_5$ shows similar magnetically ordered phases to those of YMn_2O_5: a 2D-ICM and CM phases. However, we found that in a narrow temperature range of 1K around T = 38 K ($T_{CM}<T<T_D$), a 1D-ICM ordering characterized by q_M= (q_x,0,1/4) which separates the 2D-ICM and CM phases shows up as shown in Figs. 1(a) and 1(b). Correspondingly, a sharp peak (T_{c1}=38.5K) and shoulder (T_s=37.8K) in the dielectric constant were observed as shown in Fig. 1(c). This indicates that the ferroelectric phase transition at T_{c1} occurs with the onset of the 1D-ICM ordering from the 2D-ICM one. The ferroelectric and magnetic phase transitions in $ErMn_2O_5$ are summarized in Fig. 2. Note that such 1D-ICM ordering around T_{c1} was recently confirmed also in YMn_2O_5[3], which suggests that a lock-in commensurate magnetic ordering along the *c* axis is important for ferroelectricity in RMn_2O_5.

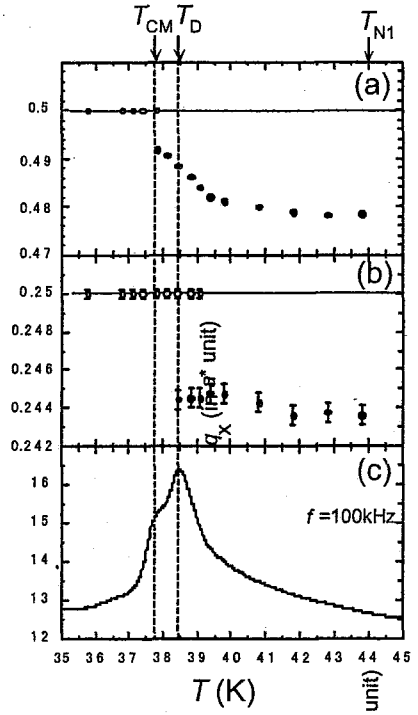

Fig.1 (a) q_x, (b) q_z, and (c) dielectric constant (100kHz), taken on heating.

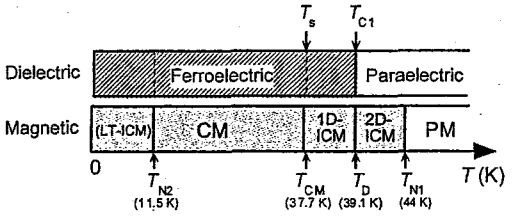

Fig. 2. Ferroelectric and magnetic phase transitions in $ErMn_2O_5$.

References

[1] I. Kagomiya et al: JPSJ **70**, Suppl. A (2001) 145.
[2] S. Kobayashi *et al.*: JPSJ **73** (2004) 1031.
[3] S. Kobayashi *et al.*: JPSJ **73** (2004) 1593.

使用施設:JRR-3M, 装置:FONDER(T2-2), 分野 : 磁気構造、磁気励起

研究テーマ：$RBaCo_2O_{5.5}$(R=Tb, Ho, Y) の逐次相転移
表　題：$NdBaCo_2O_{5.5}$ の構造とスピン状態

1-2-7

Structures and Spin States of $NdBaCo_2O_{5.5}$

M. Soda, Y. Yasui, M. Ito, S. Iikubo, M. Sato and K. Kakurai[1]

Department of Physics, Nagoya University, Chikusa-ku, Nagoya 464-8602
[1]*Advanced Science Research Center, JAERI, Tokai, Ibaraki 319-1195*

In Co-oxides, the spin state of Co ions is one of key elements to understand their physical properties. Because they often exhibit spin state change, a variety of physical behaviors are expected with the change of the difference of the electronic energies, δE between the spin states.[1,2] In $R_{1-x}A_xCoO_{3-\delta}$ (A=Sr, Ba and Ca), the substitution of R^{3+} with A^{2+} affects the effective value of δE through the introduction of hole-carriers and by changing the average ionic radius of $R_{1-x}A_x$. The electron transfer energy t seems to be also important to determine δE.[2] In $RBaCo_2O_{6-2\delta}$ (x=0.5) with relatively small size of R^{3+}, R and Ba are ordered and the oxygen-deficiency is also found to be in the ordered state.[3–5] The structure of $RBaCo_2O_{5.5}$ is formed by the linkage of alternating CoO_6 octahedra and CoO_5 pyramids along the b-axis. These systems provide a rather good opportunity to extract fundamental information how the magnetic state of Co ions within the pyramids and octahedra depend on such the local arrangements of the ligand atoms. In the present work, neutron scattering studies have been carried out on a single crystal of $NdBaCo_2O_{5.5}$ by using the spectrometer TAS-2 installed at the thermal guide of JRR-3 of JAERI in Tokai, to collect information on the spin state of Co ions in relation to the local structures.

Intensities of the neutron Bragg reflections with various indices have been measured on a single crystal of $NdBaCo_2O_{5.5}$ in the temperature range of 7-320 K, where several superlattice reflections as well as the fundamental reflections of the unit cell with the size of $\sim a_p \times 2a_p \times 2a_p$ have been found, where a_p is the lattice parameter of the cubic perovskite cell. With decreasing T from the temperature above 320 K, the intensities of several nuclear Bragg reflections change in the temperature region $T > 190$ K. At $T_c \sim 170$ K, additional intensity component appears at several nuclear Bragg points. Superlattice peaks corresponding to the G-type antiferromagnetic structure also appear (Q=(k'/2,k',l); k'=odd) at this temperature. With further decreasing T, the intensity ratios among several reflections begin to change at $T^*\sim$ 30 K. No additional reflections appear at this temperature.

At 40 K ($T^* < T < T_c$) and 7 K ($T < T^*$) the magnetic structures have been analyzed, where the spin states of Co ions within the CoO_6 and CoO_5 polyhedra are basically clarified. One of characteristics of these magnetic structures is that there is the significant difference between the magnitudes of the aligned moments of Co^{3+} ions in CoO_6 and CoO_5 polyhedra. At 40 K the magnitude μ_1 and μ_2 of Co^{3+} in the octahedra and the pyramids are 1.28(±0.04) μ_B and 2.47(±0.05) μ_B, respectively. These values indicate that Co^{3+} ions of the octahedra are in the intermediate spin (IS) state, while those of the pyramids are in the high spin (HS) state. The magnetic moments have the coplanar and canted structure, although the canting angles are different between the moments in the CoO_6 and CoO_5 polyhedra. In the region of $T < T^*$, μ_1 decreases gradually as T decreases, although the magnetic structure dose not exhibit appreciable change. The electrical resistivity ρ begins to increase rapidly at T^* with decreasing T. These results suggest that the spin state of Co^{3+} ions in the octahedra approaches the low spin (LS) state below T^*. The direct evidence for the existence of the LS state of Co^{3+} ions in the octahedra has reported in $TbBaCo_2O_{5.5}$[4] by the present authors' group.

The present results and those reported in refs. 2, 4 and 5 indicate that the spin state of Co ions depends on their local arrangement of the ligand oxygens. The ionic radius r_R of R^{3+} is important for the determination of the spin state, too: For smaller r_R, Co^{3+} in the octahedra (pyramids) prefer the LS (IS) states more, and for large r_R, they prefer the IS (HS) states more. These relationships can be understood by considering the magnitude of the energy splitting between the t_{2g} and e_g orbitals created by the crystal field: With decreasing r_R, the volume of the polyhedra increases and the energy splitting decreases, resulting in the tendency to strabilize the higher spin state. The smaller energy splitting of Co ions of pyramids have higher spin states than in the octahedra.

References

1) H. Masuda *et al.*: J. Phys. Soc. Jpn. **72** (2003) 873.
2) T. Fujita *et al.*: J. Phys. Soc. Jpn. **73** (2004) No. 7
3) D. Akahoshi and Y. Ueda: J. Solid State Chem. **156** (2001) 355.
4) M. Soda *et al.*: J. Phys. Soc. Jpn. **72** (2003) 1729.
5) M. Soda *et al.*: J. Phys. Soc. Jpn. **73** (2004) 464.

原子炉：JRR-3　　装置：TAS-2(T2-4)　　分野：中性子散乱（磁性）

研究テーマ：希土類化合物 *R*NiSn(*R*:希土類における高次磁気構造と磁場誘起磁気転移
表題：希土類化合物 DyNiSn における磁場誘起磁気転移

1-2-8 Field-Induced Magnetic Structures of Rare-Earth Intermetallics, DyNiSn

S. Kawano, K. Murogaki[1], Y. Andoh[2], M. Takahashi[3], M. Kurisu[4], G. Nakamoto[4] and T. Tsutaoka[5]

Research Reactor Institute, Kyoto University, Osaka 590-0494, Japan; [1]Graduate School of Science, Kyoto University, Kyoto 606-8502, Japan; [2]Faculty of Education and Regional Sciences, Tottori University, Tottori 680-8551, Japan; [3]Institute of Materials Science, University of Tsukuba, Ibaraki 305-8573, Japan; [4]Japan Advanced Institute of Science and Technology, Ishikawa 923-1292, Japan; [5]Faculty of Education, Hiroshima University, Hiroshima 739-8524, Japan

Ternary equiatomic rare-earth compound DyNiSn crystallizes in the orthorhombic (space group: Pnma) TiNiSi-type structure. Only Dy atom bears the magnetic moment. Magnetic properties are characterized by successive magnetic transitions at T_N=7.3 K and T_1=5.4 K with lowering temperature, and a multi-step (3 steps) metamagnetic transition at low temperatures when an external magnetic field is applied along the magnetization easy *b*-axis [1]. Szytula *et al.* have reported a sine-modulated structure with the magnetic wave vector of $\boldsymbol{Q}$=(Q_x Q_y 0) type at *T*=2 K from powder neutron diffraction measurements [2]. The detailed magnetic structures, however, are still remained unclear for field-induced as well as zero-field phases. In the present note, we report preliminary results of single crystal neutron diffraction studies on DyNiSn. Figure 1 shows a distribution of Bragg reflections in DyNiSn. Although the direction of the magnetic moment is along the easy magnetization *b*-axis, no magnetic reflection on the (1 0 0) line in the *a**-*c** plane suggests magnetic reflections on this plane to be the 3rd harmonics of main satellites in the *a**-*b** plane. Figure 2 gives the field dependence of the (0 0 1)$^+$ satellite and the (0 0 2) reflection. The increase in the (0 0 2) intensity indicates the ferromagnetic component developing by applied field, and shows an existence of two intermediate phases from 0.7 to 1.1 T and from 1.6 to 1.4 T up to a saturated state beyond 2 T. This behavior agrees with the magnetization results [1]. From 0.7 to 1.2 T a new magnetic reflection appears at (2/3 0 0). Detailed measurements and analysis are in progress.

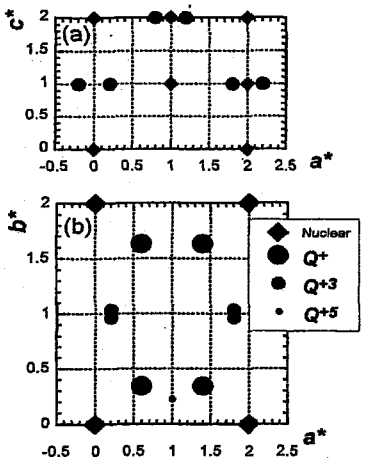

Figure 1: Schematic representation of magnetic and nuclear reflections of DyNiSn.

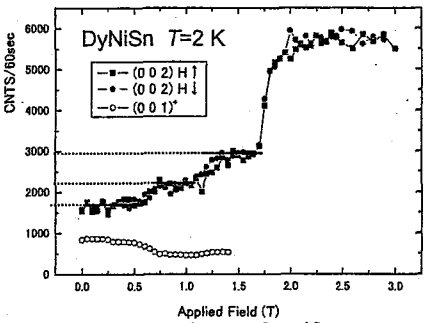

Figure 2: Field dependence of antiferromagnetic (0 0 1)$^+$ and ferromagnetic (0 0 2) reflections at 2 K.

References

[1] M. Kurisu, et al., Physica B **201** (1994) 107.
[2] A. Szytula, et al., J. Alloys and Compounds **244** (1996) 94.
[3] S. Kawano, et al., J. Phys. Chem. Solids **60** (1999) 1205.

使用施設：JRR-3M, 装置：HQR(T1-1), 分野 Magnetism

研究テーマ：$Pr_{1-x}A_xCoO_3$ (A=Ca, Sr and Ba) の圧力誘起金属・絶縁体転移
表　題：$Pr_{1-x}Ca_xCoO_3$ のスピン状態転移

1-2-9

Spin State Transition of $Pr_{1-x}Ca_xCoO_3$

T. Fujita, Y. Yasui, T. Miyashita, Y. Kobayashi, M. Sato, Y. Shimojo[1], N. Igawa[1], Y. Ishii[1] and K. Kakurai[1]

Department of Physics, Nagoya University, Furo-cho, Chikusa-ku, Nagoya 464-8602
[1]Japan Atomic Energy Research Institute, Tokai, Ibaraki 319-1195

Spin state change is a remarkable characteristic of Co oxides, which induces a variety of interesting physical behaviors. In perovskite Co oxides $RCoO_3$ (R=Y and various rare earth elements), for example, the change is often found from the low spin (LS; spin s=0; t_{2g}^6) ground state to the intermediate spin (IS; s=1; $t_{2g}^5e_g^1$) or the high spin (HS; s=2; $t_{2g}^4e_g^2$) state with increasing temperature T.[1] It indicates that the difference of the electronic energies, δE between these spin states is rather small. The value of δE is expected to increase with decreasing ionic radius r_R of R^{3+}, because the crystal field splitting Δ_c increases with decreasing r_R through the contraction of the volume(V_o) of the CoO_6 octahedra. However, it is not simple, in general, to understand the change of δE in detail only by considering Δ_c (and the Hund coupling J_H), because the Co-Co transfer energy t may also change δE mainly through the changes of Co-O-Co bond angle caused by the change of the ionic radius r_R of R^{3+}. For $R_{1-x}A_xCoO_3$ (A= Ba, Sr and Ca), we have to consider both effects of the hole doping and the δE (Δ_c)-change induced by the V_o-change.[2] External pressure can also change the value of δE. It is interesting to search for proper set of these parameters, r_R, carrier density, external pressure and so on, to obtain desired electronic state.

For $Pr_{1-x}Ca_xCoO_3$, a transition from the high temperature conducting phase to the low temperature less conducting (insulating) one has been reported by Tsubouchi *et al.*[3] in the very narrow region of $x \sim 0.5$. We have independently found a similar transition in the wide x region under the condition of high pressure $p > 5$ kbar.[4] The abrupt decrease of the magnetic susceptibility χ of $Pr_{0.6}Ca_{0.4}CoO_3$ at the transition temperature T_s with decreasing T under high pressure, can be seen as was reported at ambient pressure for $Pr_{0.5}Ca_{0.5}CoO_3$ in ref. 3. This result and those of ^{59}Co-NMR studies by the present authors' group, indicate that the transition is accompanied by the IS → LS spin state change of Co^{3+} ions with decreasing T. We have carried out further studies by various methods to clarify details of the transition and to extract more information what factors determine the spin state of the system. Here, the results of the neutron diffraction studies for the samples of $Pr_{1-x}Ca_xCoO_3$ with x up to 0.5 are briefly presented.[4] The high resolution powder diffractometer (HRPD) of JRR-3M of JAERI in Tokai was used. Rietveld analyses were carried out by using the computer program Rietan 2000.[5]

Because both the volumes V_u and V_o of the unit cell and the CoO_6 octahedra, respectively decrease significantly with increasing x in the region of the relatively large x, the value of Δ_c can be considered to increase with increasing x. However, detailed analyses of the magnetic susceptibilities χ and our NMR results indicate that δE decreases with increasing x. We think that the Co-Co transfer energy t acts an important role for the explanation of this behavior of δE. At the transition, the sudden increase of the tilting angle of the CoO_6 octahedra (or the sudden decrease of the angle α) takes place. This tilting stabilize the LS state through the reduction of t or the increase of δE in the low temperature phase.

References

1) for example, K. Asai, A. Yoneda, O. Yokokura, J. M. Tranquada, G. Shirane and K. Kohn: J. Phys. Soc. Jpn. **67** (1998) 290.
2) H. Masuda, T. Fujita, T. Miyashita, M. Soda, Y. Yasui, Y. Kobayashi and M. Sato: J. Phys. Soc. Jpn. **72** (2003) 873.
3) S. Tsubouchi, T. Kyomen, M. Itoh, P. Ganguly, M. Oguni, Y. Shimojo, Y. Morii and Y. Ishii: Phys. Rev. **B 66** (2002) 052418.
4) T. Fujita, T. Miyashita, Y. Yasui, Y. Kobayashi, M. Sato, E. Nishibori, M. Sakata, Y. Shimojo, N. Igawa, Y. Ishii. K. Kakurai, T. Adachi, Y. Ohishi and M. Sakata: J. Phys. Soc. Jpn. **73** (2004) No. 7.
5) F. Izumi and T. Ikeda: Mater. Sci. Forum **321-324** (2000) 198.

原子炉：JRR-3　　装置：HRPD(1G)　　分野：中性子散乱（磁性）

研究テーマ：特異な原子価状態におけるフラストレーション系の研究１
表題： $(Zn_xGe_{1-x})Co_2O_4$ の中性子散乱

1-2-10

Neutron Scattering Study of $(Zn_xGe_{1-x})Co_2O_4$

K. Kamazawa

Advanced Research Institute for Science and Engineering, Waseda Univ., 3-4-1 Ohkubo, Shinjuku-ku, Tokyo 169-8555, Japan

Pauli paramagnetic $ZnCo_2O_4$ takes a low spin (LS) state and spin value is S= 0, while isomorphic $GeCo_2O_4$ has electron in $d\gamma$ and it is magnetic spinel. In spinel group, Pauli paramagnetic spinels whose electrons are in $d\varepsilon$ at room temperature become superconductivity at low temperature.

Using neutron scattering measurement magnetic behavior of mixed $GeCo_2O_4$ and $ZnCo_2O_4$, i.e. $(Zn_xGe_{1-x})Co_2O_4$, were observed. The neutron scattering measurement was conducted using High-Q-Resolution triple axis spectrometer installed at T1 thermal guide at JAERI.

Fig.1 shows the 1/2 1/2 1/2 magnetic peak intensities vs. temperature for $GeCo_2O_4$ and $(Zn_{0.25}Ge_{0.75})Co_2O_4$. For $(Zn_{0.25}Ge_{0.75})Co_2O_4$, magnetic diffuse scattering exists until considerable high temperature. The magnetic diffuse scattering is considered to originate in a randomness effect of Co^{2+} and Co^{3+} in the B site. Magnetic susceptibility curve, like a spin glass behavior, also supports the neutron scattering result as shown in Fig. 2.

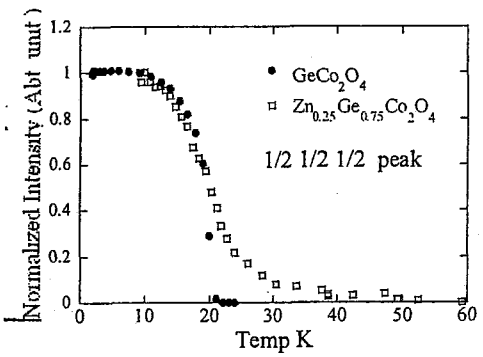

Fig. 1: The 1/2 1/2 1/2 magnetic peak intensities vs. temperature for $GeCo_2O_4$ and $(Zn_{0.25}Ge_{0.75})Co_2O_4$.

However, in the temperature dependences of the powder neutron diffraction for $(Zn_{0.5}Ge_{0.5})Co_2O_4$, the 1/2 1/2 1/2 magnetic peak does not emerge at any temperature. It indicates that static magnetic correlation does not exist anymore. It is thought that $(Zn_{0.5}Ge_{0.5})Co_2O_4$ is paramagnetic. By the way, X-ray and neutron scattering data show two phase, that is $GeCo_2O_4$ and $ZnCo_2O_4$ coexist. In addition, it was reported that $ZnCo_2O_4$ takes a normal spinel structure though stoichiometric $Zn^{2+}Co^{3+}{}_2O_4$ could not be compounded [1]. Co_3O_4; $(Co^{2+}Co^{3+}{}_2O_4)$ remains and Co^{2+} acts as impurities to A site [2]. Further measurements are required.

Acknowledgement

K. K. would like to thank Prof. Y. Tsunoda for his support as the research representative for the neutron scattering measurement applications of office procedure.

References

[1] P. Cossee, J. Inorg., Nucl., Chem., **8**, 483 (1958).
[2] W. L. Roth, J. Phys. Chem. Solids, **25**, 1 (1964).

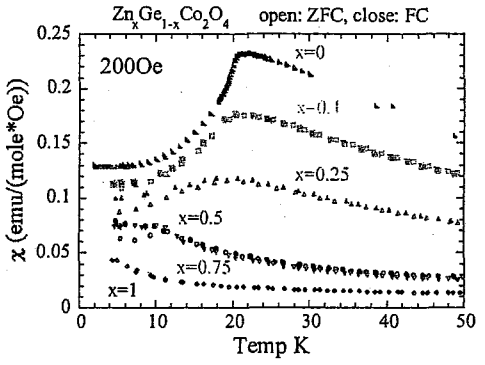

Fig. 2: Magnetic susceptibility vs. temperature at 200Oe for $(Zn_xGe_{1-x})Co_2O_4$.

使用施設：JRR-3M，装置：HQR(T1-1)，分野 Magnetism

研究テーマ：中性子散乱による機能材料構造の研究
表　題：中性子回折によるZ型Baフェライトの磁気構造とその温度依存性の研究

1-2-11

Estimation of temperature dependence of magnetic structure of Z-type barium ferrite $Ba_3Co_{1.8}Fe_{24.2}O_{41}$ by powder neutron diffraction

Y. Takada, T. Nakagawa, Y. Fukuta, T. A. Yamamoto, T. Tachibana[1], T. Shimada[1], Y. Ishii[2], N. Igawa[2]

Graduate School of Engineering, Osaka University, 2-1 Yamadaoka, Suita, Osaka 565-0871
[1]NEOMAX Co. Ltd., 2-15-17 Egawa, Shimamoto-cho, Mishima-gun, Osaka 618-0003
[2]Neutron Scattering Research Group, JAERI, 2-4 Shirane, Tokai-mura, Naka-gun, Ibaraki-ken 319-1195

1 Introduction

Co_2Z-type hexaferrite $Ba_3Co_2Fe_{24}O_{41}$ keeps high permeability even in UHF region (300 MHz - 3 GHz), because it has the easy-magnetization direction parallel to its basal plane (*ferroxplana*) and larger magnetic anisotropy. Thus, it is expected as one of promising candidate materials for commercial use in GHz components such as mobile phone, wireless LAN, inductor cores and electromagnetic absorbent materials [1-3].

In our previous works, we found that substitution of cobalt for iron improved permeability of the Z-type ferrites. The magnetization curve of $Ba_3Co_{1.8}Fe_{24.2}O_{41}$ measured by VSM indicated there are two transformation points at 540 and 680 K [1]. However, no crystal structure changes were observed in high-temperature XRD profiles. These facts mean that two magnetic changes occur in this temperature range.

The aim of this study is investigation of the temperature dependence of magnetic structure of $Ba_3Co_{1.8}Fe_{24.2}O_{41}$ with neutron diffraction.

2 Experimental

Powder sample of $Ba_3Co_{1.8}Fe_{24.2}O_{41}$ was prepared at 1573 K in oxygen atmosphere by the ceramic method.

High-temperature neutron diffraction patterns of the samples were obtained using HRPD installed at JRR-3 in JAERI. Neutron wavelength was 1.823 Å, monochromized by the Ge(331) reflection. The powder sample was cast in a vanadium folder with 15 mm in diameter. Diffraction patterns in the range of 2θ = 2.5 - 162.5° were measured at various temperatures lower than 773 K in vacuum. Angle step was 0.05° and duration time at each step was 500 sec.

3 Results and discussion

Figure 1 is the closeup of neutron diffraction peaks of 2θ = 19 - 26° at 294 K, 523 K, 573 K and 773 K. These diffraction peaks are mainly attributed to magnetic scattering. The diffraction pattern at 773 K is completely due to nuclear scattering because measurement temperature is higher than its Curie temperature (about 683 K) and magnetic order completely disappears. Comparing peak intensities at 523 K with those at 573 K, peaks due to the reflections from (0010) and (0012) planes rapidly vanish. On the other hand, the peak due to (100) increases. This means that magnetic structure changes in this temperature region. Figure 2 shows the temperature dependence of angles of magnetic moments against c-axis determined from the Rietveld analyses for the neutron diffraction patterns. The angle of magnetic moments turns rapidly from the direction parallel to *c*-plane to *c*-axis in the temperature region from 523 K to 573 K. The property of $Ba_3Co_{1.8}Fe_{24.2}O_{41}$ as *ferroxplana* loses above 523 K.

References

1) T. Tachibana et al., Proceedings of ICF-8, Kyoto and Tokyo, Japan; JSPPM (2000) 888-890.
2) T. Tachibana et al., J. Magn. Magn. Mater. 262 (2003) 248-257.
3) T. Nakagawa et al., J. Am. Ceram. Soc. Jpn. (Submitted).

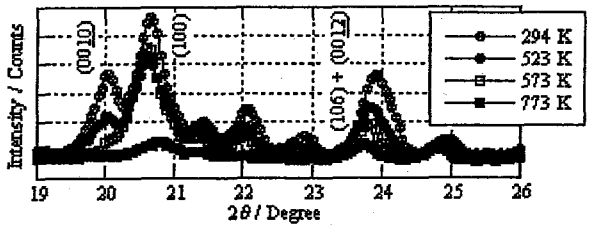

Figure 1: Neutron diffraction patterns of $Ba_3Co_{1.8}Fe_{24.2}O_{41}$ at 2θ = 19 - 26° at 294 K, 523 K, 573 K and 773 K.

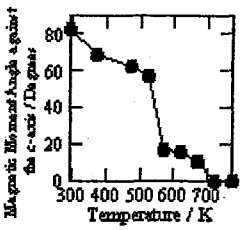

Figure 2: Temperature dependence of angles of magnetic moments against c-axis.

原子炉：JRR-3　　装置：HRPD(1G)　　分野：中性子散乱（磁性）

研究テーマ：特異な原子価状態におけるフラストレーション系の研究２
表題： $GeCo_2O_4$における高スピン状態ー低スピン状態移転

1-2-12 High spin -low spin state transition in $GeCo_2O_4$

K. Kamazawa, I. Kagomiya, S. Park*, T. J. Sato*,and S. -H. Lee*.

Advanced Research Institute for Science and Engineering, Waseda Univ., 3-4-1 Ohkubo, Shinjuku-ku, Tokyo 169-8555, Japan
**NIST Center for Neutron Research, 100 Bureau Drive, Stop 8562 Gaithersburg, MD 20899-8562.*

Previous authors have researched $GeCo_2O_4$ normal spinel. However, some behaviors are still unclarified. Magnetic behavior obtained from powder neutron diffraction indicates a 2D character, though the cubic $GeCo_2O_4$ is a true 3D compound [1]. A spin value estimated from magnetic susceptibility at high temperature shows S=3/2 [1], while hyperfine field of Fe^{2+} in $GeCo_2O_4$ indicates the spin value S=1/2 at low temperature [2]. In addition, the 1/2 1/2 1/2 reflection is stronger than the 3/2 1/2 1/2 and 3/2 3/2 1/2 reflections, and magnetic diffuse scattering is accompanied around only the former reflection. In the present report, neutron scattering results with a large single crystal are summarized. The measurement was performed using High-Q-Resolution triple axis spectrometer installed at T1 thermal guide at JAERI. Fig.1 shows temperature dependences of the 002 reflection which is forbidden in spinel structure. The 002 reflection is usually observed in spinels, because oxygen is large and oxygens which surround the A-site spread out to the <111> direction, and the B-sites distort torigonalally to the <111> direction. However, though ion of the A-site is small and *u*-parameter of Ge-spinel is said to be *u*=0.375, ion of the B-site is anomalously large and local lattice distortion becomes larger than any other spinels. Actually, the 110 reflection which isn't seen in usual spinel is observed as sample mosaic in every Ge-spinel single crystal [4]. That is, $GeCo_2O_4$ is locally distorted from high temperature. To down the crystal field energy, high-spin (S=3/2) to low-spin state (S=1/2) transition occur at T_N=21K, and local distortion becomes larger. The transition is observed as temperature variations of the sample mosaic at all nuclear Bragg peak points. The occurrence of the 2D character is reasonable phenomenon due to a local arrangement of Ge-spinel structure. The strength of antiferromagnetic peaks can explain the structure factor of nearest neighbor interaction [3]. The fluctuation and details are published in Ref.[4].

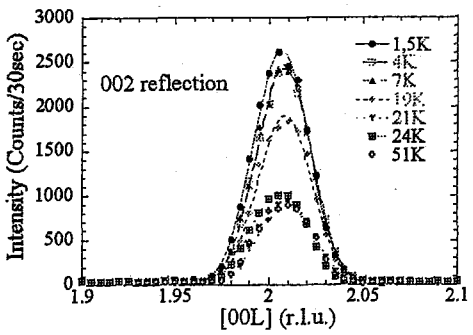

Fig. 1: Temperature dependences of the 002 reflection for $GeCo_2O_4$ single crystal.

Acknowledgement

K. K. would like to thank Prof. Y. Tsunoda for his support as the research representative for the neutron scattering measurement applications of office procedure.

References

[1] J. Hubsch, J. Magn. Magn. Mat. 66, (1987) 17
[2] F. Varret *et. al.*, J. Phys. Chem. Solids, 35 (1974) 215
[3] Y. Yamada *et. al.*, Phys. Rev. B 66, 064401 (2002)
[4] Kamazawa *et. al.*, unpublished.

使用施設：JRR-3M，装置：HQR(T1-1)，分野 Magnetism

研究テーマ：ランタノイドとイリジウムを含む複合酸化物の磁気構造
表　題：トリプルペロブスカイト $Ba_3Fe_2ReO_9$ の磁気構造

1-2-13

Crystal and Magnetic Structures of Triple Perovskite $Ba_3Fe_2ReO_9$

M. Wakeshima, K. Yamamura, Y. Hinatsu, N. Igawa[1], and Y. Ishii[1]

Division of Chemistry, Graduate School of Science, Hokkaido University, Sapporo 060-0810
[1]NSRC, JAERI, Tokai, Ibaraki 319-1195

The crystal structure and magnetic properties of the triple-perovskite type compound $Ba_3Fe_2ReO_9$ were investigated. Through magnetic susceptibility measurements, this compound showed complicated magnetic behavior below 450 K. The Mössbauer spectrum measurements indicated that a half of the Fe ions showed the magnetic ordering below 450 K and the other half of Fe ions did below 320 K. In order to elucidate these behaviors, powder neutron measurements were performed at 10 K and 300 K with a High Resolution Powder Diffractometer (HRPD) in the JRR-3M reactor with a neutron incident wave length (λ = 1.82268 Å).

Neutron diffraction profile measured at 300 K shows that $Ba_3Fe_2ReO_9$ crystalizes in the 6H-perovskite type structure (stacking sequence hcchcc) with space group $P6_3/mmc$. Figure 1(a) is illustrated the crystal structure of $Ba_3Fe_2ReO_9$. The structure consists of dimers of face-sharing octahedra separated by single corner sharing octahedra. By the Rietveld analysis, it was revealed that the Fe ions occupy the single corner site, and that the Re and Fe ions occupy the dimer sites randomly in the ratio of 1:1.

In the data collected at 10 K (Fig. 2), no additional peaks are observed and the clear enhancement of peak intensities is recognized. This result means that the magnetic unit cell is equal to the nuclear unit cell. The magnetic structure of $Ba_3Fe_2ReO_9$ was determined by the Rietveld analysis. The two octahedral transition metal sites (single corner and dimer sites) were allowed to have different magnetic moments.

The magnetic structure at 10 K is illustrated in Fig. 1(b). In this figure, only the magnetic moment of the Fe^{3+} ion is extracted. In the dimer sites, the magnetic moments of Fe^{3+} are coupled antiferromagnetically. The magnetic copling between the single corner and dimer sites is also antiferromagnetic. The direction of the magnetic moments is along the c axis. The ordered magnetic moments are listed in Table 1. These magnetic ordered moments are considerably smaller than theoretical one ($gS = 5\mu_B$) of the Fe^{3+} ions. From this result, it is suggested that the randomness of the Fe and Re ions in the dimer sites leads to the frustrations between the magnetic coplings such as a spin-glass.

Table 1: Ordered magnetic moments (μ_B) of $Ba_3Fe_2ReO_9$.

	dimer	corner
10 K	2.88(4)	2.67(7)
300 K	2.82(5)	2.53(8)

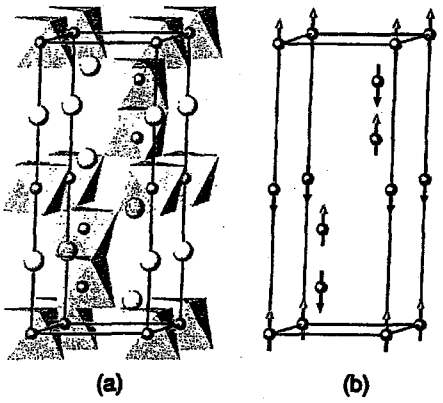

Figure 1: (a) Crystal structure of $Ba_3Fe_2ReO_9$; (b) Magnetic structure of $Ba_3Fe_2ReO_9$ at 10 K.

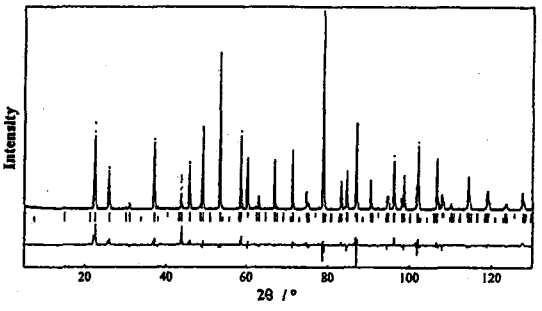

Figure 2: Neutron diffraction profile at 10 K of $Ba_3Fe_2ReO_9$.

原子炉：JRR-3　　装置：HRPD(1G)　　分野：中性子散乱（磁性）

研究テーマ：$ZnCr_2O_4$の中性子散乱
表題：$ZnCr_2O_4$の磁気散乱における磁場冷却効果

1-2-14 Field Cooling Effect in Magnetic Neutron Scattering of $ZnCr_2O_4$ Crystal IV

I. Kagomiya, A. Hatanaka[1], H.Yanagihara[1], K. Kohn, K. Nakajima[2], E. Kita[1], K.Kakurai[2] and K. Siratori[3]

Department of Physics, Waseda University, 3 Shinjyuku-ku, Tokyo 169-8555, Japan
[1]Institute of Applied Physics, Tsukuba University, Tsukuba, Ibaraki 305-8573, Japan
[2]Advanced Science Research Center Japan Atomic Energy Institute, Ibaraki 319-1195, Japan
[3]Hosei University, Koganei, Tokyo 184-8584, Japan

A cubic normal spinel $ZnCr_2O_4$ is considered as a typical example of geometrically frustrated spin systems. This crystal has a first-order magnetic transformation at about 12 (±1) K. The magnetic structure below this temperature has not been determined yet and that is the aim of our study.

As was stated in the previous report,[1] magnetic Bragg reflections appear below T_N at (h, k, $l/2$) and (h, $k/2$, $l/2$), on the basis of the chemical unit cell, with an extinction rule: present only when $h + k = 2n + 1$, for the former. We have concluded that the magnetic unit cell is composed of 8 chemical cells, (2×2×2), containing 128 Cr^{3+} ions. This cell dimension seems too large to determine the magnetic structure by powder diffraction data.

The crystal undergoes a lattice deformation, to the tetragonal (or the orthorhombic), below the magnetic transition point. The lattice constant along the c axis was reported to be slightly, the order of 1/1000, smaller compared with that along the a axis. Moreover, magnetic cooling along the 〈111〉 axes affects the intensity of magnetic reflections, as was described in the previous report. Thus, the magnetic symmetry of the ordered phase of $ZnCr_2O_4$ is monoclinic or lower and there are 12 kinds of magnetic domains, at least. For the determination of the magnetic structure, elimination of the magnetic domains is indispensable.

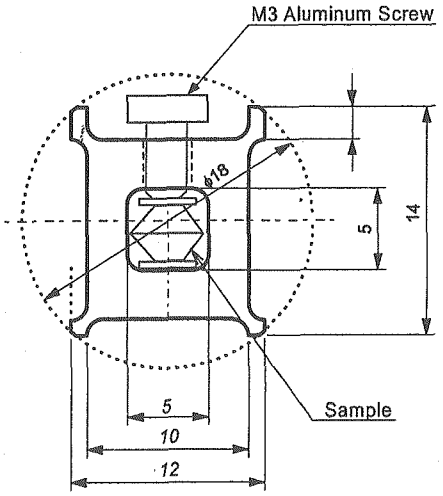

Fig.1. An aluminum sample holder.
Uni-axial pressure was generated by an aluminum screw.

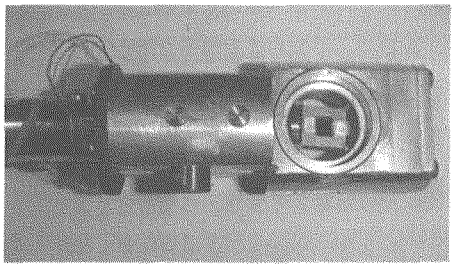

Fig. 2. Sample rotating mechanism.

To make the specimen single-domain, we applied uniaxial pressure along the [001] axis of a single crystal grown with a Bi_2O_3 flux, whose dimension is approximately

使用施設：JRR-3M, 装置：PONTA(5G), 分野 Magnetism

$4 \times 4 \times 4$ mm^3.[3], by an aluminum screw (see Fig. 1). The specimen was set in a sample holder that can rotate around a horizontal axis, with the [110] parallel to the rotation axis. See Fig. 2. A vertical magnetic field of 6 T was applied along the [1 −1 1] axis during cooling of the specimen through the magnetic transition point of about 12 K.

Prior to the magnetic field cooling experiment, we confirmed the pressure dependence of the neutron magnetic diffraction with HQR diffractometer equipped with a closed cycle He refrigerator. The pressured axis was set parallel[100] and perpendicular[001] to the diffraction plane (001). It was found that there were clear differences in diffraction patterns for samples cooled with and without pressure from the Fig. 3.

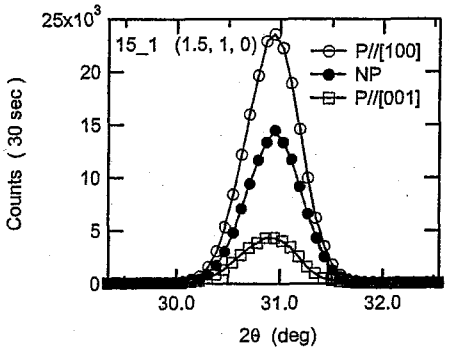

Fig. 3. Pressure dependence of (3/2, 1, 0) magnetic reflections measured with and without(NP) pressure along [100] and [001].

The effect of pressure is different for the direction of pressure. From this result, the uniaxial pressure is confirmed for realizing single domain structure.

Diffraction data at 2.5 K were collected with PONTA diffractometer installed at JRR-3M in JAERI with the incident wavelength of 1.637 Å. Measurements were performed within the (001), (1, -1, 0) and (1, -1, 1) plane. Measured peaks are 35 in total. In Table1, peaks equivalent in the cubic paramagnetic phase are compared.

Very unfortunately, an accident of the reactor, in the last September, prevented us to meåsure the reference data, peak intensities for the case of the specimen cooled without field and stress. Because of the absorption and diffraction of neutrons due to the tools for the compression and rotation, the accuracy of the absolute value of peak intensities is limited. Analysis of the data will be made after the experiment is completed.

References

[1] I. Kagomiya, M. Toki, Y. Hata, K. Kohn, K. Nakajima, E. Kita, K. Kakurai and K. Siratori: this report **9** (2003) 805.

Table 1. Peak intensities of (1, 0, 1/2) magnetic diffractions.

(1, 0, 1/2)			Direction cosine of magnetic field			
			0.26	0.77		
			1	1	average	pressure effect
Direction cosine of pressure	0.	1	3500	5000	4000	1000
	0.45	1	5500	18000	12000	5000
	0.89	1				1500

研究テーマ：先端偏極中性子散乱によるスピン一格子物性の研究
表　題：スピンギャップ系 $TlCuCl_3$ の結晶構造

1-2-15

Crystal Structure of the Spin Gap System $TlCuCl_3$

A. Oosawa, Y. Ishii, K. Kakurai and H. Tanaka[1]

Advanced Science Research Center, JAERI, Tokai, Ibaraki 319-1195
[1]*Res. Cent. for Low Temperature Physics, Tokyo Institute of Technology, Oh-okayama, Meguro-ku, Tokyo 152-8551*

Spin gap system $TlCuCl_3$ has been attracting much interest because this system shows the various quantum phase transitions. It has been reported that this system crystallizes in a monoclinic structure which belongs to the space group $P2_1/c$ [1]. However, in the recent neutron diffraction experiments for single crystal $TlCuCl_3$, the very weak nuclear reflections were observed for $\boldsymbol{Q} = (h, 0, l)$ with odd l at low temperature, which should be forbidden in the space group $P2_1/c$ [2]. This means that this system may undergo a structural phase transition to lower symmetry at low temperature. In order to investigate the crystal structures at low temperature, we carried out the neutron powder diffraction experiments.

The preparation of single crystals of $TlCuCl_3$ has been reported in ref. 3. $TlCuCl_3$ powder was obtained by grinding up the single crystals using the agate mortar with pestle in atmosphere for approximately ten minutes. The neutron powder diffraction patterns were measured on HRPD installed at JRR-3 in JAERI. The obtained diffraction patterns were analyzed by Rietveld method using RIETAN-2000 [4].

The obtained neutron powder diffraction patterns of $TlCuCl_3$ for $T = 10$ and 297 K are shown in the figure. From the Rietveld refinements, it was found that the obtained patterns for $T = 10$ and 297 K can be reproduced by the crystallographic parameters, as shown in the table, with the space group $P2_1/c$, as denoted by the thick lines in the figure. This means that $TlCuCl_3$ has no structural phase transition, thus we infer that the observed nuclear peaks for odd l in the single crystal neutron diffraction experiments was not due to the intrinsic structural phase transitions to lower symmetries, but due to the extrinsic effects, such as impurities and lattice defects. It was also found that the obtained patterns include the lines of a little amount of $CuCl_2 \cdot 2H_2O$ and $CuCl_2$, which may be due to the deliquescence by the grinding in atmosphere. It is noted that the isotropic displacement parameters B have large values for $T = 297$ K, which is consistent with the X-ray powder diffraction experiments in related system $KCuCl_3$ [5]. It is unusual and may be related to the anomalous spin-lattice correlations in this system [6].

References

1) K. Takatsu, W. Shiramura and H. Tanaka: J. Phys. Soc. Jpn. **66** (1997) 1611.
2) H. Tanaka, A. Oosawa, T. Kato, H. Uekusa, Y. Ohashi, K. Kakurai and A. Hoser: J. Phys. Soc. Jpn. **70** (2001) 939.
3) A. Oosawa, M. Ishii and H. Tanaka: J. Phys.: Condens. Matter **11** (1999) 265.
4) F.Izumi and T.Ikeda:Mater.Sci.Forum **321-324** (2001) 538.
5) M. Hanawa, Y. Ohishi and Y. Moritomo: private communications.
6) A. Oosawa, K. Kakurai and H. Tanaka: see in this JAERI-Review.

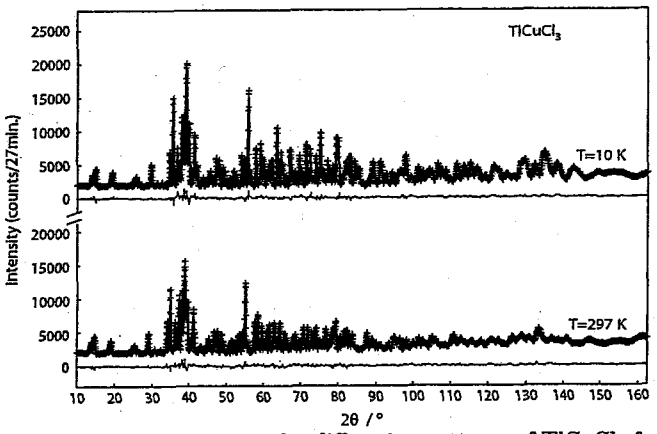

Upper figure: Neutron powder diffraction patterns of $TlCuCl_3$ for $T = 10$ K and 297 K. The thick and thin lines denote the calculated pattern and the difference between the observed pattern and the calculated that, respectively. Right table: Crystallographic parameters of $TlCuCl_3$ obtained by Rietveld refinements.

● $T = 10$ K

$$\begin{cases} a = 3.9207\text{Å}, b = 14.050\text{Å}, c = 8.7907\text{Å} \\ \alpha = 90°, \beta = 95.608°, c = 90° \end{cases}$$

	x	y	z	$B(\text{Å}^2)$
Tl	0.779	0.170	0.554	0.308
Cu	0.236	0.050	0.158	0.359
Cl(1)	0.272	0.195	0.262	0.389
Cl(2)	0.679	-0.006	0.319	0.458
Cl(3)	-0.181	0.097	-0.036	0.334

● $T = 297$ K

$$\begin{cases} a = 3.9755\text{Å}, b = 14.137\text{Å}, c = 8.8656\text{Å} \\ \alpha = 90°, \beta = 96.399°, c = 90° \end{cases}$$

	x	y	z	$B(\text{Å}^2)$
Tl	0.776	0.170	0.553	2.194
Cu	0.241	0.051	0.150	1.254
Cl(1)	0.265	0.194	0.263	1.561
Cl(2)	0.678	-0.007	0.318	1.253
Cl(3)	-0.179	0.097	-0.035	1.350

原子炉：JRR-3　　装置：HRPD(1G)　　分野：中性子散乱（磁性）

研究テーマ:直交ダイマー系 $SrCu_2(BO_3)_2$ の圧力効果
表題:直交ダイマー系 $SrCu_2(BO_3)_2$ における量子相転移の観測

1-2-16 Study of Pressure Effect on the Ground State Properties of $SrCu_2(BO_3)_2$

H. Kageyama,[1] M. Nishi,[2] A. Lappas,[3] N. Aso,[2] K. Kakurai,[4] Y. Ueda[2]

[1]*Department of Chemistry, Graduate School of Science, Kyoto University, Kyoto 606-8502*
[2]*Institute for Solid State Physics, The University of Tokyo, 277-8582*
[3]*FORTH-IESL, Vassilika Vouton, PO Box 1527, Heraklion711-10, Crete, Greece*
[4]*Advanced Science Research Center, JAERI, Tokai, Ibaraki 319-1195*

The layered oxide $SrCu_2(BO_3)_2$ has a magnetic network, which is topologically equivalent to that conceived by Shastry and Sutherland nearly two decades ago. Experimental studies on this material revealed exotic magnetic properties including exact dimer ground state with a gap of 34 K in the spin-excitation spectrum, quantized magnetization plateaux at 1/3, 1/4 and 1/8 of the Cu full moment [1]. Our neutron scattering provided the direct evidence that a one-triplet excitation is almost localized due to the orthogonality of neighboring dimers in the Shastry-Sutherland lattice [2, 3], while later neutron experiment shows that the DM interaction makes the triplet excitation dispersive to some extent [4].

This material is theoretically believed to be very close to the quantum phase baundaries to the ordered state and plaquette singlet state, see Fig. 1 [5]. Thus the application of pressure may modify the exchang coupling constant, leading to a phase transition. In fact, the magnetic susceptibility show the tendency that the spin gap decreases with increasing pressure.

With a hope to induce phase transition to the antiferromagnetic state, we performed neutron diffraction measurement using a clamping type pressure cell made by Al_2O_3, which yields as much as 25 kbar. The experiment was curried out on ISSP-PONTA spectrometer installed at 5G beam port of the Japan Research Reactor 3M (JRR-3M) in Japan Atomic Energy Research Institute, Tokai establishment. Several pieces of single crystals of high quality were used, and the reciprocal lattices of (h,h,l) and (h,k,0) were investigated extensively. Unfortunately, we could not detect any trace of magnetic peaks. It may be that this material is still in a dimer-singlet state even at 25 kbar, or the new phase is the plaquette singlet phase. Even if the material is in the ordered phase, a big amount of neutron absorption from the pressure cell might hinder from observing magnetic peaks from the specimen. Improvement of pressure cell might be encouraged.

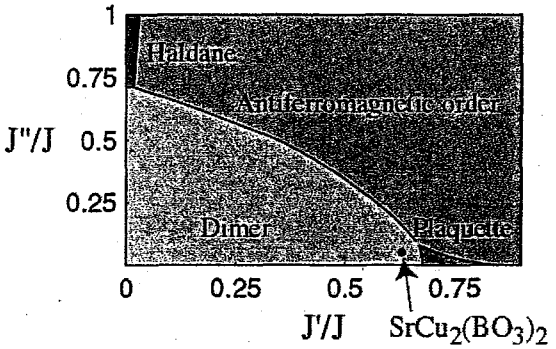

Figure 1: The theoretical phase diagram for the Shastry-Sutherland model proposed by Koga [5].

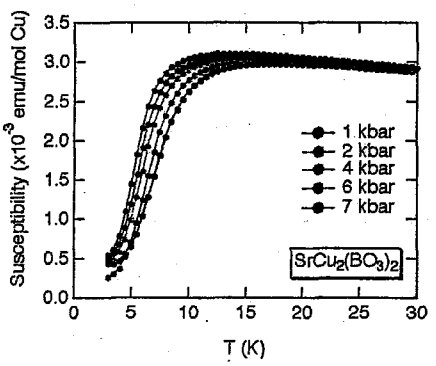

Figure 2: Magnetic susceptibility of $SrCu_2(BO_3)_2$ under high pressures [6].

References

[1] H. Kageyama et al., Phys. Rev. Lett. **82** (1999) 3168.
[2] H. Kageyama et al., Phys. Rev. Lett. **84** (2000) 5876.
[4] N. Aso et al., J. Phys. Soc. Jpn. **71** Suppl. A, (2001) 177.
[4] O. Cepas et al., Phys. Rev. Lett. **87** (2001) 167205.
[5] A. Koga, J. Phys. Soc. Jpn. **69** (2000) 3509.
[6] H. Kageyama et al., Physica B **329** (2003) 1020.

使用施設:JRR-3M, 装置:PONTA(5G), 分野 low-dimensional magnetism

研究テーマ：先端偏極中性子散乱によるスピン－格子物性の研究
表　題：先端偏極中性子解析装置 CRYOPAD の基本性能

1-2-17

CRYOPAD on the Triple-axis Spectrometer TAS-1 for Spherical Polarimetry

M. Takeda, M. Nakamura, Y. Shimojo, K. Kakurai, E. Lelièvre-Berna[1], F. Tasset[1] and L. -P. Regnault[2]

Advanced Science Research Center, Japan Atomic Energy Research Institute, 2-4 Shirakata Shirane, Tokai, Naka, Ibaraki, 319-1195 Japan

[1] *Institut Laue-Langevin, 6 rue Jules Horowitz BP 156 - 38042 Grenoble Cedex 9, France*

[2] *CEA-Grenoble, Département de Recherche Fondamentale sur la Matière Condensée, SPSMS-MDN, F-38054 Grenoble Cedex 9, France*

CRYOPAD (CRYOgenic Polarization Analysis Device) is a novel instrument which makes it possible to measure the spherical changes of neutron-spin polarization in the scattering processes of magnetic materials[1-3]. ILL and CEA-Grenoble, in the framework of EC/ENPI, and JAERI, in the framework of the MoU between ILL and ASRC JAERI, have designed and assembled three third generation CRYOPADs at ILL (CRYOPADUM project), optimized both for elastic and inelastic neutron scattering. One is installed on the ILL instrument D3 (Millennium Project) and the other on the CEA-Grenoble instrument IN22. The JAERI CRYOPAD has been successfully installed on the triple-axis spectrometer TAS-1 at JRR-3 in this fiscal year.

CRYOPAD consists of a couple of Nb Meissner screens and a hybrid precession torus (HPT) which has two independent hybrid precession coils: HPC_in and HPC_out. In order to cool the Nb screens into the superconducting state the screens are attached to the bottom of liquid He bath of cryostat as a concentric circle. In a normal operation on TAS-1 typical liquid-He-consumption rate is 12 % (= 2 ℓ) a day. Autonomy is more than one week. The two Nb magnetic shields screen the stray fields of the HPT and an earth-magnetic-field. The residual magnetic fields are less than 0.3 (nT) inside the sample chamber where the measurements of spin rotation can be performed with the accuracy of 0.5 deg for 14.7 meV neutrons.

HPC_in controls rotation of the incident beam polarisation vector around the horizontal axis, perpendicular to the wave vector, $\vec{k_i}$, and HPC_out that of scattered neutrons around the axis perpendicular to $\vec{k_f}$. The fields produced by the two coils are decoupled by the Nb screens and a Nb frame surrounding the yoke of HPC_in coil to control the spin rotation of incident and scattered neutrons independently. In addition to the HPT, nutators at just outside the outer Nb screen control the direction of polarization vector in the plane perpendicular to $\vec{k_i}$ and $\vec{k_f}$. The combination of the HPT and nutators enables to perform spherical polarization analysis.

The neutron-spin control has been checked by using PG(004) Bragg reflection, whose scattering angle is almost equal to 90.0 deg for 14.7 meV neutrons as shown in Fig. 1. The results are summarized in Table 1 associated with expected values of the final polarization. The deviation from 1 or 0 stems from the instrumental imperfection such as incomplete polarization and uncontrolled rotation due to the residual field. Anyway the off-diagonal terms are negligibly small. This indicates that we can spherically control the neutron spin as desired and that the door to a new world of research on magnetism is now open at JAERI.

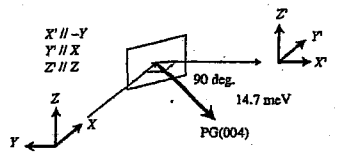

Figure 1: Experimental set-up for checking spin handling by combination of the nutators and HPCs (HPC_in and HPC_out).

Table 1: Directions of polarization of incident beam (In), direction to be analyzed (Detection), measured final polarization (P_f), and expected final polarization.

In	Detection	P_f	
		(measured)	(expected)
Z	Y' (// +X)	-0.031 ± 0.010	0.0
Z	X' (// -Y)	-0.021 ± 0.012	0.0
Z	Z' (// +Z)	0.910 ± 0.003	1.0
Y	Y' (// +X)	0.003 ± 0.002	0.0
Y	X' (// -Y)	-0.915 ± 0.003	-1.0
Y	Z' (// +Z)	0.021 ± 0.010	0.0
X	Y' (// +X)	0.919 ± 0.003	1.0
X	X' (// -Y)	-0.008 ± 0.006	0.0
X	Z' (// +Z)	0.017 ± 0.012	0.0

We are much indebted to N. Kernavanois, E. Bourgeat-Lami, S. Pujol and X. Tonon for their assistance in assembling CRYOPAD at ILL.

References

1) F. Tasset, Physica B 156-157 (1989) 627.
2) F. Tasset, P. J. Brown, E. Lelièvre-Berna, T. Roberts, S. Pujol, J. Allibon, E. Bourgeat-Lami, Physica B 267-268 (1999) 69.
3) L. P. Regnault, B. Geffray, P. Fouilloux, B. Longuet, F. Mantegezza, F. Tasset, E. Lelièvre-Berna, E. Bourgeat-Lami, M. Thomas, Y. Gibert, Phisca B 335 (2003) 255.

原子炉：JRR-3　　装置：TAS-1(2G)　　分野：中性子散乱（磁性）

研究テーマ:熱中性子三軸スピンエコー実験方法の開発
表題:スピンエコー法によるイジング型パーコレーション磁性体の動的臨界現象の研究
1-2-18

Neutron spin echo study on the critical spin dynamics in the percolating Ising magnet

S. Itoh, K. Iwasa[1], K. Kakurai[2], M. Nishi[3] and K. Nakajima[2]

High Energy Accelerator Research Organization, Tsukuba, 305-0801; [1]Tokyo Metropolitan University, Hachioji, 192-0397; [2]Japan Atomic Energy Research Institute, Tokai, 319-1195; [3]University of Tokyo, Tokai, 319-1106

The two-dimensional (2D) antiferro-magnet, Rb_2CoF_4, has been reported to be well described by the 2D Ising model, and it has been experimentally confirmed that its critical dynamics obeys the dynamical scaling, $\Gamma = \kappa^z$, where Γ is the damping constant, κ is the inverse correlation length, and z is the dynamical critical exponent [1]. On the other hand, recent theoretical developments have revealed that the critical dynamics in a percolating 2D Ising system does not obey the standard dynamical scaling. The spin dynamics is determined by thermal activation over energy barriers resulting from the non-uniform geometry of the percolating network. As the result, the damping constant, $\Gamma(T)$ drops faster than any power of $\kappa(T)$ with decreasing the temperature (T), or, in terms of the dynamical scaling, the effective dynamical exponent diverges at the critical point [2].

Previously, in order to investigate the critical spin dynamics in the percolation system, we measured inelastic neutron scattering from the percolating 2D Ising antiferromagnet, $Rb_2Co_{0.6}Mg_{0.4}F_4$, with the magnetic concentration very close to the percolation threshold (c_p=0.593), on the IRIS spectrometer at ISIS [3]. The energy resolution was 4 μeV on IRIS. We found that the observed $\Gamma(T)$ (width of the quasi elastic spectrum) was well described by the percolation theory as shown in Fig.1 (a).

At present, we performd neutron spin echo experiments to measure $\Gamma(T)$ in $Rb_2Co_{0.6}Mg_{0.4}F_4$ (T_N=23K) on the PONTA spectrometer installed at the 5G port at JRR3M in JAERI (Tokai). Figure 1 (b) shows the Fourier time dependence of the NSE signal (corrected by the instrumental polarization), $P_{NSE}(t)$, measured at T = 43 K and 62 K. The damping constant was determined by fitting P_{NSE} (t) to exp(-Γt), and the obtained values were plotted in Fig. 1 (a). The present result is in a good agreement with that on IRIS.

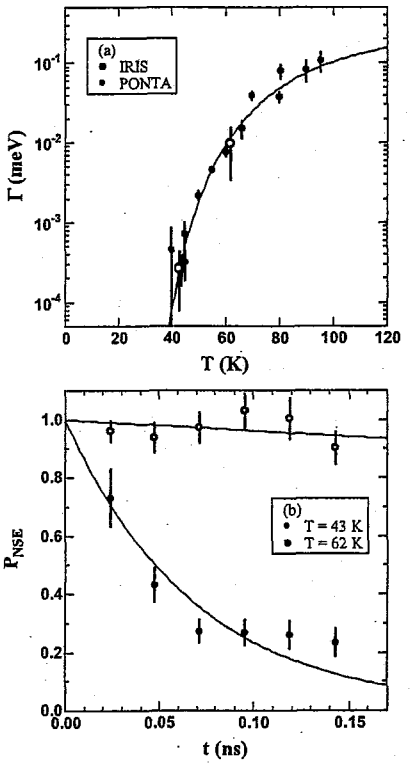

Figure 1: Critical spin dynamics in $Rb_2Co_{0.6}Mg_{0.4}F_4$, (a) the damping constant $\Gamma(T)$, and (b) the NSE signal at T = 43 K and 62 K. The solid line in (a) is the theoretical curve and those in (b) are the fitted curves.

References

[1] M. T. Hatchings et al., Phys. Rev. Lett 49 (1982) 386.
[2] C. L. Henley, Phys. Rev. Lett. 54 (1985) 2030.
[3] S. Itoh et al., J. Phys. Soc. Jpn 70 (2001) 3107.

使用施設:JRR-3M, 装置: PONTA(5G), 分野 Magnetism

研究テーマ：Ce 化合物強相関伝導系における特異な磁気相
表　題：CeP の圧力下における強磁性の研究

1-2-19

Study of Ferromagnetism of CeP under High Pressure

D. Kawana, T. Osakabe[1], A. Hannan, M. Kohgi

Department of Physics, Tokyo Metropolitan University, Hachioji, Tokyo 192-0397
[1]Advanced Science Research Center, JAERI, Tokai, Ibaraki 319-1195

CeP shows unusual properties due to its very low carrier density (0.01/f.u.) [1]. Its magnetic properties under high pressures are especially interesting. Above about 0.5 GPa it showes complex magnetic structures composed of double layers of ferromagnetic Ce(001)-plane with a large moment value of about 2 μ_B sandwitching the type-I antiferromagnetic structure of Γ_7 Ce ions at low temperatures [2]. Above about 10 K (T_{C1}) the Γ_7 Ce layers become paramagnetic, while the ferromegnetic double layers keep ordering up to the upper critical temperature T_{C2}. The period of the structure decreases from 9 to 4 Ce-layers with increasing pressure up to about 1.7 GPa. The magnetic structures around 2 GPa are similar to those of CeSb and CeBi at ambient pressure. The resistivity measurement [3] indicates that T_{C2} becomes maximum ($\sim$ 50 K) at about 3 GPa. Above the pressure, T_{C2} decrease with increasing pressure and disappeares at about 6 GPa. The above facts indicate that the $4f$ electron state of CeP shows a drastic chage from a localized state to a non-magnetic itinerant one in the pressure range 0 - 6 GPa. In order to investigate this process from the microscopic point of view , we study the compound by means of neutron diffraction technique under high pressures. From the previous experimental results, it was revealed that, in the pressure range between 2.5 and 2.8GPa, a ferromagnetic phase appears at low temperatures below around 30 K, while another phase, 3* ($\uparrow\uparrow \circ \downarrow\downarrow \circ$), appears above this temperature [4]. It was also revealed that only a ferromagnetic phase exists at low temperatures under a pressure above about 3.2 GPa. [5] In order to extend the study of the pressure dependence of the feromagnetic state of CeP at higher pressures, we performed an experiment at the triple-axis-spectrometer TAS-1(2G) installed at JRR-3 reactor, JAERI. To apply a pressure on the sample, we used a sapphire anvil cell. The sample of 0.3 × 0.2 × 0.08 mm^3 was set in a hole of phosphorous bronze gasket, with a little ammount of ruby powder for pressure calibration and Daphne7373 as pressure transmitting medium. We observed a temperature dependence of the peak intensity of 200 Bragg peak, where a ferromagnetic component is superimposed on the nuclear Bragg scattering, at 3.9 GPa. With decreasing temperature, the peak intensity increases at about 40 K. However, due to low counting statistics, an accurate determination of the transition temperature is difficult as shown in Fig. 1. However, the saturation moment of the ferromagnetic state at the lowest temperature is estimated to be 1.3±0.3 μ_B by comparing the integrated intensity of the peak at 1.5 K with that at 55 K. This value is rather small compared to the magnetic moment of a fully polarized Ce^{3+} ion (2.14 μ_B). The present results is consistent with the view point that the the $4f$ electron state of CeP approaches to a delocalized state at presures above 3 GPa. However, more accurate estimation of T_{C2} and saturation moment is required for the detailed discussion of the interesting phenomena of CeP though the experimental limitation is quite severe for a neutron diffraction experiment in such a high pressure region.

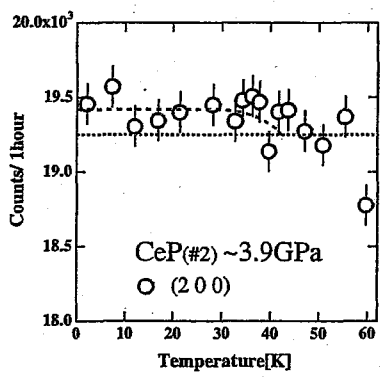

Figure 1: Temperature dependence of peak intensity of 200 peak of CeP at 3.9 GPa.

References

1) T. Suzuki *et al.*: Physica B, **186-188** (1993) 347.
2) M. Kohgi *et al.*: Physica B, **281-282** (2000) 417.
3) N. Môri *et al.*: Physcal Properties of Actinde and Rare Earth Compounds JJAP Series **8** (1993) 182.
4) A. Hannan *et al.*: Applied Phys A, **74** (2002) S565.
5) D. Kawana, Master Thesis (2004, Tokyo Metropolitan University)

原子炉：JRR-3　　装置：TAS-1(2G)　　分野：中性子散乱（磁性）

研究テーマ：三次元ハイゼンベルグ型パーコレーション磁性体の臨界散乱

表題：ハイゼンベルグ型パーコレーション磁性体 $RbMn_{0.31}Mg_{0.69}F_3$ の臨界スピン動特性

1-2-20

Critical spin dynamics in Heisenberg percolating antiferromagnet, $RbMn_{0.31}Mg_{0.69}F_3$

S. Itoh, K. Iwasa[A], R. Kajimoto[B], M. J. Bull[C], N. Aso[D] and M. A. Adams[C]

High Energy Accelerator Research Organization, Tsukuba; [A]Tohoku University, Sendai; [B]Japan Atomic Energy Research Institute, Tokai; [C]Rutherford Appleton Laboratory, UK; [D]Institute for Solid State Physics, The University of Tokyo, Tokai

We investigated the critical spin dynamics in $RbMn_{0.31}Mg_{0.69}F_3$, the three-dimensional Heisenberg percolating antiferromagnetic system, of which magnetic concentration is very close to the percolation concentration for a cubic lattice (c_P=0.312). The temperature (T) dependence of the static magnetic correlation function was measured with the double axis mode on the triple axis spectrometer, GPTAS. The incident energy was chosen to be 13.6 meV and the collimation was mainly 40'-10'-10'. The resolution was measured to be 0.006 rlu (FWHM) for the longitudinal direction, and 0.005 rlu for the transverse direction. The scan was performed along the longitudinal direction at around the magnetic superlattice point (1/2, 1/2, 1/2). A single-crystal sample was mounted on the dilution refrigerator, and the experiments were performed at T = 25 mK ~ 3 K, and the background signal was measured at around 70 K. Also, the static correlation function was measured on the crystal analyzer spectrometer, PRISMA, at ISIS, with the diffraction mode, at T = 1.5 ~ 22 K. We determined the T dependence of the inverse magnetic correlation length, $\kappa(T)$, from the static correlation function, as shown in Fig. 1 (a). The observed $\kappa(T)$ was well fitted to $\kappa(T) = \kappa_0 + A|(T - T_N)/T_N|^{\nu}$, and κ_0 = 0.011 rlu, T_N = 4.0 ± 0.5 K and ν = 0.73 ± 0.14 were obtained. We also measured the damping constant of the critical scattering at the superlattice point (1/2, 1/2, 1/2) on the high energy resolution spectrometer, IRIS at ISIS (energy resolution: 15 μeV). As shown in Fig. 1 (b), the T dependence of the damping constant, was fitted to $\Gamma(T) = C(T-T_N)^y$ with T_N = 4.0 K for T ≥ 10K, and the exponent was determined to be y = 1.42 ± 0.09. Assuming the dynamical scaling, $\Gamma = \kappa^z$, the dynamical critical exponent was determined to be z = 1.9 ± 0.4. The obtained exponents, ν and z, were in agreement with those for the homogeneous system, $RbMnF_3$, where ν = 0.701 ± 0.011 and z = 1.46 ± 0.13 [1].

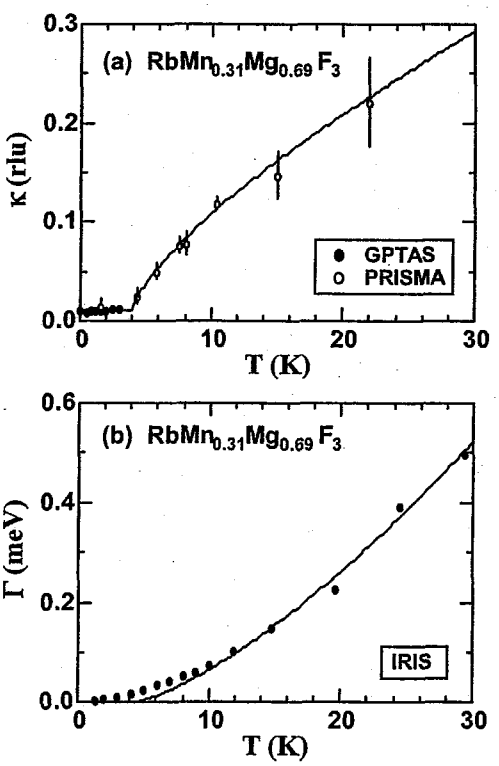

Figure 1: Critical spin dynamics in $RbMn_{0.31}Mg_{0.69}F_3$. The sold lines are the fitted curves.

References

[1] A. Tucciarone et al., Phys. Rev. B **4** (1971) 3206.

使用施設：JRR-3M, 装置：GPTAS(4G), 分野 Magnetism

研究テーマ：Ni 置換した希薄ホールドープ $La_{2-x}Sr_xCuO_4$ における反強磁性
表　題：希薄ホールドープ $La_{2-x}Sr_xCuO_4$ の反強磁性状態における Ni 不純物効果
1-2-21

Ni impurity effects on the antiferromagnetic state in the lightly hole-doped $La_{2-x}Sr_xCuO_4$

H. Hiraka, T. Machi[1], N. Watanabe[1], Y. Itoh[1], M. Matsuda[2] and K. Yamada

Institute for Materials Research, Tohoku University, Sendai 980-8577
[1] *Superconductivity Research Laboratory, International Superconductivity Technology Center, Tokyo 135-0062*
[2] *Advanced Science Research Center, JAERI, Tokai, Ibaraki 319-1195*

La_2CuO_4, the parent material of the monolayer superconductor $La_{2-x}Sr_xCuO_4$ (LSCO), is one of the typical two-dimensional antiferromagnet. It is well known that the Néel temperature T_N ($\sim$ 320 K) is very sensitive to hole doping and the three-dimensional antiferromagnetic order disappears when doped by the amount of 2% Sr. Recent magnetization measurements [1,2], however, indicated that T_N increases by $\sim$ 100 K with Zn- or Ni-substitution in the lightly hole-doped phase of LSCO ($x \sim 0.01$), suggesting strong correlation between the hole motion and the magnetic interaction. In order to clarify the interesting antiferromagnetic state directly, magnetic neutron study using single crystals is highly desirable.

Neutron diffraction measurements were carried out on the triple-axis spectrometer TAS-2, which is installed at the beam port T2-4 of JRR3M in JAERI (Tokai). Thermal neutron beam (E_i = 13.5 meV) was selected by the monochromator of PG(002) reflection. $La_{2-x}Sr_xCu_{1-y}Ni_yO_4$ single crystals of $x = 0.01$ and $0.01 \leq y \leq 0.10$ were grown by the traveling-solvent-floating-zone method, and characterized by magnetization and electrical resistivity measurements. The cylindrical samples with dimensions of about $4\phi \times 20$ mm were set up in the $(h, k, 0)$ or $(h, 0, l)$ scattering plane (*Bmab* notation). We mainly measured magnetic Bragg reflections of $(1, 0, 2n)$, $(0, 1, 2n+1)$ and $(1, 2n, 0)$, where n is integal.

Figure 1 shows the Ni-doping dependence of T_N in the antiferromagnetic phase of LSCO ($x = 0.01$). T_N drastically increases with y and it peaks at $y_{cr} = 0.03 \sim 0.04$, in agreement with magnetic susceptibility measurements. The highest T_N reaches up to $\sim$ 310 K, which is comparable to T_N of La_2CuO_4. Further, we observed that the magnetic-intensity pattern changes across the Ni concentration of y_{cr}. As shown in Fig. 1, it is regarded as a result of spin rotation by 90° in the CuO_2 planes, that is, from S//b-axis (realized in La_2CuO_4, Cu-type) into S//a-axis (realized in La_2NiO_4, Ni-type) with Ni substitution.

The striking recovery of T_N can be explained as a reduction of the magnetic frustration (or the magnetic instability) due to the hole-carrier localization near Ni impurities. This carrier-locaization picture is consistent with the increased resistivity measured for the Ni doped compounds. In our conjecture, the hole carrier is supposed to occupy not the O-2p orbitals but the Ni-3d orbitals in the CuO_2 planes over the low Ni doping. In other words, it results in Ni^{3+} states with $S = 1/2$ for small y. However, further Ni doping will provide Ni^{2+} states because of the finite hole numbers, and finally the magnetic anisotropy associated with $S = 1$ may trigger off the uniform spin rotaion above y_{cr}.

Furhter investigation using neutron scattering techniques is now in progress to clarify this intriguing antiferromagnetic state.

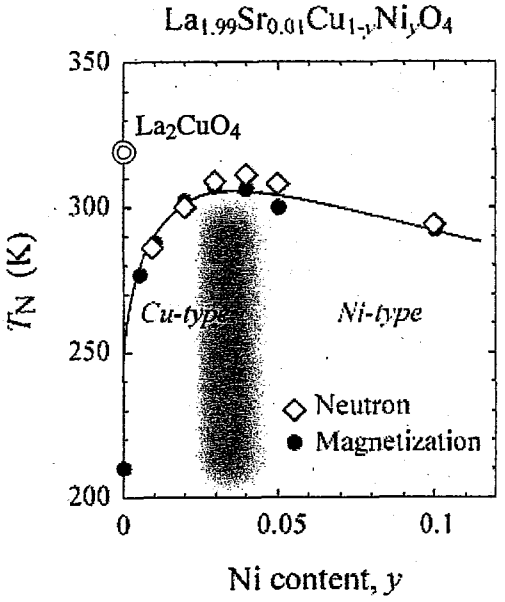

Figure 1: Magnetic phase diagram for Ni doped LSCO (x = 0.01). In the shadow region, a two phase mixture (Cu-type and Ni-type) or a uniform spin rotation ($0 < \phi < 90°$) is expected.

References

1) M. Hücker, V. Kataev, J. Pommer, J. Harras, A. Hosni, C. Pflitsch, R. Gross, and B. Büchner: Phys. Rev. B 59 (1999) R725.
2) T. Machi, I. Kato, R. Hareyama, N. Watanabe, Y. Itoh, N. Koshizuka, S. Arai, and M. Murakami: Physica C 388-389 (2003) 233.

原子炉：JRR-3　　装置：TAS-2(T2-4)　　分野：中性子散乱（磁性）

研究テーマ：hp13 型 RMn_6Sn_6 合金の中性子散乱による研究

表題：hp13 型 RMn_6Sn_6 合金の中性子散乱による研究

1-2-22 Neutron Diffraction Study on $Y_{1-x}Dy_xMn_6Sn_6$ Alloys

T. Hori[1], H. Shiraishi[1], K, Ohoyoama[2] and Y. Yamaguchi[2]

[1]*Shibaura Institute of Technology, Saitama-City, Saitama, 337-8570*

[2]*IMR, Tohoku University, Sendai, Miyagi, 980-8577*

It has been reported that YMn_6Sn_6 alloy with the hp13 type ($MgFe_6Ge_6$ type) layer structure shows an inhomogeneous helical antiferromagnetism with the Néel temperature $T_N = 333$ K and the paramagnetic Curie temperature $\theta_P = 394$ K [1,2]. It should be noticed that Mn atom layers on 6i (1/2, 0, z_2) and (1/2, 0, $-z_2$) sites are well separated by Sn atom layers on 2c (1/3, 2/3, 0), 2d (1/3, 2/3, 1/2) and 2e (0, 0, z_1) sites and Y atom layer on 1a (0, 0, 1/2) site. The magnetic moments of Mn atom are ferromagnetically arrangemed in the same c-plane.

Recently, we have made also similar measurements on YMn_6Sn_6 alloy, and obtained interesting results; the magnetization approaches saturation around 11 T at 77 K [6]. The isotypic alloy $DyMn_6Sn_6$ shows a simple ferrimagnetism with the Curie temperature $T_C = 393$ K and $\theta_P = 138$ K [1,7]. In the present work, we have extended the studies to $Y_{1-x}Dy_xMn_6Sn_6$ alloys, which are found to have the hp13 type structure in whole composition range ($0 \leq x \leq 1.0$).

The magnetic ordering temperature increases linearly with increasing x ($T_N = 333$ K for $x = 0$ and $T_C = 398$ K for $x = 1.0$).

The magnetization for YMn_6Sn_6 alloy reaches the saturation around 13 T; the saturation magnetization corresponds to the ferromagnetic moment of 13.5 μ_B per chemical formula (= 2.3 μ_B per Mn atom). The magnetization for the alloys with $x \leq 0.4$ reaches also the saturation in a field around 5 T. The ferromagnetic moment from the saturated magnetization, μ_F (μ_B / f. u.), decreases linearly with increasing x. It means that the magnetic moments of Mn and Dy atoms, μ_{Mn} and μ_{Dy}, keep constant values for the whole composition range ($0 \leq x \leq 1.0$); $\mu_{Mn} = 2.3\mu_B$ per Mn atom and $\mu_{Dy} = 10\mu_B$ per Dy atom.

We have made neutron diffraction experiments for the $Y_{0.5}Dy_{0.5}Mn_6Sn_6$ alloy at temperatures of between 10 K and 480 K. It has been confirmed from the Rietveld analysis that Sn occupies 2c, 2d and 2e sites with $z_1 = 0.159$, Y and Dy occupy randomly 1a site and Mn occupies 6i sites with $z_2 = 0.253$ at 480 K. The atomic occupancies, z_1 and z_2 are almost independent of the temperatures down to 10 K.

Figure 1 shows the observed and calculated neutron diffraction pattern for the $Y_{0.5}Dy_{0.5}Mn_6Sn_6$ alloy ($x = 0.5$) at 10 K. We have also obtained from the Rietveld analysis of the observed data that all magnetic moments of Mn ($\mu_{Mn} = 2.3\mu_B$ per Mn atom) are ferromagnetic and antiparallel to the magnetic moments of Dy atom ($\mu_{Dy} = 10\ \mu_B$ per Dy atom), and an angle θ between the direction of the magnetic moments and c−axis is 43°.

The magnetic moments of Mn and Dy atoms decreases monotonically with increasing temperature.The angle θ keeps almost constant at temperatures between 10 and 200 K, increases abruptly around 250 K, and finally reachs to 90° at 295K.

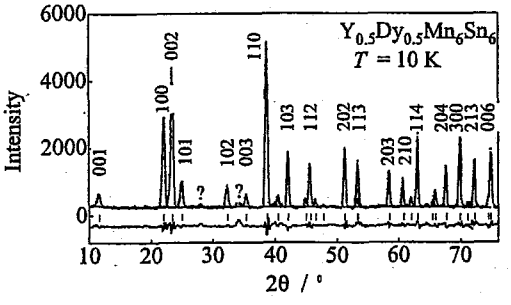

Fig. 1. Observed (+) and calculated (a line) neutron diffraction patterns for $Y_{0.5}Dy_{0.5}Mn_6Sn_6$ at 10 K. The difference between the observed and calculated intensities is shown by the lower curve.

使用施設：JRR-3M, 装置： T1-3 (HERMES), 分野： 2. Magnetism

研究テーマ：高圧下における幾何学的スピンフラストレーション系の研究
表　題：スピンフラストレーション系 $ZnFe_2O_4$ 単結晶の磁気散漫散乱の磁場効果
1-2-23

Magnetic field effects on the diffuse scattering of a spin-frustrated spinel ferrite $ZnFe_2O_4$ single crystal

K. Kamazawa, K. Katano[1] and Y. Tsunoda[2]

Advanced Research Institute for Science and Engineering, Waseda Univ., 3-4-1 Ohkubo, Shinjuku-ku, Tokyo 169-8555, Japan

[1] *Neutron Scattering Group, Advanced Science Research Center, Japan Atomic Energy Research Institute, Tokai, Ibaraki 319-1195, Japan*

[2] *Department of Applied Physics, School of Science and Enginnering, Waseda University, 3-4-1 Ohkubo, Shinjuku-ku, Tokyo 169-8555, Japan*

In the previous paper we reported that magnetic diffuse scattering of neutrons is located along and slightly inside of the first Brillouin zone boundary (BZB) of the FCC structure for a frustrated spinel ferrite $ZnFe_2O_4$ [1]. The intensity distribution of these diffuse scattering was well reproduced by an RPA calculation [2] using a weak ferromagnetic coupling for the nearest neighbor spins and the antiferromagnetic coupling for the third neighbor spins. However, we also found another type of diffuse scattering located around the (4 0 0) and (4 4 0) nuclear Bragg peak positions which are explained by the structure factor of the B-site atoms. These diffuse scatterings indicate the ferromagnetic short range order of the spins at the B-site. We refer to this diffuse scattering as the ferromagnetic diffuse scattering. In order to clarify the details of this ferromagnetic diffuse scattering, we performed neutron scattering measurements on a $ZnFe_2O_4$ single crystal under applied magnetic fields.

In the neutron scattering measurements, we used TAS-2 triple-axis spectrometer installed at the T2 thermal guide of JRR-3M, Tokai, Japan. The incident neutron wave vector was ki = 2.66Å. A pyrolitic graphite (PG) analyzer and a thick PG filter were used. The full-width at the half-maximum (FWHM) of the energy resolution was about 0.8 meV.

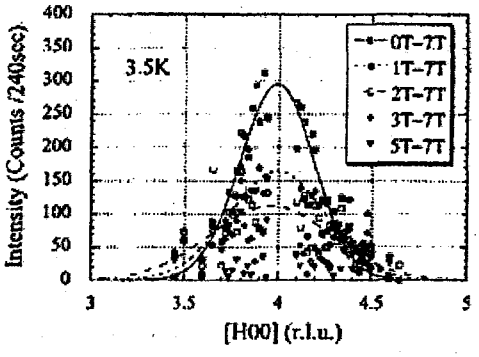

Figure 1: Magnetic field dependences of the elastic diffuse scattering obtained by scanning along the [1 0 0] axes at 3.5 K.

Since diffuse scattering data were taken through the analyzer, the spin fructuations with characteristic time shorter than 10^{-11}s were discarded. Neutron scattering experiments were performed in the cubic (HK0) zone, and magnetic fields were applied in the [0 0 1] direction. Figure 1 shows the line profiles obtained by scanning along the [H 0 0] direction at 3.5K under the magnetic field of 0, 1, 2, 3, 5, and 7T. The intensity of the diffuse peak located around the (4 0 0) nuclear Bragg peak decreases dramatically with increasing magnetic field. On the other hand, the strong diffuse peak around the (3 0 0) RLP, which is an equivalent one to that distributed along the first BZB, does not show appreciable field dependence. This point was confirmed in the measurements of the diffuse peak around the equivalent (1 0 0) RLP. In order to check the localization of this diffuse scattering to a Bragg peak position under the magnetic field, the (4 0 0) Bragg peak intensity was carefully examined under the various fields. However, no evidence of the ferromagnetic longrange order was observed even in the field of 7T. This result is consistent with the DC magnetic susceptibility data which just decrease with increasing magnetic field and shows no anomaly.

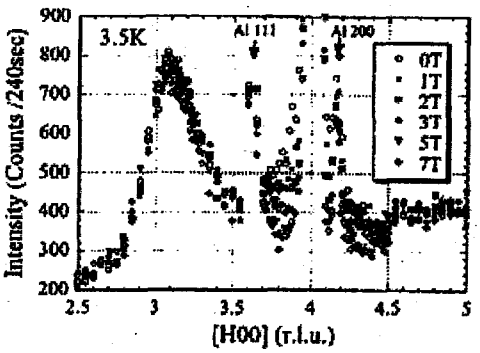

Figure 2: Magnetic diffuse scattering obtained by subtraction of the scan in 7T from that in each magnetic field at 3.5 K.

原子炉：JRR-3　　装置：TAS-2(T2-4)　　分野：中性子散乱（磁性）

Magnetic diffuse scattering intensities obtained by subtraction of the scan in 7T from that in each magnetic field at 3.5K are shown in Fig. 2. It indicates that with increasing the magnetic field the FWHM of the diffuse peak increases with decreasing intensity, suggesting that the ferromagnetic clusters are subdivided into small clusters. These experimental results therefore suggest that the ferromagnetic correlations in $ZnFe_2O_4$ are weakened rather than are strengthened in the magnetic field though it seems to be contrary to the expected sense.

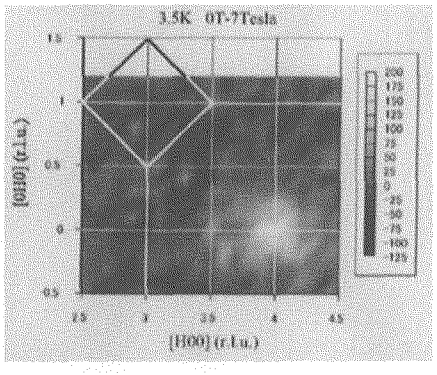

Figure 3: Subtracted contour map around the (4 0 0) Bragg peak position studied at 3.5 K. The solid lines indicate the Brillouin zone boundaries of the FCC structure.

Figure 3 shows the subtracted data (I(H=0T)-I(H=7T)) in an elastic contour map around the (4 0 0) Bragg peak position studied at 3.5 K. Ferromagnetic diffuse scattering distributes almost spherically, indicating that the ferromagnetic spin correlation is isotropic. As described before, the magnetic diffuse scattering around (4 0 0) decreases in magnetic field, however, the scattering around (3 0 0) and along the BZB does not change appreciably in the field. One effect that might be expected under the magnetic field is a change in inelastic scattering which shows very low-frequency dispersion relations in zero magnetic field. We hence studied inelastic scattering energy spectra at the (1.8 0 0) and (3.8 0 0) RLPs under the various magnetic fields at 3.5 K.

The data obtained at the (1.8 0 0) RLP are given in Fig. 4. No appreciable change in the energy spectrum was observed even at 7T. Similar results were obtained at the (3.8 0 0) RLP where the field sensitive ferromagnetic diffuse scattering was observed as an elastic component as shown before. Previously we studied magnetic diffuse scattering of the same normal spinel ferrite $CdFe_2O_4$, using a single crystal specimen. Although the atomic configuration of Fe^{3+} ions in $CdFe_2O_4$ is just the same as that of $ZnFe_2O_4$, the location of the magnetic diffuse peak was completely different [3]. The diffuse peak intensity in the former distributs in the second zone of the FCC Brillouin

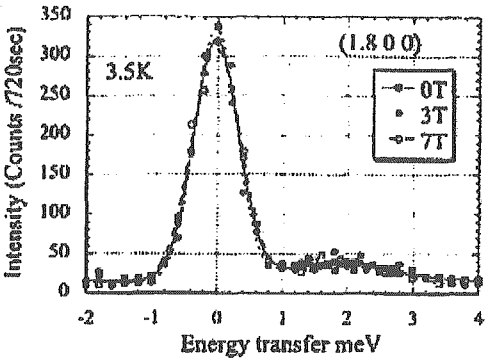

Figure 4: Magnetic field dependences of the energy spectra studied at the (1.8 0 0) RPL at 3.5 K.

zone boundary (BZB), while that in the latter is in the first zone of the FCC BZB as mentioned before. Furthermore, in $CdFe_2O_4$, ferromagnetic diffuse scattering located around the (4 0 0) nuclear Bragg peak position was not observed. Thus, the spin correlations in these systems are entirely different. The ferromagnetic diffuse scattering which is very sensitive to the applied magnetic field observed here is a characteristic of $ZnFe_2O_4$. Further measurements over a wider region in the reciprocal lattice space are desired to clarify these distinctive features of the field-sensitive diffuse scattering in the $ZnFe_2O_4$ system.

References

1) K. Kamazawa, *et al.*, Phys. Rev. B 68 (2003) 024412.
2) Y. Yamada, *et al.*, Phys. Rev. B 66 (2002) 064401.
3) K. Kamazawa, *et al.*, Phys. Rev. B 70 (2004) 024418.

研究テーマ:銅酸化物超伝導体 $La_{2-x}Sr_xCuO_4$ の磁気揺らぎに対する磁性不純物効果
表題:Ni 置換反強磁性体 $La_{2-x}Sr_xCuO_4$ の磁気特性

1-2-24 Magnetic properties of Ni-doped antiferromagnet $La_{2-x}Sr_xCuO_4$

H. Hiraka[1], A. Fukaya[1], K. Yamada[1], M. Matsuda[2], T. Machi[3], N. Watanabe[3], and Y. Itoh[3]

[1]Institute for Materials Research, Tohoku University, Katahira 2-1-1, Aoba-ku, Sendai 980-8577, Japan; [2]Advanced Science Research Center, Japan Atomic Energy Research Institute, Tokai, Ibaraki 319-1195, Japan; [3]Superconductivity Research Laboratory, International Superconductivity Technology Center, 1-10-13 Shinonome, Koto-ku, Tokyo 135-0062, Japan

La_2CuO_4, the parent material of the superconductor $La_{2-x}Sr_xCuO_4$ (LSCO), is considered as one of the typical two-dimensional antiferromagnet. It is well known that the Néel temperature T_N (~320 K) is very sensitive to hole doping and the three-dimensional antiferromagnetic order disappears when doped by the amount of 2% Sr. Recent magnetization measurements [1, 2], however, indicated that T_N increases by ~100 K with Zn- or Ni-substitution in the lightly hole-doped phase of LSCO (x~0.01), suggesting strong correlation between the hole motion and the magnetic interaction. In order to clarify the interesting antiferromagnetic state directly, magnetic neutron study using single crystals is highly desirable.

Neutron diffraction measurements were carried out on the 2-axis spectrometer KSD, which is installed at the beam port T1-2 of JRR3M in JAERI (Tokai). Thermal neutron beam (Ei =35.2 meV) was selected by the monochromator of Ge (311) reflection. $La_{2-x}Sr_xCu_{1-y}Ni_yO_4$ single crystals of x=0.01 and y=0.01 were grown by the traveling-solvent-floating-zone method, and characterized by magnetization and electrical resistivity measurements. The cylindrical sample with dimensions of 4ϕ× 22 mm was set up in the (h,k,0) scattering plane (*Bmab* notation).

Figure 1 (upper) shows the temperature dependence of the magnetic Bragg reflection (1,0,0) in $La_{1.99}Sr_{0.01}Cu_{0.99}Ni_{0.01}O_4$. The angle-integrated Bragg intensity shows a normal thermal evolution with T_N ~280 K, in agreement with that from susceptibility measurements. However, the peak intensity suddenly drops at about 100 and 200 K, associated with the peak broadening (lower). Besides, the (1,0,0) transverse scan itself became somewhat a multi-peak structure near those two temperatures (inset). This unexpected thermal behavior occurred twice, whereas we could not observe thereafter. Further investigation using other crystals with different resolution is now in progress.

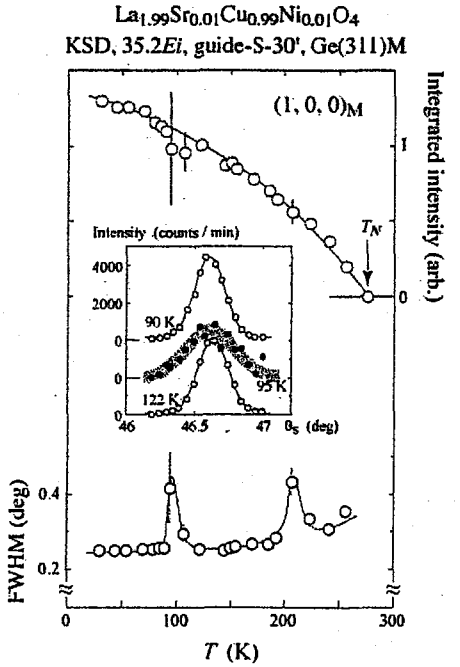

Fig. 1 Magnetic (1,0,0) reflection: [upper] θs-integrated intensity, [lower] FWHM, [inset] rocking curves across the broadening temperature.

References

[1] M. Hücker *et al.*, Phys. Rev. B **59**, R725 (1999).
[2] T. Machi *et al.*, Physica C **388-389**, 233 (2003).

使用施設:JRR-3M, 装置:KSD(T1-2), 分野:2.Magnetism

研究テーマ：中性子散乱によるウラン化合物の物性研究
表　題：反転対称性のない重い電子系超伝導体 $CePt_3Si$ の反強磁性秩序と超伝導の共存及び磁気励起の研究
1-2-25

Magnetic structure and low energy excitation in a non-centrosymmetric heavy fermion superconductor $CePt_3Si$

N. Metoki[1], K. Kaneko[1], T. D. Matsuda[1], A. Galatanu[1], T. Takeuchi[2], S. Hashimoto[2], T. Ueda[2], R. Settai[2], Y. Ōnuki[1,2], N. Bernhoeft[3]

[1] *ASRC-JAERI, Tokai, Naka, Ibaraki 319-1195*
[2] *Graduate School of Science, Osaka University, Toyonaka, Osaka 560-0043*
[3] *DRFMC, CEA/Grenoble, 38054 Grenoble Cedex 9, France*

$CePt_3Si$ is a heavy fermion superconductor with non-centrosymmetric structure (space group $P4mm$)[1)]. This compound exhibits antiferromagnetic order at $T_N = 2.2$ K and enters into a heavy fermion superconducting state at $T_{SC} \approx 0.75$ K. We have carried out neutron scattering experiments in order to reveal the magnetic structure and the coexistence with superconductivity. We observed a low energy exciatation which showed the heavy fermion quasi-elastic and inelastic nature based on the crystal field level splitting[2)].

Neutron scattering experiments were carried out on thermal and cold triple-axis spectrometers TAS-1, TAS-2, and LTAS. Elastic scattering was measured with neutron beam at $E = 14.7$meV monochromatized/analyzed with PG crystals, while inelastic scattering was measured with fixed final energy $E_f =$ 3.5, 14.7 and 30.5 meV.

We observed clear antiferromagnetic peaks with the propagation vector $Q_0 = (0\ 0\ 1/2)$ below T_N with use of polycrystalline sample. The magnetic reflections were also clearly observed on a single crystalline sample. Figure 1 shows the temperature dependence of the (0 0 1/2) and (1 0 1/2) intensities with normalizing the signal intensity. It should be noted that the antiferromagnetic intensity remains almost constant below T_{SC}, indicating that the antiferromagnetic order coexists with the heavy fermion superconductivity. As shown in Fig. 2 the integrated intensity of the antiferromagnetic reflections can be explained with the model calculation based on the magnetic structure shown in the inset of Figure 2. The ferromagnetic sheets of Ce moments stacked antiferromagnetically along the c-axis. The obtained magnetic moment of

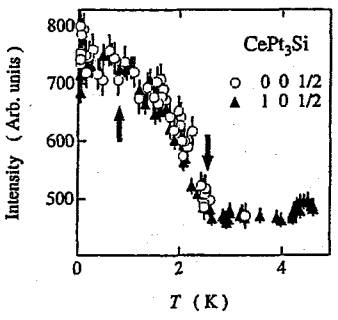

Figure 1: The intensity of (0 0 1/2) and (1 0 1/2) magnetic reflection as a function of temperature, shown by open circles and closed triangles, respectively.

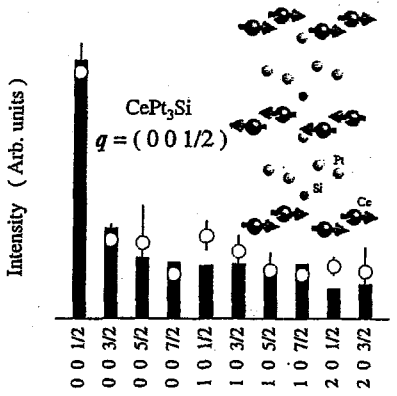

Figure 2: The integrated intensity of the antiferromagnetic reflections of $CePt_3Si$. The open circles are the experimental data, while bars are model calculation based on the magnetic structure shown in the inset. Note in-plane direction of the magnetic moment is unclear due to multi-domain structure.

原子炉：JRR-3　　装置：LTAS(C2-1)　　分野：中性子散乱（磁性）

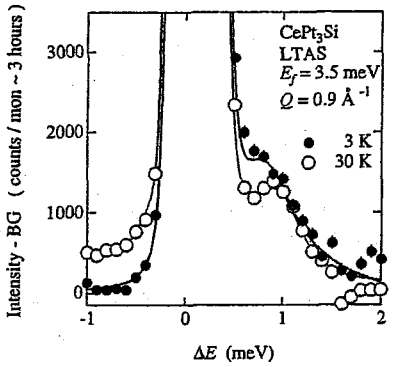

Figure 3: Low energy magnetic response of polycrystalline $CePt_3Si$. The solid and open circles represent data measured at 3 K and 30 K, respectively.

$0.16\pm0.01\,\mu_B$/Ce is strongly suppressed from the effective moment of Ce^{3+} ion $2.54\,\mu_B$/Ce. This remarkable reduction is consistent with a presence of Kondo-like interaction[1]. The direction of the magnetic moment lying in the c-plane could not be determined because of the domain structure.

Inelastic scattering experiments have been carried out on a polycrystalline sample. The low energy excitation spectra at $Q=0.9\,\text{Å}^{-1}$ for $T=3$ and 30 K with $E_f=3.5$ meV are shown in Fig. 3. Note that the background has been subtracted. A clear inelastic peak at $\Delta E\approx 1$ meV at $T=30$ K is found to coexist with a quasi-elastic response, where the quasi-elastic response increases in intensity with decreasing temperature. The existence of the low-energy excitation ≈ 1 meV is consistent with the broad specific heat anomaly around $T=2$ K [1], which integrates to an entropy change of $R\ln 2$ at ≈ 25 K. The Schottky anomaly was observed in specific heat and thermal expansion on single crystal sample. Thus this low energy excitation can be concluded as the magnetic exitation base on low lying crystalline field level. We also observed a magnetic response at 24 meV in addition to some phonon scattering. This peak can be considered as the second crystal field level. The J multiplet of the Ce^{3+} ion splits into three doublets in a given point symmetry.

The excitation energies $\Delta E\approx 1$ meV and 24 meV are consistent with a step-like behavior observed in the electrical resistivity around 10 K and 100 K [1]. We found that the magnetic susceptibility is almost isotropic and well explained in terms of the mean field calculation based on the crystal field level scheme assuming $\Gamma_7(0\,\text{meV})-\Gamma_6(1\,\text{meV})-\Gamma_7(24\,\text{meV})$[2,3]. The almost isotropic magnetization curve and the metamagnetic behavior are also clearly reproduced by this level scheme[3].

The magnetic structure of the $CePt_3Si$ may be relevant in connection with discussions of the pairing symmetry in this compound. The magnetic propagation vector $\boldsymbol{Q_0}=(0\,0\,1/2)$ implies two interpenetrating, Néel magnetic sublattices which are ferromagnetic in the c-plane. Within a localized $4f$ model, on simultaneous space-time inversion a given magnetic sublattice is centrosymmetric and a pairing of spin-triplet character may be favorable. However, hybridization with Pt and Si breaks this degeneracy and a combination of these two competing effects may be relevant to the microscopic coexistence of the superconductivity and antiferromagnetic order.

Our low energy data showed the overlap of the quasi-elastic component with the width of ≈ 0.4 meV and the first crystal field level at 1meV, indicating that the kondo energy has the comparable energy scale to that of the the first excited state with different orbital from the ground state. This is related to the strong reduction of the Ce magnetic moment. This result indicates that the magnetic as well as quadrupolar degree-of-freedom in the quasi-quartet ground state may play important role for the magnetism and the superconductivity. It is now highly interesting to establish the low lying modes relevant to the heavy quasi-particles and superconductivity as achieved in UPd_2Al_3 [4].

References

1) E. Bauer *et al.*, Phys. Rev. Lett. 92 (2004) 027003.
2) N. Metoki *et al.*, J. Phys.: Condens. Matter 16 (2004) L207.
3) T. Takeuchi *et al.*, J. Phys.: Condens. Matter, 16 (2004) L333.
4) N. Metoki *et al.*, Phys. Rev. Lett. 80 (1998) 5417.

研究テーマ:強磁性と反強磁性スピン相関が競合する系の磁性
表題:MnPt 合金における正方格子歪みと磁気構造

1-2-26 **Magnetic structure and tetragonality in MnPt alloy**

H. Hama, T. Ikeda and Y. Tsunoda

Sch. of Sci. and Eng. Waseda University, 3-4-1 Ohkubo, Shinjuku, Tokyo 169-8555 Japan

A CuAu-I type PtMn alloy shows an antiferromagnetism and has rather high Neel temperature (T_N=913 K). Nowadays, the material is considered to be an important substance for the application to the GMR devices. The magnetic structure of PtMn alloy previously reported, however, was contradictory. Last year, we reported the magnetic structure determined using a PtMn single crystal sample with single magnetic domain. At room temperature, Mn spins show anti-parallel coupling on the c-plane and the moments are parallel to the c-axis. At T_T=740 K, however, a magnetic phase transition takes place; the easy axis changes from the c-axis to the axis in the c-plane. The change of the easy axis should have strong coupling with the tetragonality (1−c/a) of the crystal.

A careful examination of the tetragonality and the magnetic Bragg peak intensity were studied using the T1-1 triple axis spectrometer and we found a strong correlations between the shrinkage of the c-axis and the (1 0 1) magnetic Bragg peak intensity. Experimental results are given in the Fig. 1. At around T_S=580 K which is far below the magnetic phase transition temperature, the tetragonalty (1−c/a) starts increasing rapidly with increasing temperature. At T_S, the (1 0 0) magnetic Bragg peak intensity also starts decreasing rapidly and the (1 0 1) peak intensity starts increasing. At T_T, the (1 0 1) peak intensity shows maximum value, then, start decreasing with temperature increasing up to T_N. The (1 0 0) peak intensity shows anomaly around T_T and the negative slope of (1−c/a) has the maximum value between T_T and T_N. Experimental data suggest that the change of the easy axis starts at around T_S, then continuously inclination angle from the c-axis increases with increasing temperature and at T_T, the easy axis reaches in the c-plane. Thus, the transition at T_T is not the spin flip phase transition in normal meanings but the continuous change of the easy spin axis. The origin of the change of the easy axis is the drastic contraction of the c-axis at high temperature.

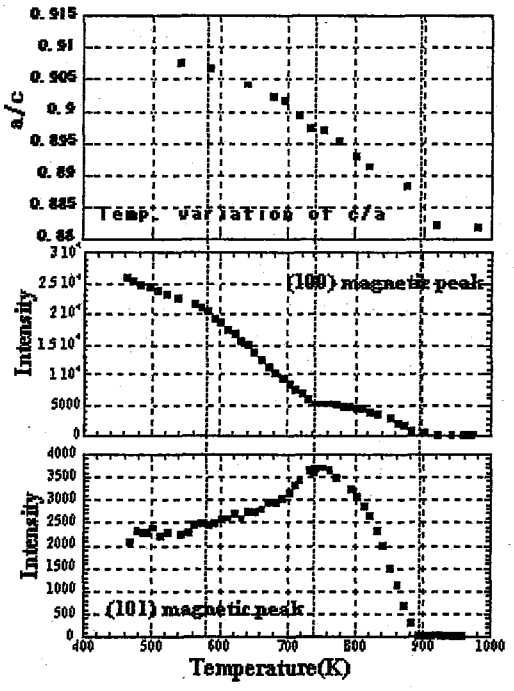

使用施設:JRR-3M, 装置:T1-1, 分野 Magnetism

研究テーマ：中性子散乱によるウラン化合物の物性研究
表　題：$NpFeGa_5$ の磁気構造
1-2-27

Magnetic structure of $NpFeGa_5$

E. Yamamoto[1], N. Metoki[1], K. Kaneko[1], D. Aoki[2], Y. Homma[2], Y. Shiokawa[2], Y. Ōnuki[1,3]
[1]*ASRC-JAERI, Tokai, Naka, Ibaraki 319-1195*
[2]*IMR, Tohoku University, Oarai, Ibaraki 311-1313*
[3]*Graduate School of Science, Osaka University, Toyonaka, Osaka 560-0043*

Actinide based '115' compounds have been attracted much attention, after the discovery of the high-T_C heavy fermion superconductivity in $PuCoGa_5$.[1)] So far no superconductivity has been reported in U- and Np-'115' compounds. Strong itinerant character of $5f$ bands in U-'115' would favor Pauli-paramagnetic or itinerant antiferromagnetic state, whereas the magnetism looks to be the most stable in Np system. The remarkable difference might be due to the character of $5f$ electrons. We have studied the magnetic structure of $NpFeGa_5$ on the thermal triple axis spectrometers TAS-1 and TAS-2.

The antiferromagnetic reflections were observed with the antiferromagnetic propagation vector $\boldsymbol{q}$=(1/2 1/2 0) as shown in Fig. 1. The integrated intensities of the (1/2 1/2 l) peaks are plotted in Fig. 2. It is notable that the integrated intensity is strong for odd l and weak for even l. We found that this feature can be reproduced with assuming a ferrimagnetic structure due to Np and Fe magnetic sublattices as shown in the inset of Fig. 2. The in-plane moment direction cannot be determined because of the multi-domain structure. The magnetic moments were derived as 0.24 μ_B/Fe and 0.86 μ_B/Np, respectively. The magnetic interactions of $NpFeGa_5$ are completely opposite to that of $NpCoGa_5$ with one more $3d$ electron. Furthermore Co has no magnetic moment, and the moment direction is also different.

The existence of Fe moment indicates that the $5f$-$3d$ hybridization is rather important in Np system. In U-'115' system, however, the U-$5f$ and Ga-$4p$ hybridization band plays dominant role for the transport and magnetic properties. This difference is most likely due to the different $5f$ character in Np and U compounds.

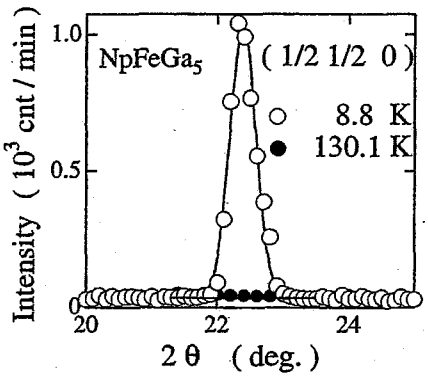

Figure 1: The radial scan at (1/2 1/2 0) in $NpFeGa_5$.

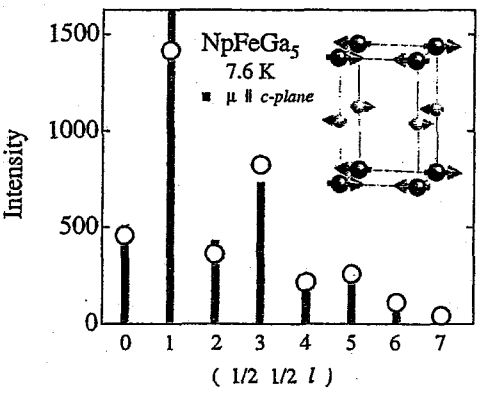

Figure 2: The Integrated intensity of AFM reflection of $NpFeGa_5$. Open circles denote the experimental data and the bars are the model calculation, assuming the magnetic structure shown in the inset.

References

1) J. L. Sarrao *et al.*, Nature **420**, 297 (2002).

原子炉：JRR-3　　装置：TAS-1(2G)　　分野：中性子散乱（磁性）

研究テーマ：重い電子系の磁性

表題：$Ce(Ni_{1-x}Pd_x)_2Ge_2$ の磁気臨界点近傍の磁気相図

Magnetic Phase Diagram of $Ce(Ni_{1-x}Pd_x)_2Ge_2$ proximate to the magnetic instability

1-2-28

T. Fukuhara and H. Kadowaki*

*Department of Liberal Arts and Sciences, Toyama Prefectural University, Kosugi, Toyama 939-0398, Japan; * Department of Physics, Tokyo Metropolitan University, Hachioji-shi, Tokyo 192-0397, Japan*

Recently, the spin fluctuation of heavy fermion compound $CeNi_2Ge_2$, which shows pronounced Non-Fermi-liquid behavior, have been investigated intensively. The spin fluctuation having a wave vector $\mathbf{k}_1$ = (0.23, 0.23, 1/2) was observed, and the spectral shape is well described by the Lorentzian form with Γ_Q~4 meV [1]. On the other hand, spin fluctuations having a Gaussian shape with an energy width of 0.6 meV and 0.9 mev grow below about 20 K for $\mathbf{k}_2$ = (1/2, 1/2, 0) and $\mathbf{k}_3$ = (0, 0, 0.7), respectively [2]. The open question is the origin of the appearance of second low-energy spin fluctuations. To get insight into the nature of these spin fluctuations, it is desired to investigate the spin fluctuation of $Ce(Ni_{1-x_c}Pd_{x_c})_2Ge_2$ where x_c is the palladium concentration at the magnetic instability. However, the x_c has not been established yet. Figure 1 indicates a tentative magnetic phase diagram of $Ce(Ni_{1-x}Pd_x)_2Ge_2$ based on the previous neutron scattering experiments using single crystals, where x was determined by the energy dispersion x-ray analysis.

Previous results of the neutron scattering experiment for the x = 0.10 single crystal using a dilution refrigerator indicated that a faint magnetic reflection appears at very low temperature around the wave vector **Q** ~ (1/2, 1/2, 1) which corresponds to $\mathbf{k}_2$ observed in $CeNi_2Ge_2$. [3] We have reinvestigated the same crystal by using a ^{3}He refrigerator, and no apparent magnetic reflection was observed along (1/2, 1/2, L) line at T = 0.4 K, suggesting T_N < 0.4 K at x = 0.10.

As shown in Fig. 1, T_N determined by the

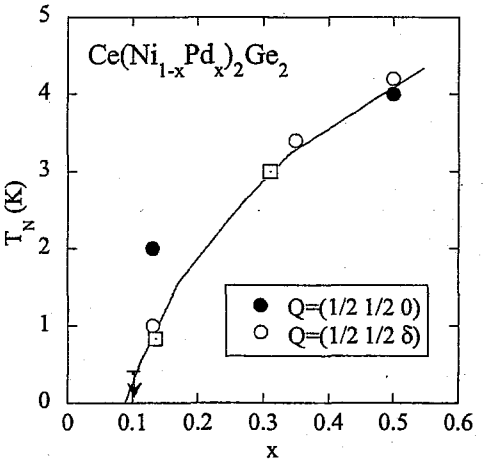

Figure 1: Tentative magnetic phase diagram of $Ce(Ni_{1-x}Pd_x)_2Ge_2$. A solid curve is guide to the eyes. Open square denotes the T_N determined by the Hall coefficient measurements. For x=0.10, T_N is below 0.4K,

Hall coefficient measurements well agrees with that determined by the neutron scattering experiments, where the magnetic ordering has the incommensurate propagation vector, **k** = (1/2, 1/2, δ) ; δ ~ 0.1. Hence, to estimate x_c precisely, the Hall coefficient measurements for x ≤0.10 is expected to be appropriate, because of the difficulty of the observation of a magnetic reflection near x_c.

For x = 0.13 and 0.50, another weak magnetic reflection having a commensurate propagation vector **k** = (1/2, 1/2, 0) appears, and the details are yet to be clarified.

Refernces

[1] B. Fåk et al., J. Phys. : Condens. Matter **12** (2000) 5423.
[2] H. Kadowaki et al., Phys. Rev. B **68** (2003) 120402(R).
[3] T, Fukuhara et al., J. Phys. Soc. Jpn. A **39** (1989) 5867.

使用施設：JRR-3M，装置：HQR(T1-1)，分野 Magnetism

研究テーマ：中性子散乱によるウラン化合物の物性研究
表　題：$NpCoGa_5$の磁気構造と磁気相図及びメタ磁性転移
1-2-29

Magnetic structure, phase diagram, and metamagnetic transition in $NpCoGa_5$

N. Metoki[1], K. Kaneko[1], E. Colineau[2], N. Bernhoeft[3], D. Aoki[4], Y. Homma[4], Y. Shiokawa[4], E. Yamamoto[1], Y. Ōnuki[1,5]

[1]*ASRC-JAERI, Tokai, Naka, Ibaraki 319-1195*
[2]*EC-JRC, Institute for Transuranium Elements, D-76125 Karlsruhe, Germany*
[3] *DRFMC, DEA/Grenoble, 38054 Grenoble Cedex 9, France*
[4]*IMR, Tohoku University, Oarai, Ibaraki 311-1313*
[5]*Graduate School of Science, Osaka University, Toyonaka, Osaka 560-0043*

Actinide based '115' compounds have been attracted much attention, after the discovery of the heavy fermion superconductivity in $PuCoGa_5$[1]. The existence of the superconductivity in Ce and Pu compounds and the absence in U and Np ones are theoretically studied and discussed. Strong itinerant character of $5f$ bands in U-'115' would favor Pauli-paramagnetic or itinerant antiferromagnetic state, whereas the magnetism looks to be the most stable in Np system. We have studied the magnetic structure and the metamagnetic transition in $NpCoGa_5$ on the cold and thermal triple axis spectrometers LTAS and TAS-2.

We observed (1 1 0.5) antiferromagnetic reflection as shown in Figure 1(a), which disappears above T_N. The absence of the (0 0 0.5) antiferromagnetic reflection as shown in Fig. 1(b) indicates that magnetic moment of Np is parallel to the c-axis.

The deduced magnetic structure is shown in the inset of Fig. 2. The Np magnetic moment is directed along the tetragonal c-axis and exhibits ferromagnetic order in the basal plane. The ferromagnetic sheets are stacked antiferromagnetically along the c-axis. This magnetic structure is the same as the $UPtGa_5$ and $UPdGa_5$.[2–4], which are iso-structural and iso-electronic compounds with the same number of valence electrons, assuming itinerant $5f$ electrons.

Figure 2 summarizes the integrated intensity of the antiferromagnetic reflections on the $(h\,h\,l)$ scattering plane. The observed intensity can be well reproduced by the model calculation, assuming magnetic from factor for Np^{3+} free ion. The magnetic moment of Np was estimated as $0.8(1)\,\mu_B$. It is in good agreement with a value obtained by a recent Mössbauer spectroscopy measurement[5].

High field neutron scattering experiments have been carried out in order to clarify the magnetic structure under magnetic field. We found that the (1 1 -1.5) antiferromagnetic peak observed for H=0 T at T=1.6 K completely disappeared for H=4.6 T. It means that a simple ferromagnetic structure is stabilized in the high field phase.

Figure 3 indicates the field dependence of the (1 1 -1.5) antiferromagnetic peak height.

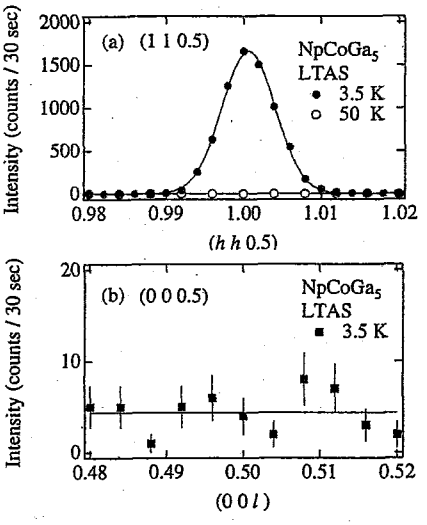

Figure 1: (a) The (1 1 0.5) antiferromagnetic peak of $NpCoGa_5$. (b) The $(0\,0\,l)$ scattering profile at the (0 0 0.5) antiferromagnetic Bragg point.

原子炉：JRR-3　　装置：LTAS(C2-1)　　分野：中性子散乱（磁性）

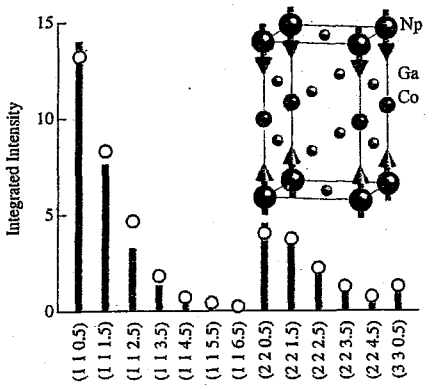

Figure 2: Integrated intensity of antiferromagnetic reflections of $NpCoGa_5$. Open circles denote the experimental result and the bars are the model calculation for the magnetic structure shown in the inset.

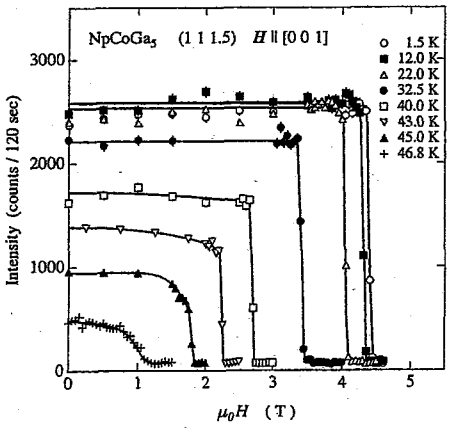

Figure 3: The field dependence of the (1 1 -1.5) antiferromagnetic peak intensity of $NpCoGa_5$. The field is applied parallel to the c-axis.

The antiferromagnetic Bragg intensity showed very little field dependence below $H_c(T)$ in the low temperature region for T <40 K. The Bragg intensity dropped suddenly to the background level for $H > H_c(T)$, indicating a sharp transition from the antiferromagnetic to the ferromagnetic structure at $H_c(T)$.

When the temperature is close to the antiferromagnetic ordering temperature T_N=47 K, the antiferromagnetic Bragg intensity decreases slightly with increasing $H < H_c(T)$. The jump remains sharp and the intensity is the same as the background level for $H > H_c(T)$. However for T=46.8 K, just below T_N=47K, the antiferromagnetic Bragg intensity exhibits a gradual field dependence around H=1 T. The metamagnetic transition field was plotted as a function of temperature to reveal the magnetic phase diagram as shown in Fig. 4.

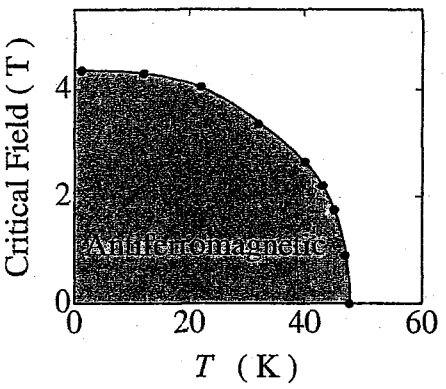

Figure 4: The H-T magnetic phase diagram of $NpCoGa_5$. The hatched area indicates the antiferromagnetic phase. The paramagnetic phase with a field induced ferromagnetic component is realized in the other region.

The metamagnetic transition of $NpCoGa_5$ is a spin flop of the Np magnetic moment. The weak spin flop field H_c=4.4 T at 1.5 K in comparison with the magnetic ordering temperature T_N=47K can be understood in terms of the two dimensional magnetic interaction. We assume the strong in-plane ferromagnetic interaction between the nearest neighbor Np spin on the same plane, while the out-of-plane antiferromagnetic coupling is weak. The in-plane interaction plays dominant role for the magnetic ordering, where the ordered temperature has the energy scale of J. The ferromagnetic sheets can remain unchange, throughout the spin flop transition, that is why the spin flop field can be weak.

References

1) J. L. Sarrao *et al.*, Nature **420**, 297 (2002).
2) Y. Tokiwa *et al.*, J. Phys. Soc. Jpn **71** (2002) 725.
3) K. Kaneko *et al.*, Phys. Rev. B **68** (2004) 214419.
4) S. Ikeda, *et al.*, J. Phys. Soc. Jpn **72** (2003) 2622.
5) E. Colineau*et al.*, Phys. Rev. B **69** (2004) 184411.

研究テーマ： S=1/2 カゴメ格子系 Cu3Bi(SeO3)2O2X (X=Cl, Br, I) の磁気構造

1-2-30 S=1/2 カゴメ様格子磁性体 $Cu_3Bi(SeO_3)_2O_2Cl$ の基底状態

Ground State of the S=1/2 Kagomé-like Lattice System $Cu_3Bi(SeO_3)_2O_2Cl$

A. Fukaya, H. Hiraka, K. Oyama and K. Yamada

Institute of Material Research, Tohoku University, Aobaku Katahira 2-1-1 Sendai 980-8577

The Heisenberg antiferromagnet with nearest-neighbor exchange interaction in kagomé lattice is one of the typical geometrical-frustrated systems. Model compounds of the kagomé lattice with spin values of S=2/3 (Cr^{3+}) and S=5/2 (Fe^{3+}) have extensively been studied. In the S=1/2 kagomé system, both geometrical frustration and quantum effect are expected to play important roles in the magnetism. Therefore, many theoretical works have been done. In contrast, few experimental study had been performed for S=1/2, since no model compound had been found. Quite recently, however, several candidate compounds of S=1/2 kagomé systems have been synthesized, and these compounds triggered several experimental studies.

In order to study the ground state of the S = 1/2 kagomé system, we chose $Cu_3Bi(SeO_3)_2O_2Cl$, which crystal structure at room temperature has recently been reported as a model material [1]. The magnetic susceptibility of the synthesized powder sample is shown in Fig. 1. A sharp peak is observed at ~27 K.

In this neutron scattering measurement on HQR, the powder sample was measured by a 2 θ scan. The wave length of the incident neutron was 2.457 Å. The temperature dependence of the integrated intensity around 2θ=28.6 deg (d=4.97 Å) is shown in Fig. 2. The intensity starts to increase at T~130 K. This increase is caused by a structural phase transition, since no significant anomaly is not observed above 27 K in the susceptibility. At present, we have not succeeded in determining the crystal structure below ~130 K.

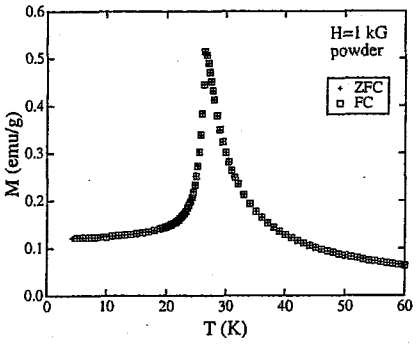

Fig. 1. Magnetic susceptibility of $Cu_3Bi(SeO_3)_2O_2Cl$.

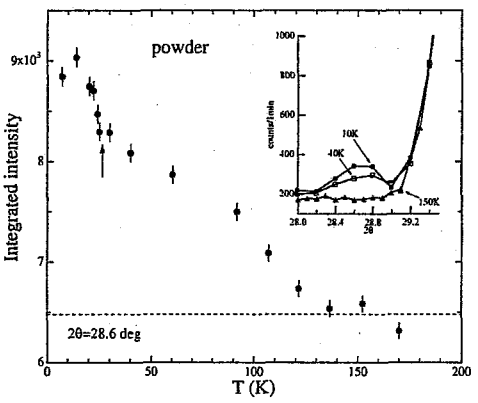

Fig. 2. Temperature dependence of the integrated intensity around 2θ=28.6 deg. The arrow at ~27 K shows the temperature where the sharp peak is observed in the susceptibility. The dotted line shows a background level. The inset shows the profile around 2θ=28.6 deg.

With decreasing the temperature, the intensity again exhibits an anomalous increase at ~27 K corresponding to the sharp peak in the magnetic susceptibility shown in Fig. 1. Then the increase in the intensity suggests a magnetic transition. Thus, the ground state of $Cu_3Bi(SeO_3)_2O_2Cl$ is expected to be a long-range ordered state. In this study, existence of the magnetic scattering was found only at several reflections. However, the intensity of magnetic scattering is superposed on the nuclear peaks. This result suggests that the unit cell of the magnetic structure is equal to that of the crystal.

References

[1] P. Millet *et al.*, J. Mater. Chem. **11**, 1152 (2001).

使用施設：JRR-3M，装置： T1-1 (HQR)，分野： 2. Magnetism

研究テーマ：中性子を用いた f 電子系化合物の研究
表　題：$5f$ 遍歴反強磁性体 $UPdGa_5$ の磁気特性
1-2-31

Magnetic properties of $5f$ itinerant antiferromagnet $UPdGa_5$

S. Ikeda[1,2], N. Metoki[1,3], Y. Haga[2], K. Kaneko[2], T. D. Matsuda[2] and Y. Ōnuki[1,2]

[1] *Advanced Science Research Center, Japan Atomic Energy Research Institute, Tokai, Naka, Ibaraki 319-1195, Japan*
[2] *Graduate School of Science, Osaka University, Toyonaka, Osaka 560-0043, Japan*
[3] *Department of Physics, Tohoku University, Sendai 980-8578, Japan*

Actinide compounds incorporating $5f$ electrons have attracted much attention on account of their unusual magnetic and electronic properties such as heavy fermions and unconventional superconductivity. Especially, a recent discovery of high-T_c heavy fermion superconductors $PuCoGa_5$[1] and $PuRhGa_5$[2] with the tetragonal $HoCoGa_5$-type crystal structure (space group $P4/mmm$) was a highly interesting topic in condensed matter physics. Prior to the Pu system, isostructural compounds $UTGa_5$ (T: transition metal) were studied from a viewpoint of electronic and magnetic properties. $UTGa_5$ with T=Fe, Ru, Os, Co, Rh and Ir shows Pauli-paramagnetic behavior, whereas T=Ni[3,4], Pd[5,6] and Pt[3,7,8] exhibits itinerant antiferromagnetism below the Néel temperatures T_N= 86 K, 31 K, and 26 K, respectively. In this paper we report the magnetic structure of $UPdGa_5$ studied by means of neutron scattering on a single-crystalline sample[6].

Figure 1 shows the temperature dependence of the magnetic susceptibility in $UTGa_5$ (T : Ni , Pd and Pt) for the field along the a- (the [1,0,0] direction) and c-(the [0,0,1] direction) axes, χ_a and χ_c, respectively. The magnetic susceptibility in $UPdGa_5$ is very small, less than 4×10^{-3} emu/mol. This susceptibility is much smaller than that of a U^{3+} free ion and/or a localized system UPd_3. Both χ_a and χ_c exhibit a weak temperature dependence, as shown in Fig. 1(b). The temperature dependence of the susceptibility above T_N can not be explained with the Curie-Weiss law. There exists a small magnetic anisotropy with $\chi_a > \chi_c$. We note that the small magnetic susceptibility with the weak temperature dependence would be understood based on an itinerant character of the $5f$ electrons. It should be also noted that the magnitude, temperature dependence, and anisotropy of the magnetic susceptibility in $UPdGa_5$ show intermediate behavior between $UNiGa_5$ and $UPtGa_5$. The susceptibility of $UPdGa_5$ exhibits a clear anomaly at the Néel temperature T_N= 31 K. The susceptibility showed anisotropic behavior; χ_c decreases steeply below T_N while the decrease of χ_a is smaller than χ_c. Similar anisotropy in χ below T_N has been reported in $UNiGa_5$ and $UPtGa_5$, as shown in Fig. 1 (a) and (c), respectively. It indicates that the uranium moments orient parallel to the c-axis.

Figure 2 shows neutron diffraction profiles at

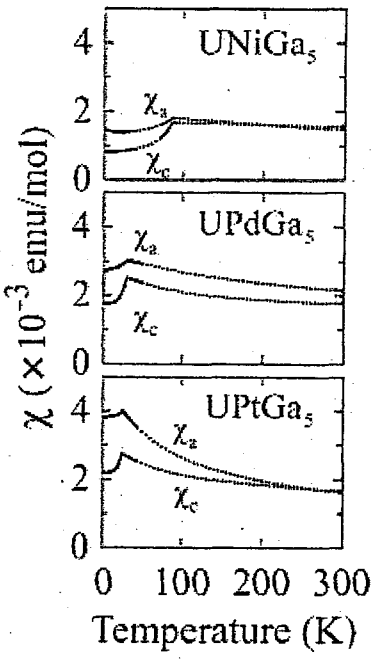

Figure 1: Temperature dependence of the magnetic susceptibility in (a) $UNiGa_5$, (b) $UPdGa_5$ and (c) $UPtGa_5$ for $H//[1,0,0]$(a-axis) and $H//[0,0,1]$(c-axis).

(1 1 0.5) and (0 0 1.5) measured below and above T_N. The antiferromagnetic reflections were observed at (h 0 l/2) and (h h l/2) superlattice positions with integer h and l on the (h0l) and (hhl) scattering planes. Therefore we conclude that the antiferromagnetic propagation vector is q=(0 0 1/2); the magnetic moments couples ferromagnetically in the basal plane, and this ferromagtic layer stacks antiferromagnetically along the c-axis. The absence of the magnetic peak at (0 0 1.5), as shown in Fig. 2(b), indicates that the direction of the magnetic moment is parallel to the c-axis. The integrated intensity of the antiferromagnetic peaks as denoted by open circles in Fig. 3 is well reproduced by the model calculation shown by bars, assuming this magnetic structure. The magnetic moment μ was determined to be $0.33\mu_B$/U at 3.0 K. The magnetic structure in $UPdGa_5$ has been predicted by Kaneko *et al.* to be the same type as in $UPtGa_5$ from the temperature dependence of the

原子炉：JRR-3　　装置：TAS-1(2G)　　分野：中性子散乱（磁性）

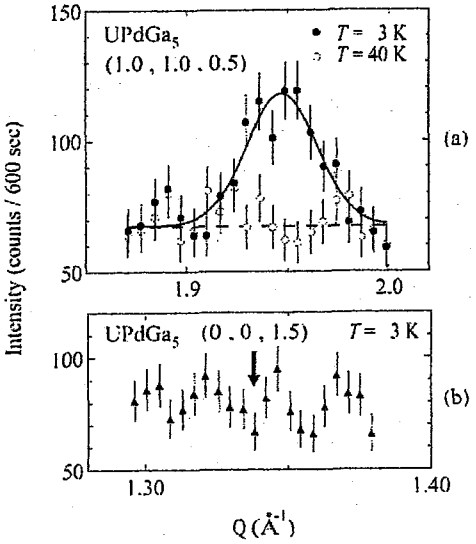

Figure 2: Neutron diffraction profiles at (a) (1 1 0.5) and (b) (0 0 1.5) in $UPdGa_5$ measured at 3.0 K ($< T_N$) and 40 K ($> T_N$) shown by open and closed circles, respectively.

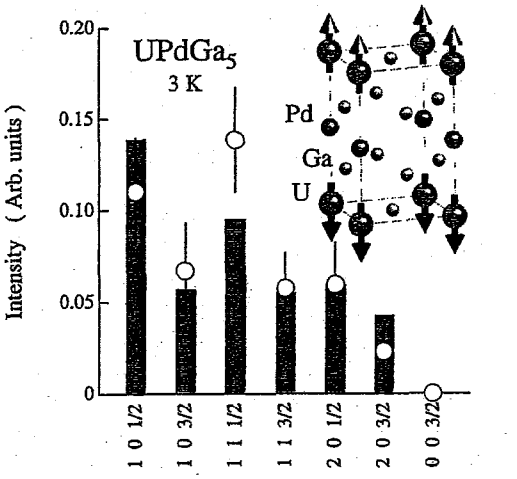

Figure 3: Integrated intensity of antiferromagnetic reflection of $UPdGa_5$. Open circles represent the experimental result and the bars denote the calculated one assuming the magnetic structure shown in the inset. The magnetic moment of uranium is deduced to be 0.33 μ_B.

lattice constant[9]. Their prediction of the magnetic structure for $UPdGa_5$ is consistent with the one determined from the present neutron diffraction experiment. The magnetic structure of $UNiGa_5$ and $UPtGa_5$ has been studied[10]. $UNiGa_5$ has a Néel-type ordering, namely, the adjacent uranium moments are aligned in opposite directions. On the other hand, the uranium moments in $UPtGa_5$ order ferromagnetically in the basal c-plane and couple antiferromagnetically along the c-axis. This difference implies a sign change of the nearest neighbor interaction. This is not understood from the results of band calculation, because these compounds have almost the same topology of the Fermi surface in the paramagnetic state[11,12]. Tokiwa *et al.* discussed about it from a viewpoint that the orbital contribution of $5f$ electrons would be essential in the magnetic structure[10]. Kaneko *et al.* revealed that the local stress in the UGa_3 block in their crystal structure exhibits the systematic change, which would be related to the change of the magnetic structure[9].

Recently Hotta reported theoretical calculation of the magnetic phase diagram based on j-j coupling scheme[13]. It is pointed out that the narrow region with the q=(0 0 1/2) antiferromagnetic structure realized in $UPdGa_5$ and $UPtGa_5$ appears in the phase diagram with introducing a splitting of the Γ_8 level. This is consistent with a recovery of the magnetic anisotropy with increasing the uniaxial stress on UGa_3 layer observed in $UPdGa_5$ and $UPtGa_5$. In contrast, there is a wide stable region for the magnetic structure with q=(1/2 1/2 1/2) realized in $UNiGa_5$. Further studies should be expanded into Np or Pu compounds with miltiple $5f$ electron systems.

References

1) J. L. Sarrao, L. A. Morales, J. D. Thompson, B. L. Scott, G. R. Stewart, F. Wastin, J. Rebizant, P. Boulet, E. Colineau and G. H. Lander, Nature **420** (2002) 297.
2) F. Wastin, P. Boulet, J. Rebizant, E. Colineau and G. H. Lander, J. Phys. Condens. Matter.**15** (2003) S2279.
3) Yu. N. Grin, P. Rogl and K. Hiebl, J. Less-Common Met. **121** (1986) 497.
4) Y. Tokiwa, Y. Haga, E. Yamamoto, D. Aoki, N. Watanabe, R. Settai, T. Inoue, K. Kindo, H. Harima and Y. Ōnuki, J. Phys. Soc. Jpn. **70** (2001) 1744.
5) V. Sechovský, L. Havela, G. Schaudy, G. Hilsher, N. pillmayr, P. Rogl and P. Fiscer, J. Mag. Mag. Mater. **104-107** (1992) 11.
6) S. Ikeda, N. Metoki, Y. Haga, K. Kaneko, T.D. Matsuda, A. Galatanu and Y. Ōnuki: J. Phys. Soc. Jpn. **72** (2003) 2622.
7) Y. Tokiwa, S. Ikeda, Y. Haga, T. Ōkubo, T. Iizuka, K. Sugiyama, A. Nakamura and Y. Ōnuki: J. Phys. Soc. Jpn. **71** (2002) 845.
8) S. Ikeda, Y. Tokiwa, Y. Haga, E. Yamamoto, T. Okubo, M. Yamada, N. Nakamura, K. Sugiyama, K. Kindo, Y. Inada, H. Yamagami and Y. Ōnuki: J. Phys. Soc. Jpn. **72** (2003) 576.
9) K. Kaneko, N. Metoki, G. H. Lander, N. Bernhoeft, Y. Ishii, S. Ikeda, Y. Tokiwa, Y. Haga and Y. Ōnuki: Phys. Rev. B **68** (2003) 214419.
10) Y. Tokiwa, Y. Haga, N. Metoki, Y. Ishii and Y. Ōnuki: J. Phys. Soc. Jpn. **71** (2002) 725.
11) H. Yamagami, Acta Phys. Pol. B **34** (2003) 1201.
12) H. Yamagami, Physica B **312-313** (2002) 297.
13) T. Hotta: Phys. Rev. B **70** (2004) 054405.

研究テーマ：6H-ペロブスカイト構造をもつ $Ba_3LnM_2O_9$(Ln = La ~ Lu, Y ; M = Ru)の磁気構造
表題： 6H-ペロブスカイト $Ba_3MSb_2O_9$(M = Mn and Co)の磁気構造

1-2-32

Magnetic Structure of 6H-Perovskites $Ba_3MSb_2O_9$ (M = Mn and Co)

Y. Doi, Y. Hinatsu, and K. Ohoyama*

*Division of Chemistry, Graduate School of Science, Hokkaido University, Sapporo 060-0810, Japan; * Institute for Materials Research, Tohoku University, Sendai 980-8577, Japan*

Quaternary oxides $Ba_3MSb_2O_9$ (M = Mn and Co) have a 6H-perovskite-type structure (Fig. 1). This structure is represented as a framework consisting of the corner-sharing MO_6 octahedron and face-sharing Sb_2O_9 dimer. The magnetic ions (Mn^{2+} or Co^{2+}) form a triangular array in *ab* plane. Their magnetic susceptibility and specific heat measurements show an antiferromagnetic transition at 10.0 K (Mn) and 2.3 K (Co).

In order to determine their magnetic structure, neutron diffraction measurements were performed above and below T_N. using the high efficiency and resolution powder diffractometer, HERMES, of Institute for Materials Research, Tohoku University, installed at the JRR-3M Reactor in JAERI (Tokai). The wavelength of a neutron incident is 1.8035 Å. The data were analyzed by the Rietveld technique.

The diffraction pattern for $Ba_3CoSb_2O_9$ at 10 K is well refined using the crystal structure with the space group $P6_3/mmc$, while that for $Ba_3MnSb_2O_9$ at 20 K indicates that it has a monoclinically distorted structure with space group $C2/c$ ($a_{mono} \approx a_{hex}$, $b_{mono} \approx \sqrt{3}a_{hex}$, $c_{mono} \approx c_{hex}$, $\beta_{mono} \approx 90°$).

The data below T_N for both compounds show some additional diffraction peaks at lower angles. For $Ba_3CoSb_2O_9$, they are indexed with $h = n_1 \pm 1/3$, $k = n_2 \pm 1/3$, and $l = 2n_3 + 1$ (n_i: integer). We analyzed data using a magnetic unit cell of $\sqrt{3}a_{hex} \times \sqrt{3}a_{hex} \times c_{hex}$, in which the Co sites are divided in six sublattices. The value of l is odd for all the magnetic reflections, thus we assumed that the magnetic moment of Co ion at (x, y, 0) is antiparallel to that at (x, y, 1/2). As the result of the Rietveld analysis, it was found that $Ba_3CoSb_2O_9$ adopts the so-called 120° structure, in which the direction of the magnetic moment of one sublattice is parallel to the *c*-axis (Fig. 2). The ordered magnetic moment of the Co^{2+} ion is 1.35(3) μ_B.

The magnetic structure of the $Ba_3MnSb_2O_9$ is almost the same as that of $Ba_3CoSb_2O_9$ except for the direction of ordered magnetic moments. In this case, all the magnetic moments are lying in the *ab* plane. The ordered magnetic moment of the Mn^{2+} ion is 4.07(2) μ_B.

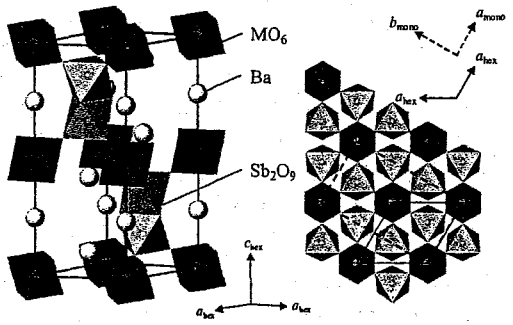

Figure 1: Schematic crystal structures of 6H-perovskite-type oxides $Ba_3MSb_2O_9$ (M = Mn and Co).

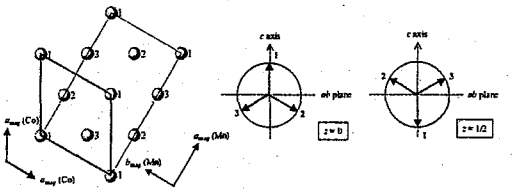

Figure 2: Magnetic structure of 6H-perovskites $Ba_3MSb_2O_9$ (M = Mn and Co). Diamagnetic ions are omitted. For $Ba_3MnSb_2O_9$, magnetic moments of Mn^{2+} are lying in *ab* plane.

使用施設：JRR-3M，装置：HERMES(T1-3)，分野：Magnetism

研究テーマ：多重極限環境下における中性子散乱実験法の研究
表　題：新しいウラン化合物 $U_3Ni_5Al_{19}$ の反強磁性秩序
1-2-33

Antiferromagnetic Ordering in a Ternary Uranium Compound $U_3Ni_5Al_{19}$

Y. Haga[1], N. Metoki[1], K. Kaneko[1] and Y. Ōnuki[1,2]
[1] *Advanced Science Research Center, JAERI, Tokai, Ibaraki 319-1195*
[2] *Graduate School of Science, Osaka University, 560-0043*

$U_3Ni_5Al_{19}$ crystallize in a peculiar flat orthorhombic structure (space group Cmcm) with the lattice parameters $a = 4.092$, $b = 15.947$ and $c = 26.974$ Å. Uranium atoms align along the a-axis with the same spacing 4.092 Å. Twelve uranium atoms in the unit cell occupy two crystallographic $4c$ and $8f$ sites of very similar local environments. Magnetic susceptibility $\chi(T)$ with field along the c-axis shows a sharp cusp at 23 K, implying an antiferromagnetic ordering. These antiferromagnetic moments are aligned ferromagnetically by a relativly weak magnetic field of 7 T at low temperature. Such a ferromagnetic moment is not observed when the field is applied along a or b directions, suggesting strong magnetic anisotropy along the c-axis. [1)]

In order to clarify the antiferromagnetic state we have performed neutron scattering experiments. Single crystals of a typical dimension of 1 x 1 x 5 mm^2 were grown from an aluminum flux with the starting composition UNi_2Al_{20}. Neutron scattering experiments were performed at the triple-axis spectrometer TAS-2 with an incident neutron energy of 14.7 meV monochromatized by a vertically bent PG monochromator. Higher order contamination was removed by 8 cm thick PG filter. The $(h\ 0\ l)$ and $(0\ k\ l)$ scattering planes were measured in order to study the magnetic structure.

Figure 1 shows an example of the scattering profile of the (044) Bragg peak above and below the transition temperature 23 K. We found a strong temperature dependence of the intensity across 23 K. Such temperature dependence was observed also on other Bragg peaks. This result indicates that the magnetic scattering is always superimposed on the nuclear Bragg peaks. Figure 2 is the temperature dependence of the (205) Bragg intensity measured with the fixed counter position at the peak maximum. We observed clear increase of the peak intensity due to the magnetic ordering below 23 K. The peak intensity above 23 K corresponds to the scattering intensity of (205) nuclear reflection. The background is denoted by dashed line in Fig. 2. The observed magnetic scattering can be attributed to the antiferromagnetic (AFM) ordering, since the absence of the ferromagnetic moment is shown by the $\chi(T)$ measurements. The AFM Bragg peaks with integer reflection indices indicate that the size of the magnetic unit cell is the same as the structural one. Furthermore no antiferromagnetic peak was observed at super lattice positions; the magnetic reflections appear at the nuclear Bragg positions. Within our experimental sensitivity, no (h00) magnetic peak was observed. The absence of the (h00) magnetic reflection could be explained from the direction of the magnetic moment, which would be parallel to the a-axis. This is consistent with the susceptibility data and the metamagnetic behavior.

In summary, we have investigated the antiferromagnetic state of a new uranium compound $U_3Ni_5Al_{19}$. The magnetic Bragg peaks were superimposed on the nuclear reflections, indicating that the magnetic unit cell is the same as the chemical one.

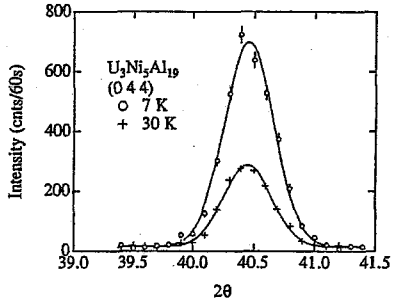

Figure 1: Neutron scattering profile of (440) reflection for $U_3Ni_5Al_{19}$ above and below 23 K

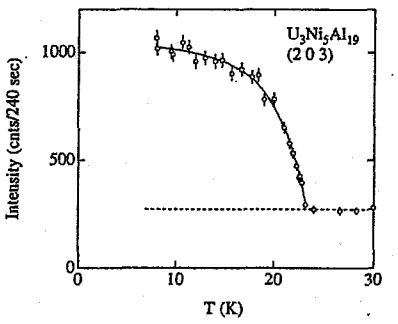

Figure 2: Temperature dependence of the (502) reflection intensity of $U_3Ni_5Al_{19}$.

References

1) Y. Haga *et al.*, to be published in the proceedings of SCES04.

原子炉：JRR-3　　装置：TAS-2(T2-4)　　分野：中性子散乱（磁性）

研究テーマ： UGe_2 における強磁性と超伝導の共存状態の研究

1-2-34 UGe_2 の強磁性と超伝導の中性子散乱による研究

Neutron Scattering Study on Magnetism and Superconductivity in UGe_2

Naofumi Aso[1], Hiroyuki Nakane[2], Noriaki K. Sato[2], Gaku Motoyama[3], Yoshiya Uwatoko[1], Tetsuya Takeuchi[4], Yoshiya Homma[5], Yoshinobu Shiokawa[5], Kazuma Hirota[1]

[1] *ISSP U. Tokyo,* [2] *Dept. Phys., Nagoya Univ.,* [3] *Fac. Sci., Himeji Inst. Tech.*
[4] *Low Temp. Center, Oosaka Univ.* [5] *IMR Tohoku Univ.*

Interplay of ferromagnetism and superconductivity has been one of central issues in the condensed matter physics and a ferromagnet UGe_2 [1, 2, 3] give us a good opportunity to study this fundamental problem. In this work, we present results on elastic neutron scattering experiments under high pressure up to 1.6 GPa at temperatures T down to 60 mK. particularly concentrating on the superconducting region in UGe_2 to understand the interplay between superconductivity and ferromagnetism. A single crystal was grown by Czochralsky pulling method with a tetra-arc furnace.[4] The pressure was generated by a beryllium-copper based piston-cylinder clamp device using Fluorinert as a pressure transmitting medium and was estimated by determining the change in lattice parameter of the NaCl. Elastic neutron scattering experiments has been performed on cold neutron triple-axis spectrometer HER (C1-1) with configuration shown in Fig. 1.

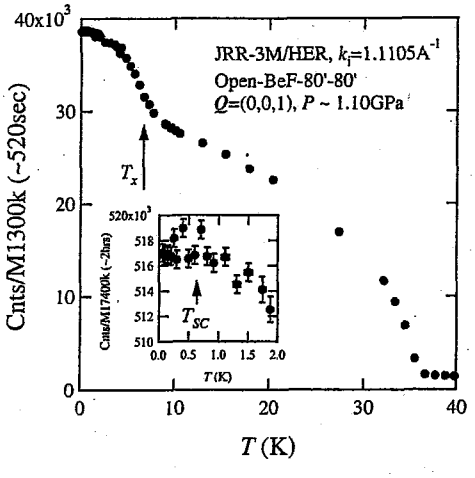

Fig. 1. Temperature dependence of Bragg peak intensities at Q = (0,0,1) under $P \sim 1.10$ GPa. Inset shows the detailes below $T < 2$ K.

Figure 1 shows the temperature dependence of the peak intensities at a magnetic Bragg Q = (0,0,1) under $P \sim 1.10$ GPa ($< P_{x,T=0}$). In addition to a ferromagnetic transition with $T_{Curie} = 36$ K, an sharp change around $T_x \sim 7$ K can be recognized as marked with an arrow in Fig. 1, which is consistent with the previous measurements.[2] Inset illustrates the details below $T < 2$ K with better statistics, showing a flat behavior below $T = 1$ K through T_{SC}. There is no "distinct" changes in intensities by passing through T_{SC}. We also carried out the similar measurements under $P \sim 1.25$ GPa (not shown here), where no T_x transition (i.e. $P > P_{x,T=0}$) and no changes in intensities below T_{SC} can be observed. We also performed scans of the magnetic Bragg peak profiles along b^* - and c^* - directions at Q = (0,0,1) both above and below T_{SC} under $P \sim 1.10$ GPa and ~ 1.25 GPa The line widths estimated by fitting are found to be constant both above and below T_{SC}.

Why no change can be observed in the ferromagnetic Bragg peaks ? Two reasons can be considered as follows; (1) The effect of superconductivity on the magnetic Bragg peak is if the some fluctuation affecting the superconductivity is not in the elastic channel. (2) The pressure studied in this work may not be controlled to the superconductivity optimal pressure P_{opt}, since recent detailed ac susceptibility measurements[3] exhibits that the $P_{opt} \sim 1.20$ GPa and its pressure range is very narrow.

References

[1] S.S. Saxena et al., Nature (London) 406 (2000) 587.
[2] A. Huxley et al., Phys. Rev. B63 (2001) 144519.
[3] H. Nakane et al., to be submitted.
[4] G. Motoyama et al., Phys. Rev. B65 (2002) 020510.

使用施設：JRR-3M，装置： C1-1 (HER)，分野： 2. Magnetism

研究テーマ：多重極限環境下における中性子散乱実験法の研究
重い電子系超伝導体 $PrOs_4Sb_{12}$ の磁気励起

1-2-35

Magnetic Excitations in Heavy-Fermion Superconductor $PrOs_4Sb_{12}$

K. Kuwahara, K. Iwasa*, M. Kohgi, K. Kaneko[1], S. Araki[1,**], N. Metoki[1,2], H. Sugawara[***], Y. Aoki and H. Sato

Department of Physics, Tokyo Metropolitan University, Tokyo 192-0397
[1]*Advanced Science Research Center, JAERI, Ibaraki 319-1195*
[2]*Department of Physics, Tohoku University, Sendai 980-8578*

The filled skutterudite compound $PrOs_4Sb_{12}$ is the first Pr-based heavy-fermion (HF) superconductor with the superconducting transition temperature $T_c = 1.85$ K. [1,2] The large specific heat jump $\Delta C/T_c \sim 500$ mJ/K^{2}mol at T_c suggests that heavy quasiparticles are formed at low temperatures and participate in a superconducting transition. Considering the occurrence of the field-induced antiferroquadrupolar (AFQ) ordering above ~5 T below ~1 K, [3,4] interestingly, the HF superconductivity of $PrOs_4Sb_{12}$ seems to be mediated by a nonmagnetic quadrupolar interaction.

We have studied magnetic excitations in a single crystal of this material by inelastic neutron scattering (INS) at low temperatures under high magnetic fields. The single crystal sample (about 4 g) used in the present experiment is the same as that used in a previous elastic neutron experiment. [4]. The sample was mounted at the mixing chamber of a ^{3}He-^{4}He dilution refrigerator with a superconducting magnet. INS experiments were performed on the cold neutron triple axis spectrometer LTAS at the JAERI.

Figure 1 shows the energy spectra of excitations with different Q vectors along [1,0,0] and [1,1,0] directions at the lowest temperature in a zero magnetic field. The well-defined crystal field (CF) excitations at 0.7 meV are observed at (1.6,1.6,0), (1.9,1.9,0) and (2.1,0,0), as reported in the previous INS experiment of the polycrystal sample [1]. The widths of the INS peaks at (1.6,1.6,0) and (1.9,1.9,0) are about 0.3 meV (FWHM), slightly larger than the instrumental resolution. At (2.8,0,0), on the other hand, the energy of the INS peak is about 0.5 meV and the peak becomes very broad and asymmetrical. These results show that the magnetic excitations at 0.7 meV soften at the zone boundary along the [1,0,0] direction. The observed softening may originate from the intersite interaction between Pr ions. Taking into account the fact that (1,0,0) is the modulation vector of the field-induced AFQ phase [4], the observed softening may be ascribed to quadrupolar instability with the same wave vector. Such dispersive modes are well known as magnetic excitons in singlet ground-state systems. The observed behavior might be due to the exciton caused by a nonmagnetic quadrupolar interaction.

Under magnetic fields, the observed field dependence of excitations is better reproduced by a CF level scheme with a singlet ground-state [4]. In a high resolution experiment, furthermore, the change of the excitation spectra at (1,0,0) was observed on passing through the superconducting transition temperature, suggesting some correlation between the magnetic response and the superconductivity.

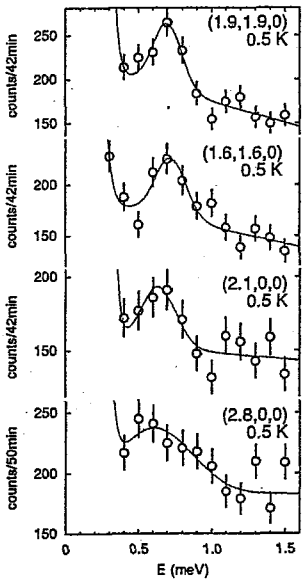

Figure 1: Energy spectra of excitations in $PrOs_4Sb_{12}$ with different Q vectors at the lowest temperature in a zero magnetic field. Lines are guides to the eyes.

References

1) M. B. Maple *et al.*: J. Phys. Soc. Jpn. **71** (2002) Suppl. 23.
2) E. D. Bauer *et al.*: Phys. Rev. B **65** (2002) 100506(R).
3) Y. Aoki *et al.*: J. Phys. Soc. Jpn. **71** (2002) 2098.
4) M. Kohgi *et al.*: J. Phys. Soc. Jpn. **72** (2003) 1002.

* Present address: Department of Physics, Tohoku University, Sendai 980-8578.
** Present address: Graduate School of Science, Osaka University, Osaka 560-0043.
*** Present address: Department of Mathematical and Natural Sciences, Faculty of Integrated Arts and Sciences, Tokusima University, Tokushima 770-8592.

原子炉：JRR-3　装置：LTAS(C2-1)　分野：中性子散乱（磁性）

研究テーマ:RPdSn (R = Tb, Dy, Ho, Er)**の磁気構造**
表題: DyPdSn **の中性子回折**
1-2-36

Neutron Diffraction Studies on DyPdSn

Y. Andoh, M. Kurisu[1], G.. Nakamoto[1], T. Tsutaoka[2] and S. Kawano[3]

Department of Environmental Sciences, Tottori University, Tottori 680-8551, Japan; [1]Japan Advanced Institute of Science and Technology, Ishikawa 923-1292, Japan; [2]Graduate School of Education, Hiroshima University, Hiroshima 739-8524, Japan; [3]Research Reactor Institute, Kyoto University, Osaka 590-0494, Japan

Ternary equiatomic rare-earth compounds, *R*PdSn (*R* = Tb, Dy and Ho), crystallize in the orthorhombic (*Pnma*) TiNiSi-type structure. TbPdSn and HoPdSn exhibit a multi-step metamagnetic transition at low temperatures, when the magnetic field is applied along the easy magnetization direction of the *b*-axis [1]. Neutron diffraction measurements have shown that TbPdSn and HoPdSn have two kinds of magnetic reflections with different propagation vectors $\boldsymbol{Q}_1$ = (1 0 0.45) and $\boldsymbol{Q}_2$ = (0 ~0.4 1) at 1.8 K [2]. Our recent magnetic measurements of polycrystalline samples have revealed that there are two magnetic phases in DyPdSn ; T_N = 7.0 K and T_t = 4.8 K. However, no information about the magnetic structure of DyPdSn has been reported so far. In the present work, we have carried out the neutron diffraction studies on DyPdSn as part of continuous studies of the magnetic properties of *R*PdSn compounds. Samples were prepared by arc-melting of stoichio- metric amounts of the components (3N of Dy, Pd and 5N of Sn). The neutron diffraction measurements were made using the HQR spectrometer of JRR-3M of JAERI at Tokai.

Figure 1 shows the powder neutron diffraction pattern at 1.6 K and 14K. There are three magnetic reflections at 1.6 K. With increasing temperature these magnetic reflections vanish at T_t = 4.8 K. The magnetic propagation vector at 1.6 K is determined to be $\boldsymbol{Q}_M$ = (0.21 0 0.66). This value is different from those of TbPdSn and HoPdSn. The observed and calculated 2θ with $\boldsymbol{Q}_M$=(0.21 0 0.66) are listed in Table 1. More detailed neutron diffraction studies using a single crystal are now in progress.

REFERENCES

[1] Y. Andoh et al., Meeting Abstract of Phys. Soc. Jpn. **54** Part 3 (1999) 365.
[2] Y. Andoh et al., Activity Report On Neutron Scattering Research, Vol. 7 (2000) 104.

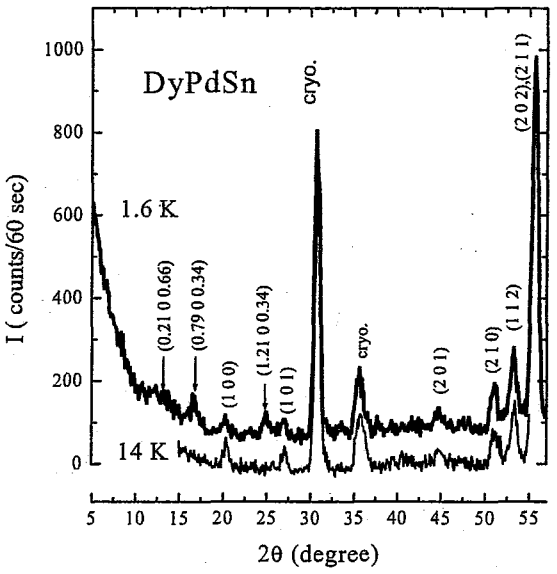

Figure 1 Powder neutron diffraction patterns of DyPdSn at 1.6 K and 14K. Arrow indicates the magnetic reflection.

Table 1: Observed and calculated 2θ of magnetic and nuclear reflections at 1.6 K

Index	$2\theta_{obs.}$	$2\theta_{cal.}$	$2\theta_{obs.}$-$2\theta_{cal}$
M(0 0 0)$^+$	12.3	12.4	-0.1
M(1 0 0)$^-$	16.7	17.0	-0.3
(1 0 0)	20.2	20.2	0.0
M(1 0 0)$^+$	24.9	25.2	-0.3
(1 0 1)	26.9	26.9	0.0
(2 0 1)	44.8	44.9	-0.1
(1 1 2)	53.2	53.0	0.2
(2 0 2)	55.7	55.4	0.3
(2 1 1)		56.0	-0.3

使用施設:JRR-3M, **装置:**HQR(T1-1), **分野** Magnetism

研究テーマ：$SrFe_{1-x}Co_xO_{3-\delta}$の磁気構造と特異な異常ホール効果
表題：$SrFe_{1-x}Co_xO_{3-\delta}$の磁場中の磁気構造

1-2-37 Magnetic Structure of $SrFe_{1-x}Co_xO_{3-\delta}$ under External Magnetic Field

Y. Yasui, M. Soda, S. Iikubo, T. Ido, M. Sato, K. Kakurai[1] and M. Nishi[2]

[1]*Department of Physics, Nagoya University, Furo-cho, Chikusa-ku, Nagoya 464-8602*
[2]*Advanced Science Research Center, JAERI, Tokai, Ibaraki 319-1199*
[3]*Institute for Solid State Physics, The University of Tokyo, 106-1 Shirakata, Tokai, 319-1106*

The spin system of the perovskite $SrFe_{1-x}Co_xO_{3-\delta}$ has a helical structure in the region of x<0.2, where the modulation vector $\boldsymbol{q}$ is ~0.212[111]. [1] For x > 0.2, non-trivial magnetic structure is realized with spontaneous moment. The hysteretic behavior of the magnetization observed in the measurements with varying T up and then down after zero field cooling indicates that the system has the reentrant spin-glass phase. The H-dependence of the Hall resistivities ρ_H observed for x=0.4~0.6 has not been understood well by an ordinary equation $\rho_H=R_0H+4\pi R_sM$. (Detailed magnetic and transport properties of powder samples of $SrFe_{1-x}Co_xO_{3-\delta}$ were reported by authors' group in ref. 2.) We pay attention to the relationship between the non-trivial magnetic structure and the anomalous Hall resistivity, because the problem seems not to be understood by existing classical theories. For example, H- and T-dependence of ρ_H of the pyrochlore molybdate $Nd_2Mo_2O_7$ with non-trivial magnetic structure cannot be well understood.[3,4]

In the studies on this problem, a possible role of the spin chiral order has been proposed.[5,6] Although the present authors' group have shown that the idea cannot describe the behavior of the Hall resistivity ρ_H, it is interesting to search systems in which effects of the spin chirality χ (where χ is defined as $\chi\equiv \boldsymbol{S}_1\cdot(\boldsymbol{S}_2\times\boldsymbol{S}_3)$ for three spins $\boldsymbol{S}_1$, $\boldsymbol{S}_2$ and $\boldsymbol{S}_3$) on the behavior of ρ_H can be explicitly found. From this point of view, it is also interesting, as pointed out by Tatara and Kawamura[7] to investigate the behavior of ρ_H in the spin glass state. It is important to clarify the relationship between the spin chiral order and the anomalous behavior of ρ_H to study the detailed magnetic structure of $SrFe_{1-x}Co_xO_{3-\delta}$.

A single crystal of $SrFe_{0.43}Co_{0.57}O_{2.84}$ was prepared[2] and used in the present study. Neutron diffraction measurements have been carried out in the external magnetic field $\boldsymbol{H}$ applied vertically (//[1$\bar{1}$0]) up to 5T at HQR (T1-1) at JRR-3M of JAERI in Tokai.

Figure 1 shows the T-dependence of the 001 and 001/2 reflection intensities taken at H=0 for $SrFe_{0.43}Co_{0.57}O_{2.84}$, where these reflections appear with decreasing T at T_C~150 K. With further decreasing T, the intensities of these reflections begin to decrease at T_g~80 K, which is considered to be due to the occurrence of the reentrant spin glass phase. The superlattice peaks appear [$\boldsymbol{Q}$=(h,h,1/2), (h,h,3/2), (1/2,1/2,k), (3/2,3/2,k), etc. (h,k,integer)] with

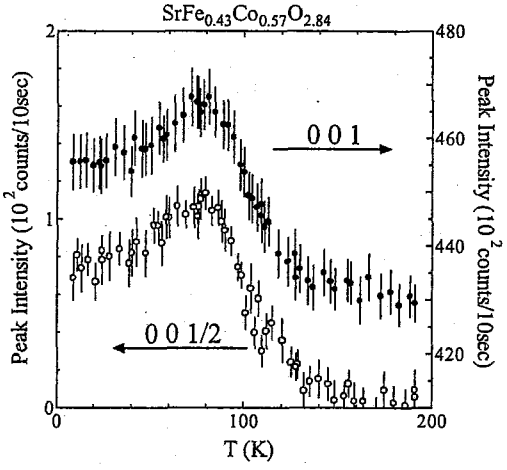

Figure 1: Temperature dependence of the scattering intensities of 001 and 001/2 reflections take at H=0 of $SrFe_{0.43}Co_{0.57}O_{2.84}$.

使用施設：JRR-3M，装置：HQR(T1-1)，分野 Magnetism

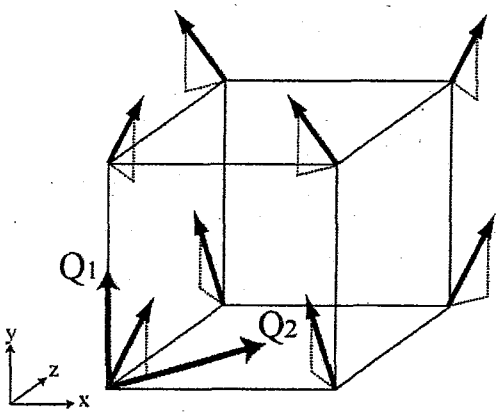

Figure 2: One of spin structure models of $SrFe_{0.43}Co_{0.57}O_{2.84}$ which can explain the observed magnetic reflection intensities taken at T=88K under zero magnetic field. Black and gray arrows indicate the directions of the magnetic moments and modulation vectors, respectively.

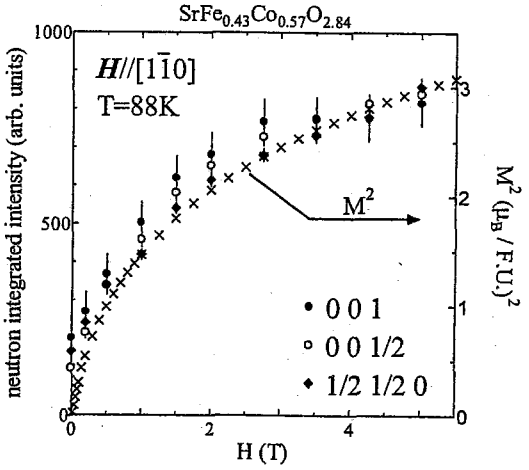

Figure 3: H-dependence of the magnetic scattering intensity of 001, 001/2 and 1/21/20 reflections at T=88K is shown together with the H-dependence of M^2.

decreasing T at T_C. Because the superlattice reflections corresponding to the modulation vector $\boldsymbol{Q}_1$=(0,0,1/2) and $\boldsymbol{Q}_2$=(1/2,1/2,0) are observed below T_C, the magnetic structure is not simple. One of the model of the magnetic structure which can explain the magnetic reflection intensities at T=88 K is shown in Fig. 2. The net magnetizations are along one of the four fold crystallographic axes, and we have chosen this to be the z-axis in Fig. 2. The direction of each moment deviates from the z-axis by ~20°. The value of the magnetic moments is estimated by comparing the magnetic reflection intensities with the nuclear Bragg intensities, to be about 1.1μ_B. This value is consistent with the one estimated from the M-H curve.

Figure 3 shows H-dependence of the magnetic scattering intensities of 001, 001/2 and 1/21/20 reflections taken at T=88K, where we find that the H-dependence is similar to the that of the square of the magnetization M^2. The value of the ferromagnetic component of the moment estimated from the intensities of *hhk* reflections, is ~1.7μ_B at H=5T, which is consistent with that of the magnetization. It is interesting that not only the reflection intensities at the ferromagnetic Bragg points but also those at the superlattice points have the similar increase with increasing H, because it implies, roughly speaking, that the magnitude of all the moments increase by a constant factor $\alpha(H)(>1)$ with the spin structure being kept unchanged. Further analysis is necessary to determine the precise magnetic structure and to clarify the relationship between the non-trivial magnetic structure and the Hall resistivity.

References

[1]T. Takeda, Y. Yamaguchi and H. Watanabe: J. Phys. Soc. Jpn. **33** (1972) 967.
[2]T. Ido, Y. Yasui and M. Sato: J. Phys. Soc. Jpn. .**72** (2003) 357.
[3]S. Yoshii, S. Iikubo, T. Kageyama, K. Oda, Y. Kondo, K. Murata and M. Sato: J. Phys. Soc. Jpn. **69** (2000) 3777.
[4]Y. Yasui, S. Iikubo, H. Harashina, T. Kageyama, M. Ito, M. Sato and K. Kakurai: J. Phys. Soc. Jpn. .**72** (2003) 865.
[5]Y. Taguchi, Y. Oohara, H. Yoshizawa, N. Nagaosa and Y. Tokura: Sience **291** (2001) 2573.
[6]K. Ohgushi, S. Murakami and N. Nagaosa: Phys. Rev. **B 62** (2000) R6065.
[7]G. Tatara and H. Kawamura: J. Phys. Soc. Jpn. .**71** (2002) 2613.

研究テーマ：Li 置換 CuO の磁気転移

表題：中性子粉末回折による $Cu_{1-x}Li_xO$ の磁気転移の研究

1-2-38 Neutron Diffraction Study of Magnetic Transition in $Cu_{1-x}Li_xO$

X.G. Zheng, T. Mori, K. Ohoyama*, H. Hayashida**, and A. Hoshiko **

Faculty of Science and Engineering, Saga University, Saga 850-8502, Japan
**Institute for Materials Research, Tohoku University, Sendai 980-8577, Japan*
***Graduate School of Sciences, Kyushu University, Fukuoka 812-8581, Japan*

Hole doping into antiferromagnetic CuO is of great interest for studying the effect on magnetic interaction especially because CuO might be a simple reference material for the high-T_c superconducting cuprates. Recent observation of a charge stripe-like structure in cupric oxide, CuO, raised renewed interest in this simplest copper oxide.[1] Heavy Li substitution in $Cu_{1-x}Li_xO$ (x = 0.16) can be realized.[2] A superlattice reflection, which is the same as that reported for slightly nonstoichiometric CuO, is observed in $Cu_{1-x}Li_xO$. The present study aims to investigate the evolution of the magnetic transition as well as the magnetic structure in this compound. A special interest is whether the charge superlattice has an associated magnetic structure.

Neutron diffraction experiment was carried out at several temperatures using powder sample of $Cu_{1-x}Li_xO$ (x = 0.16) at T1-3 (HERMES).

Undoped CuO transits into an incommensurate order at T_{N1} = 230 K and commensurate one at T_{N2} = 213 K with propagation vector (1/2 0 −1/2). 12-hr neutron diffraction on $Cu_{1-x}Li_xO$ (x = 0.16) did not produce high-resolution spectra to enable the determination of a possible magnetic structure associated with the charge superlattice. However, a magnetic reflection at peak (10-1) was clearly recognized (Fig. 1), suggesting the same basic magnetic structure as that of the undoped CuO. A quick temperature scan showed magnetic transition near 90 K, in consistency with a previous independent μSR experiment (Fig. 2).

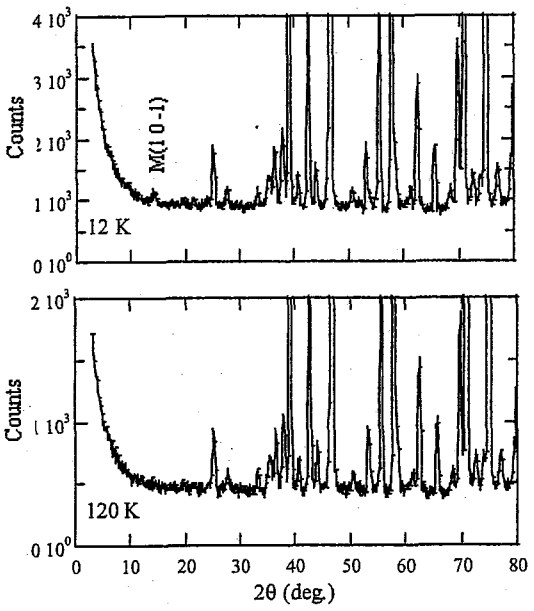

Figure 1: Neutron diffraction patterns for $Cu_{0.84}Li_{0.16}O$ at 12 K (upper) and 120 K (lower).

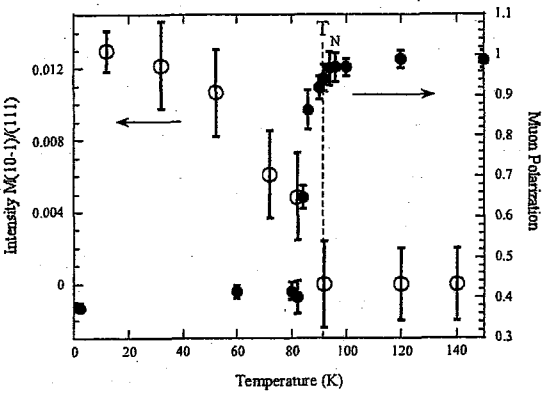

Figure 2: Temperature dependence of the neutron diffraction intensity of a magnetic peak (1/2 0 −1/2) and muon polarization for $Cu_{0.84}Li_{0.16}O$.

References

[1] X.G. Zheng et al., PRL **85** (2000) 5170.
[2] X.G. Zheng et al., PRB **69**, (2004) 094510; *ibid* **67** (2003) 214516.

使用施設：T1-3，装置：HERMES，分野 Magnetism

研究テーマ:遷移金属カルコゲナイドの Ba_2LnMX_5 の磁性
表題:$CaNdFeO_4$ の結晶構造と磁気構造

1-2-39

Crystal and Magnetic Structure of $CaNdFeO_4$

M. Wakeshima, S. Oyama, Y. Hinatsu, and K. Ohoyama*

*Division of Chemistry, Graduate School of Science, Hokkaido University, Sapporo 060-0810, Japan; * Institute for Materials Research, Tohoku University, Sendai 980-8577, Japan*

The layered perovskite type oxide $CaNdFeO_4$ is crystallized in an orthorhombic K_2NiF_4 type structure with space group: *Bmab*. In temperature dependence of its magnetic susceptibilities and specific heats, two anomalies were observed at around 7 K and 35 K. The ^{57}Fe Mössbauer spectra suggested that the anomalies at 7 and 35 K correspond to an antiferromagnetic ordering of Nd^{3+} ion and a change in the direction of magnetic moment of Fe^{3+} ion, respectively.

In order to elucidate these magnetic behavior of $CaNdFeO_4$, the powder neutron diffraction measurements were preformed using the high efficiency and resolution powder diffractometer, HERMES, of Institute for Materials Research, Tohoku University, installed at the JRR-3M with a neutron incident wave length (λ = 1.8207 Å). The magnetic structures were determined by the Rietveld technique.

Figure 1 shows the variation to temperature in the intensities of the magnetic Bragg reflection. Below 50 K, the discontinuous changes of intensities are observed. This is the typical characterization of the magnetic phase transition and consists with the results of Mössbauer spectra. The magnetic structure of Fe^{3+} is determined at 50 and 2 K and illustrated in Figure 2. From these magnetic structures, it is confirmed that the antiferromagnetic arrangement of the magnetic moment of Fe^{3+} changes 90 degrees from the *b*-axis to the *c*-axis. The ordering of the Nd^{3+} moment occurs when the temperature is decreased through 40 K and its ordered moment increases with decreasing temperature. It is supposed that the spin-reorientation transition observed in $CaNdFeO_4$ is induced by the onset of local magnetic interactions between the neodymium and iron sublattices.

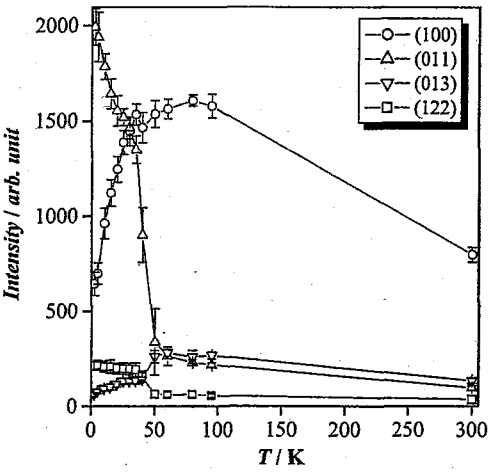

Figure 1 Temperature dependence of the intensities of the magnetic Bragg reflection for $CaNdFeO_4$.

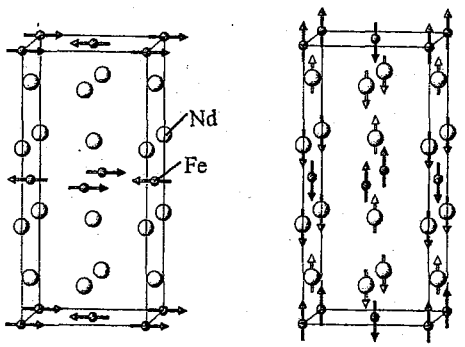

Figure 2 Magnetic structures of $CaNdFeO_4$.

使用施設:JRR-3M, 装置:HERMES(T1-3), 分野 Magnetism

研究テーマ:酸化物磁性体の超交換相互作用
表題:酸化物磁性体$(Ba_{1-x}Sr_x)_2Zn_2Fe_{12}O_{22}$および$Ba(Fe_{1-x}Sc_x)_{12}O_{19}$の超交換相互作用

1-2-40 Superexchange Interaction of $(Ba_{1-x}Sr_x)_2Zn_2Fe_{12}O_{22}$ and $Ba(Fe_{1-x}Sc_x)_{12}O_{19}$

S. Utsumi, and N. Momozawa*

*Center for Frontier Electronics and Photonics, Chiba University, 1-33 Yayoi, Inage, Chiba 263-8522, Japan; *Faculty of Science and Technology, Tokyo University of Science, 2641 Yamazaki, Noda 278-8510, Japan*

A hexagonal ferrite, $Ba_2Zn_2Fe_{12}O_{22}$, has a ferrimagnetic structure at all temperatures below the Curie point, T_C=392 K. Therefore, it is difficult to estimate the strength of superexchange interactions. Sr-containing $(Ba_{1-x}Sr_x)_2Zn_2Fe_{12}O_{22}$ can have a helimagnetic structure with the propagation vector along the *c*-axis in the Sr-rich crystals, where x is the Sr concentration ranging from 0 to 1.0 and all magnetic moments in the $(Ba_{1-x}Sr_x)_2Zn_2Fe_{12}O_{22}$ system lie in the *c*-plane. The purpose of this study is to estimate the strength of superexchange interactions from the viewpoint of the helimagnetic structure. The superexchange interactions are quantitatively discussed using the molecular field approximation.

Single crystals of $(Ba_{1-x}Sr_x)_2Zn_2Fe_{12}O_{22}$ were grown by the method of spontaneous crystallization from Na_2O-Fe_2O_3 flux. Neutron diffraction experiments were carried out on the single crystals at T=8 K with a KSD diffractometer installed at JRR3M in JAERI (Tokai). The local lattice distortion and the cation redistribution caused by the Sr-substitution were examined by the analyses of the nuclear scattering intensities. The helimagnetic structure was determined from the magnetic scattering intensities. The superexchange interaction was discussed based on free energy, and its strength was estimated.

There are competing superexchange interactions among Fe magnetic moments lying on the j=4, 5 and 8 layers of the $(Ba_{1-x}Sr_x)_2Zn_2Fe_{12}O_{22}$ system. Figure 1

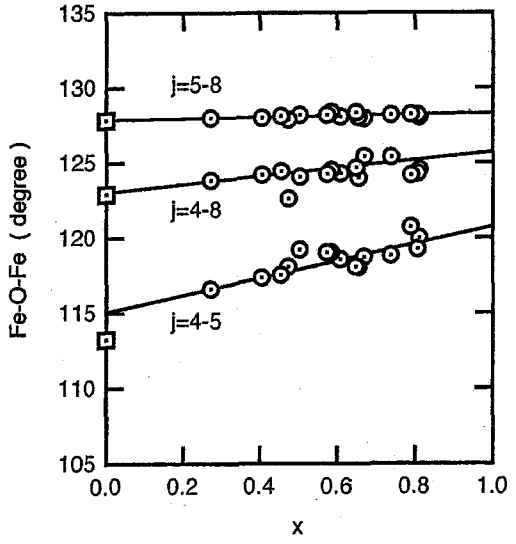

Figure 1: Dependence of the angles Fe-O-Fe of the competing superexchange interactions on x.

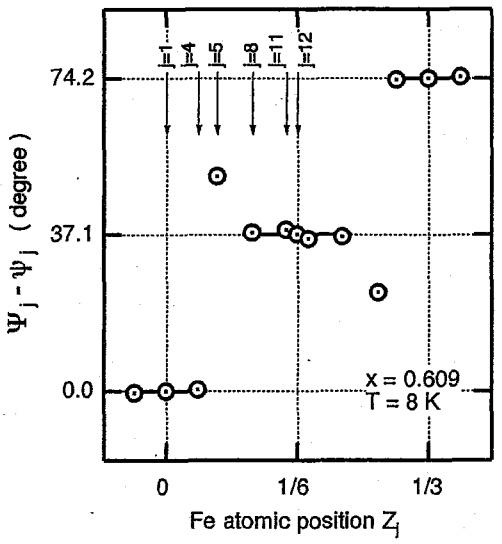

Figure 2: The helimagnetic structure of $(Ba_{1-x}Sr_x)_2Zn_2Fe_{12}O_{22}$ (x=0.609, T=8 K). The vertical axis indicates the turn angle of magnetic moments in the *c*-plane, and the horizontal axis the Fe atomic position z_j.

使用施設:JRR-3M, 装置:T1-2:KSD, 分野 Magnetism

shows the x dependence of angles Fe-O-Fe of the superexchange interactions between j=4-5, 4-8 and 5-8. The strengths of the competing superexchange interactions are strong, medium and weak in order of j=5-8, 4-8 and 4-5. Furthermore, the strength of the superexchange interaction between j=4-5 is supposed to become strong by the Sr-substitution.

Figure 2 shows the magnetic structure of $(Ba_{1-x}Sr_x)_2Zn_2Fe_{12}O_{22}$ (x=0.609, T=8 K). The turn angle ϕ_0 of the helix is 74.2°. There are two kinds of bunches, that is, large and small ferrimagnetic bunches, and they rotate helically with equal angular intervals of $\phi_0/2$ (=37.1°). The small ferrimagnetic bunch is composed of j=1 and 4 magnetic moments, and the large ferrimagnetic bunch of j=8, 11 and 12 magnetic moments. And furthermore, j=5 magnetic moment entirely deviates from the large and small ferrimagnetic bunches because of φ_5=50.8°. The helimagnetic structure for the $(Ba_{1-x}Sr_x)_2Zn_2Fe_{12}O_{22}$ system can be characterized by the turn angle ϕ_0 of the helix and the direction φ_5 of j=5 magnetic moment. Figure 3 shows the x dependence of ϕ_0 and φ_5 at T=8 K.

If the superexchange interaction energy $E_{jj'}^{ex}$ is written with the form of $E_{jj'}^{ex} = -J_{jj'}\mu_j\mu_{j'}\cos(\Psi_{j'} - \Psi_j)$, the free energy gives ϕ_0 and φ_5 in following equation:

$$\cos\left(\frac{\phi_0}{2}\right) = \frac{1}{2}\cdot\frac{\gamma J_{45}}{J_{58}}\left[\left(\frac{J_{58}}{\gamma J_{45}}\right)^2 - \left(\frac{J_{58}}{\gamma J_{48}}\right)^2 + 1\right],$$

$$\cos(\varphi_5) = \frac{1}{2}\cdot\frac{\gamma J_{48}}{J_{58}}\left[\left(\frac{J_{58}}{\gamma J_{45}}\right)^2 - \left(\frac{J_{58}}{\gamma J_{48}}\right)^2 - 1\right].$$

Here, γ is the parameter which indicates the cation distribution. By using these equations and the data of Fig. 3, the ratios of exchange integrals, J_{45}/J_{58} and J_{48}/J_{58}, were estimated as shown in Fig. 4. These values and the result of Fig. 1 are consistent with each other.

The Sr-substitution induces the local lattice distortion in the $Ba_2Zn_2Fe_{12}O_{22}$ lattice. As a result, since the superexchange interaction between j=4-5 magnetic moments remarkably increases, the helimagnetic structure appears. The strengths of the superexchange interactions were determined from the viewpoint of the free energy. The study on $Ba(Fe_{1-x}Sc_x)_{12}O_{19}$ is being carried out.

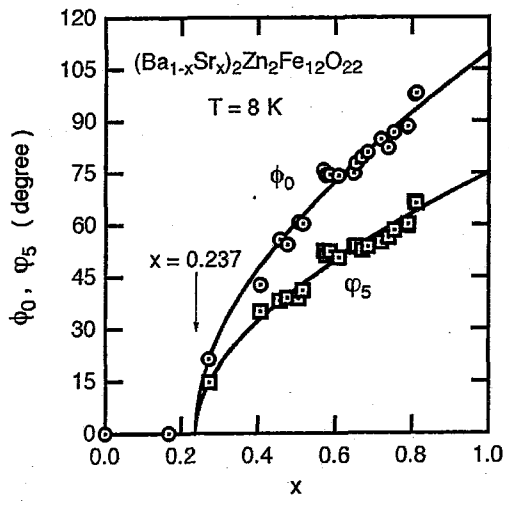

Figure 3: Dependence of ϕ_0 and φ_5 on x for the $(Ba_{1-x}Sr_x)_2Zn_2Fe_{12}O_{22}$ system at T=8 K.

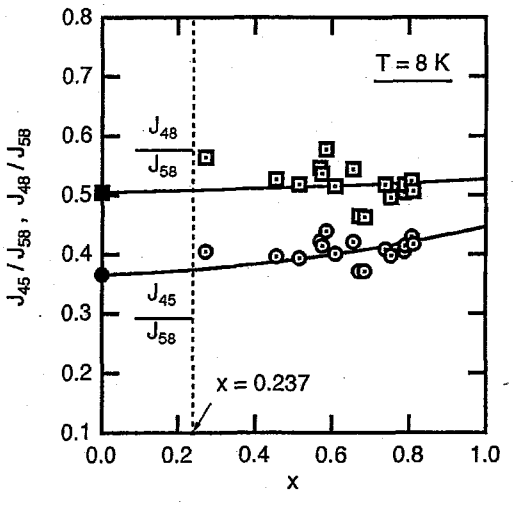

Figure 4: The determined values of J_{45}/J_{58} and J_{48}/J_{58} as a function of x. The helimagnetic structure appears at x>0.237.

研究テーマ：R_7Rh_3 (R = Tb, Dy, Ho, Er)の磁気構造
表題：Tb_7Rh_3の中性子回折

1-2-41

Neutron Diffraction Studies on Tb_7Rh_3

T. Tsutaoka, T. Tokunaga, Y. Andoh[1], S. Kawano[2], G. Nakamoto[3], and M. Kurisu[3]

Graduate School of Education, Hiroshima University, Hiroshima 739-8524, Japan
[1]Faculty of Regional Sciences, Tottori University, Tottori 680-8551, Japan
[2]Research Reactor Institute, Kyoto University, Osaka 590-0494, Japan
[3]Japan Advanced Institute of Science and Technology, Ishikawa 923-1292, Japan

The rare earth compound Tb_7Rh_3 crystallizes in the hexagonal Th_7Fe_3-type structure with three different crystallographic sites of Tb. The bulk magnetic measurements indicated three magnetically ordered states: antiferromagnetic below T_N = 91 K, ferrimagnetic below T_C = 73 K and antiferromagnetic below T_t = 27 K [1]. In the ferrimagnetic phase, the *c*-axis ferromagnetic component exists. We have previously reported that the propagation vector is $\boldsymbol{Q}$ = (0 0 1/3) at 1.5 K; the Q_z value does not change up to T_N [2]. In this work, we have performed the Rietveld analysis (software: *FullProff*) on the powder diffraction data taken at 5 K. The neutron diffraction measurement was made using the HQR spectrometer of JRR-3M of JAERI at Tokai.

Figure 1 shows a neutron diffraction pattern at 5 K. The observed and calculated patterns are denoted by open circles and the full line,

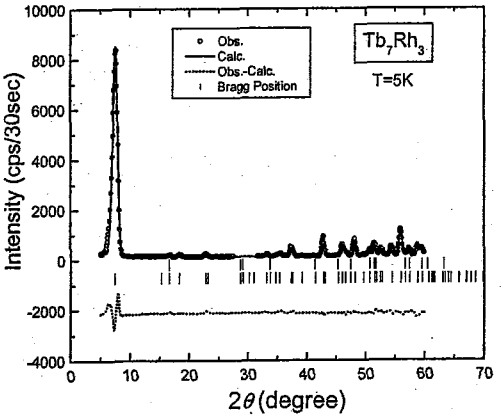

Fig.1 Neutron diffraction pattern of Tb_7Rh_3 at 5 K.

respectively. Vertical bars give possible Bragg peak positions. The observed and calculated integrated intensities of the magnetic reflections are listed in Table 1. The magnetic propagation vector was determined to be $\boldsymbol{Q}$ = (0 0 0.3312). The magnetic moment of Tb is 9.0 μ_B for the sites 1 and 2, 6.3 μ_B for the site 3, respectively. Figure

Table1. Observed and calculated integrated intensities of magnetic reflections at 5 K.

h	*k*	*l*	F_M(obs)	F_M(calc)
0	0	0.3312	1182.034	1124.715
1	0	0.3312	7.898	6.095
0	1	0.3312	5.481	4.230
1	0	0.6688	18.787	6.252
1	1	0.6688	13.853	1.870
2	0	0.3312	5.640	1.813
1	0	1.3312	32.756	11.334
0	1	1.3312	22.484	7.780
0	2	0.6688	93.535	78.500
0	0	1.6688	7.588	15.825
0	1	1.6688	168.700	188.283
1	1	1.3312	1.602	1.774
2	0	1.3312	46.400	50.440
2	1	0.6688	98.501	91.842
2	0	1.6688	45.310	42.350
0	0	2.3312	83.274	88.323
2	1	1.3312	143.755	153.811
0	1	2.3312	98.080	134.009

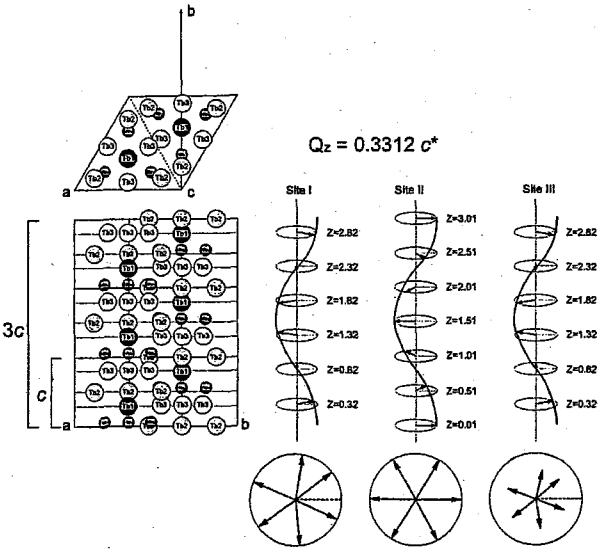

Fig.2 Magnetic structure of Tb_7Rh_3 at 5 K.

3 shows a possible helical magnetic structure of Tb_7Rh_3 at 5 K. Helical angle at the site 2 is 59.6°. The phase shift of each site is small.

References

[1] Y. Nakamori et al., Physica B **304** (2001) 1.
[2] T. Tsutaoka et al., J. Phys. Soc. Jpn. **70** (2001) Suppl. A 212.

使用施設：JRR-3M, 装置：HQR(T1-1), 分野 Magnetism

研究テーマ： クロマイト MCr_2O_4 の磁気構造 - $FeCr_2O_4$ $(M = Fe)$ -
表題： $CoCr_2O_4$ の中性子散乱

1-2-42 Neutron scattering of $CoCr_2O_4$

K. Tomiyasu, J. Fukunaga, Y. Tsunoda and K. Kohn
Department of Applied Physics, School of Science and Engineering, Waseda University, 3-4-1 Ohkubo Shinjuku Tokyo 169-8555

$CoCr_2O_4$ crystallizes into the normal spinel structure; magnetic Co^{2+} ions occupy A-sites and magnetic Cr^{3+} ions occupy B-sites. The magnetic moments consist of a ferrimagnetic and a spiral components, and Menyuk *et al* reported that both the components exhibit long-range order below T_S = 27 K.[1] In the last year, however, we reinvestigated the magnetic ordering of $CoCr_2O_4$ by neutron scattering, and found that the satellite reflection is diffusive, that is to say, the spiral component exhibits short-range order, even in lowest temperature phase. In the present manuscript, we report the temperature dependence of the spiral correlation length and of the spiral fluctuation.

A single crystal of $CoCr_2O_4$ was prepared by one of the present authors (K. K.) using the flux method. The crystal size is about $6 \times 6 \times 4$ mm^3. Neutron scattering experiments were performed on the T1-1 and C1-1 triple axis spectrometers installed at guide tubes of JRR-3M, Tokai, Japan. The energy of the incident neutrons was fixed at 13.5 meV in the T1-1 experiments and at 3 and 10 meV in the C1-1 experiments.

Figure 1 shows the temperature dependence of the line width κ of the 1.38 1.38 0 satellite reflection. As the temperature decreases, the line width gradually decreases and becomes almost constant at T_F. This fact means that the spiral correlation length ξ is about 0.8 nm at 50 K, increases and almost saturates around 3.1 nm at T_F with decreasing the temperature, because the value of ξ is obtained by taking an inverse of κ.

Figure 2 shows the temperature dependences of the 1.38 1.38 0 satellite peak intensity of the elastic component, which were taken at the center of the satellite peak with two energy (frequency) resolutions of 10 and 160 GHz. As the temperature decreases, the satellite reflection appears above 50 K and around 24 K in the 160 and 10 GHz resolution experiments, respectively. The two curves trace each other below $T_S' = 18$ K. Since the dynamic component that is slower than the energy resolution is observed as elastic scattering, these data indicate the following facts. The spiral fluctuation becomes slower with decreasing the temperature. The spiral component fluctuates with frequency that is faster than order of 100 GHz above 24 K, fluctuates with frequency of order of 10 GHz between 24 K and T_S' and falls within 10 GHz below T_S'.

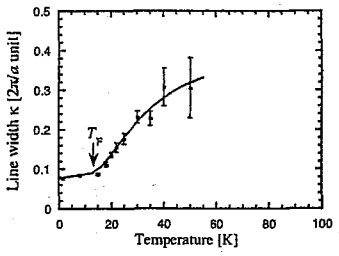

Fig. 1. Temperature dependence of the line width of the satellite reflection after correction of the Cooper and Nathans' resolution function.

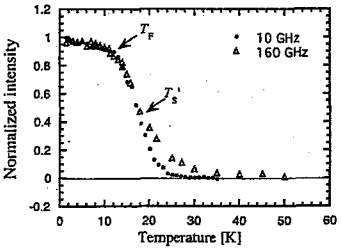

Fig. 2. Temperature dependences of the peak intensity of the elastic component taken at the center of the satellite peak with the energy resolutions 10 and 160 GHz. The intensities are normalized by extrapolating those to at 0 K.

References

[1] N. Menyuk and K.Dwight and A. Wold: J. Phys. (Paris) **25** (1964) 528.

使用施設：JRR-3M, 装置： T1-1 (HQR), C1-1 (HER) , 分野： 2. Magnetism

研究テーマ： クロマイト MCr_2O_4 の磁気構造と磁気揺らぎ – $NiCr_2O_4$ $(M = Ni)$ –
表題： $NiCr_2O_4$ の磁気構造と磁気揺らぎ

1-2-43 Magnetic structure and fluctuation of $NiCr_2O_4$

K. Tomiyasu[1] and I. Kagomiya[2†]

[1]*Department of Applied Physics, School of Science and Engineering, Waseda University, 3-4-1 Ohkubo Shinjuku Tokyo 169-8555*

[2]*Advanced Research Center of Science and Engineering, Waseda University, 3-4-1 Ohkubo Shinjuku Tokyo 169-8555*

†*Present address: National Institute of Advanced Industrial Science and Technology, Tsukuba 305-8568*

The ferrimagnets $MnCr_2O_4$, $CoCr_2O_4$ and $NiCr_2O_4$ crystallize into the normal spinel structure; magnetic Mn^{2+}, Co^{2+} and Ni^{2+} ions occupy A-sites and magnetic Cr^{3+} ions occupy B-sites. Furthermore, the magnetic moments in all these chromites are composed of a ferrimagnetic (longitudinal) and an antiferromagnetic (transverse) components.[1, 2, 3, 4, 5] Therefore, the magnetism of all these chromites is expected to be similar to each other. However, although ordering of the two magnetic components in $MnCr_2O_4$ and $CoCr_2O_4$ occurs at T_C (= 43 and 97 K) and T_S (= 18 and 25 K) separately, that in $NiCr_2O_4$ was reported to occur at T_C (= 65 K) simultaneously.[1, 2, 3] In addition, the magnetic structure of $NiCr_2O_4$ reported previously [4, 5] is too complex compared to that of $MnCr_2O_4$ and $CoCr_2O_4$ [1, 2]. To resolve these mismatches, we reinvestigated the magnetic ordering of $NiCr_2O_4$ below T_C by neutron powder diffraction.

A powder specimen of $NiCr_2O_4$ was synthesized from a stoichiometric mixture of NiO and Cr_2O_3 at 1200 °C in air. No extra lines, which cannot be explained by the spinel structure, are observed in an X-ray powder diffraction pattern of the present sample at room temperature. Neutron diffraction experiments were performed on the T1-1 and C1-1 triple axis spectrometer installed at a thermal guide of JRR-3M, Tokai, Japan. The energy of the incident neutrons was fixed at 13.5 meV in the T1-1 experiments and at 3 and 10 meV in the C1-1 experiments.

Figure 1 shows the neutron powder diffraction patterns at 100 K, 50 K and 15 K. The fundamental reflections and the Q = (0,0,1) superlattice reflections are observed at 15 K. The former and latter reflections come from the ferrimagnetic component and the antiferromagnetic component, respectively.

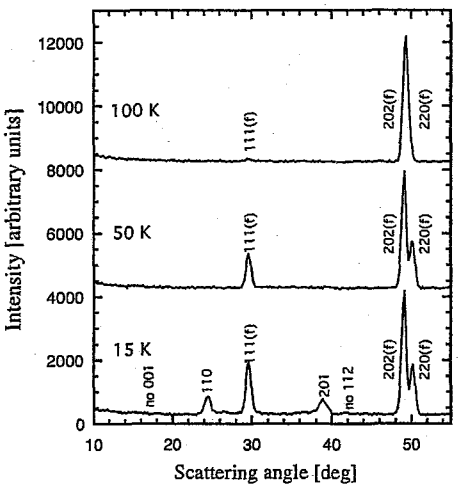

Fig. 1. Neutron powder diffraction patterns at 100 K, 50 K and 15 K. The symbol (f) means fundamental reflection.

Figure 2 shows the temperature dependence of the peak intensity of these reflections. As the temperature decreases, only the longitudinal component appears at T_C = 74 K, and the transverse component emerges at $T_S' = 35$ K.

Table 1 gives the experimental integrated intensity of magnetic scattering. The experimental magnetic scattering integrated intensity of the fundamental reflections was obtained by subtracting the data at 100 K from those at 15 K, and that of the superlattice reflections was obtained by subtracting the data at 50 K from those at 15 K. To determine the magnetic structure of $NiCr_2O_4$

使用施設：JRR-3M, 装置： T1-1 (HQR), C1-1 (HER) , 分野： 2. Magnetism

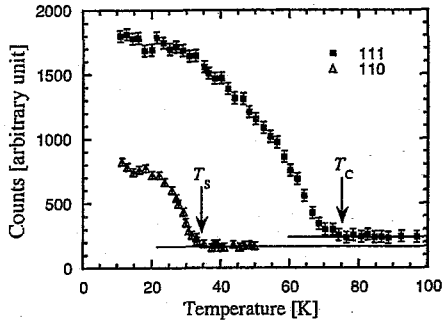

Fig. 2. Temperature dependence of the peak intensity of the 111 fundamental and the 110 superlattice reflections.

Table 1. Experimental and best-fit calculated magnetic scattering intensity. The symbol N.O. means that no reflection was observed within statistical uncertainty.

hkl	experimental	calculated
001	N.O.(< 70)	0
110	499	533
201	429	423
112	N.O.(< 80)	100
002 + 200	N.O.(< 80)	0
111	1430	1426
220 + 202	N.O.(< 150)	149
R-factor	-	1.0%

at 15 K ($T < T_S$), these intensities at 15 K were calculated so as to best fit the observed values in a least squares method. The best-fit new magnetic structure model, which is as simple as other chromites $MnCr_2O_4$ and $CoCr_2O_4$, is shown in Figure 3.

Figure 4 shows temperature dependence of the 110 peak intensity measured by using two incident energy 3 and 10 meV. As the temperature decreases, the 110 reflection appears at 32 and 35 K in 3 and 10 meV experiments, respectively. This fact means that the magnetic fluctuation of the transverse component gradually becomes slower with decreasing the temperature, since the lower incident energy gives the higher resolution of energy.

In this way, the mismatches among the chromites have been solved by the present reinvestigation. However, the present magnetic structure of $NiCr_2O_4$ is not proposed by

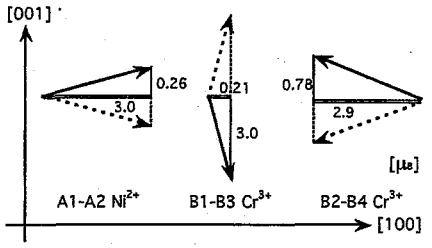

Fig. 3. The new magnetic structure model of $NiCr_2O_4$ below $T_S = 31$ K. The transverse component exhibits collinear (only up or down) antiferromagnetic ordering described by propagation vector $Q = (0,0,1)$.

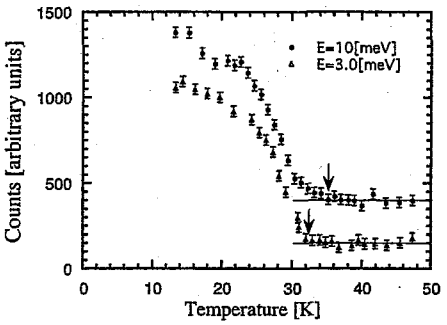

Fig. 4. Temperature dependence of the 110 peak intensity measured by using two incident energy.

the KDLM theory and LKDM theory, which solves the Heisenberg Hamiltonian for the $3d$-metal MCr_2O_4.[6, 7] More detailed theory is required to explain the magnetic structures of the $NiCr_2O_4$.

References

[1] J. M. Hastings and L. M. Corliss: Phys. Rev. **126** (1962) 556.

[2] N. Menyuk and K.Dwight and A. Wold: J. Phys. (Paris) **25** (1964) 528.

[3] E. Prince: J. Appl. Phys. **32** (1961) 68S.

[4] E. F. Bertaut and J. Dulac: Acta. Crystallogr. **A28** (1972) 580.

[5] E. F. Bertaut and J. Dulac: Acta. Crystallogr. **A36** (1980) 157.

[6] T. A. Kaplan and K. Dwight and D. H. Lyons and N. Menyuk: J. Appl. Phys. **32** (1961) 13S.

[7] D. H. Lyons and T. A. Kaplan and K. Dwight and N. Menyuk: Phys. Rev. **126** (1961) 540.

研究テーマ：Sr2NiWO6 の磁気形状因子

表題：規則型複合ペロブスカイト酸化物反強磁性体のスピン密度分布

1-2-44 Spin Density Distribution in Ordered Complex Perovskites

Y. Todate[1], H. Kimura[2], and Y. Noda[2]

[1] *Department of Physics, Ochanomizu University, Otsuka, Bunkyo-ku, Tokyo 112-8610*

[2] *IMRAM, Tohoku University, Katahira, Aoba-ku, Sendai 980-8577*

Among many composite oxides with perovskite-related structure the compounds with B-site ordering of magnetic and non-magnetic ions form a face-centered magnetic lattice and usually show the type-II antiferromagnetic (AF) ordering at low temperatures. It is interesting to compare static and dynamic properties of magnetic moments between prototypical monoxides such as NiO and these ordered perovskites which exhibit similar magnetic ordering on the fcc lattice because, despite considerable difference in the ionic environment, apparent similarities[1] in the magnetic properties would conversely suggest some difference in the form of localized moments in the ordered perovskites. In connection to this, it has also been argued [2] that the electron-spin transfer due to the covalent bonding effect may be observed in the magnetic form factor in smaller Q-region. The magnetic ordered perovskite is therefore the best suited material for this study because of the large, doubled unite cell dimension which gives the magnetic reflections inside $\sin(\theta)/\lambda \sim 0.1$ and also because of its simple structure.

In order to obtain information on the magnetic moment distribution in Ni-based ordered AF perovskites, single crystal diffraction experiment has been carried out on FONDER at JRR-3M in JAERI. Collection of nuclear and magnetic reflections from cubic Ba_2NiWO_6 was carried out at 8K. The Néel temperature is 48K and the sample size was 4.4mmϕ×3.0mm$h$. The nuclear and magnetic reflection intensities have been converted into absolute scale assuming the reported Fm3m cubic structure.[2] Because of the type-II AF structure, there are four types of incompatible magnetic domains with different spin orientation factors to be corrected. Magnetic reflections were grouped into these four groups and the corrected data are plotted in Fig. 1. The domain distribution seems to be nearly equal and somewhat larger magnetic scattering factor has been obtained compared with the value $S = 1.0$ ($2.2\mu_B$) expected for Ni^{2+}. Furthermore, Q-dependence is flatter than the calculated form factor and even flatter than the observed form factor for NiO.[3] Another feature to be noted is a dip around $\sin(\theta)/\lambda \sim 0.13$. It is not conclusive at the present time whether these differences are originated in the different spatial distribution of the magnetic moment including the orbital contribution. Comparison would be desirable in the whole (higher) Q-region.

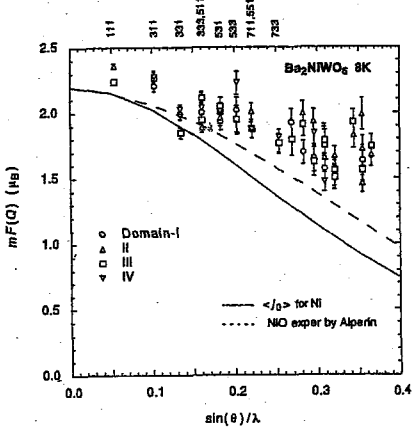

Fig. 1. Observed magnetic structure factor $mF(Q)$. Calculated and observed magnetic form factors for NiO[4] are also compared.

References

[1] Y. Todate: J. Phys. Chem. Solids **60** (1999) 1173.

[2] J. Hubbard and W. Marshall: Proc. Phys. Soc. **86** (1965) 561.

[3] S. Nomura and T. Kawakubo: J. Phys. Soc. Jpn. **17** (1962) 1771.

[4] H. A. Alperin: J. Phys. Soc. Jpn. suppl. B-III **17** (1962) 12.

使用施設：JRR-3M, 装置： T2-2 (FONDER), 分野： 2. Magnetism

研究テーマ： $Ho_{1-x}Y_xB_2C_2$ の長周期磁気構造
表題： $Tb_{0.5}Y_{0.5}B_2C_2$ の粉末中性子回折

1-2-45 Neutron Powder Diffraction of $Tb_{0.5}Y_{0.5}B_2C_2$

A. Tobo[1], M. Haino[1], K. Ohoyama[2] and H. Onodera[1]
[1] *Fac. of Science, Tohoku Univ., Aramaki, Aoba, Sendai, Miyagi 980-8578*
[2] *Institute for Materials Research, Tohoku Univ., Katahira, Aoba, Sendai, Miyagi 980-8577*

RB_2C_2 (R: Rare Earth) shows complicated magnetic behavior due to an antiferroquadrupolar (AFQ) ordering and an antiferromagnetic (AFM) ordering. TbB_2C_2 is antiferromagnet with $T_N = 21.7$ K, but the AFQ order is induced by magnetic fields [1, 2]. In order to investigate the mechanism of magnetic field induced AFQ phase, we try changing the strength of interactions in TbB_2C_2 by substituting nonmagnetic Y^{3+} ion for Tb^{3+} ion.

The $Tb_{0.5}Y_{0.5}B_2C_2$ compound was synthesized by conventional argon arc technique. In fig. 1, we show the temperature dependence of low-field magnetization M. A kink is observed at 4.9 K. Neutron powder diffraction experiments were performed using the high efficiency and resolution powder diffractometer HERMES (T1-3) installed at JRR-3M, JAERI. For the measurements, we prepared the powder sample using 99.5 % enriched ^{11}B, since the natural B atoms strongly absorb neutrons.

In fig. 2, we show the neutron powder diffraction patterns of $Tb^{11}B_2C_2$ and $Tb_{0.5}Y_{0.5}{}^{11}B_2C_2$. The antiferromagnetic structure of $Tb^{11}B_2C_2$ is described by a main propagation vector $(1\ 0\ \frac{1}{2})$ accompanied with a small $(0\ 0\ \frac{1}{2})$ component, a long periodic $(1 \pm \delta\ \pm \delta\ 0)$ component and an anomalous diffusive component distributed widely around (1 0 0) [1]. For $Tb_{0.5}Y_{0.5}{}^{11}B_2C_2$, the magnetic reflections that are correspond to propagation vectors $(1\ 0\ \frac{1}{2})$ and $(1 \pm \delta\ \pm \delta\ 0)$ are observed. The magnetic moments which correspond to propagation vector $(1\ 0\ \frac{1}{2})$ for $Tb^{11}B_2C_2$ and $Tb_{0.5}Y_{0.5}{}^{11}B_2C_2$ are $\sim 5.8\mu_B$ and $\sim 1.6\mu_B$, respectively. The magnetic reflections that are correspond to $(1 \pm \delta\ \pm \delta\ 0)$ for $Tb_{0.5}Y_{0.5}{}^{11}B_2C_2$ is relatively large, although the peaks are very broad. There is no evidence of the AFQ order at $H = 0$ for $Tb_{0.5}Y_{0.5}B_2C_2$, and we consider that the basic magnetic structure of $Tb_{0.5}Y_{0.5}B_2C_2$ is basically the same as that of TbB_2C_2.

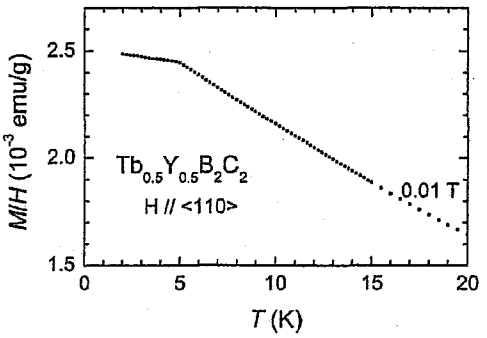

Fig. 1. Temperature dependence of magnetization M measured with a field of 0.01 T apllied pararell to $\langle 1\ 1\ 0 \rangle$.

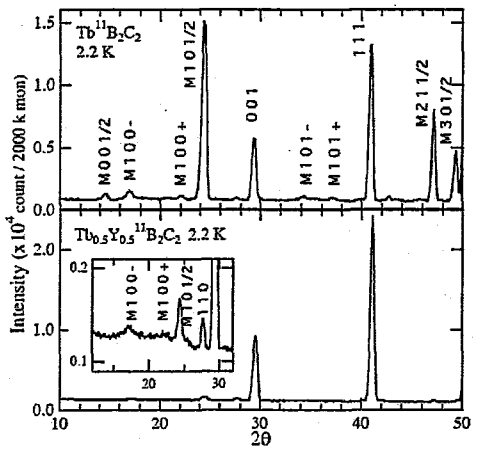

Fig. 2. Neutron powder diffraction patterns of $Tb^{11}B_2C_2$ [1] and $Tb_{0.5}Y_{0.5}{}^{11}B_2C_2$ at 2.2 K. The magnetic reflections are denoted by the letter M.

References

[1] K. Kaneko *et al.*: J. Phys. Soc. Jpn. **70** (2001) 3112.
[2] K. Kaneko *et al.*: Phys. Rev. B **70** (2003) 012401.

使用施設：JRR-3M, 装置： T1-3 (HERMES) , 分野： 2. Magnetism

研究テーマ：三角格子反強磁性体 $CuFeO_2$ における異常磁気励起

1-2-46 三角格子反強磁性体 $CuFe_{1-x}Al_xO_2$ の熱誘起相における磁気構造変化

Reinvestigation of Magnetic Structures for the Thermally Induced States of $CuFe_{1-x}Al_xO_2$ (x=0.00, 0.02 and 0.05) Using Four-Circle Neutron Diffractometer

N. Terada[1], T. Kawasaki[1], S. Mitsuda[1] and H. Kimura[2]

[1]*Department of Physics, Faculty of science, Tokyo University of Science, 1-3 kagurazaka, shinjuku-ku, Tokyo, 162-0825*

[2]*Institute of Multidisciplinary Research for Advanced Materials, Tohoku University, Sendai 980-8577*

As one of the model materials of frustrated triangular lattice antiferromagnet (TLA), the delafossite compound $CuFeO_2$ has been extensively studied. Although $CuFeO_2$ is considered to be a Heisenberg spin TLA with $S=\frac{5}{2}$ of orbital singlet Fe^{3+}, it shows features of Ising spin TLA; particularly, a sinusoidally amplitude-modulated magnetic structure with magnetic moments along the c-axis (PD(0°)) is realized as the thermally induced state.[1] Recently, we suggested that a small amount of non-magnetic impurity gives a dramatic change from the quasi-Ising to Heisenberg in character.[2, 3], where we inferred that a proper screw type magnetic structure shown in Fig. 1(a) is realized in the IM state of $CuFe_{1-x}Al_xO_2$ with x=0.02, through the measurement restricted to (hhl) zone. The intensity data observed in the (hhl) zone, however, can be explained by a sinusoidally amplitude-modulated structure with the moments canted at 45° degrees from the c-axis toward the $\langle 1\bar{1}0\rangle$ direction (PD(45°)), which is shown in Fig.1(b), as well as the proper screw type structure. This time, in order to determine the magnetic structures of the IM state in $CuFe_{1-x}Al_xO_2$ with x=0.02 and x=0.05, we performed neutron diffraction measurements using FONDER diffractometer that can survey magnetic Bragg peaks three-dimensionally.

As clearly seen in the index l-dependences of the spin orientation factors beyond the (hhl) zone shown in Figs. 1(c) and (d), the observed spin orientation factors were explained not by the proper screw type structure but by the PD(45°) structure, suggesting that the PD(45°) structure is realized in the IM states of both x=0.02 and 0.05 samples. It should be emphasized that the diffusive magnetic excitation spectrum observed in the IM state[3] is consistent not with the static proper screw type structure but with the thermally fluctuating PD(45°) structure.

In addition to these measurements, we performed the measurement for the PD state in the x=0.00 sample, using FONDER. The result was not inconsistent with the PD(0°) structure.

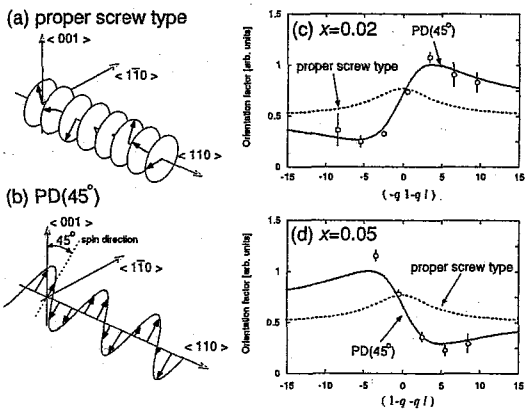

Fig. 1. Schematic drawings of (a) proper screw type magnetic structure and (b) PD(45°) structure. Typical index l-dependences of spin orientation factors (c) along (-q 1-q l) in the x=0.02 sample and (d) along (1-q -q l) in the x=0.05 sample: open circles show observed spin orientation factors after extinction correction, and solid and broken lines show the calculated ones.

References

[1] S. Mitsuda et al, J. Phys. Soc. Jpn. 67, 4026 (1998).

[2] N. Terada et al, J. Phys. Soc. Jpn. 73, 1442 (2004).

[3] N. Terada et al, J. Magn. Magn. Mater. 272-276S, E997-E998 (2004)

使用施設：JRR-3M，装置： FONDER(T2-2)，分野： 2. Magnetism

研究テーマ： 三角格子反強磁性体 $CuFeO_2$ における異常磁気励起

1-2-47 三角格子反強磁性体 $CuFe_{1-x}Al_xO_2$ における希釈-温度磁気相図

Magnetic Phase Diagram of Triangular Lattice Antiferromagnet $CuFe_{1-x}Al_xO_2$

N. Terada[1], T. Kawasaki[1], T. Fujii[1] and S. Mitsuda[1]

[1]*Department of Physics, Faculty of science, Tokyo University of Science, 1-3 kagurazaka, shinjuku-ku, Tokyo, 162-0825*

Delafossite compound $CuFeO_2$ has been extensively investigated as one of ABO_2-type materials for triangular lattice antiferromagnet. In spite of the Heisenberg spin of orbital singlet Fe^{3+} (S=$\frac{5}{2}$, L=0) magnetic ions, *quasi-Ising character* is stabilized with delicate balance of competing exchange interactions.[1] Recently, we reported the significant difference between the successive magnetic phase transitions of $CuFe_{1-x}Al_xO_2$ with x=0.00 and x=0.02, suggesting that the quasi-Ising character of the x=0.00 sample disappears in the x=0.02 sample by a small amount of non-magnetic Al^{3+} impurity.[2, 3] This time, in order to investigate the critical concentration "x_C" between x=0.00 and x=0.02, where the quasi-Ising chracter disappears, we have performed elastic neutron diffraction experiments for the single-crystals of $CuFe_{1-x}Al_xO_2$ with x=0.010 and x=0.015, using HQR and GPTAS.

As shown in Fig. 1(a), with decreasing temperature from paramagnetic state, a magnetic Bragg reflection, indexed as (q_{PD} q_{PD} $\frac{3}{2}$), appears below $T_{N1}^{x=0.010} \sim 14$K, where the incommensurate wave number q_{PD} continuously shifts toward the commensurate 4-sublattice reciprocal lattice point of ($\frac{1}{4}$ $\frac{1}{4}$ $\frac{3}{2}$). With further decreasing temperature, the wave number finally jumps to the 4-sublattice point below $T_{N2}^{x=0.010} \sim 8$K. Thus, although $T_{N2}^{x=0.010}$ shifts toward low temperature side from $T_{N2}^{x=0.000} \sim 10.5$K, the behavior of the wave number, which characterizes these states, qualitatively coincide with that of the x = 0.000 sample, suggesting that the quasi-Ising character seen in the x = 0.000 sample remains in the x = 0.010.

As shown in Fig. 1(b), with decreasing temperature from paramagnetic state in the x=0.015 sample, a magnetic Bragg reflection (q_{IM}-reflection) appears below $T_{N1}^{x=0.015} \sim 14$K, where the wave number q_{IM} is almost independent of temperature. With further decreasing temperature, the integrated intensity $I_{q_{IM}}$ starts to decrease below $T_{N2}^{high} \sim 10.5$K; instead, another reflection of q_{LT}-reflection start to grow in the "coexistence region" ($T_{N2}^{low} \leq T \leq T_{N2}^{high}$). Moreover, below T_{N2}^{low}, in addition to the q_{LT}-reflection, the other reflections, q'_{LT}- and ($\frac{1}{2}$-q'_{LT})-reflection, appear in the LT state. Thus, the successive magnetic phase transitions of the x=0.015 sample coincide with those of the x=0.020 sample except the shift of T_{N2}^{low} and T_{N2}^{high}.

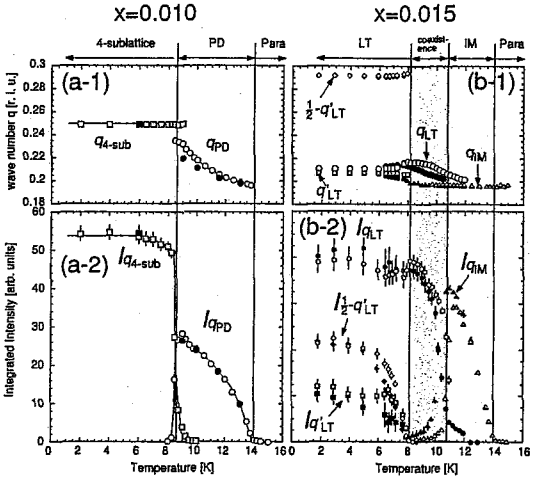

Fig. 1. Temperature dependences of (1) propagation wave number q and (2) integrated intensity of magnetic Bragg reflections in $CuFe_{1-x}Al_xO_2$ with (a) x=0.010 and (b) x=0.015. Open and closed symbols are used for increasing and decreasing temperature processes, respectively. Shading denotes the coexistence region between T_{N2}^{high} and T_{N2}^{low}.

References

[1] S. Mitsuda et al, J. Phys. Soc. Jpn. 67, 4026 (1998).

[2] N. Terada et al, J. Phys. Soc. Jpn. 73, 1442 (2004).

[3] N. Terada et al, submitted to Phys. Rev. B.

使用施設：JRR-3M, 装置： HQR(T1-1), TAS(4G) , 分野： 2. Magnetism

研究テーマ： 三角格子反強磁性体 $CuFeO_2$ における異常磁気励起

1-2-48 三角格子反強磁性体 $CuFeO_2$ における異常磁気励起

Anomalous Magnetic Excitation on Triangular Lattice Antiferromagnet $CuFeO_2$

N. Terada[1] and S. Mitsuda[1]

[1]*Department of Physics, Faculty of science, Tokyo University of Science, 1-3 kagurazaka, shinjuku-ku, Tokyo, 162-0825*

ABO_2-type compound with delafossite structure is a good example of geometrically frustrated triangular lattice antiferromagnet (TLA). $CuFeO_2$ has been extensively investigated as one of ABO_2-type TLA model materials. In spite of the Heisenberg spin character of orbital singlet Fe^{3+} (S=$\frac{5}{2}$, L=0) magnetic ions, $CuFeO_2$ shows *quasi-Ising* character with the delicate balance of competing exchange interactions.[1] In fact, our recent study showed the quasi-Ising character easily disappears by a small amount of non-magnetic Al^{3+} impurity, observing the changes in both successive magnetic phase transitions[2] and H-T magnetic phase diagram.[3] Our preliminarly measurements of spin-wave dispersion curves for $CuFeO_2$ and $CuFe_{0.98}Al_{0.02}O_2$ suggested that the quasi-Ising chracter seen in $CuFeO_2$ disappears and the original Heisenberg spin character is retrieved.[4] However, the dispersion curve for $CuFe_{0.98}Al_{0.02}O_2$ was taken in the low energy region around the one of the magnetic Bragg points with $q \sim 0.21$. This time, in order to obtain the whole dispersion relation over the zone, we have performed inelastic neutron scattering on $CuFe_{0.98}Al_{0.02}O_2$, using GPTAS and HER.

The spin-wave dispersion curves, which consist of two spin-wave branches, "higher" and "lower" energy branch, are shown in Fig. 1, . While the "lower" energy branch starts from $h \sim 0.21$ and 0.29, there is an energy gap for the "higher" energy branch whose bottom position is $h \sim 0.21$. Comparing this results with spin-wave branches observed for $CuFeO_2$ shown in the inset of Fig. 1, we found that the energy gap of "lower" energy branch in $CuFeO_2$ goes to zero in $CuFe_{0.98}Al_{0.02}O_2$; on the other hand, the "higher" energy branch of $CuFeO_2$ almost remains unchanged in $CuFe_{0.98}Al_{0.02}O_2$. Note here that the magnetic orderings in the LT phase in $CuFe_{0.98}Al_{0.02}O_2$ are characterized by three propagation wave numbers, q_{LT}, q'_{LT} and $\frac{1}{2}$-q'_{LT} with $q_{LT} \sim q'_{LT} \sim 0.21$.[2] Considering the magnetic orderings in the LT phase, we infer that "softening" of the "lower" energy branch causes Heisenberg magnetic orderings with q'_{LT} and $\frac{1}{2}$-q'_{LT}, and the "higher" energy branch with the gap corresponds to the magnetic ordering with q_{LT}. Thus the ordering with q_{LT} must have Ising-like character.

In addition to these measurements, we also performed inelastic neutron scattering for $CuFe_{0.95}Al_{0.05}O_2$, using HER. As a result, diffusive magnetic excitation spectrum was observed down to 2K.

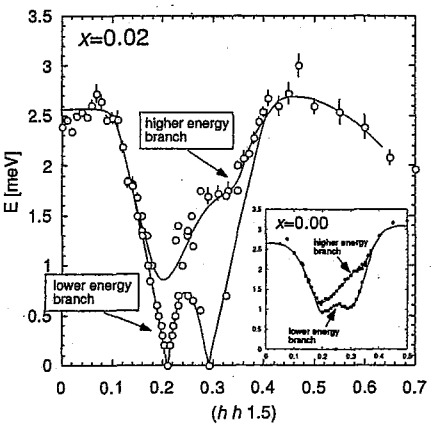

Fig. 1. Spin-wave dispersion relation along the ($hh\frac{3}{2}$) at $T \sim 4$K in $CuFe_{0.98}Al_{0.02}O_2$. The inset show the spin-wave dispersion relation of $CuFeO_2$. Solid lines are guide for the eyes.

References

[1] S. Mitsuda et al, J. Phys. Soc. Jpn. 67, 4026 (1998).

[2] N. Terada et al, J. Phys. Soc. Jpn. 73, 1442 (2004).

[3] N. Terada et al, submitted to Phys. Rev. B.

[4] N. Terada et al, J. Magn. Magn. Mater. 272-276S, E997-E998 (2004)

使用施設：JRR-3M, 装置： HER(c1-1), GPTAS(4G) , 分野： 2. Magnetism

研究テーマ： $Pt_{1-c}Mn_c$ ($c < 0.16$) の磁気構造揺らぎ
表題： $Pt_{1-c}Mn_c$ ($c < 0.16$) の磁気構造揺らぎ

1-2-49 Magnetic Fluctuation in $Pt_{1-c}Mn_c$ ($c < 0.16$)

M. Takahashi[1], K. Ohshima[1], T. Shishido[2] and K. Hirota[3]
[1] *Institute of Materials Science, University of Tsukuba, Tsukuba 305-8573*
[2] *Institute for Materials Research, Tohoku University, Sendai 980-8577*
[3] *Institute for Solid State Physics, The University of Tokyo, 106-1 Shirakata, Tokai, 319-1106*

The magnetism of $Pt_{1-c}Mn_c$ between 0.12 to 0.16 is very unique. The magnetic structure changes drastically with a little change of atomic arrangement and Mn concentration, while magnetic susceptibility always shows a spin-glass like behavior.[1] In the ordered alloys with the ABC_6 type structure, fourfold splitting along [011] and [0$\bar{1}$1] with incommensurate maxima at $1/2, \pm 0.06, \pm 0.06$ and $1/2, \pm 0.06, \mp 0.06$ appears with diffuse scattering around $1/2, 0, 0$ in c=0.125, while in c=0.144, commensurate superlattice peaks appear at $1/2, \pm 1/4, 0$ and $1/2, 0, \pm 1/4$. The incommensurate peaks are due the SDW formation, while the commensurate ones are due to antiferromagnetic interaction between near-neighbor Mn atoms. In order to understand the relation between the magnetic structure and spin-glass like behavior, inelastic neutron scattering measurements were performed on the ordered $Pt_{1-c}Mn_c$ with $c = 0.125$ at TOPAN(6G) in JRR-3M. Temperature dependence of the line profile along [100] at 0.0 meV in the upper part of Fig. 1 shows that both incommensurate peaks (at h=$\pm$0.06) and commensurate peaks (at h = $\pm 1/4$) decrease their intensities with increasing temperature. On the other hand, at 1.5 meV (in the lower part of the figure), diffuse intensity with maxima at h$\sim$ $\pm$0.06 and $\pm$0.25 increases with increasing temperature. The inelastic scattering pattern of 1.5 meV on the (hk0) scattering plane at 40 K in Fig. 2 shows anisotropic diffuse rods along [100] and [010]. The distribution and temperature dependence of the inelastic intensity show quite similar behavior as observed in c=0.144 sample in which SDW peaks do not appear. The results indicate that dynamical fluctuations of the SDW survive in these samples.

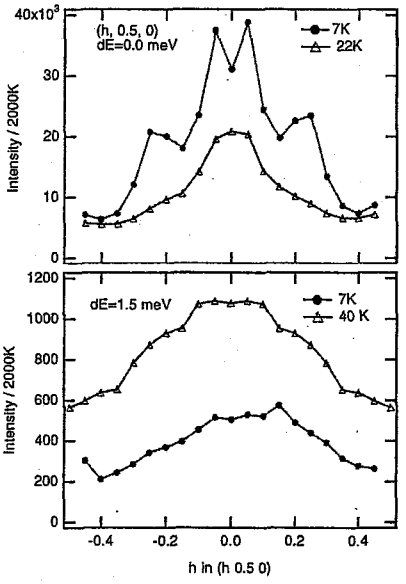

Fig. 1. Temperature dependence of the line profile along [100] at 0.0 meV (upper) and 1.5 meV (lower).

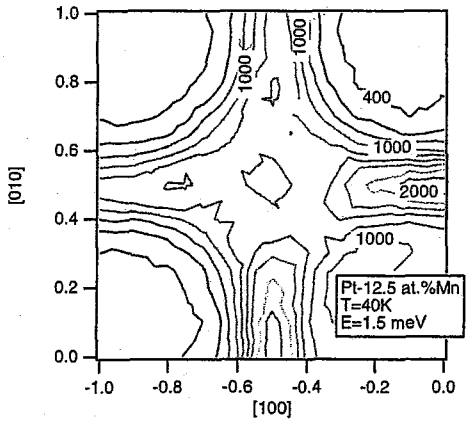

Fig. 2. Inelastic scattering pattern on the (hk0) plane at 40 K for 1.5 meV.

References

[1] M,Takahashi *et al.*: Phys. Rev B, to be published.

使用施設：JRR-3M，装置： 6G(TOPAN)，分野： 2. Magnetism

申請時のテーマ:三元系 Ni_2In 型金属間化合物の磁気構造
表題:$(Mn_{1-x}T_x)_{65}Sn_{35}$ (T=Ti, Cr)の中性子回折と磁性

1-2-50

Magnetic and Neutron Diffraction Study on Ni_2In type $(Mn_{1-x}T_x)_{65}Sn_{35}$ (T=Ti,Cr)

H.Shiraishi, T.Hori, K.Ohoyama[a], Y.Yamaguchi[a]

Shibaura Institute of Technology, Oomiya, Saitama 337-8570, Japan
[a]*Institute of Materials Research, Tohoku University, Sendai 980-8577, Japan*

The compound $(Mn_{1-x}T_x)_{65}Sn_{35}$ (T=Ti, Cr) is a single phase of Ni_2In type for $0 \leqq x < 0.3$. In Cr system, both a and c decrease a little with increasing x, though, in Ti system it increased rapidly reflecting the larger atomic radius of Ti than that of Mn. The σ-T curve for x=0.25 in Cr system shows a small concave region at T_t as shown in Figure 1. The χ_{ac}-T curve for x=0.25 shows two anomalies clearly at T_f and T_t as shown in the inset of Figure 1. The neutron diffraction experiments were carried out for x=0.25 in Cr system at several temperatures. The neutron diffraction intensity for paramagnetic state at T=200K were analyzed by the Rietveld refinement methods. The determined distribution of atoms among the sublattice is as follows: 2(a) sites is occupied by Mn (0.87)+Cr(0.13), 2(d) sites is occupied by Mn(0.618)+ Cr (0.37) and 2(c) sites is occupied by Sn(1.00). In the temperature $T \leqq T_t$, the diffraction pattern shows one extra magnetic (001) reflection indicating the presence of an antiferromagnetic component lying in the basal plane. As the magnetic

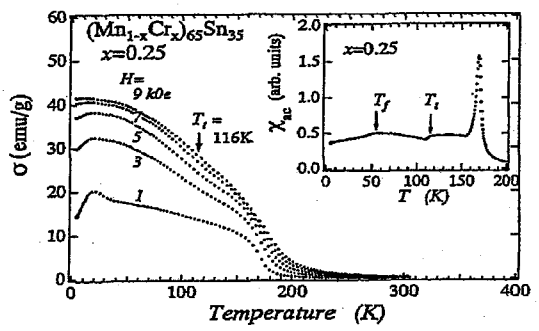

Fig.1. The σ-T curve and χ_{ac}-T curve (inset) for x=0.25.

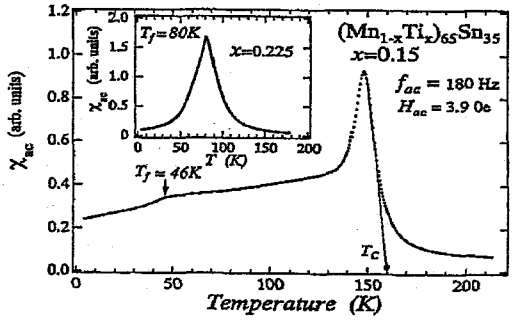

Fig.2. The χ_{ac}-T curve for x=0.15 and x=0.225 for Ti system.

contribution to the (002) reflection is negligible, the ferromagnetic component is parallel to the c axis. So the magnetic structure of $(Mn_{1-x}Cr_x)_{65}Sn_{35}$ is noncollinear type in the temperature $T \leqq T_t$, and changes to collinear type at $T > T_t$. The magnetic structure at $T \leqq T_t$ is similar to the canted spin arrangement at low temperatures in MnCoSn[1]. The χ_{ac}-T curve for x=0.15 in Ti system is shown in Figure 2. The sharp peak in higher temperature is Hopkinson peak for ferrimagnetic Curie temperature T_c. The χ_{ac}-T curve also shows a change of curvature at the ferrimagnetic to re-entrant spin glass-like state transition temperature T_f. The x dependence of T_c changes similarly to that of σ. The inset of Figure 2 shows a cusp of χ_{ac}-T curve for x=0.225. The χ_{ac}-T curve for $0.225 \leqq x \leqq 0.3$ shows only a cusp, indicating the direct transition between a paramagnetic state and a spin-glass state.

[1] W.Bazela, A.Szytula, W.Zajac, Solid State Commun. **38** (1981) 875.

Reacter(JRR-3M), Facility(T1-3), Field(Magnetism)

研究テーマ:強磁性と反強磁性相互作用が競合する系の磁性
表題:$(Pd_{1-X}Ag_X)_{90}Mn_{10}$ スピングラスの中性子散乱

1-2-51

Spin-glass state of $(Pd_{1-x}Ag_x)_{90}Mn_{10}$ Alloys

Kenzo Sato, Yoichi Ito and Yorihiko Tsunoda

Sch. of Sci. & Engi. Waseda University, 3-4-1 Ohkubo, Shinjuku, Tokyo 169-8555 Japan

Both PdMn and AgMn alloys are typical spin-glass systems. The origin of the glass like behavior of those magnetic systems is considered to come from the freezing of the SDW clusters which are a reflection of the parallel shaped Fermi surfaces of Pd and Ag metals. However, the direction and distance of the parallel Fermi surfaces for Pd are completely different from those for Ag; For Pd metal, parallel planes are normal to the cubic axis, resulting that the SDW satellite diffuse peaks are observed at $1\mp\delta\ 0\ 0$ on the [1 0 0] axis. For Ag metal, the parallel Fermi surfaces are nearly normal to the [1 1 0] axis, resulting in the $1\ 1/2\mp\delta\ 0$ diffuse satellite reflections. PdAg alloy forms continuous solid solutions in all concentration range. Thus, we can observe the continuous change of the Fermi surfaces through the SDW satellite peak positions. Purpose of the present investigation is to observe this point.

Single crystal specimens of $(Pd_{1-x}Ag_x)_{90}Mn_{10}$ alloys with X=0.1, 0.15 and 0.3 were prepared by the Bridgman method. Neutron scattering measurements were performed at the T1-1 triple axis spectrometer. The experimental data obtained by scanning along the [1 0 0] axis are given in Fig. 1. In this figure, the data at paramagnetic phase are subtracted to obtain the magnetic contribution. The satellite diffuse peak positions slightly shift towards the 1 0 0 reciprocal lattice point with increasing Ag concentration.

This is completely inconsistent with the theoretical calculations; the calculation predicts that the hole surface shrinks with increasing Ag concentration, indicating that the satellite peak position should shift towards the original point with increasing Ag concentration.

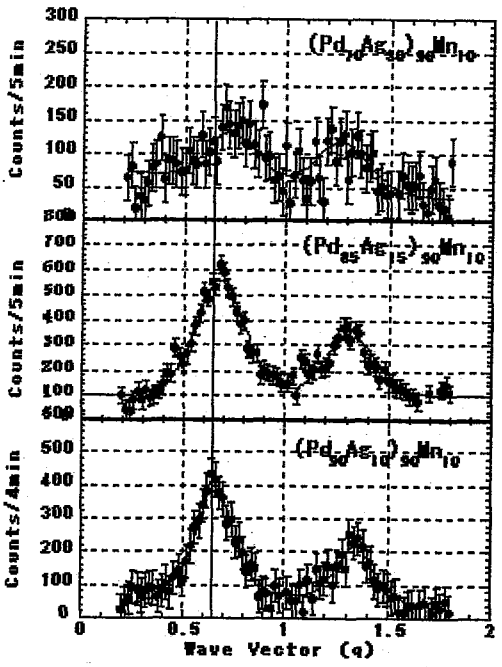

Fig.1 Magnetic diffuse peaks obtained for (PdAg)Mn alloys

The discrepancy would be explained by the segregation of the system; although PdAg alloy forms continuous solid solution in whole concentration range, PdMn alloy is more stable than AgMn alloy and the PdAgMn system segregates into PdMn and Ag. Thus, if we replace a part of Pd into Ag in the PdMn alloy, the effective Mn concentration of PdMn alloy increases with increasing Ag concentration, resulting that the satellite peak position shifts towards the 1 0 0 reciprocal lattice point. This is consistent with the experimental data. Thus, although PdAg alloy forms continuous solid solution, the spin-glass like behavior of (PdAg)Mn alloy would be that of PdMn alloy.

使用施設:JRR-3M, 装置:T1-1, 分野: Magnetism

研究テーマ： p型 ZnMgRE(RE: 希土類元素) 準結晶の磁性

1-2-52 p 型 Zn-Mg-RE 準結晶の磁気相関

Magnetic correlations in the p-type icosahedral Zn-Mg-RE quasicrystals

T. J. Sato[1,3] and A. P. Tsai[2,3,4]

[1] *NSL, ISSP, University of Tokyo, Tokai, Ibaraki 319-1106, Japan*
[2] *IMRAM, Tohoku University, Sendai 980-8577, Japan*
[3] *SORST-JST, Kawaguchi Saitama 332-0012, Japan*
[4] *MEL, NIMS, Sengen, Tsukuba, 305-0047, Japan*

Quasicrystals are characterized by sharp Bragg reflections with a point symmetry that is forbidden in a periodic lattice, such as the five-fold symmetry. Magnetism of quasicrystals has been a fundamental issue of study since its discovery; the face-centered-icosahedral Zn-Mg-RE (RE: rare-earth) quasicrystals are the play ground for the magnetic study to date, whereas the recently-discovered primitive (p-) icosahedral Zn-Mg-RE quasicrystals are totally unexplored. In the present study we have performed neutron elastic and inelastic scattering experiments on the powder samples of the p-Zn-Mg-Ho quasicrystals.

The neutron scattering experiments were performed at the triple-axis spectrometer 4G-GPTAS. Incident neutron energy was fixed to 14.5 meV with using a PG filter to eliminate higher harmonics contamination. Shown in Fig. 1 is temperature difference of the scattering intensity observed at the low temperature $T = 3$ K and the paramagnetic temperature $T = 30$ K; the difference can reasonably represent the magnetic scattering component. The development of the short-range magnetic correlations is clear from the significant diffuse scattering peak appearing at $Q \simeq 0.55$ Å^{-1} Note that the pattern is quite similar to that observed in the f-Zn-Mg-RE quasicrystals [1]. Shown in Fig. 2 are the representative inelastic scattering spectra observed at $Q \simeq 0.55$Å^{-1}, recorded at several temperatures. An outstanding feature of the inelastic spectrum is the temperature independence of the scattering intensity for the $E > 0$ side. This independence is not an experimental error, as the intensity for the $E < 0$ side increases at elevated temperatures. This temperature independence requires a particular temperature dependence of the intrinsic spectral weight function in the quasicrystalline spin system.

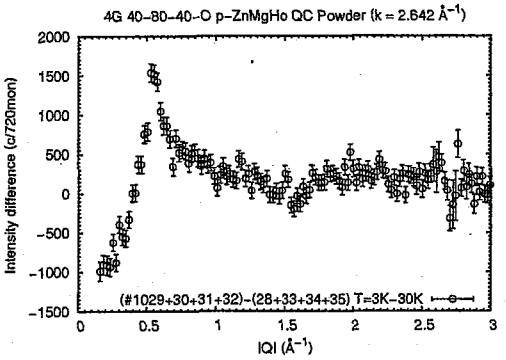

Fig. 1. Temperature difference $(I(3\text{ K}) - I(30\text{ K}))$ of the powder diffraction intensity of the p-Zn-Mg-Ho quasicrystal.

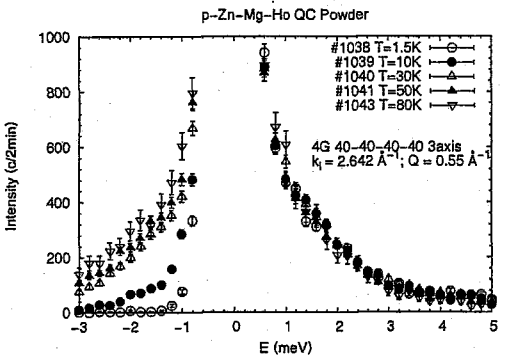

Fig. 2. Inelastic neutron scattering spectra of the p-Zn-Mg-Ho quasicrystal. Spectra at several different temperatures are shown.

References

[1] T. J. Sato *et al.* : Phys. Rev. Lett. 81 (1998) 2364.

使用施設：JRR-3M，装置： 4G (GPTAS), C11 (HER) ，分野： 2. Magnetism

研究テーマ： $PrPb_3$ の反強四重極秩序
表題： 反強四重極秩序物質 $PrPb_3$ における磁場誘起反強磁性

1-2-53 Field Induced Antiferromagnetism in the AFQ system $PrPb_3$

Takahiro Onimaru[1], Toshiro Sakakibara[1], Takashi Tayama[1], Naofumi Aso[1], Hideki Yoshizawa[1], Dai Aoki[2], Yoshichika Ōnuki[3], Tatsuya Kawae[4], Tetsuo Kitai[5] and Tetsuya Takeuchi[6]

[1] *Institute for Solid State Physics, University of Tokyo, Kashiwa 277-8581*
[2] *Institute for Materials Research, Tohoku University, Sendai 980-8577*
[3] *Department of Physics, Osaka University, Osaka 560-0043*
[4] *Department of Applied Physics, Kyushu University, Fukuoka 812-8581*
[5] *Faculty of Engineering, Kyushu Institute of Technology, Kitakyushu 804-8585*
[6] *Low Temperature Center, Osaka University, Toyonaka, Osaka 560-0043*

Antiferroquadrupolar (AFQ) ordering in the intermetallic f electron compounds has been attracting much attention in these years. $PrPb_3$ crystallizes in a simple $AuCu_3$-type cubic structure, and it has a Γ_3 non-Kramers doublet in the crystalline-electrical-field (CEF) ground state. There is a second order transition at 0.4 K with a lambda type anomaly in the specific heat.[1] From various experiments, it is considered that an AFQ ordering of Γ_3−type quadrupolar moments occurs. However, up to present, no microscopic evidence for the AFQ OP of $PrPb_3$ has been reported yet. In order to detect a possible induced AF moment in the AFQ phase, we have performed neutron diffraction experiments on $PrPb_3$ in a magnetic field.

In the present work, we used the 6mm cube single crystal grown by the Bridegeman method. Neutron diffraction measurements were performed using the triple-axis spectrometer GPTAS (4G) installed at the JRR-3M research reactor in Japan Atomic Energy Research Institute. Neutrons with a wave length of 2.35 Å were obtained by the (002) reflection of pyrolytic graphite (PG) for both the monochromator and the analyzer with 40'-80'-80'-80' collimation. We chose the (hkk) scattering plane, and the magnetic field was applied along the [01$\bar{1}$] direction perpendicular to the scattering plane. The sample was sealed in a aluminum cell with helium gas, and mounted on a mixing chamber of a ^{3}He−^{4}He dilution refrigerator.

Fig. 1 shows the results of q-scans along the line with $q=(\frac{1}{2}kk)$ at various temperatures in a magnetic field of H=5 T. At much lower temperature than 0.35 K, we clearly observed a magnetic reflection at $q=(\frac{1}{2}\delta\delta)$ with δ=0.062. Under the same condition, we have also observed magnetic reflections at some equivalent points $q=(\frac{3}{2}\delta\delta)$ and $(\frac{3}{2}\ 1+\delta\ 1+\delta)$. From these results, we propose a magnetic structure which is induced by the magnetic field above 3 T. The propagation vector is $k=(\frac{1}{2}\delta\delta)$ with δ=0.062, and the magnetic moments oscillate with the amplitude of 0.127 μ_B. The direction of the magnetic moments are perpnendicular to the magnetic field, therefore, the AFQ order parameter in the ordered phase above 3 T would be O_2^2−type. We have performed the q-scans along other lines including the principal points such as $(\frac{1}{2}00)$, $(0\frac{1}{2}\frac{1}{2})$ and $(\frac{1}{2}\frac{1}{2}\frac{1}{2})$, but we could not detect any magnetic reflections other than $(\frac{1}{2}\delta\delta)$ with δ=0.062

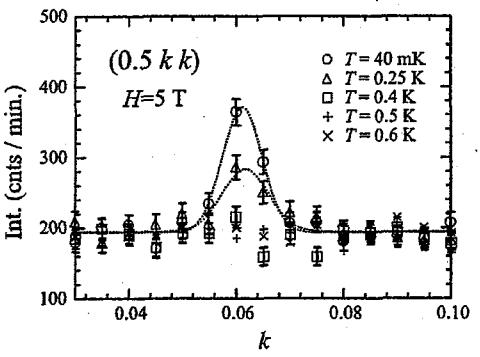

Fig. 1. Q-scans along the line with $q=(\frac{1}{2}kk)$ in a magnetic field of 5 T at various temperatures T=0.04 K(○), 0.25 K(△), 0.4 K(□), 0.5 K(+) and 0.6 K(×).

References

[1] E. Bucher, K. Andres, A. C. Grossard and J. P. Maita: J. Low Temp. 2 (1972) 322.

使用施設：JRR-3M, 装置： 4G (GPTAS) , 分野： 2. Magnetism

研究テーマ：四極子秩序物質 RB_2C_2 での異常磁気散漫散乱の三次元分布測定
1-2-54 希土類化合物 ErB2C2 での磁気散漫散乱の三次元分布測定

Three dimension measurements of magnetic diffuse scattering in the rare earth compound ErB_2C_2

K. Ohoyama[1], H. Kimura[2], Y. Noda[2], K. Kaneko[3], A. Hino[1], A. Tobo[4], and H. Onodera[4]
[1]*Institute for Materials Research, Tohoku University, Sendai 980-8577*
[2]*Institute of Multidisciplinary Research for Advanced Materials, Tohoku University, Sendai 980-8577*
[3]*Advance Science Research Center, Japan Atomic Research Institute, Tokai 319-1195*
[4]*Department of Physics, Graduate School of Science, Tohoku University, Sendai 980-8578*

The tetragonal compounds RB_2C_2 (R=rare earth) show various magnetic and quadrupolar behaviour due to competition between antiferroquadrupolar (AFQ) and antiferromagnetic (AFM) interactions. Of this system, ErB_2C_2 is worthy of note in spite that no AFQ ordering is realised, because anomalous magnetic diffuse scattering with characteristic profiles, which can not be understood only by simple spin correlations, is observed above T_N in the square region in the c^* plane surrounded by the (1-δ,$\pm\delta$,0) and (1+δ,$\pm\delta$,0) reciprocal positions, which correspond to the magnetic long periodicity [1, 2, 3].

The purpose of the present work is observing profile along the c^* axis of the characteristic magnetic diffuse scattering in ErB_2C_2 by FONDER, to clarify its three dimensional distribution.

The single crystalline sample was grown by the Czochralski method with a tri-arc furnace from the mixtures of 99.9% pure Er, 99.5% enriched ^{11}B and 99.999% pure C. The neutron diffraction experiments were performed on the four-circle neutron diffractometer FONDER[4]. The wavelength of the neutron beam was 1.2402 Å, monochromatised with a Ge311 crystal.

Figure 1 shows the contour map of the magnetic diffuse scattering at T=14.4 K in the $(1, k, l)$ plane observed on FONDER. As shown in Fig.1, the three dimensional measurement of the diffuse scattering shows no remarkable structure along the c^*. Moreover, the profile along the c^* axis is a simple lorentzian type one; the width of the diffuse scattering along the c^* is independent of the positions in the (h, k, 0) plane. From the fitting with a Lorentzian function with resolution convolution, the corrlation length was estimated to be ~15Å. In comparison with the complicated profile in the c^* plane, the profiles along the c^*axis are simple as shown in Fig.1, though the broadening is comparable to those in the c^* plane[3]. This means that the spin correlation in the c^* plane is important to understand of magnetic properties of ErB_2C_2.

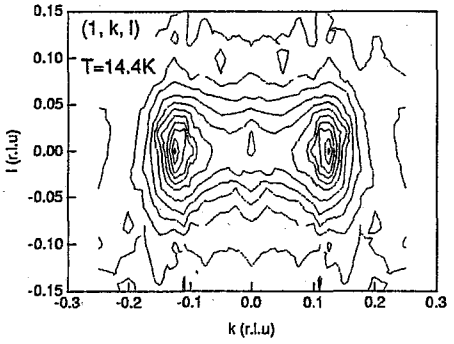

Fig. 1. Contour map of the magnetic diffuse scattering of $Er^{11}B_2C_2$ at T=14.4 K in the $(1, k, l)$ plane observed on FONDER. The data were observed only in the $k \leq 0$ region; the contour map in $k > 0$ is the mirror image of the data in $k \leq 0$.

References

[1] K. Ohoyama *et al.*: J. Phys. Soc. Jpn. **71** (2002) 1746.
[2] K. Ohoyama *et al.*: J. Magn. Magn. Mat. **272-276** (2004) E461.
[3] K. Ohoyama *et al.*: cond-mat/0403101.
[4] Y. Noda *et al.*, J. Phys. Soc. Jpn. **70**, Suppl. (2001) 456.

使用施設：JRR-3M，装置： T2-2 (FONDER)，分野： 2. Magnetism

研究テーマ： 四極子秩序物質 RB_2C_2 でのスピン格子ダイナミクス

1-2-55 反強四極子秩序物質 HoB_2C_2 での磁気励起

Magnetic Excitations in the antiferroquadrupolar ordering compound HoB_2C_2

K. Ohoyama[1], K. Kaneko[2], A. Tobo[3], K. Hirota[4], T. Matsumura[3], and H. Onodera[3]
[1]*IMR, Tohoku Univ., Sendai 980-8577*
[2]*ASRC, JAERI, Tokai 319-1195*
[3]*Dep. of Physics, Tohoku Univ., Sendai 980-8578*
[4]*NSL, ISSP, Univ. of Tokyo, Tokai 319-1106*

The tetragonal RB_2C_2 (R=rare earth) system shows characteristic magnetic and quadrupolar behaviour caused by competition between antiferroquadrupolar (AFQ) and antiferromagnetic (AFM) interactions [1, 2, 3]. The AFQ orderings in RB_2C_2 are unique phenomena, because the strict $4f$ ground states by crystal electric field with tetragonal symmetry have no degree of freedom on quadrupolar moments; therefore, it was thought that quadrupolar orderings can never be realised in rare earth tetragonal compounds before the discovery of the AFQ orderings in RB_2C_2.

Important characteristics of the AFQ orderings in RB_2C_2 are as follows: (i) the AFQ ordering temperature, T_Q of DyB_2C_2 is 24.7 K, which is nearly ten times higher than those of typical AFQ ordering rare earth compounds [1]. (ii) the AFQ ordering in HoB_2C_2 is realised at T_Q=4.5 K below the magnetic ordering temperature, T_N=5.9 K [2]. (iii) in TbB_2C_2, the AFQ ordering is induced by applying magnetic field [3].

We expect that the AFQ orderings in RB_2C_2 probably yield anomalies of dynamic properties because the lattice and spin systems in RB_2C_2 must be coupled by the AFQ orderings through the strong LS coupling. Therefore, we performed inelastic scattering experiments on a single crystalline sample of $Ho^{11}B_2C_2$ on the triple axis spectrometer TOPAN at 6G beam hole of JRR3-M of JAERI(Tokai). The experimental conditions were as follows; collimation was 15-30′-S-PG-30′-B, E_f=14.7 meV.

Figure 1 shows an energy spectrum at T=1.65 K, where the AFQ and AFM orderings are realised. As shown in Fig.1, excitations were observed at ϵ=3 and 6 meV around the (1,0,0) position, at which an AFM Bragg peak is observed below T_Q; the magnetic origin of the excitations is evident because the peaks disappear when temperature increases up to 50 K.

Though we observed energy spectra around (1,0,0), the magnetic excitations at ϵ=3 and 6 meV show no obvious q dependence. This probably means that these magnetic excitations are due to crystal electric field effects. In the present experiments, we could not find any indication of magnon. Therefore, measurements in lower energy regions below ~2 meV must be important to understand dynamic properties in HoB_2C_2.

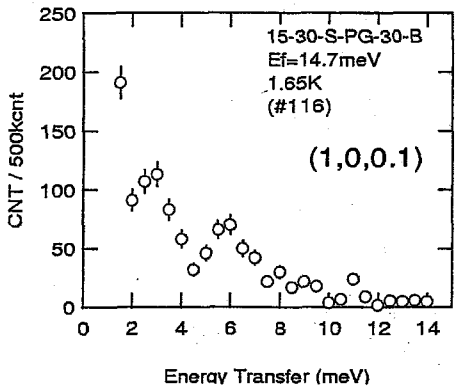

Fig. 1. Energy spectrum of $Ho^{11}B_2C_2$ at (1,0,0.1) obtained on TOPAN at T=1.65 K.

References

[1] H. Yamauchi *et al.*: J. Phys. Soc. Jpn. **68** (1999) 2057.
[2] H. Onodera *et al.*: J. Phys. Soc. Jpn. **68** (1999) 2526.
[3] K. Kaneko *et al.*: Phys. Rev. B. **68** (2003) 012401.

使用施設： JRR-3M, 装置： 6G(TOPAN), 分野： 2. Magnetism

研究テーマ：特異な原子価状態におけるフラストレーション系の研究３
表題：$GeFe_2O_4$ における 90 度 Fe-O-Fe 相互作用

1-2-56 The 90 degrees Fe-O-Fe interaction of $GeFe_2O_4$

Y. Noma, K. Kamazawa[#*], I. Kagomiya[*], K. Tomiyasu, K. Ohyama[**], and Y. Tsunoda

Dept. of Appl. Phys., School of Science and Enginnering, Waseda Univ., 3-4-1 Ohkubo, Shinjuku-ku, Tokyo 169-8555, Japan
[*]Advanced Research Institute for Science and Engineering, Waseda Univ., 3-4-1 Ohkubo, Shinjuku-ku, Tokyo 169-8555, Japan
[**]Inst. for Material Res., Touhoku Univ.

$GeFe_2O_4$ has a normal spinel structure, and its spin value is S=2. Isomorphic ferrites of $ZnFe_2O_4$ [1] and $^{110}CdFe_2O_4$ [2] have been observed some of us and described that the ion radius of the A site affect the angle and distance between the B-site, which play an important role in the magnetic behavior of spinel ferrites. Although a spin value is different and orbital moment is not zero, however, since the ion radius is $Ge^{4+}<Zn^{2+}<Cd^{2+}$, a strong ferromagnetic interaction is expected between the nearest neighbor Fe ions. Therefore, its behavior was observed by powder neutron diffraction using HERMES installed at T1 thermal guide at JAERI. Fig.1 shows temperature dependences of powder neutron diffraction for $GeFe_2O_4$. The magnetic diffuse scattering emerges almost the same as 2-theta position of $ZnFe_2O_4$, and the 1/2 1/2 1/2 magnetic Bragg peak which is common to the Ge-spinels is observed. It is considered to come from separate phase rather than uniform magnetic behavior. At least, however, it turns out that $GeFe_2O_4$ (electron's number is d=6) is not in low-spin state. In addition smaller A-site, e.g. Ge^{4+}, indicates that the nearest neighbor Fe-Fe interaction does not become antiferromagnetic. Although 95% of B-site is Fe^{2+} deduced from the Möossbauer spectra, in the present stage it was not confirmed whether remaining 5% acts greatly, because stoichiometric sample creation is hard. It is reported that a nature of spinel is different by integer or half-integer spin value recently [3]. $GeFe_2O_4$ has also integer spin value S=2. The approach from the viewpoint is also interesting, however there is a Jahn-Teller effect, careful inspections are required. The Jahn-Teller effect and L#0 does not affect magnetic behavior greatly at the present data. In conclusion, the present results support the model of the ~90 degrees Fe-O-Fe interaction described in Ref. [1] and [2].

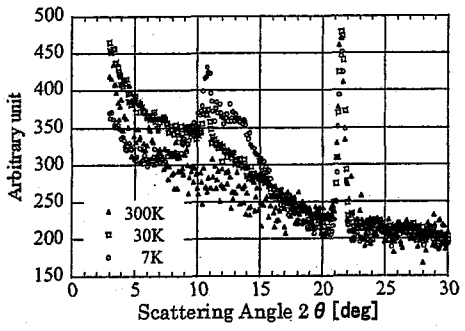

Fig. 1: Temperature dependences of powder neutron diffraction profile for $GeFe_2O_4$.

[#]Corresponding author;
E-mail address: kamazawa@waseda.jp
(K. Kamazawa).

References

[1] K. Kamazawa *et al.*, Phys. Rev. B **68**, 024412 (2003).
[2] K. Kamazawa *et al.*, To be published., Phys. Rev. B.
[3] M. K. Crawford *et al.*, Phys. Rev. B **68**, 220408 (2003).

使用施設：JRR-3M，装置：HQR(T1-1)，分野 Magnetism

研究テーマ:誘電・磁性複合系RbCoBr3の中性子散乱
表題:歪んだ三角格子イジング反強磁性体TlCoCl3の中性子散乱による研究
1-2-57

Neutron Diffraction Study of Distorted-Triangular-Lattice Ising-like Antiferromagnet $TlCoCl_3$

Y. Nishiwaki[1], K. Iio[1], T. Kato[2], and Y.Oohara[3]

[1] *Department of Physics (Cond.Mat.Phys.), Graduate School of Science and Engineering, Tokyo Institute of Technology, 2-12-1 Oh-okayama, Meguro-ku, Tokyo 152-8551*

[2] *Faculty of Education, Chiba University, 1-33 Yayoi-cho, Inage-ku, Chiba 273-8522*

[3] *Neutron Scattering Laboratory, Institute for Solid State Physics, University of Tokyo, Shirakata 106-1, Tokai, Ibaraki 319-1106*

$TlCoCl_3$ is a $KNiCl_3$-family triangular lattice antiferromagnet with the Ising spins. The lattice is distorted from the prototype $CsNiCl_3$-structure through structural phase transitions at T_{st2} =165 K, T_{st3} =75 K and T_{st4} =68 K.[1] The temperature dependence of the dielectric constant is quite similar to that of $RbMnBr_3$, of which the lowest-temperature structure is proposed as an orthorhombic *Pbca* structure with a unit cell $2a \times \sqrt{3}a \times c$.[2] This structure is also a candidate of the lowest-temperature structure of $TlCoCl_3$, but any diffraction experiment was not yet carried out. Additionally, there had been no experimental and theoretical studies of the Ising spin system of the zigzag-row model, the latter corresponds to the triangular-lattice exchange interactions with the *Pbca*-type distortion.[2]

We performed single-crystal neutron diffraction measurements of $TlCoCl_3$ at HQR(T1-1), JRR-3M, Tokai. The peak intensity of the nuclear Bragg reflection was measured as a function of temperature, as shown in Fig.1. The unit cell is enlarged from (a, a, c) to $(\sqrt{3}a, \sqrt{3}a, c)$ in the temperature range $T_{st4} < T < T_{st2}$. And $T < T_{st4}$, our result is similar to the results of $RbMnBr_3$, which indicate that lowest-temperature structure of $TlCoCl_3$ is probably the *Pbca* orthorhombic structure. However, we cannot decide the crystal structure uniquely because we presently measured only (h, h, l) line scans.

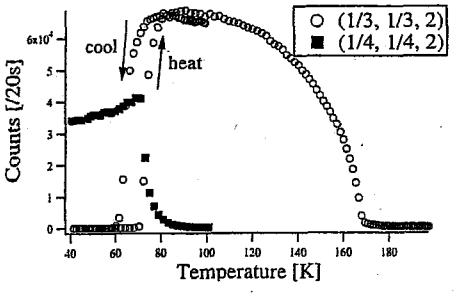

Fig. 1. The temperature dependence of the nuclear peak heights for **Q**=(1/3,1/3,2) and (1/4,1/4,2)

For the magnetic Bragg peaks, we obtained the q-scan profiles along the direction $(h, h, 1)$, as shown in Fig. 2. The diffraction pattern is quite similar to the commensurate phase of $RbMnBr_3$ under magnetic fields.[2] Accordingly, the Ising spins of $TlCoCl_3$ must be arranged in an up-up-down-down manner with triple-domain formation.

For regorous treatments, powderd-sample experiments to identify the crystal structure are planned.

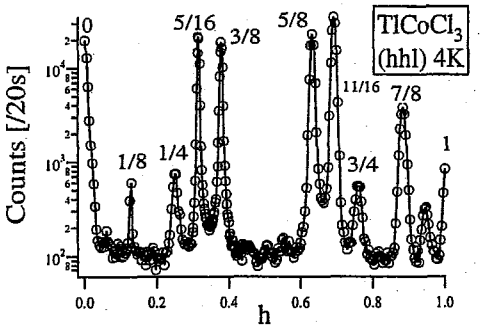

Fig. 2. The q-scan profiles along $(h, h, 1)$.

References

[1] Y. Nishiwaki *et al.*: J. Phys. Soc. Jpn. **72** (2003) 2608.

[2] T. Kato: J. Phys. Soc. Jpn. **71** (2002) 300.

使用施設：JRR-3M，装置： HQR(T1-1)，分野： 2. Magnetism

研究テーマ：二本脚梯子系におけるスピン・ダイナミックス
表題：二本脚梯子系 $Sr_{0.33}V_2O_5$ におけるスピン・ギャップの観測

1-2-58 Observation of Spin-Gap in the Two-Leg Ladder System $Sr_{0.33}V_2O_5$

M. Nishi[1], M. Isobe[2] and Y. Ueda[2]

[1]*Neutron Science Laboratory, ISSP, University of Tokyo, Tokai 319-1106, Japan*
[2]*Material Design and Characterization Laboratory, ISSP, University of Tokyo, Kashiwa 277-8581, Japan*

Spin 1/2 two-leg ladder antiferromagnets have been extensively studied with great interest because of their fundamental quantum nature. Physical properties of $Sr_{0.33}V_2O_5$ have been studied [1, 2]. Above the structural transition temperature 165K the conductivity of this compound shows metallic behavior and below 165 K this behaves as an insulator with spin gap of 53 K from the temperature dependence of magnetic susceptibility. From the structural point of view, $Sr_{0.33}V_2O_5$ can be regarded as a two-leg spin ladder system. The inelastic neutron scattering measurements were carried out on the ISSP-PONTA triple axis spectrometer (5G) at JRR-3M of JAERI in Tokai with the fixed final neutron energy 30.5meV using $Sr_{0.33}V_2O_5$ powder sample. In the results of the experiments the spin gap energy is obtained as 6 meV (see Fig. 1) and the Q-dependence of the energy is almost flat. This means the exchange interaction along the rung is 6 times as large as that along the leg like CaV_2O_5 [3]. The spin gap disappeared at 33 K corresponding with the energy of 2.8 meV. In the case of orthogonal dimmer system $SrCu_2(BO_3)_2$ the spin gap collapses also at lower temperature than the spin gap energy. These phenomena are considered as the effect of topological frustrations.

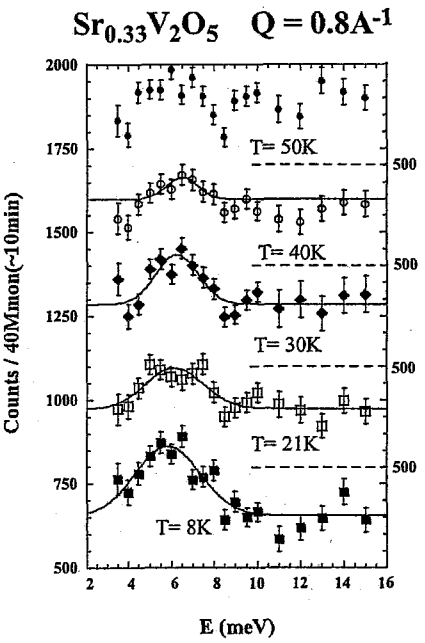

Fig. 1. Neutron scattering profiles at Q = 0.8 A^{-1} at several temperatures.

References

[1] Y. Ueda, J. Phys. Soc. Jpn. **69** (2000) Suppl. B 149.

[2] H. Yasuoka, J. Phys. Soc. Jpn. **69** (2000) Suppl. B 161.

[3] T. Ohama, M. Isobe and Y. Ueda, J. Phys. Soc. Jpn. **70** (2001) 1801.

[4] H. Kageyama et al., Phys. Rev. Lett. **84** (2000) 5876.

使用施設：JRR-3M, 装置：PONTA(5G), 分野 Magnetism

研究テーマ： 光誘起相転移を起こす $RbMn[Fe(CN)_6]$ の磁気構造決定
表題： 光誘起構造変化を起こす $RbMn[Fe(CN)_6]$ の強磁性磁気秩序

1-2-59 Ferromagnetic Spin-Ordering in Photo-reactive $RbMn[Fe(CN)_6]$[1]

Y. Moritomo[1,2], A.Kuriki[3], K. Ohoyama[4], H. Tokoro[5], S. Ohkoshi[5], K. Hashimoto[5] and N. Hamada[6]
[1]*Department of Applied Physics, Nagoya University, Nagoya 464-8603*
[2] *PRESTO, JST*
[3]*Department of Crystalline Materials Science, Nagoya University, Nagoya 464-8603*
[4]*Institute for Materials Research, Tohoku University, Sendai 980-8577*
[5]*Research Center for Advanced Science and Technology, University of Tokyo, Tokyo 153-8904*
[6]*Faculty of Science and Technology, Science University of Tokyo, Chiba 278-8510*

In $RbMn[Fe(CN)_6]$,[2] two kinds of magnetic elements, *i.e.*, Fe and Mn, form a three-dimensional NaCl-type structure bridged by CN^- ions. Recently, Tokoro *et al.* has reported suppression of magnetization by irradiation of one-pulse laser shot at 3 K. This observation suggests photo-induced ferromagnetic-to-antiferromagnetic transition, perhaps mediated by some photo-induced structural change. To clarify this novel photo-induced phenomenon, we first have to determine the spin structure of the ground state (*before photo-irradiation*). Crytallographically, $RbMn[Fe(CN)_6]$ belongs to the tetragonal space group ($I\bar{4}m2$; $Z = 2$) at low temperatures, in which Fe and Mn elements locate at $2a$ and $2b$ site, respectively. The low temperature valence state is considered to be high-spin Mn^{3+} (d^4; $S = 2$) and low-spin Fe^{2+} (d^6; $S = 0$) state.

The Figure shows neutron powder patterns at 5 K ($\leq T_C$; thick curve) and at 20 K ($\geq T_C$: thin curve) for $RbMn[Fe(CN)_6]$. In the middle panel, we show magnetic components of the neutron powder pattern. No trace of (002) magnetic Bragg reflection is observed, indicating that the easy axis is along c. In the Bottom panel, we plotted calculated intensities $I_{M,cal}$ of the magnetic Bragg reflections with ferromagnetic alignment of the Mn^{3+} local spins along c. $I_{M,cal}$ well reproduces the observed magnetic Bragg reflections, even though the experimental error bars are rather large due to the overlapped intense nuclear Bragg reflections. Magnitude of the moment is estimated to be 3.2(7) μ_B, which is consistent with the saturated magnetization (3.3 μ_B at 7 T) at 3 K.

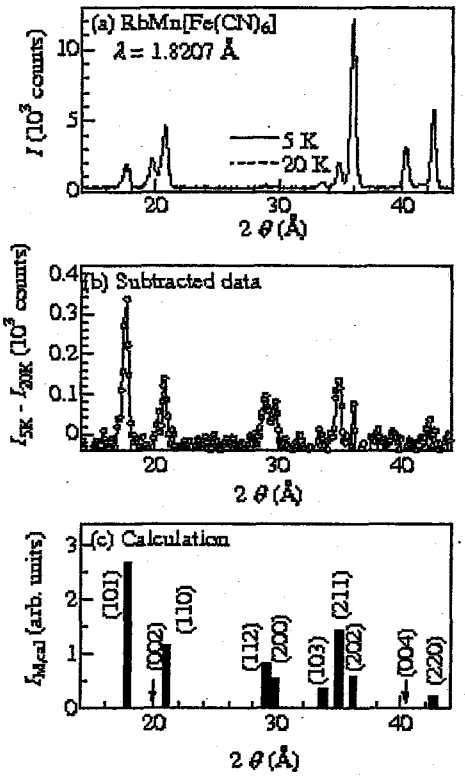

Fig. 1. (a) Neutron powder patterns at 5 K ($\leq T_C$; thick curve) and at 20 K ($\geq T_C$: thin curve) for $RbMn[Fe(CN)_6]$. (b) Subtracted neutron powder pattern (I_{5K} -I_{20K}, where I_{5K} and I_{20K} are the powder patterns at 5 K and 20 K, respectively.) (c) Calculated intensities $I_{M,cal}$ of the magnetic Bragg reflections with ferromagnetic alignment of the Mn^{3+} local spins along c.

References

[1] Y. Moritomo, *et al.*, J. Phys. Soc. Jpn. **72**, 456 (2003).
[2] S. Ohkoshi, *et al.*, J. Phys. Chem. **106** 2423 (2002).

使用施設：JRR-3M, 装置： T1-3 (HERMES) , 分野： 2. Magnetism (m)

研究テーマ:界面効果を利用したCr薄膜のスピン構造制御

1-2-60 Sn単原子層挿入されたエピタキシャルCr(011)/Sn人工格子におけるCrのスピン構造

Spin Structures of Cr in Epitaxial Cr(011)/Sn Multilayers with Monatomic Sn Layers

K. Mibu, N. Jiko*, and M. Takeda**

*Research Center for Low Temperature and Materials Sciences, Kyoto University, Uji, Kyoto 611-0011, Japan; *Institute for Chemical Research, Kyoto University, Uji, Kyoto 611-0011, Japan; **Advanced Science Research Center, JAERI, Tokai, Ibaraki 319-1195, Japan*

Magnetic structures of epitaxial Cr(011)/Sn multilayers, where monatomic Sn layers are periodically embedded in Cr, were studied by neutron diffraction measurements using a triple-axis spectrometer, TOPAN, at JRR-3M. The scans were carried out through the Cr(100) and Cr(010) reciprocal points (Fig. 1), around which magnetic peaks due to antiferromagnetic structures are expected to appear. It had already been found by previous measurements that the commensurate antiferromagnetic (CAF) structure is stabilized down to low temperatures for [Cr(8.0 nm)/Sn(0.2 nm)] multilayer [1], in which the thickness of Cr is comparable with the wavelength of spin-density wave (SDW) modulation in bulk Cr.

For [Cr(16.0 nm)/Sn(0.2 nm)] multilayer, it was found that the CAF structure is stabilized at room temperature and an incommensurate SDW (ISDW) phase with the wave vector along the [010] or [001] direction appears at low temperatures together with the CAF phase (Fig. 2). The results are in contrast with those on Cr(001)/Sn multilayers with the same Cr layer thicknesses, where an ISDW structure with the modulation along the perpendicular direction to the film plane is stabilized at low temperatures [2,3]. In the former multilayers, the growth orientation does not agree with the direction of the nesting vector of bulk Cr. Therefore, the nesting effect, which acts to make the antinode of ISDW in (100), (010), or (001) atomic planes, and the interface effect, which tends to pin the antinode at the (011) atomic plane of the Cr/Sn interface, compete with each other. This competition is thought to be the origin of the instability of the ISDW phase.

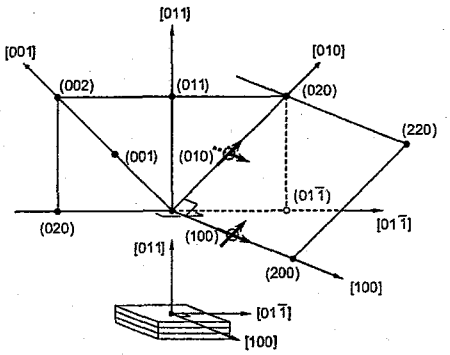

Figure 1: Configuration for neutron diffraction measurements on Cr(011)/Sn multilayers.

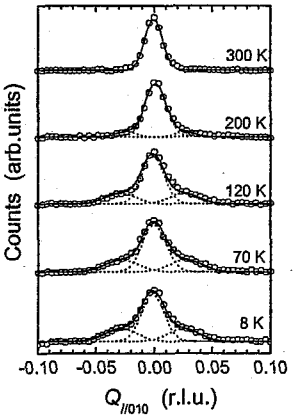

Figure 2: Neutron diffraction patterns for [Cr(16.0 nm)/Sn(0.2 nm)] multilayer around the Cr(100) point along the [010] direction at various temperatures. The abscissa is expressed by the reciprocal lattice units of $2\pi/d_{010}$.

References

[1] N. Jiko *et al.*, J. Magn. Magn. Mater. **272-276** (2004) 1233.

[2] M. Takeda *et al.*, J. Phys. Soc. Jpn. **69** (2000) 1590.

[3] K. Mibu *et al.*, Phys. Rev. Lett. **89** (2002) 287202.

使用施設:JRR-3M, 装置:TOPAN(6G), 分野 Magnetism

研究テーマ：ZrNiAl型とTiNiSi型結晶構造をとるTbPtSn化合物の磁気構造
表題：TbPtSn化合物の中性子回折

1-2-61 **Neutron Diffraction Study on TbPtSn**

M. Kurisu, G. Nakamoto, Do Thi Kim Anh, Y. Andoh[1], T. Tsutaoka[2], and S. Kawano[3]

Japan Advanced Institute of Science and Technology, Ishikawa 923-1292, Japan
[1]*Faculty of Environmental Sciences, Tottori University, Tottori 680-8551, Japan*
[2]*Graduate School of Education, Hiroshima University, Hiroshima 739-8524, Japan*
[3]*Research Reactor Institute, Kyoto University, Osaka 590-0494, Japan*

The rare-earth compound TbPtSn has two types of crystal structures of orthorhombic and hexagonal, respectively, depending on the sample preparation method. Here we report the results of the specific heat and neutron diffraction measurements on the samples with hexagonal symmetry. The ingots of TbPtSn compound were prepared by arc-melting the constituent elements. The bulk magnetic measurements were made using a SQUID magnetometer. The specific heat was measured using a PPMS. The neutron diffraction measurements were carried out by using the HQR spectrometer of JRR-3M of JAERI at Tokai in the temperature range from 1.5 K to 300 K.

The X-ray and neutron diffraction measurements on the powder sample have shown that TbPtSn has the hexagonal ZrNiAl structure with the lattice constants of a=7.4429 and c=3.9997 Å. The bulk magnetic measurements have indicated that the hexagonal TbPtSn orders antiferromagnetically below 12.5 K. The magnetization curve indicates the metamagnetic transitions at 20 kOe and 50 kOe at 1.8 K. The specific heat measurement has also indicated an anomaly at 12.5 K as shown in Fig. 1.

The powder neutron diffraction pattern at 4 K is described well by the magnetic propagation vector (0.75 0.75 0.50). It is more interesting to note that a new phase appears at 11 K with increasing temperature as indicated in Fig. 2. In the specific heat curve, an appreciable change is found in the slope of the curve around 11 K. Detailed analysis is in progress on the diffraction patterns.

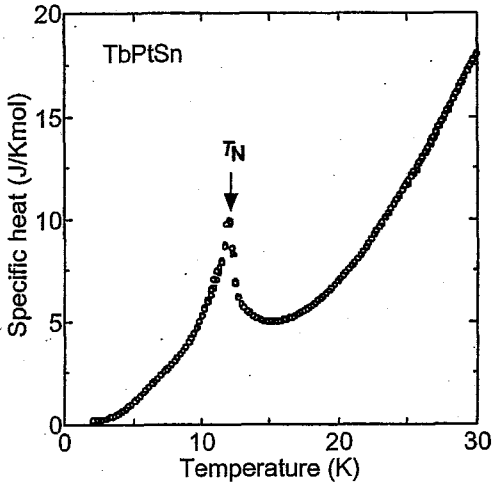

Fig.1. Specific heat of TbPtSn.

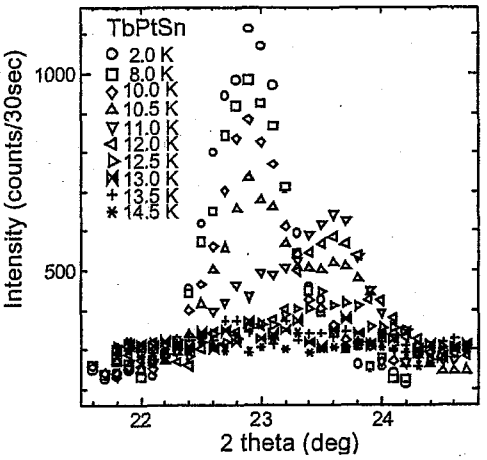

Fig2. Thermal variation of the (100)- magnetic reflection of TbPtSn.

使用施設：JRR-3M, 装置：HQR (T1-1), 分野：Magnetism

研究テーマ：CeB_2C_2におけるスピン密度分布の観測
表題：CeB_6の磁気形状因子の観測

1-2-62

Magnetic Form Factor in CeB_6

Y. Kousaka[1], H. Ichikawa[1], M. Togasaki[1], M. Saitoh[1], N. Okada[2], E. Nishibori[2], M. Sakata[2], K. Hirota[3], M. Nishi[3], K. Kakurai[4], M. Takada[5], Y. Noda[6], S. Kunii[7] and J. Akimitsu[1]

[1]*Department of Physics and Mathematics , Aoyama-Gakuin Univ., 5-10-1 Fuchinobe, Sagamihara 229-8558;* [2]*Department of Applied Physics, Nagoya Univ., Furo-cho, Chikusa-ku, Nagoya 464-8603;* [3]*Institute for Solid State Physics, The Univ. of Tokyo, 106-1 Shirakata, Tokai 319-1106;* [4]*Japan Atomic Energy Research Institute (JAERI), 2-4 Shirakata, Tokai 319-1195;* [5]*SPring-8, 1-1-1 Kouto Mikazuki-cho, Sayo-gun, 679-5198;* [6]*IMRAM, Tohoku Univ., 2-1-1 Katahira, Aoba-ku, Sendai 980-8577;* [7]*Department of Physics, Tohoku Univ., Aoba, Aramaki, Aoba-ku ,Sendai 980-8578*

A typical dense Kondo compound CeB_6 has a cubic CsCl-type structure with a space group of $Pm\bar{3}m$. It shows mysterious magnetic phase transitions at low temperature: paramagnetic state, antiferro-quadrupolar ordering and antiferro-magnetic ordering. The phases are denoted as phase I, II and III, respectively.

Recently, we reported the spin density distribution in CeB_6, analyzed by maximum entropy method (MEM) using polarized neutron diffraction technique, and concluded that the magnetic moment exists not only on the Ce site, but also inbetween the B sites [1]. On the other hand, Givord *et al.* pointed out that our result was distorted by an extinction effect, and the magnetic moment was localized only on the Ce site after correcting the extinction effect [2]. However they ignored the results whose F_N were weak in the MEM analysis. Therefore we measured the extinction free magnetic form factors including weak F_N reflections.

The single crystal was grown by the floating zone method using enriched ^{11}B to avoid the large neutron absorption due to ^{10}B. The polarized neutron diffraction experiment was performed at PONTA (5G), JRR-3M reactor in JAERI (Tokai). The experimental condition was 1.6K under an applied magnetic field of 5.9T parallel to the <110>-axis (phase II).

In order to estimate how the extinction effect affects the observed intensity, we measured some intensities of nuclear scattering at 10K (phase I), and determined an extinction parameter by solving Zachariasen's differential equations [3].

Finally we obtained the extinction free magnetic form factors by using the extinction parameter [Fig.1]. The corrected results are different from the non-corrected ones. In addition, we must pay attention to the results in (114) and (116) reflections which Givord ignored in the MEM analysis. These are the same with Givord's quantitatively. In order to check whether the results of weak F_N are essential or not, additional experiment is now in progress.

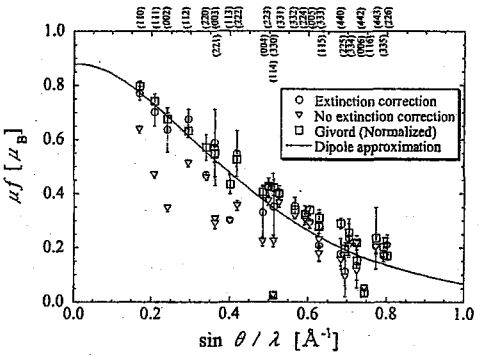

Fig.1 The observed magnetic form factors.
The open triangles and open circles denote our non-corrected and corrected results, respectively. The open squares denote Givord's corrected ones, which are normalized by magnetization, because their experimental condition is different from ours.

References

[1] M. Saitoh et al.: J. Phys. Soc. Jpn. **71** (2002) 2369.
[2] F. Givord et al.: J. Phys.: Condens. Matter **15** (2003) 3095.
[3] P. J. Becker and P. Coppense: Acta. Cryst. **A30** (1979) 129.

使用施設：JRR-3M, 装置：PONTA(5G), 分野 Magnetism

研究テーマ：電子ドープ系銅酸化物超伝導体の不純物効果

1-2-63 電子ドープ型超伝導体 $Pr_{0.89}LaCe_{0.11}Cu_{1-y}Zn_yO_{4-y}$ の不純物置換効果

Impurity effect on the spin correlation of the n-type superconducting cuprate $Pr_{0.89}LaCe_{0.11}Cu_{1-y}Zn_yO_{4-y}$

M. Fujita, A. Hino, H. Goka and K. Yamada

Institute of Material Research, Tohoku University, Aobaku Katahira 2-1-1 Sendai 980-8577

Interplay between superconductivity and magnetic order is one of the current topics in high-T_c cuprates, where magnetic interaction is widely believed to play a vital role for the superconducting paring. To study the interplay the effects of 3*d*-transition metal impurities into Cu-site on the spin correlation have been investigated. In fact, many studies on the impurity-effect have been performed for hole-doped (*p*-type) cuprates and revealed a competitive relation between the static spin correlation and superconductivity. On the other hand, most of studies on the effect of Cu-site impurities in electron-doped (*n*-type) cuprates have been focused on the degradation of superconductivity.

Here, we report the preliminary result of neutron scattering experiment to study the Zn impurity-effect on the magnetic order of n-type cuprate $Pr_{0.89}LaCe_{0.11}Cu_{1-y}Zn_yO_{4-y}$. In this system, the as-grown sample (y=0) without Zn shows the Néel order below around T_N=200 K. Upon reducing the oxygen content by heat treatment, the Néel order is drastically degraded around y=0.03 and disappears beyond around y=0.05. For the present neutron scattering experiment we grew single crystals by using a traveling-solvent-floating-zone method. The as-grown crystals were annealed under Ar-gas flow to control the oxygen content. In the neutron scattering experiment we monitored the temperature dependence of the magnetic Bragg peak intensity at (1/2 1/2 1) in the tetragonal I4/mmm notation for samples with various oxygen concentrations. In Fig.1, the Néel temperatures are compared between samples with and without Zn impurity as a function of y. For the y values less than 0.04 the T_N does not change by the 2% substitution of Zn impurities though a slight increase in the T_N is suggested for y>0.04.

The Zn-impurity effect shows a clear contrast between *p* and *n*-type doping. For the former, the doped holes induce magnetic frustration and form themselves charge segregation or stripes which dramatically disconnect the interlayer magnetic coupling and easily destroy the Néel order. In such situation, due to charge localization Zn impurities prohibit the holes from forming charge segregation and then the Néel order slightly recovers. On the other hand, the doped electrons dominantly take Cu-3*d* orbital and form $3d^{10}$ nonmagnetic Cu-site. Therefore, doped electrons gradually dilute the Néel order. Similar to electron doping the $3d^{10}$ nonmagnetic state of Zn is also expected to dilute the Néel order in n-type cuprates. On the contrary, the effect of 2% of Zn substitution on the magnetic order was negligibly small. If 2% of Zn corresponds to the oxygen content y=0.01, we should see the effect. Systematic study is highly required to solve this discrepancy.

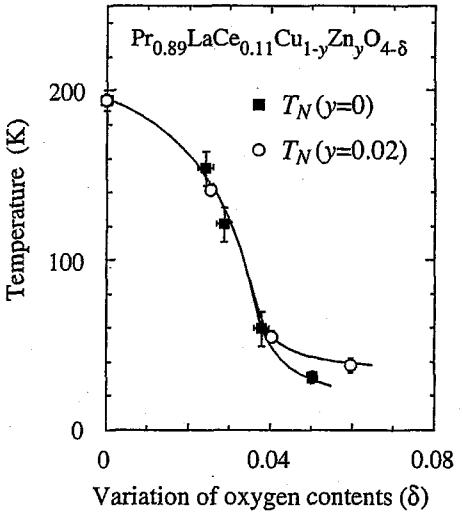

Fig. 1. The Néel temperatures of $Pr_{0.89}LaCe_{0.11}Cu_{1-y}Zn_yO_{4-y}$ with (open circles) and without Zn substitution(closed squares).

使用施設：JRR-3M，装置： C1-1 (HQR), 6G(TOPAN)，分野： 2. Magnetism, Superconductivity

This is a blank page.

1. 中性子散乱 3)超伝導現象

1. Neutron Scattering 3) Superconductivity

This is a blank page.

研究テーマ：極端条件下中性子散乱による銅酸化物高温超伝導体の磁気相関の研究
表　題：電子ドープ型高温超伝導体の静的磁気相関に対する磁場効果

1-3-1

Effect of magnetic field on static spin correlation in electron-doped system

M. Fujita, M. Matsuda[1], S. Katano[1] and K. Yamada

Institute for Materials Research, Tohoku University, Katahira, Sendai 980-8577
[1]Advanced Science Research Center, Japan Atomic Energy Research Institute, Tokai, Ibaraki 319-1195

1 Introduction

Mechanism of high-T_c superconductivity mediated by spin fluctuations is one of the central topics in highly correlated electron systems. Studies of spin correlations in the hole-doped high-T_c cuprates such as $La_{2-x}Sr_xCuO_4$ (LSCO) have intensively been carried out by neutron scattering experiments, and show an intimate relation between spin correlations and superconductivity[1]. Recent neutron-scattering measurements on the LSCO with x around 1/8 revealed a large enhancement of the long-ranged incommensurate (IC) magnetic order under the field[2]. Lake *et al.*, furthermore, found a tendency of the stabilization in the magnetic ordering in the vortex state of the optimally doped LSCO and discussed that the IC antiferromagnetic (AF) insulator is a possible ground state after suppressing the superconductivity by magnetic fields[3].

In order to test the universality of the field-effect on the spin correlations, that is, the relation between magnetism and superconductivity in the cuprates superconductors, comprehensive study on the electron-doped system is indispensable. Quite recently, Kang *et al.* performed neutron-scattering measurement on well-known electron-doped system of $Nd_{2-x}Ce_xCuO_4$ (NCCO) with x=0.15 (T_c=25 K) and reported a huge enhancement of magnetic order under the field[4]. However, in that system, a field-effect on Nd^{2+} magnetic moment is expected to be predominant, and therefore, the results may conceal the inherent nature of Cu^{2+} spins that would play an important role for superconductivity. Thus, experiments using samples with negligible effects from large rare-earth magnetic moments are required. We hence performed neutron scattering measurements under the magnetic fields up to 9 T on a single crystal of superconducting $Pr_{0.89}LaCe_{0.11}CuO_4$, in which the effect of rare-earth moments is negligible compared with that in NCCO[5].

2 Results and Discussion

In this sample, a fairly small intensity from the magnetic order was observed in the zero-field at the tetragonal (0.5 1.5 0) reciprocal position, where corresponds to AF zone center in the as-grown non-superconducting samples[6]. In Fig. 1, we show the temperature-dependence of the magnetic peak intensity after subtracting background estimated at high temperatures. In zero-field, the intensity at 3 K normalized with the sample volume is ~5 % of that in the as-grown sample, and T_N of 27±4 K is much lower than that of 200±5K in the as-grown non-superconducting sample[6]. (T_N is the onset temperature for the appearance of magnetic intensity upon cooling.) These results suggest that a competitive relation between the AF order, and superconductivity and show that the AF order is dramatically degraded in the present SC sample by the oxygen reduction.

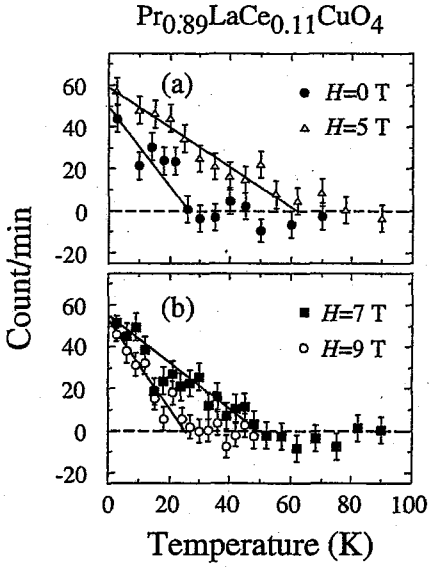

Figure 1: Temperature dependence of the peak-intensity measured under the magnetic field of (a) 0 and 5 T, and (b) 7 and 9 T at the tetragonal (0.5 1.5 0) position after subtracting the background at high temperature. Solid lines are guides to the eyes.

Applying the field of 5 T, T_N increases up to ~60 K and the low-temperature peak-intensity at 5 T is also enhanced with the rate of ~20 % of that at 0 T. In the hole-doped LSCO, on the other hand, T_N does not change even though the peak-intensity increases under the field with the factor of 2. The enhancement of TN, therefore, indicates a different field-dependence of the enhanced antiferromagnetism between the electron- and hole-doped systems.

Further increasing the field, the peak-intensity at

原子炉：JRR-3　　装置：TAS-2(T2-4)　　分野：中性子散乱（超伝導）

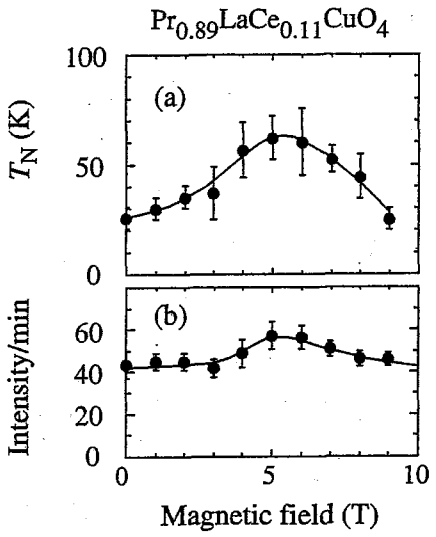

Figure 2: Field-dependence of (a) the onset temperature for the magnetic ordering temperature and (b) the peak-intensity at 3 K.

low temperature decreases possibly owing to a cant of spins from the CuO_2 planes. More importantly, T_N decreases in connection with the reduction of the peak-intensity, suggesting that the enhancement (the degradation) of the AF order in the electron-doped system is characterized by the simultaneous increase (decrease) in T_N and the intensity. In Fig. 2, we present the field-dependence of T_N and intensity measured at 3 K.

The field dependence of the intensity at (0.5 0 0)/(1.5 0 0) shows no observable enhancement. At this reciprocal lattice point, however, Kang *et al.*, observed a huge increase in the intensity[4]. This discrepancy may be attributed to the difference of sample preparation, and the ordering of the magnetic moments on the Nd atoms. We just note here that this point is not the AF zone center of the as-grownsample. Our results show that the enhancement of the AF ordering under magnetic field is a common feature of the cuprate high-T_c superconductors, and the ground state when the superconductivity is suppressed is the antiferromagnetic insulator.

Finally, we discuss the difference in the spin correlations in the electron- and hole-doped systems. At each field, temperature-dependence of the peak-intensity shows a linear change, which is typical for the defect-induced magnetism in correlated Fermi systems. Recent μSR results for the PLCCO system showing the reduction of both volume fraction of magnetically ordered region and staggered moment upon electron-doping near the AF and SC phase boundary. These results suggest the existence of antiferromagnetically ordered islands on the SC background in the present sample, and that the magnetic property in the AF island itself changes by electron-doping. On the other hand, in the LSCO system, evidence for the stripe formation of doped-hole was found. In this case, magnetic property in the AF region separated by charge-river would persist upon hole-doping. Therefore, the character of doped antiferromagnetism between hole- and electron-dope systems associated with the charge distribution is somewhat different. This may be related with the different field-dependence of spin correlations in two systems. In order to clarify the common high-T_c mechanism, further study on magnetism is needed.

References

1) K. Yamada *et al.*: Phys. Rev. B. **57**, 6165 (1998).
2) S. Katano *et al.*: Phys. Rev. B. **62**, R14677 (2000), B. Lake *et al.*: Nature (London), **417**, 299 (2002).
3) B. Lake *et al.*: Sience, **291**, 1759 (2001).
4) H.J. Kang *et al.*: Nature (London), **423**, 522 (2003).
5) M. Fujita *et al.*: Phys. Rev. B. **67**, 014514 (2003).
6) M. Fujita *et al.*: Physica C **392-396**, 130 (2003).

研究テーマ： 重い電子系 URu_2Si_2 の隠れた秩序と圧力誘起反強磁性
表題： $U(Ru_{1-x}Rh_x)_2Si_2$ ($x \leq 0.05$) における隠れた秩序と反強磁性

1-3-2 Hidden Order and Antiferromagnetism in $U(Ru_{1-x}Rh_x)_2Si_2$ ($x \leq 0.05$)

H. Amitsuka[1], M. Yokoyama[2], S. Itoh[1], I. Kawasaki[1], K. Tenya[1] and H. Yoshizawa[3]
[1] *Graduate School of Science, Hokkaido University, N10W8 Kitaku, Sapporo 060-0810*
[2] *Faculty of Science, Ibaraki University, 2-1-1 Bunkyoh, Mito 310-8512*
[3] *Institute for Solid State Physics, The University of Tokyo, 106-1 Shirakata, Tokai, 319-1106*

The relationship between the phase transition at $T_o = 17.5$ K and the weak antiferromagnetism in URu_2Si_2 has been intensively investigated since the finding of an unusually small antiferromagnetic (AF) moment below $\sim T_o$.[1, 2] Recent microscopic investigations performed under hydrostatic pressure P shed new light on this issue, by revealing that the inhomogeneous AF order develops with increasing P.[3, 4] This ascribes the weak AF moment at ambient pressure to the effects of AF volume fraction, and convinces us that the 99 % of the system is occupied by unidentified "hidden order" (HO).

Quite recently, we performed neutron-scattering experiments under uniaxial stress σ, and found that the AF phase is also enhanced by applying σ along the tetragonal basal plane.[5] On the basis of a crystal-strain model, we pointed out that the c/a ratio (η) is an intrinsic parameter that yields the competition between HO and the AF order. The analyses also predict that a slight increase in η of $\sim$ 0.1 % may induce the AF order of nearly the full volume fraction.

The axial type lattice distortion may be expected not only by compression but also by alloying. In $U(Ru_{1-x}Rh_x)_2Si_2$, HO phase is known to be suppressed at $x \sim 0.04$, and then to be replaced by a new AF state with a complex multi-Q structure in the range between $x \sim 0.1$ and 0.3. The X-ray powder diffraction measurements revealed that the 0.1 % increase of η could be achieved at $x \sim 0.02$. It is thus expected that the inhomogeneous AF state is significantly induced by a small amount of Rh-doping. In order to verify this possibility, we have performed neutron scattering experiments on $U(Ru_{1-x}Rh_x)_2Si_2$ ($x \leq 0.05$).[6]

The elastic and inelastic neutron scattering measurements were performed on the triple-axis spectrometer GPTAS (4G) located at the JRR-3M research reactor of JAERI. For elastic scattering, we used the neutron momentum $k = 2.66$ Å^{-1} and the 40'-80'-40'-80' horizontal collimators. For inelastic scattering, we performed constant-Q scans at $Q = (1, 0, 0)$ with the fixed final momentum $k_f = 2.65$ Å^{-1}.

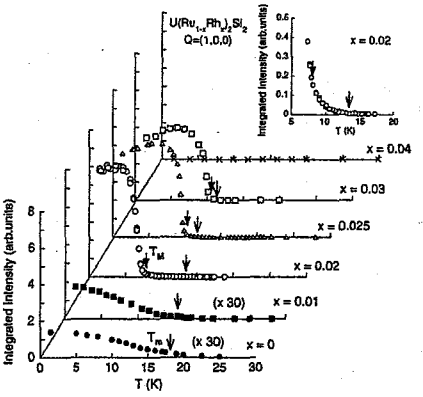

Fig. 1. Temperature variations of the integrated intensity for the (100) magnetic reflections of $U(Ru_{1-x}Rh_x)_2Si_2$ ($x \leq 0.04$). The enlargement for $x = 0.02$ between 5 K and 20 K is shown in the inset.

Displayed in Fig. 1 are the T variations of the integrated intensity $I(T)$ of the (100) magnetic reflection for $x \leq 0.04$. For $x \leq 0.01$, $I(T)$ shows an unusually slow development with decreasing T. The onset of this weak reflection T_m slightly decreases from $\sim$ 17.5K ($x = 0$) to $\sim$ 15.9 K ($x = 0.01$). In contrast, in the range $0.02 \leq x \leq 0.03$, $I(T)$ exhibits a dramatic T variation. At $x = 0.02$, $I(T)$ slightly develops below $T_m \sim 13.7$ K, and shows an abrupt increase at $\sim$ 7.7 K ($\equiv T_M$). The increase of $I(T)$ at T_M is sharper than that expected from the typical second-order phase transition. Similar $I(T)$ curves are obtained for $x = 0.025$ and 0.03, where the interval between T_m and T_M be-

使用施設：JRR-3M, 装置： 4G (GPTAS), 分野： 3. Strongly Correlated Electron Systems

comes narrower. For $x = 0.04$, on the other hand, no anomaly is found down to 1.4 K.

In Fig. 2, we plot T_o, T_m and T_M, and μ_o as a function of x, where the T_o is obtained from the $C(T)$ measurements. Note that the estimation of μ_o is based on the assumption that the AF order is homogeneous. The results indicate that the HO occupies the system as the majority phase competing with a small amount of the AF phase in the $x - T$ region $T_M < T < T_m (x \leq 0.03)$. On the other hand, the development of μ_o seen below T_M for $x \geq 0.02$ is considered to be due to the increase in the volume fraction of the AF phase. Our recent ZF-μSR measurements support this description. We also found that the magnetic excitation observed at $Q = (1, 0, 0)$ below T_m disappears in the AF region below T_M(Fig. 3).

All of these experimental results compare reasonably well with the features obtained by the previous high-P and σ measurements on the pure compound: (i) HO and AF phases compete with each other via a first-order phase transition, (ii) η governs the switching of the two phases, (iii) magnetic excitations at $Q = (1, 0, 0)$ in HO vanish in the AF phase, and (iv) a bicritical point exists in the $x - T$ phase diagram, implying the presence of biquadratic coupling between the HO and AF order parameters. Because there is no restriction by pressure cells, it is expected that further insights on the unusual two-phase competition will be obtainable from detailed studies using this system.

References

[1] T.T.M. Palstra *et al.*: Phys. Rev. Lett. **55** (1985) 2727.

[2] C. Broholm *et al.*: Phys. Rev. Lett. **58** (1987) 1467.

[3] H. Amitsuka *et al.*: Phys. Rev. Lett. **83** (1999) 5114.

[4] K. Matsuda *et al.*: Phys. Rev. Lett. **87** (2001) 087203.

[5] M. Yokoyama *et al.*: J. Phys. Soc. Jpn. **71** (2002) Suppl., p. 264; Acta Phys. Pol. B. **34** (2003) 1067.

[6] M. Yokoyama *et al.*: J. Phys. Soc. Jpn. **74** (2004) 545.

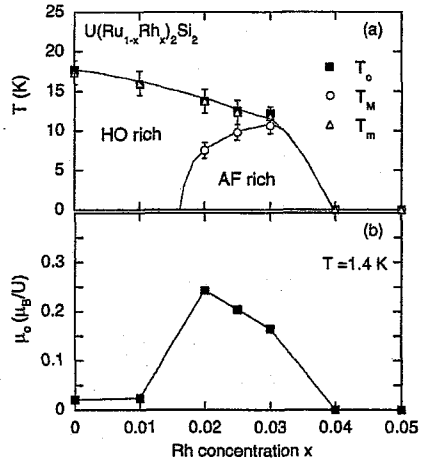

Fig. 2. T = 8.5 K (a) The transition temperature T_o, the onset temperatures of the magnetic Bragg peak T_m and T_M, and (b) the staggered moment μ_o as a function of Rh concentration x. The lines are guides to the eye.

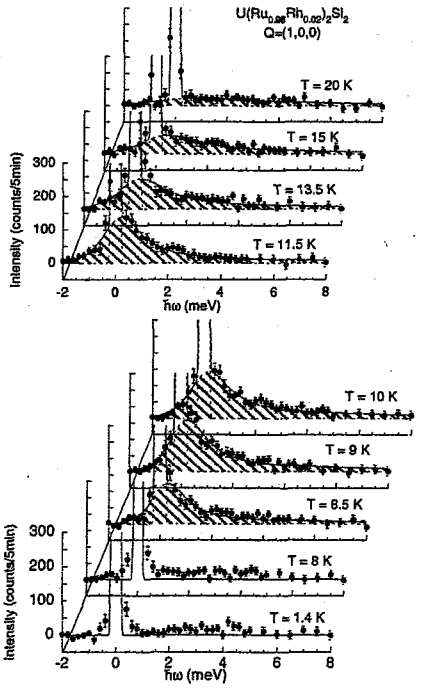

Fig. 3. Temperature variations of constant-Q scans for $Q = (100)$ in $U(Ru_{0.98}Rh_{0.02})_2Si_2$. Incoherent scattering and instrumental background are subtracted. The lines and shading are guides to the eye.

研究テーマ:重い電子系反強磁性体 Ce_7Ni_3 の磁場誘起磁気秩序相の磁気構造
表題:重い電子系反強磁性体 Ce_7Ni_3 の磁場誘起磁気秩序相の磁気構造

1-3-3 Field-Induced Magnetic Phase in a Heavy-Fermion Antiferromagnet Ce_7Ni_3

K. Umeo, K. Motoya*, N. Aso**, H. Kadowaki***, T. Takeuchi****, and T. Takabatake

*Dep. of Quantum Matter, ADSM, Hiroshima Univ., 1-3-1 Kagamiyama, Higashi-Hiroshima 739-8530, Japan; * Fac. of Science and Technorogy, Tokyo Univ. of Science, Noda 278-8510, Japan; ** ISSP, Univ. of Tokyo, 106-1 Shirakata, Tokai 319-1106, Japan; *** Dep. of Physics, Tokyo Metropolitan Univ. Hachioji-shi, Tokyo, 192-0397, Japan; **** Cryogenic Center, Osaka Univ. Toyonaka, Osaka 560-0043, Japan*

The heavy-fermion compound Ce_7Ni_3 with the hexagonal Th_7Fe_3-type structure undergoes two antiferromagnetic phase transitions at T_{N1} = 1.9 K and T_{N2} = 0.7 K. [1] Below T_{N1}, a spin-density-wave (SDW) develops with an incommensurate modulation vector of $0.22c^*$. [2] As shown in Fig. 1, T_{N1} and T_{N2} vanish above 0.3 T when the magnetic field B is applied along the c axis, magnetic easy axis. For $B//c$>0.6 T, another field-induced magnetic (FIM) phase appeared below 0.5 K, which was found by magnetoresistance, specific-heat C, and magnetization M measurements. [3] The findings of a small entropy gain of 0.1Rln2 and the very small increase of magnetization of 0.005 μ_B at the phase boundary suggested that the FIM transition may be associated with the ordering of Ce_{III} with the small moment of 0.1 μ_B. The separation of the FIM phase from the SDW phase was attributed to large spin fluctuations originated from a geometrical frustration in a hexahedron made of Ce_I and Ce_{III} atoms in Ce_7Ni_3. In order to determine the magnetic structure of the FIM phase, the neutron diffraction study for single crystal of Ce_7Ni_3 has performed in the temperature range 0.04 K $\leq T \leq$ 1 K and field range $0 \leq B \leq 5$ T.

A single crystal of Ce_7Ni_3 was grown by a Czochralsky pulling method using a radio-frequency induction furnace with a hot tungsten crucible. In order to decrease defects, strains and impurity ions, the as-grown crystal was heat-treated by the technique of the solid-state electrotransport in a high vacuum. Neutron diffraction experiments on a single-crystal sample were performed using triple-axis spectrometer 4G-GPTAS installed at JRR-3M in JAERI (Tokai). Neutron energy was fixed at 30.5 meV. The sample was cooled down to 0.04 K by a ^{3}He-^{4}He dilution refrigerator. Magnetic fields up to 5T were applied by a superconducting solenoid.

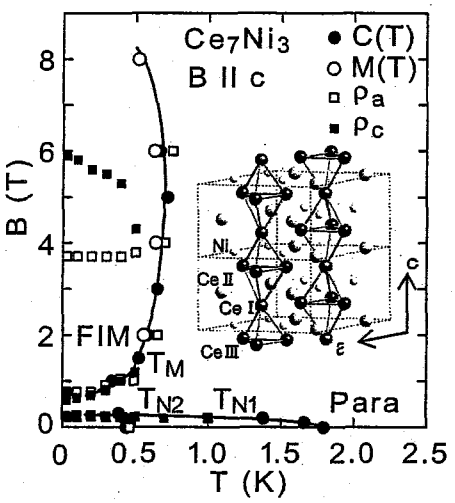

Figure 1: Magnetic field($B \| c$) vs temperature phase diagram of Ce_7Ni_3. The solid lines are a guide to the eye. The inset shows that two Ce_I atoms and three Ce_{III} atoms form a hexahedron stacking along the c axis of Ce_7Ni_3.

At first, we have scanned along a (00l) line. No magnetic reflection at (00l) for $0<l<1$ has been detected at T=50 mK and $0 \leq B \leq 5$ T. By the scan in the (hh0) lines, magnetic reflections were observed at (1/3 1/3 0) in the FIM phase. Thus, the magnetic unit cell is treble that of the chemical unit

使用施設:JRR-3M, 装置:4G GPTAS, 分野: Strongly Correlated Electron Systems

cell in the c plane. Figure 2 shows the temperature dependence of the scan around h=1/3 at B=3T. The peak vanishes at 0.7K, which corresponds with the boundary of FIM phase as shown in Fig. 1.

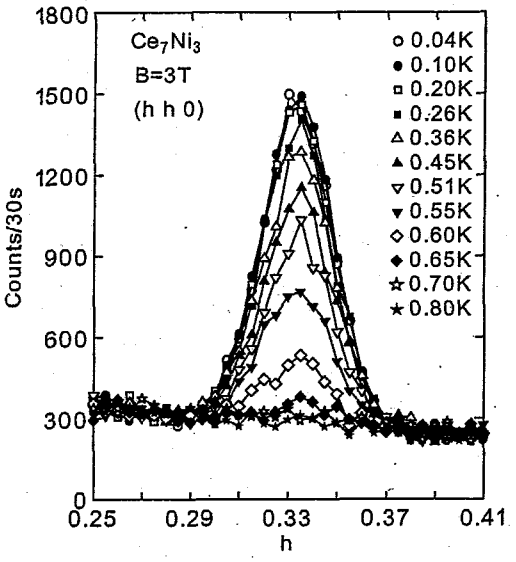

Figure 2: Temperature dependence of the scan along (hh0) line around h=1/3 in Ce_7Ni_3 at the magnetic field of 3T.

The temperature dependence of the intensity of the magnetic reflection (4/3 1/3 0) at low fields for $B \leq 1.5$ T is shown in Fig. 3. The temperature at which the slope has a maximum coincides with the boundary of the FIM phase in Fig. 1. However, there is a tail of the magnetic reflection up to 1 K, which is beyond the phase boundary. Furthermore, as shown in the inset of Fig. 3, the weak intensity at the same Q-vector exists even in the field range 0.3 T< B < 0.7 T, where no anomaly was found in the measurements of C, M and μSR [4]. The new boundary found by the neutron diffraction study is shown in Fig. 4. The phase between the SDW and FIM phase is now denoted by a small moment state (SMS). The presence of the SMS phase should be a result of large spin fluctuations associated with the magnetic frustration.

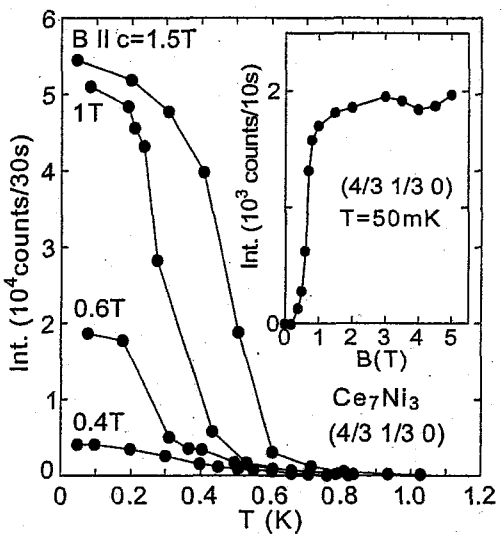

Figure 3: Temperature dependence of the intensity of magnetic reflection at (4/3 1/3 0) in various fields applied along the c axis in Ce_7Ni_3. The inset shows the field dependence of intensity at T=50mK.

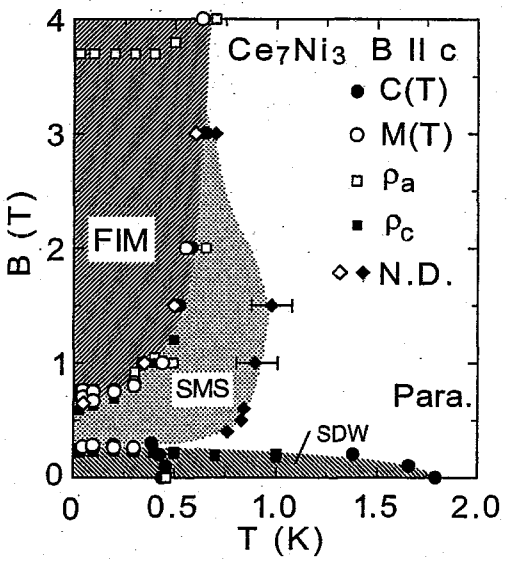

Figure 4: Magnetic field($B \| c$) vs temperature phase diagram of Ce_7Ni_3. The small moment state (SMS) is found by the present neutron diffraction study.

References

[1] K. Umeo *et al.*, J. Phys. Soc. Jpn, **66**, 2133 (1997).
[2] H. Kadowaki *et al.*, J. Phys. Soc. Jpn, **69**, 2269 (2000).
[3] K. Umeo *et al.*, Phys. Rev. B **67**, 144408 (2003).
[4] A. Schenck *et al.*, Physica B **326**, 394 (2002).

研究テーマ： 遍歴電子反強磁性体 CrB_2 の磁気構造と磁気揺らぎ
表題： 遍歴電子反強磁性体 CrB_2 の磁気構造の決定

1-3-4 Magnetic Structure of Itinerant Antiferromagnet CrB_2

H. Ichikawa[1], T. Nemoto[1], N. Motoyama[1], J. Akimitsu[1], K. Iwasa[2]
[1] *Department of Physics, Aoyama-Gauin Univ., 5-10-1 Fuchinobe, Sagamihara, 229-8558*
[2] *Department of Physics, Tohoku Univ., Aoba, Aramaki, Aoba-ku ,Sendai 980-8578*

One of the interesting problems in magnetism is that magnetic electrons show a different behavior, e.g. itinerant and/or localized state by controlling the carrier concentration, temperature and pressure, etc. We have many unsolved problems, for instance, the electronic state of the CuO_2-planes in high T_c cuprates. For these problems, we have two approaching. One is a theoretical approach starting from the weakly magnetic limit, i.e. itinerant picture. The other is an approach from the strong magnetic limit, i.e. localized picture. The theoretical progress based on the self-consistent renormalization theory (SCR-theory) of spin fluctuation has solved the magnetism in itinerant ferro- and antiferromagnets. On experimental side, the studies of metallic compounds with microscopic probe, neutron scattering and NMR, have played a special role to understand the magnetism in these materials.

In this study, we focused on CrB_2, of which crystal structure is AlB_2-type ($P6/mmm$). CrB_2 reveals itinerant antiferromagnetism below 88K[1]. Two problems, however, are still remained in magnetism of CrB_2 that it is positioned at the weak limit or the strong limit. Second one is that magnetic structure of CrB_2 has not yet been determined. In order to determine the magnetic structure, we carried out neutron diffraction measurements.

Liu *et al.* calculated the energy band of CrB_2 by using the KKR method in the muffin-tin potential approximation, and suggested that a spin density wave (SDW) arose along the c-axis due to the nesting of the seventh band Fermi surface[2]. On experimental side, Funahashi *et al.* carried out a neutron diffraction measurement by using single crystal and determined the magnetic structure. They found the helical structure in the [110]*-c* plane[3]. However, we believe that the magnetic structure of CrB_2 has not yet been determined because their samples of ^{11}B which has a small absorption coefficient for neutrons was not used, and only a few refrections could be observed for limitation of equipment. We prepared both powders and large single crystal grown by floating zone method using ^{11}B powder.

The neutron diffraction measurement was performed using the Tohoku University spectrometer, TOPAN in the JRR-3M reactor at Tokai. Energy of the incident neutrons was set at 30.1 meV ($\lambda = 1.65$ Å) and temperature was set at 10 K.

We successfully measured many magnetic reflections in neutron diffraction using large single crystal. However, the obtained propagation vectors τ_i of AF structure are $\tau_1 = 0.285\langle 110\rangle^*$, $\tau_2 = 0.285\langle 2\bar{1}0\rangle^*$ and $\tau_3 = 0.285\langle \bar{1}20\rangle^*$ which can be understood mostly within Funahashi's model. It is suggested that magnetic structure of CrB_2 can be understood by SDW model or helical one.

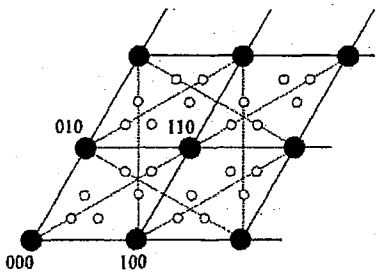

Fig. 1. satellite diffraction positions in the reciprocal lattice of the hexagonal plane.

References

[1] Y. Kitaoka *et al.*: J.Phys.Soc.Jap.**49** (1980) 493.
[2] S. H.Liu *et al.*: Phys.Rev.B **11** (1975) 3463.
[3] S. Funahashi *et al.*: Solid State Comm. **23** (1977) 859.

使用施設：JRR-3M, 装置： 6G (TOPAN) , 分野： 3. Strongly Correlated Electron Systems

研究テーマ：高温超伝導体 $La_{2-x}Ba_xCuO_4$ における電荷・スピンゆらぎと超伝導の相関

1-3-5 $La_{2-x}Ba_xCuO_4$ でのホール濃度が 1/8 からずれることによるストライプ揺らぎへの影響

Effect of deviation from 1/8-doping on the stripe fluctuation in $La_{2-x}Ba_xCuO_4$

H. Goka[1], M. Fujita[2], T. Adachi[3], T. Manabe[3], Y. Koike[3] and K. Yamada[2]

[1] *Department of Physics, Kyoto University, Kyoto 606-8502*

[2] *Institute for Materials Research, Tohoku University, Katahira 2-1-1, Aoba-ku, Sendai 980-8577*

[3] *Department of Applied Physics, Graduate School of Engineering, Tohoku University, Aoba-yama 05, Aoba-ku, Sendai 980-8579*

In $La_{2-x}Ba_xCuO_4$, the high-T_c superconductivity is fully suppressed at a specific hole concentration of ~1/8, where spin and charge stripe orders are stabilized. To investigate the stripe fluctuation in this system and its relation with the superconductivity, we have studied the low-energy spin fluctuation in $La_{1.90}Ba_{0.10}CuO_4$. In this sample, bulk superconductivity appears with T_c(onset)~22 K, while spin and charge stripe orders remain at low temperatures.

Figure 1 shows the temperature dependence of half width at half maximum κ and incommensurability δ of magnetic peak at ω=3 meV. At low temperatures both values are nearly independent of temperature but drastically change around the structural transition at T_{d2} similar to the case of x=1/8. Therefore, the stability of low-energy stripe fluctuations are closely coupled with crystal structure. Above T_{d2} in the low temperature orthorhombic(LTO) phase, δ decreases and κ increases with increasing the temperature, suggesting a degradation of stripe correlations in the LTO phase. In this figure, the results from the x=1/8 sample are also plotted as broken lines. (T_{d2} in the x=1/8 sample is 60 K.)

In Fig. 2, magnetic peak-profiles at 6 meV are compared between x=0.10 and 1/8 samples. As seen in the figure, peak widths at ~30 K are comparable to the resolution limited value (~30 Å) for both samples. At 200 K, however, no clear peak is observed in x=0.10, while a broad peak still exists in x=1/8. These observations suggest that spatial correlation of low energy spin fluctuation is easily destroyed by the deviation from 1/8-doping in the LTO phase. In other words, stripe correlation at 1/8 doping is specifically robust. Therefore, 1/8 doping may influence magnetic properties in many high-T_c cuprates irrespective of crystal structure.

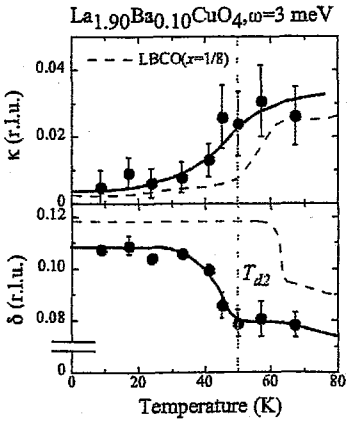

Fig. 1. Temperature dependence of half width at half maximum κ and incommensurability δ at 3 meV in $La_{2-x}Ba_xCuO_4$ (x=0.10). Broken lines are results of x=1/8.

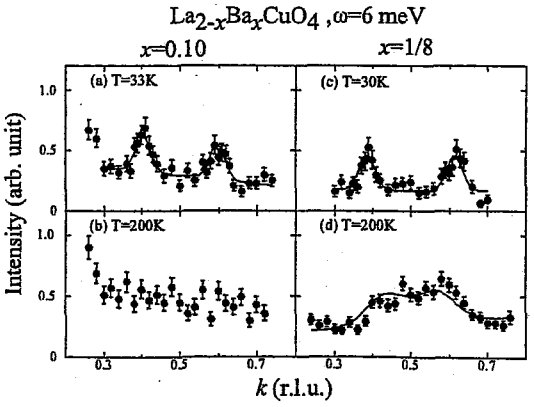

Fig. 2. Peak profiles of constant-E scan at 6 meV. The scans were performed around (0.5,0.5) along k direction. (a):x=0.10, T=33 K, (b):x=0.10, T=200 K, (c):x=1/8, T=30 K and (d):x=1/8, T=200 K.

使用施設：JRR-3M, 装置：C1-1(HER), 6G(TOPAN), T1-2(KSD), 分野：3. Strongly Correlated Electron Systems

研究テーマ： 高温超伝導体 $La_{2-x}Ba_xCuO_4$ における電荷・スピンゆらぎと超伝導の相関
表題： $La_{1.875}Ba_{0.125}CuO_4$ におけるストライプ融解

1-3-6 Thermal melting of stripe correlations in $La_{1.85}Ba_{0.15}CuO_4$

M. Fujita, H. Goka and K. Yamada
Institute for Materials Research, Tohoku University, Katahira 2-1-1, Sendai 980-8577

Antiferromagnetic spin fluctuations in a doped CuO_2 plane are widely believed to have a fundamental connection with the mechanism of high-T_c superconductivity. Extensive neutron scattering measurements on $La_{2-x}Sr_xCuO_4$ have revealed an intimate relationship between the incommensurate (IC) low-energy spin fluctuations and the superconductivity.[1] However, up to now, the physics behind the IC spin fluctuations remains controversial.

The concept of fluctuating stripes[2,3] provides an appealing explanation of the magnetic fluctuations; however, there is an alternative school of thought that argues for an explanation in terms of Fermi-surface-nesting effects.[4] This controversy is tied to the issue of whether charge-stripe order is incompatible with superconductivity. It is clear experimentally that static ordering of charge stripes is correlated with a depression of T_c but are the excitations of the stripe-ordered state different in nature from those in a state without static stripe order?

To address these issues, we present a neutron scattering study of $La_{2-x}Ba_xCuO_4$ with $x = \frac{1}{8}$. This is the material in which high-temperature superconductivity was first discovered[5] and in which the anomalous suppression of T_c at $x = \frac{1}{8}$ was first observed.[6] Neutron scattering experiments were performed by thermal and cold neutron triple-axis spectrometers, TOPAN and HER.

Within the low-temperature-tetragonal (LTT) phase, superlattice peaks indicative of spin and charge stripe orders are observed below 50 K. For excitation energies $\hbar\omega \leq 12$ meV, we have characterized the magnetic excitations that emerge from the incommensurate magnetic superlattice peaks. In the ordered state, these excitations are similar to spin waves. Following these excitations as a function of temperature, we find that there is relatively little change in the Q-integrated dynamical spin susceptibility for $\hbar\omega \sim 10$ meV as stripe order disappears and then as the structure transforms from LTT to the low-temperature-orthorhombic (LTO) phase at 60K. As seen in Fig. 1, the Q-integrated signal at lower energies changes more dramatically through these transitions. The continuous evolution through the transitions provides direct evidence that the incommensurate spin excitations in the disordered state are an indicator of dynamical charge stripes.

References

[1] K. Yamada *et al.*: Phys. Rev. B **57** (1998) 6165.
[2] J. Zaanen *et al.*: Phys. Rev. B **53** (1996) 8671.
[3] S.A. Kivelson *et al.*: Rev. Mod. Phys. **75** (2003) 1201.
[4] Q. Si *et al.*: Phys. Rev. B **47** (1993) 9055.
[5] J.G. Bednorz and K.A. Müller: Z. Phys. B **64** (1986) 189.
[6] A.R. Moodenbaugh *et al.*: Phys. Rev. B **38** (1988) 4596.

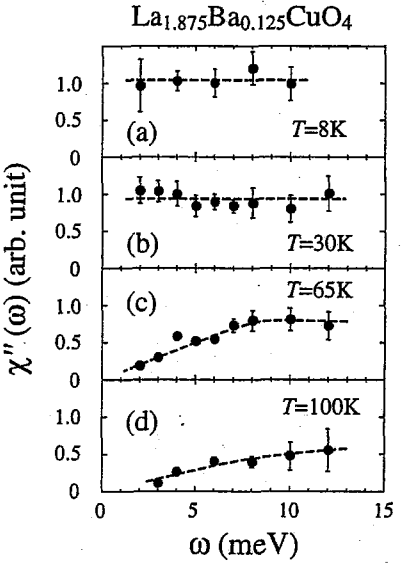

Fig. 1. Local spin susceptibility as a function of ω in $La_{1.875}Ba_{0.125}CuO_4$ at (a) 8 K, (b) 30 K, (c) 65 K, and (d) 100 K. Dashed lines are guides to the eye.

使用施設：JRR-3M, 装置： C1-1(HER), 6G(TOPAN) , 分野： 3. Superconductivity

研究テーマ： Sr_2RuO_4 の異方的スピン揺動とｐ波超伝導

1-3-7 Sr_2RuO_4 の異方的スピン揺らぎに関する研究

Neutron scattering study of the anisotropic spin fluctuation in Sr_2RuO_4

H. Kawano-Furukawa[1,2], M. Urata[3], T. Nagata[1], H. Yoshizawa[4] H. Kadowaki[5], and Pengcheng Dai[6]

[1] *Department of Physics, Ochanomizu Univ. Tokyo 112-8610*
[2] *PRESTO, Japan Science and Technology Corporation, Saitama 332-0012*
[3] *Graduate School of Humanities and Sciences, Ochanomizu Univ., Tokyo 112-8610*
[4] *Neutron Scattering Laboratory, I.S.S.P., Tokyo Univ., Ibaraki 319-1106*
[5] *Department of Physics, Tokyo Metropolitan University, Tokyo, 192-0397*
[6] *Department of Physics and Astronomy, The Univ. of Tennessee, Knoxville, 37996-6393, USA and Condensed Matter Sciences Division, ORNL, Oak Ridge, Tennessee 37831-6393, USA*

Sr_2RuO_4 is a superconductor ($T_c = 1.5$ K) discovered in 1994[1]. NMR- and μSR measurements have established that the superconducting state of this material is likely to be a spin-triplet with p-wave symmetry[2, 3]. Due to its very simple electronic structure, compared with other materials[4, 5], Sr_2RuO_4 has been studied intensively as an ideal material where p-wave superconductivity may be realized. A particularly interesting question is whether any magnetic fluctuation plays any important role in the realization of the p-wave superconducting state of this material.

Instead of behaving as a conventional ferromagnet, band structure calculations predict that the magnetic susceptibility of this material should have a peak at $\mathbf{q} \sim$ (1/3 1/3 0) [6], and this was indeed confirmed by inelastic neutron scattering [7]. After these findings, some theoretical groups predicted that such a spin fluctuation with c-axis anisotropy might stabilize p-wave superconductivity [8, 9, 10].

From NMR measurements Ishida *et al.* reported anisotropic behavior of the spin susceptibility of this system[11]. In NMR measurements one can measure spin-lattice relaxation time, T_1 and the $1/T_1T$ corresponds to the $\mathbf{q}$-integrated spin susceptibility, $\sum_{\mathbf{q}} \frac{\chi''(\mathbf{q},\omega)}{\omega}|_{\omega\to 0}$. These authors concluded that the dynamical spin susceptibility exhibits c-axis anisotropy with a factor of ~ 3, and that such an anisotropic behavior most likely originates from the spin susceptibility at $\mathbf{q}_0 = (0.3\ 0.3\ 0)$.

Neutron scattering is an ideal technique to investigate the $\mathbf{q}$ dependent dynamical spin susceptibility. In addition, because neutrons are scattered by the local spins whose components are perpendicular to the scattering vector $\mathbf{Q}$, one can determine if there are anisotropies in the dynamical spin fluctuations. In order to investigate the anisotropic behavior of the spin susceptibility at $\mathbf{q}_0 =$ (0.3 0.3 0), we have performed unpolarized inelastic neutron scattering experiments. A detailed account of the experimental procedures and results were reported in a previous publication [12].

We grew large single crystals of Sr_2RuO_4 by the floating zone method. The T_c(onset) values for our samples were determined to be 1.4 $\sim$ 1.6 K by resistivity measurements. The neutron scattering experiments were performed using the triple axis spectrometer GPTAS installed at the JRR-3M reactor in JAERI, Tokai, Japan. Neutrons with $k_f = 3.83$ Å^{-1} and combinations of collimators 40'-80'-40'-80' (from the monochromator to the detector) were utilized. A pyrolitic graphite (PG) filter was set after the sample position to eliminate higher order contaminations. We prepared 3 composite samples (each sample contained 8 $\sim$ 10 crystals) with different scattering planes, (h k 0), (h h l) and ($0.7h$ $0.3h$ l). The lengths of the tetragonal reciprocal lattice vectors were $a^* = b^* =$ 1.63 Å^{-1} and $c^* = 0.49$ Å^{-1}.

The intensity of the magnetic scattering is proportional to the square of the magnetic form factor f_Q^2 and to the orientation factor $G(\theta)$[13]. If the electronic distributions are isotropic in real space, the magnetic form

使用施設：JRR-3M，装置： GPTAS(4G)，分野： 3. Strongly Correlated Electron Systems

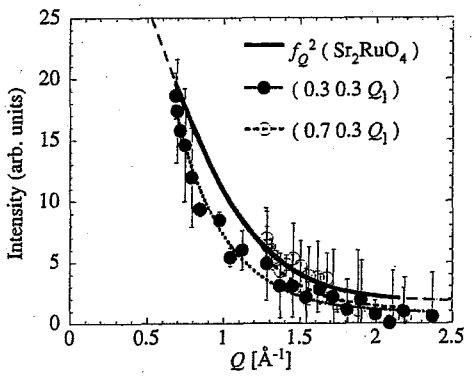

Fig. 1. Q dependence of scaled intensity observed at (0.3 0.3 Q_l) and (0.7 0.3 Q_l) and 4 K. Conservatively, error bars are put with 2 sigma. The full line is the square of magnetic form factor of Sr_2RuO_4, $f_Q^2(Sr_2RuO_4)$, determined in the present study (See text). Broken lines are fitting curves with anisotropic factor of 2.8. After ref. [12]

factor f_Q decreases monotonically with increasing a scattering vector $\mathbf{Q}$. The θ in the orientation factor G is the angle between the scattering vector $\mathbf{Q}$ and the a-b plane; $G(\theta)$ is $\mathbf{Q}$ independent when the susceptibility is isotropic but shows a different $\mathbf{Q}$ dependence when the susceptibility is anisotropic. If the susceptibility is isotropic, the magnetic intensity is scaled only by f_Q^2. Therefore, by measuring the $\mathbf{Q}$ dependence of the magnetic intensity against f_Q^2, one can investigate any anisotropic behavior of the dynamical spin susceptibility.

As the magnetic form factor for the Ru moments in the metallic/superconducting Sr_2RuO_4 is unknown, we first tried to determine it by measuring the spin susceptibility in the (h k 0) plane and assuming isotropic spin fluctuations in the a-b plane. The determined form factor is depicted as a thick solid line in the Fig. 1. The magnetic form factor for Sr_2RuO_4, $f_Q^2(Sr_2RuO_4)$, decreases faster than that for Ru^+ in Q.

In order to evaluate the θ dependence, we performed a series of constant-E scans along (0.3 0.3 Q_l) and (0.7 0.3 Q_l) with $E = 4$ meV and 8 meV, respectively. The Q_l dependence of the integrated intensity (0.3 0.3 Q_l) and (0.7 0.3 Q_l) shows a very broad peak centered at $Q_l = 0$ (not shown), indicating the strong two dimensionality of the spin fluctuations. This result lets us treat each data points with different Q_l independently.

In Fig. 1 the Q dependence of the intensity measured along (0.3 0.3 Q_l) and (0.7 0.3 Q_l) (after resolution corrections, a background subtraction and a scaling due to energy difference) are depicted. This figure clearly shows that the intensities for both (0.3 0.3 Q_l) and (0.7 0.3 Q_l) scans decrease faster than $f_Q^2(Sr_2RuO_4)$ with increasing Q. This observation indicates that the spin susceptibility has c-axis anisotropy. By fitting to the appropriate formulae we estimate an anisotropic factor $\chi_c''/\chi_{a,b}''$ of $\sim$ 2.8 $\pm$ 0.7. Thus we concluded that the incommensurate antiferromagnetic fluctuations observed at $\mathbf{q}_0$ = (0.3 0.3 0) exhibit c-axis anisotropy with an anisotropic factor of $\sim$2.8, which is in good agreement with the NMR result ($\sim$ 3) [11].

References

[1] Y. Maeno *et al.*, **372**, 532 (1994).
[2] G. M. Luke *et al.*, Nature (London) **394**, 558 (1998).
[3] K. Ishida *et al.*, Nature (London) **396**, 658 (1998).
[4] H. Tou *et al.*, Phys. Rev. Lett. **80**, 3129 (1998).
[5] K. Ishida *et al.*, Phys. Rev. Lett. **89**, 037002 (2002).
[6] I. I. Mazin *et al.*, Phys. Rev. Lett. **79**, 733 (1997).
[7] Y. Sidis *et al.*, Phys. Rev. Lett. **83**, 3320 (1999).
[8] T. Kuwabara *et al.*, Phys. Rev. Lett. **85**, 4586 (2000).
[9] M. Sato *et al.*, J. Phys. Soc. Jpn. **69**, 3505 (2000).
[10] K. Kuroki *et al.*, Phys. Rev. B **63**, 060506 (2001).
[11] K. Ishida *et al.*, Phys. Rev. B **64**, 100501 (2001).
[12] T. Nagata *et al.*, Phys. Rev. B **69**, 174501 (2004).
[13] As a text, see Neutron Scattering with a triple-Axis Spectrometer (Basic Techniques), G. Shirane, S. M. Shapiro and J. M. Tranquada, Cambridge university press.

研究テーマ： 金属-絶縁体転移近傍の強相関電子材料の熱電特性と磁性の相関
表題： 強相関電子系 $Na_{0.75}CoO_2$ の磁性と電子状態

1-3-8 Electronic structure and magnetism of $Na_{0.75}CoO_2$ in strongly correlated electron systems

H. Okabe[1], M. Matoba[1], K. Ohoyama[2], T. Kyomen[3], and M. Itoh[3]

[1] *Graduate School of Sci.&Tech., Keio University, 3-14-1 Hiyoshi, Yokohama 223-8522*
[2] *Institute for Materials Research, Tohoku University, 2-1-1 Katahira, Sendai 980-8577*
[3] *Materials and Structures Laboratory, Tokyo Institute of Technology, 4259 Nagatsuta, Yokohama 226-8503*

The discovery of giant thermoelectricty in $Na_{0.6}CoO_2$ [1] and superconductivity in $Na_{0.35}CoO_2{\cdot}1.3H_2O$ [2] has triggered a wave of extensive studies on the electronic structure of a parent material Na_xCoO_2 (x=0.35~1.0) [3-6] Most, however, did not consider the effect of Na location on Co sites; considering that the only role of Na ions is as an electron donor to the CoO_2 framework. Here, we have focused on one of the sodium cobaltites $Na_{0.75}CoO_2$, and calculated its electronic structure by considering the Na location [7].

$Na_{0.75}CoO_2$ crystallizes in a hexagonal structure (space group $P6_3/mmc$) consisting of two-dimensional layers of edge sharing CoO_6 octahedra and partially occupied Na ions. Strictly speaking, Na ions occupy crystallographic $6h(x, 2x, 1/4)$ [8], so that we should employ structure parameters obtained by the HERMES [9] experiment and Rietveld refinement on $Na_{0.75}CoO_2$ to determine the Na location in the band calculations. Na ions occupy these two $6h$ sites with an approximate composition ratio of 1:2 (Na(1) : Na(2) = 0.071 : 0.162). As shown in Fig.1, we tentatively made a supercell ($2\times2\times1$) taking into account the Na location as randomly as possible. In the calculation, the supercell gives 4 crystallographically different Co sites due to the location of the Na ions.

We used the full potential linearized plane wave method as implemented in Wien2k code [10] and its LDA+U extension: a Hubbard type on-site Coulomb interaction added to the local density approximation (LDA). The computational detail was described in the paper [7]. Figure 2 shows the density of states (DOS) and the electronic band structure of $Na_{0.75}CoO_2$ with and without U, respectively. The most remarkable feature is that a narrow manifold just above the Fermi energy is found in the calculation results that include U ($\sim$ 5.0 eV [11]). This is mostly constructed by a Co^{4+} like manifold (Co(2) in Table 1) splitting from the Co 3d-O 2p manifold in the top of the valence band.

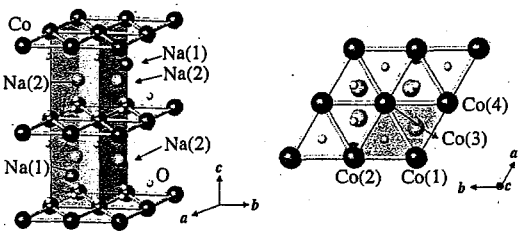

Fig. 1. $2\times2\times1$ supercell of $Na_{0.75}CoO_2$, where the shaded area identifies a unitcell of Na_xCoO_2 (x = 0.35, 0.55 ~ 0.75).

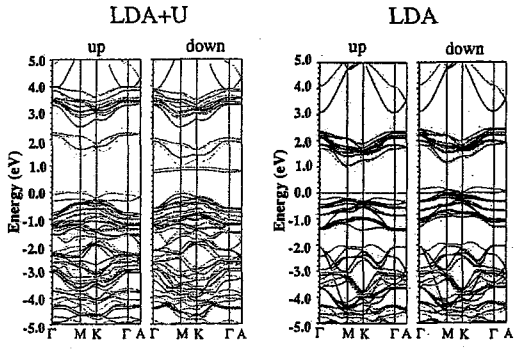

Fig. 2. Total DOS and band structure of $Na_{0.75}CoO_2$ with and without the on-site Coulomb repulsion U.

We found unusual distributions of Co magnetic moments from the results of the LDA+U calculation. As listed in Table 1, the magnetic moments of Co ions are significantly different at each Co site: the Co(2)

使用施設：JRR-3M, 装置： T1-3 (HERMES) , 分野： 3. Strongly Correlated Electron Systems

Table 1. Magnetic moments of Co ions (M_{Co}) and Co-Na bond lengths (d_{nn}, d_{ave}) which are distances from nearest neighboring Na ions and average distances from nearest six Na ions, respectively.

site	$M_{Co}(\mu_B)$	d_{nn}(Å)	d_{ave}(Å)
Co(1)	0.0017	2.7373	3.3830
Co(2)	0.6792	3.2588	3.4254
Co(3)	0.0075	3.0404	3.3528
Co(4)	0.0114	3.0404	3.6377

ion has a magnetic moment hundreds times larger than that of the Co(1) ion. This result is closely related to the bond distance between the Co ion and it ' s nearest neighboring Na ions. As the Co-Na bond length decreases, cobalt oxidization is suppressed and the Co ion closes in on a Co^{3+}(low spin, $s = 0$) state. On the other hand, a long Co-Na bond length leads to the promotion of cobalt oxidization; a Co^{4+}(low spin, $s = 1/2$) like state appears. In an early report of LDA band structure on $Na_{0.5}CoO_2$, all Co ions tended to possess an equivalent ($Co^{3.5+}$) valence state [3]. Our results, however, indicate a tendency for charge disproportionation ($2Co^{3.25+} \rightarrow Co^{3.25+\delta} + Co^{3.25-\delta}$) in $Na_{0.75}CoO_2$.

When the bond distances between Co and Na ions determine the valence states and the magnetic moments of Co ions, no long-range magnetic order appears. Because Na ions are located randomly in $6h$ sites, magnetic Co^{4+} ions are also located randomly in the crystal. Hence, the most dominant magnetic ground state is probably that of a spin-glass-like short-range ordered state. This picture is supported by our earlier studies in which: (i) magnetic anomalies with spin-glass-like characteristics were observed below 13 K, indicating short-range ferromagnetic coupling [12], and (ii) there were no signs of magnetic long-range order detected by neutron powder diffraction down to 2K [11]. Furthermore, from our calculations the average magnetic moment of all Co ions are estimated to be $0.176\mu_B$. This is in good agreement with the experimental value of approximately $0.18\mu_B$ measured by μ^+SR spectra [13].

It should be noted that our tentative supercell is just one of many possible patterns of random Na locations. It is likely that Na ions are unevenly distributed in the actual material. Additionally, there are local distortions of oxygen ions caused by the random Na location. These effects, however, would affect the degree of charge deviation (δ) of Co ions in each case. Therefore, the existence of charge disproportionation ($4Co^{3.25+} \rightarrow 3Co^{3+} + Co^{4+}$) revealed by our computational approach is essential for $Na_{0.75}CoO_2$. This result shows that magnetic Co^{4+} ions are located randomly in the crystal, indicating that the magnetic ground state of $Na_{0.75}CoO_2$ is the spin-glass-like short-range ordered state.

Acknowlegements

We are grateful for helpful discussions with Prof. I. Terasaki (Waseda University), Dr. T. Motohashi (Tokyo Institute of Technology), and Prof. S. Anzai (Keio University). One of us (M. Matoba) wishes to thank the Asahi Glass Foundation.

References

[1] I. Terasaki, Y. Sasago, and K. Uchinokura, Phys. Rev. B **56**, R12685 (1997).
[2] K. Takada *et al.*, Nature **422**, 53 (2003).
[3] D. J. Singh, Phys. Rev. B **61**, 13397 (2000).
[4] D. J. Singh, Phys. Rev. B **68**, 20503 (2003).
[5] J. Kunes, K. W. Lee, and W. E. Pickett, cond-mat/0308388.
[6] J. Ni and G. M. Zhang, cond-mat/0305423.
[7] H. Okabe *et al.*, J. Appl. Phys. **95**, 6831 (2004).
[8] Y. Ono *et al.*, J. Phys. Soc. Jpn. **70** Suppl. A, 235 (2001).
[9] K. Ohoyama *et al.*, Jpn. J. Appl. Phys. **37**, 3319 (1998).
[10] P. Blaha *et al.*, *WIEN2k, An Augmented Plane Wave + Local Orbitals Program for Calculating Crystal Properties* (Karlheinz Schwarz, Techn. Universitat Wien, Austria, 2001).
[11] M. Matoba *et al.*, *to be submitted.*
[12] T. Takeuchi *et al.*, Physica B **312-313**, 719 (2002).
[13] J. Sugiyama *et al.*, Phys. Rev. B **67**, 214420 (2003).

研究テーマ：化学的な乱れの入った系における量子相転移の動的臨界現象

1-3-9 乱れた近藤格子系 $Ce(Ru_{0.5}Rh_{0.5})_2Si_2$ のスピンダイナミクス

Spin dynamics of strongly disordered Kondo-lattice system $Ce(Ru_{0.5}Rh_{0.5})_2Si_2$

Y. Tabata[1], T. Taniguchi[1], N. Osaka[1], S. Kawarazaki[1], H. Kadowaki[2] and N. Aso[3]

[1] *Graduate School of Science, Osaka University, Toyonaka, Osaka 560-0043*

[2] *Department of Physics, Tokyo Metroporitan University, Hachioji, Tokyo 192-0397*

[3] *Institute for Solid State Physics, The University of Tokyo, 106-1 Shirakata, Tokai, 319-1106*

A number of heavy fermion compounds and alloys show deviations of thermal and transport properties from predictions of Landau Fermi liquid (FL) theory, so-called non-Fermi liquid (NFL) behavior. Several mechanisms leading to the NFL behavior have been proposed. In systems close to a magnetic quantum critical point (QCP) the coupling of the conduction electrons to critical spin fluctuation can lead the NFL behavior. In other systems, such as $UCu_{5-x}Pd_x$ [1], the NFL properties are thought to be a consequence of the interplay of strong chemical disorder and many body effects. A. H. Castro Neto et al. have suggested the similarity between the disordered Kondo lattice system and the Ising spin glass system in transverse magnetic field, and have predicted the existence of the quantum Griffiths singularity in the vicinity of a QCP[2].

$Ce(Ru_{0.5}Rh_{0.5})_2Si_2$ is a pseudo-binary Kondo-lattice compound showing the NFL behavior in the specific heat, magnetic susceptibility and electrical resistivity[3]. The macroscopic properties suggest that the origin of the NFL behavior in this material is quantum Griffiths singularity[4, 5]. In order to clarify the NFL properties from the microscopic and the dynamical aspect, we have studied the spin dynamics of $Ce(Ru_{0.5}Rh_{0.5})_2Si_2$ by the inelastic neutron scattering experiments.

The inelastic neutron scattering experiments were performed on the triple-axis spectrometer HER at the JRR-3M reactor of Japan Atomic Energy Research Institute(JAERI). The typical energy resolution using a fixed E_f = 4.4 meV condition was about 0.2 meV (FWHM) at the elastic position.

Figure 1 shows results of constant-Q scan with $\boldsymbol{Q}$ = (1/2 1/2 0) at T = 1.5 and 50 K.

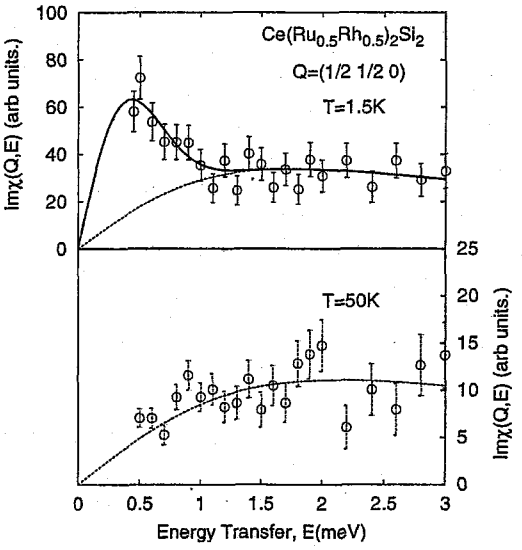

Fig. 1. Constant-Q scans with the scattering wave vector $\boldsymbol{Q}$ = (1/2 1/2 0) at T = 1.5 and 50 K. The solid line is a fit to Lorentzian with an additional Gaussian term, $\mathrm{Im}\chi(\boldsymbol{Q},E) = \mathrm{Im}\chi_{\mathrm{L}}(\boldsymbol{Q},E) + \mathrm{Im}\chi_{\mathrm{G}}(\boldsymbol{Q},E)$, for the data at 1.5K. The dashed lines represents the Lorentzian term in $\mathrm{Im}\chi(\boldsymbol{Q},E)$. The data at 50 K is well described by single Lorentzian term.

At 50 K, the data is well described by the Lorentzian form

$$\mathrm{Im}\chi_{\mathrm{L}}(\boldsymbol{Q},E) = \chi_L(\boldsymbol{Q})\frac{E/\Gamma_{\boldsymbol{Q}}}{1+(E/\Gamma_{\boldsymbol{Q}})^2}$$

with $\Gamma_{\boldsymbol{Q}}$ = 2.2 meV $\simeq$ 25 K, which is similar value to the Kondo temperature estimated from the uniform susceptibility[3] An additional low energy structure below 1 meV is observed in the spectrum at 1.5 K. The higher energy (> 1 meV) spectrum can be well described by the Lorentzian with $\Gamma_{\boldsymbol{Q}}$ = 1.8 meV. We have tried to parameterize the low energy data by adding either another Lorentzian or a Gaussian term to

使用施設：JRR-3M，装置： C1-1 (HER)，分野： 3. Strongly Correlated Electron Systems

$\mathrm{Im}\chi_{\mathrm{L}}(\boldsymbol{Q}, E)$. The additional Gaussian form

$$\mathrm{Im}\chi_{\mathrm{G}}(\boldsymbol{Q}, E) = \sqrt{\pi}\delta\chi(\boldsymbol{Q})\frac{E}{\gamma_{\boldsymbol{Q}}}\exp\left(-\left(\frac{E}{\gamma_{\boldsymbol{Q}}}\right)^2\right)$$

provides a better fit. The solid line in Fig. 1 is the best fit to $\mathrm{Im}\chi_{\mathrm{L}}(\boldsymbol{Q}, E) + \mathrm{Im}\chi_{\mathrm{G}}(\boldsymbol{Q}, E)$ for the data at 1.5K. The energy width of the Gaussian is estimated about 0.54 meV. The NFL behavior in this material should be due to this additional low energy fluctuation. The Gaussian type low energy term was also observed in another NFL material $CeNi_2Ge_2$[6]. In $Ce(Ru_{0.5}Rh_{0.5})_2Si_2$, both the low energy Gaussian and the high energy Lorentzian terms hardly depend on the scattering wave vector $\boldsymbol{Q}$, which indicates that both terms come from local spin fluctuation. Unfortunately, the energy resolution in this experiment is not enough high to clarify the details of the structure of the low energy spectrum. Higher energy resolution experiments are required.

References

[1] O. O. Bernal et al., Phys. Rev. Lett. **75**, 2023 (1995).

[2] A. H. Castro Neto et al., Phys. Rev. Lett. **81**, 3531 (1998).

[3] T. Taniguchi et al., J. Phys. Soc. Jpn. **68**, 2026 (1999).

[4] Y. Tabata et al., Phys. Rev. Lett. **86**, 524 (2001).

[5] Y. Tabata et al., J. Magn. Magn. Mater. **272-276**, 197 (2004)

[6] H. Kadowaki et al., Phys. Rev. B **68**, 140402R (2003)

研究テーマ： 金属秩序型、無秩序型 RBaMn$_2$O$_6$ の結晶構造及び磁気構造
表題： ペロブスカイト型Mn酸化物 RBaMn$_2$O$_6$ における A サイトランダムネス効果

1-3-10 A-site Randomness effect on perovskite manganites, RBaMn$_2$O$_6$

T. Nakajima[1], H. Yoshizawa[2] and Y. Ueda[1]
[1] *Institute for Solid State Physics, MDCL, the University of Tokyo, Kashiwa, 277-8581*
[2] *Institute for Solid State Physics, NSL, the University of Tokyo, Tokai, 319-1106*

We have investigated the structures and electromagnetic properties of the A-site disordered Ba-based manganite $R_{0.5}$Ba$_{0.5}$MnO$_3$ (R = Y and rare earth elements) and compared $R_{0.5}$Ba$_{0.5}$MnO$_3$ with not only the A-site ordered manganite RBaMn$_2$O$_6$ but also ordinary disordered manganites $R_{0.5}A_{0.5}$MnO$_3$ (A = Ca and Sr) [1, 2, 3]. The structures and magnetic properties were studied by neutron powder diffraction using HERMES installed at T1-3 port of JRR-3M in JAERI (Tokai).

The disordered form $R_{0.5}$Ba$_{0.5}$MnO$_3$ has a primitive cubic perovskite cell with no tilt of MnO$_6$ octahedra. The characteristic electronic states of perovskite manganites are absent in $R_{0.5}$Ba$_{0.5}$MnO$_3$ and magnetic glassy states govern the electronic state of $R_{0.5}$Ba$_{0.5}$MnO$_3$. The magnetic glassy states could be due to the disorder effect that hinders the long-range magnetic ordering and could occur as a result of the competition between randomly distributed ferromagnetic and antiferromagnetic interactions.

The A-site randomness effect has been investigated in Pr-compounds with various degrees of Pr/Ba randomness at the A-sites. The A-site randomness suppresses both ferromagnetic and A-type antiferromagnetic transitions in PrBaMn$_2$O$_6$. Figure 1 shows the phase diagram for the electromagnetic properties as a function of degree of the A-site order. The A-site order stabilizes AFM(A) state associated with a $d_{x^2-y^2}$ orbital order (layer type), because the layer type order of R/Ba and consequently the distorted MnO$_6$ octahedra introduce 2-dimensionality in the crystal structure. The increase of the A-site disorder makes AFM(A) state unstable because of the decrease of structural anisotropy (2-dimensionality). On the other hand, it is advantageous to FM state generated by an isotropic double exchange interaction and it leads to FM state for 25~35% A-site ordered PrBaMn$_2$O$_6$. However, the effect of large cation size difference between Pr and Ba is simultaneously enhanced by the A-site disorder and finally results in magnetic glassy state in the strong disordered compound. In conclusion the A-site randomness in Ba-based manganites clearly suppresses not only FM transition but also AFM(A) transition and leads to magnetic glassy state. We observed a similar randomness effect on Nd-compounds.

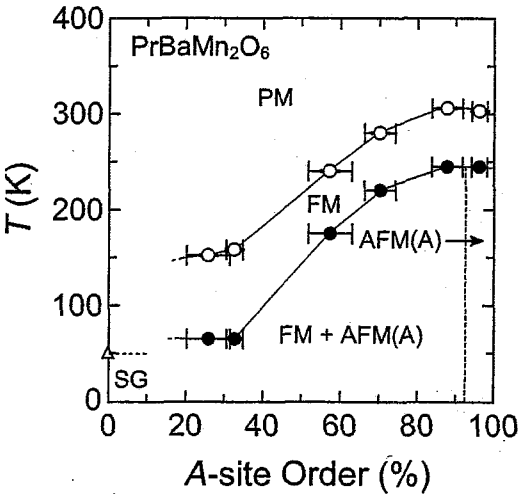

Fig. 1. The phase diagram for the electromagnetic properties of PrBaMn$_2$O$_6$ as a function of the A-site order.

References

[1] T. Nakajima *et al.*: J. Phys. Soc. Jpn. **71** (2002) 2843.
[2] Y. Ueda *et al.*:J. Phys: Condens. Matter **16** (2004) S573.
[3] T. Nakajima *et al.*: J. Phys. Soc. Jpn. (in press)

使用施設：JRR-3M, 装置： T1-3 (HERMES) , 分野： 3. Strongly Correlated Electron Systems

研究テーマ：Na_xCoO_2 における Na 層の乱れとその構造物性
表題：熱電変換材料 Na_xCoO_2 の結晶構造

1-3-11 Crystal structure of thermoelectric materials: Na_xCoO_2

H. Nakatsugawa and K. Nagasawa

Division of Materials Science and Engineering, Graduate School of Engineering, Yokohama National University
79-5 Tokiwadai, Hodogaya Ward, Yokohama 240-8501 Japan

Four polycrystalline Na-richer samples of γ -Na_xCoO_2 were prepared by the RH technique[1,2] to precisely control the sodium content. Starting powders of Na_2CO_3 and Co_3O_4 were mixed and calcined at 1153K for 12h in air. Then, the samples were reground, pressed into pellets and sintered at 1193K for 12h in air. Finally, the pellets were cooled in the furnace to room temperature at a rate of 1K/min. The resulting powder sample was characterized by neutron diffraction (ND) and inductively coupled plasma atomic-emission spectrometry (ICP-AES) analysis. The ND patterns showed good identification of the samples as the γ phase, and there was no indication of the presence of other prototypes or residual raw materials. The molar ratio of metal ions in the samples for γ -Na_xCoO_2 was determined to be Na : Co = (i) 0.77(6) : 1 , (ii) 0.78(3) : 1 , (iii) 0.79(9) : 1, and (iv) 0.82(6) : 1 by the ICP-AES analysis.

We performed powder ND experiments at 10 and 300K on the Kinken powder diffractometer for high efficiency and high resolution measurements, HERMES, of Institute for Materials Research (IMR), Tohoku University, installed at the JRR-3M reactor in Japan Atomic Energy Research Institute (JAERI), Tokai Establishment. An incident neutron wavelength λ =1.82035(7) Å was obtained from a Ge(311) monochromater. The fine powder sample was sealed in a vanadium cylinder with helium gas, and mounted at the cold head of a closed cycle He-gas refrigerator. The ND data were collected on thoroughly ground powders by a multi-scanning mode in the 2theta range from 10° to 153° with a step width of 0.10°.

The structure determination of γ -Na_xCoO_2 was analyzed using the Rietveld analysis program, RIETAN-2000. The charge density distributions at room temperature were visualized by an elaborate method, which are combination of the MEM and the Rietveld refinement of the XRD data.

The powder ND data showed that the specimens for x=0.77(6), 0.78(3), 0.79(9), and 0.82(6) had the P2-type hexagonal structure which was assigned to $P6_3/mmc$ (No.194) at 10K and room temperature. In Figs.1(a) and 1(b), the results of the Rietveld refinement at 10K are shown for (a) x=0.77(6) and (b) x=0.79(9). No impurity peak was detected in the present powder ND measurements. The weighted profile reliability factors of the Rietveld refinement, R_{wp}, were (a) 7.66% and (b) 7.15%. The reliability factors based on the integrated intensities, R_I, were (a) 6.43% and (b) 7.13%. There are two kinds of prisms, i.e., $Na1O_6$ and $Na2O_6$ prisms. The $Na1O_6$ prism at *2b* site shares two sets of three oxygen atoms with upper and lower one CoO_6 octahedara, respectively. On the other hand, the $Na2O_6$ prism at *2d* site shares two sets of three oxygen atoms with upper and lower three CoO_6 octahedara, respectively. Judging from the ionic radius of Na^+ for six coordinations (1.02Å), the Na^+ ions cannot fully occupy the adjacent *2b* and *2d* sites because of the Na1-Na2 distances. Thus, the sodium ions are randomly distributed at the *2b* and *2d* sites with different occupancies. Sodium content was determined to be 0.776 (*2b*:0.255 + *2d*:0.521) for γ -$Na_{0.78}CoO_2$ and 0.799 (*2b*:0.265 + *2d*:0.534) for γ -$Na_{0.80}CoO_2$ which are in good agreement with that obtained by the ICP-AES chemical analysis.

使用施設：JRR-3M, 装置：HERMES(T1-3), 分野 Strongly Correlated Eldctron Systems (c)

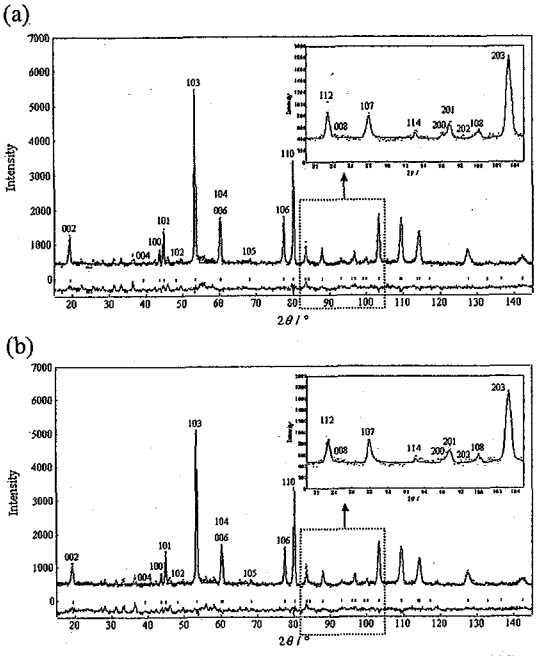

Figure 1: Rietveld fitting of ND data for (a) x=0.77(6) and (b) x=0.79(9) at 10K.

The number of observed XRD structure factors derived in the Rietveld analysis at room temperature were 24 for each set of data, which were used for further MEM analysis. Following the Rietveld analysis, the MEM analysis was carried out with a computer program, MEED, using 50×50×100 pixels. In the MEM imaging, any kind of deformation of electron densities is allowed as long as it satisfies the symmetry requirements. This method enables us to visualize more detailed features included in the observed data like the bonding electron distribution associated with hybridized orbitals.

In Figs.2(a) and 2(b), the three-dimensional representation of the MEM charge densities for samples of (a) x=0.77(6) and (b) x=0.79(9) together with the MEM charge densities in the (002) plane for both samples. An equi-contour surface is drawn only for the lower density region. In these figures, there are O−O network of the electron density due to the O2*p* – O2*p* orbital hybridization. There found to be an obvious overlapping of the charge density between O−O network and Co for x=0.77(6), but no significant overlapping for x=0.79(9). This is the direct observation of decrease of the Co − O hybridization in the CoO_2 layer with increasing the sodium content from x=0.77(6) to 0.82(6). In particular, the change in the electron density distribution should be attributed to the increase of the lattice parameter *a* and the Co−O distance with increasing x.

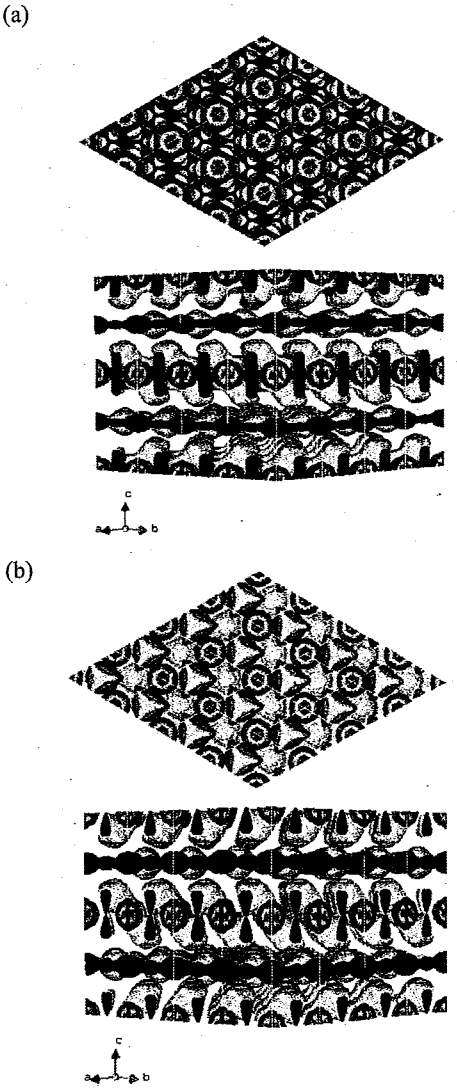

Figure 2: Three-dimensional representation of the MEM charge distribution at room temperature for (a) x=0.77(6) and (b) x=0.79(9).

References

[1] T.Motohashi *et al.* Appl.Phys.Lett. **79** pp. 1480 - 1482 (2001).
[2] T.Motohashi et al. Phys.Rev. B **67** pp. 064406-1 – 064406-5 (2003).

研究テーマ：マンガン酸化物の電荷整列相に及ぼすBサイト置換効果
表題：$Nd_{1/2}Ca_{1/2}(Mn_{0.95}M_{0.05})O_3$の不純物誘起強磁性と不純物状態

1-3-12 Impurity-induced ferromagnetism and impurity states in $Nd_{1/2}Ca_{1/2}(Mn_{0.95}M_{0.05})O_3$[1]

Y. Moritomo[1], K. Murakami[1], H. Ishikawa[1], M. Hanawa[1], A. Nakamura[1] and K. Ohoyama[2]
[1] *Department of Applied Physics, Nagoya University, Nagoya 464-8603*
[2] *Institute for Materials Research, Tohoku University, Sendai 980-8577*

The charge-ordered (CO) phase, which is frequently observed in half-doped manganites e.g., $Nd_{1/2}Ca_{1/2}MnO_3$ and $Pr_{1/2}Ca_{1/2}MnO_3$, is known to be amenable to the external perturbations, such as, (a) magnetic field[2], (b) hydrostatic and chemical pressure[3] and (c) B-site substitution.[4] This amenability of the CO state can be ascribed to the strong competition of the CO state with the ferromagnetic metallic (FM) state due to the double-exchange mechanism.[5] Among the perturbations, B-site substitution effect on the CO phase is rather complicated, since the B-site impurity is usually expected to be advantageous for the insulating CO state. Here, we have investigated impurity effects on the lattice structure and the electronic state for the 5 % B-site substituted $Nd_{1/2}Ca_{1/2}(Mn_{0.95}M_{0.05})O_3$ (M = Cr, Co, Ni, Ru, Zn, Fe, Cu, Sc, Nb and Cd).

The Figure shows temperature variation of magnetization M for $Nd_{1/2}Ca_{1/2}(Mn_{0.95}M_{0.05})O_3$. As temperature decreases, M shows a broad peak at $\sim$ 250 K and then decreases. This suppression of M is originated in the charge-ordering transition. Even though the anomaly at $\sim$ 250 K is blurred by substitution by Zn, Fe, Cu, Sc, Nb and Cd, no trace of the ferromagnetism is observed down to the lowest temperature. By contrast, in the Cr-, Co-, Ni- and Ru-doped sample, the $M-T$ curve steeply increases as temperature decreases, indicating a ferromagnetic transition: T_C = 240 K for M = Ru, 150 K for M = Cr and 90 K for M = Ni and Co. We found a strong correlation between the ferromagnetism and the density of state (DOS) of the impurity d-state at the Fermi level E_F, suggesting that the ferromagnetism can be ascribed to the enhanced one-electron bandwidth of the Mn3d-Md hybridized band.

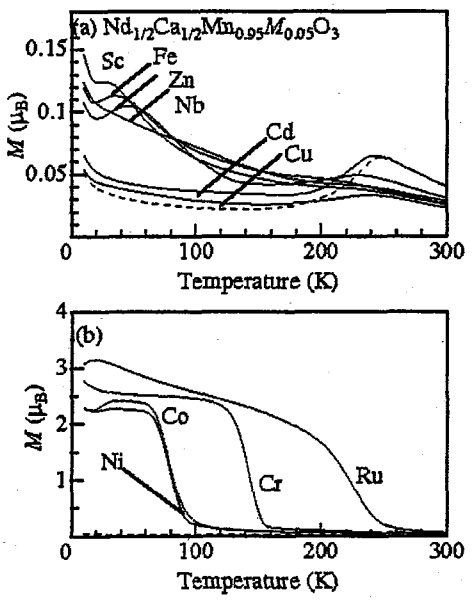

Fig. 1. Temperature variation of magnetization M for $Nd_{1/2}Ca_{1/2}(Mn_{0.95}M_{0.05})O_3$: (a) M = Zn, Fe, Cu, Sc, Nb and Cd, and (b) M = Cr, Co, Ni and Ru. M was measured under a field of 0.5 T in the warming run after cooling down to 10 K in the zero field (ZFC). The broken curve is for the non-doped $Nd_{1/2}Ca_{1/2}MnO_3$.

References

[1] Y. Moritomo, *et al.*, Phys. Rev. B**69**, 212407 (2004).
[2] Y. Tomioka, *et al.*, Phys. Rev. B **53**, R1689 (1996).
[3] Y. Moritomo, *et al.*, Phys. Rev. B **55**, 7549 (1997).
[4] B. Raveau, *et al.*, J. Solid State Chem., **130**, 162 (1997).
[5] P. W. Anderson and H. Hasagawa, Phys. Rev. **100**, 675 (1955).

使用施設：JRR-3M，装置：T1-3 (HERMES)，分野：3. Strongly Correlated Electron Systems.(c)

研究テーマ:f電子系化合物における価数揺動状態
1-3-13:TmTeの圧力下金属相における非弾性磁気散乱

Inelastic Neutron Magnetic Scattering in the Metallic Phase of TmTe under High Pressure

T. Matsumura, H. Ishida, K. Hirota*, and M. Nishi*

*Department of Physics, Graduate School of Science, Tohoku University, Sendai 980-8578, Japan; * Institute for Solid State Physics, The University of Tokyo, 106-1 Shirakata, Tokai 319-1106, Japan*

TmTe is a magnetic semiconductor with an energy gap ~0.35 eV between the 4f13 level and the bottom of the 5d conduction band. Application of pressure reduces the gap, which closes at ~2 GPa. At ambient pressure TmTe exhibits characteristic properties of localized f electrons such as antiferroquadrupolar ordering; antiferro-magnetic transition occurs at 0.5 K. In the metallic phase above 2 GPa, a ferro-magnetic order appears with Tc=15 K [1], which decreases with increasing the presure. The resistivity also exhibits anomalous behavior above 2 GPa that reminds the Kondo effect [2].

The aim of the present study is to examine magnetic excitations near the insulator to metal transition (IMT). At ambient pressure the excitation is of crystal field levels. At high pressures near and above 2 GPa, we expect some signature of valence fluctuation and ferromagnetic correlations.

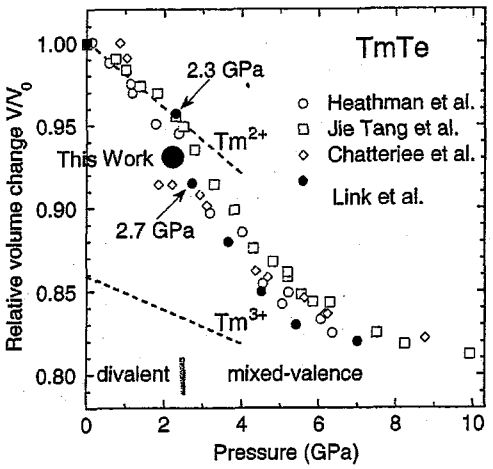

Figure 1: Volume-pressure diagram of TmTe.

The pressure was applied in a McWhan-type cell which can go up to ~3GPa. The volume of the sample was 5mm in diameter and 8mm in length. The pressure was determined by the variation of lattice constant of NaCl. The position in the volume-pressure diagram in this work is indicated in Fig. 1.

Neutron scattering experiment was performed with the PONTA 3-axis spectrometer at the 5G port of JRR-3M in JAERI(Tokai). Although we expected that the sample had entered the metallic phase, the ferro-magnetic order was not observed even at 4 K. This shows that the pressure of this work was just before the IMT.

Figure 2 shows the excitation spectra at Q=(1.5 0 0); this is of magnetic one since the intensity decreases with Q. The data can be fit to a Lorentzian at E=0 with Γ=1.6 meV, which is seems to reflect more unstable 4f state than at P=0.

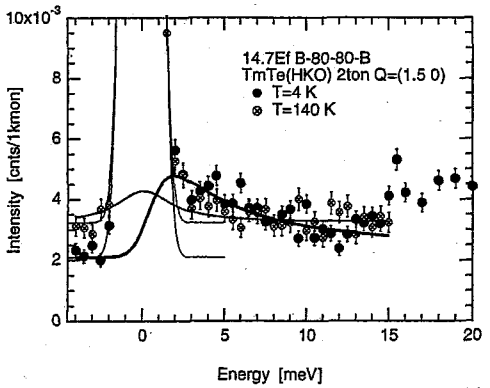

Figure 2: Excitation spectra of TmTe under high pressure at 2.1GPa.

References

[1] P. Link et al., Phys. Rev. Lett. **80** (1998) 173.
[2] T. Matsumura et al., Phys. Rev. Lett. **78** (1998) 1138.

使用施設:JRR-3M, 装置:PONTA(5G), 分野 Strongly Correlated Electron Systems

研究テーマ： 金属—絶縁体転移近傍の強相関電子材料の熱電特性と磁性の相関
表題： フラストレートした強相関電子系 $Na_{0.75}CoO_2$ の磁性

1-3-14 Magnetic nature of $Na_{0.75}CoO_2$ in frustrated and correlated systems

M. Matoba[1], T. Takeuchi[1], H. Okabe[1], and K. Ohoyama[2]
[1] *Graduate School of Sci. & Tech., Keio University, 3-14-1 Hiyoshi, Yokohama 223-8522*
[2] *Institute for Materials Research, Tohoku University, 2-1-1 Katahira, Sendai 980-8577*

Extensive investigations of magnetic frustration on unique spin systems (triangle, kagome, etc.) have been performed during the last two decades, since the magnetic frustration lead various ground states without long range order: cooparative paramagnets, spin glasses, spin liquids and spin ices [1]. Futhermore, a novel Co oxide, $Na_xCoO_2 \cdot yH_2O$ is the first to be discovered superconducting Co oxide with T_c=5 K [2] in highly frustrated and strongly correlated systems.

In this report, we focus on defects-induced mixed valent material $Na_{0.75}CoO_2$ (space group $P6_3/mmc$) and we would like to discuss the magnetism [3-6] of Na_xCoO_2 in highly frustrated and strongly correlated nature. The crystal structure of Na_xCoO_2 [7-9] are resemble to that of α-$NaFeO_2$ [7], which geometric frustration and self dilution effects are expected on strongly correlated CoO_2 sheets. In addition, unconventional magnetic nature are observed in $Na_{0.75}CoO_2$ [3, 4]. Our lack of understanding these complex effects on the strongly correlated electron systems is highlighted by attempts to interpretate the magnetic frustration on Na_xCoO_2. This is thus our motivation for this investigation.

A well-ordered powder sample of $Na_{0.75}CoO_2$ was carefully prepared and characterized by powder x-ray diffraction, Rietveld refinement, wavelengh dispersive x-ray spectroscopy, and x-ray photoemission spectroscopy. All DC magnetic measuements were carried out by the commercial SQUID magnetometer (Quantum Design, MPMS), and the neutron powder diffraction (NPD) patterns were obtained with Kinken powder diffractometer [10] for high efficiency and high resolution measurements (HERMES) installed at the T1-3 beam hole of the guide hall at the Japan Research Reactor 3M (JRR-3M) in Japan Atomic Energy Research Institute (JAERI).

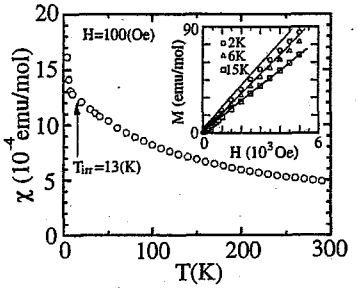

Fig. 1. Temperature dependence of χ_{FC} of $Na_{0.75}CoO_2$ (H=100 Oe). The inset shows the magnetization at 2 K, 6 K, and 15 K.

Figs. 1 and 2 show DC temperature-dependent magnetic susceptibility curves (χ_{FC} and χ_{ZFC}) for polycrystalline $Na_{0.75}CoO_2$, whose NPD patterns were obtained by the HERMES experiment, in the field cooled (FC) and the zero-field cooled (ZFC) conditions. The χ data don't show a broad maxium indicative of two-dimensional antiferromagnetic long range order as normally seen for antiferromagnetic K_2NiF_4-type compounds [3, 11]. However, the magnetic enhancement below 13 K or rather the itinerant weak ferromagnetic behaviour are observed. This fact is consistent with the prediction by the results of band calculation [12]. Now, the χ data (in Fig. 1) for the temperature range 10 K to 300 K can be fitted to the following Curie-Weiss law,

$$\chi(T) = \chi_0 + C/(T-\theta) \qquad (1)$$

where $\chi_0 = 8.554 \times 10^{-5}$ emu/mol including the Landau, Pauli and Van Vleck terms, C is the Curie constant (μ_{eff}=1.13μ_B) and $\theta = -130.4$ K is the Weiss temperature. Spin only value for Co^{3+} ($t_{2g}^6 e_g^0$:S=0) and Co^{4+} ($t_{2g}^5 e_g^0$:S=1/2) are 0 and 1.73 μ_B, respectively. This temperature dependence of $\chi(T)$ therefore indicates the coexistence of localized spins and itinerant electrons in $Na_{0.75}CoO_2$. At low temperatures, the turin-

使用施設：JRR-3M，装置： T1-3 (HERMES)，分野： 3. Strongly Correlated Electron Systems

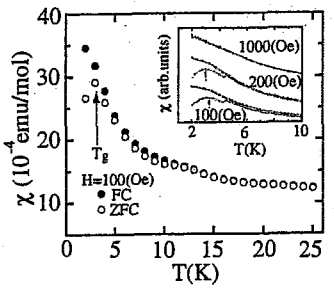

Fig. 2. Temperature dependence of χ_{FC} and χ_{ZFC} of $Na_{0.75}CoO_2$ at low tenperature rigions. The inset shows the χ data near T_g at several magnetic fields.

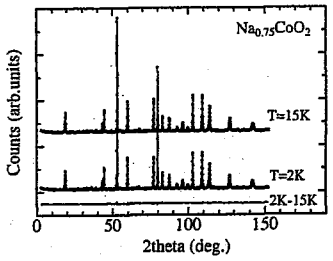

Fig. 3. Neutron powder diffraction (NPD) data obtained at low temperatures.

ing point between χ_{FC} and χ_{ZFC} is seen at 13 K in Fig. 2. Then, we have performed magnetization studies to reveal its magnetic nature at distinctive temperatures (2 K, 6 K, and 15 K), as shown in the inset of Fig. 2. Linear relation is only found at 15 K. Small devaiation at 2 K and 6 K suggests short range ferromagnetic coupling. And spin glass like cusp transition is observed near 3 K in the χ_{ZFC} data. As shown in the inset of Fig. 1, magnetic field dependent characterisics of the χ data indicate that some kind of short range order surely exists [3].

The NPD patterns for 2 K and 15 K are identical as shown in Fig. 3. If the inflection point at 13 K in the χ data were originated from magnetic long-range order, the NPD patterns should show magnetic Bragg peaks at 2 K, or the intensities of the crystallographic peaks should change due to the magnetic contribution. However, no differences are found for the HERMES experiment, thus indicating that no magnetic long range order is present down to 2 K. Furthermore, the absence of broad features at 2 K suggests that no magnetic short-range order is present below T_g=3 K. However, due to the weak magnetic moment of Co^{4+} (S=1/2) and the fact that the sample resembles a fairly dilute magnetic system, potential broad features might be too weak to be observable.

In summary, $Na_{0.75}CoO_2$ is not the conventional itinerant paramagnet but shows the coexistence behaviour of localized spins and itinerant electrons. Irrevesible temperature T_{irr}=13 K and cusp transition temperature T_g=3 K are observed throughout DC χ_{FC} and χ_{ZFC} experiments. The investigation of low-temperature NPD experiments reveals that no magnetic long-range order is present in the NPD patterns.

Acknowlegements

We are grateful for helpful discussions with Prof. I. Terasaki (Waseda University) and Dr. T. Motohashi (Tokyo Institute of Technology). One of us (M. Matoba) wishes to thank the Asahi Glass Foundation.

References

[1] A. P. Ramirez, Annu. Rev. Mater. Sci. **24**, 453 (1994).
[2] K. Takada *et al.*, Nature **422**, 53 (2003).
[3] T. Takeuchi *et al.*, Physica B **312-313**, 719 (2002).
[4] T. Motohashi *et al.*, Phys. Rev. **67**, 64406 (2003).
[5] M. Matoba *et al.*, *Proceedings of the 9th Symposium on Thermoelectric Conversion Research Committee of Japan (TEC2003, Tokyo, 2003)*, p.72.
[6] H. Okabe *et al.*, J. Appl. Phys. **95**, 6831 (2004).
[7] R. J. Balsys and R. L. Davis, Solid State Ionics **93**, 279 (1996).
[8] I. Terasaki, Y. Sasago, and K. Uchinokura, Phys. Rev. B **56**, R12685 (1997).
[9] T. Motohashi *et al.*, Appl. Phys. Lett. **79**, 1480 (2001).
[10] K. Ohoyama *et al.*, Jpn. J. Appl. Phys. **37**, 3319 (1998).
[11] M. Matoba *et al.*, Physica B **312-313**, 630 (2002).
[12] D. J. Singh, Phys. Rev. B **61**, 13397 (2000).

研究テーマ： 金属-絶縁体転移近傍の強相関電子材料の熱電特性と磁性の相関
表題： 強相関電子系 CoO_2 平面を有する層状オキシ硫化物 $Sr_2Cu_2CoO_2S_2$ の磁性

1-3-15 Magnetism of layered cobalt oxysulfide $Sr_2Cu_2CoO_2S_2$ with strongly correlated CoO_2 square-planes

M. Matoba[1], S. Okada[1,2], T. Takeuchi[1], Y. Kamihara[1], K. Ohoyama[3], and Y. Yamaguchi[3]
[1] *Graduate School of Sci. & Tech., Keio University, 3-14-1 Hiyoshi, Yokohama 223-8522*
[2] *Faculty of Sci. & Tech., Waseda University, Tokyo 169-8555 and CREST, Japan Sci. & Tech. Agency, Tokyo 108-0075*
[3] *Institute for Materials Research, Tohoku University, 2-1-1 Katahira, Sendai 980-8577*

Many layered transition-metal (TM) oxides and sulfides have been the subject of the intense experimental and theoretical investigations due to their interesting physical properties including superconductivity, charge density waves, and two-dimensional (2D) magnetism [1]. $Sr_2Cu_2CoO_2S_2$ is indeed a prototypical example which represents a combination of TM oxide and sulfide layers; it has a prototypical stacking sequence $-Sr-Cu_2S_2-Sr-CoO_2-Sr-$ [2, 3], as schematically depicted in the inset of Fig. 1. In this article, we report *unknown magnetic and electronic nature* of $Sr_2Cu_2CoO_2S_2$ [3, 4, 5, 6].

A polycrystalline sample of $Sr_2Cu_2CoO_2S_2$ was carefully prepared by the solid state reaction described elesewhere [3, 4, 5, 6]. Obtained black polycrystalline samples were characterized by a neutron powder diffraction (NPD) by the high efficiency and high resolution measurements (HERMES) [7], a x-ray photoemmission spectroscopy (XPS) and a superconducting quatum interference device (SQUID) magnetometer.

Figures. 1(a) and 1(b) show magnetic susceptibilities (χ) and $d\chi T/dT$ of $Sr_2Cu_2CoO_2S_2$ as a function of temperature, indicating the complicated magnetic behaviour due to *unkown magnetic origins*. In this article, we would like to limit the discussion to the magnetic feature above 150K. Above 150K, the behaviour of χ shows a broad maxium indicative of 2D antiferromagnetic coupling [8]. On the other hand, the antiferromagnetic transition temperature (T_N) can be obtained from measurements of the magnetic contribution $d\chi T/dT$, which is proportinal to the heat capacity [9]. Consequently, T_N can be determined to be 200K

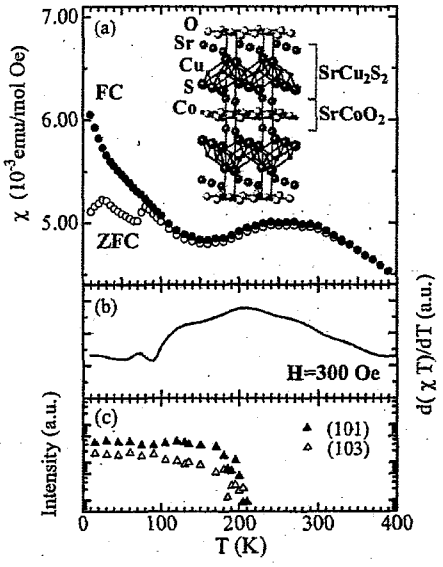

Fig. 1. Temperature dependences of field cooled (FC) and zero-field cooled (ZFC) magnetic susceptibilities (a), its derivative ZFC curve, and typical magnetic neutron intensities (c) of $Sr_2Cu_2CoO_2S_2$ (space group I/4mmm).

from the $d\chi T/dT$ curve. The T_N is indeed almost consistent with the temperature below which magnetic NPD peaks originated from antiferromagnetic CoO_2 planes appear, as shown in Fig. 1(c). The indices of magnetic reflections peaks are the same as those normally seen for antiferromagnetic K_2NiF_4-type compounds with square-planar NiF_2-type planes.

The line shape of Cu $2p$ XPS spectrum with no clear satellite is quite smilar to that of Cu_2O ($Cu_2^+O^{2-}$), as shown in Fig. 2. The XPS spectra of CuO ($Cu^{2+}O^{2-}$) and $NaCuO_2$ ($Na^+Cu^{3+}O_2^{2-}$) have well-defined satellites at higher binding energy side of the main peak. It is thus concluded that

使用施設：JRR-3M，装置： T1-3 (HERMES)， 分野： 3. Strongly Correlated Electron Systems

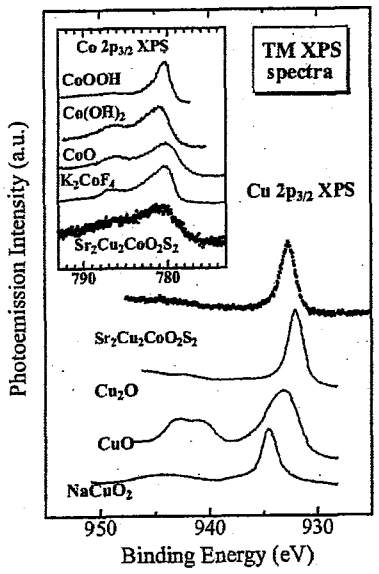

Fig. 2. Cu $2p$ and Co $2p$ XPS spectra of $Sr_2Cu_2CoO_2S_2$ in comparisson with those of reference compounds.

the Cu ion in $Sr_2Cu_2CoO_2S_2$ is in the monovalent state or "Cu^+" state. On the other hand, Co $2p$ XPS spectra of $Sr_2Cu_2CoO_2S_2$ have a strong satellite, as shown in the inset of Fig. 2, which is quite similar to those of strongly correlated Co compounds such as K_2CoF_4 [11]. We therefore analyzed the spectra by the CoO_4 cluster model [12] to estimate the O $2p$-to-Co $3d$ charge transfer energy $\Delta(\sim 4\text{eV})$ and the on-site $d-d$ Coulomb repulsion energy $U(\sim 5\text{eV})$. The cluster model analysis suggests that the electronic nature of the CoO_2 planes belongs to a strongly correlated electron system, as listed in Table 1.

In summary, we has been investigated magnetism and electronic nature in the novel layered oxysulfide $Sr_2Cu_2CoO_2S_2$. $Sr_2Cu_2CoO_2S_2$ is the antiferromagnet with $T_N(=200\text{K})$ obtained from measurements of the NPD and the magnetic contribution $d\chi T/dT$. The χ shows a broad maxium indicative of 2D antiferromagnetic nature, which is not originated from the $Cu_2^+S_2$ layers but the strongly correlated $Co^{2+}O_2$ square-planes revealed by the XPS measurement.

Table 1. The charge transfer energy Δ, the Coulomb repulsion energy U, and the hybridization energy T obtained by the CI cluster model analysis in comparison with the reference data [10, 11].

compounds	Δ (eV)	U (eV)	T (eV)
$Sr_2Cu_2CoO_2S_2$	4.2	5.0	2.0
$CoBr_2$	3.4	4.5	2.0
$CoCl_2$	5.0	4.5	2.0
CoO	5.7	5.1	2.0
K_2CoF_4	7.5	4.5	2.0
CoF_2	8.6	4.5	2.0

Acknowlegements

We are grateful for helpful discussions with Prof. S. Anzai (Keio Univ.), Prof. I. Terasaki (Waseda Univ.) and Dr. H. Kito (AIST). One of us (M. Matoba) wishes to thank the Asahi Glass Foundation. The HERMES measurement was performed under the inter-university cooperative research program of the Institute for Materials Research, Tohoku University.

References

[1] R. Cava, Science **247**, 656 (1990).
[2] W. J. Zhu *et al.*, J. Am. Chem. Soc. **119**, 12398 (1997).
[3] M. Matoba *et al.*, Jpn. J. Appl. Phys. **39**, 498 (2000).
[4] M. Matoba *et al.*, J. Phys. Soc. Jpn. **70**, Suppl. A64 (2001).
[5] M. Matoba *et al.*, Physica B **312-313**, 630 (2002).
[6] S. Okada *et al.*, J. Phys. Chem. Solids **63**, 983 (2002).
[7] K. Ohoyama *et al.*, Jpn. J. Appl. Phys. **37**, 3319 (1998).
[8] R. Navarro *et al.*, Physica B **83**, 97 (1976).
[9] M. E. Fisher, Philos. Mag. **17**, 173 (1962).
[10] S. -J. Oh, *Core-level spectroscopy in condensed systems*, ed. by J. Kanamori and A. Kotani (Springer-Verlag, Berlin, 1987) p.125.
[11] L. Sangaletti, F. Parmigiani, and E. Ratner, Phys. Rev. B **57**, 10175 (1998).
[12] T. Saitoh *et al.*, Phys. Rev. B **52**, 7934 (1995).

研究テーマ：La2-xSrxCuO4 のオーバードープ相における低エネルギースピン揺動

1-3-16 La2-xSrxCuO4 のオーバードープ相における低エネルギースピン揺動

Spin Fluctuation of Overdoped $La_{2-x}Sr_xCuO_4$ Studied by Neutron Scattering

C. H. Lee[1], H. Hiraka[2] and K. Yamada[2]

[1] *AIST, 1-1-1 Umezono, Tsukuba, Ibaraki 305-8568, Japan*

[2] *Institute for Materials Research, Tohoku University, Sendai 980-8577, Japan*

The interplay between magnetism and superconductivity is one of the most interesting and important issues in the physics of the cuprate high temperature superconductors. To clarify the mechanism of high-Tc superconductivity in term of magnetism, intensive studies have been carried out using neutron scattering. $La_{2-x}Sr_xCuO_4$ (LSCO) is one of the most simple high-T_c cuprates and has an advantage that it can be doped in a wide range of carrier concentration. It is, thus, considered that LSCO is a suitable system for studying spin fluctuations, systematically. To date, spin fluctuations of underdoped and optimally doped region have been studied in details, whereas, there is only preliminary studies for overdoped region. In this work, therefore, we have studied spin fluctuations of overdoped region for $La_{2-x}Sr_xCuO_4$ using inelastic neutron scattering techniques and compared the results with that of underdoped region.

Inelastic neutron scattering measurements were performed using the triple-axis spectrometer TOPAN in JRR-3M of JAERI at Tokai. The incident (final) neutron energy was fixed at E_i (E_f) = 14.75 meV or 13.75 meV using the (002) reflection of a pyrolytic graphite monochromator and an analyzer. The typical horizontal collimator sequence was 40'-100'-S-60'-80' where S denotes the sample position. In order to increase the sample volume, two or three single crystalline rods were assembled and mounted in an Al container filled with He thermal exchange gas.

Fig. 1 shows energy dependence of dynamical spin susceptibility $\chi''(\omega)$ below T_c for x = 0.10, 0.18, 0.20 and 0.23. In overdoped region, spin gap, which opens below T_c, disappears monotonically as Sr concentration increases, but the suppression of $\chi''(\omega)$ below ω = 6 meV is still observed in x = 0.23. The spin gap will, finally, be completely disappeared in x = 0.25[1]. For x = 0.18, even a spin pseudo gap is present around $T = T_c$[2]. In contrast, for underdoped samples of x=0.10 showing similar superconducting transition temperatures (T_c) with x = 0.20, no suppression of $\chi''(\omega)$ at low energy region is observed. Possibly, an extra low energy component in underdoped samples is induced by inhomogeneity originated from Sr doping and/or stripe which are suppressed in overdoped region by sufficient hole concentration. Further studied should be carried out to clarify the mechanism of high-T_c superconductivity.

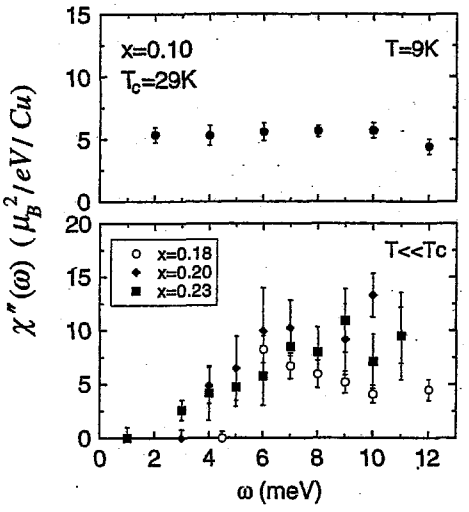

Fig. 1. Energy dependence of $\chi''(\omega)$ for the x = 0.10, 0.18, 0.20 and 0.23 samples at $T \ll T_c$.

References

[1] C. H. Leeet *al.* : J. Phys. Soc. Jpn. **69** (2000) 1170.

[2] C. H. Leeet *al.* : Phys. Rev. B **67** (2003) 134521.

使用施設：JRR-3M, 装置：6G(TOPAN), 分野：3. Strongly Correlated Electron Systems

研究テーマ： 重い電子系化合物 URu_2Si_2 の磁気形状因子
表題： 重い電子系化合物 URu_2Si_2 の磁気形状因子

1-3-17 Magnetic Form Factor in the Heavy-Electron System URu_2Si_2

K. Kuwahara[1], H. Sagayama[1], M. Kohgi[1], M. Nishi[2], K. Nakajima[3] and H. Amistuka[4]

[1] *Department of Physics, Tokyo Metropolitan University, Tokyo 192-0397*
[2] *Institute for Solid State Physics, The University of Tokyo, Tokai 319-1106*
[3] *Neutron Science Research Center, Japan Atomic Energy Research Institute, Tokai 319-1195*
[4] *Graduate School of Science, Hokkaido University, Sapporo 090-0810*

The tetragonal heavy-electron compound URu_2Si_2 undergoes two successive phase transitions; a puzzling phase transition at T_o = 17.5 K and a superconducting transition at $T_C = \sim 1$ K. To study the electronic state of 5f electrons of this compound, we have measured the magnetic form factor of the field induced moment in the paramagnetic state with polarized neutrons.

In the previous polarized neutron experiment using the single crystal with thickness of 1.0 mm [1], the observed magnetic form factor f is close to the free ion value as other U-based intermetallic compounds, as shown in Fig 1. Interestingly, the obtained magnetic moment of 5f electrons μ ($0.07\mu_B$/U) was smaller than the value of the bulk magnetization ($1.0\mu_B$/U). However there is a possibility that this disagreement is due to the extinction effect or the multiple scattering. Therefore we have performed neutron experiment using smaller sample.

A single crystal of URu_2Si_2 was grown in a tetra-arc furnace using the Czochralski pulling method. It was cut into rectangular parallelepiped. The sample thickness is 0.5 mm. The polarized neutron experiment has been done using the three axis spectrometer PONTA (5G) installed in the research reactor JRR-3M, Tokai. The sample was set inside a superconducting magnet with the c-axis vertical to the ($hk0$) scattering plane. Polarized neutrons of wavelength λ = 1.01Å were produced by a Heusler alloy monochromator and a set of collimator OPEN-80'-80'-OPEN (2-axis mode) was used. Form factor measurements were performed in the paramagnetic state at T = 60 K in an applied magnetic field of 6 T along the c-axis. To correct the incomplete neutron polarization, the flipping efficiency was measured for all reflection points.

Figure 1 shows the magnetic amplitudes μf of URu_2Si_2 as a function of $\sin\theta/\lambda$. The observed magnetic amplitudes of the sample with thickness of 0.5 mm agree with those with thickness of 1.0 mm within statistical errors except for the strong Bragg reflection point (2,0,0). Therefore the extrapolated value at $\frac{\sin\theta}{\lambda} = 0$ is smaller than the bulk magnetization value even in the present study using the smaller sample. This result may suggest some contribution other than 5f electrons to the bulk magnetization of URu_2Si_2.

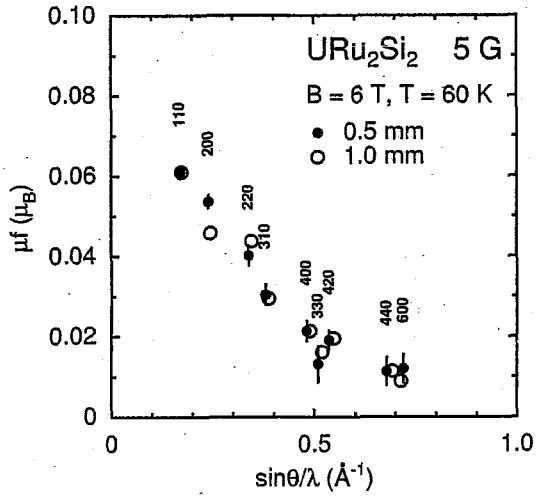

Fig. 1. The magnetic amplitudes μf of the sample with thickness of 0.5 mm (closed circles) and the sample with thickness of 1.0 mm (open circles) as a function of $\frac{\sin\theta}{\lambda}$ for URu_2Si_2 at T = 60 K and B = 6 T ($\parallel$ c-axis). Note that the bulk magnetization value is $1.0\mu_B$/U.

References

[1] K. Kuwahara*et al.*: ISSP Activity Report on Neutron Scattering Research, **10** (2003) 154.

使用施設：JRR-3M，装置： 5G(PONTA)，分野： 3. Strongly Correlated Electron Systems

研究テーマ： Zn 置換した $La_{2-x}Sr_xCuO_4$ 高温超伝導体における低エネルギー磁気励起・静的磁気相関とその磁場効果に関する研究

1-3-18 高温超伝導体 $La_{1.85}Sr_{0.15}CuO_4$ における低エネルギー磁気励起の磁性・非磁性不純物置換効果

Magnetic and non-magnetic impurity effects on the low-energy spin excitations in the high-T_c superconductor $La_{1.85}Sr_{0.15}CuO_4$

M. Kofu[1,2], H. Kimura[3], and K. Hirota[2]

[1] *Department of Physics, Tohoku University, Sendai 980-8578*

[2] *Institute for Solid State Physics, The University of Tokyo, 106-1 Shirakata, Tokai 319-1106*

[3] *Institute of Multidisciplinary Research for Advanced Materials, Tohoku University, Sendai 980-8577*

In high-T_c cuprates, it is well known that impurities substituting for the Cu sites suppress superconductivity. Non-magnetic impurity Zn decreases the superconducting transition temperature T_c more strongly than magnetic impurity Ni, unlike BCS superconductors. In previous neutron scattering studies, impurity-free $La_{1.85}Sr_{0.15}CuO_4$ shows a "spin gap" below $\omega = 4$ meV in the energy spectrum indicating antiferromagnetic(AF) incommensurate spin excitations [1]. Since the spin gap opens below T_c, the relation between the gap and the superconductivity has been discussed. Moreover, a recent work shows that Zn induces a novel spin state in the spin gap, which we call *in-gap* state, and that the state becomes more dominant and more static with increasing Zn-doping [2]. In this study, we focus on magnetic impurity Ni. We investigated Ni effects on the low-energy spin excitations and compared the results of Zn and Ni-doped samples.

Neutron scattering experiments were performed with the TOPAN spectrometer installed at 6G beam port. Detailed experimental conditions are denoted in Fig. 1. Single crystals of Zn and Ni doped $La_{1.85}Sr_{0.15}CuO_4$ were grown by a traveling solvent floating zone method. The onsets of T_c estimated from shielding signals are 29.2 K for $La_{1.85}Sr_{0.15}Cu_{0.992}Zn_{0.008}O_4$ and 31.6 K for $La_{1.85}Sr_{0.15}Cu_{0.991}Ni_{0.009}O_4$.

At the base temperature, for the Zn-doped sample, the spin excitations are induced at $\omega = 2$ meV or higher energy. While for the Ni-doped sample, no magnetic signals appear at $\omega = 3$ meV(Fig. 1). These results suggest that both Zn and Ni have a tendency to fill the spin gap, and that Ni has a weaker effect on the low spin excitations as compared with Zn. These results seem to correspond to the suppression of T_c. However, it is not clear whether the effects on the spin excitation for both the samples are same, in other words, whether Ni induce the in-gap state similar to Zn. To clarify this uncertainty, we will carry out studies for other concentration of Ni and perform experiments of high-energy spin excitation for Zn and Ni doped samples.

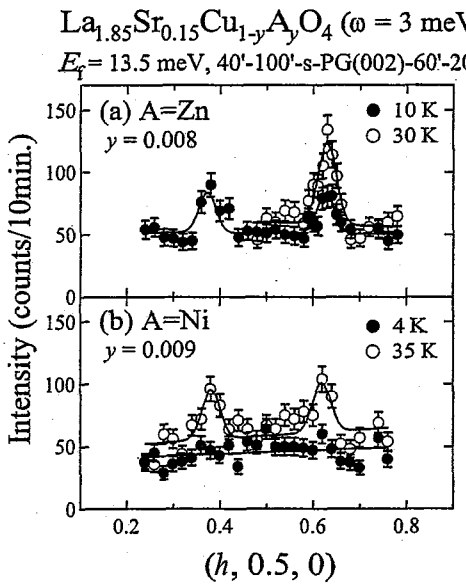

Fig. 1. q-profiles of spin excitation at $\omega = 3$ meV for (a) $La_{1.85}Sr_{0.15}Cu_{1-y}Zn_yO_4$ ($y = 0.008$) and (b) $La_{1.85}Sr_{0.15}Cu_{1-y}Ni_yO_4$ ($y = 0.009$). Filled and open circles correspond to the data below and above T_c, respectively.

References

[1] K. Yamada *et al.*: Phys. Rev. Lett. **75**, 1626 (1995).

[2] H. Kimura *et al.*: Phys. Rev. Lett. **91**, 067002 (2003).

使用施設：JRR-3M，装置： 6G (TOPAN)，分野： 3. Strongly Correlated Electron Systems (c)

研究テーマ： $YTiO_3$ の磁気構造解析による軌道のイメージング
表題： 強磁性 $YTiO_3$ の磁気形状因子の観測

1-3-19 Observation of a magnetic form factor of ferromagnetic $YTiO_3$

H. Kimura[1], S. Komiyama[1], K. Kadoshita[1], Y. Noda[1], S. Miyasaka[2], and Y. Tokura[2]
[1] *IMRAM, Tohoku University, Sendai 980-8577*
[2] *Fac. of Eng. and Tech., University of Tokyo, Tokyo 113-8656*

$YTiO_3$ shows a ferromagnetic order at $T_C \sim 35$ K. It has been believed that the ferromagnetic order originates from antiferro-orbital ordering, which occurs at much higher temperature than T_C. In fact, it is shown by a polarized neutron analisys that a magnetic form factor for Ti^{3+} spin ($S = 1/2$) well discribes the modeled antiferro-orbital order[1]. In the present study, we have performed a magnetic structure analysis of ferromagnetic $YTiO_3$ to obtain the precise magnetic form factor, by using unpolarized neutron diffraction.

The measurements were performed with FONDER installed at T2-2 beam port in JRR-3M guide-hall. The wavelength of neutron is 1.24 Å. Data collection of nuclear and magnetic Bragg reflections were carried out at 10 K and 45 K. The total number of nuclear and magnetic Bragg reflections are 114 points at each temperature.

Crystal structure analysis was performed at 45 K, which well describes a *Pbnm* structure with a reliability factor of 4 %. As seen in Fig. 1(a), (0 -2 0) intensity starts increasing around 32 K with decreasing temperature, showing that a ferromagnetic order appears at $T_C \sim 32$ K. A large error bar in Fig. 1(a) is due to a quite huge intensity of the nuclear reflection in contrast with a weak intensity of the magnetic reflection. This means that it is difficult to extract the purely magnetic contributions from the observed data. In fact, we could obtain very limited number of promising magnetic reflections. We subtracted the intensities at 45 K from those at 10 K and converted the results into the absolute magnetic structure factor using a scale factor obtained by the crystal structure analysis at 45 K. Thus the magnetic form factor for Ti^{3+} spin, $\mu<J_0>$, was experimentally obtained from the observed magnetic structure factor based on the $G_xA_yF_z$-type spin configuration[2]. Figure 1(b) shows the observed and calculated magnetic form factor as a function of $\sin\theta/\lambda$. The figure shows that the observed value (open circles) well reproduces the calculated one (solid line) but there are some small differences between them, indicating that the form factor might not be described by a simple $<J_0>$ term. The present results have shown that the neutron 4-circle diffractometer FONDER is useful for determining a precise magnetic form factor.

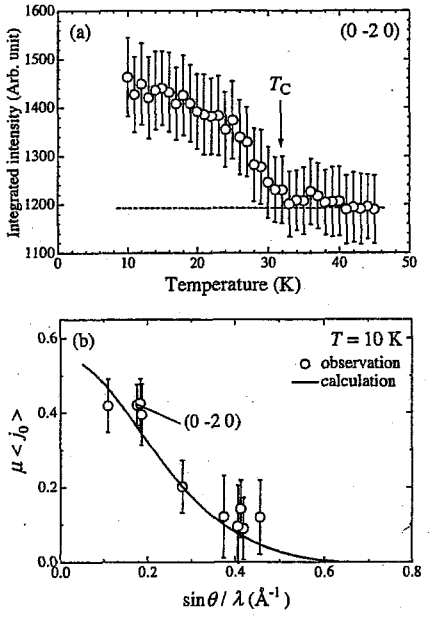

Fig. 1. (a); The integrated intensity of (0 -2 0) reflection as a function of temperature. (b); The magnetic form factor for Ti^{3+} ion as a function of $\sin\theta/\lambda$. Open circles and a solid line correspond to observed and calculated ($\mu = 0.55\ \mu_B$[2]) values, respectively.

References

[1] H. Ichikawa *et al.* : Physica B. 281&282 (2000) 482.
[2] C. Ulrich *et al.* : Phys. Rev. Lett. **89** (2002) 167202.

使用施設：JRR-3M, 装置： T2-2 (FONDER) , 分野： 3. Strongly Correlated Electron Systems

1-3-20

研究テーマ：重い電子系の量子臨界領域の磁気秩序の研究
表題：近藤格子化合物 $Ce(Ru_{0.9}Rh_{0.1})_2(Si_{1-y}Ge_y)_2$ における"遍歴"から"局在"への磁気秩序様式の変化

Alternation between the "itinerant" and "lolcalized" antiferromagnetic order in the Kondo-lattice compound $Ce(Ru_{0.9}Rh_{0.1})_2(Si_{1-y}Ge_y)_2$

S. Kawarazaki[1], Y. Tabata[1], Y. Okita[1], C. Kanadani[1] and Y. Uwatoko[2]
[1] *Graduate School of Science, Osaka University, Toyonaka, Osaka 560-0043*
[2] *Institute for Solid State Physics, The University of Tokyo, Kashiwa-shi, Chiba 277-8581*

In the Kondo-lattice systems, two types of magnetic order can be exist, that is, an itinerant and a localized magnetic orders. The former is a spontaneous magnetic polarization of the heavy quasi-particle band (quasi-particle band regime), whereas the latter is formed by the localized spin through the RKKY-interaction (RKKY-regime).

In the course of searching for an alternation of the scheme of the magnetic order, we have studied the magnetic properties of the pseudo-binary alloy system $Ce(Ru_{0.9}Rh_{0.1})_2(Si_{1-y}Ge_y)_2$. The base material $Ce(Ru_{0.9}Rh_{0.1})_2Si_2$ is known as an archetypal Kondo-lattice compound which shows a spin density wave (SDW) transition[3]. By substituting Ge for Si, one can effectively apply negative pressure to the SDW phase through the lattice expansion and the SDW phase is shifted to the antiferromagnetic order formed by the localized spins[1, 2]. The neutron scattering experiments were performed on the triple-axis spectrometer GPTAS at the JRR-3M reactor of Japan Atomic Energy Research Institute(JAERI).

Figure 1 (a) shows the pressure dependences of the amplitudes of the magnetic modulation, μ, at $T = 1.5$ K in the $Ce(Ru_{0.9}Rh_{0.1})_2(Si_{1-y}Ge_y)_2$ for $y = 0$, 0.13, 0.20 and 0.25 respectively. The μ is reduced as increasing the pressure due to the development of the cf-hybridization. The long-range magnetic orders for $y = 0$, 0.13 and 0.20 collapse around $P_c \simeq 0.5$, 1.2 and 1.3 GPa respectively. The μ for $y = 0.25$ is nearly unresponsive to P below 1.2 GPa.

The magnetic wave number, q in $\boldsymbol{Q} = (0\ 0\ q)$, is shown as a function of pressure for each Ge-concentration in Fig. 1 (b). The q hardly depends on the pressure in the $y = 0$ and 0.25 compounds, where $q \simeq 0.39$ and 0.35 respectively. On the other hand, the q shows strong pressure dependence in the intermediate Ge-concentration region, for $y =$

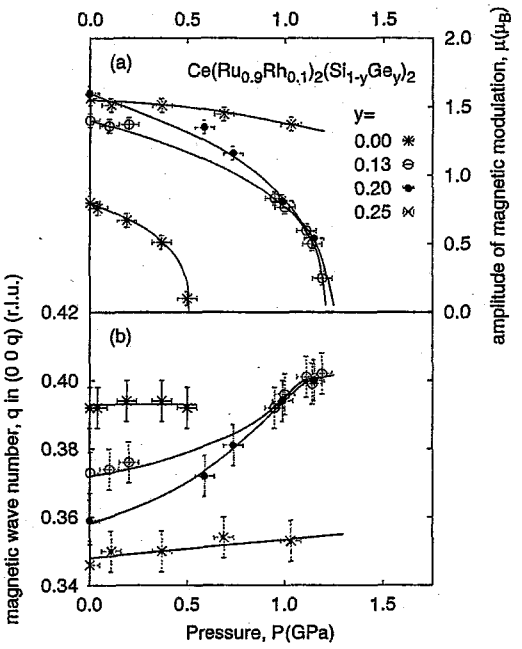

Fig. 1. (a) The amplitudes of the magnetic modulation μ and (b) the magnetic wave number q in $Ce(Ru_{0.9}Rh_{0.1})_2(Si_{1-y}Ge_y)_2$ for $y = 0$, 0.13, 0.20 and 0.25 as functions of the pressure. The solid lines in (a) and (b) are guides to eyes.

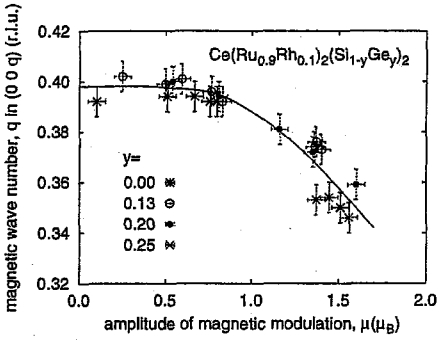

Fig. 2. The μ-dependence of the q for each Ge-concentration under hydrostatic pressure. The solid line is guide to eyes

使用施設：JRR-3M，装置：4G (GPTAS)，分野：3. Strongly Correlated Electron Systems

0.13 and 0.20, where the value of the q increases up to ~ 0.4 successively as increasing the pressure, and is saturated near P_c.

The weak P-dependence of the μ for $y = 0.25$ indicates that the nature of the f-electrons is strongly localized and the magnetic order is in the RKKY-regime, where the Fermi surfaces (FS) are constructed by the "bare" conduction electrons. On the other hand, in the $y = 0$ compound, the μ is reduced rapidly by applying pressure, which indicates the itinerant nature of the magnetic order. Thus, in this compound, the cf-coherence must have already grown up and the FS of the heavy quasi-particles have already constructed even at ambient pressure. The values of q for $y = 0$ or 0.25, which are nearly unresponsive to P, are determined by the respective FS's, i.e. the bare conduction electron FS (BCE-FS) or the heavy quasi-particles one (HQP-FS).

The continuous shift of the value of the q in the intermediate Ge-concentration region should correspond to the continuous change of the FS between the BCE- and the HQR-FS due to a pressure-induced evolution of the cf-coherence. In order to investigate the relation between the shifts of the value of the q and the evolution of the cf-coherence, we shows the μ-dependence of the q for each Ge-concentration under pressure in Fig. 2. In the high μ-region ($\mu > 1.0\mu_B$), the value of the q is changed successively as reflecting the growing up of the cf-coherence, whereas the saturation of the value of the q is clearly found for $\mu < 0.8\ \mu_B$, where is in the quasi-particle band regime and the evolution of the cf-coherence should be saturated.

References

[1] K. Watanabe, Y. Uwatoko, Y. Tabata, H. Kadowaki, C. Kanadani, T. Taniguchi, S. Kawarazaki, J. Phys. Soc. Jpn. 72 (2003) 1751.

[2] Y. Tabata, K. Watanabe, T. Taniguchi, C. Kanadani, S. Kawarazaki, Physica B 329-333 (2003) 508

[3] S. Kawarazaki, M. Sato, H. Kadowaki, Y. Yamamoto, Y. Miyako, J. Phys. Soc. Jpn. 66 (1997) 2473

研究テーマ：RMnO$_3$の軌道秩序と磁気秩序
表題：RMnO$_3$のスピン波励起

1-3-21 Magnon Excitations in RMnO$_3$

R. Kajimoto[1,*], H. Mochizuki[2], H. Yoshizawa[2], H. Shintani[3], T. Kimura[3,†], and Y. Tokura[3]
[1] *Neutron Science Laboratory, KEK, Tsukuba 305-0801, Japan*
[2] *Neutron Science Laboratory, ISSP, University of Tokyo, Tokai 319-1106, Japan*
[3] *Department of Applied Physics, University of Tokyo, Tokyo 113-8656, Japan*

Perovskite manganese oxides RMnO$_3$ show an interesting variation of the spin structure with decreasing the ionic radius of R: the layered (A-type) structure (R = La, Pr, Nd) → the incommensurate (IC) sinusoidal structure (R = Tb, etc.) → the up-up-down-down structure (R = Ho). This change of the magnetic structure was explained as a competition between spin interactions caused by the combination of the GdFeO$_3$-type distortion and the staggered-type ordering of e_g orbitals of Mn ions [1]. To reveal the origin of the variation of the spin structure in RMnO$_3$, we have performed a neutron scattering study on single crystals of PrMnO$_3$ and TbMnO$_3$, and measured magnetic excitations. Most of the measurements were performed at 4G (GPTAS) with E_f = 13.7 meV. Part of the measurements were carried out at C1-1 (HER) with E_f = 5 meV.

Upper panel of Fig. 1 shows the observed peak positions in the energy spectra at 10 K as a function of Q. Solid lines are fits to the Heisenberg model of magnons in an A-type antiferromagnet taking only nearest-neighbor couplings into account. The fit gives $8J_1S$ = 9.0(3) meV and $4J_1'S$ = −4.8(5) meV, where J_1 and J_1' are the nearest neighbor coupling of spins within the ab plane and that along the c axis, respectively. Lower panel of Fig. 1 shows contour plots of the excitation spectra in TbMnO$_3$ at 10 K. Dotted lines are a calculated magnon dispersion relation of an A-type antiferromagnet with $8J_1S$ = 2.5 meV, $4J_1'S$ = −4 meV, and J_2 = $-0.5J_1$ or 0, where J_2 is the next-nearest-neighbor coupling within the ab plane. The observed excitations are well described as magnons in the A-type antiferromagnet with finite J_2, except for a momentum region around the wave vector of the IC magnetic structure q_{IC} = (0, 0.28, 1). We further investigated the excitations around q_{IC} with better energy resolution at C1-1, and found that the excitations

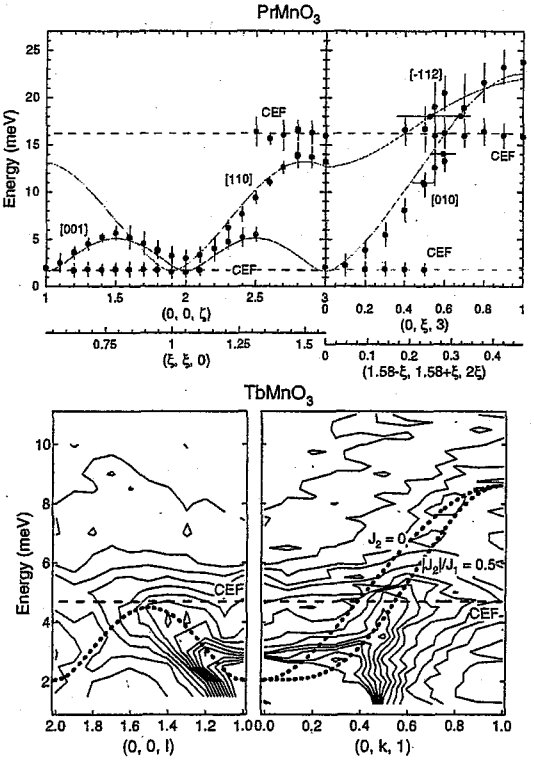

Fig. 1. (Upper panel) Magnon dispersion relation of PrMnO$_3$ at 10 K. Error bars indicate the half widths of the observed spectra. Solid lines are fits to the Heisenberg model for the A-type antiferromagnetic ordering taking only the nearest-neighbor coupling J_1 into account. "CEF" labels the excitations due to the crystalline electric field of Pr. (Lower panel) Contour plots of the excitation spectra in TbMnO$_3$ at 10 K. Dotted lines are the magnon dispersion relation of the A-type antiferromagnet. In the right part of the figure (Q = (0, k, 1)), each dotted line indicates the dispersion for J_2 = 0 and that for $J_2 = -\frac{1}{2}J_1$.

soften and split into two or three modes around q_{IC}.

In table 1 are summarized J's derived from the analyses. One can clearly see that the exchange interaction within the ab plane systematically decreases as the radius of R is reduced, while that along the c axis is independent of R. These observations are consistent to the model

使用施設：JRR-3M，装置：4G (GPTAS), C1-1 (HER)，分野：3. Strongly Correlated Electron Systems

based on the combination of the $GdFeO_3$-type distortion and the orbital ordering.

	large ← radius of R → small		
	$LaMnO_3$ [2]	$PrMnO_3$	$TMnO_3$
$8J_1S$ (meV)	13.36(18)	9.0(3)	~2.5
J_2			$\sim -0.5J_1$
$4J_1'S$ (meV)	−4.84(22)	−4.8(5)	~−4

Table 1. Summary of J's obtained by the A-type magnon model.

References

[*] Present address: Neutron Science Research Center, JAERI, Tokai 319-1195, Japan.

[†] Present address: Los Alamos National Laboratory, Los Alamos, New Mexico 87545, USA.

[1] T. Kimura, S. Ishihara, H. Shintani, T. Arima, K. T. Takahashi, K. Ishizaka, and Y. Tokura, Phys. Rev. B **68**, 060403(R) (2003).

[2] K. Hirota, N. Kaneko, A. Nishizawa, and Y. Endoh, J. Phys. Soc. Jpn. **65**, 3736 (1996).

研究テーマ：RMnO$_3$の軌道秩序と磁気秩序
表題：TbMnO$_3$の磁気構造

1-3-22 Magnetic Structure of TbMnO$_3$

R. Kajimoto[1,*], H. Yoshizawa[2], H. Shintani[3], T. Kimura[3,†], and Y. Tokura[3]
[1] *Neutron Science Laboratory, KEK, Tsukuba 305-0801, Japan*
[2] *Neutron Science Laboratory, ISSP, University of Tokyo, Tokai 319-1106, Japan*
[3] *Department of Applied Physics, University of Tokyo, Tokyo 113-8656, Japan*

TbMnO$_3$ shows an incommensurate sinusoidal spin ordering with $q_{Mn} \sim 0.295b^*$ below $T_N \sim 41$ K with spins oriented along the [010] direction. q_{Mn} decreases as temperature is lowered, then locked at $q_{Mn} = 0.28b^*$ below $T_{lock} \sim 30$ K [1, 2]. Very recently, it was found that the spontaneous electric polarization P parallel to the c axis appears below T_{lock}. Moreover, the magnitude or the direction of P can be drastically changed by applying a magnetic field [3]. The magnetic control of the ferroelectric polarization will provide an attractive possibility of new magnetoelectric devices. These recent discoveries in TbMnO$_3$ motivated us to reinvestigate the magnetic properties of this material. Here, we report the result of a neutron diffraction study on the elastic properties of the magnetic ordering in TbMnO$_3$. The measurement was performed at 4G-GPTAS with $k_i = 2.57$ Å.

Figure 1 shows neutron scattering profiles along the $(0, k, 0)$ and $(0, k, 1)$ lines at 4 K, 10 K, and 55 K. At 4 K, surprisingly many superlattice reflections due to the magnetic moments of both Mn and Tb ions are observed at every position with $k \approx n/7$ (n = integers), while only the Mn peaks are observed at 10 K. The magnetic reflections due to the Mn ordering were observed at $(h, k \pm q_{Mn}, l)$ with $q_{Mn} = 0.28$, where solid vertical lines are drawn in Fig. 1. The observed Mn peaks can be classified into four groups depending on the values of h, k, and l as A-type ($h + k$ = even and l = odd), G-type ($h + k$ = odd and l = odd), C-type ($h + k$ = odd and l = even), and F-type ($h + k$ = even and l = even). Though the strong A-type reflections and weak G-type reflections are already observed by the previous studies [1, 2], the C-type and F-type reflections are firstly observed in the present study. A preliminary analysis of the magnetic structure shows that the intensities of the A-type peaks are consistent with the sinusoidal model with spins parallel to the b axis as reported by Quezel *et al* [1]. Analysis of the G-type peaks gave the similar result. For the C-type and F-type peaks, however, we failed to satisfactorily reproduce the observed intensities, though the existence of the peaks on the $(0, k, 0)$ line indicates the spin arrangements have substantial x or z components.

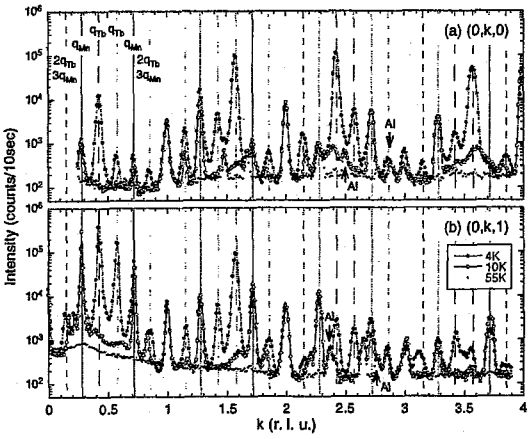

Fig. 1. Neutron diffraction profiles along (a) the $(0, k, 0)$ line and (b) the $(0, k, 1)$ line at 4, 10, and 55 K. Vertical lines indicate the positions of the Mn ($k \approx$ integer ± 2/7 and 6/7) and Tb ($k \approx$ integer ± 3/7 and 6/7) superlattice peaks. "Al" denotes diffractions from the aluminum sample cell.

Figures 2(a)-(d) show temperature dependences of the scattering intensities of the Mn magnetic peak. All the intensities start to increase at $T_N^{Mn} = 46$ K. There are two distinct anomalies in the temperature profiles below T_N^{Mn}: with decreasing temperature, the slopes show upturns at $T_{lock} = 28$ K, and then a drastic drop of the A-type peak (a) or increases of the others (b)-(d) below $T_N^{Tb} = 7$ K. The former temperature coincides with the temperature where the wave vector of the Mn ordering locks at its low temperature value. The latter anomaly is concomitant with the ordering of the Tb moments. All the weak (G, C, and F) components show a similar temperature depen-

使用施設：JRR-3M，装置：4G (GPTAS)，分野：3. Strongly Correlated Electron Systems

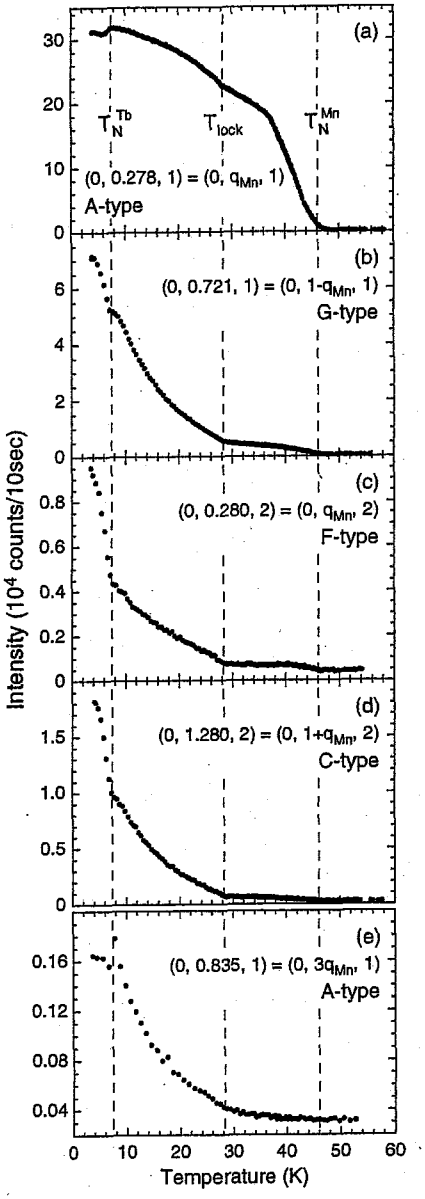

Fig. 2. (a)-(d) Temperature dependences of the intensities of the Mn superlattice peaks of (a) *A*-type, (b) *G*-type, (c) *F*-type, and (d) *C*-type. (e) Temperature dependence of the intensity of the Mn third harmonics at (0, 0.835, 1) = (0, $3q_{Mn}$, 1).

dence, and they gradually develop below T_N^{Mn}. Their temperature dependence is quite different from the sharp increase of the *A*-type component, suggesting that the weak components arise from some secondary effect. One of probable causes is the development of the ordering of the Tb moments, which is manifested by the steep increase of these components in compensation for the *A*-type component on the (quasi) long-range ordering of the Tb moments (Fig. 2). In addition to the fundamental ($1q_{Mn}$) peaks described above, we also observed the third harmonics ($3q_{Mn}$) of each type of the Mn ordering at $(h, k \pm 3q_{Mn}, l)$ (dashed lines in Fig. 1). (Though we could not detect the third harmonics for the *F*-type ordering, it may be because of the weakness of the fundamental ($1q_{Mn}$) *F*-type peaks.) The existence of the higher harmonics of the Mn ordering means that the spin ordering is not an ideal sinusoidal wave. The ratio of the intensity of the $3q_{Mn}$ peak to that of the $1q_{Mn}$ peak is $\sim 10^{-2}$. This value is much smaller than that for an ideal square wave (1/9), indicating the deviation of the spin arrangement from the sinusoidal wave is quite small. In Fig. 2(e) is shown the temperature dependence of the intensity of the $3q_{Mn}$ peak of the *A*-type ordering. It gradually develops below T_{lock}, indicating that the sinusoidal ordering pattern of the Mn moments becomes distorted at $T < T_{lock}$.

References

[*] Present address: Neutron Science Research Center, JAERI, Tokai 319-1195, Japan.

[†] Present address: Los Alamos National Laboratory, Los Alamos, New Mexico 87545, USA.

[1] S. Quezel, F. Tcheou, J. Rossat-Mignod, G. Quezel, and E. Roudaut, Physica B **86-88**, 916 (1977).

[2] J. Blasco, C. Ritter, J. García, J. M. de Teresa, J. Pérez-Cacho, and M. R. Ibarra, Phys. Rev. B **62**, 5609 (2000).

[3] T. Kimura, T. Goto, H. Shintani, K. Ishizaka, T. Arima, and Y. Tokura, Nature (London) **426**, 55 (2003).

研究テーマ：四重極秩序を示す重い電子系 $PrFe_4P_{12}$ における磁気状態

1-3-23 $PrFe_4P_{12}$ の反強四重極相における秩序変数と磁気励起

Order Parameters and Magnetic Excitation in the AFQ Ordered Phase of $PrFe_4P_{12}$

K. Iwasa[1], L. Hao[1], K. Kuwahara[2], M. Kohgi[2], H. Sugawara[3],
Y. Aoki[2], H. Sato[2], T. D. Matsuda[4], J. -M. Mignot[5], A. Gukasov[5], and M. Nishi[6]

[1] *Dept. of Physics, Tohoku University, Sendai 980-8578, Japan*
[2] *Dept. of Physics, Tokyo Metropolitan University, Hachioji, Tokyo 192-0397, Japan*
[3] *Dept. of Mathematical and Natural Sciences, Tokushima University, Tokushima 770-8502, Japan*
[4] *A. S. R. C., Japan Atomic Energy Research Institute, Tokai 319-119, Japan*
[5] *Laboratoire Léon Brillouin, CEA-CRNS, 91191 Gif sur Yvette Cedex, France*
[6] *Institute for Solid State Physics, University of Tokyo, Kashiwa 277-8581, Japan*

We performed a polarized neutron diffraction measurement at the spectrometer 5G (PONTA), in order to determine the order parameters in antiferro-quadrupolar (AFQ) ordered phase of $PrFe_4P_{12}$ [1]. Figure 1 shows the results of $|F_N+F_M|^2$ and $|F_N-F_M|^2$ at several superlattice points at 1.6 K and 3.6 T measured by switching the spin directions of incident neutrons applied along the cubic [0, 0, 1] axis. $|F_N|$ and $|F_M|$ represent a nuclear structure factor and a magnetic one, respectively. The different values of $|F_N+F_M|^2$ and $|F_N-F_M|^2$ at each points means interference of scattering amplitudes from the Fe-ion displacement in the atomic superlattice as observed in the X-ray diffraction experiment [2] and the magnetic-field-induced antiferromagnetic component. The observed pattern can be explained by the model based on the Fe displacement obeying the four-fold rotational symmentry around the [0,0,1] axis and the antiferromagnetic component along the magnetic field applied to the [0,0,1] axis. This fact indicates that the dominant order parameter of 4f-electron quadrupole is $O_2^0=(3J_z^2-J(J+1))/2$ at this condition.

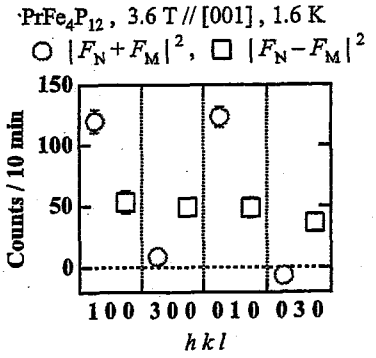

Fig. 1. Neutron spin-flipping measurements of $|F_N \pm F_M|^2$ at various reflections.

By inelastic neutron scattering experiment for a single-crystal sample performed at C1-1 (HER) as well as at 4F2 in Laboratoire Léon Brillouin, France, we observed magnetic response in the AFQ ordered phase. Figure 2 shows the spectra at (0, 2, 0) and (0, 1, 0) at 3.5 K, and sharp magnetic excitation is seen at 1.4 meV.] It is noticeable that the maximum intensity appears at the Brillouin zone center and the minimum at the zone boundary, indicating the ferromagnetic fluctuation consistent with the positive Weiss temperature of magnetic susceptibility. Such characteristic collective excitation is expected to be associated with the low-lying AFQ ordering.

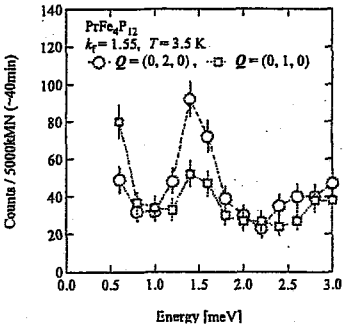

Fig. 2. Inelastic spectra at 3.5 K.

References

[1] L. Hao *et al.*: Acta Physica Polonica B **34** (2003) 1113.
[2] K. Iwasa *et al.*: Physica B **312-313** (2002) 834.

使用施設：JRR-3M, 装置：5G(PONTA), C1-1(HER) 分野：3. Strongly Correlated Electron Systems

研究テーマ:$LaCoO_3$ 中の中間スピン状態と結合した格子変形とスピン転移の動的性質のフォノン散乱による研究
表題:$LaCoO_3$ 中の 100K スピン転移に伴うフォノン異常

1-3-24 Phonon Anomaly associated with the 100 K Spin-state Transition in $LaCoO_3$

K. Asai, M. Suzuki, Y. Kobayashi, T. S. Naing, K. Yamada*[1], M. Akimitsu*[2], J. Akimitsu*[3], P. Manuel*[4], J. M. Tranquada*[5], and G. Shirane*[5]

*Dept. Appl. Phys. and Chem., The University of Electro-communications, Tokyo 182-8585, Japan; *[1]IM R, Tohoku University, Sendai, 980-8577, Japan; *[2]Shibaura Institute of Technology, Saitama 330-8570, Japan; *[3]College of Science & Engineering, Aoyama Gakuin University, Sagamihara 229-8551, Japan; *[4]ISIS, RAL, Didcot OX110QX, UK; *[5]BNL, New York 11973 USA*

The magnetic anomaly of $LaCoO_3$ around 100 K has been ascribed to a broad spin-state transition from the nonmagnetic low spin (LS) to an intermediate spin state (IS; S=1) [1]. However, the nature of the "Jahn-Teller active" IS state, especially its orbitals, has not been clarified. The purpose of the present neutron experiment is to find evidence for any orbital order or fluctuation by investigating phonons of $LaCoO_3$.

The neutron scattering experiment was performed with TOPAN at JRR-3M in JAERI (Tokai) on (h,k,k) plane of the pseudo-cubic reciprocal space for crystals consisting of four rhombohedral twins.

Figure 1 shows the energy spectra at the R-point (2.5,1.5,1.5) at selected temperatures. We found two phonon peaks at about 13 and 22 meV at 8 K. The phonon energies decrease remarkably with increasing temperature, down to about 10 and 20 meV at 200 K. From a symmetry consideration, the observed phonons are revealed to be identical with those found in the Raman spectroscopy by Sugai et al [2]. The temperature dependence in both studies is consistent.

The lowering of the phonon energies associated with population of the IS state suggests that these phonons couple with some motion of the IS-Co^{3+} orbitals which has the same symmetry with the phonons. Recently, a static orbital order of the IS-Co^{3+} was proposed by an x-ray diffraction study [3]. If the order, or its fluctuation, takes place, the phonon energy at the R-point will decrease as observed. Further study to elucidate the q-region of the softening around the R-point is in progress.

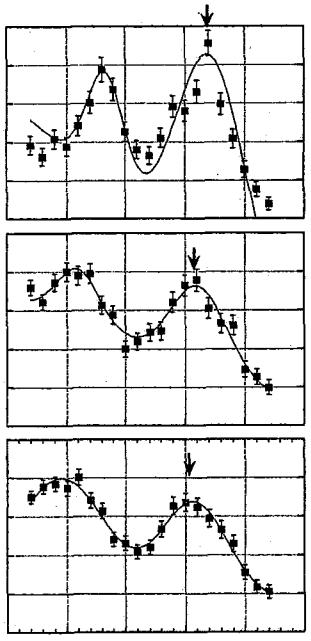

Figure 1: Energy spectra at (2.5,1.5,1.5) after correcting the Bose factor. The arrows and lines are guides for eyes.

References
[1] For example, K. Asai et al., J. Phys. Soc. Jpn. **67** (1989) 290.
[2] S. Sugai et al., TMS News Letters. **5** (2004) 89.
[3] G. Maris et al., Phys. Rev. B **67** (2003) 224423.

使用施設:JRR-3M, 装置:TOPAN(6G), 分野:強相関電子系

研究テーマ：$La_{2-y-x}Nd_ySr_xCuO_4$の磁気励起スペクトルと"stripe"
表題：$La_{1.6-x}Nd_{0.4}Sr_xCuO_4$の磁気励起スペクトル

1-3-25 Studies on the Magnetic Excitation Spectra of $La_{1.6-x}Nd_{0.4}Sr_xCuO_4$

S. Iikubo[1], M. Ito[1], Y. Yasui[1], M. Soda[1], M. Sato[1], K. Kakurai[2] and M. Nishi[3]

[1]*Department of Physics, Nagoya University, Furo-cho, Chikusa-ku, Nagoya 464-8602*
[2]*Advanced Science Research Center, JAERI, Tokai, Ibaraki 319-1199*
[3]*Institute for Solid State Physics, The University of Tokyo, 106-1 Shirakata, Tokai, 319-1106*

In order to investigate the relationship between the superconductivity and the "stripe" order (or the "stripe" fluctuations), magnetic excitation spectra of $La_{1.6-x}Nd_{0.4}Sr_xCuO_4$ have been measured by neutron inelastic scattering on a sample of aligned crystals with x~1/8, which exhibit "stripe" order at low temperature.

Special attention has been paid to what effects of "stripes" can be found in the behavior of the spectra $\chi''(\boldsymbol{q}, \omega)$, where $\boldsymbol{q}$ and ω are the wave vector and the energy of the magnetic excitations.

In the studies on $YBa_2Cu_3O_y$(YBCO), we have reported that characteristics of $\boldsymbol{q}$-, ω- and T- dependences of $\chi''(\boldsymbol{q},\omega)$ found in our experiments can be well reproduced by model calculations which do not consider effects of "stripes" fluctuations. The result indicates that the fluctuations of "stripes" (so-called dynamical "stripes") may not exist, or may not, at least, play an important role in realizing the high-T_c superconductivity [1, 2], even if they exist. In the calculations of the generalized susceptibility $\chi(\boldsymbol{q},\omega)$, the expression $\chi(\boldsymbol{q},\omega)=\chi^0(\boldsymbol{q},\omega)/\{1+J(\boldsymbol{q})\,\chi^0(\boldsymbol{q},\omega)\}$has been used, where $\chi^0(\boldsymbol{q},\omega)$ is the susceptibility of the effective band without the exchange coupling $J(\boldsymbol{q})$ among Cu-Cu electrons. We note here that consideration of the experimentally observed large energy broadening Γ of the quasi particles, is very important in the analyses.

For a sample of $La_{1.6-x}Nd_{0.4}Sr_xCuO_4$ with x=0.12, following effects of the ordered "stripes" or dynamical "stripes" on $\chi''(\boldsymbol{q},\omega)$ have been found[3]: The fluctuating "stripes" reduce the Γ value. It has been also found that $\chi''(\boldsymbol{q},\omega)$ observed in this system can not be reproduced by the above expression. In this report, we show differences of the behaviors of $\chi''(\boldsymbol{q},\omega)$ between the samples with x=0.12 and 0.18. The data of $\chi''(\boldsymbol{q}, \omega)$ was taken with the triple axis spectrometer ISSP-PONTA installed at JRR-3M of JAERI in Tokai.

For x=0.12, the "stripe" ordering occurs at T_e~69 K. The structural transition to the low temperature tetragonal (LTT) phase and the magnetic ordering also occur at around T_e with decreasing T.[3] For x=0.18, the structural transition and the magnetic ordering occur at ~80K and T_m~20K, respectively. We have not found the superlattice peaks which correspond to the charge ordering.

The magnetic excitation spectra observed for x=0.12, have incommensurate(IC) peaks at $\boldsymbol{Q}$=(0.5,

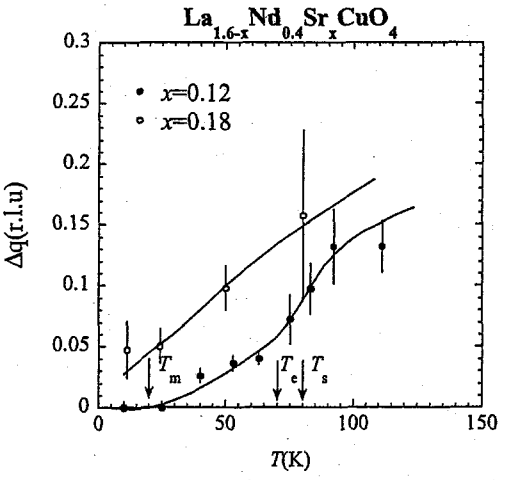

Fig. 1: Temperature dependence of the peak width $\Delta\boldsymbol{q}$ (FWHM) of the magnetic excitation spectra for ω=2.5meV. Filled and open circles represent the data for x=0.12 and 0.18, respectively.

使用施設：JRR-3M，装置：PONTA(5G)，分野：3. Strongly Correlated Electron Systems

0.5±δ) in the whole ω region (up to 12 meV) at temperatures between 10 K<T<142 K. For x=0.18, Data of $\chi''(q,\omega)$ have been collected at temperatures between 11 K<T<200 K with the fixed transfer energies of 2.5, 3, 6, 8 and 10 meV. The peak widths for x=0.18 are much broader than those of the peaks observed at the corresponding energies for x=0.12. Figure 1 shows the T-dependence of the intrinsic widths Δq of the IC peaks deduced at ω=2.5 meV by deconvoluting the resolution function. For x=0.12, the values of Δq decrease down to the very small value with decreasing T through T_e. The decrease of Δq with decreasing T even above T_e simply indicates that the growth of the "stripe" correlation makes the peak width narrower. For x=0.18, the values of Δq are larger than the value for x=0.12 in the whole temperature region, which indicates that the "stripe" fluctuations are weaker for x=0.18 than for x=0.12.

The data of $La_{1.6-x}Nd_{0.4}Sr_xCuO_4$ have been analyzed similarly to the case of YBCO. For this system, the ratios, t_0:t_1:t_2 of the effective band parameters 1:-1/6:-1/15 are used. (For these ratios, the sharpest IC peaks are obtained within the restriction that the parameters can reproduce the shape of the Fermi surface.) We have found that for x=0.12, the observed IC peaks are too sharp to be reproduced by the calculation, even when we use a Γ value as small as 2 meV. Figure 2 shows the observed profiles at 65 K (>T_m) for the sample with x=0.18 . The broad peak structure at all the ω values can be well reproduced by using a common scale factor and Γ~20 meV.

We have also analyzed $\chi''(q,\omega)$ of $La_{2-x}Sr_xCuO_4$ and shown that the existence of the large dip of the Γ–x curve at x~1/8.[4]The result indicates that the effect of the dynamical "stripes" can be clearly seen in $La_{2-x}Sr_xCuO_4$ at around x=1/8, too. On the other hand, in YBCO, the Γ–x curve does not have such a dip structure.

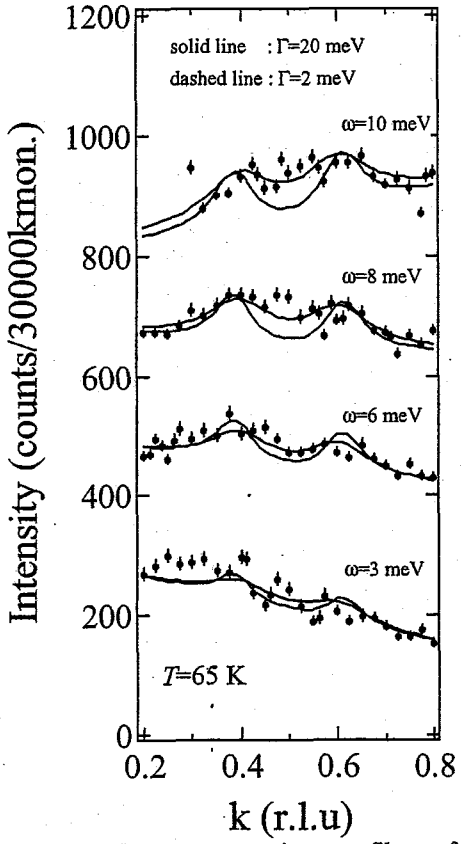

Fig. 2 Neutron scattering profiles of the magnetic excitations taken at T=65 K are shown at various energies, for a single crystal of $La_{1.42}Nd_{0.4}Sr_{0.18}CuO_4$. Lines represent the results of the profile fittings carried out by using the model shown in the text.

References

[1] M. Sato, M. Ito, H. Harashina, M. Kanada, Y. Yasui, A. Kobayashi and K. Kakurai : J. Phys, Soc. Jpn **70** (2001) 1342.

[2] M. Ito, H. Harashina, Y. Yasui, M. Kanada, S. Iikubo, M. Sato, A. Kobayashi and K. Kakurai : J. Phys, Soc. Jpn **71** (2002) 265.

[3] M.Ito, Y. Yasui, S. Iikubo, M. Soda, M. Sato, A. Kobayashi, K. Kakurai: J. Phys. Soc. Jpn.72 (2003) 1627.

[4] M. Ito, Y. Yasui, S. Iikubo, M. Soda, A. Kobayashi, M. Sato, K. Kakurai, C-H Lee and K. Yamada : J. Phys, Soc. Jpn **72** (2004) 991

研究テーマ： $R(=\mathrm{Y, La})\mathrm{VO_3}$ の軌道秩序の観測

1-3-26 YVO_3 の軌道秩序の研究

Observation of Orbital Ordering in YVO_3 by Polarized Neutron Diffraction Method

H. Ichikawa[1], M. Togasaki[1], Y. Kousaka[1], S. Soma[1], J. Akimitsu[1], T. Matsumura[2], K. Iwasa[2]
[1] Department of Physics, Aoyama-Gauin Univ., 5-10-1 Fuchinobe, Sagamihara, 229-8558
[2] Department of Physics, Tohoku Univ., Aoba, Aramaki, Aoba-ku ,Sendai 980-8578

$R\mathrm{VO_3}$ (R:Y and rare earth elements) are prototypical Mott-Hubbard type insulators with the V electron configurations of $3d^2$. It is suggested that the C-type antiferromagnetic (AF) state and G-type orbital ordering (OO) are stabilized when the ionic radius of R site is large, and G-type AF and C-type OO are stabilized when it is small. YVO_3 is located near the phase boundary, so it has several phase transitions. It is considered that (C-type+ G-type) AF and G-type OO are realized in the intermediate temperature phase ($T_{N2} = 77\ \mathrm{K} < T < T_{N1} = 116\ \mathrm{K}$) and G-type AF and C-type OO are realized in the low temperature phase ($T < T_{N2}$)[1, 2].

In this study, we carried out the polarized neutron diffraction measurement to observe the magnetic form factors of V^{3+} in YVO_3 at low temperature phase. The neutron diffraction measurement was performed using the Tohoku University spectrometer TOPAN in the JRR-3M reactor at Tokai. Heusler alloy was used as a polarizer and energy of the incident neutrons was set at 80 meV (λ = 1.011 Å). The magnetic form factor on each V^{3+} site i is defined as f_i, the magnetic form factor f observed in ($h\ k\ 0$) plane can express $f = (f_1 - f_3) \pm (f_2 - f_4)$. If the simple d_{yz}/d_{zx} C-type OO which is generally suggested is realized, f_i becomes $f_1 = f_3$ and $f_2 = f_4$, so magnetic form factor f must be 0. However, we observed non zero value magnetic form factors (Fig. 1).

To reproduce the observed magnetic form factors, we have made some model calculations and the best fitted model is shown in Fig. 2. We concluded that our observed magnetic form factors come from the coplex terms of orbitals which make the orbital magnetic moments and the OO pattern is not simple d_{yz}/d_{zx} C-type one. However, our calculation does not converge perfectly now and we will make more precious analysis.

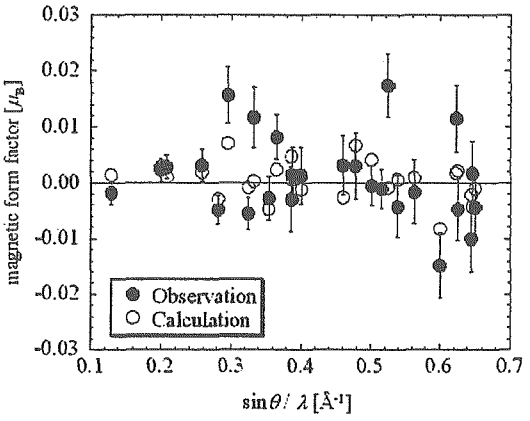

Fig. 1. Observed(closed circle) and calculated(open circle) magnetic form factors of YVO_3.

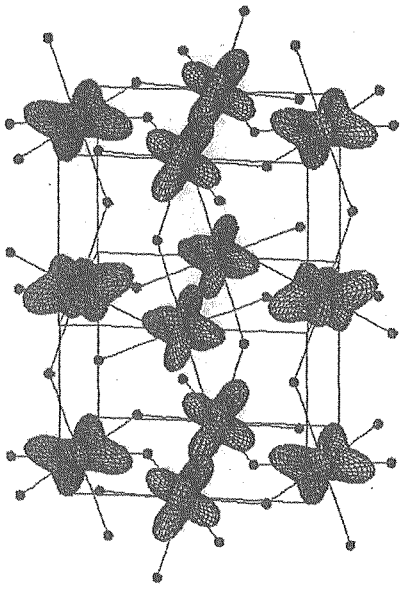

Fig. 2. A schematic view of the orbital ordering in YVO_3.

References

[1] G. R. Blake et al.: Phys. Rev. B 65 (2002)174112.
[2] C. Ulrich et al.: Phys. Rev. Lett 91 (2003)257202.

使用施設：JRR-3M, 装置： 6G (TOPAN) , 分野： 3. Strongly Correlated Electron Systems

研究テーマ： Fe_3O_4 の軌道秩序の観測

1-3-27 $Ca_{1.8}Sr_{0.2}RuO_4$ の軌道秩序の研究

Observation of Orbital Ordering in $Ca_{1.8}Sr_{0.2}RuO_4$ by the Polarized Neutron Diffraction Measurements

H. Ichikawa[1], S. Soma[1], Y. Kousaka[1], J. Akimitsu[1], S. Nakatsuji[2], Y. Maeno[2], T. Matsumura[3], K. Iwasa[3]

[1] Department of Physics, Aoyama-Gauin Univ., 5-10-1 Fuchinobe, Sagamihara, 229-8558
[1] Department of Physics, Kyoto Univ., Oibuncho, Kita-shirakawa, Sakyo, Kyoto, 606-8502
[2] Department of Physics, Tohoku Univ., Aoba, Aramaki, Aoba-ku ,Sendai 980-8578

The charge, spin and orbital degrees of freedom have been attracted much attention since they produce a wide variety of phenomena in strongly correlated electron systems. Although the charge and spin ordered states can be easily observed by the electron, x-ray and neutron diffraction techniques, it has been believed that the orbital ordered state itself is difficult to observe. In 1976, however, Akimitsu and Ito succeeded in directly observing the orbital ordered state by using the polarized neutron diffraction.

In this study, we focused on the quasi-two dimensional $Ca_{2-x}Sr_xRuO_4$, providing a complex phase diagram which involves the Mott insulator ($0 < x < 0.2$) and the superconductivity ($x = 2.0$). The competition between the d_{xy} orbital which leads to the Stoner ferromagnetism and d_{yz}/d_{zx} orbital leading to the localized antiferromagnetism causes much variable phenomena. In particular, the metamagnetic transition by applying the magnetic field introduces the drastic change of the orbital ordered state in $Ca_{1.8}Sr_{0.2}RuO_4$[1].

We performed the polarized neutron diffraction measurements to observe the new orbital ordered states under the magnetic field of 6 T in $Ca_{1.8}Sr_{0.2}RuO_4$ using the Tohoku University spectrometer TOPAN in the JRR-3M reactor at Tokai. Heusler alloy was used as a polarizer and energy of the incident neutrons was set at 32.4 meV (λ = 1.59 Å). We succeeded in observing the d_{xy}-like orbital which lies in RuO_2 layer by Fourier transforming the observed magnetic form factors (Fig. 1).

However, we confirmed recently the large reduction of the observed intensity caused by the secoundary extinction effect in this material and we should reexamine the magnetic form factors by correcting the extinction effects.

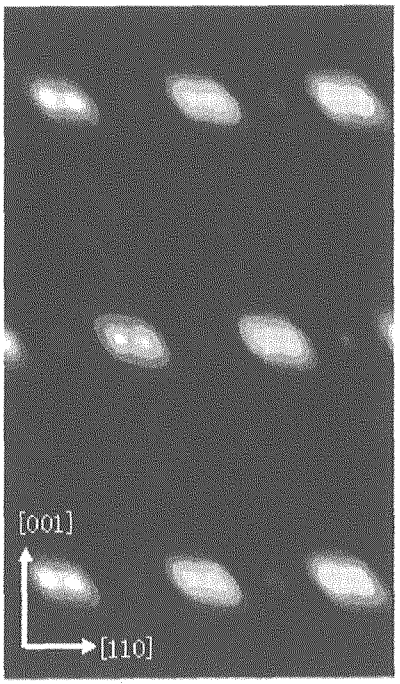

Fig. 1. The observed spin density map in $Ca_{1.8}Sr_{0.2}RuO_4$.

References

[1] S. Nakatsuji et al.: Phys. Rev. Lett. 90 (2003)137202.

使用施設：JRR-3M，装置： 6G (TOPAN)，分野： 3. Strongly Correlated Electron Systems

1. 中性子散乱 4)非晶質・液体

1. Neutron Scattering 4) Amorphous・Liquid

This is a blank page.

研究テーマ：超イオン導電体中の原子熱振動
表　題：超イオン導電体ガラス $(AgI)_{0.8}$-$(Ag_2MoO_4)_{0.2}$ の原子熱振動
1-4-1

Themal Vibration of Superionic Conducting Glass $(AgI)_{0.8}$-$(Ag_2MoO_4)_{0.2}$

D. Hosaka, A. Thazin, T. Shimoyama, T. Sakuma, H. Takahashi[1], M. Arai[2] and Y. Ishii[2]

Faculty of Science, Ibaraki University, Mito, Ibaraki 310-8512
[1]*Faculty of Engineering, Ibaraki University, Hitachi, Ibaraki 316-8511*
[2]*Advanced Science Research Center, JAERI, Tokai, Ibaraki 319-1195*

AgI-Ag_2MoO_4 is a good model system to understand the relationship among structure and transport properties in disordered materials. The glasses with composition AgI-Ag_2MoO_4 belong to fast ion conducting (FIC) glasses which can be used as electrolytes in solid state electrochemical devices[1].

It was observed that the structure features of AgI-doped glasses are as follows; (1) the glass network structure is unaffected by the addition of AgI; (2) the neutron structure, $S(Q)$, exhibits a prepeak at low $Q \sim 0.6$ - 0.9 Å^{-1} and (3) a strong Ag-I correlation is observed in the radial distribution function around 2.8 Å. At previous work, we utilized X-ray diffraction for studying of thermal vibration of AgI doped glasses and present work we employed neutron scattering in order to perform the structural analysis of $(AgI)_{0.8}$-$(Ag_2MoO_4)_{0.2}$ glass.

AgI and Ag_2MoO_4 were mixed and melted in a pyrex bottle at 600 ℃. The sample was poured on a stainless-steel block and pressed by another block.

The neutron scattering experiments were performed at TAS-1 in JRR-3M reactor of JAERI. The measured Q-range is from 0.9 Å^{-1} to 10.5 Å^{-1} which corresponds to the scattering angle from 5° to 120° with the neutron wavelength of 1.0 Å. For low temperature experiments aluminium cans are used with heat exchange gas and the GM-type cryostat was used in this work. The measurements were performed at 10, 150 and 300 K and the intensity data were obtained with every 0.05 Å^{-1}.

The data were corrected for absorption, multiple scattering, container and background effects using Placzek correction method resulting in the total differential cross section. After the incoherent scattering intensity was subtracted from the corrected intensity, the coherent intensity which is related to the structure was obtained. The coherent intensity was normalized at large-Q range, then the structure $S(Q)$ was derived as shown in Fig.1.

The absolute value of $S(Q) - 1$ for these glasses increases slightly with the increase of temperature. The differences of the structure factors $S_{10K}(Q) - S_T(Q)$ were obtained from the observation values of these glasses at 150 and 290 K. There can be noticed that the deviations of the differences from zero increase as the temperature increases. The maximums of the differences appear at Q=2.05, 3.16, 5.12, 7.11 Å^{-1} and the minimums are at Q= 2.58, 3.9, 6.02, 8.03 Å^{-1} in this glass. The positions of Q of the maximums and minimums almost correspond to those in Fig.1 at 10, 150 and 290 K.

The results of analysis, it was obtained that Debye-Waller temperature parameter B increases with the increase of temperature. The values of $B_T - B_{10K}$ are 0.5 and 0.9 Å^2 at T=150 and 290 K, respectively. This tendency of the temperature dependence is similar to that of the crystalline superionic conductors nAgI-$3Ag_2O$-$2V_2O_5$ and AgI-$AgPO_3$[2]. The relation between the Debye-Waller temperature parameter B and the mean-square displacement of atoms $\langle u^2 \rangle$ is shown as the equation $B=8\pi^2\langle u^2 \rangle$. The calculated values of the effective mean-square displacement $\langle u^2 \rangle_T - \langle u^2 \rangle_{10K}$ are 0.019 and 0.0342 Å^2 at T=150 and 290 K respectively. It was found that the value of Debye-Waller temperature parameter and mean square displacement of these glasses increase with the temperature.

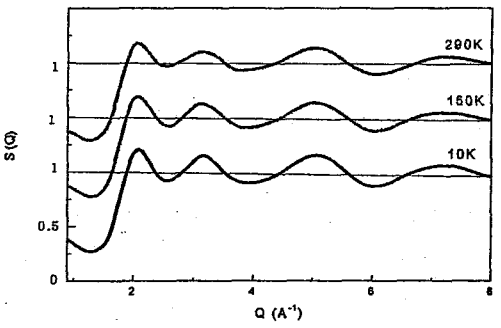

Figure 1: Structure factor $S(Q)$ of $(AgI)_{0.8}$-$(Ag_2MoO_4)_{0.2}$ glasses at 10, 150 and 290 K.

References

1) T. Minami and M. Tanaka : *J. Solid. State. Chem.* **32** (1980) 289.
2) A. Thazin, M. Arai, T. Sakuma and H. Takahashi : *Solid State Ionics* **150** (2002) 291.

原子炉：JRR-3　　装置：TAS-1(2G)　　分野：中性子散乱（液体・不規則物質）

研究テーマ：対イオン結合法による新しい高分子ミセルの創製と構造解析
1-4-2 中性子小角散乱法による DMF-NMF 二成分溶液の混合状態の研究

Mixing State of DMF-NMF Binary Solutions Studied by Small-Angle Neutron Scattering

T. Takamuku,[a] T. Kumai,[a] K. Fujii,[b] Y. Umebayashi,[b] and S. Ishiguro[b]

[a]*Department of Chemistry and Applied Chemistry, Faculty of Science and Engineering, Saga University, Honjo-machi, Saga 840-8502, Japan;* [b]*Department of Chemistry, Faculty of Science, Kyushu University, Hakozaki, Higashi-ku, Fukuoka 812-8581, Japan*

N,N-Dimethylformamide (DMF) and *N*-methylformamide (NMF) have often been used as solvents for organic reactions and metal-ion complexation. A DMF molecule involves the carbonyl oxygen atom (C=O) as a proton acceptor, while an NMF molecule involves the NH group as a proton donor, together with the carbonyl oxygen atom. It is expected that NMF molecules form chain-like clusters through intermolecular hydrogen bond between the C=O and NH groups. In addition, NMF can form intermolecular hydrogen bond with DMF. Hence, it is interesting to see how DMF and NMF molecules are bonded with each other to form solvent clusters in their binary solutions.

Here, to clarify the mixing state of DMF and NMF molecules at molecular level, small-angle neutron scattering (SANS) measurements have been made on DMF-NMF binary solutions over the DMF mole fraction range of $0.1 \leq x_{DMF} \leq 0.9$ at 25 °C. The sample solutions were prepared by mixing deutrated DMF (DMF-d_7) with undeutrated NMF to obtain the high contrast scatterings from DMF-d_7 and NMF molecules.

The present SANS experiments were carried out using the SANS-U spectrometer at a reactor JRR-3M in JAERI, Tokai. The momentum transfer Q ($= 4\pi\lambda^{-1}\sin\theta$; λ the wavelength, 2θ the scattering angle) range covered was 0.02–0.15 Å [1]. The SANS intensities on SAUS-U were corrected for background, absorption, and cell scattering and normalized by using the scattering of lupolen [2].

Figure 1 shows the SANS intensities for the DMF-d_7 - NMF binary solutions at 25 °C at various x_{DMF}. As seen, the significant SANS intensities are not observed for the binary solutions over the DMF mole fraction range investigated.

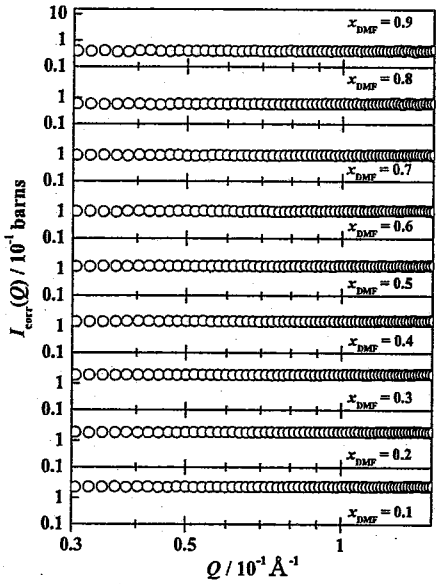

Figure 1: SANS intensities for DMF-d_7 - NMF binary solutions at various x_{DMF}.

Thus, the present results suggest that DMF and NMF molecules are homogeneously mixed with each other in the binary solutions, but solvent clusters of each amide are not significantly formed in the binary solutions. It is likely that intermolecular hydrogen bond between DMF and NMF plays an important role in the mixing of the amides.

References

[1] Y. Ito, M. Imai, and S. Takahashi, *Physica B*, **889**, 213 (1995).
[2] G. D. Wignall and F. S. Bates, *J. Appl. Cryst.*, **20**, 28 (1987).

JRR-3M, SANS-U(C1-2), Glasses & Liquids

研究テーマ：超イオン導電体における乱れ
表　題：バナジウム酸銀系超イオン電導ガラスにおける FSDP の起源

1-4-3

Origin of FSDP for Superionic Silver Vanadate Glasses

H. Takahashi, Y. Sanao, T. Sakuma[1] and Y. Ishii[2]

Faculty of Engineering, Ibaraki University, Hitachi 316-8511
[1]Faculty of Science, Ibaraki University, Mito 310-8512
[2]Advanced Science Research Center, JAERI, Tokai, Ibaraki 319-1195

We have investigated the medium range order in AgI containing superionic glasses in terms of the diffraction peak in low q region. Small peak observed around 5 to 10 nm^{-1} in q space is often called the first sharp diffraction peak (FSDP). FSDP was observed in silver vanadate glasses with and without AgI addition by X-ray diffraction. No FSDP was found by neutron diffraction. So it is considered that FSDP arises from the density fluctuation of vanadium oxide glass network. Another FSDP was found in 0.67(AgI)-0.33($3Ag_2O$-$2V_2O_5$) glass by the elastic neutron scattering experiment[1)]. In the present investigation, detailed FSDP measurements using triple-axis spectrometer were performed for several glasses with different AgI content in order to obtain information about the origin of FSDP.

Powder glass sample filled into a cylindrical vanadium container of 10 mm in diameter was used as a specimen. Elastic and total neutron scattering experiments for x(AgI)-(1-x)($3Ag_2O$-$2V_2O_5$) glasses, where x = 0.3, 0.5, 0.6 and 0.67, were performed by LTAS at JRR-3. The incident neutron wavelength of 0.483 nm is employed. The scattering data was recorded in the range $1.0 \leq Q \leq 10.0$ nm^{-1} at room temperature.

Figure 1 shows the elastic neutron scattering profiles for x(AgI)-(1-x)($3Ag_2O$-$2V_2O_5$) glasses. The diffraction profile for x = 0.67 glass is essentially the same as the previous one obtained by TAS-2. The separation of FSDP from the tail of non-scattered beam is improved by using the longer wavelength of neutron in the present investigation. It is reconfirmed that FSDP could not be detected from the total scattering experiments as before. FSDP is observed above x = 0.5 by elastic neutron scattering. Sub-figure indicates the composition dependence of FSDP position. FSDP position extrapolated to x = 0.3 falls around q = 0.8 in this sub-figure. It is clear that no FSDP is found at x = 0.3. Therefore the critical AgI concentration for the formation of FSDP, in other words medium range structure, lies between x = 0.3 and 0.5. Composition dependence of the molar volume also suggests the structure change in the same AgI concentration. Structure change assumed by FSDP measurement is consistent with the results of the molar volume. FSDP observed by neutron scattering originates from the correlation between Ag, I and/or O based on the coherent scattering length of the elements. Since doped AgI concentration strongly affects the appearance of FSDP, it is natural to conclude that AgI microdomain is formed above critical AgI concentration. Domain size is considered to increase with AgI concentration as shown in the figure. It is verified that AgI containing silver vanadate system precipitates AgI crystal beyond x = 0.7. So AgI microdomain is assumed to act as a nuclear of AgI microcrystal. The fact that FSDP could not be detected by neutron diffraction suggests that inelasitic and quasielastic scatterings due to the low-energy diffusive motion of Ag ion obscure the structural information in the medium range order.

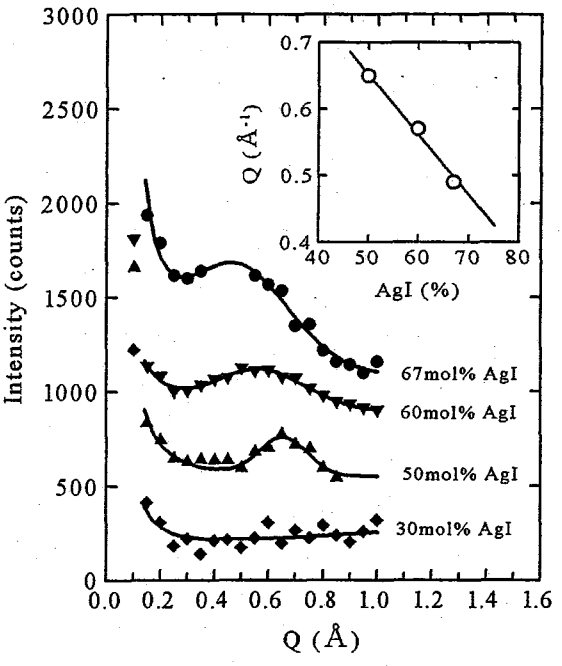

Figure 1: AgI Concentration dependence of FSDP for silver vanadate glasses.

References

1) H. Takahashi, N. Rikitake, T. Sakuma and Y. Ishii : Solid State Ionics, **168** (2004) 93.

原子炉：JRR-3　　装置：LTAS(C2-1)　　分野：中性子散乱（液体・不規則物質）

研究テーマ:液体金属、混合系の構造
課題:液体 Ge-Sn 混合系の構造

1-4-4

Neutron diffraction study of liquid germanium-tin mixtures

S. Takeda, Y. Kawakita, H. Shigeta, S. Fujita, Y. Kato

Department of Physics, Faculty of Sciences, Kyushu University, Ropponmatsu, Fukuoka 810-8560 Japan

There are several single-element liquids with anomalous static structure factors that have a shoulder in the high momentum transfer region of the first peak of the structure factor. Si, Ge and Sn are classified into same group and those structure factors have also the shoulder behind the main peak. Among them, Si and Ge have attracted attention because of the semiconductor-metal transition which occurs on melting accompanied with volume contraction[1].

In general, if the elements belong to the same family and the same property, the liquid mixture will be expected to be an ideal one. The mixture of liquid Ge-Si is expected to be an ideal one from the phase diagram, while the mixture of liquid Ge-Sn expected to have a segregation tendency.[2]

It is therefore interesting to obtain the precise information on the structure of liquid Ge-Sn mixtures and to investigate the structural change of liquid by adding Sn, and also the temperature dependence of the mixed system.

The diffraction measurements of liquid Ge-Sn mixtures were carried out at several concentrations and temperatures at He atmospheric pressure utilizing HERMES installed at the JRR-3M. The measurements have been performed for liquid Ge-Sn mixture over a wide temperature range from the melting temperature to 1500°C to investigate the structural change of the liquid by adding Sn atoms, and also the temperature dependence of mixed system. The wavelength of neutron beam was 1.8196 Å. The purities of Ge and Sn samples were 99.9999 % and 99.999 %, respectively.

In case of the measurements above 1000°C, a bulk sample was inserted into the cylindrical cell made of glassy carbon. The diameter of the cell was 9.8 mm and its wall thickness was 0.2 mm. The furnace was 1800°C-Furnace constructed by AS Science Products, Ltd and the heater consists of two concentric cylinders made of 0.05-mm -thick niobium foils and has 8 thermal shields around the irradiative heater element. The temperature of the sample was measured by a tungsten-rhenium thermocouple. Helium gas was introduced to keep the liquid sample stable in the carbon cell. Our experimental procedures are described in detail elsewhere[3]. In case of the measurement under 1000°C, a bulk sample was sealed into the cylindrical quartz cell[4].

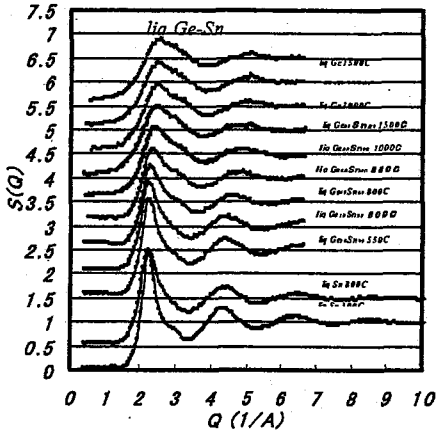

Fig. 1 Structure factors of liquid Ge-Sn mixtures at several temperatures. Structure factors of liquid Ge and Sn are cited from the references.[3,4,5]

The diameter of quartz cell was 10.0 mm and its wall thickness was 0.3 mm.

使用施設:JRR-3M, 装置:HERMES, 分野 liquids

The structure factors, $S(Q)$, in the range of momentum transfer Q up to 6.70 $Å^{-1}$ were obtained by a standard procedure which includes absorption correction, subtraction of scattering from the cell, normalization using the spectra for vanadium and reduction of multiple scattering contributions.

As shown in the figure, the temperature dependence of the structure factors of $Ge_{80}Sn_{20}$ is not so large, but the height of the main peak decreases slightly with increasing temperature. The peak position moves slightly to the high-Q side. The peak position is 2.40 $Å^{-1}$ at 1000C, and it becomes 2.44 $Å^{-1}$ at the highest temperature, 1500C. The shoulder around 3.3 $Å^{-1}$ becomes inconspicuous and almost disappears at high temperature and the temperature dependence is similar to that for liquid Ge. The temperature dependence of the structure factor is larger in Sn rich region in Ge rich region. In the mixture of 60and 40 at% Ge, there can be evaluated the relatively large value in the long wave length limit and it suggests the fluctuations and also the segregation tendency in the liquid state.

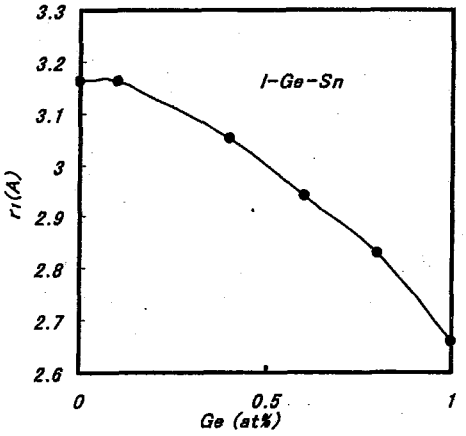

Fig. 2 Concentration dependence of first peak position for g(r) of liquid Ge-Sn mixtures.

The pair correlation functions are obtained by the Fourier transform of observed structure factors. The concentration dependence of the first peak position of g(r) are shown in Fig. 2. As shown in the figure, the peak position moves large r region with Sn concentration in Ge rich region, while that value dose not change so much with Ge in Sn rich region. The temperature dependence of first peak position is rather large in Sn rich region, while that is small in Ge rich region. That may reflect the open structure of liquid Ge and Ge rich concentration.

Our results suggest that the excess Sn atoms substitute the Ge atmos in the liquid mixtures in Ge rich region. Since the liquid Ge has a open structure as the homogeneous metallic phase with loose packing, and temperature dependence of the first peak position in the liquids mixtures are expected to be small in Ge rich region. However, the substitution of Ge atom by Sn may results in the significant effects for the liquid structure. Our experimental results will be described in detail elsewhere[6].

This study was financially supported by the Japan Aerospace Exploration Agency (JAXA).

References

1) V.M. Grazov , S.N. Chizhevskaya and N.N. Glagsleva: in *Liquid Semiconductors* (Plenum, New York, 1969) Chap. 3.

2) M. Hansen and K. Anderko, *Constitution of Binary Alloys,* (McGraw-hill, 1958).

3) Y. Kawakita, S. Takeda, T. Enosaki, K. Ohshima, H. Aoki, T. Masaki and T. Itami: J. Phys. Soc. Jpn. **71** (2002) 366.

4) S. Takeda, S. Tamaki and Y. Waseda; J. Phys. Soc.

5) H. Aoki, T. Masaki, S. Munejiri, Y. Ishi, T. Kamiyama and T. Itami: Annual Reports NASDA-TMR-010019E (2000), P91.

6) S. Takeda, H. Shigeta, S. Fujita, Y. Kawakita, T. Masaki, T. Itami: to be submitted to J. Non-Cryst. Solids.

研究テーマ:超臨界水-アルコール系の中性子小角散乱
表題:超臨界エタノールの中性子小角散乱

1-4-5

Small-Angle Neutron Scattering of Supercritical Ethanol

Nobutaka Yamamoto[1], Koji Yoshida[1], Toshio Yamaguchi[1], and Michihiro Nagao[2]

[1]*Department of Chemistry, Faculty of Science, Fukuoka University, Fukuoka 814-0180, Japan*
[2]*Institute for Solid State Physics, The University of Tokyo, Tokai 319-1106, Japan*

Introduction

Supercritical water (SCW) has novel properties not available under ambient conditions and is used as a medium in various chemical reactions in SCW technology, such as decomposition of hazardous organic compounds like PCB, dioxin, etc. In the meantime, a co-solvent effect of alcohols on the chemical reactions in SCW was found, i.e. addition of methanol into SCW moderates the condition of SCW reactions. It is interesting to note that the poorer the co-solvent effect the longer the hydrophobic group of alcohols. In order to understand an underlying mechanism of the co-solvent effect and further develop the SCW technology, it is essential to investigate the structure of supercritical alcohol-water mixtures on both microscopic and mesoscopic scales.

So far, we have elucidated the microscopic structural information, in particular, about hydrogen bonding, through interatomic distance and coordination number for SCW [1] and supercritical methanol (SCM) [2], by X-ray and neutron diffraction, and for supercritical methanol-water mixture by Raman scattering method. Furthermore, in our previous proposal, we measured small-angle neutron scattering (SANS) of methanol, 1-propanol, and methanol-water mixtures under a supercritical condition and discussed a correlation between density fluctuations and chemical reactivity of SCW. These studies have suggested that chemical reactions in SCW take place effectively near the critical point and that solvent clusters in water-alcohol mixtures play an important role in the chemical reaction of SCW.

In this work, we have measured SANS spectra of supercritical ethanol (SCE) to reveal density fluctuations as a function of temperature and pressure (density) and compare its mesoscopic structure with those of other alcohols.

Experiment

SANS spectra of supercritical deuterated ethanol were measured on the SANS-U spectrometer of the Institute for Solid State Physics of the University of Tokyo, installed at a beamline of a cold source in JRR-3M. We used a high-pressure high-temperature SANS cell (Toyo Koatsu). Fig. 1 shows the high temperature and high-pressure system used for the measurements. A sample solution was injected into a cell with a syringe under vacuo. The pressure was controlled with a high-pressure pump. The sample to detector distance was 4 m, where the Q-range obtained was from 0.008 to 0.15 $Å^{-1}$. The thickness of a sample in a cell is 10mm.A typical measurement time of a sample was 40 min. Measurements were also made for luporen polymer used for normalization, an empty cell, and empty background.

The reduced pressure range (P_C=6.30 MPa) measured was 1.17 to 1.97 at the reduced temperatures T_r=1.02, 1.04, and 1.07 (T_C=516.3 K).

Measurements of an aqueous mixture of ethanol under the supercritical conditions failed because of accidental cracks of sapphire windows in the course of measurements.

使用施設:JRR-3M, 装置:SANS-U, 分野 4 Glass & Liquid

Results and Discussion

To estimate density fluctuations of SCE, the Ornstain-Zernike plots were made according to the equation,

$$\frac{1}{I(Q)} = \frac{\xi^2}{I(0)} \cdot Q^2 + \frac{1}{I(0)}$$

where $I(Q)$ and $I(0)$ are the scattering intensities of a sample at Q and Q=0, respectively. Q is the scattering vector (=$4\pi/\lambda\sin\theta$, λ the wavelength, θ the scattering angle), and ξ is the correlation length of the concentration fluctuation by forming a cluster is expressed.

Fig. 2 shows pressure dependence of the correlation length obtained at the various temperatures. The correlation lengths of ethanol gradually decrease as increasing reduced temperatures as expected. A maximum of the correlation lengths was found as in the cases.

A detail study of the clusters is in progress.

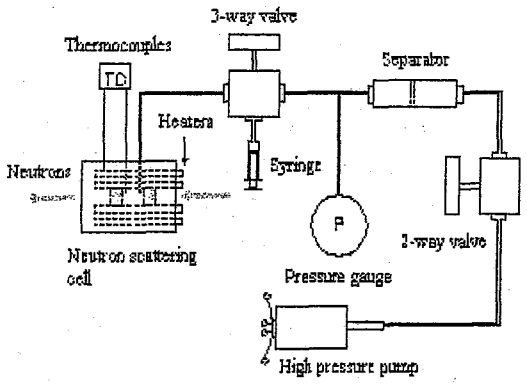

Fig. 1. The high-temperature and high-pressure systems used for SANS measurements

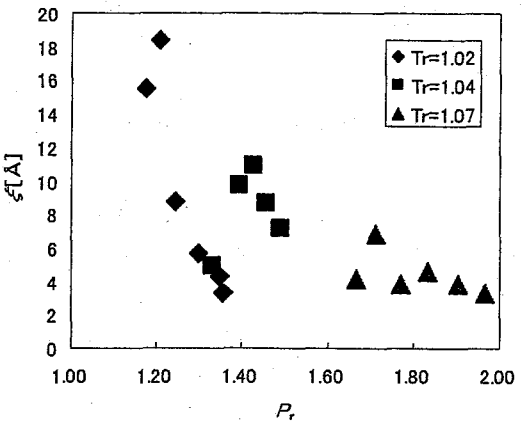

Fig. 2. Pressure dependence of correlation length of SCE at various supercritical temperatures.

References

[1] T. Yamaguchi, *J. Mol. Liq.*, **78**, 43 (1998).

[2] T. Yamaguchi, C. J. Benmore, A. K. Soper, *J. Chem. Phys.*, **112**, 8976 (2000).

研究テーマ：水－tert-ブタノール混合溶液中のゆらぎ構造とダイナミクス
表題：スピンエコー法による－tert-ブタノール－水混合系のスローダイナミクス
1-4-6

Slow Dynamics of *tert*-Butanol-Water Mixture by Neutron Spin Echo Technique

Koji Yoshida, Toshio Yamaguchi[1], Michihiro Nagao[2], and Hideki Seto[3]

[1]*Department of Chemistry, Faculty of Science, Fukuoka University, Fukuoka 814-0180, Japan*

[2]*Institute for Solid State Physics, University of Tokyo, Tokai 319-1106, Japan*

[3]*Department of Physics, Faculty of Sciences, Kyoto University, Kyoto 606-8502, Japan*

Introduction

Many anomalous properties in aqueous alcohol mixtures have been found to be related to inhomogeneities at the microscopic level. We have demonstrated that anomalies in various physicochemical properties of alcohol-water mixtures in a water-rich region are explained by the formation of molecular aggregates or microinhomogeneities in the mixtures[1]. The dynamic properties of alcohol-water mixtures, such as *n*-butoxyethanol-water, have also been investigated by neutron spin echo measurements [2].

Small-angle X-ray scattering [3] and light scattering measurements [4] observed large concentration fluctuations in *tert*-butanol (TBA) – water mixtures. However, dynamics of microinhomogeneities on a mesoscopic scale has not yet been revealed in TBA-water mixture. The neutron spin echo (NSE) technique is a unique tool to investigate the dynamics of system in a timescale of 0.1-100 ns in a mesoscopic spatial structure of 10-10^3 Å. In this study, NSE measurements have been carried out to reveal the dynamics of the molecular aggregation in a TBA-water mixture.

Experiment

An NSE spectrometer is equipped at the $C_{2\text{-}2}$ cold neutron guide port of JRR-3M at JAERI. The scattering vector Q covered was 0.01 - 0.10 $Å^{-1}$. The Fourier time was varied from 0.15 to 15 ns. The measuring time was about 8 h for each Q range at fixed temperatures. A plate of Grafoil was measured for resolution correction.

Tert-butanol (TBA) (over 98 atom%D, Kanto Kagaku), C_4H_9OD, whose hydroxyl part is deuterated (note that the hydroxyl hydrogen of the alcohol exchanges with water hydrogen), and D_2O (99.95 atom%D, CEA) were used without further purification. The sample solution was 10 mol% TBA in D_2O and sealed in a quartz cell of 2 mm thickness. The temperature was controlled within ±0.1 °C with a thermostat to circulate water.

Results and Discussion

The NSE method measures the energy transfer of neutrons at an extremely high energy resolution as a phase shift in the Larmor precession of each neutron spin in a magnetic field. The intermediate correlation function $I(Q,t)$ is defined by the following equation as a function of the wave vector Q and Fourier time t.

$$I(Q,t) = N^{-1}\sum_{k,l}\left\langle \exp\left(iQ\cdot r_k(t)\right)\exp\left(iQ\cdot r_l(0)\right)\right\rangle \qquad (1)$$

Here, N is the number density. The bracket means an ensemble average. In the case of neutron quasielastic scattering, $I(Q,t)$ can be obtained directly from the amplitude of the NSE signal at the spin echo condition. The $I(Q,t)$ obtained from NSE experiments was fitted to the following equation on the basis of the Brownian motion,

$$I(Q,t)/I(Q,0) = \exp(-\Gamma t) \qquad (2)$$

where Γ is the relaxation rate. Figure 1 shows the Q-dependence of the relaxation rate. The diffusion coefficient D was obtained from the following equation,

$$\Gamma = DQ^2 \quad (3)$$

The values of D are summarized in Table 1. The value at 25 °C is smaller than the diffusion constants (9.3 and 3.1×10^{-10} m^2 s^{-1}) of water and TBA, respectively, obtained from NMR in a TBA-water mixture at the same mole fraction of TBA [5]. Thus, the NSE values seem to reflect the motion of molecular aggregates because the NMR data are related to the translational motion of single molecules of water and alcohol. An apparent activation energy, E_a, of the diffusion process obtained from temperature dependence of the NSE diffusion constants is 28.3 ± 0.6 kJ mol^{-1}, which is larger than the hydrogen bonding energy deduced from the translation of water molecule (19 kJ mol^{-1}) in pure water [6]. This implies that the hydrogen bonding is strengthened due to hydrophobic hydration in the mixtures and consistent with the results of the static structure by neutron diffraction [7].

It is worthwhile to compare the present results with the previous one in *n*-butoxyethanol(BE)-water mixture that has the lower critical solution temperature (LCST). In Figure 1, the values of $\Gamma(Q)$ are well fitted to a function of square of Q. On the other hand, $\Gamma(Q)$ in the BE-water mixtures is proportional to $Q^{-2.6}$ at 37 °C. The apparent non-linearity in the $\Gamma(Q)$–Q^2 plots in the BE-water mixture seems to arize from development of inhomogeneities near the LCST. On the other hand, the present NSE results have suggested that clusters in the TBA-water mixture do not drastically change with temperature. This finding is consistent with the results obtained from SAXS that the correlation length of concentration fluctuations changes only slightly with increasing temperature in a TBA-water mixture[4].

The present conclusion on the dynamics of the molecular aggregation in the TBA -water mixture should be confirmed by further NSE experiments under different TBA concentrations, which are now in progress.

1. K. Yoshida, T. Yamaguchi, A. Kovalenko, F. Hirata, J. Phys. Chem. B, **106**, 5042 (2002).

2. K. Yoshida, T. Yamaguchi, T. Otomo, M. Nagao, Y. Kawabata, H. Seto, T. Takeda, Appl. Phys. **A74** [Suppl.], S386 (2002); J. Mol. Liq. in press.

3. N. Ito, T. Fujiyama, Y. Udagawa, Bull. Chem. Soc. Jpn. **56**, 379 (1983).

4. K. Nishikawa, T. Iijima, J. Phys. Chem. **97**, 10824 (1993).

5. W. S. Price, H. Ide, Y. Arata, J. Phys. Chem. A **107**, 4784 (2003).

6. L. A. Woolf, J. Chem. Soc. Faraday I . **72**, 1267 (1976).

7. D. T. Bowron, J. L. Finney, and A. K. Soper, *J. Phys. Chem. B* **102**, 3551 (1998).

Table 1. Diffusion constants ($D \cdot 10^{11}$/m^{2}s^{-1}) of the TBA-water mixtures

	$x_{BE} = 0.10$
15°C	6.0±0.2
25°C	8.6±0.1
45°C	17.8±0.6

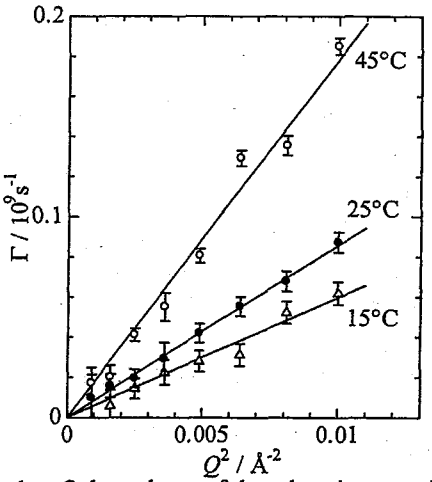

Fig. 1. Q-dependence of the relaxation rates $\Gamma(Q)$ in the TBA-water of 0.10 mole fraction at various temperatures.

研究テーマ：高機能イオン交換体中における水分子間水素結合構造
表題：イオン交換樹脂中における水分子間水素結合構造

1-4-7 Hydrogen-Bonded Structure of Water Molecules in Ion Exchange Resins

Y. Kameda, K. Yamanaka*, M. Sasaki, K. Tsuji, S. Oomori, Y. Amo, and T. Usuki

Department of Material and Biological Chemistry, Faculty of Science, Yamagata University, Yamagata 990-8560, Japan

**Plant and Equipment Division, Organo Corporation, Tokyo 136-8631, Japan*

Ion exchange resins provide wide applications in extensive fields of chemical and biological sciences. Considerable efforts have been made to investigate the ion exchanging mechanism within the resin, which is necessary to improve its performance. However, structural information on absorbed water molecules in the microscopic level has not yet been deduced.

In the present report, we describe the results of neutron diffraction measurements on cation and anion exchange resins absorbing H/D isotopically substituted water molecules in order to obtain structural information on the hydrogen-bonded network among water molecules inside the resin.

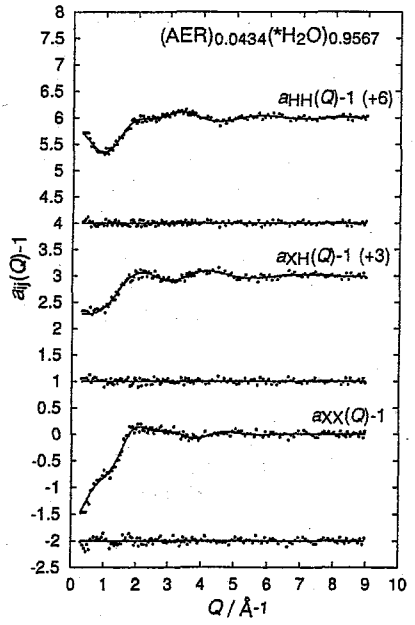

Figure 1: Circles: Observed H-H, X-H, and X-X partial structure factors, $a_{ij}(Q)$, for water molecules absorbed in anion exchange resin (AER). Solid lines: The best-fit of calculated $a_{ij}(Q)$. The difference between observed and calculated $a_{ij}(Q)$ is shown below.

Neutron diffraction measurements for cation exchange resins (CER, AMBERLITE® IR124H) and anion exchange resins (AER, AMBERLITE® IRA402BL) both absorbing D_2O (99.9 % D), ^0H_2O (35.9 % D) and $^{0\text{-}2}H_2O$ (67.9 % D), were carried out at 25 °C using the ISSP 5G (PONTA) diffractometer installed at the JRR-3M research reactor in Japan Atomic Energy Research Institute (JAERI), Tokai, Japan. The incident neutron wavelength, λ = 1.089(4) Å, was employed. Scattered neutrons were collected over the angular range of $3 \leq 2\theta \leq 102°$ which corresponds to $0.30 \leq Q \leq 8.97$ Å^{-1} ($Q = 4\pi\sin\theta/\lambda$). Measurements were made in advance for dehydrated CER and AER, an empty SiO_2 cell, a vanadium rod of 8 mm in diameter, and an instrumental background. After correction for the background, absorption

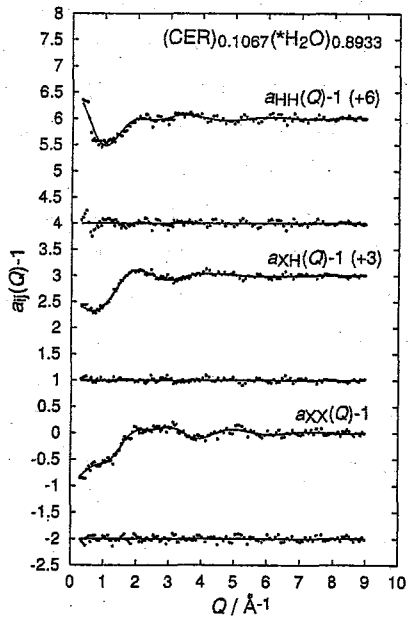

Figure 2: Same notations as in Fig. 1, except for water molecules absorbed in cation exchange resin (CER).

使用施設：JRR-3M, 装置：PONTA(5G), 分野 Glasses & Liquids

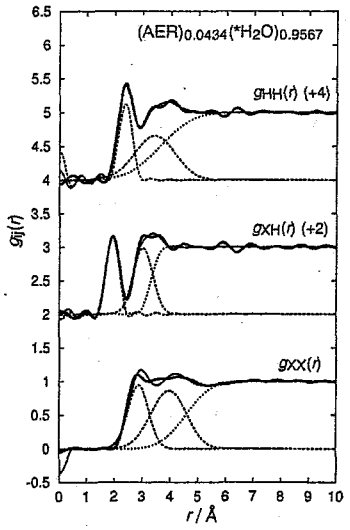

Figure 3: Circles: Observed H-H, X-H, and X-X partial pair correlation functions, gij(r), for water molecules absorbed in anion exchange resin (AER). Solid lines: The Fourier transform of the solid lines in Fig. 1. Contributions from both the short- and long-range interactions are denoted by broken and dotted lines, respectively.

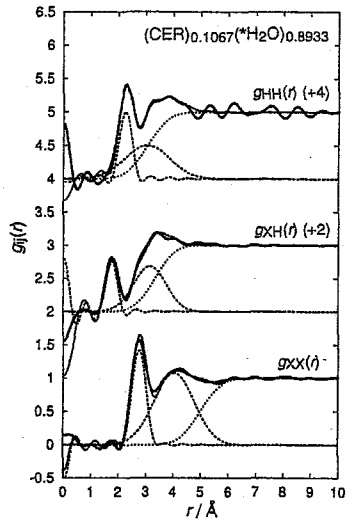

Figure 4: Same notations as in Fig. 1, except for water molecules absorbed in cation exchange resin (CER).

and multiple scattering, the observed count rates were converted to the normalized scattering cross section. Scattering cross sections observed for the dehydrated resins were then subtracted from the observed scattering cross sections for wet samples in order to cancel out intra- and intermolecular contributions within the resin.

Partial structure factors, $a_{HH}(Q)$, $a_{XH}(Q)$ and $a_{XX}(Q)$ (X: Atoms involved in the sample except for hydrogen) for AER and CER samples were derived by combining observed scattering cross sections for samples with different H/D isotopic compositions as shown in Figs. 1 and 2, respectively; the procedure has been described in our previous paper [1].

Partial pair correlation functions, $g_{HH}(r)$, $g_{XH}(r)$ and $g_{XX}(r)$ for AER and CER, were obtained by the Fourier transform of observed partial structure factors, which are represented in Figs. 3 and 4, respectively.

In order to determine structural parameters for the hydrogen-bonded intermolecular interaction between water molecules, the least squares fitting procedure was applied to the observed partial structure factors, $a_{ij}(Q)$, as shown in Figs. 1 and 2. The present value of the nearest neighbor O···H distance for the AER, r_{OH} = 1.95(1) Å, agrees well with that reported for aqueous 8 mol% NH_4Cl (r_{OH} = 1.91(1) Å) [2] and for aqueous 10 mol% LiBr (r_{OH} = 1.91(1) Å) [3] solutions, and for the pure water (r_{OH} = 1.85 Å) [4], which suggests that the hydrogen-bonded network similar to that in the pure water is maintained inside the AER. On the other hand, considerably shorter intermolecular O···H distance (r_{OH} = 1.78(1) Å) was observed for the present CER sample. This implies that the hydrogen-bonded network among water molecules within the CER is strongly affected by the presence of the H_3O^+, which is known to exhibit very short intermolecular hydrogen-bonded distance between the nearest neighbor water molecule (r_{OH} = 1.69(2) Å) [1] in concentrated aqueous acidic solutions.

References

[1] Y. Kameda, T. Usuki, and O. Uemura, *Bull. Chem. Soc. Jpn.*, **71** (1998) 1305.

[2] Y. Kameda, K. Sugawara, T. Usuki, and O. Uemura, *J. Phys. Soc. Jpn.*, **70** (2001) Suppl. A, pp. 362.

[3] Y. Kameda, M. Imano, M. Takeuchi, S. Suzuki, T. Usuki, and O. Uemura, *J. Non-Cryst. Solids*, **293-295** (2001) 600.

[4] A. K. Soper and M. G. Phillips, *Chem. Phys.*, **107** (1986) 47.

This is a blank page.

1. 中性子散乱 5)高分子

1. Neutron Scattering 5) Polymer

This is a blank page.

研究テーマ：高分子の結晶構造
表　題：重水素化ポリエチレンの結晶構造

1-5-1

Crystal Structure of Deuterated Polyethylene

Y. Takahashi and T. Kumano

Department of Macromolecular Science, Graduate School of Science, Osaka University Toyonaka, Osaka 560-0043, Japan

Neutron diffraction has several advantages in comparison with X-ray diffraction for crystalline polymers.[1-3] In the previous paper,[3] the crystal structure of deuterated polyethylene was determined in temperature range 10 - 300K by using the neutron diffraction on the equator measured for the fiber specimen by powder diffractometer, and the angle ϕ between the molecular plane and the b-axis and the rigid body temperature parameters were determined. On the other hand, the diffractometer BIX-3 and neutron imaging plate were developed by Niimura's group. In the present study, the neutron crystal structure analysis is carried out by using three-dimensional data measure by BIX-3 and neutron imaging plate.

The film of the commercially supplied deuterated polyethylene was made by a hot press and stretched in boiling water. The films were stacked and rolled up the cylinder with diameter 5mm.

The neutron diffraction was measured with BIX-3 and neutron imaging plates. The digital data of eight imaging plates were summed up in order to improve the signal to noise ratio. The integrated intensities were estimated according to the method developed for X-ray.[4] Digtal data for one pixel of reflection arc are summed along the arc with constant 2θ and the summed intensities are plotted against a layer line. From the one-dimensional intensity curve thus obtained, the integrated intensity was estimated.

The structure refinement was made by the rigid body least-squares method.[5] The parameters to be refined are the azimuthal angle between the molecular plane and the a axis, θ, the translational temperature parameters, T_{11}, T_{12}, T_{22}, and T_{33}, and the librational temperature parameter, ω_{33}. Finally, the least-squares refinement converged to the discrepancy factorR = 0.184. The value θ is estimated to be 46.3^o (standard deviation: 1.5^o), which corresponds well to the value 45.1^o (1.3^o) determined in the previous paper.[3] Translational temperature parameters, T_{11}, T_{12}, snf T_{22}, are 2.58 (0.67), 1.40 (0.66), and 2.54 (0.71), respectively, which correspond well to T_{aa} = 2.49 (0.42), T_{ab} = 0.66 (0.53), and T_{bb} =2.43 (0.47) determined in the previous paper[3] within the accuracy of the standard deviations. The librational temperature parameter ω is 0.52 (0.52), which also corresponds to the value 1.04 (0.44) determined in the previous paper.[3]

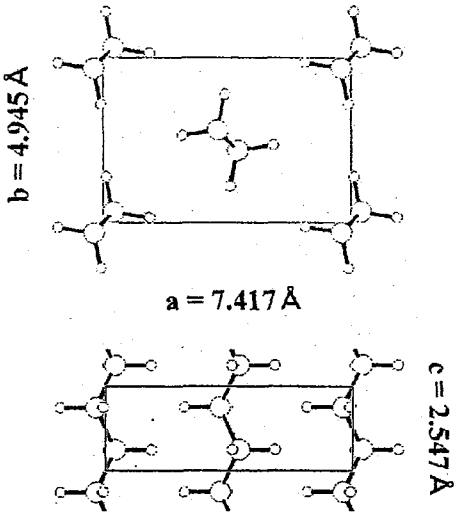

Figure 1: Crystal Structure of Polyethylene.

Acknowledgement

The authors express their thanks to Drs N. Niimura, I. Tanaka, and K. Kurihara of JAERI for neutron diffraction measurements.

References

1) Y. Takahashi: "Neutron Structure Analysis of Crystalline Poymers", Recent Res. Devel. in Macromol. Res., **3** (1998) 265.
2) Y. Takahashi: "Neutron Diffraction by Crystalline Polymers", ACS Symposium Series **739**, "Scattering from Polymers" edited by P. Cebe, B. S. Hsiao, and D. J. Lohse, Chapter 5, 74 (2000).
3) Y. Takahashi: Macromolecules **31** (1998) 3868.
4) Y. Takahashi and H. sul, tobe published.
5) Y. Takahashi, T. Sato, H. Tadokoro, and Y. Tanaka: J. Polym. Sci. Polym. Phys. Ed., **11** (1973) 233.

原子炉：JRR-3　　装置：BIX-3M(1GB)　　分野：中性子散乱（高分子）

研究テーマ：トリアシルグリセロールの準安定相の結晶構造に関する研究
表題：中性子線回折をもちいた脂質化合物の構造化学的研究

1-5-2

Structural Analysis of Metastable Phase of Triacylglycerols; the Order of the Acyl Chain packing

Akita Chikayo, Kawaguchi Tatsuya and Kaneko Fumitoshi

Graduate School of Science, Osaka University, 1-1 Machikaneyama, Toyanaka 563 – 0046, Japan

Triacylglycerols (TAGs) are major constituents of natural fats and oils and widely used as raw materials for many industrial products.

Depending on the crystallization conditions, TAGs crystallize into various solid modifications, which are different in lateral packing of the hydrocarbon chains, so-called subcell. There are three kinds of solid modifications for most TAGs: the stable phase β with the triclinic parallel (T//) subcell, and two metastable phases β' and α with the orthorhombic perpendicular (O⊥) and hexagonal (H) subcells. According to the previous studies using IR and Raman spectroscopy and X-ray diffraction, the metastable phases β' and α have lower regularity as to the lateral packing of hydrocarbon chains than the stable phase β.

In this study, we tried to evaluate the microdomain size and distortions of hydrocarbon chains in the lateral directions for the three modifications of tristearin by coherent neutron elastic scattering using fully duetrated specimens tristearin (SSS) $[C_3D_5(O_2C(CD_2)_{16}CD_3)_3]$, which removed a strong background due to incoherent scattering of hydrogen atoms.

Fig.1 shows the powder diffraction diagram of each phase at room temperature measured with HERMES of JRR3M in JAERI. In the region around s = 0.24 Å^{-1} (s = 2sinθ/λ), the β phase exhibited three intense reflection due to the (010), ($\bar{1}$10) and (100) planes of the T// subcell.

Unlike X-ray diffraction, the second order reflection could be observed clearly around 0.46 Å^{-1} because the scattering length does not depend on the scattering angle. The profiles at 0.24 Å^{-1} and 0.46 Å^{-1} regions were decomposed into the first and second order reflections.

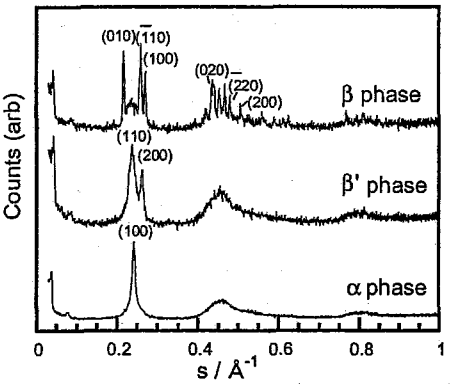

Fig. 1. Powder diffraction diagram of each phase at room temperature

Using the paracrystal theory of Hosemann [1], the integral breadth (δ*b*) of each reflection in the β phase was plotted versus the square of its order (h^2), so that the relative statistical deviation *g* and the average number *N* of netplane spacing could be estimated. The obtained *g* values listed in Table 1 were similar to that of the polyethylene (PE) single-crystal specimen [2], which means that the lateral packing of hydrocarbon chains has a long-range structural order in the β phase.

Table 1 Relative statistical deviation *g* and the average number *N* of netplane spacing

β phase of tristearin						PE	
N			*g* (%)			*N*	*g*
100	110	010	100	110	100	110	110
57	33	73	2.0	0.9	2.0	80	2.1

As for the β' phase, two broad reflections due to the (110) and (200) planes of the O⊥

使用施設：JRR-3M, 装置：HERMES, 分野 Softmatter

subcell were observed around s = 0.25 Å^{-1}. However, only a broadened peak was observed in the 0.4 – 0.5 Å^{-1} region at room temperature, where the second order reflections were expected to appear. Similar features were confirmed for the scattering profile of the α phase. It was suggested that the structural correlation of hydrocarbon chains in the lateral direction decreased rapidly with distance in the β' and α phases. On cooling, the several peaks appeared in the 0.4 – 0.5 Å^{-1} region, suggesting that the lateral order of hydrocarbon chains increased as shown in Fig.2.

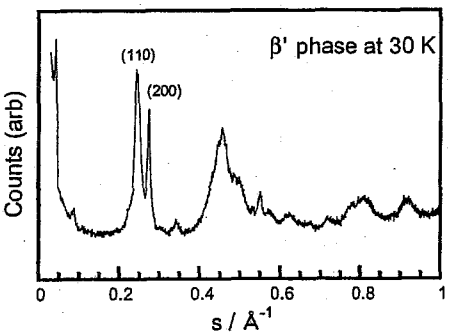

Fig. 2. Powder diffraction diagram of the β' phase at 30 K.

However, since several general reflections (hkl) such as (011), (111) and (201) reflections of the (O⊥) subcell appeared in the same region simultaneously, the detailed profile analysis on the (220) and (400) reflections could not been performed this time.

The separation of the (220) and (400) reflections from the other general reflections is required for the detailed analyses. Now, we are preparing an experiment using a oriented specimen.

References

[1] R. Hosemann, S. N. Bagchi, Direct Analysis of Diffraction by Matter, North-Holland Publ. Co., Amsterdam, 1962.
[2] F. J. Balta-Calleja, R. Hosemann, W. Wilke, Makromol. Chem. **92** (1966) 25.

研究テーマ：中性子イメージングプレートを利用した合成高分子の精密結晶構造解析への初挑戦
表　題：中性子イメージングプレートによるポリエチレン結晶の水素原子位置抽出
1-5-3

The First Success in Direct Extraction of Hydrogen Atoms in Polyethylene Crystal

K.TASHIRO, I.TANAKA[1,2], T.OOHARA[1], N.NIIMURA[1,2], S.FUJIWARA[1],
K. KURIHARA[1], and T. KAMAE

Graduate School of Science, Osaka University, Osaka 560-0043
[1]*Advanced Science Research Center, JAERI, Tokai, Ibaraki 319-1195*
[2]*Faculty of Engineering, Ibaraki University, Hitachi, Ibaraki 316-8511*

When we try to estimate the limiting physical properties of polymer crystals, we need to know the atomic positions in the crystal lattices, in particular the positions of hydrogen atoms as exactly as possible. However, even for the low-molecular-weight compounds, it has been difficult to extract the hydrogen atomic positions using an X-ray structure analysis technique. The situation is worse for polymer crystals, which show quite poor X-ray diffraction patterns because of small crystallite size. In a previous paper[1)] we succeeded in extracting the hydrogen atoms by calculating the Fo-Fc Fourier map based on the X-ray imaging-plate system. This success was based on the usefulness of 2-dimensional imaging plate detector. It may be possible to know the hydrogen atom positions in more exact and direct manner by taking the 2-dimensional neutron diffraction patterns of the uniaxially-orineted deuterated polymer materials using a neutron imaging plate system[2)]. As reported here, we have succeeded to pick up the hydrogen atom positions of orthorhombic polyethylene crystal by collecting the diffraction data for uniaxially-oriented fully-deuterated (H) and hydrogeneous (H) polyethylene samples using a JAERI neutron imaging plate system BIX-3. The thus clarified hydrogen atom positions were refined and were compared with X-ray diffraction and electron diffraction results[3)].

On the basis of the 2-dimensional neutron fiber diagrams taken for the uniaxially-oriented D and H polyethylene samples, the Fourier maps were calculated. As shown in Figure 1, the positive and negative density peaks of hydrogen atoms were detected clearly for the D and H polyethylene samples, respectively. In particular the Fo-Fc maps made the positions more clear. The structure parameters were refined on the basis of least-squares method. The reliability factors were 0.135 for 29 reflections of the D sample and 0.191 for 17 reflections of the H sample. Of course the X-ray structure analysis gave essentially the same crystal structure but the hydrogen atom positions could not be refined reasonably[1)]. The refinement of both the hydrogen and carbon positions could be successfully made for the first time on the basis of neutron diffraction data. On the other hand, from the electron diffraction pattern measured for polyethylene single crystal grown from the solution, 45 reflections were collected in total. The direct method allowed us to extract the hydrogen atoms and the final reliability factor was 0.176. However, the structure parameters were not as reasonable as those obtained by X-ray and neutron diffraction data. This is because of modification of relative intensities of diffraction spots due to the so-called multiple scattering effect in the single crystal.

In conclusion, we have succeeded in evaluating the hydrogen atomic positions as exactly as possible on the basis of 2-dimensional neutron diffraction patterns taken for D and H polyethylene samples. Although a fully deuterated sample is difficult to prepare the usefulness of combining this sample with neutron diffraction technique is clear as described here.

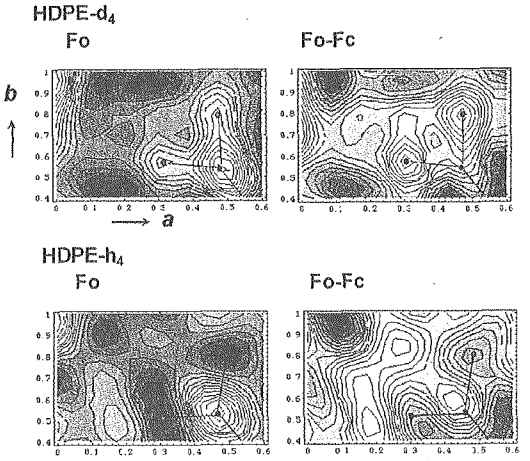

Figure 1: Fourier neutron density maps obtained for uniaxially-oriented (top) deuterated and (bottom) hydrogeneous polyethylene samples.

References

1) K. Tashiro, H. Asanaga, K. Ishino, R. Tazaki, and M. Kobayashi, J. Polym. Sci.: Part B: Polym. Phys. **35** (1997) 1667.
2) N. Niimura, Y. Karasawa, I. Tanaka, J. Miyahara, K. Takahashi, H. Saito, S. Koizumi, and M. Hidaka, Nucl. Instrum. Meth. Phys. Res. A. **349** (1994) 521.
3) K. Tashiro, I. Tanaka, T. Oohara, N. Niimura, S. Fujiwara, T. Kamae, Macromolecules **37** (2004) 4109.

原子炉：JRR-3　　装置：BIX-1 & 3(1G-A)　　分野：中性子散乱（高分子）

研究テーマ:中性子反射率測定に基づく(ナノフィラー/高分子)ハイブリッド超薄膜の安定性評価
表題:中性子反射率測定に基づく(ナノフィラー/高分子)ハイブリッド超薄膜の安定性評価

1-5-4

Neutron Reflectivity Study on the Stability of Ultrathin (Nanofiller/Polymer) Hybrid Films

N. Hosaka[1], H. Sakata[1], A. Takahara[1,2]

*Graduate School of Engnieering[1], Institute for Materials Chemistry and Engineering[2], Kyushu University, 6-10-1 Hakozaki, Higashi-ku, Fukuoka, 812-8581, Japan**

Polymer thin films used in numerous technological applications become ever thinner with the miniaturization of devices. However, such films are not stable, and will dewet from the substrate above glass transition temperature. The key to whether a film is stable or not on a certain substrate is given by Young's equation for the spreading coefficient [1],

$$S = \gamma_B - (\gamma_A + \gamma_{AB}) \qquad (1)$$

where γ_A, γ_B and γ_{AB} are the surface energies of the polymer film, substrate and polymer-substrate interface, respectively. If the spreading coefficient is negative, then the film is unstable.

Previous study showed that the addition of polyhedral oligomeric silsesquioxanes (POSS) to the polystyrene (PS) thin films led to an inhibition of dewetting in the films [2]. This inhibition effect can be attributed to the changes of the energetics of the surface and interface of the film caused by the segregation of POSS. In this study, neutron reflectivity (NR) technique is used to determine the structures of the PS films with octacyclopentyl-POSS (cPOSS: Figure 1).

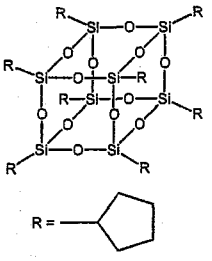

Figure 1: Chemical structure of cPOSS.

NR measurements were performed on a thin deuterated PS (d-PS) films containing 10 wt% cPOSS prepared on acid-cleaned Si wafer by spin-casting, and conducted on MINE with 8.8 Å of incident neutron beam. NR curve of the as-cast film was shown in Figure 2. The solid line is model reflectivity data based on the scattering length density profile shown in the inset. As shown in the scatteling length density profile, roughend structure was observed at the surface and polymer-substrate interface of the film, which can be attributed to the segregation of cPOSS on the surface and interface. NR measurement was also performed on the d-PS film with 10 wt% cPOSS annealed at 403 K for 120 min. The film was roughened through annealing process, however, the critical angle was the same as that of the as-cast film. It was revealed that the film was maintained even after annealing without dewetting from the substrate. Segregation of cPOSS on the surface and interface, and stabilization of the films.was confirmed.

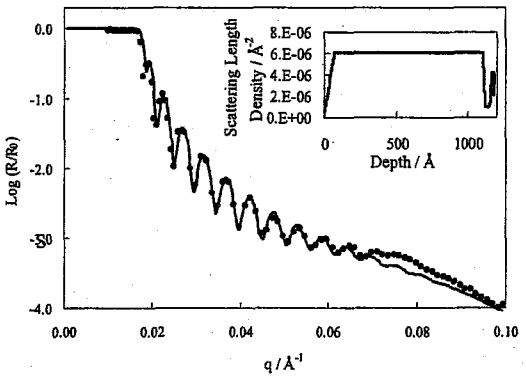

Figure 2: NR curve of as-cast d-PS film with 10 wt% cPOSS. The inset shows the scattering length density profile.

References

[1] G. Krausch, *J. Phys.: Cpndens. Matter*, **9**, 7741-7752 (1997).

[2] N. Hosaka, R. Matsuno, K. Yamamoto, D. Kawaguchi, K. Tanaka, H. Otsuka, A. Takahara, *Trans. Mater. Res. Soc. Japan*, **29**[1], 161-164 (2004).

使用施設:JRR-3M, 装置:MINE(C3-1-2), 分野 Softmatter

研究テーマ：中性子散乱によるソフトマターの構造と機能の研究
表　題：リビングアニオン重合過程の中性子散乱測定によるその場解析
1-5-5

Direct In-situ Observations in Living Anionic Polymerization by Small Angle Neutron Scattering

K. Yamauchi[1], H. Hasegawa[1], T. Hashimoto[1,2], H. Tanaka[1,2], R. Motokawa[2], S. Koizumi[2]

[1] *Graduate School of Engineering Kyoto University, Nishikyo-ku, Kyoto, 615-8510*
[2] *Japan Atomic Energy Research Institute(JAERI), Tokai, Ibaraki, 319-1195*

Small angle neutron scattering (SANS) has been a powerful technique to study dynamics of physical processes in polymer systems such as order-disorder transition of block copolymers, shear-induced phase transition of polymer blends, etc. SANS is also extremely useful to study chemical reactions in polymer systems such as polymerization, etc. We can look at not only concentration changes by chemical reactions but also structural changes (primary, secondary, and higher-order structures) by time-resolved SANS measurement.

In this study, we would like to present the preliminary results of our SANS study on the synthesis process of polyisoprene-*block*-poly(d_8-styrene) (PI-*block*-dPS). A mixture of isoprene, d_8-styrene, and d_6-benzene in the ratio of 1:1:2 by weight was introduced into a quartz cell under argon atmosphere. A solution of *sec*-butyllithium was added to the mixture via the syringe technique to give a little yellow color solution on isoprene anion. In the non-polar solvent it is known that the reactivity of isoprene is much larger than that of styrene resulting in the formation of PI-*block*-dPS block copolymer (Figure 1). As soon as *sec*-butyllithium was added to the mixture, time-resolved SANS measurement was started with the SANS-J instrument installed to JRR-3M research reactor with neutron wavelength of 0.7 nm at JAERI, Tokai, Japan. Time-resolved SANS intensity profiles were obtained with 5 min interval. The solution of living polymer in the quartz cell kept at 30 ℃ without stirring.

The resulting block copolymer was characterized by GPC (Gel Permeation Chromatography). The number-average molecular weight M_n and polydispersity index M_w/M_n values of polymmers were calculated from GPC on the basis of polystyrene calibration. Characteristics data of PI-*block*-dPS was shown in Table 1.

Table 1: Characteristics of PI-*block*-dPS diblock copolymer

Sample	M_n	M_w/M_n
PI-*block*-dPS	1.41×10^5	1.03

The SANS profiles as shown in Figure 1 exhibited four different time region (Region 1-4) in terms of the number, position and intensity of scattering peaks. In Region 1, only the intensity at low q increased with time suggesting the growth of PI chains. In Region 2, a peak appeared at q = 0.2 nm^{-1} and the intensity increased with time while the peak position remained constant. Moreober, GPC results suggested that the molecular weight was constant in Region 2. These results means block polymer chains are not grown in Region 2. In region 3, the peak position rapidly shifted toward smaller q and its intensity increased suggesting the growth of dPS blocks attached to the PI blocks. In this time region, the order-order transition (abrupt change in the width of the peak and appearance of the higher-order peaks at $3^{1/2}$ and $7^{1/2}$ positions of the first-order peak) was also observed. In Region 4, the order-order transition from cylinders to lamellae was observed induced by the further growth of the dPS blocks suggested by the positional changes of the higher order peaks to the integer multiples of the first-order peak. Time-resolved SANS results suggested that the stepwise growth of PI-*block*-dPS diblock copolymer chain and microphase separated structure.

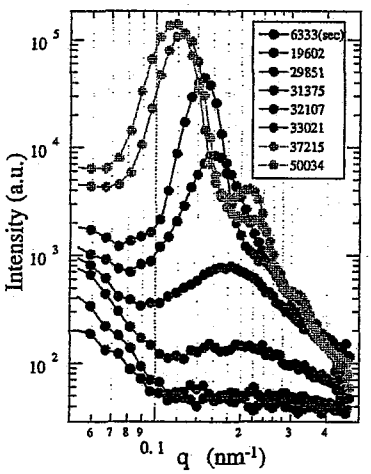

Figure 1: Time dependence of the SANS profiles in the living anionic polymerization of isoprene/styrene mixture in benzene.

原子炉：JRR-3　　装置：SANS-J(C3-2)　　分野：中性子散乱（高分子）

研究テーマ：3504ゲルの体積相転移とミクロ相分離挙動へのゲルサイズ依存性
表題：小角中性子散乱による弱荷電ゲル微粒子の構造解析

1-5-6 Small-Angle Neutron Scattering Study on Microstructure of Weakly Charged Polymer Gel Particles

F. IKKAI[1] and M. SHIBAYAMA[2]

[1]L'ORÉAL Tsukuba Center, 5-5 Tokodai, Tsukuba, Ibaraki 300-2635, Japan;
[2] ISSP, The Univ. of Tokyo, Tokai, Naka-gun, Ibaraki 319-1106, Japan

INTRODUCTION

Weakly charged polymer gels consisting of *N*-isopropyl acrylamide (NIPAm) and its ionized derivative show volume phase transition above a critical temperature. At the same time, the transition is known to involve formation of microphase separation, resulting in an appearance of a scattering peak in small-angle scattering profile.[1] From the scattering vector, q_m, ≈ 0.02 Å^{-1}, at the peak position, the characteristic length, D, of the phase separation was estimated to be 200 ~ 300 Å. However, if the gel size is equal to D, does the phase separation as well as volume phase transition take place above the transition temperature? The purpose of this small-angle neutron scattering (SANS) study is to investigate gel-size dependence of the microphase separation in weakly charged polymer gel.

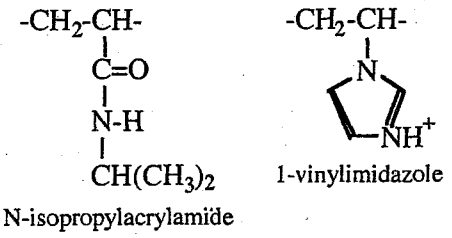

Fig. 1 Chemical structures of gel components

EXPERIMENTAL

To do the experiment, we prepared NIPAm gel particles having different diameters. The particles were prepared by heat-induced emulsion copolymerization of NIPAm, 1-vinylimidazole (VI), and *N,N'*-methylene-bis-acrylamide (BIS) using ammonium persulfate (APS) and sodium dodecylbenzenesulfonate (SDS) as the initiator and the surfactant, respectively. (Fig. 1) The monomer aqueous solutions were put into a 300 mL round-bottom flask and the copolymerization was carried out for 2 h at 60 °C with stirring under N_2 atmosphere.[2] The size of gel particles depended on SDS concentration and stirring rate. After the polymerization, residual monomers and SDS were removed by dialyzing against 0.1 N HCl and ionized water.

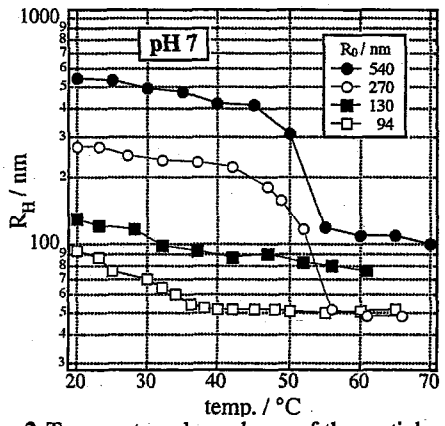

Fig. 2 Temperature dependence of the particle size for NIPAm/VI gels with different R_0's.

RESULTS & DISCUSSION

Fig. 2 shows temperature dependence of the particle size for NIPAm/VI gels with different R_0's, where R_0 is the initial particle size at 20 °C. The gel particles having R_0 = 540 nm and 270 nm collapsed suddenly at ca. 52 °C, indicating a volume phase transition. On the other hand, those having R_0 = 130 nm and 94 nm gradually shrank and did not show any volume transition. This clearly indicates that the volume phase transition of the weakly charged gels depends on the gel size. Fig. 3 shows the SANS profiles for the particles having R_0 =

使用施設：JRR-3M，装置：SANS-U(C1-2)，分野 Softmatter

130 nm at 20 °C (before transition) and 75 °C (after transition). Two profiles showed different features. At 20 °C, the

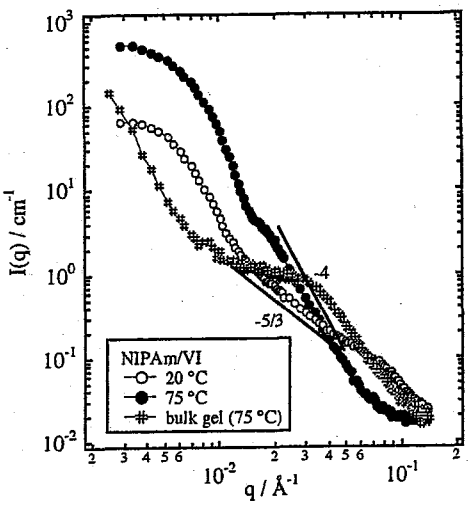

Fig. 3 SANS profiles of NIPAm/VI particle gels at 20 °C (swelling state) and 75 °C (shrinking state), and bulk gel (#) at 75 °C

slope of the profile at high q range was –5/3, which means that the particle interface consists of random coil of polymer chains. On the other hand, at 75 °C, the Porod law was observed at the high q range, indicating that the particles have a clear interface above the transition temperature. Furthermore, because the SANS profile at 75 °C showed the first to third peaks of particle scattering, we fitted it with a particle scattering function as follows.

$$\frac{d\int}{d\int}(q) = \frac{w}{d_p}(\int_{b,p}\int\int_{b,s})^2 \int \frac{\int\int W_R(R)W_f(\int)V(R)\int^2(qR)dRd\int}{\int\int W_R(R)W_f(\int)V(R)dRd\int} \quad (1)$$

where $\Phi(qR)$, $W_R(R)$, and $W_\lambda(\lambda)$ are the isolated particle scattering factor, the particle-size distribution function, and the wavelength distribution function, respectively, as shown below.

$$-(qR) = \frac{3[sin(qR) - qR\cos(qR)]}{(qR)^3} \quad (2)$$

$$W_R(R) \sim \exp\left|\frac{(R \mid \overline{R})^2}{2\mid_R^2}\right| \quad (3)$$

$$W_\mid(\mid) \sim \exp\left|\frac{(\mid \mid \overline{\mid})^2}{2\mid_\mid^2}\right| \quad (4)$$

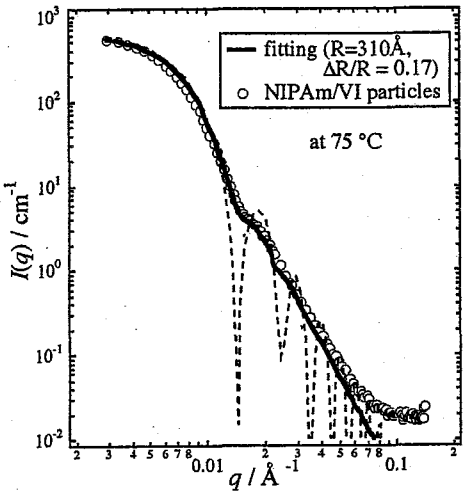

Fig. 4 Fitting result of SANS profile for NIPAm/VI gel particles at 75 °C

Fig. 4 shows the fitting result of SANS profiles for NIPA/VI gel particles at 75 °C. The result shows that the gel particles have 330 Å of radius and 17 % of particle size distribution. It should be noted that the so-called phase separation peak at 0.02 Å^{-1} was not observed for these particles. As also shown in Fig. 3, the macroscopic bulk gel of NIPAm/VI copolymer showed a phase separation broad peak above the transition temperature. That is, gel particles producing no volume phase transition do not show a phase separation peak for SANS. This probably means that the particle size with a few hundreds nm order is not large enough to form phase separation in the particle.

REFERENCES

[1] Shibayama, M. et al. *J. Chem. Phys.* **1992**, 97, 6842.
[2] Ito, S. et al. *Langmuir* **1999**, 15, 4289.

研究テーマ：自己組織化を活用したブロック共重合体のラジカル重合の制御
表　題：中性子小角散乱法によるソープフリー乳化重合の観察
1-5-7

Small-angle Neutron Scattering Observation on Soap-Free Emulsion polymerization of poly (*N*-isopropylacrylamide)-*block*-poly (ethylene glycol)

R. Motokawa, T. Nakahira, M. Annaka[1], T. Hashimoto[2] and S. Koizumi[2]

Department of Materials Technology, Chiba University, Inage-ku, Chiba 263-8522
[1]*Department of Chemistry, Kyushu University, Fukuoka 812-8581*
[2]*Advanced Science Research Center, JAERI, Tokai, Ibaraki 319-1195*

A living ionic polymerization method ideally provides mono-dispersed and high molecular weight macromolecules. However it is difficult to obtain poly (*N*-isopropylacrylamide) (PNIPA) by the living anion polymerization method. This is because the amide group on *N*-isopropylacrylamide (NIPA) cannot be protected from anionic activation and from there a sub-polymerization process occurs to produce a branched polymer. To obtain the mono-dispersed linear polymer, there is a classical method of heterogeneous polymerization in a poor solvent, that is emulsion polymerization. It was reported that radical polymerization in the emulsion can provides the high molecular weight and mono-dispersed polymer. It is believed that the confined space of the emulsion strongly restricts bimolecular terminal reactions. Inclusion polymerization has a similar advantage to control radical.

We focus on the heterogeneous polymerization method as a nano-reaction vessel and aim to observe its polymerization process by small-angle neutron scattering (SANS) measurement. Along the interest, we designed a soap-free emulsion polymerization system to synthesize a new amphiphilic block copolymer of poly (*N*-isopropylacrylamide) - *block* - poly (ethylene glycol) (NE). PNIPA in water is famous for a distinct volume change due to dehydration at around 34°C. Utilizing the strong solvent-selectivity appearing above 34°C, the NE block copolymer forms a self-assembled micelle where radically activated PNIPA chains are packed in a core and the poly (ethylene glycol) (PEG) chains form corona.

We performed small-angle neutron scattering (SANS) measurements at research reactor JRR-3 of JAERI, at Tokai. We employed two SANS spectrometers of pinhole and double crystal Bonse-Hart types named SANS-J and PNO, respectively. SANS-J covers a q-range of $0.03 \leq q \leq 1$ nm^{-1} and the incident neutron of $\lambda = 0.65nm(\Delta\lambda/\lambda = 13\%)$. NIPA monomer and PEG were dissolved in D_2O, then $Ce(NO_3)_6(NH_4)_2$ was added to the solution as a redox initiator. The polymerization solutions were filled in a quartz cell of 2 mm thickness, which gives transmittance of 70%. The sample temperature was controlled for polymerization temperature at 25°C, 34°C, 40°C, 50°C and 60°C. Then, we polymerize the NE block copolymer under the neutron beam. The double crystal spectrometer PNO is able to cover a q-region of ultra small-angle neutron scattering (USANS) of $10^{-4} \leq q \leq 10^{-2}$nm^{-1}, λ=0.2 nm. The sample specimens were prepared the same as SANS-J.

Figure 1 shows the q-profiles for end polymerization products of different polymerization temperatures. In the temperature range above 34°C, we observed the asymptotic q-behavior, $I(q) \sim q^{-4}$, originating from the interfacial structure of aggregated emulsion. In the q-profiles, the crossovers of asymptotic q-behaviors are clearly seen as indicated by arrows of $q=1/\xi$. These values of ξ reflect micelle size and become smaller as polymerization temperature increase. We consider that the PNIPA core strongly aggregates and dehydrates toward 60°C. As polymerization temperature increases, we obtain smaller molecular weight, M_n, of end products (NE) and molecular weight distribution, M_w/M_n, become relatively narrow distributions between 1.4 and 1.6. It seems quiet probable that the value of M_n and M_w/M_n has a connection with micelle structure. On the other hand, we observed Ornstein-Zernike type scattering at 25°C, which indicates that polymerization proceeds in the homogeneous solution system and molecular weight distributions of end products (NE) are broader $M_w/M_n \sim 2.5$.

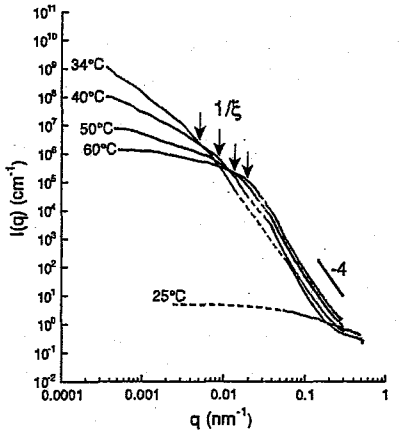

Figure 1: SANS profiles were obtained for end polymerization mixture at different polymerization temperature, 25°C, 34°C, 40°C, 50°C and 60°C.

原子炉：JRR-3　　装置：SANS-J(C3-2)　　分野：中性子散乱（高分子）

研究テーマ:ゲスト成分が誘起する界面活性剤／水系の秩序-秩序転移
表題:ゲスト成分の添加によるラメラ膜間相互作用の変調

1-5-8 Inter-Lamellar Interaction Modulated by Addition of Guest Components

M. Imai, R. Mawatari, K. Nakaya and S. Komura*

Department of Physics, Ochanomizu University2-1-1 Otsuka, Bunkyo, Tokyo 112-0012, Japan
** Department of Chemistry, Faculty of Science, Tokyo Metropolitan University*
Minami-Osawa, Hachioji 192-0397, Japan

The complex systems consisting of surfactant membranes and polymers or colloidal particles are widely recognized in the fields of biological membranes, drug carrier systems, lubricants, food, etc. and have acquired great interest from scientific and industrial points of view. The systems show characteristic phase behavior as a result of modification of inter-membrane interaction induced by the guest components. We followed the inter-membrane interaction by means of SANS-U (C1-2) and NSE (C2-2) instruments at JRR3M in JAERI (Tokai).

Figure 1 shows the change of SANS profiles with addition of (a) neutral polymer (polyethylene oxide) and (b) hard-sphere colloidal particle into the lamellar phase of nonionic surfactant $C_{12}E_5$/water system. Unfortunately, there is no visible Bragg peak in the SANS profile of dilute surfactant (Φ_{C12E5}=0.045) sample without guest species, because of the large membrane fluctuations. By the addition of PEO chains the scattering functions keep the initial profile until ρ_{PEO}~0.03 % and then the scattering intensity at low q region increases with increase of ρ_{PEO}, which is due to the phase separation. On the other hand, the addition of colloidal particles brings the sharpening of the first Bragg peak and even the emergence of the second harmonic. Thus the inter-lamellar interactions induced by the addition of the guest components strongly depends on the nature of the guest species.

In the case of surfactant lamellar + polymer system, the confined polymer chains prefer large space between the lamellar layers. This results in the decrease of the layer compression modulus and brings lamellar-lamellar phase separation due to the conservation of surfactant layer. On the other hand, the spherical colloidal particles confined between the flexible lamellar membranes suppress lamellar fluctuations and bring a repulsive inter-lamellar interaction. The behavior of lamellar layer containing colloidal particles is well described by the entropical repulsive inter-lamellar interaction driven by the steric hindrance.

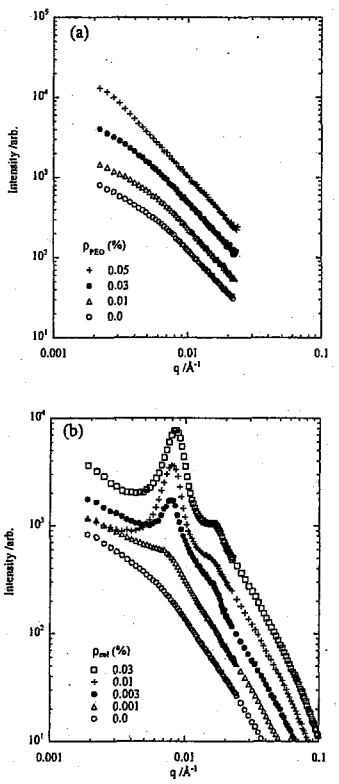

Fig. 1 SANS profiles of lamellar phase confining guest components, PEO (a) and colloidal particle (b), at constant surfactant volume fraction Φ_{C12E5}=0.045 with varying the guest components fraction.

使用施設:JRR-3M, 装置:SANS-U(C1-2), NSE(C2-2) 分野 Softmatter

研究テーマ：リビングラジカル重合法を用いた高分子合成過程の小角中性子散乱法によるその場観察
表　題：RAFT 重合によるポリスチレン合成過程の小角中性子散乱法によるその場観察
1-5-9

Small-angle Neutron Scattering Study on Living Radical polymerization with Reversible-Additon-Fragmentation-chain-Transfer (RAFT polymerization) Process of Styrene

Naosuke Mukawa, Ryuhei Motokawa[2], Mikihito Takenaka, Takeji Hashimoto and Satoshi Koizumi[1]

Graduate School of Engineering, Kyoto University, Kyoto 615-8510, Japan
[1]*Advanced Science Researchi Center, JAERI, Tokai-mura, Ibaraki 319-1195, Japan*
[2]*Department of Materials Technology, Chiba University, Inage-ku, Chiba 263-8522, Japan*

Living radical polymerization has recently emerged as one of the more effective technique for a preparation of well-defined polymer-structures by controlling molecular weight, molecular weight distribution and tailored architecture. There are several approaches have been reported and we paticularly aim at a process of reversible addition-fragmentation chain transfer(RAFT process). The approach utilizes readily available thiocarbonylthio compounds as chain transfer agents (RAFT agents) to confer living character to the polymerization. We expected that there are any structures or behaivors controll the molecular weight and molecular weight distribution during RAFT polymerization. So we investigated polymerization process of polystyrene with RAFT by using time-resolved SANS measurement.

SANS-J instrument at Japan Atomic Energy Reserch Institute(JAERI) JRR-3M research reactor was used for this study with neutron wavelength of 0.65nm. The polymerization of d6-styrene monomer was performed with benzene as solvent and 2,2'-Azobis-isobutyronitrile (AIBN) as initiator and 1-phenylethyl phenyldithioacetate (1-PEPDTA;Figure 1) as RAFT reagent at 60 °C in quartz cell of 2mm thickness. The final polymer concentretion was 50wt% and the molecular weight of the resulting polystyrene was about 20,000.

Figure 2 shows the time change in the scattering intensity after the onset of initiation. The polymerization process of styrene can be divided into the following two regions: (i) In region I or time t $\leq$ 600 min, the scattering intensity increased with time at all observed q region, which reflects the progress of the polymerization. Moreover, the relatively steep slope appears at q $\leq$ 0.3 nm-1 in the late stage of Region I, indicating that the heterogeneity is also formed due to the aggregation of the end functional group of RAFT in polymers. The fact of the formation of the heterogeneity agrees with the observation of the increases in turbidity of the samples at 420 min. (ii) In region II or t $\geq$ 600 min, the intensity at q $\geq$ 0.3 nm-1 hardly changed while the intensity decreases with time at q $\geq$ 0.3 nm-1 and then the power law behaivors of q^{-4} , which reflects the domain structure with sharp interface appears at 1200min. This change indicating that the heterogeneity have coarsened with time and that the sharp interface have developed in the later stage of the region II.

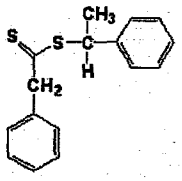

Figure 1: 1-PEPDTA.

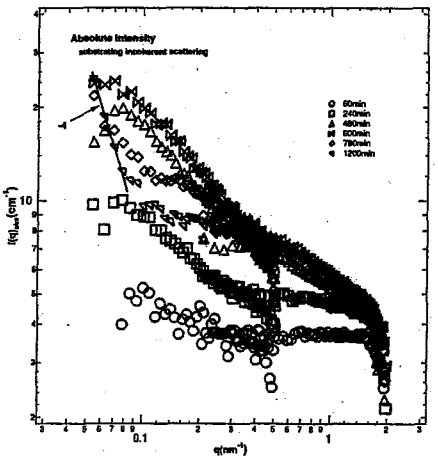

Figure 2: SANS profiles were obtained for in-situ observation of d6-polystyrene polymerization process at 60 ℃.

原子炉：JRR-3　　装置：SANS-J(C3-2)　　分野：中性子散乱（高分子）

研究テーマ:PNIPA 水溶液およびハイドロゲルの圧力誘起相転移

1-5-10 PNIPA 水溶液およびハイドロゲルの圧力誘起相転移

Pressure-Induced Phase Transition of Poly(N-isopropyl acrylamide) Aqueous Solutions and Gels

K. Isono, S. Okabe, T. Karino, I. Nasimova, M. Shibayama

Institute for Solid State Physics, The University of Tokyo, 106-1 Shirakata, Tokai 319-1106, Japan

Poly(N-isopropyl acrylmide) (PNIPA) polymers are known to be environment-sensitive polymers. Upon a slight change of an environmental variable, such as temperature, solvent composition, or hydrostatic pressure, PNIPA gels undergo either a swelling or shrinking transition. The pressure-sensitivity is ascribed to non-zero volume change of mixing, which is sensitive to the hydrostatic pressure. At low pressures and temperatures, PNIPA solutions and gels are in one phase, while they undergo phase separation at high temperatures and pressures. The phase diagram is a parabolic function with a maximum at a certain pressure $P = P_c$ in the pressure-temperature (P-T) plane. The P-T phase diagrams of 690 mM PNIPA solution and gel are shown in Figure 1.

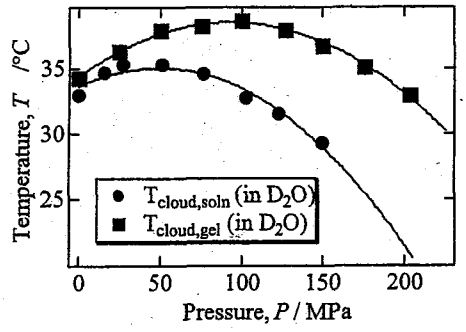

Figure 1: Phase diagram of 690 mM PNIPA solution and gel. Solid lines are drawn by the curve-fitting with a parabolic function.

The critical pressures, P_c, and temperatures, T_c, are (P_c, T_c) = (48.2 MPa, 35.3 °C) and (93.0 MPa, 38.6 °C) respectively for the solution and the gel.

The Small-angle neutron scattering (SANS) technique was used to investigate the structure changes that occurs in the system with pressurizing and consider the role of cross-links in the structure factor of polymer gels.

In general, the scattering intensity for polymer solutions in the semidilute regime is given by Lorentzian (or Ornstein-Zernike) function, i.e.

$$I(q) = \frac{I(0)}{1+\xi^2 q^2}, \qquad (1)$$

where ξ is a correlation length.

If a polymer solution is cross-linked, $I(q)$ is perturbed. According to Panyukov and Rabin [1], the structure factor, $S(q)$ are given by sum of correlators of the thermal fluctuations $G(q)$ and of the static density inhomogeneities $S(q)$

$$S(q) = G(q) + C(q) = \frac{g_q}{1+wg_q} + \frac{\nu_q}{(1+wg_q)^2} \qquad (2)$$

where g_q, ν_q and w are functions depending on interaction parameter, χ, average number of monomers between the cross-links, N_X, and polymer volume fraction at sample preparation, ϕ_0, and observation, ϕ. In this investigation as-prepared polymer gels, i.e., gels obtained directly after polymerization without further treatment, are studied. For as-prepared gels away from their critical saturation threshold, the following equation can be obtained by substituting $\phi = \phi_0$

$$S_q \cong \frac{S_L(0)}{1+\xi^2 q^2} + \frac{S_{SL}(0)}{(1+\xi^2 q^2)^2}. \qquad (3)$$

Therefore, the scattering function for as-prepared polymer gels is given by a sum

使用施設:JRR-3M, 装置:SANS-U(C1-2), 分野 Softmatter

of Lorentz (L) and squared-Lorentz (SL) functions.

Pressure-dependent SANS experiments were carried out with high-pressure cell at SANS-U with 7 Å of incident neutron beam. The q range was 0.01-0.08 $Å^{-1}$. The pressure was scanned at given temperatures.

Figure 2 shows the $I(q)$ for 690 mM PNIPA solutions in D_2O at 32 °C. $I(q)$ is a monotonically decreasing function of q, but it increase by increasing pressure, P. The solid lines are the fit with eq. 1, i.e. L function. The fitting is quite successful. This means that PNIPA solutions can be described as semidilute polymer solutions.

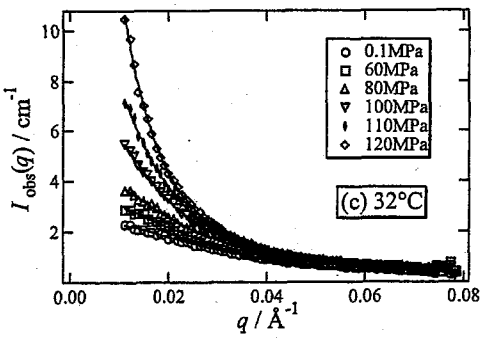

Figure 2: SANS intensity, $I(q)$, for PNIPA solution obtained at various pressures at T = 32 °C. The solid lines are fits with a Lorentz function.

The correlation lengths, ξ, were estimated from fitting results for various temperatures and pressures. It was found that ξ increased with increasing P. However, each of the ξ curves showed a cusp at high pressures. This cusp indicates the pressure at which a phase separation takes place before divergence of ξ at spinodal i.e. bimodal points. It was found that the spinodal curve, T_{sp}, seems to merge the bimodal curve, T_b, at the critical point.

Figure 3 shows Kratky plots, i.e., $q^2I(q)$ vs q, with pressure for the gel at T = 34.2 °C. It is very clear from this plot that the non-Lorentzian behavior is observed for the gel at high pressures (P > 100 MPa). Hence, the sum of L and SL functions was used for the fitting according to the eq. 3. It was also found that at T = 20 °C at low pressures (0.1 < P < 120 MPa) scattering profiles had only the L component, while the SL component became significant with increasing T and/or P. Figure 4. shows the fraction of the SL component, X_{SL} as a function of pressure for T = 20, 30 and 34.2 °C. At T = 34.2 °C, the major component is the SL i.e. the static inhomogeneity. Thus it can be concluded that inhomogeneites usually observed for polymer gel do not appear in the as-prepared gels observed at the same conditions. However, they became dominant near the spinodal. [2]

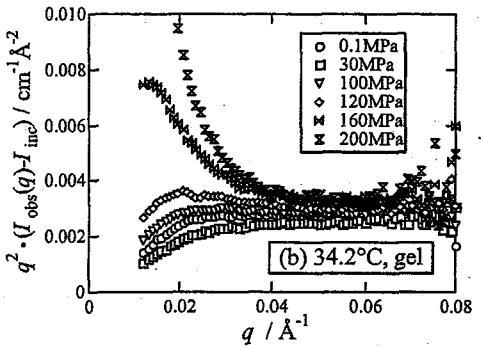

Figure 3: Kratky plot for PNIPA gel obtained at various pressures at T = 34.2 °C.

Figure 4: Pressure dependence of the fraction of SL component variation, X_{SL}, for PNIPA gels observed at various temperatures.

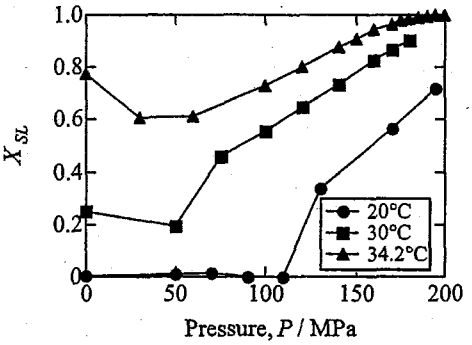

References

[1] Panyukov, S.; Rabin, Y. *Phys. Rep.* 1996, 269, 1

[2] Shibayama, M.; Isono, K.; Okabe, S.; Karino, T.; Nagao, M.

研究テーマ：高分子溶液のダイナミクスに関する研究
表　題：高分子準希薄溶液の核生成成長における粘弾性効果
1-5-11

Viscoelastic effects on the nucleation and growth in semi-dilute polymer solution

M.TAKENAKA, N.IWASE , T.HASHIMOTO and S.KOIZUMI[1]

Department of Polymer Chemistry, Graduate School of Engineering , Kyoto University, Kyoto 606-8501
[1]Advanced Science Research Center, JAERI, Tokai, Ibaraki 319-1195

Recently, it has been found that the dynamical assymmetry between constituent components in a mixture causes the coupling between stress and diffusion during phase separation processes of mixture due to the asymmetric stress division. .This coupling is called "viscoelasitc effects" and has been found to causes shear-induced phase separations in polymer sollution and non exponential decay in dynamic scattering near equilibrium. The strength of the effects of viscoelacity is characterized by the viscoelastic length ξ_{ve} defined by

$\xi_{ve} = (\frac{D\eta_0}{3K_{os}})^{0.5}$ (1),

where D, η_0, and K_{os} are, respectively, the interdiffusion coefficient, the zero-shear viscocity, and the osmotic compressibility. In order to estimate ξ_{ve}, we need to obtain the value of K_{os}. Thus in this study we measured the scattering function of the polymer solution and estimates K_{os}. We used deutrated polystyrene (dPS,weight average molecular weight $=5.0 \times 10^6$)/Diethyl Malonate(DEM) sample.We used three samples, dPS/DEM=2/96, 4/96, 6/94 (wt/wt). The SANS experiment were performed at SANS-J. Figure 1 shows the temperature dependence of the scatterd intensity I(q) of dPS/DEM=4/96. We fitted the scattered intensity, I(q), with the structure factor calculated with random phase approximation, and estimated the interaction parameter χ and K_{os} of dPS/DEM polymer solutions. Figure 2 shows the temperature dependence of χ and K_{os}. χ decreased with temperature while K_{os} increased with temperature. The temperature dependence of χ can be expressed by ,

$\chi = A(\phi) + \frac{B(\phi)}{T}$ (2)

where T is absolute temperature and $A(\phi)$ and $B(\phi)$ depend on ϕ_{PS}. Next, we estimated spinodal temperature with the obtained T dependence of χ. The interaction parameter at Spinodal point, χ_s , can be calculated by ,

$\chi_s = \frac{v_0}{2}(1\phi_{dPS}v_{dPS}\langle z_{dPS}\rangle + \frac{1}{\phi_{DEM}v_{DEM}})$ (3)

where ϕ_i is volume fraction, v_i is the molar volume, $\langle z_i \rangle$ is weight-average degrees of polymerization for ith components, and v_0 denote reference molar volume of the solution. We estimated the spinodal tempetrature by substituting χ_s into eq.(2). Figure 3 shows the spinodal curve of dPS/DEM, indicating that the dPS/DEM solution has an Upper Critical Soution Temperature type phase diagram.

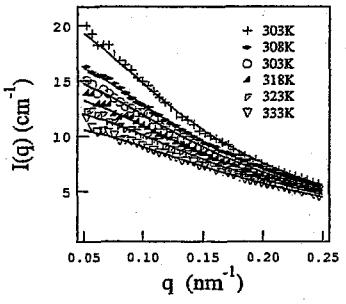

Figure 1: SANS profiles for dPS/DEM=4/96 (wt/wt).

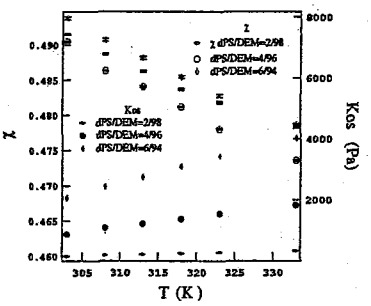

Figure 2: The temperature-dependence of χ and K_{os} of dPS/DEM solutions.

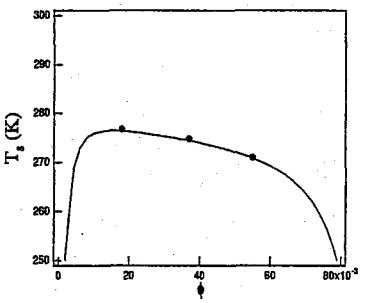

Figure 3: Spinodal Curve plot as a function of volume fraction of polystyrene ϕ.

原子炉：JRR-3　　装置：SANS-J(C3-2)　　分野：中性子散乱（高分子）

研究テーマ：トポロジカルゲルのゾルーゲル転移と不均一性解析

1-5-12 トポロジカルゲルのゾルーゲル転移と不均一性解析

Small Angle Neuron Scattering from Slide-Ring Gels under Deformed State

T. Karino[1,2], M. Shibayama[1,2], Y. Okumura[1,3] T. Kataoka[3] and K. Ito[1,3]

[1] *CREST, JST*

[2] *Institute for Solid State Physics, University of Tokyo, 106-1 Shirakata, Tokai, 319-1106*

[3] *Graduate School of Frontier Sciences, University of Tokyo, Kashiwa, Chiba, 277-8561*

Polymer gels are made of polymer networks by connecting linear polymer chains. In most cases, cross-links are introduced randomly via covalent bond and are permanent. As a result, polymer gels have spatial inhomogeneities[1].

Recently, polyrotaxane gels, consisting of α–cyclodextrin (CD) and poly(ethylene glycol) (PEG), were synthesized by Okumura et al[2]. Cross-links of polyrotaxane gels can move freely along the polymer chains. This indicates that the gel is allowed to reduce their spatial inhomogeneities by sliding cross-links. We call this type of gel a slide-ring gel (SR gel).

We investigated specific features of SR gels by comparing them with conventional chemical gels[3], and demonstrated sliding capability of cross-links under uniaxial deformation. In this work, limitations of the performance of sliding were evaluated by small angle neutron scattering under uniaxial deformationas a function of cross-links density.

Fig.1 shows the two-dimensional scattering intensity functions of a SR gel at C_x=0.6wt%. The stretching direction was horizontal. In undeformed state ($\lambda\sim1.0$), the scattering function is isotropic. By stretching ($\lambda\sim1.8$), however, the scattering function shows the so-called normal butterfly pattern, which is a prolate isointensity pattern in the direction perpendicular to the stretching direction. This means that the cross-links slide along the polymer chain so as to reduce spatial inhomogeneities. As a result, the scattering functions show a normal butterfly patterns in $C_x > 1.0$wt%.

Fig.2 shows the two-dimensional scattering intensity functions of SR gel at C_x=2.0wt%. At $\lambda\sim1.8$, the scattering function shows an abnormal butterfly pattern, i.e., prolate patterns parallel to the stretching direction. Conventional chemical gels show an abnormal butterfly pattern. Such abnormal butterfly patterns were observed at $C_x > 2.0$wt%. It is concluded that an increase of cross-links density degrades the mobility of cross-links, resulting in an increase in the spatial inhomogeneities by stretching.

These results indicate that cross-links density strongly influences the mobility of cross-links. Thus, a normal–abnormal butterfly pattern transition was observed.

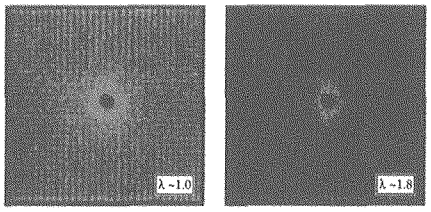

Fig. 1. Butterfly pattern of slide-ring gel in low cross-links density(C_x =0.6wt%).

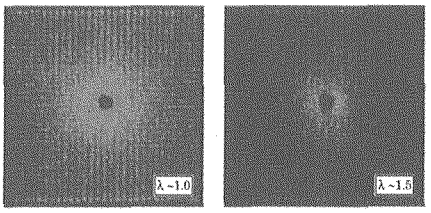

Fig. 2. Butterfly pattern of slide-ring gel in high cross-links density(C_x =2.0wt%).

References

[1] Shibayama, M. *Macromol. Chem. Phys.* **1998**, *199*, 1.

[2] Okumura, Y. ; Ito, K. *Adv. Mater.* **2001**, *13*, 485.

[3] Karino, T. ; Shibayama, M. ; Okumura, Y. ; Ito, K. *Macromolecules* accepted.

使用施設：JRR-3M, 装置： C1-2 (SANS-U) , 分野： 6. Softmatter

研究テーマ：中性子散乱によるソフトマターの構造と機能の研究
表　題：ニオブ酸化物ナノシートの中性子散乱による観察

1-5-13

Observation of Niobates Nanosheets in Aqueous Solutions by Neutron Scattering

D. Yamaguchi[1], N. Miyamoto[2], S. Koizumi[1], T. Nakato[3,2], and T. Hashimoto[4,1]

[1] *Advanced Science Research Center, JAERI, Tokai, Ibaraki 319-1195*
[2] *PRESTO, Japan Science and Technology Corporation*
[3] *Graduate School of Bio-Applications and Systems Engineering (BASE), Tokyo University of Agriculture and Technology, 2-24-16 Naka-cho, Koganei-shi, Tokyo 184-8588*
[4] *Department of Polymer Chemistry, Graduate School of Engineering, Kyoto University, Katsura, Kyoto 615-8510*

Exfoliation of inorganic layered materials into their unit layers has been paid attention because of their properties to form nanohybrids with other molecules. Among these layered materials, the layered niobates such as $K_4Nb_6O_{17}$ have high potential for application since they present excellent phptoactive properties. Recently it is shown that the exfoliated nanosheets of $K_4Nb_6O_{17}$ exhibit peculiar liquid crystalline behavior[1]. In this study the structure of exfoliated $K_4Nb_6O_{17}$ nanosheets in the aqueous solutions were investigated by small-angle and ultra-small-angle neutron scattering spectrometers (SANS-J and PNO).

An interesting feature of $K_4Nb_6O_{17}$ nanosheets is a variety of lateral sizes, which is controlled by breaking large single crystal of $K_4Nb_6O_{17}$ with using ultrasonication, while the fixed thickness of 1.8 nm[1]. The liquid crystallinity is dependent on the lateral size and concentration of the nanosheets, that is, at higher concentration or larger lateral size of nanosheets, the solution exhibits liquid crystalline phase while at lower concentration or smaller lateral size, the solution is in the isotropic phase. However, a nonintuitive scattering behavior of lateral size dependence was observed on SANS measurement. That is, as the lateral size was decreased, the scattering peaks sharpened and the higher order scattering maxima came to appear, suggesting the degree of order increased.

Our speculation for this discrepant tendency between SANS observation and general phase behavior (above described) is following; The $K_4Nb_6O_{17}$ nanosheet has a specific bending modulus and the persistent length of the nanosheet is inversely proportional to the bending modulus. The nanosheets whose lateral sizes are bigger than the persistent length are naturally expected to be in bent (or crumpled) state. Therefore, in the case of nanosheets, whose lateral size is smaller than the persistent length and which are regarded as unbending and flat disk, they might form the liquid crystalline phase in which the distance between nanosheets are nearly constant at anywhere. While in the case of nanosheets which have extremely large lateral size compared to the persistent length, they might form the liquid crystalline phase where the intersheet distance is not constant but has a large distribution due to the crumple of each sheet.

To obtain further information about the structure

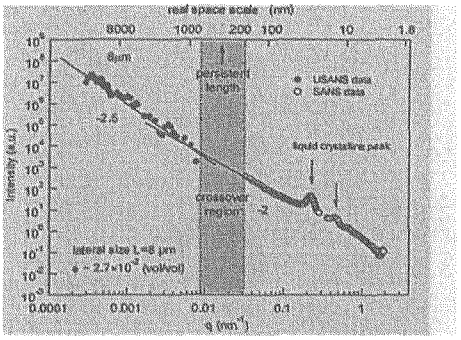

Figure 1: Combined SANS and USANS profiles for $K_4Nb_6O_{17}$ aqueous solution whose lateral size L=8μm and concentration ϕ=2.7×10^{-2} (vol/vol).

of nanosheets the ultra-small-angle neutron scattering (USANS) measurement was performed. Figure 1 show the combined data of SANS and USANS for the nanosheet solution of which lateral size is 8 μm. As we can see in Figure 1, the USANS profile of nanosheet does not have any characteristic peaks but show a monotonic power law scattering of which index is slightly smaller than -2 (ca. -2.5). Supposing that the value of index, -2.5 obtained by the power law scattering of USANS, corresponds to the mass fractal dimension, it is suggested that the nanosheets take neither perfectly flat shape (of which mass fractal dimension is -2) nor perfectly collapsed shape (of which mass fractal dimension is -3) but partially bent and/or crumpled shape[2]. Thus, the USANS data constructively support our speculation for nonintuitive lateral size dependence of SANS data. In the case of nanosheet whose lateral size is ca. 8μm, the persistent length is estimated to be hundreds of nm from the crossover q region, where the power law index changes from -2.5 to -2. We can regard the niobate nanosheet, i.e., the elementary layer of $K_4Nb_6O_{17}$ crystal, as a softmatter, even though it is an inorganic crystal.

References

1) Miyamoto, N.; Nakato, T. *J. Phys. Chem. B*, **2004**, *108*, 6152.
2) Abraham, F. F.; Nelson, D. R. *J. Phys. (France)*, **1990**, *51*, 2653.

原子炉：JRR-3　　装置：PNO(3G)　　分野：中性子散乱（高分子）

研究テーマ： 両親媒性分子膜の熱揺らぎに対する温度・圧力効果
表題： 両親媒性二分子膜の熱揺らぎに対する圧力効果

1-5-14 Pressure Effects on Thermal Fluctuations of Amphiphilic Bilayers

Y. Kawabata[1], M. Nagao[2], N. Yamada[3] and S. Okabe[2]
[1] *Tokyo Metropolitan University, Hachioji, 192-0397, Japan*
[2] *Institute for Solid State Physics, The University of Tokyo, Tokai, 319-1106*
[3] *Faculty of Integrated Arts and Sciences, Hiroshima Univ., Higashihiroshima, 739-8521*

Amphiphiles in water self-assemble to form various mesoscopic structures such as lamellar, micelle, hexagonal and so on. In a nonionic surfactant $C_{16}E_6$/water system, amphiphilic bilayers are formed (lyotropic liquid crystal) under a certain condition [1]. It is known that this lyotropic liquid crystal structure is changed by shear stress, temperature and so on. Pressure is also important thermodynamic parameter. However, pressure effects on the lyotropic liquid crystal structure have not been investigated.

In this study, we investigated the pressure effects on the static and dynamic structure of the lyotropic liquid crystal by means of small angle neutron scattering (SANS) and neutron spin echo (NSE).

The SANS experiments were carried out using the SANS-U spectrometer of JRR-3M, JAERI, Tokai. The camera distance was 2 m and the incident neutron wavelength λ was 4.7 Å. The momentum transfer Q ranged over $0.04 \leq Q \leq 0.15$ Å^{-1}. Pressure was changed from $0.1 \leq P \leq 140$ MPa with fixed at $T = 53$ °C, where the liquid crystal phase appears.

Figure 1 shows the pressure dependencies of the SANS profile at $T = 53$ °C. The bragg peak position Q_0 corresponding to the repeat distance between bilayers was out of the Q range ($Q_0 \approx 0.04$), because the used neutron wavelength is shorter than that of the usual setting ($\lambda = 7.0$ Å) due to the tilt angle of the neutron velocity selector (NVS). We found that the micellar phase is induced about at 110 MPa from the lamellar phase at ambient pressure, and that the repeat distance $d = 117$ Å in the lamellar phase at ambient pressure decreases to the half of that at $P = 140$ MPa ($d \approx 60$ Å). From an observation with the eyes, the phase induced at $P = 140$ MPa is 2-phase region, where

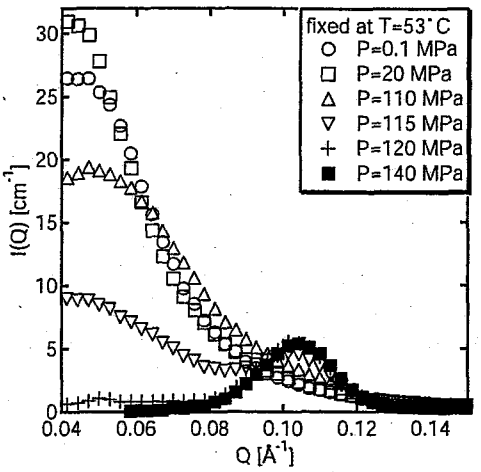

Fig. 1. Pressure dependencies of SANS profile at $T = 53$ C°. At $P = 90$ MPa, a lamellar phase is formed through the co-existence phase of micellar and lamellar phase.

the upper region of the sample is the lamellar phase and the lower region is water-rich phase. The neutron beam irradiated the upper region of the sample.

The tendency of the decrease of d is the same as that observed in the experiments under the shear stress. Under the shear stress, d decreases to the thickness of the bilayers [2]. It has been considered that the decrease of the repeat distance is due to the suppression of the thermal fluctuation of bilayers, which plays an role as the steric interaction between bilayers. Therefore, we tried to measure the thermal fluctuation of bilayers at high pressure by means of NSE.

The NSE experiments were performed at the ISSP-NSE spectrometer at JAERI. The wavelength of the incident neutron beam was 7.14 Å. The measured spatial and temporal regions are $0.04 \leq q \leq 0.14$ Å^{-1} and $0.15 \leq t \leq 15$ ns, respectively. Pressure was changed from 0.1 MPa to 82 MPa with fixed

使用施設：JRR-3M, 装置： C1-2 (SANS-U), C2-2 (NSE), 分野： 6. Softmatter

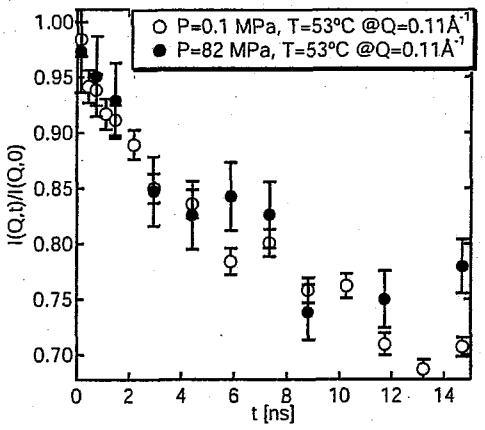

Fig. 2. The intermediate correlation functions at $P = 0.1$ and $P = 82$ MPa. The scattering vector Q is set to 0.11 $Å^{-1}$.

at $T = 53$ °C due to the limitation of the performance the high pressure cell.

Figure 2 shows the intermediate correlation functions at $P = 0.1$ and $P = 82$ MPa. This result indicates that the pressure effect is not remarkable in the time range to 15 ns and below 80 MPa.

References

[1] S. S. Funari *et al.*, *J. Phys. Chem*, **98**, 3015 (1994).

[2] T. Kato *et al.*, *Langmuir* to be published.

研究テーマ：中性子散乱によるソフトマターの構造と機能の研究
表　題：デンドリマーを鋳型として用いたパラジウム微粒子の合成過程の中性子小角散乱による研究

1-5-15

Preparation of Palladium Nanoparticles with Dendrimers As Observed by SANS

H. Tanaka, T. Hashimoto, H. Ito, K. Naka, Y. Chujo, and S. Koizumi[1]

Department of Polymer Chemistry, University of Kyoto, Kyoto 615-8510
[1]Advanced Science Research Center, JAERI, Tokai, Ibaraki 319-1195

It is well known that metal nanoparticles exhibit quantum mechanical properties, and which makes them promising materials for various kinds of applications in nanotechnology. The patterning of the metal nanoparticles into organized structures is quite essential to achieve useful properties for chemical, optical, magnetic, and electronic devices. One of the superior methodologies for controlling the organized structures involves the chemical cross-linking by organic ligands. Recently,Chujo et al. have found that by employing a cubic silsesquioxane[1)] or a polyamidoamine (PAMAM) dendrimer as such a cross-linker, it becomes attainable to organize palladium nanoparticles into spherical aggregates *via* self-organized templates in methanol solutions without any external force.

In this report, we focus on the structure formation mechanism of palladium nanoparticles prepared through alcoholic reduction of the mixture of palladium acetate in *N, N*-dimethylformamide and PAMAM dendrimer in methanol at 50 ℃, by means of *in-situ* SANS and SAXS measurements. SANS measurements were performed with SANS-J at the guide hall of the reactor JRR-3M in JAERI.

Figure 1 shows SANS and SAXS profiles obtained during the reduction process. The scattered intensity $I(q)$ is plotted as a function of scattering vector q defined by $q=(4\pi/\lambda)\sin(\theta/2)$, with θ and λ being the scattering angle and the wavelength of incident beam, respectively. It should be noted that SANS measurements cover relatively lower q region, $q<0.1\mathrm{nm}^{-1}$, on the other hand, SAXS cover higher q region, $q>0.1\mathrm{nm}^{-1}$. The scattering vector q can be expressed with characteristic length ξ, $q=2\pi/\xi$, therefore, SANS profiles can provide information on the structure with relatively larger size, ξ >60nm, and SAXS profiles provide rather smaller structure,ξ <60nm.

The time change of SANS and SAXS profiles show quite different features, that while SANS profiles show almost same tendency independent of the reaction time, where the form factor from assembly of dispersed spheres with average diameter of 80nm as shown by solid curve are clearly observed even from 20 minutes after preparing the solutions, SAXS profiles exhibit distinct change as reaction proceeds, where the scattered intensity gradually increase with time, indicating the formation of palladium nanoparticles of 5nm in average diameter as shown by dotted curve.

The experimental results described above are quite indicative of the formation mechanism of spherical aggregates. It can be schematically depicted in Figure 2. First, palladium ions and PAMAM dendrimers associated to form spherical domains with average diameter 80nm just after mixing of the two solutions due to attractive interactions between palladium ions and PAMAM dendrimers. Second, within such spherical domains, reductions of palladium ions were occurred, forming nanoparticles of 5nm in average diameter, during the course of which the spherical domains of 80nm diameter were maintained and served as templates for nanoparticle formation.

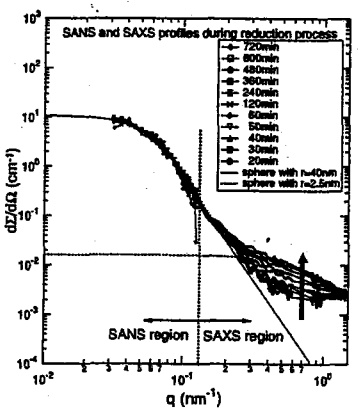

Figure 1: Time-resolved SANS and SAXS profiles during reduction process.

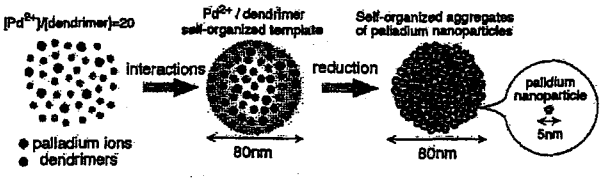

Figure 2: Schematic illustration of self-organizing process of palladium nanoparticles.

References

1) K. Naka, H. Ito, and Y. Chujo, *Nano. Lett.*, **2**, 1183 (2002)

原子炉：JRR-3　　装置：SANS-J(C3-2)　　分野：中性子散乱（高分子）

研究テーマ:せん断流動場下におけるポリエチレンの結晶化過程

1-5-16超高分子量成分を含むポリエチレンブレンドのシシカバブ構造解析

Structural Analysis of Elongated Polyethylene Blends with High Molecular Weight Components

G. Matsuba, T. Kanaya, Y. Ogino, S. Sakamoto, K. Nishida, and M. Shibayama*

*Institute for Chemical Research, Kyoto University, Gokasho, Uji, 611-0011 Japan; *Institute for Solid State Physics, The University of Tokyo, 106-1 Shirakata, Tokai, 319-1106 Japan*

Thorough knowledge of flow-induced crystallization in polymer melts is essential to control industrial processing methods such as extrusion, injection, and blow molding and resultant product properties. It is widely accepted that the sheared polymer melts exhibit an increased rate of crystallization and a different morphology, that is the so-called "shish-kebab" structure, compared with those of a quiescent melt. The shish-kebab structures can be observed in polyethylene [1], isotactic polypropylene [2], 6-6 nylon [3] and so. In this report, we studied the structure of elongated polyethylene blends using small angle neutron scattering (SANS) technique.

In this study, the components in blends are ultra-high molecular weight protonated polyethylene (hPE) with weight average molecular weight (M_w) of 2000000 and deuterated polyethylene (dPE) with M_w of 200000. The blend of hPE and dPE with the hPE fraction of 1 wt % was prepared with the co-precipitation method. SANS measurements were carried out with SANS-U spectrometer (C1-2) at JRR-3M reactor in Japan Atomic Energy Research Institute (JAERI), Tokai, Japan. The wavelength of neutron is 7 Å and the sample -to-detector distance was 4000 and 8000 mm.

Figure 1 shows the 2D SANS and small angle x-ray scattering (SAXS) images of elongated blend with hPE and dPE at drawing ratio (DR) of 6. The elongational direction is vertical. An equatorial streak exists in the 2D SANS image, while no streaks exist in the 2D SAXS image. These results suggest there exist small amount of fibrils or shishs in the blend. In addition, it is considered that the shish structure is mainly composed of the ultra-high molecular weight component because the scattering contrast between hPE and dPE is quite high, confirming that the deuterium labeling method is valuable in this experiment. Meanwhile, the droplet-like spots parallel to the elongational direction is assigned to long spacing of the kebab structure or the oriented lamella stacks.

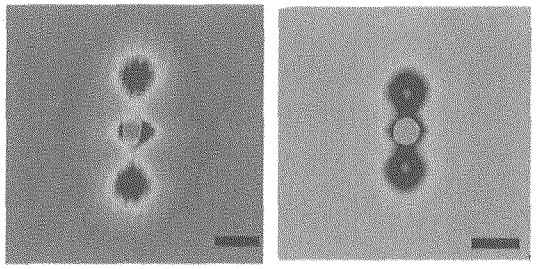

Figure 1: 2D SANS (left) and SAXS (right) images for PE blend with drawing ratio of 6. The scale bar is q = 0.02 Å^{-1}. The elongational direction is vertical.

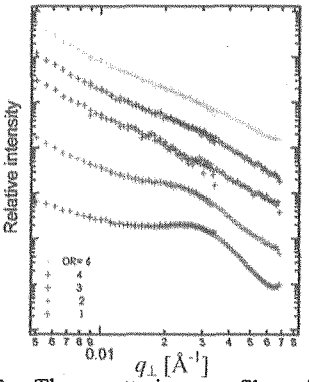

Figure 2: The scattering profiles, in log-log presentation perpendicular to the elongational direction for SANS measurements as a function of the drawing ratio.

使用施設:JRR-3M, 装置:SANS-U(C1-2), 分野 Softmatter

From the 2D SANS images, the intensity profiles along the equatorial were extracted as a function of the scattering vector, $q_\perp$ ($=4\pi\sin\theta/\lambda$), perpendicular to the elongational direction. Figure 2 shows the SANS intensity profiles perpendicular to the elongational direction at several DR, and each profile was shifted along the intensity axis for convenience. The scattering profiles in Figure 2 have some information about the shish structure.

We assumed that the equatorial streaks are due to the shish structure and the shape is represented by a cylinder several micron high. The scattering function of the cylinder is given by

$$I(q_\perp) = \int \frac{\sin^2(q_\perp H\cos\theta)}{{q_\perp}^2 H^2\cos^2\theta} \frac{4J_1^2(q_\perp R\sin\theta)}{{q_\perp}^2 R^2\sin^2\theta} \sin\theta d\theta$$

where $q_\perp$, R and $2H$ are scattering vector in the vertical direction to the long axis, radius and height of cylinder, respectively, and $J_1(x)$ is the first Bessel function. We calculated this equation for cylinders with radius 1 Å, 10 Å, 22 Å, 35 Å and 50 Å assuming that its height is 7.5 μm and compared with the observed scattering function after convoluting with the resolution function of SANS-U spectrometer. The result is shown in Figure 3, showing the best agreement with the 22 Å case for the drawing ratio of 6. This result indicates that the cylinder includes about 40 polyethylene chains. The radius of cylinder evaluated is listed in Table 1 as a function of DR. The radius of shish structure decreases with increasing the DR.

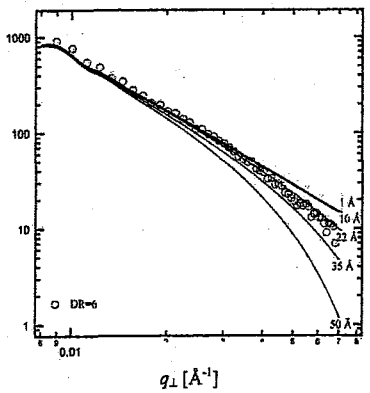

Figure 3: The observed SANS intensity for drawing ratio of 6 (open circle) and the calculated curves for a cylinder 7.5 μm long and several radius of 1 Å, 10 Å, 22 Å, 35 Å and 50 Å

Figure 4 shows the profiles taken along the meridian from 2D SANS image (Figure 1) as a function of the scattering vector, $q_{//}$, parallel to the elongational direction. Each profile was shifted along the intensity axis for convenience. The peak corresponding to the long period spacing around $q_{//}$ = 0.023 Å^{-1} (about 270 Å) at DR =1 shifts toward smaller $q_{//}$ with DR. The long spacing period increases with DR. For the correlation function calculated from Figure 4, the increasing long period is caused by inter-lamellae amorphous layers stretched out.

Drawing Ratio	Radius [Å]
2	35
4	30
5	25
6	22

Table 1: The drawing ratio dependence of the diameter for cylinder.

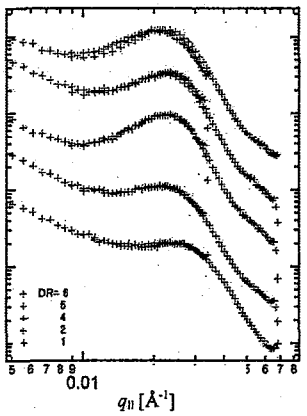

Figure 4: The SANS scattering profiles, in log-log presentation, parallel to the elongational direction as a function of the drawing ratio.

References

[1] A.J. Pennings et al, Kolloid Z.Z. Polym., **237** (1969) 21.
[2] R.H.Sorani et al., Physica A, **304** (2002) 145.
[3] B.S.Hsiao et al., J. Appl. Cryst., **30** (1997) 1084.

研究テーマ：中性子散乱によるソフトマターの構造と機能の研究
表　題：酵素触媒重合によるセルロースの人工合成過程の中性子小角散乱によるその場観察

1-5-17

In-situ SANS Observation of Enzymatic Polymerization of Artificial Cellulose

H. Tanaka, T. Hashimoto, K. Kurosaki[1], M. Ohmae[1], S. Kobayashi[1], and S. Koizumi[2]

Department of Polymer Chemistry, University of Kyoto, Kyoto 615-8510
[1]*Department of Materials Chemistry, Kyoto University, Kyoto 615-8510*
[2]*Advanced Science Research Center, JAERI, Tokai, Ibaraki 319-1195*

Enzymatic polymerization was first reported by Kobayashi et al. in 1991, as the first successful way of synthesizing artificial cellulose *via* a nonbiosynthetic pathway [1],utilizing β-cellobiosyl fluoride as an activated subtrate monomer, and the cellulase, which had been generally used as an enzyme for hydrolysis reaction of cellulose, as rather polymerization catalyst, and an organic (acetonitrile) /aqueous (acetate buffer) solvent system (Figure 1). It was found that this method could provide highly regio- and stereo-controlled cellulose with a degree of polymerization of about 22 glucose units. However, detailed information about the mechanism of enzymatic polymerization has not been fully understood yet.

In this study, we have investigated the self-assembling process of cellulose synthesized *via* enzymatic polymerization *in situ* to elucidate the mechanism of this reaction, by means of time-resolved Small-Angle Neutron Scattering (SANS) measurement with SANS-J at JAERI, JRR-3M research reactor.

Figure 2 shows time-evolution of SANS profiles obtained in the course of polymerization process. Here the scattered intensity I(q) is double logarithmically plotted as a function of the magnitude of the scattering vector q, defined by $q=(4\pi/\lambda)\sin(\theta/2)$,where λ and θ represent the wavelength and the scattering angle, respectively. The SANS profiles were corrected for the background scattering and the transmittance for the further analysis.

It should be noted that before polymerization the scattering profile for enzyme solution obeys Porod law or q^{-4} especially at lower q region, q<0.1nm^{-1} as indicated by the slope q^{-4} in the figure , which reflects a sharp interface composed of the enzyme associations with more than several hundreds of nanometers in size. On the other hand, once polymerization reaction has started, throughout the reaction process, the scattered intensity shows the power law of $q^{-\alpha}$ at almost all q range observed in this experiment, with α being between 3.0 and 4.0 , indicating that cellulose synthesized form aggregated structure with self-similar surface having surface fractal dimension D_s given by $D_s=6-\alpha$.

It is also worth noting that, as polymerization proceeds, α tends to decrease from 4.0 to 3.7 and finally approach toward the finite value of 3.7 as shown in the figure, therefore, surface fractal dimension D_s increase from 2.0 toward 2.3. This means that, just after polymerization has started, first aggregated structures with sharp interface are formed, and as polymerization proceeds, the surface become rougher due to the successive formation of cellulose around the structure.

These results suggest that the enzymatic polymerization is expected to occur on or near the surface of the self-assembled enzymes with a sharp interface, and cellulose thus synthesized maintain its position near the surface, and then, together with newly synthesized cellulose, formed the aggregated structure with rougher surface charcterized by fractal dimension D_s around the enzyme associations.

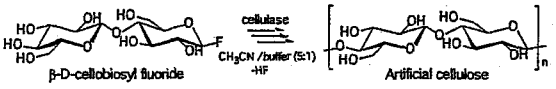

Figure 1: Scheme for enzymatic polymerization of cellulose

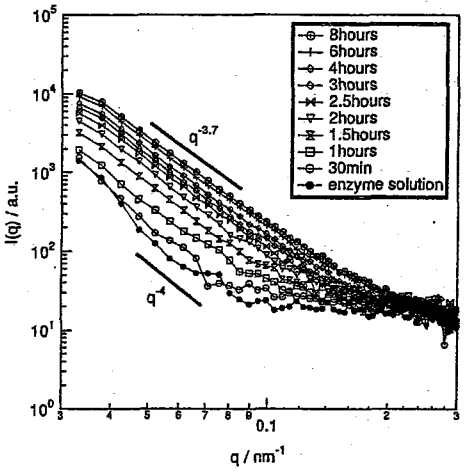

Figure 2: Time evolution of SANS profiles obtained during enzymatic polymerization.

References

1) S. Kobayashi, K. Kashiwa, T. Kawasaki, S. Shoda, *J. Am. Chem. Soc.*, **113**, 3079 (1991)

原子炉：JRR-3　　装置：SANS-J(C3-2)　　分野：中性子散乱（高分子）

研究テーマ:ブロックコポリマーミセルの自己組織化挙動の解明
表題:ブロックコポリマーミセルのコア架橋反応により合成されたナノ微粒子の構造解析

1-5-18 Structural Analysis of Nanoparticles Prepared by Core-Cross-Linked Block Copolymer Micelles

K. Matsumoto, H. Hasegawa, and H. Matsuoka

Department of Polymer Chemistry, Graduate School of Engineering, Kyoto University, Katsura, Kyoto, 615-8510, Japan

Block copolymers self-assemble to form micelles in solvents selective for one of the blocks. The core of the micelle consists of an insoluble block, and the shell consists of both a soluble block and the solvent [1]. Such micelle formation has attracted much attention for industrial and biomedical applications [2, 3]. Compared to the micelles of low molecular weight surfactants, the block copolymer micelles are generally larger, ranging from several nanometers to tens of nanometers. Additionally, they are more stable due to their slow exchange between associated and non-associated molecules. These properties are quite advantageous in the constructing nano-scale materials. By cross-linking the core of the micelle, we can obtain nanoparticles with shell-forming polymers grafted from the particle surface.

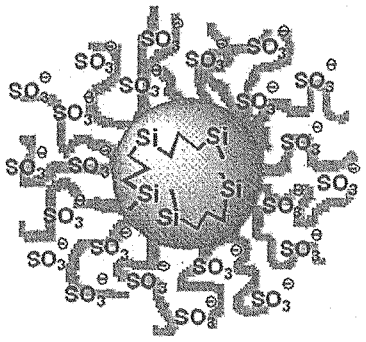

Figure 1: Image of sodium poly(styrenesulfonate)-grafted nanopaticles

We have synthesized sodium poly(styrenesulfonate)-grafted polymer nanoparticles (Figure 1) starting from poly(*p*-((1-methyl)silacyclobutyl)styrene-*block*-poly(neopentyl *p*-styrenesulfonate) (polySBS-*b*-polySSPen) (Figure 2) [4,5]. In this study we examined the structure of the block copolymer micelles in organic solvent by small-angle neutron scattering (SANS).

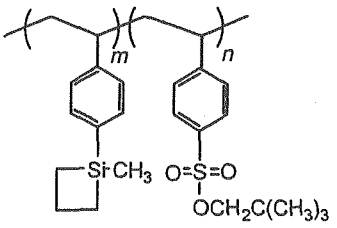

Figure 2: Chemical structure of polySBS-*b*-polySSPen

An acetone-d_6 solution (1wt%) of SBS_{113}-*b*-$SSPen_{134}$ was prepared, and SANS of the sample was measured by SANS-U of JRR-3M in JAERAI. Figure 3 shows an example of SANS profiles. A strong scattering at small angle regions clearly indicates an existence of block copolymer micelles. The data were analyzed by model fitting. The solid line is a calculated profile assuming core-shell sphere model whose core consists of polySBS and the shell consists of polySSPen shell and acetone-d_6. The calculated profile fitted the experimental data well at the small angle region. We consider that the deviation at large angle region may be due to the contribution of scattering from the individual chain (blob scattering). In fact, a Debye function can reproduce the scattering behavior at large

使用施設:JRR-3M, 装置:SANS-U(C1-2), 分野 Softmatter

angle region well as shown in Figure 3. The fitting parameters were listed in Table. Radius of the overall micelle (R_s) 17.5 nm is very close to the hydrodynamic radius (17 nm) obtained from dynamic light scattering measurement of the same micelle solution, suggesting the accuracy of the SANS analysis. The aggregation number of the micelle is calculated to be 39. The graft density of the corona chain was calculated to be 0.023 chains/nm^2. After the core-cross-linked by ring-opening polymerization and hydrolysis of the corona chains, core-cross-linked nanoparticles with corona chains consisting of sodium polystyrenesulfonate were obtained.

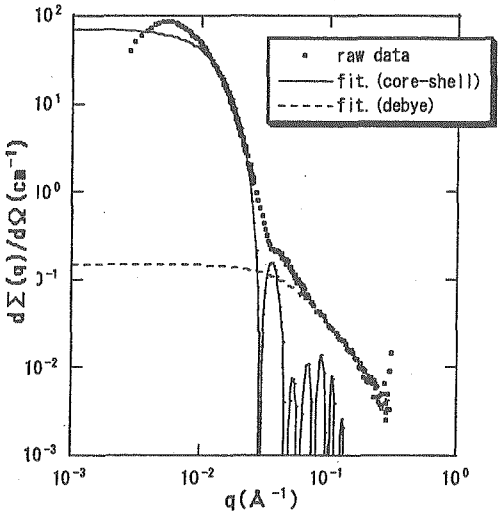

Figure 3: SANS profile for 1wt% SBS_{113}-*b*-$SSPen_{134}$ in acetone-d_6. Solid line is a profile calculated using core-shell sphere. Dotted line is a Debye function.

Table: Structural Parameters for SBS_{113}-*b*-$SSPen_{134}$ obtained by SANS Analysis

R_c [nm]	R_s [nm]	R_g [nm]	N_{agg}
11.5	17.5	2.9	39

R_c: radius of core, R_s: radius of overall micelle, R_g: radius of gyration of corona chain, N_{agg}: aggregation number

To examine the nanostructure of the particle in dry-state, atomic force microscopy observation was carried out on micro slide glass. Figure 4 shows a typical AFM image for sodium poly(styrene sulfonate)-grafted nanoparticles. The AFM observation clearly indicated the obtained particles are fairly nomodisperse spherical nanoparticles.

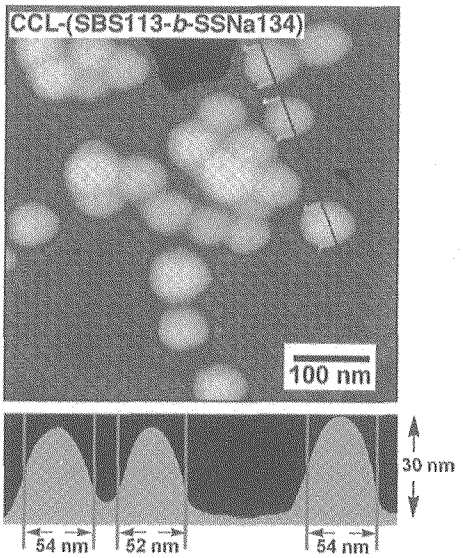

Figure 4: A typical AFM image of sodium poly(styrene sulfonate)-grafted particles.

The ionic-polymer-grafted nanoarticles synthesized here are expected not only as new functional materials but also as fundamental academic samples for investigation of polyelectrolyte brushes [6].

References

[1] I. W. Hamley, Encyclopediaof Polymer Science and Technology 3rd ed. H. F. Mark Ed., Wiley, New Jersey, 2003, vol. 1, 457-482.
[2] I. Piirma, Polymeric Surfactants. Surfactant Science Series, Marcel Dekker, New York, 1992, Vol. 42.
[3] B. Lindman, P. Alexandridis, Eds., Amphiphilic Block Copolymers, Elsevier, Amsterdam, 2000.
[4] K. Matsumoto, H. Hasegawa, and H. Matsuoka, Trans. MRS-J. 29, 23 (2004).
[5] K. Matsumoto, H. Hasegawa, and H. Matsuoka, Tetrahedron, in press.
[6] P. Kaewsaiha, K. Matsumoto, H. and Matsuoka, Langmuir, in press.

研究テーマ：中性子散乱によるソフトマターの構造と機能の研究
表　題：中性子小角散乱による架橋ポリテトラフルオロエチレン電解質膜の構造解析

1-5-19

Structural Analysis of Polymer Electrolyte Membranes Based on Crosslinked Polytetrafluoroethylene by Small-Angle Neutron Scattering

T. Yamaki, M. Asano, R. Motokawa[1], S. Koizumi[1] and M. Yoshida

Takasaki Radiation Chemistry Research Establishment, JAERI, Takasaki, Gunma 370-1292
[1]Advanced Science Research Center, JAERI, Tokai, Ibaraki 319-1195

Polymer electrolyte fuel cells (PEFCs) have received much attention in the transportation and portable power fields. The proton exchange membrane (PEM) is a vital component in the PEFCs; this membrane acts as a separator to prevent mixing of the reactant gases and as an electrolyte for transporting protons from the anode to the cathode. The sulfonated fluorocarbon polymer membrane, *e.g.*, Nafion, is the PEM material widely used for this type of applications.

Our efforts have been independently focused on the development of novel PEM materials by radiation-induced graft polymerization of vinyl monomers (*e.g.*, styrene) into a fluorocarbon polymer film followed by sulfonation[1]. The use of radiation-crosslinked polytetrafluoroethylene (PTFE) films for the γ-ray-graft substrates enabled us to prepare the polymeric membranes with a much larger ion-exchange capacity (IEC) and moderate osmotic swelling property in water[2]. Importantly, the crosslinking process of PTFE should be necessary for improving membrane performances.

The understanding and optimization of swelling and proton conductivity of our membranes require information on the microstructure and on its modification. Such information also leads to a deep insight into the dynamical properties inside the membrane from the molecular to macroscopic level. Therefore, the aim of this work is to clarify the structure of the crosslinked-PTFE based membranes under different external conditions using small-angle neutron scattering (SANS).

All the PEMs were prepared by our established procedure[1]. The vacuum-dried membranes in the acid form were stored in deuterated water before use. SANS experiments were carried out with the SANS-J instrument at the JRR-3M research reactor of JAERI. The scattering intensity was measured as a function of q, the magnitude of scattering vector. q is related to the scattering angle, θ, by the relationship $q = (4\pi/\lambda)\sin\theta$, where λ is the wavelength of the incident neutron beam (0.65 nm). The q range was varied from 0.03 to 2 nm^{-1}.

Figure 1 shows the SANS profile of the membrane based on 130-kGy crosslinked PTFE (IEC = 2.0 meq g^{-1}) together with that of Nafion for comparison. Nafion exhibited a characteristic scattering peak around $q = 1.4$ nm^{-1}, corresponding to a Bragg distance of 4.2 nm. This so-called "ionomer peak" is due to a microphase separation between the hydrophilic ionic domains and hydrophobic polymer matrix. According to the previous SANS experiments, water in Nafion was found to be localized and form pools embedded in the matrix. In contrast, an entirely different profile was obtained for our membrane: an intense small-angle upturn in intensity and no well-defined peak. This demonstrates that the crosslinked-PTFE sulfonic acid membranes will possess the structural properties which cannot be rationalized by the so far presented models.

Based on the above preliminary results, more thorough investigation of the membranes prepared under different conditions is now in progress. A number of other studies including scattering at the smaller q range, investigation at various humidity levels, and quantitative interpretation of the data should be performed to understand the complex structure present in our hydrated membranes.

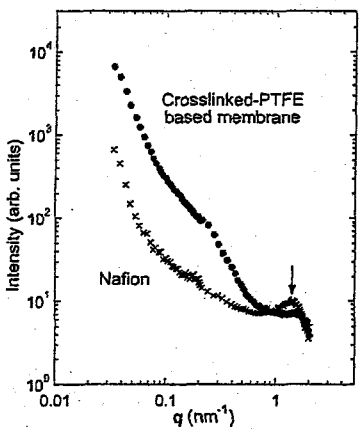

Figure 1: SANS profiles of the crosslinked-PTFE based electrolyte membrane and Nafion, both of which were swollen in deuterated water. The arrow indicates the "ionomer peak" on the pattern of Nafion.

References

1) T. Yamaki, M. Asano, Y. Maekawa, Y. Morita, T. Suwa, J. Chen, N. Tsubokawa, K. Kobayashi, H. Kubota and M. Yoshida : Radiat. Phys. Chem. 67 (2003) 403.
2) T. Yamaki, K. Kobayashi, M. Asano, H. Kubota and M. Yoshida : Submitted to Polymer.

原子炉：JRR-3　　装置：SANS-J(C3-2)　　分野：中性子散乱（高分子）

研究テーマ：非イオン界面活性剤が作るラメラ相の構造に対するずり流動場効果と膜のダイナミックス
表題：非イオン界面活性剤/水系におけるずり流動場誘起転移

1-5-20 Shear-Induced Transformation in a Nonionic Surfactant/Water System

K. Miyazaki, Y. Kawabata, and T. Kato'

Department of Chemistry, Tokyo Metropolitan University, Hachioji, Tokyo 192-0397, Japan

In the past 10 years, much attention has been paid to the effects of shear flow on the structure of a lamellar phase owing to the development of the apparatus which enables us to determine their structures directly under shear flow. In the previous studies, we have measured small-angle neutron scattering (SANS) on the lamellar phases of a nonionic surfactant $C_{16}H_{33}(OC_2H_4)_7OH$ ($C_{16}E_7$) in D_2O at 48 and 55 wt% and 70°C under shear flow for the shear rates 10^{-3}–10 s^{-1} which is much lower than those for other studies reported so far. In the present study, measurements have been made for the sample containing 40 wt% of $C_{16}E_7$ at 70°C.

Measurements of SANS were carried out at the instrument SANS-U of Institute for Solid State Physics of University of Tokyo in JRR-3M at Tokai with a Couette shear cell [1].

Figure 1 shows shear rate dependences of the repeat distance and the peak height of for the perpendicular, transverse, and parallel orientations. In the range 0.1 - 0.3 s^{-1}, the repeat distance (d) decreases rapidly with increasing shear rate and takes a minimum value (referred to as d^* hereafter). Although the repeat distance at rest for the 40 wt% sample is larger than those for the 48 and 55 wt% samples, d^* is around 5 nm and depends on concentration only slightly.

It should be noted that d^* is nearly equal to the total film thickness, i.e., the sum of the thicknesses of the hydrophobic and hydrophilic layers at rest obtained from analyses of peak position and line shape of small angle X-ray scattering reported before [2]. The present results strongly suggest local segregation into water-rich and surfactant-rich regions.

Figure 1b demonstrates that the peak heights decrease significantly with increasing shear rate before the abrupt decrease of d for all the principal orientations, suggesting that lamellar domains are substantially shrunk by shear flow.

References
[1] Y. Takahashi et al., J. Soc. Rheol. Jpn. **28** (2000) 187.
[2] K. Minewaki et al. Langmuir **17** (2001) 1864.

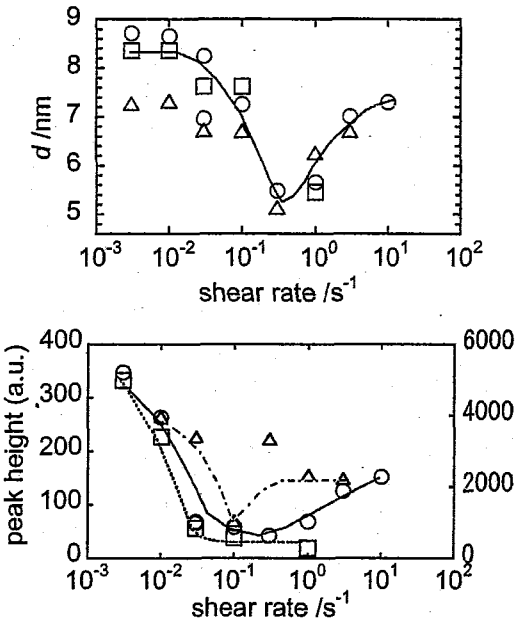

Fig. 1 Shear rate dependences of the repeat distance (a) and peak height (b) for the perpendicular (○), transverse (□), and parallel (Δ) orientations at 40 wt% at 70°C. The different symbol sizes correspond to different runs. In the lower figure, the left ordinate indicates the peak height for the perpendicular and transverse orientations while the right ordinate for the parallel orientation.

使用施設：JRR-3M, 装置：SANS-U(C1-2), 分野 Soft matter

研究テーマ：両親媒子系複雑液体の構造とダイナミクス

表題：中性子スピンエコー法による DPPC/D_2O/$CaCl_2$ 系における脂質二重層膜のスローダイナミクスの研究

1-5-21 Neutron Spin Echo Study on Slow Dynamics of Lipid Bilayers in the DPPC/D_2O/$CaCl_2$ System

T. Takeda[1], N. L. Yamada[2], Y. Kawabata[3], H. Seto[4] and M. Nagao[5]

[1]*Faculty of Integrated Arts and Sciences, Hiroshima University, Higashi-Hiroshima 739-8521*

[2]*Graduate School of Bio-Sphere Science, Hiroshima University, Higashi-Hiroshima 739-8521*

[3]*Graduate School of Science, Tokyo Metropolitan University, Hachioji 192-0397*

[4]*Graduate School of Science, Kyoto University, Kyoto 606-8502*

[5]*NSL, ISSP, University of Tokyo, Tokai, Naka, Ibaraki 319-1106*

In the dipalmitoylphosphatidylcholine (DPPC)/water system, there are various multilamellar phases, in which lipid bilayers and water are stacked alternately. The lamellar repeat distance d_l varies greatly with an addition of salt in the DPPC/water system. In order to study dynamics in undulation of lipid bilayers, NSE experiments have been carried out on the dilute lamellar liquid crystalline phase in the DPPC/D_2O/$CaCl_2$ system with d_l longer than 500 Å so as to avoid the effect on the single membrane dynamics from neighbouring sheets of membranes[1].

For sample preparation, 3wt% DPPC was dispersed in D_2O solution with 7mM $CaCl_2$. The NSE experiments were performed using ISSP-NSE at C2-2 port of JRR-3M in JAERI(Tokai). The bending moduli of the membrane κ estimated from the results of the NSE experiments using the theory presented by Zilman and Granek (ZG)[2] decrease monotonically with increasing temperature as shown in Fig. 1 and with increasing d_l as shown in Fig. 2. The values of κ obtained from the sample with 3wt% DPPC are nearly the same as that obtained using the method of electric-field-induced bending deformation of the cylindrical tubes[3]. The estimated values of κ depend strongly on d_l even in case of d_l longer than 500Å as shown in Fig. 2.

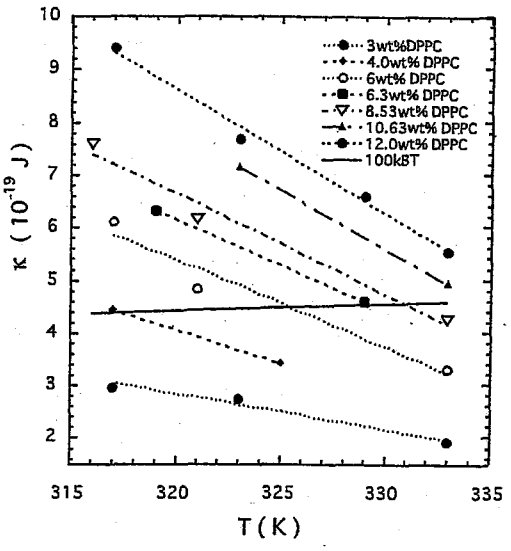

Fig. 1. Temperature dependence of the estimated bending modulus κ obtained from NSE experiments. The solid line indicates 100 k_BT.

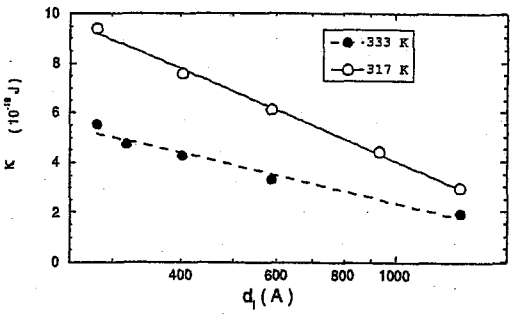

Fig. 2. Dependence of the estimated κ on the lamellar repeat distance d_l obtained from NSE experiments.

References

[1] T. Takeda *et al.*: AIP CP **708** (2004)118.

[2] A. G. Zilman and R. Granek: Phys. Rev. Letters **77** (1996) 4788.

[3] M. Mishima*et al.*: Chem. Phys. Lipids **110** (2001) 27.

使用施設：JRR-3M, 装置：NSE(C2-2), 分野：6. Soft Matters

研究テーマ：トリブロック共重合体ミクロ相分離系の流動中性子散乱とレオロジー
表題：フタル酸ジブチル中における BSB トリブロック共重合体ミクロ相分離網目構造の
1-5-22 流動破壊と回復挙動

Shear-Induced Disruption and Recovery of Microphase-Separated Network Structure of a BSB Triblock Copolymer in Dibutyl Phthalate

H. Watanabe, Y. Matsumiya, T. Kanaya, and Y. Takahashi*

Institute for Chemical Research, Kyoto University, Uji, Kyoto 611-0011, Japan;
** Department of Molecular & Materials Sciences, IGSES, Kyushu University, Fukuoka 812-8581, JAPAN*

Recently, shear effects on rheological and structural properties were investigated for a butadiene-styrene (BS) diblock copolymer forming a micellar lattice in an S-selective solvent, DBP [1]. Disruption of this lattice under the shear and a time required for the recovery after cessation of the shear were strongly influenced by the B/S concentration fluctuation.

For a similar, regular network structure of a BSB triblock copolymer in DBP, the middle S block takes either the loop or bridge configurations, the former being similar to the tail configuration in the BS diblock system but the latter being absent in that system. Some bridges should be converted to the loops under steady shear, and the recovery of the BSB network may be affected by this conformational change, in addition to the concentration fluctuation.

To test this hypothesis, we have examined the rheological and structural properties of a 30 wt% DBP solution of a BSB triblock copolymer (M_S = 53.9 × 10^3, M_B = 13.3 × 10^3 for each B block) at 25°C. The rheological measurements were conducted in a cone-plate geometry with a rheometer (ARES, Rheometrics). The SANS measurements were made with the SANS-U spectrometer at the Neutron Scattering Laboratory, Institute for Solid State Physics, University of Tokyo (Tokai, Ibaragi) in a Couette flow cell before, during, and after imposition of the steady shear. The incident beam was in the direction of the velocity gradient, and the profiles were detected in a velocity-velocity plane. No shear-orientation was detected.

Figure1 shows SANS profiles of the 30wt% BSB/DBP system under steady shear at various shear rates ($\dot{\gamma}$). At equilibrium ($\dot{\gamma}$ = 0), the BSB network structure (the B cores connected by the middle S blocks) has a long-range order in the alignment of the B domains. Under the shear, this order is disrupted and the heaviest disruption occurs at $\dot{\gamma}$ = 1 s^{-1}, not at higher and/or lower $\dot{\gamma}$.

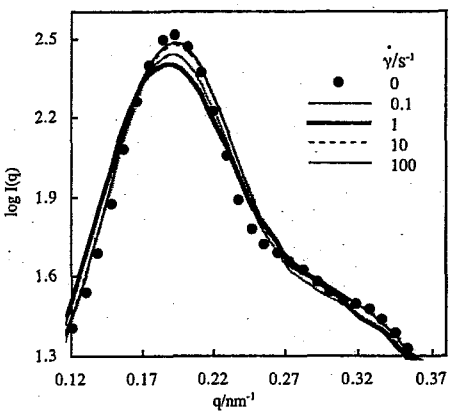

Figure 1 Rheo-SANS profile of the 30 wt% BSB/DBP system at 25°C.

This non-monotonic disruption with increasing $\dot{\gamma}$ is similar to that observed for a BS micellar lattice system [1]. This similarity suggests that the B/S concentration fluctuation governing the disruption in the BS system also plays an important role in the BSB system. To test this expectation, we conducted linear viscoelastic tests for the BSB system just after cessation of the shear. The results are shown in Figure 2.

使用施設：JRR-3M, 装置：SANS-U(C1-2), 分野 Softmatter

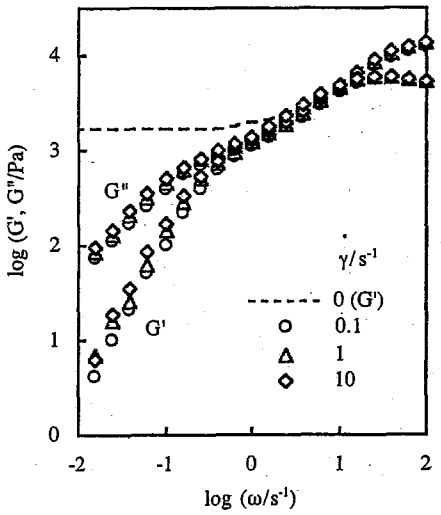

Figure 2 Viscoelastic moduli of the 30 wt% BSB/DBP system just after shear at 25°C.

Figure 2 demonstrates that the storage and loss moduli G' and G'' of the BSB system after the shear at various γ (≥ 0.1 s^{-1}) are hardly dependent on γ and exhibit two relaxation domains. The fast relaxation seen at $\omega \geq 1$ s^{-1} is attributable to the relaxation of individual BSB chains.

The slow relaxation (at $\omega < 1$ s^{-1}) seen for the sheared BSB system at 25°C was similar, in the relaxation intensity, to that of the same system at 34°C $\cong T_{ODT}$. In addition, in a frequency scale ω_r normalized by the chain relaxation frequency, the relaxation processes at 25°C and 34°C emerged at the same ω_r. The relaxation at 34°C is assigned to the concentration fluctuation, as noted for many copolymer systems at T $\cong T_{ODT}$ [2]. Thus, the slow relaxation of the sheared BSB system at 25°C is also attributable to the B/S concentration fluctuation. This assignment is similar to that for the BS system [1].

Under this assignment, the characteristic frequency of the concentration fluctuation ω_f is estimated from the G' and G'' data; $\omega_f \cong 0.3$ s^{-1} for the sheared BSB system. The heaviest disruption of the BSB network under the steady shear occurs at $\gamma = 1$ s^{-1} $\cong \omega_f$ (cf. Figure 1), suggesting that the BSB network is most heavily disrupted when the shear is fast enough to overwhelm the fluctuation but still slow for formation of the flowing plane. This feature is similar to that of the BS system [1].

However, the BSB and BS systems exhibited different behavior during the recovery of equilibrium elasticity after the shear disruption. Figure 3 shows a time t_r required for *full* recovery of elasticity of these systems. For the BS system, t_r changes with γ and shows a peak at $\gamma/\omega_f \cong 1$, meaning that the elasticity of this system sustained by the micellar lattice was most slowly recovered when the lattice was most heavily disrupted (at $\gamma \cong \omega_f$) [1].

In contrast, the elasticity of the BSB system (dotted curve in Figure 2) is sustained by the S bridges as well as the loops when the network is well ordered [3]. Figure 3 demonstrates that t_r of this system hardly changes with γ despite the fact that the heaviest disruption occurs at $\gamma \cong \omega_f$ (cf. Figure 2). This behavior suggests that a late stage of the elasticity recovery in the BSB system was governed by the reformation of the S bridges that was converted to the loops under shear: The rate-determining step for this reformation should be the pull-out of the loops resulting in the transient mixing of the S and B blocks, thereby giving the γ–insensitive t_r.

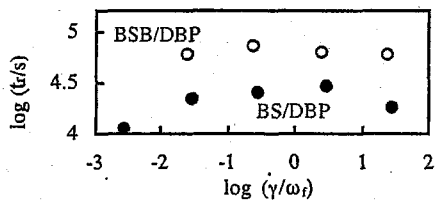

Figure 3 Elasticity recovery time of the 30 wt% BSB/DBP and 28 wt% BS/DBP systems.

References

[1] Watanabe et al., *Macromolecules* **34** (2001) 6742
[2] Bates and Fredrickson, *Annu Rev Phys Chem* **41** (1990) 525
[3] Watanabe, *Acta Polym* **48** (1997) 215

研究テーマ： リン脂質/水系における膨潤相の形成要因

1-5-23 リン脂質DPPC/水系で指組ゲル相近傍に現れる膨潤相

A swollen phase neighboring the interdigitated phase in aqueous solution of DPPC

H. Seto[1], N. L. Yamada[2], M. Hishida[1], H. Nobutou[2], M. Nagao[3] and T. Takeda[2]

[1] *Department of Physics, Kyoto University, Sakyo, Kyoto 606-8502*

[2] *Faculty of Integrated Arts and Sciences, Hiroshima University, Higashihiroshima 739-8521*

[3] *Institute for Solid State Physics, The University of Tokyo, Tokai 319-1106*

An aqueous solution of dipalmitoyl-sn-glycero-3-phosphatidylcholine (DPPC) has various phases depending on their environmental conditions such as temperature and pressure, and on adding other ingredients such as ethanol, salt, etc. In most of the phases, hydrocarbon chains of lipid molecules face each other and bilayer structure is formed and stack regularly with water layer in between. With increasing temperature, successive phase transitions are observed; a gel-to-gel (L'_β / P'_β) pretransition and a gel-to-liquid crystalline (P'_β /L_α) main transition. In these phases, the lamellar repeat distances are about 60 Å. In the P'_β phase, an intra-bilayer ripple structure was observed. The origin of these transitions has been explained in terms of the melting of hydrocarbon chains of lipid molecules; they partially melt in the ripple-gel phase and completely melt in the liquid crystalline phase.

In general, pressure has an opposite effect of temperature on a structural formation in aqueous solutions of phoshoplipids. Increasing pressure from the liquid crystalline phase induces the main transition to the ripple gel phase. A slope of a main transition temperature against pressure, dT_m/dP, is positive independent of phospholipids. [1] This implies that the main transition is controlled by a volume increase and an endothermic enthalpy change. It is known that an interdigitated gel phase is induced by further compression (above 100 MPa) from the ripple gel phase. This phase is characterized by an alternative alignment of hydrophobic headgroups and lipophilic tails of phospholipid molecules. [2]

The interdigitated structure of phospholipids is observed under various experimental conditions. Addition of small molecules, for example alcohol, is known to stabilize the interdigitated structure. [3] An origin of the stabilization by adding alcohol was understood by a model proposed by Adachi *etal.* [4], which indicated that two alcohol molecules are filled in a volume surrounded interstitially by the headgroups of phospholipid molecules.

Effects of ethanol on the *P-T* phase diagram of the DPPC aqueous solution was investigated by Kaneshina *etal.* [5] They have shown that the interdigitated phase appeared at lower pressure with adding small amount of ethanol. This result implied that the effects of pressure and ethanol on the structural formation of DPPC membranes were the same. Both mechanisms of pressure- and ethanol-induced interdigitation could be explained by a packing property of phospholipid molecules, however, an origin of the equality of these effects remains to be answered. [6]

DPPC was purchased from Avanti Polar Lipids, Inc. Deuterated water of 99.9 % purity and ethanol of 99.5 % were obtained from Isotec Inc. and Katayama Chemical Co. Ltd., respectively. All materials were used without further purification. DPPC was first milled in an agate mortar and dissolved in a water solution of ethanol at 15 wt %. Molar ratios of ethanol against water were 0, 0.3, 0.5, 0.7, 0.8 and 1.2. All the samples were incubated at 50 °C (above the main transition temperature) for about a day.

SANS experiments were carried out at SANS-U. Incident neutrons of 7 Å were selected and two-dimensional detector was placed at 1.5 m from the sample position, and the measured momentum transfer Q was $0.017 \leq Q \leq 0.2$ Å^{-1}. Exposure time for one measurement was between 300 and 1800 s. Two dimensional data were azimuthally

使用施設：JRR-3M, 装置： C1-2 (SANS-U) , 分野： 6. Softmatter

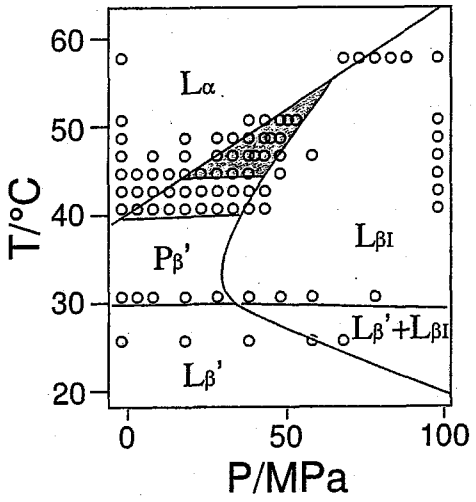

Fig. 1. A obtained phase diagram of DPPC aqueous solution with adding ethanol of 0.8M. Open circles indicate the points of SANS measurement. The swollen phase is indicated by the hatched region.

averaged and normalized to be an absolute intensity using a Lupolen standard.

SANS experiments were done at $20 \leq T \leq 90$ °C and $0.1 \leq P \leq 200$ MPa for the samples with 0M, 0.3M and 0.5M ethanol, and at $25 \leq T \leq 63$ °C and $0.1 \leq P \leq 100$ MPa for the samples with 0.7M, 0.8M and 1.2M ethanol, respectively. A $P-T$ phase diagram for the sample with 0.8M ethanol is shown in Fig. 1 as a typical example. It was consistent with the previous result [5] except an existence of a new phase neighboring the interdigitated gel phase. [7]

In Fig. 2(a), a pressure dependence of a SANS profile at $T = 41$ °C for the sample with 0.8M ethanol was shown. A Bragg peak at Q=0.09 Å^{-1} of the L_α phase at ambient pressure vanished with increasing pressure, and an intense single peak was observed between 5 MPa and 20 MPa before growing a Bragg peak due to the interdigitated phase. On the other hand, it appeared only with decreasing temperature at constant pressure as shown in Fig. 2(b). This implies that this phase with a peak at $Q \simeq 0.06$ Å^{-1} was transformed form the liquid crystalline (L_α) phase and the interdigitated gel ($L_{\beta I}$) phase, however, it was not transformed form the ripple gel (P'_β) phase.

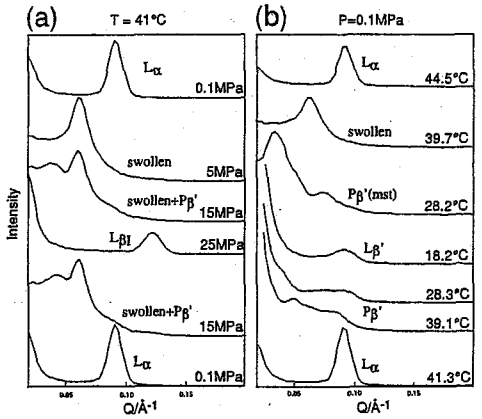

Fig. 2. (a) Pressure dependence of SANS profile for the sample with 0.8M ethanol at $T = 41$ °C and (b) temperature dependence of the sample with 1.2M ethanol at ambient pressure.

These profiles were analyzed in terms of a model proposed by Lemmich et al. [8] A thickness of lipid bilayers were the same as in the gel phases (L_β' and P_β') and a thickness of water layer between bilayers was larger than that at the other phases. Thus we named this phase as a "swollen phase". This phase was observed near the interdigitated phase for all the samples investigated, even without ethanol or at ambient pressure. The transition temperature and pressure to the swollen phase form the liquid crystalline phase decreased with increasing ethanol concentration. This behavior is the same as the interdigitated gel phase.

References

[1] R. Winter & W. -C. Pilgrim, Ber. Bunsenges., Phys. Chem. **93**, 708 (1989).

[2] L. F. Braganza & D. L. Worcester, Biochemistry, **25**, 2591 (1986).

[3] S. A. Simon & T. J. McIntosh, Biochim. Biophys. Acta, **773**, 169 (1984).

[4] T. Adachi, *etal.*, Biophys. J., **68**, 1850 (1995).

[5] S. Kaneshina, *etal.*, Chem. Lett., 1963 (1992).

[6] R. Winter, Curr. Opin. Colloid Interface Sci., **6**, 303 (2001).

[7] H. Seto, *etal.*, J. Appl. Cryst. **36**, 607.

[8] J. Lemmich, *etal.*, Phys. Rev. E, **53**, 5169 (1996).

研究テーマ:中性子反射率測定に基づく高分子超薄膜／水界面における水の構造の直接評価
表題:中性子反射率測定による(固体／水)界面での水の構造評価の予備的検討

1-5-24

Preliminary Experiment on the Analysis of Water Structure at (Solid/Water) Interface by Neutron Reflectivity

Nao Hosaka[1], Tomoyuki Koga[1] and Atsushi Takahara[1,2]

Graduate School of Enginering[1], Institute for Materials Chemistry and Engineering[2], Kyushu University, Hakozaki, Higashi-ku, Fukuoka 812-8581, JAPAN

Water at the solid interface plays an important role in blood compatibility, biofouling and so on. The structure of water at the interface might influence the initial process of biological interaction[1]. However, since it is very difficult to apply X-ray reflectivity and spectroscopic method due to the optical turbidity, a little study has been done on the analysis of the structure of water at the solid/water interface. Since a substrate such as silicon and quartz glass is highly transparent against neutron, a neutron reflectivity technique can be applied for the analysis of the scattering density profile near the solid interface. The purpose of this study is to design the sample cell for neutron reflectivity experiment at (solid/water) interface and carry out preliminary experiment of NR.

Figure 1 shows the geometry of NR measurement at the (solid/water interface). The neutron beam was irradiate through the highly polished quartz glass. The surface was cleaned with vacuum ultraviolet ray-irradiation (λ=172nm) to remove contamination at the surface. The heavy water was used as an aqueous media. NR measurements were made with the multilayer interferometer for neutrons (C-3-2-2, MINE). The incident neutrons possess the long wavelength of 1.26 nm with the resolution of 5.1 %.

As the quartz glass has a lower scattering length density (4.22×10^{-8} Å^{-2}) than D_2O(6.4×10^{-8} Å^{-2}), this allows a critical angle to be measured at low q, which serves as a useful reference for the entire reflectivity profile. The reflectivity of the quartz glass/D_2O interface is shown in Figure 2. A critical angle was clearly

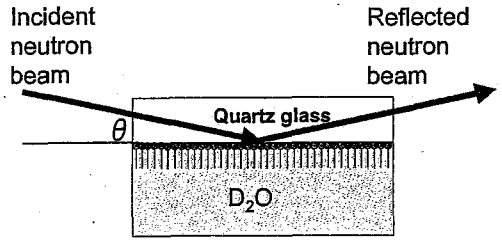

Figure 1 Schematic diagram of the sample cell used in this study.

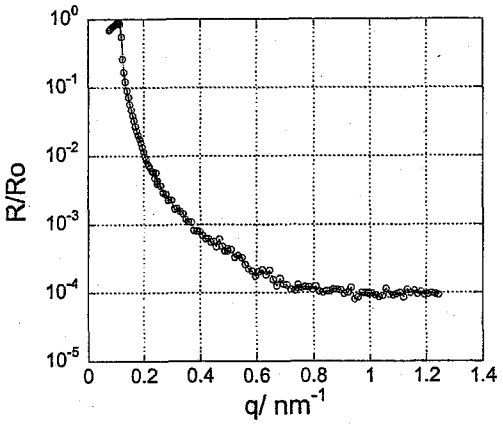

Figure 2 Neutron reflectivity profile of quartz glass.D_2O interface.

observed at q= 0.113nm^{-1}. The data seem to follow Fresnel's low at low q region. In order to compare the water structure at the hydrophobic surface, organoailane monolayer will be immobilized on the quartz glass substrate.

References

[1] T. Tsuruta, Adv. Polym. Sci., 126,2(1996)..

使用施設:JRR-3M, 装置:MINE(C3-1-2), 分野 Softmatter

研究テーマ：オイルゲル化剤による有機溶媒のゲル化に関する研究

1-5-25 小角中性子散乱によるオイルゲル化剤で形成された有機ゲルの構造に関する研究

Small-Angle Neutron Scattering Study on Organogel systems formed with Oilgelators

S. Okabe and M. Shibayama

Institute for Solid State Physics, The University of Tokyo, 106-1 Shirakata, Tokai 319-1106, Japan

"Oilgelators" are compounds which are capable of gelation for various kinds of solvents. The gel networks formed with gelators consist of needle-like structures.[1] However, the general picture of organogelation mechanism has not been clarified yet. In this study, we investigate the microscopic structures of gels formed with various types of gelators.

The gelators which we used in this study were cyclo(L-β-3,7-dimethyloctyl-asparaginyl-L-phenylalanyl), trans-(1R,2R)-bis(undecylcarbonylamino)-cyclohexane and Nε-lauroyl-Nα-stearylaminocarbonyl-L-lysine ethyl ester. They are coded as No.1, 2, and 3, respectively. The chemical structures with their critical gelation concentrations (CGCs) in toluene are shown in Scheme 1.

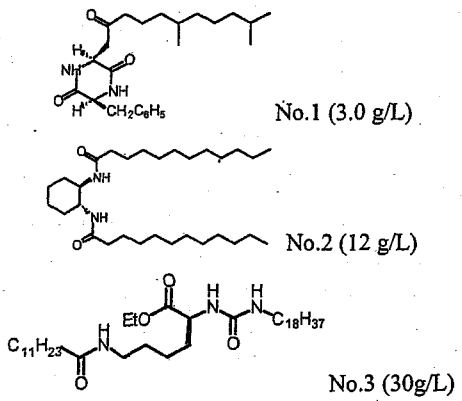

Scheme 1 Chemical structures of the gelators.

All of them are carefully designed with the following criteria. (1) Presence of long alkyl chain(s) so as to dissolve in organic solvents, (2) hydrogen-bond capability for self-assembling, (3) non-crystallinity to avoid aggregation or precipitation. In addition to these, we will demonstrate another important factor preferable for gelator in the following experiments.

The scattering functions, $I(q)$s were obtained by means of small-angle neutron scattering at the SANS-U spectrometer. The temperature of the samples, T, was controlled carefully with a water-circulating bath.

The scattering intensity, $I(q)$s, of each sample are shown in Fig.1. At high T, the $I(q)$s are almost independent of q and the level were relatively low. This means that the gelators were molecularly dispersed and

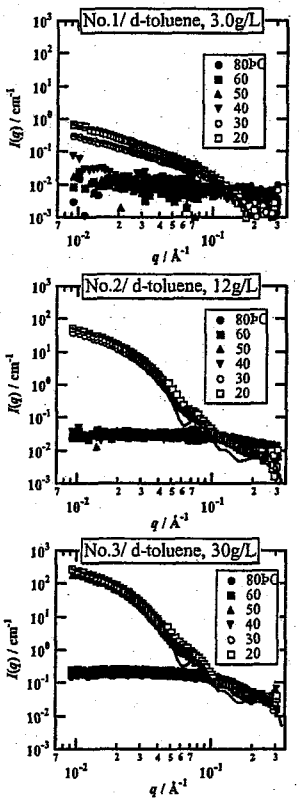

Fig. 1 T-dependence of the $I(q)$s. the solid lines are the best fit.

使用施設：JRR-3M，装置：SANS-U(C1-2)，分野 Softmatter

had no specific structure similar to those for low molecular weight solutions. With increasing T, the $I(q)$s changed drastically to have a q-dependence with high intensity. It seemed that the gelator molecules gathered each other to form a supramolecular structure. The characteristic temperatures of each system, at which scattering function became q-dependent, were consistent with the gelation temperatures obtained by light scattering experiments. And the $I(q)$s of No.2 and 3 systems at high T's were well reproduced with the theoretical function of cylindrical objects. So, the unit of the gel network is a cylinder-shaped particle. The fitted parameters were the diameter, D, and the length, L, of the cylinder. They were evaluated to be 13 and 200 nm, respectively. These parameters were not dependent on T, meaning no change in the unit of the network after gelation.

The same analysis was carried out for the $I(q)$s of No.1 system. The obtained D was 3 nm and was independent on T. On the other hand, L was 400 (at 30°C) to 3000 nm (at 20°C) and was strongly dependent on T. This means that the structure formed with No.1 molecules grew with lowering T. This implies that the network of No.1 can easily fill the space in the system in comparison with that of No.2 or 3. This seems to be the reason why the CGC of No.1 is much lower than that of No.2 and 3.

The concentration-dependence of $I(q)$s was also obtained for No.1 and 2 systems. As shown in Fig. 2, the normalized intensities by the gelator concentration, c, i.e., $I(q)/c$'s were superimposed to the master functions, respectively. This means that the shape of the unit structure did not change with c but the number density increased proportionally to c, indicating the

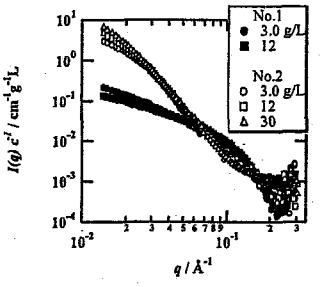

Fig. 2 Master curves of $I(q)$s for No.1 and 2 systems.

needle-like structure do not prefer to gather nor unite with each other.

Considering the above results, schematic representations of the unit structures formed by the molecules were proposed as illustrated in Scheme 2. In the case of No.1 system, the molecules are arranged parallel to the circular part of the chemical structure and has one-dimensional nature. However, in the case of No.2 and 3 systems, the molecules are stacked into relatively bulky cylinder with relatively low aspect ratio because of the steric hindrance around

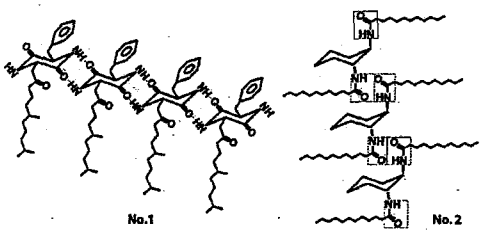

Scheme 2 Illustrations of the models of unit structures formed with gelators.

hydrogen bond-capable parts.

It is concluded that the unit structure of gel networks formed with gelators is a cylindrical assembly of gelator molecules and its high aspect ratio makes it easy to fill the space with the network.[2]

References

[1] S. Okabe and M. Shibayama et al., J. Polym. Sci. B, 42, 1841, (2004)

[2] S. Okabe et al., in preparation.

研究テーマ： 界面膜ダイナミクスの droplet 濃度依存性

1-5-26三元系マイクロエマルションの静的、動的構造の droplet 密度依存性

Droplet density dependences of the static and dynamic structures in a ternary microemulsion system

M. Nagao[1], H. Seto[2], Y. Kawabata[3], and M. Shibayama[1]

[1] *Institute for Solid State Physics, The University of Tokyo, Tokai, 319-1106*

[2] *Department of Physics, Kyoto University, Kyoto 606-8502*

[3] *Faculty of Science, Tokyo Metropolitan University, Hachioji 192-0397*

A ternary microemulsion, consisting of AOT (dioctyl sulfossucinate sodium salt), water, and oil has been intensively investigated by scattering techniques. Thus, this system is suitable to extend the structural parameters depending on the external field, such as the concentration of ingredients, temperature, pressure and so on.

A water-in-oil droplet structure is known to form under a wide concentration region with a fixed water to AOT ratio at the vicinity of room temperature [1]. A droplet density, ϕ, dependences of the static and the dynamic structures were investigated by Sheu et al. [2] by means of small-angle neutron scattering (SANS), quasi-elastic light scattering (QELS), and neutron spin echo (NSE). They obtained that the photon correlation function, $C(t)$, obtained by QELS was represented by a stretched exponential form, with the stretched exponent, β, depending on ϕ. It was unity for low ϕ, while decreased with increasing ϕ below $\phi \sim 0.6$. It was concluded that the decrease of β was due to the dynamic correlations between the spherical water droplets. This means that the dynamical mode due to the inter-droplet structure affects the experimental data, and it is difficult to understand such information independently from the experimental data, so far.

Quite recently, we succeeded in separation of the form factor, $F(q)$ (indicating the intra-structure), and the structure factor, $S(q)$ (the inter-structure), from the SANS data by using the relative form factor method [3]. Using the procedure, the ϕ dependence of $F(q)$ without the influence of $S(q)$ was deduced. The radius of droplets kept almost constant, while the polydispersity decreased with increasing ϕ below $\phi \sim 0.6$. As the next stage, we tried to separate the dynamic structure between the intra- and the inter-droplet fluctuations from the NSE data.

We performed a NSE experiment at the ISSP-NSE of JRR-3M, JAERI, Tokai. The measured samples were $\phi = 0.05$ and 0.3 for the film contrast. In the measured spatial and temporal domains ($0.02 \leq q \leq 0.10\text{Å}^{-1}$ and $0.14 \leq t \leq 14.7$ ns), it is known that the deformation motion of water droplets as well as the translational diffusion of the droplets are expected to be obtained by means of NSE from the dilute droplet microemulsion.

The translational diffusion coefficient, $D_{\rm tr}$, was measured by means of dynamic light scattering (DLS). A DLS/SLS-5000, ALV, Langen, Germany, with a 22mW He-Ne laser (Uniphase, USA) was used for the measurement at the scattering angle of 90°. The observed $C(t)$ showed the decay curve with $\beta = 1$, and $D_{\rm tr}$ was estimated to be $1.97 \times 10^{-11}\text{m}^2/\text{s}$. Both the NSE and DLS measurements were done at the temperature of 25 °C.

The obtained intermediate scattering function by NSE, $I(q,t)/I(q,0)$, from $\phi = 0.05$ was fitted by using a model describing the deformation motion of the spherical shell under the concept of the Helfrich's bending Hamiltonian [4]. Farago and Gradzielski [5] proposed the following equation,

$$I(q,t) = (4\pi)^2[F_{\rm s}(q)+F_{\rm sc}(q)+F_{\rm d}(q,t)]\mathrm{e}^{-D_{\rm tr}q^2t}. \quad (1)$$

Where, $F_{\rm s}(q)$ describes the scattering from a sphere in the absence of fluctuations, $F_{\rm sc}(q)$ gives a time independent correction for the fluctuations, and $F_{\rm d}(q,t)$ contains the correlators of the mode amplitudes. The exponential factor takes into account the translational diffusion. In the case when the contribution of $F_{\rm s}$ to the scattering intensity is

使用施設：JRR-3M, 装置： C2-2 (ISSP-NSE), 分野： 6. Softmatter

small, the term of F_d mainly contributes to $I(q,t)$. Therefore, we fitted $I(q,t)/I(q,0)$ for $\phi = 0.05$ at $q = 0.05\text{Å}^{-1}$, where the scattering intensity shows a fringe due to the shape of the form factor of the sphere, and got a decay time of about 10 ns.

On the other hand, the dynamical mode due to the inter-droplet structure will affect $I(q,t)$ for $\phi = 0.3$. In order to deduce such a contribution, we propose the following analysis procedure.[6] We assume that the double exponential decay function is observed as follows,

$$\frac{I(q,t)}{I(q,0)} = a\exp(-t/\tau_d) + (1-a)\exp(-t/\tau_p), \quad (2)$$

where, τ_d and τ_p indicate the characteristic decay times of each dynamical mode. When it is assumed that the intra- and inter-droplet structure fluctuations are independent each other, the decay mode due to the form factor and the structure factor are assigned as follows,

$$F(q,t)/F(q,0) = \exp(-t/\tau_d), \quad (3)$$
$$S(q,t)/S(q,0) = \exp(-t/\tau_p), \quad (4)$$

and

$$\frac{I(q,t)}{I(q,0)} = a\frac{F(q,t)}{F(q,0)} + (1-a)\frac{S(q,t)}{S(q,0)}, \quad (5)$$

where, $F(q,t)/F(q,0)$ and $S(q,t)/S(q,0)$ indicate the intermediate scattering function due to the form factor and the structure factor, respectively.

We assume that the deformation motion of the shape fluctuations is independent of ϕ, and the translational diffusion is changed to the collective motion of the packing properties of the water droplets with increasing ϕ. In this case, $F(q,t)/F(q,0)$ at $\phi = 0.3$ is written as,

$$\frac{F(q,t)}{F(q,0)} = \left[\frac{I(q,t)}{I(q,0)}\right]_{\phi=0.05}\exp(D_{tr}q^2t), \quad (6)$$

where, $F(q,t)/F(q,0)$ expressed only the deformation motion of the spherical shell and the translational diffusion was neglected by the exponential term.

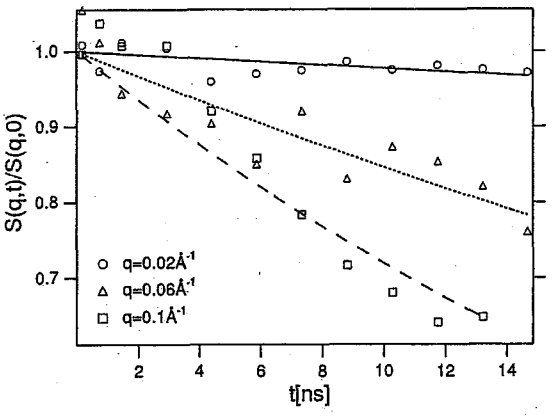

Fig. 1. The q dependence of the evaluated decay function due to the structure factor, namely, $S(q,t)/S(q,0)$. Lines are fitting results according to eq. (4). The order of τ_p is 10 to 100 ns depending on q.

When the value of a is obtained, $S(q,t)/S(q,0)$ is evaluated from the NSE data by using eq. (5). Figure 1 shows the evaluated $S(q,t)/S(q,0)$ with assuming $a = 0.5$, and eq. (4) is applied. The order of the characteristic decay time, $\tau_p \sim 100$ ns, is one order of magnitude larger than that of τ_d. This indicates that it is possible to assume that the dynamical modes due to the intra- and inter-droplet structure are independent.

In this result, the characteristic decay time due to the inter-droplet structure fluctuations is slower than that from the intra-droplet structure fluctuations and is faster than that from the translational diffusion at $\phi = 0.05$ especially at low q region.

References

[1] M. Kotlarchyk, S.H. Chen, J.S. Huang, and M.W. Kim, *Phys. Rev. A* **29**, 2054-2069 (1983).

[2] E.Y. Sheu, S.H. Chen, J.S. Huang, and J.C. Sung, *Phys. Rev. A* **39**, 5867-5876 (1989).

[3] M. Nagao, H. Seto, M. Shibayama, and N.L. Yamada, *J. Appl. Cryst.* **36**, 602-606 (2003).

[4] S.T. Milner, and S.A. Safran, *Phys. Rev. A* **36**, 4371-4379 (1987).

[5] B. Farago, and M. Gradzielski, *J. Chem. Phys.* **114**, 10105-10122 (2001).

[6] M. Nagao, H. Seto, Y. Kawabata, and M. Shibayama, *AIP CP* **709**, 92 (2004).

1. 中性子散乱 6) 生物学

1. Neutron Scattering 6) Biology

This is a blank page.

研究テーマ： Stereum purpureum 由来 Endopolygalacturonase I の中性子結晶構造解析
表題：リンゴ銀葉病菌 *Stereum purpureum* 由来エンドポリガラクツロナーゼ I の高分解能中性子結晶構造解析
1-6-1

Neutron crystallographic analysis of Endopolygalacturonase I from Stereum purpureum at atomic resolution

M. Sato[1], T. Shimizu[2], T. Nakatsu[2], and H. Kato[2]

[1]*Graduate School of Integrated Science, Yokohama City University,*
[2]*Graduate School of Pharmaceutical Sciences, Kyoto University*

Endopolygalacturonases (endoPGs, EC 3.2.1.15) catalyze the hydrolysis of the α-1,4-glycosidic linkages between adjacent α-D-galacturonic acid residues within the pectin main chain. The X-ray crystal structure analyses of endoPG I from Stereum purpureum have identified catalytic residues and accounted for general acid-base catalysis of the enzyme. It was however impossible to specify experimentally which catalytic residue is a general base or acid because no significant electron density for hydrogen atom is observed around catalytic residues.

In view of this, we prepared single crystals suitable for high resolution neutron crystal structure analysis with hanging-drop vapor diffusion method, followed by macroseeding in a sitting-drop (drop: 0.5 ml, reservoir: 4 ml) vapor diffusion.

Typical size of the crystals grown was 3.0 x 1.9 x 0.8 mm (Fig. 1). The crystals were soaked for 40 days in a reservoir solution containing 25% PEG4000, which is prepared with D_2O, and then subjected to neutron experiment. Neutron diffraction data were collected up to 1.5 Å resolution, with a completeness of 81 % and Rmerge = 0.12, using a single-crystal diffractometer (BIX-4) at JAERI.

Figure 2 shows a typical still photograph recorded on Neutron Imaging Plate (45 cm x 100 cm) with a camera length of 200 mm and an exposure time of 30 min. The initial structure, obtained from X-ray analysis, was refined with CNS, and manual modification made with O. Further refinement by simulated annealing and energy minimization is in progress.

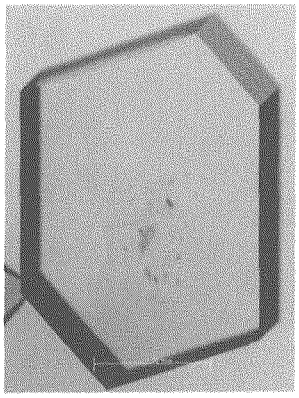

Figure 1: Typical size of the crystals grown.

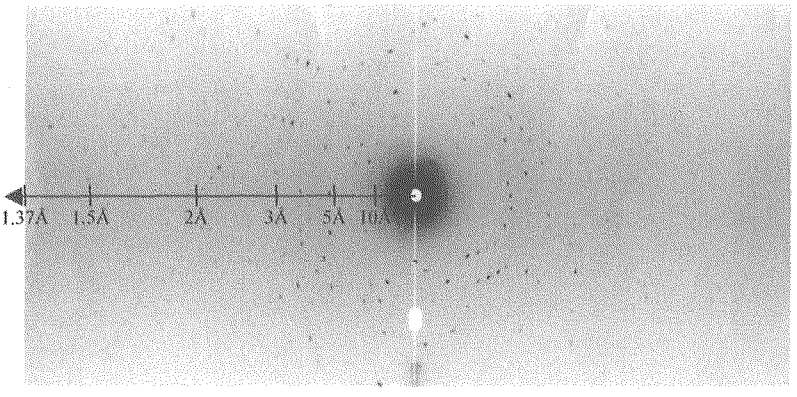

Figure 2: Typical still photograph recorded on Neutron Imaging Plate.

原子炉：JRR-3　装置：BIX-3M（1GB）　分野：中性子散乱（生物）

研究課題:コントラスト変調法によるミリストイル化タンパク質とカルモデュリン複合体の溶液構造解析
表題:コントラスト変調法によるミリストイル化タンパク質とカルモデュリン複合体の溶液構造解析

1-6-2 A Contrast Variation Study of Ca^{2+}-saturated Calmodulin Complexed with N^{α}-myristoylated NAP-22

Yoshinobu Izumi, Nobuhiro Hayashi[1], Yuji Jinbo, Tomohiro Matsufuji, Norio Matsushima[2]

Graduate School of Science and Engineering, Yamagata University, Yonezawa, Yamagata 992-8510, JAPAN;
[1]Fujita Health University, Toyoake, Aichi 470-1192 , JAPAN;
[2]Sapporo Medical University, Sapporo, Hokkaido060-8556, JAPAN

Small-angle neutron scattering (SANS) with contrast variation has been utilized to obtain the first low resolution structure of calmodulin (CaM) complexed with N^{α}-myristoylated NAP-22 (myrNAP-22). CaM binds myrNAP-22 with a 1 to 2 stoichiometry [1]. The solutions with the molar ratio of 1to 2 were prepared at a CaM concentration of 5.0 mg/mL. The neutron scattering experiments were performed with SANS-U spectrometer at 25.0 ℃.

From the plot of the square root of the extrapolated forward scattering intensity versus the $\%D_2O$ for $4Ca^{2+}$/CaM complexed with myrNAP-22, we found the matching point is about 28 $\%D_2O$ which is different from the calculated value of 36 $\%D_2O$. Figure 1 shows the Stuhrmann plot for this complex. The data point is described by equation: $R_g^2 = R_c^2 + \alpha/\rho - \beta/\rho^2$, in which R_c = 169 A, α = 1233, and β = 29350. The positive value of α indicates that denser regions are close to the periphery. The non-zero value of β indicates that the center of mass is displaced from the center of the scattering length density. Figure 2 shows the Kratky plot for this complex at 75%D_2O. The results suggest that the global structure of the complex adopts a disk-like structure.

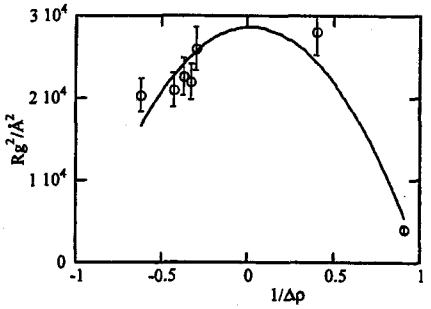

Figure 1: The Stuhrmann plot for Ca^{2+}/CaM complexed with myrNAP-22, in which R_c = 169 Å, α = 1233, and β = 29350.

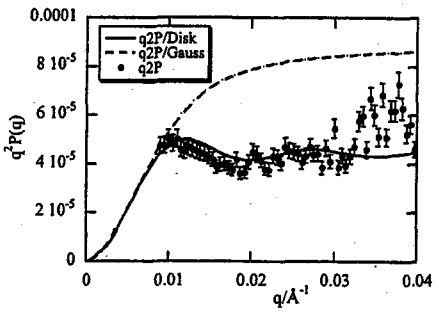

Figure 2: The Kratky plot for Ca^{2+}/CaM complexed with myrNAP-22 at 75%D_2O. Disk (solid line), Gaussian coil (broken line).

References

[1] N.Hayashi, Y.Izumi, K.Titani, and N.Matsushima, Protein Sci. 9(2000) 1905-1913.

使用施設:JRR-3M, 装置:C1-2(SANS−U), 分野:5. Biology

研究テーマ：中性子を用いた生体物質の構造に関する研究
表　題：中性子回折によって観測されたB-DNA十量体 d(CCATTAATGG) $_2$ の副溝内の複雑な水和ネットワーク

1-6-3

Complicated Water Network in the Minor Groove of B-DNA Decamer d(CCATTAATGG) $_2$ observed by Neutron Diffraction Measurements

S. Arai, T. Chatake[1], T. Ohhara, K. Kurihara, I. Tanaka[2], N. Suzuki[3], Z. Fujimoto[3], H. Mizuno[3] and N. Niimura[2]

Neutron Science Research Center, Japan Atomic Energy Research Institute, 2-4 Tokai, Ibaraki 319-1195
[1]*Chiba institute of science, 3 Shiomi, Choshi, Chiba 288-0025*
[2]*Department of Technology, Ibaraki University, Naka-Narusawa, 4-12-1 Hitachi, Ibaraki 316-8511*
[3]*National Institute of Agrobiological Sciences, 2-1-2 Kannondai, Tsukuba, Ibaraki 305-8602*

Specific hydration patterns around DNA duplex have long been recognized as one of the important determinants of nucleic acid structure (stability, polymorphism and flexibility) and nucleotide sequence recognition by proteins and drugs. In those previous studies, the observed hydration structure was obtained from the network of only the oxygen atoms of water molecules. In order to understand more fully the hydration patterns and hydrogen positions of B-DNA duplex, we have carried out both X-ray and neutron crystallographic analysis.

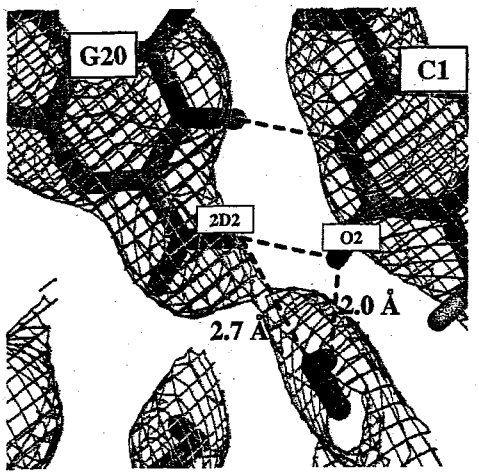

Figure 1: The inter-strand water bridge between CYT and GUA. The 2|Fo| - |Fc| nuclear density map contoured at 2.5 σ level.

The neutron diffraction experiments have been carried out by the BIX-4 neutron diffractometer installed at the JRR-3M reactor at the JAERI [1]. The DNA sequence d(CCATTAATGG)$_2$ was selected as a sample because the best condition of the crystal growth has been determined by using the crystallization phase diagram technique [2,3]. In order to avoid the high background coming from the incoherent neutron scattering of hydrogen atoms, the crystallization experiments have been carried out in D_2O solutions. The step scanning method (0.3 °) was used for data collection. The exposure time of each frame was 3-6 hours and the total time for data collection was 31 days. The crystal was sealed in a quartz capillary for measurement. In this diffraction experiment, the quartz capillary was cooled at 279 K, which was the temperature condition of the crystal growth experiments. We used two crystals to collect the whole of neutron data sets because used DNA crystals were damaged by drying, which was accidentally occurred by the temperature gradient on the quartz capillary. Moreover, we have carried out the X-ray diffraction experiments of the crystal grown in D_2O by BL-41XU installed at SPring8 synchrotron radiation facility. The diffraction images obtained from X-ray and neutron diffraction experiments were processed and scaled using the program *DENZO* and *SCALEPACK* [4]. Crystallographic refinement was performed using *CNS* [5]. We used our refined result of X-ray structural analysis as the initial model of DNA structure for neutron analysis since the unit cell parameters of the X-ray data and the neutron data were almost the same. In both the neutron and X-ray analysis, the space group was $P3_221$, with unit cell dimensions $a = b = 32.9$ Åand $c = 96.1$ Å.

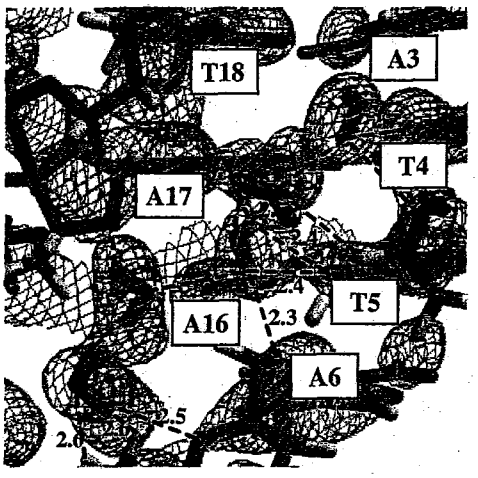

Figure 2: The spine of hydration in the minor groove determined by the neutron structural analysis.

原子炉：JRR-3　　装置：BIX-3M(1GB)　　分野：中性子散乱（生物）

To identify D_2O molecules, first the oxygen position of D_2O has been determined by X-ray analysis. Then the deuterium atoms of D_2O molecules were located by considering the direction of the hydrogen bond acceptor (N, O and P atoms) and the shape of 2|Fo| - |Fc| nuclear density map.

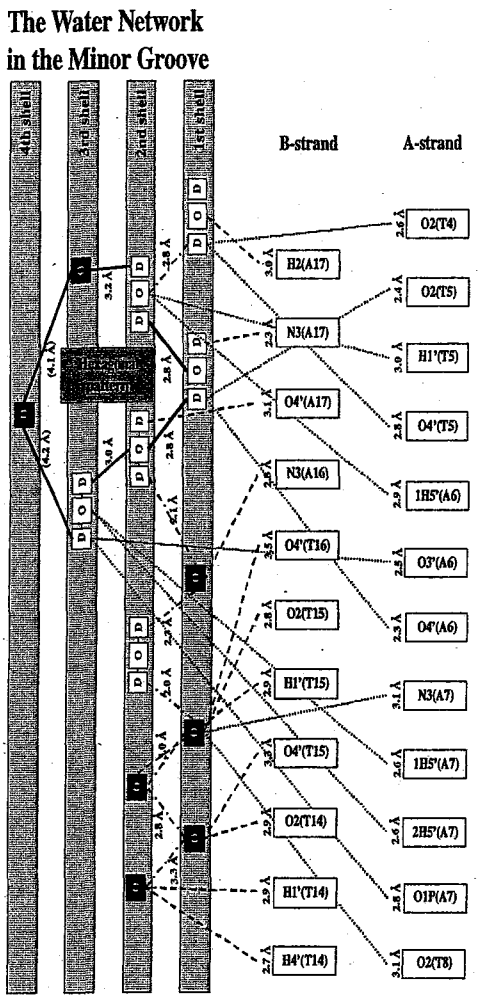

Figure 3: The schematic diagram of the hydrogen bonds network in the minor groove of d(CCATTAATGG)$_2$. The oxygen atoms of water observed by X-ray diffraction are colored in black. The hexagonal hydration pattern is shown in the bold lines.

By the neutron crystallographic analysis, many H and D atoms have been located and 27 D_2O molecules including D atoms have been determined. Fig.1 shows an example of observed water bridge. It has been well known that the spine of hydration in the minor groove of A·T-tract DNA is built by the combination of many water bridges. Especially, the previous X-ray studies had shown that the hydration pattern in the minor groove is drawn as simple hexagonal shape determined by the oxygen positions of water molecules [6]. On the other hands, by determining H and D atoms, we have succeeded in observing the complicated water network in the minor groove (Fig.2). Fig.3 shows the schematic diagram of the hydrogen bonds network in the minor groove of d(CCATTAATGG)$_2$, which has been observed by X-ray and neutron diffraction measurements. In Fig.3, the oxygen atoms of D_2O observed by X-ray analysis were superposed upon the results obtained by the neutron structural analysis. In this figure, the hexagonal hydration pattern is shown in the bold lines. It was difficult to observe the water molecules in the fourth hydration shell by the neutron diffraction measurements because the orientation of those water molecules is liable to become disorder and the maximum resolution limit in this study was not good (3.0 Å). However, as shown in Fig.3, we have found that the observed hydration network in the minor groove has shown not only the simple hexagonal pattern but also many water bridges bonded to the DNA molecules. It seems that this complexity of hydration pattern is derived from the extraordinary variety of an orientation of observed water molecules. These results suggest that many hydrogen bonds between the spine of hydration and DNA strands support the B-DNA helical structure.

This study has been carried out as a part of "Development of New Structural Biology Including Hydrogen and Hydration" in ORCS promoted by Ministry of Education, Culture, Sports, Science and Technology of Japan.

References

1) K. Kurihara, I. Tanaka, M. Refai Muslih, A. Ostermann, and N. Niimura :. J. Synchrotron Radiat. **11** (2004) 68.
2) S. Arai, T. Chatake, and N. Niimura : Acta. Cryst. **D58** (2002) 151.
3) S. Arai, T. Chatake, N. Suzuki, H Mizuno and N. Niimura : Acta. Cryst. **D60** (2004) 1032.
4) A.T. Brünger, P.D. Adams, G.M, Clore, W.L. DeLano, P. Gros, R.W. GrosseKunstleve, J.S. Jing, J. Kuszewski, M. Nilges, N.S. Pannu, R.J. Read, L.M. Rice, T. Simonson, G.L Warren : Acta Cryst. **D54** (1998) 905.
5) Z. Otwinowski and W. Minor : Methods Enzymol. **276** (1997) 307-326.
6) G. Minasov, V. Tereshko and M. Egli : J. Mol. Biol. **291** (1999) 83.

研究テーマ:タンパク質表面の水和水の動力学特性の評価
表題:タンパク質水和水のダイナミクス

1-6-4

Dynamics of Protein hydration water

Hiroshi Nakagawa, Hironari Kamikubo, Atsushi Tokuhisa and Mikio Kataoka

Department of Material Science, Nara Institute of Science and Technology

Water molecules on a protein surface affect a protein surface potential, and participate in the protein stability and function. Therefore, in order to understand a molecular mechanism of a protein function and stability, physical properties of the hydration water as well as the protein should be revealed. From the standpoint of dynamical property, the relaxation time of water molecules on the protein surface (10^{-7} $\sim 10^{-9}$sec) is larger than that of the bulk water (10^{-12}sec), and, the dynamical transition of the protein occurs only with the hydrated protein[1], suggesting that the hydration waters would play an important role in protein dynamics.

To characterize the dynamical properties of the hydration water, the temperature dependence of the incoherent elastic neutron scattering for the hydration water on the Staphylococcal nuclease (SNase) was measured using the triple axis spectrometer, HER, with energy resolution of 100μeV corresponding to the picosecond time scale. In the previous experiments, lyophilized protein powder prepared in a test tube was transferred into a cylindrical aluminum cell by hands, which makes it difficult to assess the reproducibility, and occasionally causes the anisotropy of sample shape. In the present, to reduce an anisotropic effect of sample shape on neutron scattering profile, the sample was lyophilized in the experimental cell. The mean square displacements of three samples(the hydration water, the D_2O-hydrated proteins and the dry protein) were evaluated from the momentum transfer Q dependence of the elastic scattering at the various temperatures (Figure). The scattering profile of the hydration water was calculated by the subtraction of the scattering profiles of a D_2O-hydrated protein from that of a H_2O-hydrated protein.

The mean square displacement of hydration water was suppressed below about 230K, and increases steeply above the temperature. On the contrary, in the case of D_2O-hydrated protein, we can easily found the two transitions at 150K and 230K (shown as two arrows in the figure) The latter temperature is identical to that observed in the hydration water. The transition of hydrated protein at 230K is highly affected with the hydration level, as has been previously reported. The present results revealed that the dynamical transition at 230K is closely correlated with the hydration water dynamics, while that at 150K is not directly mediated by the hydration water dynamics.

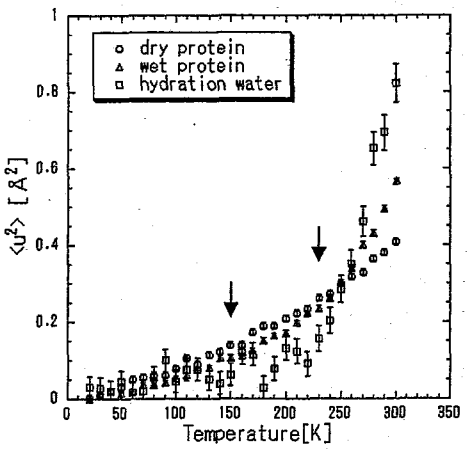

References

[1] V. Reat, R. Dunn, M. Ferrand, J.L.Finney, R. M. Daniel and J.C. Smith. Proc. Natl. Acad. Sci. USA 97,9961-6(2000)

使用施設:JRR-3M, 装置:HER(C-1-1), 分野:5.Biology

研究テーマ：中性子を用いた生体物質の構造に関する研究
表　題：インスリン結晶の中性子回折実験
1-6-5

Neutron diffraction experiments of insulin crystal

M. MAEDA[1], T. CHATAKE[1], I. TANAKA[1], K. KURIHARA[1] and N. NIIMURA[1,2]

[1]*Neutron Science Research Center, JAERI, Tokai, Ibaraki 319-1195*
[2]*Faculty of Technology, Ibaraki University, Naka-Narusawa, 4-12-1,Hitach, Ibaraki 316-8511*

Hydrogen atoms and hydration water molecules surrounding protein play important roles in many physiological functions. Neutron diffraction for protein crystallography using a neutron imaging plate system has become a powerful method for locating position of hydrogen (deuterium) atoms and bound waters of protein[1]. The cubic insulin crystal (space group $I2_13$, a=b=c=78.9Å) contains a solvent volume of 65 % and has multiple hydration layers[2]. To elucidate hydrogen and hydration in cubic insulin crystals, a large single crystal of cubic insulin for neutron protein crystallography has been grown in D_2O by using a phase diagram technique. We have succeeded in growing a large single crystal (4.0 x 4.0 x 1.3 mm^3 in volume) of cubic porcine insulin using the technique. The neutron diffraction experiments were carried out with the neutron single crystal diffractometer BIX-type installed at JRR-3M reactor in JAERI at room temperature. The crystal was sealed in quartz capillary for the measurement. The step scanning method was used for the data collection. The collection time per a frame was 55 minutes controlled by the monitor counts of direct beam in front of the crystal.

One of the results are shown as follows. The protonation and deprotonation of two nitrogen atoms ($N\pi$, $N\tau$) in imidazole ring of histidine are very important information to discuss protein crystallography. This information can be given by neutron diffraction. Figure 1 shows the $2F_o$ -F_c positive neutron density map for His5 in the B-chain(B5 His) and His10 in the B-chain(B10 His). In His5 in B-chain, $N\pi$ is protonated and $N\tau$ is deprotonated. On the contrary, in B10 His, both $N\pi$ and $N\tau$ are protonated. This means that B5 His is electrically neutral and B10 His is positively charged[3].

On the other hand, the structure of rhombohedral crystals of 2Zn insulin (space group R3, a=b=82.5Å, c=34.0Å) was initally solved at 2.8Å[4]. The structure of 2Zn insulin crystals has subsequently been refined and analyzed at 1.5Å[5]. Recently, the structure of 2Zn human insulin has been determinded at 120 K and refined to 1.0Å[6]. The first neutron protein crystallography of 2Zn insulin has been reported at 2.2Å[7], however, the difinite structure of hydrogen and hydration could not be obtained. We have tested the neutron diffraction experiment of 2Zn insulin crystal. It was found that single crystals of 2Zn insulin larger than 2 mm^3 were necessary for neutron diffraction experiments.

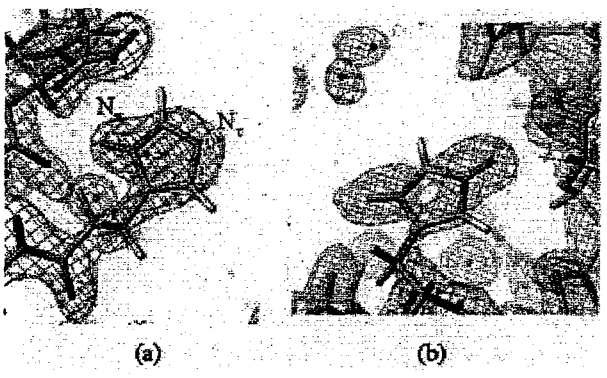

Figure 1: $2F_o$ -F_c positive nuclear density map of (a) His5 in the B-hain and (b) His 10 in the B-chain of cubic insulin

This work was supported in part by an Organized Reserch Combination System from the Ministry of Education, Culuture, Sports, Science and Technology, Japan.

References

1) N. Niimura, Y. Minezak, T. Nonaka, J-C Castanga, F. Cipriani, P. Hoghoj, M. S. Lehmann and Wilkinson (1997). Nat Struct Biol. 4 ,909-914.
2) J. Badger : Biophys.**61** (1993) 816.
3) M. Maeda, T. Chatake,I.Tanaka, A. Ostermann and N. Niimura: J. Synchrotron Rad. **11**(2004) 41.
4) M. J. Adams, T. L. Blundell, E. J. Dodson, G. G. Dodoson, M. Vijavan, E. N. Baker, M. M. Harding, D. C. Hodgkin, B. Rimmer and S. Sheat: Nature **224**(1969) 491.
5) E. N. Baker, T. L. Blundell, J. F. Cutfield, S. M. Cutfield, E. J. Dodson, G. G. Dodoson, D. C. Hodgkin, R. E. Hubbard, N. W. Isaacs, C. D. Reynolds., K. Sakabe, N. Sakabe and M. Vijavan: Philos. Trans. R. Soc. London, Ser. B. **319**(1988) 369.
6) G. D. Smith, W. A. Pangborn and R. H. Blessing: Acta. Cryst. D. **59**(2003) 474.
7) A. Wlodawer, H. Savage and G. Dodson: Acta. Cryst. B. **45**(1998) 99.

原子炉：JRR-3　　装置：BIX-3M(1GB)　　分野：中性子散乱（生物）

研究テーマ：中性子を用いた生体物質の構造に関する研究
表　題：筋肉の細いフィラメント中のトロポニンCからの中性子繊維回折
1-6-6

Neutron Fiber Diffraction of Troponin C within the Muscle Thin Filaments

S. Fujiwara[1], F. Matsumoto[1,2], and S. Deshimaru[1,2]

[1]*Neutron Science Research Center, JAERI, Tokai, Ibaraki 319-1195*
[2]*Laboratory for Structural Biochemistry, RIKEN Harima Institute, Hyogo 679-5148*

Muscle contraction occurs by sliding of the two principal components in muscle cells, the "thin" filaments and the "thick" filaments, past each other. In skeletal and cardiac muscles, the regulation of the muscle contraction is conducted through interactions of the thin filament based proteins, troponin (Tn) C, TnI, TnT, tropomyosin, and actin. To understand the molecular mechanism of the regulation of muscle contraction, it is important to obtain information of the structures of these proteins within the thin filaments.

Since the muscle contraction is triggered by binding of Ca^{2+} to TnC, we have been studying, as a first step, the structure of TnC within the thin filament by small-angle neutron scattering[1)]. It was found that TnC assumes a dumbbell-like structure, and moves toward the filament axis by binding of Ca^{2+}. It is thus important to obtain information on (possible) orientational change concomitant with this movement of TnC. Such information could be obtained from two-dimensional fiber diffraction patterns from the samples in which the filamentous axis is oriented. To explore the possibility of obtaining the orientational information of TnC within the thin filaments, we employed neutron fiber diffraction method. We prepared the native thin filaments (NTF) purified from bovine heart, and the reconstituted thin filaments containing deuterated TnC (dTnC-RTF). These samples were put into quartz capillaries of a diameter of 3 mm, and then oriented in magnetic field of 18 Tesla. Neutron fiber diffraction patterns of these oriented samples were measured with the Small-Angle Neutron Scattering Instrument (SANS-J) at the guide hall of the reactor JRR-3M in Japan Atomic Energy Research Institute. Neutrons with the wavelength of 6.5 Å($\Delta\lambda/\lambda$=12.98%) were employed, and the sample-to-detector distance was 2.0 m.

Figure 1 shows the neutron diffraction pattern of NTF. The background-subtracted pattern folded on the equator is shown. Exposure time of this pattern was 20 hours. This pattern clearly shows characteristics of the muscle thin filaments, including a strong intensity on the equator, actin-based layer lines at 59 Å, a weak cross-pattern across the equator due to tropomyosin, and at least up to 3rd layer lines of the meridional reflections due to troponin. Difference intensity of these meridional reflections between NTF and dTnC-RTF should in principle provide the reflections due only to TnC.

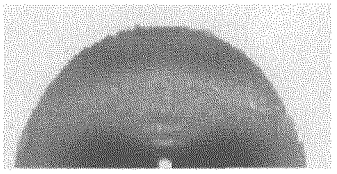

Figure 1: An example of neutron diffraction patterns of the oriented samples of the thin filaments.

Figure 2 shows the intensity distribution of these reflections. It is shown that there is a difference between the intensity distribution from NTF and those from dTnC-RTF, indicating that it is possible to extract the intensity distribution of TnC. The detailed analysis of these reflections is currently underway.

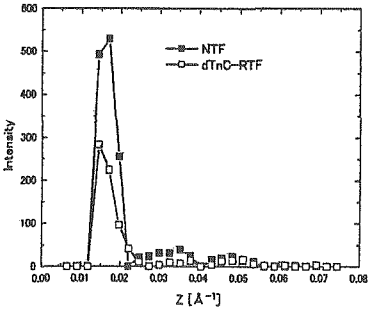

Figure 2: Intensity profiles of the meridional reflections of Tn within NTF and within dTnC-RTF.

Supported in part by the REIMEI Research Resources of Japan Atomic Energy Research Institute, and by Special Coordination Funds for Promoting Science and Technology from the Ministry of Education, Culture, Sports, Science and Technology, the Japanese Government.

References

1) F. Matsumoto *et al.*: J. Mol. Biol. (2004) in press.

原子炉：JRR-3　　装置：SANS-J(C3-2)　　分野：中性子散乱（生物）

研究テーマ：中性子を用いた生体物質の構造に関する研究
表　題：平滑筋ヘビーメロミオシンの中性子小角散乱
1-6-7

Small-Angle Neutron Scattering of Smooth Muscle Heavy Meromyosin

S. Deshimaru[1,2], S. Maruta[3], F. Matsumoto[1,2], T. Arata[4], K. Wakabayashi[5], and S. Fujiwara[1]

[1]*Neutron Science Research Center, JAERI, Tokai, Ibaraki 319-1195*
[2]*Laboratory for Structural Biochemistry, RIKEN Harima Institute, Hyogo 679-5148*
[3]*Department of Bioengineering, Soka University, Tokyo 192-8577*
[4]*Department of Biology, Graduate School of Science, Osaka University, Osaka 560-0043.*
[5]*Department of Mechanical Science and Bioengineering, Graduate School of Engineering Science, Osaka University, Osaka 560-8531*

Muscles are composed of two kinds of filaments, actin-based "thin" filaments and myosin-based "thick" filaments. The interaction between actin and the "head" region of myosin, during which one ATP is hydrolyzed, makes these filaments slide past each other, thereby contracting muscles. The molecular mechanism of this muscle contraction and its regulation is one of the most important problems in biophysics, as it is a typical example of energy transduction mechanisms of living organisms. In vertebrate smooth muscles, the acto-myosin interaction is regulated by phosphorylation of myosin. One myosin molecule contains two heads, each of which hydrolyzes ATP, and an interaction between these two heads has been shown to be important in this myosin-linked regulatory mechanism. Knowledge of the structure of the two heads in the myosin molecule could therefore provide insight into the interaction between these two heads. In order to obtain structural information of the two heads in myosin in solution, we carried out neutron scattering experiments of smooth muscle heavy meromyosin (HMM), a proteolytic fragment of the myosin molecule which contains two heads.

Smooth muscle HMM was prepared by digestion of purified chicken gizzard myosin by V8 protease, followed by the purification with gel-filtration chromatography. To detect possible conformational changes of HMM under different structural states, we prepared four kinds of samples: unphosphorylated HMM, unphosphorylated HMM in the presence of ADP-BeF_X, an ATP-analogue which mimics ATP binding state, phosphorylated HMM (pHMM), and pHMM in the presence of ADP-BeF_X. A concentration series of HMM solution in D_2O was prepared for each state. Small-angle neutron scattering experiments were done on these samples. The measurements were done with the Small-Angle Neutron Scattering Instrument (SANS-J) at the guide hall of the reactor JRR-3M in Japan Atomic Energy Research Institute. Neutrons with a wavelengh of 6.5 Å($\Delta\lambda/\lambda$=12.65%) were employed. The measurements were done at sample-to-detector distances of 6.0 m and 1.5 m.

Data taken at the two sample-to-detector distances were merged to obtain scattering curves covering Q-ranges (Q=$4\pi\sin\theta/\lambda$, where 2θ is the scattering angle and λ the wavelength of neutrons) as wide as possible. Figure 1 shows the merged scattering curve extrapolated to zero protein concentration of each sample. Differences in the scattering curves are observed, particularly in the initial slopes of the curves and a bump in the region around Q=0.07Å^{-1}, indicating that the conformations of HMM under different states are different. Analysis by the Guinier plots of these curves showed that radii of gyration of HMM under these states were different, indicating again the conformational changes of HMM under the different states. A detailed analysis with model calculations is currently underway.

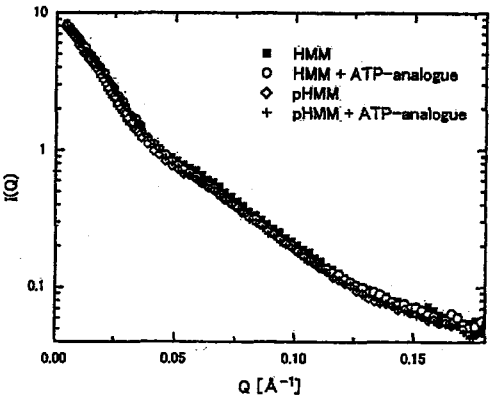

Figure 1: Scattering curves of HMM in the different states. The merged curves taken at the different sample-to-detector distances are shown. Filled squares denote the scattering curve of HMM, open circles denote that of HMM in the presence of ATP-analogue, open diamonds denote that of pHMM, and crosses denote that of pHMM in the presence of ATP-analogue.

This study was supported in part by Special Coordination Funds for Promoting Science and Technology from the Ministry of Education, Culture, Sports, Science and Technology, the Japanese Government.

原子炉：JRR-3　　装置：SANS-J(C3-2)　　分野：中性子散乱（生物）

研究テーマ：細胞における蛋白質の高次構造化不全と細胞の異常死に関する研究 (II)
表　題：遺伝子から合成された脳蛋白質の自己集合に関する中性子散乱研究
1-6-8

Neutron scattering study on self-assembly of tau molecules in water

S. Naito[1], M. Furusaka[1], S. Fujiwara[2], J.Suzuki[2], Y. Kobayashi[3], and N. Niimura[2]

[1]*High Energy Accelerator Research Organization, Tsukuba, Ibaraki 305-0801*
[2] *Japan Atomic Energy Research Institute, Ibaraki 319-1195*
[3]*College of Science and Technology, Nihon University, Tokyo101-8308*

An abnormal protein aggregation in cells causes cellular degeneration and death, and finally end up with grave disorders. Alzheimer's disease, an age-related dementia, is characterized by amyloid plaques and neurofibrillary tangles. Both are formed from abnormally aggregated protein; the plaques contain the AP peptide (a breakdown product of membrane protein) aggregated into fibers, the tangles contain tau protein aggregated into paired helical filaments (PHFs). In order to understand the origin of the disease it is important to understand the abnormal state of these proteins (resulting from proteolysis, phosphorylation, or other modifications including disulfide bond (SS) formation) and the subsequent aggregation. We have preliminarily studied the self-assembly of keratin proteins causing normal cell death of keratinocyte. The two types of keratin molecules form 8-mer consisting of 4 pieces of coiled-coil dimmer in the early stage of cell death[1].

We synthesized gene-expressed tau (46Kda,consisting of 448a.a.). SANS were conducted at SANS-J [neutron wavelength (λ=11.4 Å), sample distance (L=10m)] situated at the end of a cold-neutron guide tube from the JRR-3 reactor and at the SWAN, small and wide angle diffractometer at the KENS (Pulsed Neutron Scattering Facility in KEK). Figure 1 shows the SANS profile of tau solution in the buffer (12mg in 1 ml of 50 mM HEPES buffer, pH 7.8 containing 5mM DTT). Tau formed multimers without intermolecular disulfide bondings. Double logarithmic SANS plot profiles of tau in the buffer solution showed straight line that has a slope of –2 ($0.002<q<0.007$). This suggests that tau exists as bent rod-like molecules. In order to analyze the scattering intensity function in detail, a cross-section analysis was applied. For the medium scattering angle region, the scattering intensity of a rod-like particle of length L and the mean-square radius of cross section $\langle R_{cs}^2\rangle$ were separated into the axial factor $I(q)_{thin}$ and the cross-sectional factor, $I(q)_{cs}$.

$$I(q) = I(q)_{thin} I(q)_{cs}$$

$\langle R_{cs}^2\rangle^{1/2}$ measures the cross-sectional dimension.

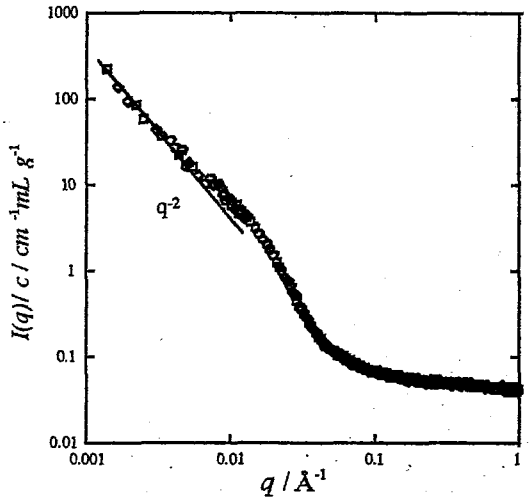

Figure 1:SANS profiles of tau aq. soln. at pH 7.8.

of the particle rather than the overall dimension. Here, q is the magnitude of scattering vector ,$I(q)_{thin}$ is approximated by Lp/q and, in the scattering vector region of $q^2\langle R_{cs}^2\rangle < 1$, I_{cs} is proportional to $\exp\{-1/2\langle R_{cs}^2\rangle q^2\}$. In this q region, therefore,

$$\ln I(q)q = \ln I(0)q - 1/2\langle R_{cs}^2\rangle q^2,$$

and the plot of $\ln(I(q)\,q)$ vs. q^2 forms a straight line whose slope is $\langle R_{cs}^2\rangle$. $I(0)$ is the zero-angle scattering intensity. R_{cs} is related to the radial distribution of scattering density. The real diameter (r) of rod-like tau was estimated by,

$$r = \sqrt{2}\, R_{cssq}$$

The diameter rod-like tau aggregate was estimated to be *ca.* 18Å. The diameter of the rod-like tau aggregate consisted of PHF's (cross-liked by SS bond) observed in neurocyte of Alzheimer's disease is 10 nm. Tau may recognize each other in a special way and aggregate easily if tau exists alone. The reason tau having less crystalline structure, such as a-helix and b-sheet, forms rod structure has been unknown, especially in neurocyte of Alzheimer's disease.

Reference

1) S.Naito *et al.*, JAERI-Review 2004-005, 17.

原子炉：JRR-3　装置：SANS-J (C3-2)　分野：中性子散乱（生物）

This is a blank page.

1. 中性子散乱 7) 基礎物理学・中性子光学

1. Neutron Scattering 7) Fundamental Physics Neutron Optics

This is a blank page.

研究テーマ：オルソ重水素を用いた高輝度超冷中性子生成法の開発
表　題：オルソ重水素を用いた高輝度超冷中性子生成法の開発

1-7-1

Development of high intensity ultracold neutron production with ortho-deuterium

M. Utsuro, M. Tanaka[1], K. Mishima[2], Y. Nagai, T. Shima, Y. Fukuda[3], T. Kohmoto[3], T. Momose[4], A. Moriai[5], K. Okumura[6], H. Yoshino[6]

Research Center for Nuclear Physics, Osaka University
[1] *Department of Sanitary Technology, Kobe Tokiwa College*
[2] *Graduate Course of Science, Osaka University*
[3] *Department of Physics, Faculty of Science, Kobe University*
[4] *Graduate Course of Science, Kyoto University*
[5] *Division of Research Reactor, Japan Atomic Energy Research Institute*
[6] *Research Reactor Institute, Kyoto University*

Ultracold neutrons(UCN) with the velocity of about 6m/s are utilized in various kinds of fundamental physics experiments on neutrons. Ortho-deuterium molecules have much attractive properties as the UCN converter material[1] lying in the rotational ground state at the low temperature below about 20K. All of the solid deuterium(SD2)-UCN sources such as LANL and PSI projects are supposed as the SD2 converter to be inserted into high radiation fields directly coupled to pre-moderators. We have proposed[2]a new concept studied here of a single crystal UCN converter of ortho-deuterium at the exit of a cold neutron guide from a pulsed source, making us rid of the high radiation load problems.

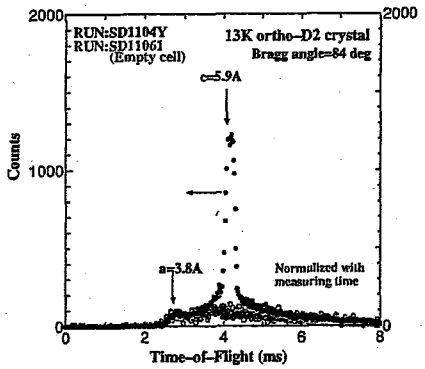

Figure 1: The measured results of the Bragg scattering experiment.

The high purity ortho-deuterium gas was prepared with the magnetic catalyser contained in an aluminum cartridge at the top of a two-stage helium refrigerator, then ortho-concentration of about 98% was attained[3]. Our UCN converter of ortho-deuterium single crystal was prepared in the $2cm^W \times 6cm^H \times 3cm^D$ crystallizing cell in the refrigerator. The crystal orientation prepared was clearly identified with the Bragg scattering as shown in Fig.1, with the time-of-flight of the chopper-pulsed cold neutron beam at the exit of C2 guide tube, JRR-3M reactor, JAERI. Further, a preliminary result of UCN production experiment is also shown in Fig.2, where the countrate in the UCN time region is in reasonable agreement with our expectation.

The present scheme applied to a high intensity pulsed neutron facility now under construction should provide the most intense UCN beam for possible joint uses of UCN.

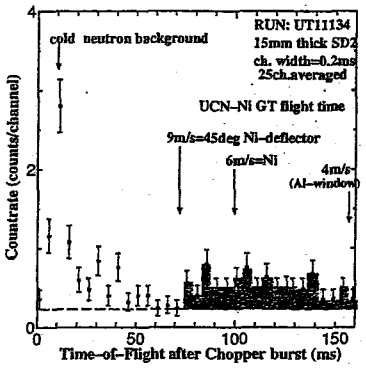

Figure 2: The measured results of the UCN production.

The present work was partially supported by the consigned research from JAERI as the "Reimei" research program in the fiscal year 2003. We especially thank to the experimental helps by Dr. Y. Aratono and Mr. K. Nakamura at the Tokai Research Establishment, JAERI.

The present refrigerator was kindly offered by the Iwatani Gas Company Ltd..

References

1) M. Utsuro and M. Hetzelt, Proc. of Internat. Con. on Inelastic Neutron Scattering (IAEA, Vienna, 1978) Vol.I, pp.67-75.
2) M. Utsuro *et al.*, Internat. Con. on Precision Measurements with Slow Neutrons, held at the Nat. Inst. Science and Technol., Gaithersburg USA, April 2004.
3) K. Mishima, "Irradiation effect of ortho deuterium for UCN source", Doctoral dissertation, Osaka Univ.(2004).

原子炉：JRR-3　　装置：NRG(7R, C2-3-3-1)　　分野：中性子散乱（基礎物理）

研究テーマ：高Q多層膜スーパーミラーの中性子反射率特性評価
表題：高Q中性子多層膜スーパーミラーの開発

1-7-2 Development of Neutron Supermirrors with High-Qc Reflection

K. Ikeda[1], T. Adachi [1], T. Shinohara [1], T. Morishima [1], T. Oku[2], and K. Sakai[3]
[1] *Image Info. Res. Unit, RIKEN, 2-1 Hirosawa, Wako, 351-0198*
[2] *Adv. Sci. Res. Center, JAERI, 2-4 Shirane Shirakata, Tokai, 319-1195*
[3] *Fac. of Science, Tokyo Inst. Tech., 2-12-1 Ookayama, Meguro-ku, 152-8551*

Neutron supermirrors with both a large critical angle and a curved surface are expected to enhance the intensity of utilizable neutrons, to reduce the size of optical devices, and to facilitate the handling of neutrons. In order to realize curved-surface supermirror devices, we have developed a supermirror fabrication system using magnetron sputtering with facing targets and a sample stage with eight movable axes.

Using this system, we have fabricated Ni/Ti supermirrors with critical reflection angles θ_c of 4 times the critical angle of total reflection of natural Nickel ($4Qc$) and the total numbers of deposited layers of 468, 542, 922 and 1634 on silicon substrates 3 inches in diameter and 3 mm in thickness. As shown in Fig.1, the reflectivity of supermirrors achieved approximately 50% at their θ_c and supermirrors with more than 542 layers had reduced reflectivity at angles smaller than θ_c.

Cross sectional images of the supermirror with 1634 layers observed by Transmission Electron Microscopy (TEM) are shown in Fig.2. The layers were smoothly deposited near the substrate, while the non-multilayered pillar structure appeared locally across a number of layers in the middle portion of the deposited layers. The scattering of neutrons by this structure prevented the incident neutrons to have Bragg's reflection and reach layers below the non-multilayered structure and that resulted in the degradation of reflectivity at both θ_c and angles smaller than θ_c. Then the multilayered structure was reestablished near the surface of the mirror as the thickness of monolayers increased so much that each interface between layers was not able to interfere with neighboring interfaces. This reemergence of a multilayered structure led to the recovery of reflectivity when the incidence angle approached around 0.87 degree equal to Qc.

Some techniques such as mixing carbon into Ni layers, ion-beam polishing of deposited layer surfaces, reactive sputtering, have to be introduced so that non-multilayered pillar structures do not appear in the deposited layers and the fabrication of practical supermirrors with $4Qc$ or with thousands of layers are achieved. [1, 2]

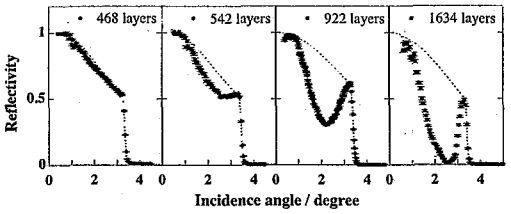

Fig. 1. Reflectivity vs. incidence angle for cold neutrons on 4Qc supermirrors with the different number of deposited layers. Dots show the experimental results and lines show the ones calculated by the optical potential method using the Debye-Waller factor as the index of interface roughness between layers.

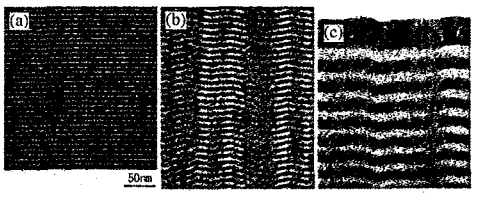

Fig. 2. Cross sectional TEM images of the 4Qc supermirror with 1634 layers, where (a), (b), and (c) show the bottom, middle, and top parts of the mirror, with monolayer thicknesses of approx. 36 Å, approx. 45 Å, and 115 – 425 Å, respectively. The black and white layers are Ni and Ti respectively.

References

[1] K. Soyama*et al.*: Physica B **311** (2002)130.
[2] M.S. Kumar*et al.*: Physica B **276-278** (2000)142.

使用施設：JRR-3M，装置：C3-1-2-2 (MINE)，分野：8. Fundamental Physics & Neutron Optics

研究テーマ：スペース長の大きな Beam Splitting Etalon を用いた Jamin 型冷中性子干渉計の開発と基礎物理への応用
表題：ギャップ長 189μm のビームスプリッティングエタロン

1-7-3 Beam splitting etalons with a spacing of 189μm thickness

M. Kitaguchi[1,3], H. Funahashi[1], K.Taketani[1], T. Nakura[1],
M. Hino[2], Y. Otaké[3] and, H. M. Shimizu[3]

[1] *Department of physics, Kyoto University, Kyoto 606-8502, Japan*
[2] *Research Reactor Institute, Kyoto University, Kumatori 590-0494, Japan*
[3] *RIKEN (The Institute for Physical and Chemical Research), Wako 350-0198, Japan*

A large dimensional interferometer for long wavelength neutrons has the advantage to increase the sensitivity to small interactions. Multilayer mirror is suitable for Bragg reflection of cold neutrons. We demonstrated Jamin-type interferometer for cold neutrons using 'beam splitting etalons (BSEs),' which enables us to align the four independent multilayer mirrors in the interferometer within required precision [1]. For wide applicability of the interferometer, it is important to enlarge the separation between two paths. The separation depends on the spacing between two mirrors in a BSE, which was 9.75μm in the above demonstration. We have developed BSEs with the spacing of 189μm in order to separate the two paths perfectly.

The present BSE can provide the two parallel paths corresponding to two spin components. A magnetic mirror deposited in the limited area on one of the BSE plate reflects only up-spin component of the incident beam and a non-magnetic mirror on the other plate reflects down-spin component that is transmitted through the magnetic mirror (Fig.1). The etalon plate has a diameter of 54 mm and its clear aperture has a diameter of 42 mm. The mirrors were fabricated by the vacuum evaporation at KURRI. The magnetic mirror has eight bilayers made of permalloy45 ($Fe_{55}Ni_{45}$) and germanium. The non-magnetic mirror also has eight bilayers made of nickel and titanium. Both multilayers have the same effective lattice constant of about 24 nm. Figure 2 shows the reflected beam profiles for the up-spin and the down-spin by scanning of a slit with 0.1 mm width in the back of the BSE. The experiment was performed at cold neutron beam line MINE2 at the JRR-3M reactor in JAERI (Tokai). The beam had a wavelength of 0.88 nm. We observed that the two paths reflected by the BSE were separated spatially corresponding to up- and down-spin components. The BSE can also split the incident beam according to the amplitude by reflection off the non-magnetic half mirror at the next to the magnetic mirror.

By using a pair of these BSEs, interferometer with two separated paths can be constructed. We are preparing for high-precision measurement of the topological Aharanov-Casher effect [2] with the interferometer.

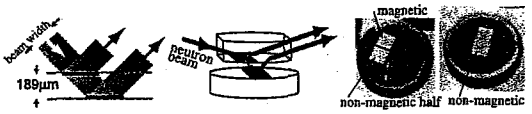

Fig. 1. [left,center] Beam separation using BSE with spacing 189μm thickness. [right] The photograph of the etalon plates before assembly. Magnetic mirror and non-magnetic half mirror has the area of 12 mm wide and 11 mm high. Non-magnetic mirror on the other plate has the area of 12 mm wide and 24 mm high.

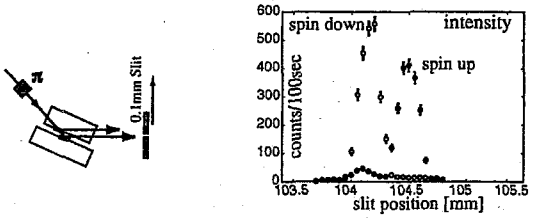

Fig. 2. Beam profile for each spin component. The incident beam was provided by a polarizer mirror and a π flipper.

References

[1] M. Kitaguchi *et al.*: Phys. Rev A **67** (2003)033609
[2] A. Cimmino *et al.*: Nucl. Instrum. Methods Phys. Res. A **440** (2000)579

使用施設：JRR-3M，装置：C3-1-2 (MINE)，分野：8. Fundamental Physics & Neutron Optics

研究テーマ： Beam Splitting Etalon (+, +, −, −) 4回反射による高分解能準弾性散乱分光装置の開発
表題： 4エタロン (++−−) 配置による中性子スピンエコー分光装置

1-7-4 Neutron spin echo spectrometer using four etalons with the (++−−) arrangement

M. Kitaguchi[1,4], H. Funahashi[1], T. Nakura[1], K. Taketani[1], M. Hino[2], S. Tasaki[3], R. Maruyama[3], Y. Otake[4], and H. M. Shimizu[4]

[1] *Department of Physics, Kyoto Univ., Kitashirakawa, Kyoto, 606-8502*
[2] *Research Reactor Institute, Kyoto Univ., Kumatori, Osaka, 590-0494*
[3] *Department of Nuclear Engineering, Kyoto Univ., Yoshida, Kyoto, 606-8501*
[4] *RIKEN, 2-1 Hirosawa, Wako, Saitama, 351-0198*

A new type of neutron spectrometer which is equivalent to neutron spin echo has been tested by using four 'beam splitting etalons.'

Beam splitting etalon (BSE) is a neutron optical device which splits and superposes optical paths. The BSE divides incident neutrons into two parallel beams with large spatial separation and large relative phase according to the gap of the etalon [1].

Neutron spin echo (NSE) is an unique method which measures the energy transition of quasi-elastic scattering with the difference of spin rotation of a neutron between before and after the scattering [2]. A BSE using a magnetic mirror makes the two spatial beams corresponding to up- and down-spin components. The relative phase between the two components is equivalent to spin rotation. The (++) arrangement of two BSEs (Fig.1) makes large relative phase and superposes spatially the two spin components at sample position. The relative phase is

$$\phi = 4\pi 2D \sin\theta/\lambda_n,$$

where D is the spacing of the BSEs, θ is the incident angle to the BSE, and λ_n is the neutron wavelength. A pair of (++) arrangements before and after the sample is equivalent to spin echo system [3]. In this case the fourier time τ, which characterize the performance of spin echo system, is written as

$$\tau = 4mD\lambda_n \sin\theta/h,$$

where m is neutron mass and h is Planck's constant. Neutron spin echo spectrometer enables us to study slow dynamics in the order of the fourier time. The fourier time depends on the spacing of BSEs. Long fourier time has the advantage in investigation of soft material science and biophysics, and can be realized by using large-spacing BSEs. Such spectrometer will be much smaller than conventional NSE, which makes neutron Larmor precession by large magnetic field.

Test experiments have been performed with four BSEs with spacing of 9.75 μm at cold neutron beam line MINE2 at the JRR-3M reactor in JAERI(Tokai). The beam had a wavelength of 8.8Å and a bandwidth of 2.7% in FWHM. In this case fourier time is 1.5 nsec. We have observed interference fringes equivalent to spin echo signal with the contrast of 30% without sample by scanning of phase-shifter-coil current. We are continuing test experiments to study the characters of the spectrometer using BSEs precisely.

References

[1] M. Kitaguchi *et al.*: Phys. Rev A **67** (2003)033609.
[2] F. Mezei, Z. Phys. **255** (1972)146.
[3] T. Ebisawa *et al.*: Phys. Lett. A **259** (1999)20.

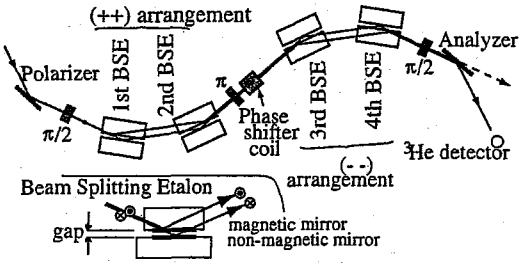

Fig. 1. Neutron spin echo spectrometer using four BSEs.

使用施設：JRR-3M, 装置： C3-1-2 (MINE-1), 分野： 8. Fundamental Physics & Neutron Optics

1. 中性子散乱 8)装　置

1. Neutron Scattering　8) Instrument

This is a blank page.

研究テーマ：静電場試料浮遊加熱装置をもちいた極限環境における融液構造測定
表　題：静電場試料浮遊加熱装置をもちいた極限環境における融液構造測定

1-8-1

Development of Electrostatic Levitation Furnace for Neutron Scattering Experiments of High Temperature Liquids

T. Masaki, T. Ishikawa, P. -F Paradis, Y. Arai, N. Igawa[1], Y. Ishii[1], and S. Yoda

Japan Aerospace Exploration Agency, 2-1-1, Sengen, Tsukuba, Ibaragi 305-8505
[1]Neutron Science Research Center, JAERI, Tokai, Ibaraki 319-1195

In recent years, many attentions have been focused on the containerless techniques for the experimental research of high temperature melts or deeply undercooling liquids, especially for the structure analysis by neutron or X-ray scattering method [1]. Recently, JAXA has been developing levitation droplet technique due to the electro-static force either for the microgravity experiments in the International Space Station (ISS) or for the normal gravity experiment in laboratory on ground. Since this technique has merits for neutron scattering experiments, JAXA and JAERI are developing an electrostatic levitation furnace (ESL) for neutron scattering experiments of extremely high temperature melts and deeply undercooling liquids. This ESL has been developed since 2002 and the neutron diffraction of levitated sintered alumina was successfully performed at the room temperature [2]. Last year, the neutron scattering experiments was performed to study the structure of levitated liquid zirconium at 2500K with the ESL. The liquid zirconium was levitated in the ELS and kept contactless condition for eight hours. However, the diffraction data could not be taken with sufficient accuracy because the sample position was unstable due to a serious trouble on the electrical isolation of the high voltage line in the ESL.

In this year, the neutron diffraction experiment was tried again for the levitated liquid zirconium. The insulation of voltage line was improved and some of metallic parts nearby the voltage line were replaced by the ceramic parts. The experiment was successfully performed and the levitated molten zirconium at the temperature of 2100 K could be kept for twenty four hours in total. Figure 1 shows the levitated liquid zirconium in the ESL. The results of neutron diffraction experiments of liquid zirconium are shown in figure 2. The diffracted neutron from the ESL chamber and back ground intensity are subtracted. Two sharp peaks are remained on the diffraction of zirconium, which are derived from diffraction peaks of copper electrodes. The shape of scattering intensity can be regarded as a typical diffraction pattern of liquid sample. More detailed analysis of diffraction data is quite difficult because the scatter of data is rather large.

Near future, the new facility for the high intensity of neutron beam can be applicable to these kinds of experiments. At that time, the accuracy of data will be remarkably improved and the detailed analysis of undercooled liquids will be possible by using the present apparatus.

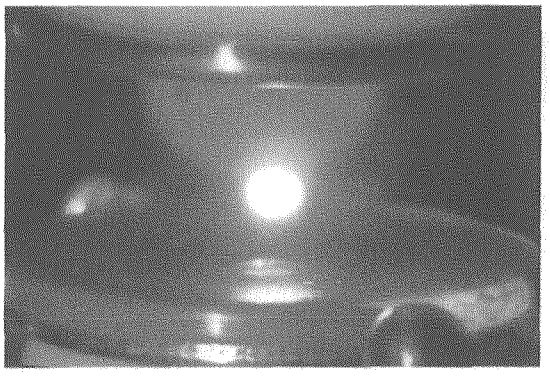

Figure 1: Levitated liquid Zr at 2100K
The bright sphere is the levitated sample. The upper and lower disks are electrodes for controlling the electrostatic field.

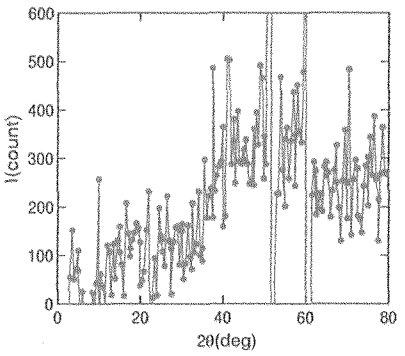

Figure 2: Neutron scattering pattern of levitated liquid Zr.

References

1) T. Schenk, D. Holland-Moritz, V. Simonet, R. Bellissent and D.M. Herlach : Phys. Rev. Lett. **89** (2002) 075507.
2) H.Aoki, P. -F. Paradis, T. Ishikawa, T. Aoyama, T. Masaki, S. Yoda, Y. Ishii and T. Itami : Rev. Sci. Instr. **74** (2003) 1147.

原子炉：JRR-3　　装置：HRPD(1G)　　分野：中性子散乱（装置）

研究テーマ：中性子イメージング用輝尽性蛍光体の研究
表　題：$CaBPO_5:Ce^{3+}$ 系輝尽性蛍光体の中性子イメージ特性

1-8-2

Neutron Imaging Characteristics of $CaBPO_5:Ce^{3+}$ Based Photostimulable Phosphors

K. Sakasai, M. Katagiri, M. Matsubayashi, T. Nakamura and Y. Kondo[1]

Neutron Scinece Research Center, JAERI, Tokai, Ibaraki 319-1195
[1] Department of Applied Physics, Tohoku University, Sendai, Miyagi 980-8579

The neutron imaging plate (NIP) has made a great success[1)] in the field of neutron scattering study but the NIP is sensitive to not only neutron but also gamma ray. Therefore, it is difficult to discriminate neutron signal from gamma ray one when the NIP is read out. To overcome the problem, the authors have been studying a $CaBPO_5:Ce^{3+}$ based material as a new neutron storage phosphor consisting of light materials.

The $CaBPO_5:Ce^{3+}$ based powder sample was prepared by firing raw materials ($CaCO_3$, H_3BO_3, $(NH_4)_2HPO_3$, and $CeCl_3 \cdot 7H_2O$) in a muffle furnace in a nitrogen atmosphereat 600°C for 2 hours and at 800°C for 2 hours. A disk-like sample with a diameter of 12 mm and a thickness of 1mm was prepared for 2D image measurement. This sample was made by the Spark Plasma Sintering (SPS) method. In the SPS method, the powder was set in a carbon vessel and then fired for 10 minutes at 800°C. The powder sample was pressed with a stress of 5 kN in a vacuum atmosphere throughout the firing.

Although the $CaBPO_5:Ce^{3+}$ sample showed Photostimulated Luminescence (PSL) after neutron irradiation, the PSL yields were not so high compared to those of $SrBPO_5:Eu^{2+}$ samples[2)]. Therefore, the authors have made $CaBPO_5:Ce^{3+}$ + CaF_2 samples (molar ratio was 1:1) and measured the PSL decay characteristics. It was confirmed that PSL yields of the $CaBPO_5:Ce^{3+}$ are significantly increased by adding CaF_2 and the ratio of $PSL_{CBPandCaF2}/PSL_{CBP}$ was 26.7, where $PSL_{CBPandCaF2}$ and PSL_{CBP} are the total PSL outputs of $CaBPO_5:Ce^{3+}$ + CaF_2 and $CaBPO_5:Ce^{3+}$ samples, respectively.

Figure 1 shows PSL yields per neutron fluence of the $CaBPO_5:Ce^{3+}$ + CaF_2 sample as a function of neutron energy. The neutron irradiation was carried out at the SANS-J Facility. As seen in the figure, the PSL yields were proportional to $E^{-0.5}$, where E is neutron energy. This is a clear evidence that the samples are sensitive to neutrons and the PSL output is proportional to the number of nuclear reactions of ^{10}B atoms with neutrons because the neutron cross section of $^{10}B(n,\alpha)Li$ is proportional to $E^{-0.5}$.

After the sample was irradiated with a collimated neutron beam with a diameter of 1.5 mm, its surface was scanned with focused laser light by using an X-Y stage controller. The neutron flux and neutron irradiation time were 2.4 x 10^4 n/cm^2/s at 0.65 nm and 30 minutes, respectively. The scanning was carried out every 0.25 mm on the sample surface. The results are shown in Fig.2. The beam intensity image can be clearly obtained.

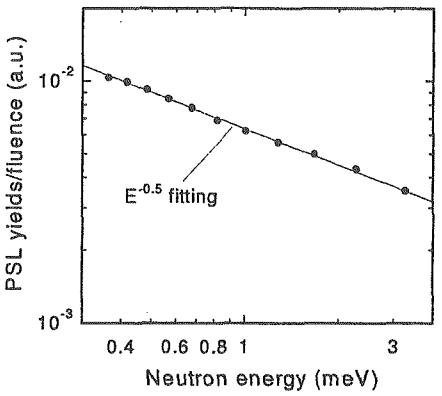

Figure 1: The PSL yields per neutron fluence of the $CaBPO_5:Ce^{3+}$ + CaF_2 sample as a function of neutron energy.

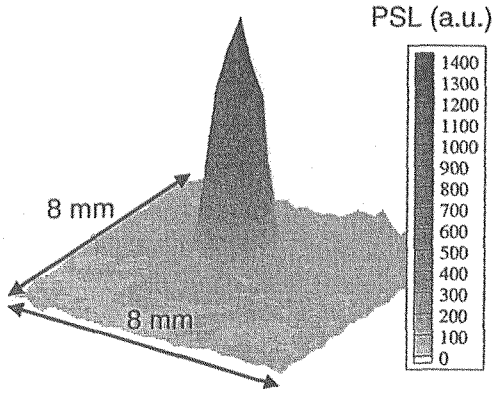

Figure 2: A collimated neutron beam image obtained with the sample. The beam size was 1.5 mmϕ.

References

1) Y. Karasawa *et al.* : Physics B, **241-243** (1998) 139.
2) K. Sakasai et al. : Applied Physics A, **74** (2002) S1589.

原子炉：JRR-3　　装置：SANS-J(C3-2)　　分野：中性子散乱（装置）

研究テーマ：多重極限環境下における中性子散乱実験法の研究
表　題：熱中性子集光デバイスの開発

1-8-3

Development of the thermal neutron focusing device

T. Osakabe and K. Soyama[1]

Advanced Science Research Center, JAERI, Tokai, Ibaraki 319-1195
[1]Neutron Science Research Center, JAERI, Tokai, Ibaraki 319-1195

The neutron focusing is an indispensable technical element in the experiments under extreme condition, such as high pressure or high magnetic field with tiny samples. The best method for compensating weak signals from tiny samples is focusing the incident neutron beam on a sample position by supermirror reflection. We have developed the thermal neutron focusing device with a lot of curved supermirrors according to the proposal of D.F.R. Mildner [1)].

Figure 1 shows the photograph of the device installed in the triple-axis spectrometer TAS-1 (2G). The device is 400 mm long and has 18 sheets of 3Qc NiC/Ti neutron supermirrors with the shape of circle. The extension of the end of each mirror meets at a focal point, which is located in 150 mm from the end of the device. Neutrons are repeatedly reflected with the same angle by the inner side of the mirror and arrive at a focal point (sample position).

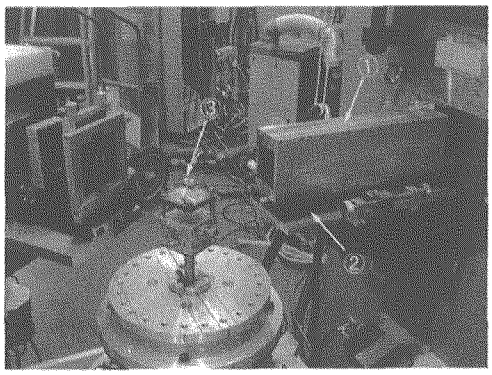

Figure 1: Photograph of the focusing device installed in the TAS-1 (2G) spectromrter. 1:focusing device, 2:adjustable stage (placed on the optical bench, 3:sample.

Figure 2(a), (b) and (c) show the neutron intensity distributions at focal length detected by the neutron IP. The intensity gains at a focal point are about 4.2, 2.7 and 2.0 for incident neutron energy of 4.9 meV, 13.7 meV and 30.5 meV respectively. Figure 2 also show the results of Monte Carlo ray-tracing simulation for the neutron intensity distributions. The each result of the measurement almost agrees with the result of simulation. This indicates that the device demonstrates the expected performance.

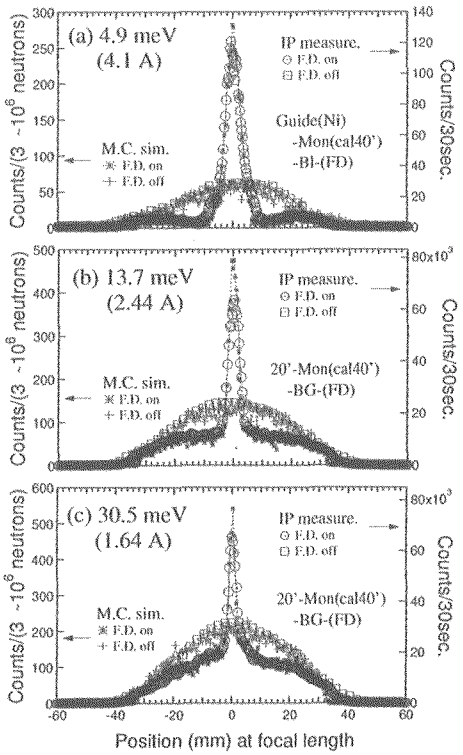

Figure 2: The neutron intensity distributions obtained by the neutron IP with or without the focusing device for the incident neutron energy of (a) 4.9 meV, (b) 13.7 meV and (c) 30.5 meV. The results of the M.C. simulation are also shown in the figures.

References

1) D.F.R. Mildner: Nucl. Instr. And Meth. A299 (1990) 416.

原子炉：JRR-3　　装置：TAS-1(2G)　　分野：中性子散乱（装置）

研究テーマ：冷中性子屈折光学系と評価用検出器の基礎研究
表　題：冷中性子光学素子と検出器の開発

1-8-4

Development of optical devices and detectors for cold neutrons

H. M. Shimizu, T. Adachi, K. Ikeda, T. Shinohara, K. Hirota, H. Sato, Y. Takizawa, S. Morita, H. Ohmori, K. Sakai[1], T. Oku[2], J. Suzuki[2], S. Satoh[3] and M. Furusaka[3]

RIKEN, Wako, Saitama 351-0198
[1]*Department of Physics, Tokyo Institute of Technology, Ohokayama, Meguro 152-8551*
[2]*Advanced Science Research Center, JAERI, Tokai, Ibaraki 319-1195*
[3]*Institute of Material Structure Science, KEK, Tsukuba, Ibaraki 305-0801*

We have developed optical devices for cold neutrons, focusing lens using MgF_2 especially.[1] Fresnel type lens has wide caliber and better transmission.[2,3] The detailed design was described before.[2] We have reported the 25 times higher performance with Focusing geometry Small Angle Neutron Scattering (F-SANS)[4] compared to Pinhole geometry Small Angle Neutron Scattering (P-SANS) last year.[1] In this report, development of fundamental nature of neutron focusing lens is described.
The performance of the compound lens was investigated using a cold neutron beam from the SANS-J instrument at the JRR-3 reactor of JAERI. A collimated neutron beam entered the lens, and the transmitted and refracted intensities were measured by a two-dimensional position sensitive detector (PSD) located at 10 m downstream from the center of the lens. The PSD has 128 × 128 position channels over a 640-mm in diameter sensitive area. The position resolution of the PSD was specified to be 5 mm.

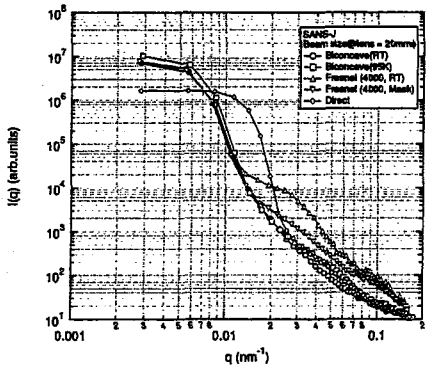

Figure 1: Measurement of the focused beam profiles comparing biconcave lens at Room Temperature (○), at 95 K (□), Fresnel lens without mask (△), with mask (▽) and no lens (◇).

Major problem of the Fresnel lens performance is undesirable refraction or reflection around back-cut region of the Fresnel structure. Those refracted or reflected neutron makes hump around direct beam. In order to solve this problem, neutron absorbing mask made by Gd. The detailed design was described before.[3] As a result, the hump around direct beam becomes 80% less by using this Gd absorbing mask.[3] This means 90% noise is reduced by Gd absorbing mask. The comparison of the beam profiles at 1.1 nm wavelength and 20 mm in diameter neutrons with/without Gd absorbing mask is shown in Fig. 1.

Meanwhile, major problem of the biconcave lens performance is less transmission with wide caliber. In order to solve this problem, the lenses were cooled at 95 K. Transmission of 27 lenses was 0.59 with 1.1 nm in wavelength and 20 mm in diameter neutron beam at room temperature. That was improved up to 0.85 at 95 K. These two profiles were also shown in Fig. 1. We also have developed two dimensional position-sensitive neutron detector (PSND) with high spatial resolution and portability. Coupling of ^{6}LiF+ZnS(Ag) scintillator in 0.3 mm thickness and 3 inches resistance dividing type photo multiplier tube (RPMT) made 30 mm × 30 mm sensitive area and 0.5-0.7 mm spatial resolution possible. In Fig. 2, full width half maximum (FWHM) of fifth peak from left side was 1.6 ch. The position resolution of the PSND was specified to be 0.5 mm. Then, FWHM for neutron beam in 0.5 mm width should be 0.8 mm. The spatial resolution is expected to be 0.63 mm by deconvolution of beam width.

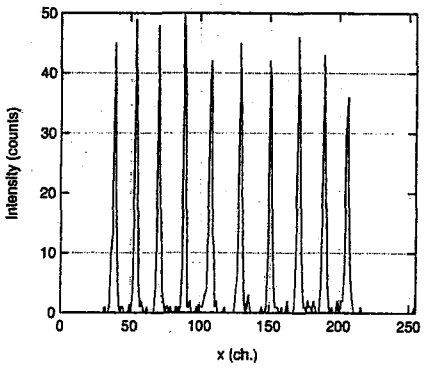

Figure 2: A typical line profile of 10 times multi shot using Cd slit in 0.5 mm width with 10 mm position shifting.

References

1) S. Koizumi, M. Matsuda and K. Kurihara:*Progress report on neutron scattering research*, (JAERI-Review 2004-005, Tokai, 2004) p. 142.
2) T. Oku, S. Morita, S. Moriyasu, Y. Yamagata, H. Ohmori, Y. Takizawa, H. M. Shimizu, T. Hirota, Y. Kiyanagi and J. Suzuki, *Nucl. Instrum. Methods A* **462** (2001) 435.
3) T. Adachi, K. Ikeda, T. Shinohara, K. Hirota, T. Oku, J. Suzuki, H. Sato, K. Hoshino, J. Guo, W. Lin, H. Ohmori, H. M. Shimizu, K. Sakai, C.-K. Loong and K. C. Littrell, *Nucl. Instrum. Methods A* **529** (2004) 112.
4) S.-M. Choi, J. G. Barker, C. J. Glinka, Y. T. Cheng and P. L. Gammel, *J. Appl. Cryst.*, **33** (2000) 793.

原子炉：JRR-3　　装置：SANS-J(C3-2)　　分野：中性子散乱（装置）

研究テーマ：中性子光学素子の開発と中性子分光法の研究
表　題：中性子磁気レンズの集光型小角散乱装置への応用に関する研究
1-8-5

A Study on Application of a Magnetic Neutron Lens to Focusing Geometry SANS Experiments

T. Oku, J. Suzuki, H. Sasao, T. Adachi[1], T. Shinohara[1], K. Ikeda[1], T. Morishima[1], K. Sakai[1], H.M. Shimizu[1]

Advanced Science Research Center, JAERI, Tokai, Ibaraki 319-1195
[1]RIKEN, 2-1 Hirosawa, Wako, Saitama 351-0198

A sextupole magnetic field functions as an ideal focusing and defocusing lens for neutrons when the neutron has positive and negative spin polarity to the local field, respectively. So far, the neutron focusing effect of sextupole magnets has been investigated experimentally and numerically [1,2]. For practical use of the lens function of a sextupole magnet in neutron scattering experiments, a sextupole magnet with a sufficiently large aperture accompanied with strong focusing power is demanded. Recently, we have developed a superconducting sextupole magnet (SSM) with an aperture of 46.8 mm in diameter which generates the sextupole magnetic field $B = (G/2)\,r^2$ with G=12,800 T/m^2, where r is the distance from the magnet axis [3].

Its neutron focusing effect has been investigated using unpolarized cold neutrons [4]. We have proposed to apply the sextupole magnet to small-angle neutron scattering experiments with focusing geometry (FSANS) to improve the q-resolution and/or measuring efficiency by focusing neutrons on the detector [5-7]. To get the advantage in the practical FSANS measurement over a conventional pinhole-geometry SANS experiment, it is necessary to employ a neutron focusing device with little scattering and absorption of the neutrons. The sextupole magnet is considered to be a suitable focusing device, because of its neutron focusing property which is free from the scattering and absorption of the neutrons. However, if neutrons with negative spin polarity are included in the incident beam, they are defocused by the sextupole magnet and, then raise the background level. Therefore, the incident beam should be well polarized in case of the FSANS experiment with the sextupole magnet. In this paper, we investigated the neutron focusing effect of the SSM using unpolarized and polarized neutrons, and discussed the feasibility of the SSM on the application to the FSANS experiments.

The SSM has a 2 m-long sextupole coil which is composed of six saddle-shaped coils. There exists non-adiabatic regions where the neutron spin is flipped; 1) around the center axis of the magnet where the sextupole magnetic field is weak, 2) around both ends of the sextupole coil where the magnetic field distribution deviates from the sextupole magnetic field distribution. We then removed these non-adiabatic regions by applying a dipole field along the beam axis using solenoid coils equipped in the SSM [8]. The detailed specifications of the SSM are described in Ref. [3]. The SSM was installed at the beamline C3-1-2-1 of JRR-3 in Japan Atomic Energy Research Institute (JAERI). The experimental setup is shown in Fig. 1. The neutrons are monochromatized by the mechanical velocity selector. The neutron wavelength is λ =13.44 Å with $\Delta\lambda/\lambda = 0.177$. The polarizer is the FeSi magnetic supermirror. We used the transmitted neutrons through the polarizer, which have negative spin polarity. The spin polarization efficiency is ~ 0.96. The transmission of the polarized neutrons with λ =13.44 Å through the polarizer is ~ 0.66. The spin flipper (SF) is a radio-frequency gradient spin flipper which was designed to be effective for the neutron beam with wavelengths longer than 4 Å and a beam size of 50 mm in diameter [9]. The neutrons with positive and negative spin polarity are incident in the SSM when the SF is on and off, respectively.

We measured 2d neutron intensity distribution using a neutron imaging plate (BAS-ND) with position resolution of 0.2 mm under several conditions as follows:

case1 SSM on, polarizer off:
The incident beam to the SSM is unpolarized.

case2 SSM on, polarizer on, SF on:
The incident beam to the SSM is polarized with positive spin polarity.

case3 SSM on, polarizer on, SF off:
The incident beam to the SSM is polarized with negative spin polarity.

case4 SSM off, polarizer on:
SSM is off.

case5 Beam shutter closed:
The incident beam to the SSM is shut out for the background measurement.

Each measuring time is 11 hours. When the SSM is on, current in the sextupole coil is $I_{ssm} = 210$ A, which corresponds to the current to produce the magnetic field gradient of $G = 8{,}235.6$ T/m^2. In this condition, the neutrons with positive spin polarity are focused on the detector (Fig. 1). When the SSM is off, $G = 0$ and the neutrons are not accelerated by the SSM. When

原子炉：JRR-3　　装置：NOP(C3-1-2-1)　　分野：中性子散乱（装置）

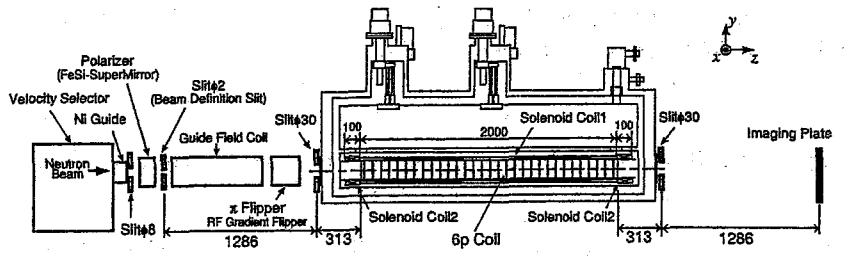

Figure 1: Experimental setup.

the polarizer is on, solenoid coils are also excited to remove the non-adiabatic regions.

The radially averaged intensity is plotted as a function of d, where d is the distance from the peak position of the 2d intensity distributions (Fig. 2). In cases 1 and 3, a shoulder was observed around $d \sim$ 23 mm, but not in case 2 (Fig. 2). Thus, the shoulder should be produced by the neutrons defocused by the SSM. The ratio of the focused to defocused neutrons by the SSM in case 2 is estimated to be 50 times larger than that in case 1, based on the polarization of $\sim$ 0.96 of the incident beam. In case 2, therefore, such a shoulder should be unobservable, because the contribution of the defocused neutrons to the intensity distribution is buried under the background level. The differences of the peak values between cases 1 and 2 and the shoulder values between cases 1 and 3 are considered to result from the neutron transmission of the polarizer.

The ratio R of the peak value to the background level of the intensity distribution of a direct beam is one of measures which are often used to evaluate SANS instruments. In general, R is desired to be larger than $\sim 10^4$. Here, we define R_{mag} as the ratio of the peak value to the level of defocused neutrons for the SANS instrument with focusing geometry using the sextupole magnet. R_{mag} $\sim$8,000 can be achieved even in the experimental condition of case 2 which is not optimized for a high R_{mag} value. Around the experimental condition of this study, R_{mag} is approximately proportional to $(\Delta\lambda/\lambda)^{-1}$. By optimizing the experimental condition, R_{mag} is expected to be increased by several times. The details of the optimization of the experimental condition will be discussed elsewhere. Therefore, the level of the defocused neutrons by the SSM can be sufficiently reduced by the same way as in this study, and $R_{mag} > \sim 10^4$ can be achieved in the FSANS experiment with the sextupole magnet.

In conclusion, we have investigated the neutron focusing effect of the SSM using unpolarized and polarized cold neutrons to discuss the feasibility of the application of the sextupole magnet to FSANS experiments. The experimental setup, which consisted of the polarizer, the spin flipper, the SSM, etc., worked as expected. By utilization of the polarizer with efficiency of $\sim$ 0.96, the level of the defocused neutrons could be reduced to be $\sim$1/8000 of the peak value of the direct beam. The level is expected to be further decreased by optimizing the experimental condition. Thus, we conclude that the sextupole magnet can be employed as a focusing device for FSANS experiments.

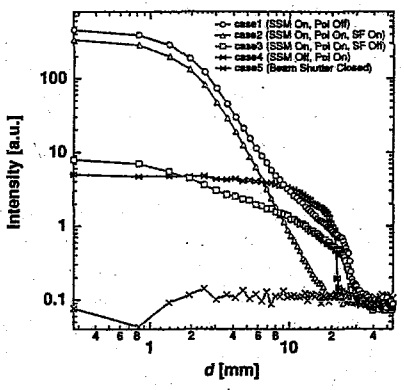

Figure 2: Radially averaged intensity. d is the distance from the intensity peak position.

References

1) H.M. Shimizu et al., NIM-A 430 (1999) 423.
2) J. Füzi et al., Appl. Phys. A 74 (2002) S210.
3) J. Suzuki et al., J. Appl. Cryst. 36 (2003) 795.
4) H.M. Shimizu et al., Nucl. Instr. and Meth. A 529 (2004) 5.
5) B. Alefeld et al., NIM-A 274 (1989) 210.
6) B. Alefeld et al., Physica B 234-236 (1997) 1052.
7) S.-M. Choi et al., J. Appl. Cryst. 33 (2000) 793.
8) M. Furusaka et al., NIM-A 529 (2004) 223.
9) T. Oku et al., Physica B 335 (2003) 226.

研究テーマ：中性子利用実験装置の開発研究
表　題：マイクロストリップを用いた二次元中性子ガス検出器の開発
1-8-6

Development of a high-performance microstrip gas chamber with a capability of track discrimination for neutron detection

T. Nakamura, S. Masaoka, H. Yamagishi, K. Soyama and K. Aizawa
Neutron Science Research Center, JAERI, Tokai, Ibaraki 319-1195

We have been developing microstrip gas chamber (MSGC) using helium-3 gas as neutron converter. The specifications expected to the MSGC detector are high detection efficiency (>60% for thermal neutrons), high spatial resolution ($< 1mm$), high neutron-gamma-ray discrimination ratio ($> 10^7$), high counting rate ($> 10^6 cps/detector$), and a moderate area. It is common that large amount of heavy gas such as CF_4 has to be filled to achieve a high spatial resolution in a conventional positioning scheme, such as charge-division or delay-line chain. However, achieving a gas gain of more than ten in such a gas condition would require an electric field strength of $\sim 10^4 V/mm$ between the microstrip electrodes, thereby, making the detector unstable due to the dielectric breakdown at the surface of the substrate.

To solve these problems and achieve the specifications, we developed the MSGC system, in which all the signal channels are read-out individually, and the incident positions of the neutrons are determined by the instrument system with a capability of secondary particle discrimination (InSPaD)[1]. The InSPaD identifies the particles - proton and triton - created in the nuclear reaction $^3He + n \rightarrow p + T$ on the basis of the track length, and determines the incident position of neutron accurately, not determined as the center of gravity. The simulation result showed a high spatial resolution less than 1 mm regardless of the gas condition using the InSPaD. Full description of the InSPaD can be found in [2]. With this system, one can use " light " gas condition without a loss of a spatial resolution, thereby, stability of the detector should be further increased.

The MSGC was manufactured by TOSHIBA Co. and can deal with charge-up at high counting rate by appropriately adjusting the resistivity of the polyimide substrate using a organic titanium coatings. Figure 1 shows the proto-type of the microstrip substrate, which measures $50 \times 50 mm^2$ mounted on the PCB socket board for individual read-out. We have made two of high pressure gas chambers; one is for the test (Figure 2) and the other is for the prototype compact chambers. For both chambers, signal channels of 160 and 561 can be fed through so that to read-out all the signals lines individually. The gas chamber withstands up to 8 atm. The windows of the chambers were made of aluminum with a thickness of 3 mm. At each channels of read-out, the signal

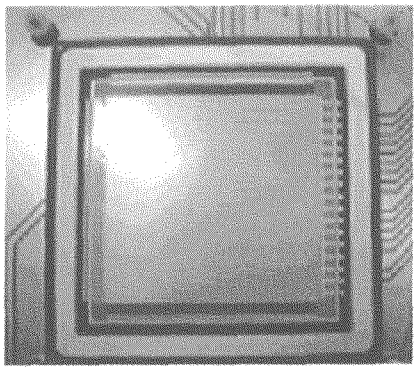

Figure 1: Microstrip substrate mounted on the PCB socket board for individual readout.

pulse were amplified, shaped and discriminated individually. We do not measure the pulse height, but only check the numbers of the fired channels (i.e. hit-detection) to ensure high count rate. The feasibility of the hit-detection method is well confirmed in x-ray [3] and in neutron detection [4]. In the InSPaD, the voltage levels of the discriminators for each channels were set identical but appropriately so that the numbers of suprathreshold channels should become different for a proton and a triton. The identification of the proton and a triton can be done using the numbers of suprathreshold channels, and the incident position of neutron can be determined by the simple logical calculation. The InSPaD realizes the identification of the particles with a simple, fast and cost-effective method, thus, ensuring high count rate, and moreover increases the signal to noise ratio of the detector system, which is attributable to the relatively high discrimination levels to differentiate a proton and a triton.

The operational principle including feasibility test of the InSPaD and the basic characteristics were confirmed using a test detector system [5]. Figure 3 shows the signal height of the event when the projected track on the plane of the anodes is at an angle to the anodes, which was estimated at $\sim 40°[sin^{-1}(4.8/7.5)]$ using a projected track length of 4.8 mm and a track length of 7.5 mm. If we set the threshold level to $10 \times 10^{-15} C$ for this event, the numbers of suprathreshold signals are two and five for the triton and proton, respectively, and the InSPaD can be used to determine the incident

原子炉：JRR-3　　装置：NOP(C3-1-2-1)　　分野：中性子散乱（装置）

position of the neutron as strip 4. This result demonstrates the feasibility of the InSPaD; in the future we will establish a full read-out system using an InSPaD.

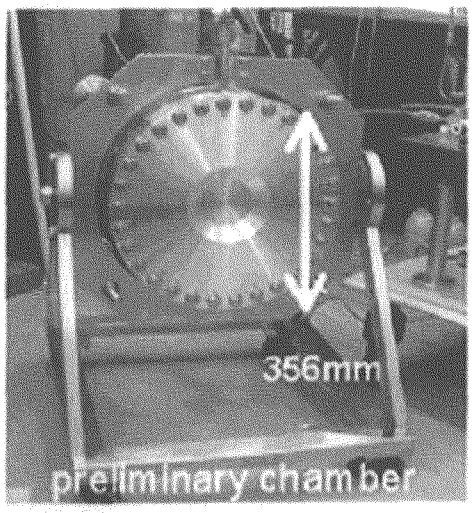

Figure 2: Test gas chamber for individually read-out, which withstands up to 8 atm.

References

1) H. Yamagishi, *et al.*: Japanese patent pending, P2000-253967.
2) H. Yamagishi, *et al.*: Rev. Sci. Instrum. **75** (2004) 2340.
3) T. Tanimori, *et al.*: Nucl. Instr. and Meth. A **436** (1999) 188.
4) T. Nakamura, *et al.*: *Proc. 16th Int. Conf. Advanced Neutron Sources (ICANS XVI), Dusseldorf,2003*, p. 441.
5) T. Nakamura, *et al.* : Nucl. Instr. and Meth. A **529** (2004) 336.

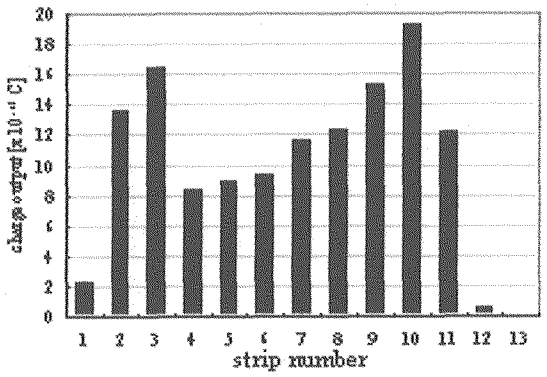

Figure 3: Signal-height distribution along the track measured event to event in a mixture of 15% C_2H_6 with helium-3 at 4 atm when the projected track in the plane of the anodes was angled about 40deg to the anodes.

研究テーマ：冷中性子画像検出器の開発
表　題：冷中性子画像検出器の開発
1-8-7

Development of cold neutron imaging detector

H. Sakurai[1], F. Tokanai[1], S. Gunji[1], S. Motegi[1], M. Kaneko[1], S. Kikuchi[1], J. Suzuki[2], T. Oku[2]

[1] *Department of Physics, Yamagata University, 1-4-12 Kojirakawa, Yamagata 990-8560, Japan*
[2] *Japan Atomic Energy Research Institute (JAERI), 2-4 Shirane Shirakawa, Tokai, Ibaraki 319-1195, Japan*

For the detection of thermal neutorns, a gas proportional counter with the fill gas of ^{3}He is frequently employed because the absorption cross section are significant for thermal neutrons. The optical capillary gas proportional counter is available to the neutron imaging with gas mixtures of ^{3}He. The nuclear reaction between a neutron and ^{3}He produces a proton with energy of 570 keV and a triton with the energy of 190 keV. For a cold neutron,these two particles are ejected to opposite sides of each other and hence the image of their tracks should be straight line in gas. Using cold neutrons at JRR-3 in JAERI,we have tested the imaging of tracks using the optical CGPC filled with a gas mixture of ^{3}He.

Figure1 is a schematic view of the optical imaging CGPC setup on the beam line of cold neutrons C3-1-2-1 at JRR-3 in JAERI. The CGPC is filled with the gas mixture ^{3}He + 8%CH_4 + 2%TMA at 1.1 atm. The energy of cold neutrons is adjusted to 0.45 meV by a velocity selector before reaching the setup. Incoming cold neutrons were confined to the centre area of the CGPC by a slit with a size of 5 mm × 5 mm made of cadmium to control the counting rate to approximately 66 cps.

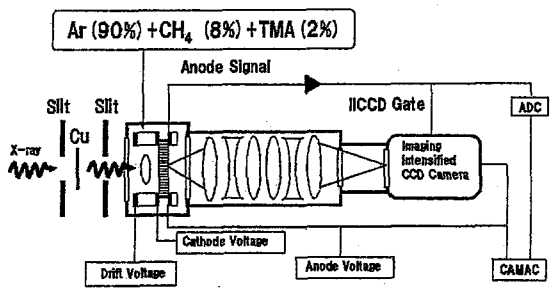

Figure 1: Schematic of the optical imaging CGPC setup on the beam line for cold neutrons at JRR-3 in JAERI.The CGPC is filled with the Penning gas mixture ^{3}He + 8%CH_4 + 2%TMA at 1.1 atm.The absorption region for cold neutron is 10 mm.The CGPC is viwed through a lens system by an IICCD.

A track image produced from the cold neutron is shown in Fig 2a. Also, Fig 2b shows the brightness distribution of the track image projected to the x-coordinate and the distribution indicates the behaviour of energy depositions along the track.The whole track length is approximately 15.2 mm on the image and there is a brighter portion with the length of 1.8 mm in the vicinity of the track end compared with the other.

Since this track image is a projection of the track to the capillary plate,the maximum lengths are estimated to 18.2 mm for the whole length and 2.2 mm for the bright portion,respectively,taking account of the gas depth.As the ranges of the triton and the proton are approximately 3.6 and 23 mm for this gas mixture from a calculation of dE/dx,the track image shows a part of track in the absorption region. Moerever,the rate of dE/dx of the triton is greater than that of the proton. These result in due to the triton and the other due to proton. Therefore,we conclude that the absorption point of neutron is in the vicinity of (430,370) at the graph of track image in Fig 2a with ambiguity of 0.5 mm.

These results indicate that the neutron absorption point can precisely determine with the the track image.

Publication:"A test of imaging by cold neutron using optical capillary gas proportional counter", NIMA(2004) in press

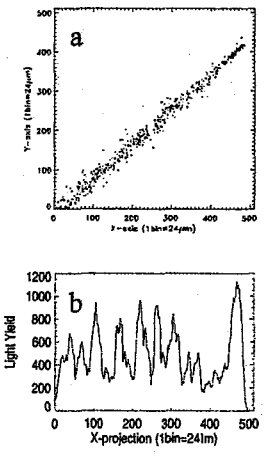

Figure 2: (a) A track image produced by absorption of a cold neutron in ^{3}He. The trace consists of a triton and a proton. (b) Light yields of the CCD for the track image which shows a projected profile of energy deposition.

原子炉：JRR-3　装置：NOP(C3-1-2-1)　分野：中性子散乱（装置開発）

This is a blank page.

1. 中性子散乱 9)残留応力

1. Neutron Scattering 9) Residual Stress

This is a blank page.

研究テーマ：円筒型炭素複合材料の残留応力の研究
表　題：２次元円筒型炭素複合材料の中性子回折法による３軸方向残留ひずみの測定
1-9-1

Residual Strain Measurements in 3-axial Directions for 2-dimensional Cylindrical Carbon-Carbon Composite by Neutron Diffraction Method

S. Baba, N. Minakawa[1], A. Moriai[1], M. Yamaji and M. Ishihara

Department of Advanced Nuclear Heat Technology, JAERI, Oarai, Ibaraki 311-1394
[1] *Department of Advanced Science Research Center, JAERI, Tokai, Ibaraki 319-1195*

The carbon fiber reinforced carbon matrix composite (c/c composite) is thought to be one of the advanced heat resistant materials in the nuclear engineering field. However, a lot of cracks are observed in manufacturing process of the ring type c/c composite due to the delamination between the fiber and the matrix by the residual stress. This is because of the different shrinkage between the fiber and the matrix during carbonization and graphitization heat treatment. The aim of the present study is to clarify the residual strain occurring in the c/c composite to improve the manufacturing process. The residual strain was measured by neutron diffraction method using the RESA (Residual Stress Analysis for neutron diffraction) in the JRR-3M (Japan Research Reactor-No.3 Modified) of JAERI. Cylindrical c/c composite after the first baking process was used in the experiment. First, the precise wavelength of neutron diffraction was determined using the standard silicon (Si) powder, National Bureau of Standards (NBS). Moreover, the most suitable line for lattice spacing of strain-free materials (d0) was determined by grinding c/c composite powder. The measured d002 diffraction intensity of the c/c composite sample showed the peak with the shoulder in the low angle site, and the intensity of the peak appears respectively at higher position with narrow width for well-graphitized parts and at lower position with wide width for not well-graphitized parts. The residual strain in 3-axes directions (radial (Fig.1), hoop and axial) was measured by changed 002 diffraction angles. The 3-axes strains were also analyzed by FEM (Finite Element Method)(Fig.2). The results of analysis by FEM that supposed the complete connection condition of the fiber and matrix are not agree with the value of measurement the strains by neutron diffraction method. Future study has necessary to carry out the analysis with precise conditions.

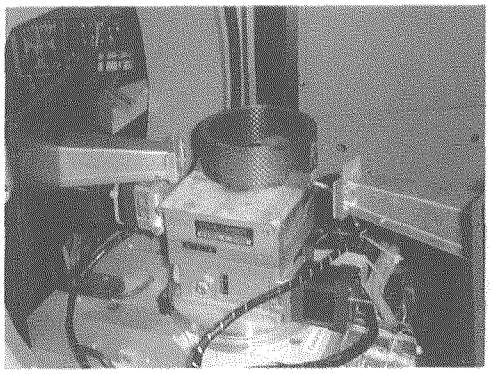

Figure 1: Set up sample on goniometer for r-direction.

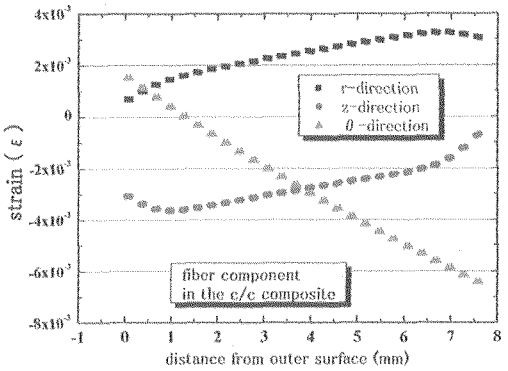

Figure 2: Estimation of 3-axial strains by FEM.

原子炉：JRR-3　　装置：RESA(T2-1)　　分野：中性子散乱（残留応力）

研究テーマ：中性子産業利用技術の開発研究
表　題：鉄鋼材料の焼入れによる残留応力発生メカニズムの解明
1-9-2

Distribution of the martensite of induction hardened S45C round bar observed by small angle neutron scattering

K. Inoue, K. Aizawa[1], A. Moriai[1] and F. Ikuta[2]

Faculty of Sience and Technology, Ryukoku University, Seta, Otsu 520-2194
[1]*Neutron Scattering Research Group, JAERI, Tokai, Ibaraki 319-1195*
[2]*Neturen Co., Ltd., Tamura, Hiratsuka 254-0013, Japan*

Induction hardening at the surface of carbon steel is usually used for industrial purpose because it extremely improves the mechanical properties of the surface, such as the wear resistance and the fatigue resistance. The hardening is accompanied by a martensitic transformation at the surface.[1)] The photographs of the induction hardened round bar and of the sliced specimen cut from the center of the bar are shown in Fig. 1. For sliced specimen, we can distinguish the martensitic region from the coexistent region of pearlite and ferrite as a contrast.

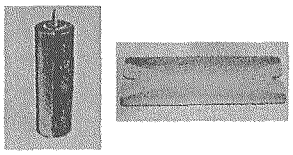

Figure 1: Photographs of the induction hardened round bar and the sliced specimen cut from the round bar.

The SEM images at each position along the central line of the sliced specimen, which corresponds to radial position on the central sectional plane of round bar, are shown in Fig. 2. We obviously see the change of the image as moving from the surface to the center. This change shows that martensite at the surface gradually change to the coexistent state of pearlite and ferrite as approaching to the center.

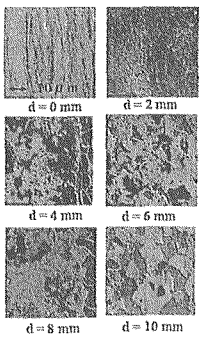

Figure 2: SEM image of the induction hardened S45C at each radial position on the central sectional plane of round bar. "d" means the distance from the surface.

To investigate the volume fraction of the martensite at each position on the center line parallel to the short side of the sliced specimen, we observed a small angle neutron scattering. SANS-J at JRR-3M was used. We covered q-range from 0.03 to 1.9 (nm^{-1}), by using the length, L, of 10 m and 1.5 m, where L means the length from the sample to the detector. The wave length of the beam was 0.679 nm, and the resolution (FWHM) was 10.33 %. The transmitted beam was very weak. This is partly because the sliced specimen has a thickness of 1mm, and partly because there exist the void, impurity and so on in the sample as it is one of the industrial utility goods. Q-dependence of the scattered beam is shown in Fig. 3..

We see that the intensity changes abruptly at around the position of 6 mm from the surface. The fact is consistent with the change of the contrast in the photograph of the sliced specimen. We have a plan to make a measurement with more thin plate, to avoid the multiple scattering. By using the Guinie plot, we will get the information about the size and the form of the martensite.

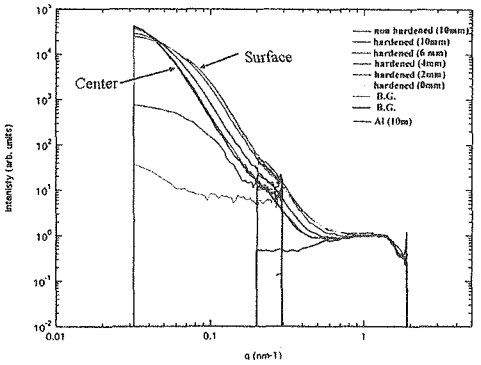

Figure 3: Q-dependence of the intensity of small angle scattered neutron beam.

References

1) K. Inoue, M. Sugimoto, N. Minakawa, A. Moriai, *et al.*:*Proceedings of International Conference on Advanced Technology in Experimental Mechanics, Nagoya, 2003*, published by The Japan Society of Mechanical Engineers. Paper No. OS04W0182. (CD edition, 6 pages).

原子炉：JRR-3　　装置：SANS-J(C3-2)　　分野：中性子散乱（残留応力）

研究テーマ：中性子産業利用技術の開発研究
表　題：鉄鋼材料の焼入れによる残留応力発生メカニズムの解明

1-9-3

Distribution of the martensite of induction hardened S45C round bar observed by very small angle neutron scattering apparatus PNO

K. Inoue, T. Hirayama, K. Aizawa[1], A. Moriai[1] and F. Ikuta[2]

Faculty of Sience and Technology, Ryukoku University, Seta, Otsu 520-2194
[1]Neutron Scattering Research Group, JAERI, Tokai, Ibaraki 319-1195
[2]Neturen Co., Ltd., Tamura, Hiratsuka 254-0013, Japan

To improve the mechanical properties, such as the wear resistance and the fatigue resistance of the industrial carbon steel, we usually make an induction hardening at the surface of the material. The hardening is accompanied by a martensitic transformation. The volume fractions of martensitic phase alter gradually according to the depth from the surface.[1)]

To get the information about the size and the form of the martensite at each position of an induction hardened S45C round bar, we have made a very small angle neutron scattering using PNO at JRR-3M. The wave length was 0.2 nm. It covered the q-range from -0.07 to 0.07 nm^{-1}.

The diameter of the round bar was 20 mm and the height was 40 mm. For the present experiment, we prepared the 1 mm thick sliced specimen cut from the center of the bar. The detail about the sample and the experiment done by SANS-J are written in another paper written by the same authors in this Progress Report.

The q-dependence of the transmitted beam at each position of the sliced specimen is shown in Fig.1. The

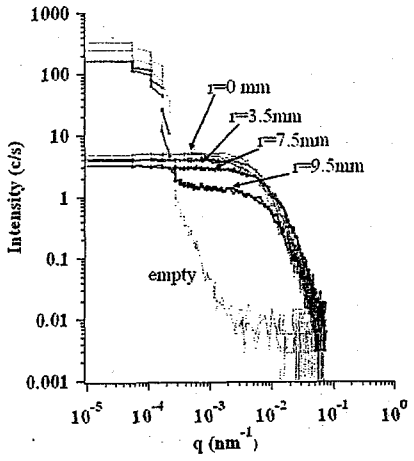

Figure 1: Q-dependence of the intensity of the transmitted beam. The letter, r, means the position on the sliced specimen, corresponding to the radius of the central sectional plane of the round bar.

transmitted beams from the center of the sliced specimen of the hardened round bar and of the non hardened round bar are shown in Fig. 2. In Fig. 2 the difference between two cases is not observed. This suggests that induction hardening does not reach to the center.

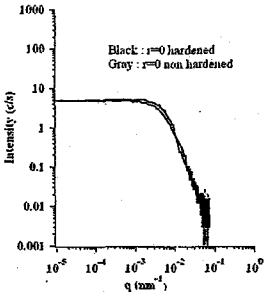

Figure 2: Q-dependence of the intensity of the transmitted beam from the center of hardened round bar and from that of non hardened one.

In Fig. 1, at r=9.5 mm, the abrupt increase of the intensity below q=3×10^{-4} nm^{-1} is observed. This fact indicates that the beam was slightly off from the edge of the sample. When we neglect this abrupt increase, we see that the intensity at the plateau becomes relatively low in case of r=9.5 mm. This will be due to the existence of the martensite at the surface of the round bar. The intensity of this plateau gradually increases as we leave from the surface of the round bar. In every case, the intensity begins to decrease above q=10^{-2} nm^{-1}. The slope of the curve is nearly q^{-4} at the center (r=0). It becomes closer to q^{-3} as we approach to the surface (r=9.5 mm).

We have a plan to connect the data obtained by PNO to the data obtained by SANS-J. Because SANS-J covers the q range from 0.03 to 1.9, we will obtain the data with wide q-range from q=0 to q=1.9. By fitting to the Guinie plot, we will get the information about the size and the form of the martensite.

References

1) K. Inoue, M. Sugimoto, N. Minakawa, A. Moriai, *et al.*:*Proceedings of International Conference on Advanced Technology in Experimental Mechanics, Nagoya, 2003*, published by The Japan Society of Mechanical Engineers. Paper No. OS04W0182. (CD edition, 6 pages).

原子炉：JRR-3　　装置：PNO(3G)　　分野：中性子散乱（残留応力）

研究テーマ：中性子 IP による高精度応力測定
表　題：d_0 不要の中性子応力測定法開発への挑戦
1-9-4

A Challenge to d_0-Disused Neutron Stress Measurement Using Area Detector

T. Sasaki[1], Y. Morii[2], N. Minakawa[2],N. Niimura[2] and Y. Hirose[1]

[1]*Department of Materials Science and Engineering, Kanazawa University, Kanazawa, Ishikawa 920-1192*
[2]*Advanced Science Research Center, JAERI, Tokai, Ibaraki 319-1195*

The aim of our study is to improve a method for determining stress inside materials with an area detector. The use of an area detector for the stress measurement can bring about an efficient use of diffraction data from the irradiated material. For example, we can obtain 360 strains from one measurement with our present measurement technique. Tough the direction of each strain is limited by the diffraction condition, there is a lot of merits in the use of an area detector. What is particularly important is the fact that we do not need a precise value of the lattice spacing in stress free sate (d_0) at the process that stress and strain are converted from the diffraction data. This strong point owes to the adoption of the principle of the stress analysis which is called the cosα method.

Since the cosα method has been firstly developed as only for the X-ray diffraction method, it is fundamentally not adequate to use it for the neutron diffraction data. However, the result of the application of the cosα method to the neutron diffraction data performed by us showed a simple relation, that is to say, a one-to-one correspondence to the mechanical condition of the material such as the applied stresses. Moreover, the cosα method can provide precise stresses through a simple data correction in which the raw diffraction data are subtracted by those that were obtained from the material treated by the stress-relief process.

All what mentioned above are the conclusions found from our first experiment[1)], in which the thickness of the specimen was 5 mm. In order to increase the degree of the practical usefulness of the method, it should also be valid to wider range of the thickness of the materials. Therefore, we planed the second experiment to examine the relation between the stresses that are output by the cosα method and those that exist in the material when the thickness of the material varies. The range of the specimen's thickness adopted in this experiment was from 1 mm to 20 mm. This report describes about its outline. The similar experimental conditions were adopted in the present experiment. Figure 1 shows the schematic of the optics which was used in the experiment.

Figure 2 shows the misfit stresses, which were calculated using the cosα method, with respect to the thickness of the specimen. The applied stress in each sample was 0 MPa. Though the residual stress might be one of the causes which contribute to the misfit

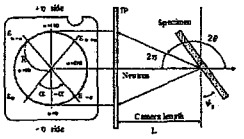

Figure 1: Experimental optics used in the experiment.

stress, the possibility would be low considering the heat treatment for the stress relief as well as the deep sampling volume due to the large penetration depth of the neutron beam. Based on our computer simulation, the misfit stresses are generated by the dependency of the shapes of the diffraction profiles on the position of the Debye-Scherrer ring. The dotted line in the figure 2 indicates the result of the computer simulation. The true line denotes the relation in case of the use of the centroid method. They are in good agreement to the experimental data. It was also found from the computer simulation that the stresses of the cosα method show one-to-one relation to the applied stresses in the material with the slope of 1.0 for every thickness that we examined. This means that the cosα method is valid for determining the mean stress in the gauge volume in the material even for the neutron diffraction data. The most valuable advantage of the cosα method in the neutron stress measurement is that the stress can be obtained without a high accuracy. It will contribute greatly to the promotion of the neutron experiment in industry.

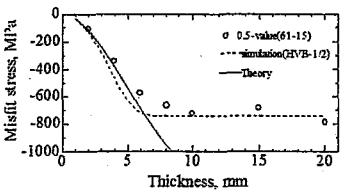

Figure 2: Experimental result on misfit stress.

References

1) T.Sasaki, N. Minakawa, Y. Morii, N. Niimura and Y. Hirose, Transactions of The Japan Society of Mechanical Engineers, vol.69, No.688, pp.1711-1716, 2003.

原子炉：JRR-3　　装置：RESA(T2-1)　　分野：中性子散乱（残留応力）

研究テーマ：レーザーピーニングした配管内面における残留応力分布測定
表　題：レーザーピーニング処理鋼表面下残留応力の非破壊測定
1-9-5

Non-destructive Measurement of Residual Stress Beneath the Surface of Laser Peened Steel

K. Akita, Y. Sano[1], T. Kubo[1], S. Ohya, H. Suzuki[2] and A. Moriai[2]

Department of Mechanical Systems Engineering, Musashi Institute of Technology, Tokyo 158-8557
[1] *Power and Industrial Systems Research and Development Center, Toshiba Corporation, Yokohama 235-8523*
[2] *Neutron Science Research Center, JAERI, Tokai, Ibaraki 319-1195*

Laser peening process is one kind of surface treatment technology using a mechanical interaction between the surface of a metallic material and the plasma induced by the irradiation of a nanoseconds-order laser pulse. The laser peening introduces compressive residual stress in surface layer, and it is effective for the improvement of fatigue strength, the corrosion resistance[1], and the prevention of stress corrosion cracking (SCC)[2]. The laser peening, therefore, has been applied to reactor core shrouds of nuclear power plants to prevent SCC.

Non-destructive measurement of the residual stress near the laser peened surface is important to understand the generation mechanism of the residual stress on laser peening. And the residual stress on inside wall of pipe welds is important to evaluate the integrity of components in nuclear reactors. However the both experiments have not been performed.

As the first stage of this study, non-destructive measurements of depth profile of residual stress near the laser peened surface was performed using neutron diffraction.

The material used for this study was a high tensile strength steel, HT1000. The size of the specimen was 40mm×40mm with the thickness of 15 mm. The HT1000 specimen was annealed by furnace cooling after keeping at 973 K for 3 hours for removing residual stress caused by machining. The fundamental wave of a Q-switched Nd: YAG laser is frequency-doubled to a water penetrable wave (λ=532 nm) by a second harmonic generator with a nonlinear optical crystal. The pulse duration is 8 ns in FWHM and the pulse frequency is 10 Hz. The specimen was driven to x- and y-directions in a water jacket during laser irradiation. The coverage C_v is defined as:

$$C_v = (\pi D^2/4) \times N_d, \qquad (1)$$

where D is the diameter of laser spot ($\simeq$1mm), N_d is the irradiation density which is the average number of laser pulses irradiated in unit area. C_v for the specimen was 2827 %. Our laser peening process in this study did not use any coating materials such as black paint. The neutron diffractometer for residual stress measurements, RESA, in JRR-3M was used to measure the residual stresses. The measured diffraction plane was α-Fe 110. The wavelength was 2.086 Å.The diffraction angle 2θ was 62 deg. The gage volume was 0.5×0.5×15 mm^3. The acquisition time was 90 seconds.

It was found non-destructively that the compressive residual stress reached about 1 mm in depth from the specimen surface. The detailed distribution of residual stress beneath the surface will be measured in the next stage.

References

1) R. Fabbro, et al., J. Laser Applications, 10, 265 (1988)
2) Y. Sano, et al., Proc. 8th Int. Conf. on Nuclear Engineering (ICONE-8), Baltimore, Paper No. 8441 (2000)

原子炉：JRR-3　　装置：RESA(T2-1)　　分野：中性子散乱（残留応力）

研究テーマ：中性子回折による構造物の残留応力測定
表　題：中性子回折法による異種金属溶接境界の材料強度評価

1-9-6

Evaluation of strength in overlaid materials by neutron diffraction

T. Ishikawa, K. Miyata, H. Yano, R. Ishikawa, Y. Morii[1], A. Moriai[1] and N. Minakawa[1]

Hitachi-Engineering Co., Ltd. Hitachi, Ibaraki 317-0073
[1]*Advanced Science Research Center, JAERI, Tokai, Ibaraki 319-1195*

Residual stress measurement inside a machine structure is important when evaluating crack progress etc. In a welding material, the stress near the welding boundary and the strength evaluation are important. We measured the residual stress by neutron diffraction, about a boundary of overlaid Nickel base alloy and Low alloy steel. The technical problem with this measurement is that diffraction might become irregular, because the Nickel base alloy of the weld metal has texture. Also, diffraction might become an interference at the boundary of a different metal. Therefore, another purpose of this measurement was to confirm this.

Figure 1 shows the form of a specimen. This specimen was Heat-treated at 621 ℃ for 24 hours at the size of 200 × 200 × 60 mm, and cut into the shown size after that. The release stress from cutting was 50 MPa or less, as a result of measuring with a strain gauge.

The RESA neutron wavelength used was 0.20858 nm. The slit width and height used was 3mm. The measurement of Young's modulus and Poison's ratio were (111)(200) of Nickel base alloy, and (110) (200) of Low alloy steel. But, the (111) diffraction of the Nickel base alloy became irregular due to its texture. And the (200) diffraction intensity of the Low alloy steel was weak, because the neutron pass length was long. Consequently in the stress analysis the Nickel base alloy was measured at(200), and the Low alloy steel was measured at (110).

Figure 2 shows the residual stress distribution around the boundary of an overlaid weld and base metal. The residual stress of the overlaid boundary was tension from 200 to 300 MPa in the X and Y direction.

This data will be used as fundamental evaluation data of crack progress and strength.

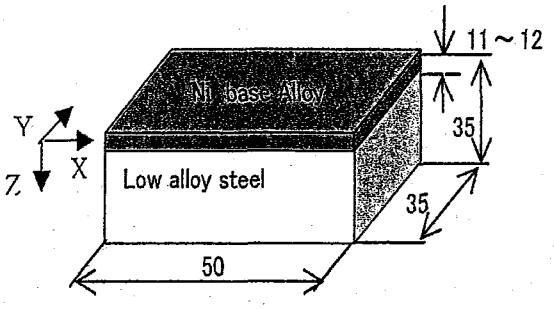

Figure 1: Geometry and dimensions of Overlaid Material specimen.

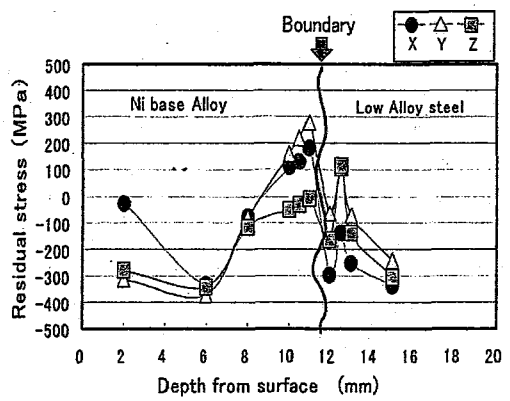

Figure 2: Residual stress distribution around the boundary of Overlaid weld and base metal.

原子炉：JRR-3　　装置：RESA(T2-1)　　分野：中性子散乱（残留応力）

研究テーマ：中性子散乱による機能材料構造の研究
表　題：形状記憶合金のき裂先端における相変態の測定

1-9-7

Phase Transformation at Crack Tip of Shape Memory Alloy TiNi

Y. AKINIWA, H. KIMURA, K. TANAKA, N. MINAKAWA[1] and Y. MORII[1]

Department of Mechanical Science and Engineering, Nagoya University, Nagoya 464-8306
[1]Advanced Science Research Center, JAERI, Tokai, Ibaraki 319-1195

1. Intruduction

The equiatomic TiNi alloy is an intermetallic compound that shows not only excellent resistance against corrosion and wear but also shape memory effect with large recovery strain and superelasticity. Though TiNi has been used for pipe couplings and the frames of glasses utilizing the shape memory effect and superelastic property [1], the practical application is limited because the fatigue properties of TiNi has not been fully clarified. In addition to the conventional use, TiNi has attracted attention as an actuator of intelligent structure in recent years and the fatigue reliability over long-term use has been recognized as an important subject in the utilization [2]. In order to evaluate the fatigue properties, it is necessary to understand the martensitic transformation at a crack tip because the stress-induced martensitic phase plays an important roll to improve the fatigue property. Judging from the past experiments by the authors, the distribution of the stress-induced martensitic transformation at a crack tip differs depending on whether the area is plane stress or plane strain. This implies that the stress condition, as well as the stress intensity factor, must be considered for the fatigue design of this material. Neutron diffraction measurement is believed to be the most suitable method to measure the martensitic transformation in plane strain condition. In this study, stress-induced martensitic transformation at a crack tip was investigated in shape memory TiNi. The cracked specimen was utilized for the measurement by neutron diffraction in order to clarify the martensitic transformation at a crack tip.

2. Material and measurement

Shape memory TiNi was heated to 450 degrees Celsius in order to introduce shape memory effect at room temperature before the neutron diffraction measurement. It is mainly composed of austenitic phase at room temperature of approximately 25 degrees Celsius without loading. A specimen in the dimension of 10 x 70 x 6 mm^3 were prepared by electrical discharge machining followed by electrolytic polishing. Due to the thickness, most of neutron diffraction is considered to be obtained from the inner part in plane strain condition. A fatigue crack was introduced from a notch in the middle of the specimen. The neutron facility of JAERI (RESA) was used for the neutron diffraction measurement. The width of the incident beam was 0.5 mm with the preset time of 1800 sec. The wave length of the beam was 0.21009 nm. The diffraction plane of (102) was employed for the measurement of the stress-induced martensitic phase at the crack tip. The measurement was conducted under the uniaxial load of 35 N.

3. Martensitic Transformation at Crack Tip

The results of the neutron diffraction at x = -500, 0, 500, 1000, 1500, 2000, 2500, 3000, 4000, 5500 micrometer, where crack tip is at x = 0 and crack propagation direction is along x axis, show that the diffraction intensity drops at x = 1500. Therefore, the distribution of the stress-induced martensitic transformation is expected to stretch about 1200 micrometer ahead of the crack tip under the applied stress intensity factor. The residual martensitic phase was also observed at the crack wake, which is believed to affect the crack closure. The results of the nano-indentation on the surface in plane stress show that the martensitic phase stretches several times larger than the present result. The suppression of the stretch of the martensitic phase at the crack tip is expected to result from the triaxiality of the stress at crack tip and the negative volume change from the austenitic to martensitic phase in TiNi.

4. Conclusion

The distribution of martensitic phase at a crack tip was measured in plane strain condition by neutron diffraction measurement. The area of the martensitic phase was found to be smaller than that in plane stress condition. However, the existence of the martensitic phase was confirmed in plane strain condition in contrast to some expectation by other researchers that it rarely exists. The results show that the stress conditions such as the thickness of a structural component must be taken into account for the fatigue design of shape memory TiNi in addition to the stress intensity factor. Further investigation is necessary for the quantitative analysis by the combination of neutron diffraction measurement for plane strain condition and atomic force microscopy on the surface for plane stress condition.

References

1) H.Sakamoto: Trans. Jpn. Inst. Met. **24** (1983) p. 665.
2) H. Tobushi: J. of JSTP **35-403** (1994) p. 910.

原子炉：JRR-3　　装置：RESA(T2-1)　　分野：中性子散乱（残留応力）

研究テーマ：組織傾斜材料の内部応力測定
表　題：金属/セラミックス傾斜機能材料の残留応力解析

1-9-8

Residual Stress Analysis of Metal/Ceramic Functionally Graded Materials

Mitsuhiko Hataya, Makoto Nakagawa, Takao Hanabusa, Kazuya Kusaka, Toshio Matsubara[1], Yukio Morii[2], Nobuaki Minakawa[2], Atsushi Moriai[2] and Hiroshi Suzuki[2]

Department of Mechanical Engineering, Tokushima University, Tokushima 770-8506
[1] Tokushima Prefectural Industrial Technology Center, Tokushima 770-8021
[2] JAERI, Tokai, Ibaraki 319-1195

It is very difficult to join a metal and a ceramic film directly, because the difference in their coefficients of thermal expansion is so large that cracks may occur in the film or a delamination may occur in an interface. A functionally graded material (FGM) is usual to relax an abrupt change in mechanical and/or physical properties at an interface of joining.

We prepared the Fe/Al_2O_3 FGM consisting five layers from iron to Al_2O_3 by spark plasma sintering (SPS). Residual stresses in each layer of FGM were measured by RESA in order to investigate the best production condition of FGM.

Table 1 shows measurement condition of residual stress. Figure 1 shows residual stress distribution in FGM. Figure 2 shows an average internal residual stress distribution.

The following results were obtained from the residual stress measurement in FGM.

- Residual stresses in all parts of Fe were tensile and increased with decreasing the volume fraction of Fe.
- Residual stresses in all parts of Al_2O_3 were compression and increased with decreasing the volume fraction of Al_2O_3.
- The difference in an average internal stress was large in the part of Fe 20%- Al_2O_3 80%.

Table 1: Conditions of residual stress measurement

Slit size (mm^2)	15(Width) × 2(Height)
Distance from sample to slits (mm)	50
Wave length (nm)	0.208022
Diffraction plane	Fe (110) Al_2O_3 (116)

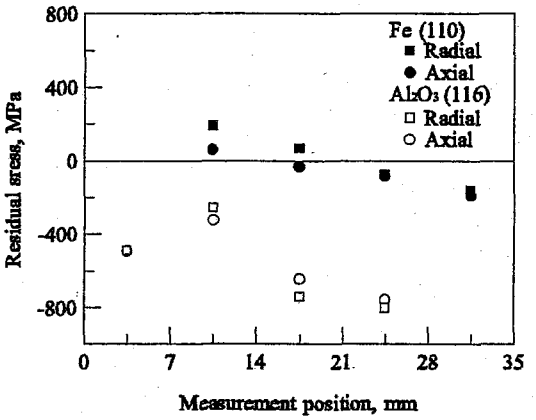

Figure 1: Residual stress distribution in FGM.

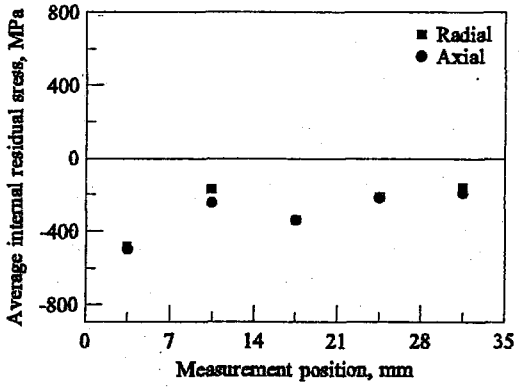

Figure 2: Average internal residual stresses (MPa).

原子炉：JRR-3　　装置：RESA(T2-1)　　分野：中性子散乱（残留応力）

研究テーマ：中性子散乱による機能材料構造の研究
表　題：中性子回折によるアルミダイカスト製品の品質評価

1-9-9

Quality Estimation of Aluminum Die-casting by Neutron Diffraction

Mitsuhiko Hataya[1], Atsushi Moriai[2], Hiroshi Suzuki[2], Yukio Morii[2], Takao Hanabusa[1] and Nobuaki Minakawa[3]

[1]Department of Mechanical Engineering, Tokushima University, Tokushima 770-8506
[2] JAERI, Tokai, Ibaraki 319-1195
[3] Advanced Machine Factory Ltd., Hitachi, Ibaraki 319-1222

In this research, we estimated quality of aluminum die-casting as a part of the application of neutron diffraction method to the industrial world. We measured residual strain in aluminum die-casting by using RESA in JRR-3. We prepared two kind of aluminum die-castings, good one and no-good one, were made by manufacturing cooperation. Their differences were distinguished with bending caused by differences of product conditions.

Figure 1 is diagram and measured positions of aluminum die-casting. Table 1 shows measurement condition of residual strain. Figure 2 shows residual strain distribution in aluminum die-casting.

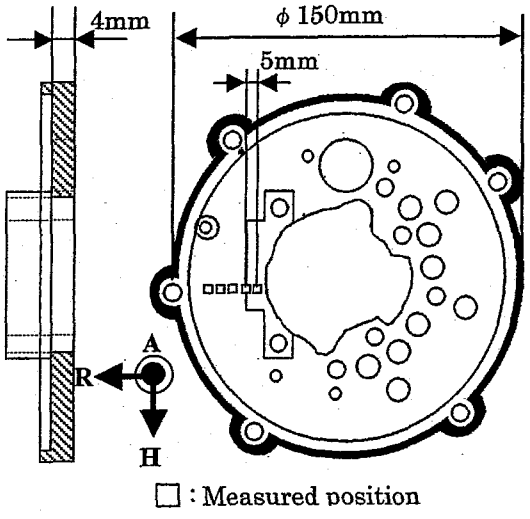

Figure 1: Diagram of aluminum die-casting.

Table 1: Conditions of strain distribution measurement

Slit size (mm)	15 (Width)×2 (Height)
Distance from sample and slit (mm)	50
Wave length (nm)	0.2087459
Diffraction plane	Al (111), (220), (311)

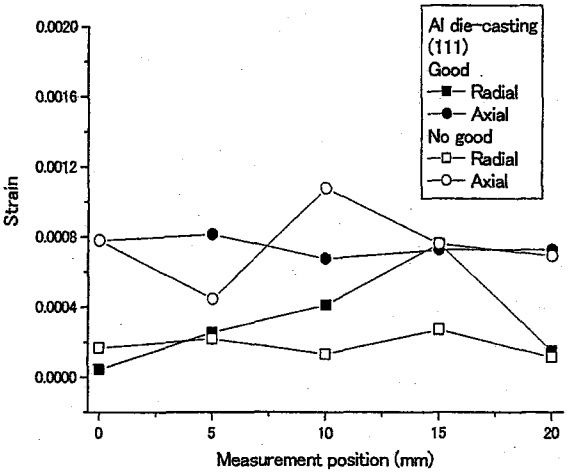

Figure 2: Strain distribution in Al die-casting.

We can see clearly difference of residual strain in aluminum die-casting between good one and no-good one from Fig.2. So, we could prove that we can estimate quality of industrial product by using neutron diffraction.

We can say from these results that neutron diffraction method is very useful for the industrial world.

原子炉：JRR-3　　装置：RESA(T2-1)　　分野：中性子散乱（残留応力）

研究テーマ：中性子散乱による機能材料構造の研究
表　題：中性子散乱による非晶質材内部応力測定の検討

1-9-10

Investigation of the residual stress measurement by the neutron scattering of an amorphous metal

Nobuaki Minakawa[1], Atushi Moriai[2], Hiroshi Suzuki[2], and Yukio Morii[2]

[1]*Advanced Machine Factory Ltd., Hitachi, Ibaraki 319-1222*
[2] *JAERI, Tokai, Ibaraki 319-1195*

Outline

The tensile strength of an amorphous metal is the mighty value over 1000MPa, which attracts attention from industrial utilization. In order that to evaluate the soundness and life of parts and manufactured goods; these are indispensable to measure an internal stress. Amorphous material must expect performing a stress measurement on the basis of the waves by scattering, in order that a diffraction line is not obtained unlike general material (material with a crystal structure). Many amorphous researches were advanced, the key was expected on the basis of the structure, which an atomic density group makes, and the test measurement was performed in that there are many tentative theories. At first trial, the relation between a diffraction line when an amorphous metal alloy crystallizes, and the scattering wave of an amorphous metal was measured.

Measurement

We used the transition metal system four components alloy as an amorphous metal specimen.

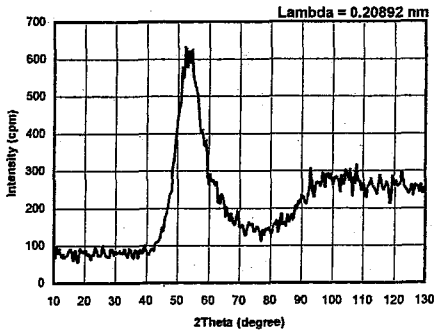

Figure 1: Neutron scattering of Amorphous.

The scattering measurement used by 0.20892nm, rotating phi axis using the neutron diffractometer for the residual stress analysis (RESA) installed in JRR-3. As a result is shown in Fig. 1. In order that temperature gradients are different, as for the terminal section of the same specimen, crystallization grows up. The scattering measurement was performed, rotating phi axis using the terminal section specimen. As a result is shown in Fig. 2.

Result

From the specimen in which crystallization proceeded, as shown in Fig. 2, diffraction lines were measured in the scattering waves. It understands that the crystallized specimen is BCC structure from the diffraction lines. The crystal lattice plane, which grows from the first wave, is (110) plane, and this result is congruous with the tentative theory relation for the atomic high density is generated from the first wave.

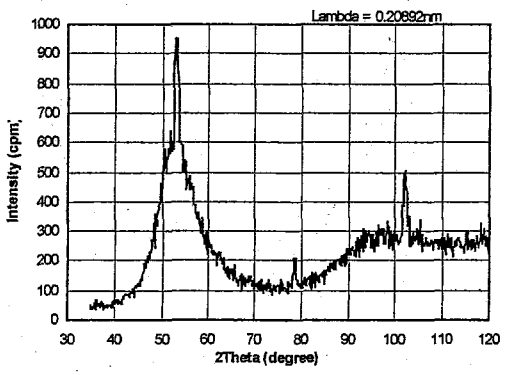

Figure 2: Neutron Diffraction of Amorphous.

原子炉：JRR-3　　装置：RESA(T2-1)　　分野：中性子散乱（残留応力）

研究テーマ：原子炉炉内構造物の溶接継手部における残留応力評価
表　題：中性子回折による NCF600 の弾性定数の測定

1-9-11

Elastic Constants Measurement of NCF600 by Neutron Diffraction - Evaluation on residual stress of weld joint in nuclear core internal structure-

R. Mizuno, A. Moriai[1], H. Suzuki[1] and Y. Morii[1]

NDE Center, Japan Power Engineering and Inspection Corporation, Yokohama 230-0044
[1]Neutron Science Research Center, JAERI, Tokai, Ibaraki 319-1195

Stress corrosion cracking (SCC) has occurred at weld joints with NCF600 material, which is Ni-based alloy, in nuclear core internal structures. Table 1 shows chemical composition of NCF600. It is important to determine the residual stress distributions inside the weld joint in order to evaluate the crack propagation by SCC. It is possible to measure the stress distributions inside bulk by neutron diffraction. Neutrons are scattered from the incident beam direction through angles 2θ, according to Bragg's law,

$$\lambda = 2d\sin\theta, \tag{1}$$

where λ is the wavelength of neutron, d is the spacing between lattice planes. Lattice strain is determined by neutron diffraction, which measures the spacing between lattice planes, according to equation (2),

$$\varepsilon = (d - d_0)/d_0, \tag{2}$$

where d_0 is the spacing between lattice planes without strain. By measured strains of three directions, stresses are determined by equation (3),

$$\begin{aligned}
\sigma_x &= \frac{E}{(1+\nu)(1-2\nu)}((1-\nu)\varepsilon_x + \nu(\varepsilon_y + \varepsilon_z)),\\
\sigma_y &= \frac{E}{(1+\nu)(1-2\nu)}((1-\nu)\varepsilon_y + \nu(\varepsilon_z + \varepsilon_x)),\\
\sigma_z &= \frac{E}{(1+\nu)(1-2\nu)}((1-\nu)\varepsilon_z + \nu(\varepsilon_x + \varepsilon_y)) \qquad (3)
\end{aligned}$$

where E is Young ' s modulus, ν is Poisson's ratio and σ_x, σ_y and σ_z are components of stress of each directions.

Hence, the elastic constants are necessary to calculate stress from measured strains. They have dependency on diffraction plane. Ni(111), Ni(200) and Ni(220) in NCF600 are available to measure the diffraction patterns because of high diffraction intensities. So the elastic constants for three lattice planes were measured by neutron diffraction. Tensile specimen of NCF600 was set and applied tensile stresses from 50 to 200MPa in steps of 30MPa. Then, the applied load was recorded by a load cell and the diffraction patterns were measured with each lattice plane for two directions; axial direction and radial direction.

Relative strains to the lattice spacing of the applied stress of 50MPa were determined from equations (1) and (2) using wavelength of neutron of 0.20868nm; d_0 is the lattice spacing on applied stress of 50MPa. Figure 1 shows the relative stress-strain diagram to 50MPa applied stress for each lattice planes. Young's modulus and Poisson's ratio for Ni(100), Ni(200) and Ni(220), respectively, are 246GPa, 0.094, 162GPa, 0.163 and 213MPa, 0.378 as shown Table 2.

Table 1: Chemical composition of NCF600 (wt%)

	C	Si	Mn	P
NCF600	≤0.15	≤0.50	≤1.00	≤0.030
S	Cr	Fe	Cu	Ni
≤0.015	14.00-17.00	6.00-10.00	≤0.50	Bal.

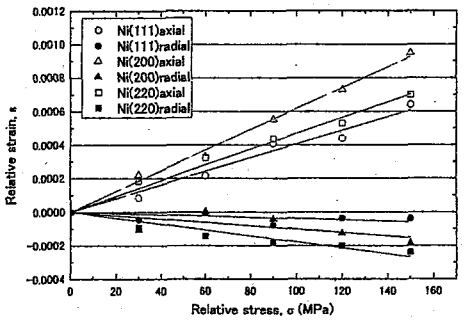

Figure 1: Stress-strain diagram for Ni(111), (200) and (220).

Table 2: Results of elastic constants measurement

	Young's modulus	Poisson's ratio
Ni(111)	246GPa	0.094
Ni(200)	162GPa	0.163
Ni(220)	213GPa	0.378

原子炉：JRR-3　　装置：RESA(T2-1)　　分野：中性子散乱（残留応力）

研究テーマ：構造用材料の残留応力および負荷荷重下での材料特性評価
表　題：強加工したフェライト鋼の復旧にともなう集合組織変化
1-9-12

Estimation of change in texture by restoration of a ferrite steel after large strain deformation

T. Suzuki, Y. Tomota, M. Uno, A. Moriai[1], T. Kamiyama[2], H. Tashiro[3]

Faculty of eng, Ibaraki Univ., Hitachi, Ibaraki 316-8511
[1]JAERI, Tokai, Ibaraki 319-1195
[2]KEK, Tsukuba, Ibaraki 305-0801
[3]Nippon Steel Co. Kamaishi, Iwate 026-8567

1. Introduction

When a ferrite steel is subjected to extremely heavy drawing, microstructure becomes nano-sized. It has been proposed that "continuous recrystallization" occurs by heavy plastic deformation[1]. Here, texture change by annealing was investigated in order to estimate the restoration process of drawn ferrite steels.

2. Experimental Procedures

A ferrite steel with the chemical compositions of 0.008C, 0.01Si and 0.13Mn was hot-forged to a bar with 5.5 mm diameter and then drawn by true strains of 2.0(2.0mm) to 6.6 (0.2mm) at the Kamaishi work of Nippon Steel Co.. The specimens were annealed at several temperatures between 373 and 1073K for 3.6 ks in vacuum. Neutron diffraction was performed at JAERI to measure the texture.

3. Results and Discussion

Figure 1 shows the texture change with annealing. The intensity of pole density at the center of 110 pole figure changes by the annealing temperature in the specimen drawn by 2.0 mm. This result suggests the change in crystal orientation occurred by recrystallization. On the other hand, the maximum intensity of pole figure hardly changed by annealing temperature in the case of the specimen drawn by 0.2 mm. It is considered that the texture evolved by sever drawing is succeeded to the annealed structure.

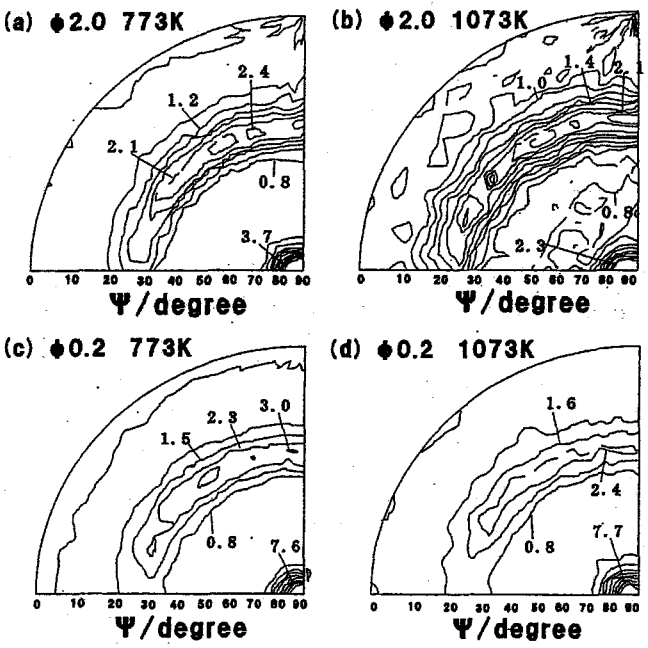

Figure 1: (110) pole figures of drawn ferrite steel annealed at (a), (c)773K and (b), (d)1073Kfor 3.6ks measured by neutron diffraction.

References

1) N. R.Tao, Z. B. Wang, W. P. Tong, M. L. Sui, J. Lu and K. Lu: Acta mater., 50(2002), pp. 4603-4616.

原子炉：JRR-3　装置：RESA(T2-1)　分野：中性子散乱（残留応力）

研究テーマ：構造用材料の残留応力および負荷荷重下での材料特性評価
表　題：高周波焼入れした鋼棒の中性子残留応力測定
1-9-13

Residual stress measurement using neutron diffraction for a quenched steel bar with induction heating

H. Tokuda[*1], Y. Tomota[*2], T. Suzuki[*3], K. Kawasaki[*4], A. Moriai[*5], N. Minakawa[*5] and Y. Morii[*5]

[*1] *Graduate student of Ibaraki University, Hitachi, Ibaraki 316-8511*
[*2] *Graduate School of Science and Engineering, Ibaraki University, Hitachi, Ibaraki 316-8511*
[*3] *Faculty of Engineering, Ibaraki University, Hitachi, Ibaraki 316-8511*
[*4] *Neturen Co. Ltd., Hiratsuka, Kanagawa 254-0013*
[*5] *Neutron Science Research Center, JAERI, Tokai, Ibaraki 319-1195*

1. Introduction

Neutron diffraction enables us to know the stress condition inside a bulky specimen, which cannot do it by other alternative method. However, several problems were found to be improved. In this study, the residual stress of a quenched SCM440 steel bar with induction heating was examined by neutron diffraction.

2. Experimental procedures

A commercially available low alloyed steel with the chemical compositions of 0.42C, 0.20Si, 0.78Mn, 0.020P, 0.011S, 0.05Ni, 1.05Cr, 0.04Cu, 0.16Mo, 0.005V in mass % was used. A round bar shown in Fig. 1 was prepared and rapidly induction-heated followed by water quenching. Then, the elastic strains remained were measured by a conventional X-ray method and neutron diffraction using a diffractometer for residual stress measurement (RESA) at JAERI, where the stress free lattice spacing was determined by the measurements for tiny coupons.

3. Results

A good agreement was found between the results obtained by the present method and those by the conventional X-ray $\sin^2\Psi$ method with a serial polishing technique where three dimensional stresses were estimated from the plane-stress data obtained.
There are however several improvements for the neutron stress measurement. In particular, the measurement for a specimen with gradient microstructure change like the present material requires the preparation of small coupons and small gauge measuring volume.

The full paper of this study will appear in the journal of ISIJ (Tetsu to Hagane: accepted for publication).

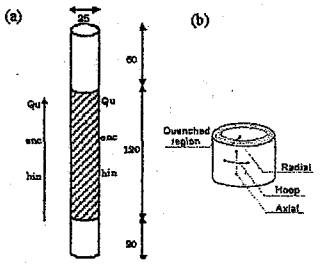

Figure 1: Geometry of a specimen quenched after induction heating (a) and definition of stress directions (b).

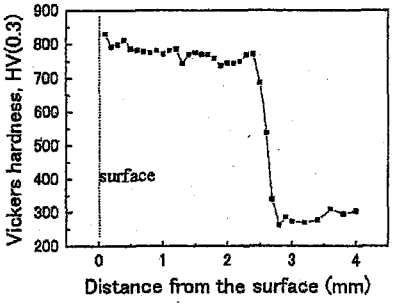

Figure 2 : Hardness distribution in the cross section of the round bar specimen.

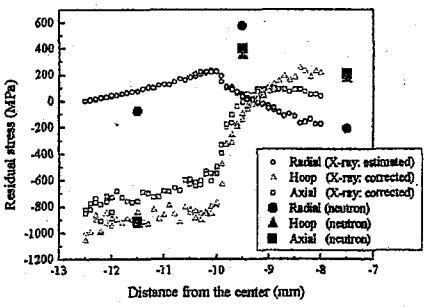

Figure 3 : Residual stresses measured by the neutron and X-ray methods as a function of distance from the center of the specimen.

原子炉：JRR-3　装置：RESA（T2-1）　分野：中性子散乱（残留応力）

研究テーマ：中性子散乱による機能材料構造の研究
表　題：新しい中性子応力測定法の開発

1-9-14

Development of New Stress Measurement Method Using Neutron Diffraction

H. Suzuki, A. Moriai, N. Minakawa[1] and Y. Morii

Neutron Science Research Center, JAERI, Tokai, Ibaraki 319-1195
[1]Advanced Machine Factory Ltd., Hitach, Ibaraki 319-1231

Neutron stress measurement method can determine the stress states by measuring the lattice strains in three orthogonal directions. In the conventional method, it is required to measure the lattice strains of the same diffraction family in all three directions. However, it is possibly difficult to measure the lattice strains of the same diffraction family in all three directions on the textured materials, and it is also possibly difficult to measure the lattice strains in all three orthogonal directions due to some reasons such as the size and the shape of the samples, etc. Furthermore, it is required to obtain the stress free lattice spacing d_0 in order to determine the residual stresses, so that the accuracy of the stress measurement depends on the accuracy of d_0 measured using the powder sample or the annealed sample. Therefore, it is very important to establish the high-versatility stress measurement method which can measure the stress states accurately under the various conditions or for the various objects.

Equation (1) shows the general formula for calculating the residual stress states in neutron diffraction technique. In conventional method, measured lattice strains in three orthogonal directions are submitted to eq.(1) and the residual stress states can be obtained by making a least square method. However, if we use this conventional principle, the tri-axial stress states can be obtained by observing the lattice strains of two or more kinds of diffraction family in only two orthogonal directions.

$$\varepsilon_{ii} = \frac{1}{E_{hkl}}\{(1+\nu_{hkl})\sigma_{ii} - \nu_{hkl}(\sigma_{11}+\sigma_{22}+\sigma_{33})\} \quad (1)$$

This proposed method was applied to evaluate the stress states of the Ni-base alloy NCF600 loaded in-situ. Measured diffraction planes were three kinds of diffraction family such as Ni{111}, Ni{200}, and Ni{220}. Changes in measured stresses almost agreed with theoretical changes within 10 MPa error. Therefore, this proposed method can determine the relative stress states accurately by observing the lattice strains in two orthogonal directions. However, if we measure the residual stress states using this method, it is required to know the stress-free lattice parameter. Therefore, stress measurement accuracy was affected by the accuracy of d_0 measured using reference samples.

Equation (2) shows the principle of the stress measurement method without using measured stress-free lattice constant a. It is possible to obtain the lattice constant and the tri-axial residual stresses by observing the lattice spacings of two or more kinds of diffraction family in two or three orthogonal directions.

$$d_{ii}\sqrt{(h^2+k^2+l^2)} = \frac{a}{E_{hkl}}\{(1+\nu_{hkl})\sigma_{ii} - \nu_{hkl}(\sigma_{11}+\sigma_{22}+\sigma_{33})\} + a \quad (2)$$

We tried to apply this new method, which can determine the residual stress states without using measured d_0, to uniaxial applied stress measurement of NCF600. Figure 1 shows the changes in lattice constant and stress states related to the applied stresses. The lattice constant a was almost constant without dependent of applied stresses, and the average value of it was about 3.5639±0.0001 Å which almost agreed with the lattice constant (3.5623±0.0003 Å) of annealed sample with 0.0016 Å error. On the other hand, the tendency of changes in stress states evaluated using proposed method coincided with theoretical change. Therefore, it is expected that this proposed method will be one of the method which can solve the problems in conventional method.

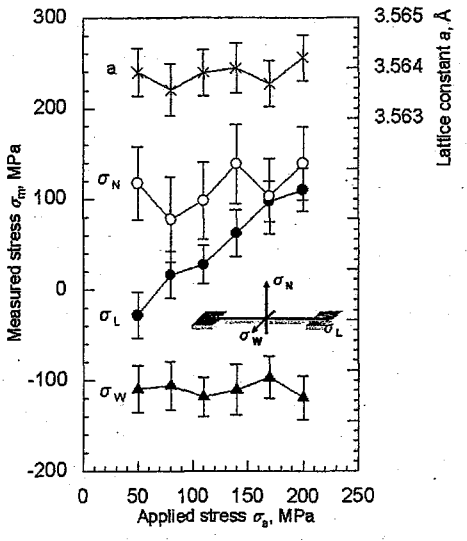

Figure 1: Changes in each stress component and lattice constant.

原子炉：JRR-3　　装置：RESA(T2-1)　　分野：中性子散乱（残留応力）

研究テーマ：中性子散乱による機能材料構造の研究
表　題：中性子回折法による Al_2O_3/YAG 二元系 MGC 材料のひずみ測定

1-9-15

Strain Measurement of Al_2O_3/YAG binary MGC by Neutron diffraction

H. Suzuki, Y. Waku[1], A. Moriai, N. Minakawa[2] and Y. Morii

Neutron Science Research Center, JAERI, Tokai, Ibaraki 319-1195
[1]UBE Industries, Ltd., Ube, Yamaguchi, 755-8633
[2]Advanced Machine Factory Ltd., Hitach, Ibaraki 319-1231

Engines or turbines are required the operation at higher temperature to improve thermal efficiency. For this purpose, it is necessary to develop a material which remains stable at very high temperature such as more than 1973 K. An Al_2O_3-$Y_3Al_5O_{12}$ (YAG) eutectic material has been recently fabricated by melting and unidirectional solidification of raw material oxides using a eutectic reaction to control precisely the crystal growth.[1)] Such kind of composite material is called melt growth composite (MGC). Al_2O_3/YAG-MGC consists of single crystal of both Al_2O_3 and YAG, and they are continuously connected and finely entangled in three-dimensions without grain boundaries. However, since thermal expansion coefficient differs in both phases, residual stresses are generated by mismatch between two phases, and it may affect the fracture mechanism and mechanical properties of the MGCs. In the present study, residual stresses in each phase of Al_2O_3/YAG-MGC were measured by using neutron diffraction.

Powder diffraction of Al_2O_3/YAG-MGC was measured using REsidual Stress Analysis (RESA) at JRR-3 in order to obtain a lattice constant in stress-free condition and to confirm the consisted phases. Figure 1 shows the result of the peak fitting of powder diffraction using REITAN-2000.[2)] It was confirmed that the measured diffraction pattern was fitted well with the calculated pattern, and that this MGC was consisted of two phases of Al_2O_3 and YAG. The lattice constants of each phase were shown as below.

Al_2O_3: a=4.7587±0.0002 Å, c=12.9923±0.0005 Å.

YAG: a=12.0055±0.0003 Å.

The lattice strains were measured in each phase of the MGC specimen with the size of 4 mm width, 3 mm thickness, and 40 mm length. Before measuring the lattice strains, the pole figure and the rocking curve were measured in some diffraction. As a result of pole figure measurement, it was confirmed that all phases were single crystal. On the other hand, the full wide half maximum of the rocking curve was approximately 1 deg to 2 deg, so that the crystallinity of MGC was comparatively low.

Table 1 shows the lattice strains in each phase of MGC. Lattice strains of some kinds of diffraction family such as YAG{532}, YAG{611}, YAG{400}, and Al_2O_3{113} were measured. Negative and positive strains correspond to compressive and tensile strains, respectively. As a result of strain measurement, it was confirmed that both of the tensile and compressive residual strains were observed in YAG phase, and the compressive residual strains existed in Al_2O_3 phase. In this study, Cd slit with aperture of 10mm width and 15mm height was utilized, so that measured lattice strains were average strain in the whole sample. Since the stress distributions in the composite materials are complex, it is very important to evaluate accurate stress distributions in MGC. Therefore, it is required to measure the lattice strains using the slit with small aperture of 1 mm × 1 mm in order to clarify the residual stress distributions in Al_2O_3/YAG-MGC.

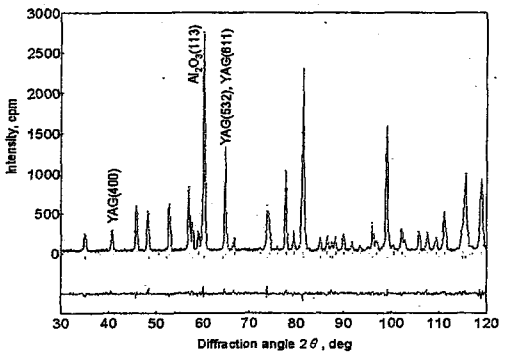

Figure 1: Diffraction pattern of Al_2O_3/YAG-MGC, and the result of fitting between measured and calculated patterns using REITAN-2000.

Table 1: Lattice strains of each phase in Al_2O_3/YAG-MGC

	Lattice strain
YAG($3\bar{5}2$)	0.00007±0.00004
YAG($2\bar{5}3$)	-0.00031±0.00004
YAG(611)	0.00020±0.00004
YAG(400)	-0.00033±0.00005
Al_2O_3($2\bar{1}3$)	-0.00046±0.00006
Al_2O_3(113)	-0.00048±0.00007

References

1) Y. Waku *et al.*, Nature, **Vol. 389, No.6646**, Sep. (1997) 49.
2) F. Izumi and T. Ikeda, Mater. Sci. Forum, 321-324 (2000) 198.

原子炉：JRR-3　　装置：RESA(T2-1)　　分野：中性子散乱（残留応力）

This is a blank page.

1. 中性子散乱 １０）その他

1. Neutron Scattering 10) Others

This is a blank page.

研究テーマ：高性能多層膜中性子偏極ミラーの開発
表題：面間隔 d の薄い多層膜偏極ミラーの開発

1-10-1 **Development of a small *d*-spacing multilayer neutron polarizer**

M. Hino, H.Sunohara *, Y.Yoshimura*, R.Maruyama*, S.Tasaki *, H.Yoshino and Y.Kawabata

Research Reactor Institute, Kyoto University, Kumatori, Osaka 590-0494, Japan
**Department of Nuclear Engineering, Kyoto University, Sakyo, Kyoto 606-8501, Japan*

A Multilayer mirror is one of the most useful devices for slow neutron experiments. A magnetic multilayer mirror consisting of ferromagnetic layers and nonmagnetic layers is useful to polarize neutron beam. Several kinds of multilayer, such as Fe/Ge, Fe/Si, FeCo/V multilayer, have been developed as neutron polarizer. Recently, Authors have developed Supersendust/Ge multilayer using vacuum evaporation technique, which were magnetically saturated in a lower external field less than 1 mT [1]. Such neutron mirrors are not only easy to handle but also energy saving devices It is very useful to miniaturize polarized neutron instruments and has realized several new experiments.

Figure 1 shows reflectivities of up (●) and down (○) spin neutron for the Supersendust($Fe_{86.8}Si_{7.5}Al_{4.5}Ti_1$)/Ge multilayer. Its *d*-spacing is estimated to be 5.8 nm and it gives at a position 5 times larger than the critical angle of nickel. The reflectivity and polarization efficiency under magnetic field of 7.5 mT are 0.73 and 0.94, respectively. It is, in our knowledge, the best reflectivity with high polarization efficiency in case of *d*-spacing of 5.8 nm. The *d*-spacings are gradually increased in order to reflect all component of the incident neutron beam, and the resolution of *d*-spacing was about 6%. This result indicates that the control of layer thickness is adequate. Here the nuclear potential values of Supersendust and germanium layers were assumed to be 190 and 94 neV, respectively. The magnetic potential value is however 69 neV. It is smaller than those of the Supersendust monolayer and resonator[2]. The reduction of magnetic potential is explained by the fact that the Supersendust layers are not saturated perfectly at the magnetic field of 7.5 mT. There is thus unexpected reflection for both spin states at the glancing angle from 1.0 to 4.0 degree, which explains that the theoretical lines in the region do not reproduce the measured values. In fact, by changing the strength of external magnetic field from 7.5 to 1.4 mT, the reflectivity and polarization efficiency goes down to 0.66 and 0.93, respectively. Though we have to remove the unexpected reflectivity, this result give us a feasibility of m=5 supermirror polarizer, which work under a low magnetic field of several mill tesla.

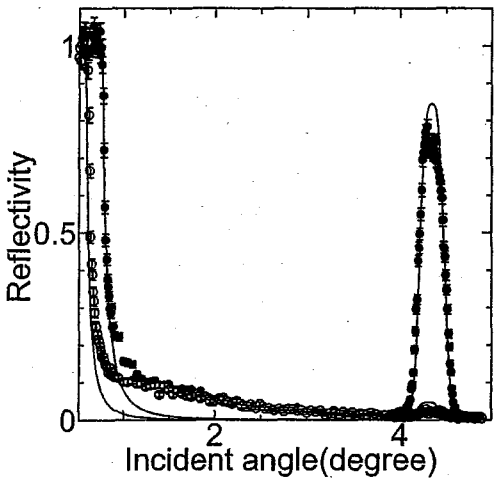

Figure 1: Reflectivities of up(●) and down(○) spin neutron for Supersendust/Ge multilayer(638 bilayers) in which *d*-spacing is 5.8nm. The solid lines is calculated from one-dimensional Schrödinger equation.

[1]M.Hino, S.Tasaki, T.Ebisawa, T.Kawai, N.Achiwa, M.Utsuro, J. Phys. Soc. Japan **70** (2001) Suppl.A 489.
[2]M. Hino, H.Sunohara, Y.Yoshimura, R.Maruyama, S.Tasaki, H.Yoshino, Y.Kawabata, Physica B(2004) in press.

使用施設：JRR-3M, MINE(C3-1-2), 7. Instrumentation

研究テーマ：強い吸収場の中性子スピン光学

1-10-2 高性能 NiC/Ti 中性子スーパーミラーの開発

Development of large-*m* NiC/Ti supermirror using ion beam sputter instrument

M. Hino, H.Sunohara*, Y.Yoshimura*, R.Maruyama*, S.Tasaki*, H.Yoshino and Y.Kawabata

Research Reactor Institute, Kyoto University, Kumatori, Osaka 590-0494, Japan
**Department of Nuclear Engineering, Kyoto University, Sakyo, Kyoto 606-8501, Japan*

A Multilayer mirror is one of the most useful devices for slow neutron experiments. Multilayer mirrors and supermirrors are applied to neutron optical devices, such as neutron guide tube [1]. The multilayer mirror consists of alternating layers of two materials with different potential energies for the neutron. It has artificial lattice spacing(*d*-spacing) and gives one-dimensional optical potentials for a neutron beam. Supermirror is a stack of multilayers with gradually increasing value of the *d*-spacing. A multilayer with small *d*-spacing and supermirror with large-***m*** is desirable to enlarge utilization efficiency for neutron scattering experiments.

Recently we succeeded in fabricating large-m Ni/Ti using ion beam sputtering technique. In this report, we show the performance of multilayer as a neutron mirror. Multilayers were deposited on silicon wafer using ion beam sputtering instrument installed in the Kyoto University Research Reactor Institute (KURRI). The polished silicon wafer is 3 inches diameter and 3mm in thickness. The measurement of reflectivity of multilayer mirrors was carried out at C3-1-2 port of the JRR-3M reactor in the Japan Atomic Energy Research Institute (JAERI). The incident wavelength is 0.88 nm and the resolution is 2.7 % in full width half maximum. The divergent angle is about 1 mrad.

Figure 1 shows comparison between reflectivity of ***m***= 3, 4, 5.1 NiC/Ti supermirrors in which number of layers are 400, 1200 and 3000, respectively. We have succeeded in fabricating ***m***=5.1 NiC/Ti supermirrors with high reflectivity. Here the number of ***m*** is a measure of critical angle in unit of critical angle of nickel. These experimental data are well reproduced by the theoretical lines with one Debye-Waller factor, which is 0.55 nm. The surface roughness of ordinary silicon substrate is 0.4~0.5 nm by using X-ray reflectometer and Zygo optical interferometer. The total thickness of ***m***=5.1 NiC/Ti multilayer is above 11 μm. It follows from this that growth of interface roughness in the NiC/Ti supermirror is estimated to be less than 0.2 nm and it does not generally depend on number of layer. This result indicates realization of large-m supermirror with higher reflectivity when we get smoother substrate.

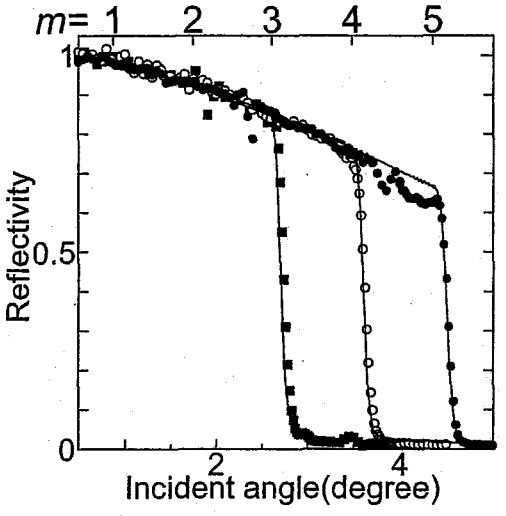

Figure 1: Reflectivity of neutrons by *m*=3(■), 4(○), 5.1(●) NiC/Ti supermirror as a function of the incident angle. The solid lines are calculated from one-dimensional Schrödinger equation including the effect of interface roughness given by one Debye-Waller factor(σ =0.55nm).

[1] F. Mezei, Comm. Phys.,1(1976)81.

使用施設：JRR-3M, MINE(C3-1-2), 7. Instrumentation

研究テーマ：ピエゾ結晶の電気的な変形制御による新しい中性子光学素子の開発研究

1-10-3 圧電性単結晶を用いた能動的中性子光学素子の可能性検証

Investigation on possibility of neutron electric optical devices based on piezoelectric single crystals

J. H. Kaneko[a*], Y. Otake[b], H. Fujimoto[c], S. Kawamura[a], M. Watanabe[a], F. Fujita[a], T. Sawamura[a], P. Mikula[d], M. Furusaka[e]

[a] *Hokkaido University, N13 W8, Kita-ku, Sapporo, 060-8628, Japan,* [b] *Riken, 2-1 Hirosawa, Wako, Saitama 351-0198, Japan,* [c] *AIST, Umezono 1-1-1, Tsukuba 305-8563, Japan,* [d] *Nuclear Physics Institute, 250 68 Rez near Prague, Czech Republic,* [e] *KEK, Oho 1-1, Tsukuba, Ibaraki, 305-0801, Japan*

A principle verification experiment of neutron electric optical devices using piezoelectric single crystals was carried out. This neutron electric optical device can change its d-spacing by applying an electric field to the crystal, which results in change of the Bragg diffraction angle[1-4]. Although an α-quartz has a small piezoelectric strain constant, an α-quartz was used in this experiment because characteristics of α-quartz are well known and it is easy to obtain high quality and large size single crystals. At first, macroscopic distortion and change of thickness caused by an applied electric field were observed by using laser interferometers. Thus, as shown in Fig. 1, double crystal diffraction measurement using 4.7 Å cold neutrons was carried out. This experiment was carried out using the ULtra Small angle scattering instrument (ULS) of the institute for Solid State Physics (ISSP), University of Tokyo, equipped at the JRR-3M reactor of the Japan Atomic Energy Research Institute. For these experiments, DC bias voltage was applied to the crystal. As shown in Fig. 2, peaks of rocking curves were shifted 14 seconds at 500 V and 2 minutes at 1000 V from their original positions. These values were approximately one figure larger than the theoretical values; therefore, these results were influenced by macroscopic bending of the crystal. From these results, it can be concluded that the possibility of neutron electric optical devices using not only change of d-spacing but also macroscopic bending of piezoelectric crystal was confirmed.

References

[1] A. Paturle et al.: Phys. Rev. B**43** (1991) 14683.
[2] H.Graafsma et al.: Acta Cryst.(1997).B**53**,565.
[3] R.Guillot et al.: Acta Cryst.(2002).A**58**(Supplement),C327.
[4] U.Pietsch et al.:J. Physics and Chemistry of Solid **62**(2001)2129.

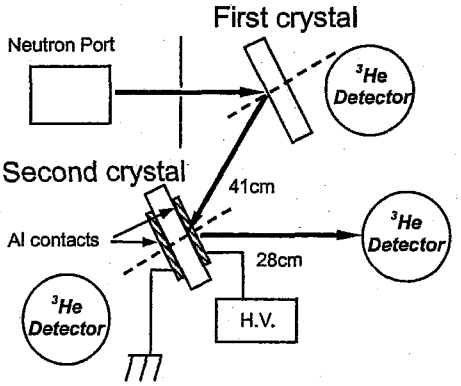

Figure 1 Experimental set-up of double crystal diffraction measurement using 4.7 Å neutrons. Neutrons were diffracted by the (110) surface of the α-quartz single crystals settled in back scattering geometry; the diffraction angle θ was approximately 73 degrees.

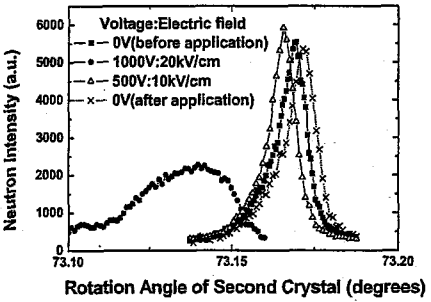

Figure 3 Changes of double crystal rocking curves by applied electric fields.

使用施設：JRR-3M, 装置：ULS(C1-3), 分野 Instrumentations

研究テーマ:多層膜中性子干渉計・反射率計
表題:中性子反射率法による固体ー固体界面の面粗度の測定

1-10-4 Measurement of the Surface Roughness at Solid-Solid Interface by Neutron Reflectometry

K. Inoue, T. Hirayama, T. Ebisawa*, S. Tasaki** and M. Hino***

*Faculty of Science and Technology, Ryukoku University, Seta, Otsu 520-2194, Japan; *NSRC, JAERI, Tokai, Ibaraki 319-1195, Japan; **Graduate School of Engineering, Kyoto University, Sakyo-ku, Kyoto 606-8501, Japan; ***Research Reactor Institute, Kyoto University, Kumatori, Osaka 590-0494 Japan,*

In the field of mechanical engineering, problems of the friction, wear and lubrication are very important. We should like to know the surface roughness in consequence of the friction. However, as the phenomena occur at solid-solid interface, there is no effective means to obtain the information concerning the profile of the interface.

Neutron beam is expected to be very suitable to obtain the information concerning the solid-solid interface because the beam penetrates far into the materials and can reach the interface. Thus, in this experiment we tried to observe the surface roughness by neutron reflectometry. The apparatus, MINE, at C3-1-2 beam port of JRR3M in JAERI(Tokai) was used. Generally, the neutron reflectometry had been used to observe the perfection of the surface flatness or to measure the thickness of very thin film. In contradiction to the traditional use, we tried to observe the roughness of the surface by reflectometer.

We prepared three Al samples, the size of which was $50 \times 50 mm^2$ and the thickness was 20 mm. The scratched surface roughness of each sample was Rmax=0.1 μ m, 0.5 μ m and 1.0 μ m. The period of the roughness was 50 μ m for Rmax=0.5 μ m and was 23 μ m for Rmax=1.0 μ m. The period was random for Rmax=0.1 μ m. Ni film was deposited onto each Al surface because the critical angle of reflection for Ni is rather large. The thickness of the film was about 100 nm. The profile of the surface roughness is shown in Fig. 1.

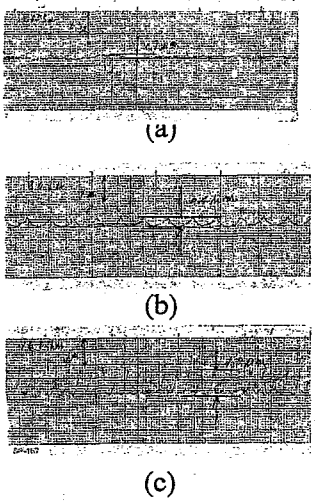

Figure 1: Roughness of the surface of Al sample coated by 100nm Ni film. (a)Rmax=0.1 μ m, (b)Rmax=0.5 μ m and (c)Rmax=1.0 μ m.

The wave length of the beam was 0.88 nm. The width of the slit for incident beam at position of 1.5 m from the sample was 0.5 mm, and the width of the slit in front of the sample was 0.2 mm. And for the reflected beam the width of the detector slit was 5 mm. The critical angle, θ_C, of Ni for this wave length, is 0.87 deg.

The reflectivity from each free surface, where the beam comes through the air, is shown in Figs. 2 (a) and (b). In Fig. 2 (b), the reflectivity is shown on a log scale. We see that the reflectivity is extremely different each other according to the roughness and to the direction of the scratch against beam direction. When Rmax=0.1 μ m, 95 % of the beam was reflected below critical angle. As Rmax becomes large, the reflectivity becomes small. For the same roughness, the reflectivity becomes small when

使用施設:JRR-3M, 装置:MINE(C3-1-2), 分野 Others

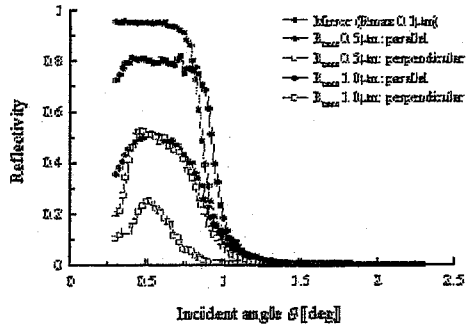

(a)

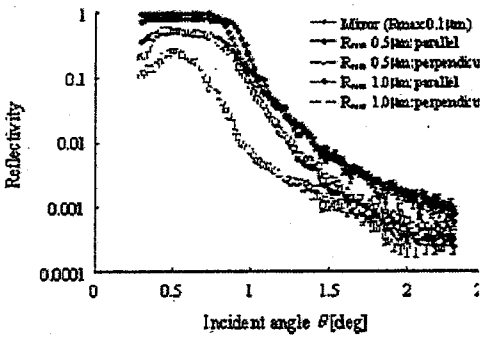

(b)

Figure 2: Reflectivity from each surface roughness. The direction of the scratch is parallel or perpendicular to the beam.

the direction of the scratch is perpendicular to the beam direction. In Fig. 2 (b), we see that the period above the critical angle is caused by the thickness of Ni film.

To investigate whether it is possible or not to observe the reflection from the solid-solid interface, we tried to observe the reflection from the interface between Si block and the sample with Rmax=0.1 μ m. The Si block had a flat surface. The incident beam came through Si block and was reflected at the interface. The result is shown in Fig. 3, where the vertical axis is shown on a log scale. In the figure, the reflectivity from the free surface of the same sample is also written.

We found that it is possible to observe the reflection from the solid-solid interface.

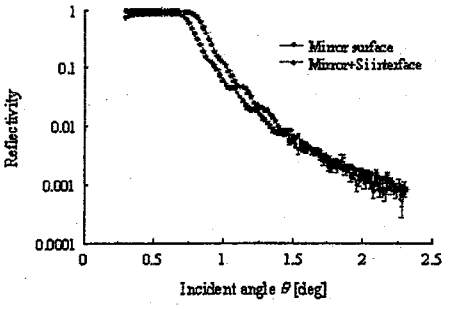

Figure 3: Reflectivity from the interface between Si flat surface and the sample with Rmax=0.1μm. The reflection from the free surface of the same sample is also shown.

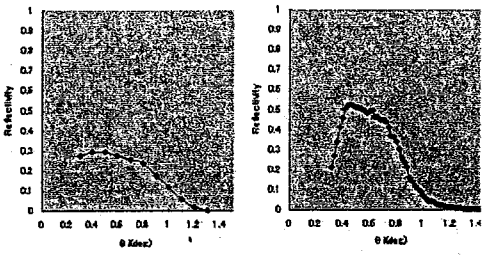

Calculation Experiment

Figure 4: Comparison of the calculated reflectivity for Rmax=0.5μm sample with the experimental one.

In that case the reflectivity becomes slightly small compared to the reflection from the free surface. We also see the period due to the thickness of Ni film.

We made a brief calculation of the reflectivity for the sample with roughness of Rmax=0.5 μ m. The result is shown in Fig. 4 with the experimental result. We see that the profile of the calculated reflectivity reproduces qualitatively the profile obtained by experiment. This calculated result will be modified when we take into the multiple scattering.

We conclude that neutron reflectometry will be a very useful method for the investigation of the change of the profile of solid-solid interface.

研究テーマ：中性子スピンエコー分光器

1-10-5 TOF-NSE 分光器用の定常電流で働くスピンフリッパーの開発

Development of Spin Flippers with Steady Current for the TOF-NSE Spectrometer

T. Takeda[1], N. L. Yamada[2], M. Nagao[3] H. Seto[4] and Y. Kawabata[5]

[1]*Faculty of Integrated Arts and Sciences, Hiroshima University, Higashi-Hiroshima 739-8521*

[2]*Graduate School of Bio-Sphere Science, Hiroshima University, Higashi-Hiroshima 739-8521*

[3]*NSL, ISSP, University of Tokyo, Tokai, Naka, Ibaraki 319-1106*

[4]*Graduate School of Science, Kyoto University, Kyoto 606-8502*

[5]*Graduate School of Science, Tokyo Metropolitan University, Hachioji 192-0397*

We designed π and $\pi/2$ flippers for a time-of-flight neutron spin echo (TOF-NSE) spectrometer at a pulsed spallation neutron source. The flippers operate with steady current for a white neutron beam. The flippers with the first modified current sheet which was made by winding Al-conductor wires[1] and with the second modified current sheet which was made of Al alloy plates[2] operated well as π and $\pi/2$ flippers. We present the results of performance tests of NSE spectrometer all Mezei-type flippers of which were replaced by the new-type π and $\pi/2$ flippers and also preliminary experiments for the performance test using a pulsed white neutron beam at PORE of KENS, KEK.

Performance tests of the new-type flippers with the second modified current sheet were carried out using ISSP-NSE at C2-2 port of JRR-3M in JAERI(Tokai). The neutron beam with the wavelength $\lambda = 7.14$ Å of its resolution $\Delta\lambda/\lambda = 18\%$ (FWHM) was used. We replaced all Mezei-type π and $\pi/2$ flippers of ISSP-NSE by the new-type one. Figure 1 shows an example of the NSE signal profile, where the normalized NSE signal amplitude P_{NSE} is 0.88 which is nearly equal to that obtained using the Mezei type one. This shows that the new π and $\pi/2$ flippers operate well as a flipper system for a NSE spectrometer.

We constructed a compact NSE spectrometer with the length of 68 cm for the performance tests of the new-type π and $\pi/2$ flippers using a pulsed white neutron beam at PORE of KENS, KEK. We set it on the sample table of ISSP-NSE and observed the NSE signal in order to find the appropriate conditions of the coil system which are independent of the neutron wavelength when the new-type flippers are used. Figure 2 shows an example of the NSE signal profile, where P_{NSE} is 0.85. This value is large enough to do the performance tests using PORE.

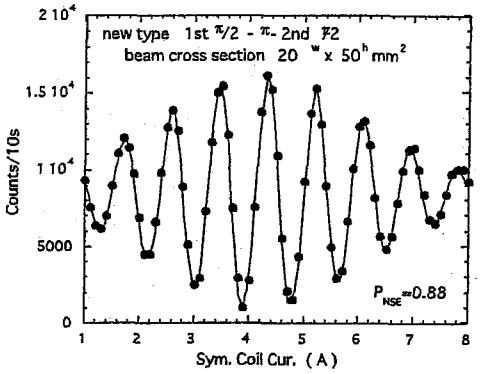

Fig. 1. Example of the NSE signal profile observed using ISSP-NSE with the new-type flipper system.

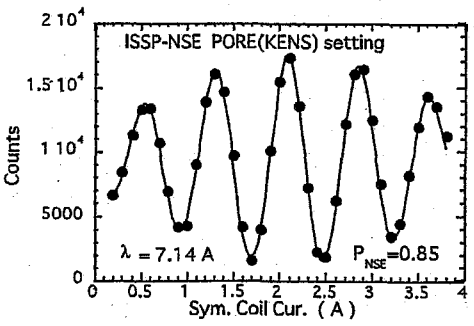

Fig. 2. Example of the NSE signal profile observed using a compact NSE spectrometer for the performance tests at PORE.

References

[1] T. Takeda *et al.*: Appl. Phys. A **74** (2002) S177.

[2] T. Takeda *et al.*: Physica B **335** (2003) 211.

使用施設：JRR-3M, 装置：NSE(C2-2), 分野： 7. Instrumentations

研究テーマ：中性子スピン干渉現象を応用した中性子スピンエコー分光法の開発
表題：MIEZE型スピンエコー分光器の開発

1-10-6 Development of MIEZE neutron spin echo method

R. Maruyama[1], T. Ebisawa[2], S. Tasaki[1], M. Hino[3], and Y. Kawabata[3]
[1] *Department of Nuclear Engineering, Kyoto University, Sakyo, Kyoto 606-8501*
[2] *Neutron Science Research Center, JAERI, Tokai, Ibaraki 319-1195*
[3] *Research Reactor Institute, Kyoto University, Kumatori, Osaka 590-0494*

We have installed MIEZE (Modulation of Intensity by Zero Effort) neutron spin echo (NSE) spectrometer. Since no spin analysis is performed downstream of the sample in a MIEZE configuration, it is suitable to measure spin-incoherent scattering, which reduces the visibility of the spin echo signal by a factor of 3 in the other NSE methods [1, 2]. We have measured spin-incoherent scattering from vanadium in order to demonstrate that it does not reduce the visibility of the spin echo signal.

The experiment was carried out using JRR-3M/C3-1-2-2 (MINE). Its arrangement is shown in Fig. 1. The continuous neutron

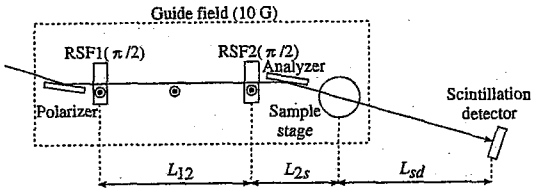

Fig. 1. Experimental arrangement of MIEZE NSE spectrometer. In this measurement, L_{12}, L_{2s} and L_{sd} are 530, 955 and 95 mm, respectively.

beam with wavelength longer than 0.80 nm was obtained as an incident beam at MINE. The polarizer and the analyzer were FeCo/V magnetic mirrors, which were fabricated with vacuum evaporation system at the Res. Reactor Inst., Kyoto Univ. The reflected beam from them was polarized into spin-up state and monochromatized with wavelength of 0.80 nm and its resolution of 10~15 %. The neutron energy transfer with spin-flip process in a resonance spin flipper (RSF) leads to the phase difference between two spin eigenstates, which were split in total energy and wave number space by RSF1(π/2). These two eigenstates were superposed by RSF2(π/2) and counted by scintillation detector. The RSFs and the detector were placed as the phase difference in wave number space was completely cancelled at the detector. The interference pattern due to the phase difference in total energy was observed as a spin echo signal.

We performed the measurements for a solid vanadium at room temperature with a scattering angle of 90° ($Q = 15.7\,\mathrm{nm}^{-1}$). The observed spin echo signals for the direct and the scattered beam are shown in Fig. 2. Its

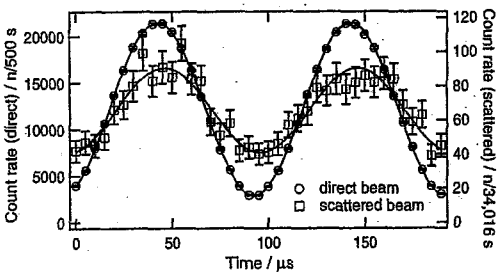

Fig. 2. Measured NSE signals for the direct and the scattered beam.

frequency is 10 kHz, which corresponds to the frequency of the oscillating field applied to RSFs. The visibility of the spin echo signals was 0.76 and 0.38 for the direct and the scattered beam, respectively. The visibility for the scattered beam of 0.38 was larger than 0.25 (i.e., 0.76/3). The decrease of the visibility from 0.76 to 0.38 was mainly caused by the difference of the path length due to the beam divergence. For the general application of this spectrometer, we must develop a high-frequency RSF, 2D PSD system and Soller type polarizer.

References

[1] P. Hank *et al.*: Physica B **234-236** (1997) 1130.
[2] T. Ebisawa *et al.*: J. Soc. Jpn. **70** Suppl. A (2001) 442.

使用施設：JRR-3M，装置：C3-1-2-2(MINE)，分野：7. Instrumentation

This is a blank page.

2. 中性子ラジオグラフィ

2. Neutron Radiography

This is a blank page.

研究テーマ：中性子ラジオグラフィによる沸騰流のボイド率計測
表　題　：超高熱流束負荷時の実験研究
2-1

Experimental Study on Void Fraction in Tight-Lattice Rod Bundles

Masatoshi Kureta, Hiroyuki Yoshida, Akira Ohnuki* and Hajime Akimoto

Japan Atomic Energy Research Institute, Tokai Research Establishment, Department of Nuclear Energy System, Tokai, Naka, Ibaraki, 319-1195, Japan

Japan Atomic Energy Research Institute (JAERI) is carrying a design study on the Reduced-Moderation light Water Reactor (RMWR) in cooperation with power companies, reactor makers and university.

The RMWR adopts a triangular tight-lattice fuel rod configuration with the gap width of about 1mm between rods, and is based on the BWR technology. The database for void fraction in such a tight bundle is indispensable to verify the numerical analysis codes in the design study.

In this paper, void fraction characteristics in the tight-lattice rod bundles are experimentally investigated. Void fraction was measured by neutron radiography (NR) technique and quick-response area-averaged void fraction meters.

Experiments were performed using two test sections ([A] 7-rod bundle with 12mm in rod diameter and 1mm gap between rods, [B] 19-rod bundle with 12mm in rod diameter and 1.3mm gap). Void fraction experiments were carried out under atmospheric pressure condition. Void fraction of air/water two-phase flow and boiling flow in [A] was measured using high-frame-rate neutron radiography (HFR-NR) and high-resolution neutron radiography (HR-NR) at the reactor room of the research reactor JRR-3M. Since neutron has a high sensitivity to thin water layer, we can not only observe but also measure the void fraction distribution in the tight rod bundle by using the neutron radiography technique. In the experiment by the NR, high void fraction of 0.5 ~ 0.92 under high gas velocity of ~max. 200m/s was measured, and behavior of two-dimensional void fraction distribution was also observed. Void fraction of air/water two-phase flow in [B] was measured by (1) conductance-type and (2) capacitance-type area-averaged void fraction measurement techniques (void fraction meter). Void probe is metallic films which were fixed at inside of the flow channel.

In the experiment by the void fraction meter, void fraction was measured under wide range of 0.07 ~ 0.9. All measurement systems have been newly developed by the JAERI and the error estimation methods of each technique were already established. Time-averaged flow-directional or area-averaged void fraction was evaluated with the quality or superficial velocities of gas and liquid phases. It was found from the observation by the HFR-NR that water lumps flows at the corner of the channel in case of air/water two-phase flow, on the other hand, water lumps disappeared at the corner in case of uniformly heated boiling condition. Fluctuation of the void fraction is about +/- 0.1 in case of RMWR simulation condition (= void fraction is about 0.8). Void fraction map was made by the present database in order to verify the numerical analysis code.

原子炉：JRR-3　装置：NRG(7R、C2-3-3-1) 分野：中性子ラジオグラフィー（熱水力）

研究テーマ：中性子ラジオグラフィによる沸騰流のボイド率計測
表題　　：中性子ラジオグラフィによる稠密14本バンドル流路内沸騰二相流のボイド率計測

2-2

中性子ラジオグラフィによる稠密14本バンドル流路内沸騰二相流のボイド率計測

呉田 昌俊、　秋本 肇
日本原子力研究所
エネルギーシステム研究部
熱流体研究グループ

中性子ラジオグラフィ（NRG）を用いた稠密バンドル内を流れる沸騰二相流の瞬時ボイド率計測技術と、ボイド率の3次元分布計測技術を開発した[1),2)]。平成15年度は、低減速軽水炉炉心を模擬した稠密14本バンドル試験体を用いて2次元ボイド率分布の時間変化と3次元ボイド率分布を計測した[3)]。

実験は、JRR-3M熱中性子ラジオグラフィ実験施設（TNRF-2）を利用した。図1にボイド率計測実験用装置の概略を示す。ボイド率の時間変化を高速度撮像中性子ラジオグラフィで、3次元空間分布を中性子トモグラフィで測定し、データを3次元表示および動画表示して観察した。

実験には、稠密14本バンドル試験体（発熱棒間隔1.3mm、棒径13.69mm、加熱長240mm）を用い、試験体内で発生する沸騰流を計測した。図2に、1ms毎に瞬時のボイド率（2次元）を計測し、蒸気泡が発生・成長する様子を可視化した結果を示す。本計測結果から、定常的な高ボイド率領域は観察されず、正味の沸騰開始点は広く分散していることがわかった。NRG技術とCT技術を融合した独自の中性子トモグラフィ技術を開発し、3次元のボイド率分布を測定した結果を図3に示す。図3より、正味の沸騰は燃料棒の狭間隙部（液速度の小さい領域）で始まること等がわかった。

本研究により、稠密バンドル内沸騰流のボイド率を1/1000秒の時間分解能、0.1mmの空間分解能で3次元計測できる技術を開発し、バンドル流路内沸騰流現象の解明に役立てた。また、得られたボイド率データは設計用ボイド率相関式の導出や、詳細数値解析コードの検証データ[4)]等に利用している。

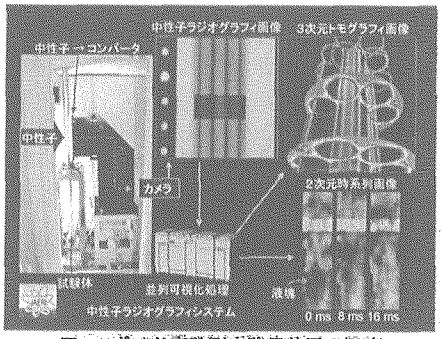

図1　ボイド率計測実験用装置の概略

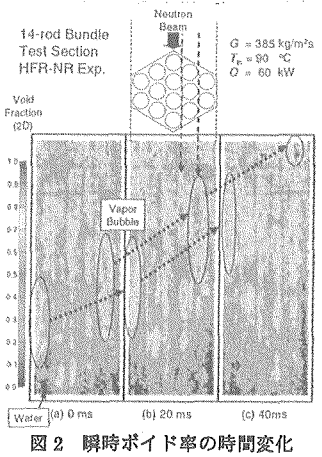

図2　瞬時ボイド率の時間変化

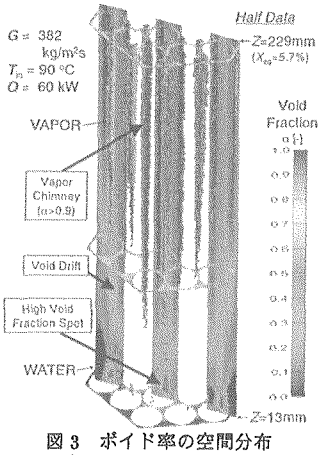

図3　ボイド率の空間分布

参考文献

1) VizJournal, インターネット, (2004).
2) 可視化情報シンポジウム, 東京, (2004).
3) 原子力学会秋の大会, D1, pp.292, 京都, (2004).
4) Proc. ICMF'04, No.226, on CD-ROM, (2004).

原子炉：JRR-3　装置：熱中性子ラジオグラフィ施設　分野：中性子ラジオグラフィ（熱水力）

研究テーマ：中性子イメージング用輝尽性蛍光体の研究
表　題：$CaBPO_5:Ce^{3+}$ 系輝尽性蛍光体の中性子照射特性
2-3

Neutron Irradiation Characteristics of $CaBPO_5:Ce^{3+}$ Based Photostimulable Phosphors

K. Sakasai, M. Katagiri, M. Matsubayashi, T. Nakamura and Y. Kondo[1]

Neutron Scinece Research Center, JAERI, Tokai, Ibaraki 319-1195
[1]*Department of Applied Physics, Tohoku University, Sendai, Miyagi 980-8579*

The neutron imaging plate (NIP) has made a great success[1] in the field of neutron scattering study but the NIP is sensitive to not only neutron but also gamma ray. Therefore, it is difficult to discriminate neutron signal from gamma ray one when the NIP is read out. To overcome the problem, the authors have been studying a $CaBPO_5:Ce^{3+}$ based material as a new neutron storage phosphor consisting of light materials.

The preparation of $CaBPO_5:Ce^{3+}$ based powder sample was described elsewhere[2]. To increase the Photostimulated Luminescence (PSL) after neutron irradiation, the authors have made $CaBPO_5:Ce^{3+}$ + CaF_2 samples (molar ratio was 1:1) and measured the PSL decay characteristics. The results are depicted in Fig.1, where the results of $CaBPO_5:Ce^{3+}$ was also shown for comparison. The neutron irradiation was carried out for 9.6 s at JAERI CNRF facility. One can see that PSL yields of the $CaBPO_5:Ce^{3+}$ are significantly increased by adding CaF_2.

Figure 2 shows a PSL output decay curve of luminescence of the neutron-irradiated $CaBPO_5:Ce^{3+}$ + CaF_2 sample. The neutron irradiation time was 100s at the TNRF. In the figure, results with a Li block (1-cm thickness) are also shown, where the block was set in front of the sample to shield it from the neutron irradiation. The ratio of $PSL_{with}/PSL_{without}$ was less than 0.09, where PSL_{with} and $PSL_{without}$ were total PSL signals in cases with and without the Li block, respectively. Since 97 % of incident neutrons were absorbed in the Li block, the influence of such intense gamma ray on the signal was less than 6 %. The figure indicates that the $CaBPO_5:Ce^{3+}$ + CaF_2 sample may be usable in such a high gamma-ray field of 2 Sv/hr.

Figure 3 shows the PSL output of the $CaBPO_5:Ce^{3+}$ + CaF_2 sample as a function of neutron fluence measured at TNRF and SANS. The $CaBPO_5:Ce^{3+}$ + CaF_2 sample has good output linearity for neutron fluence over three decades.

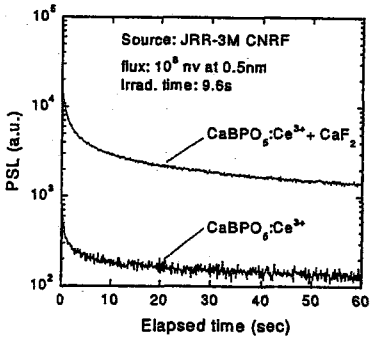

Figure 1: The PSL decay curves of $CaBPO_5:Ce^{3+}$ + CaF_2 and $CaBPO_5:Ce^{3+}$ samples.

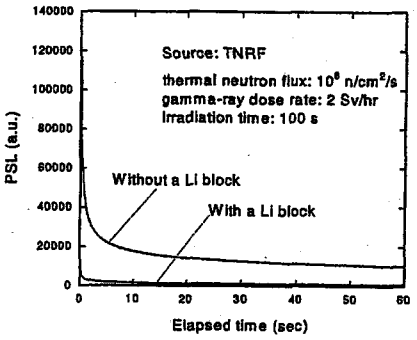

Figure 2: The PSL output decay curve of luminescence of the $CaBPO_5:Ce^{3+}$ + CaF_2 sample after neutron irradiation at TNRF.

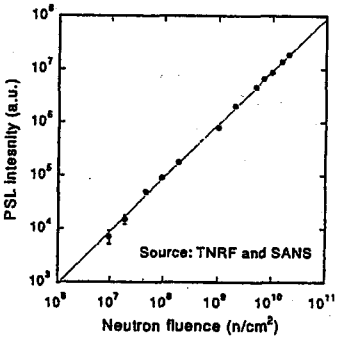

Figure 3: The PSL output of $CaBPO_5:Ce^{3+}$ + CaF_2 sample as a function of neutron fluence measured at TNRF and SANS.

References

1) Y. Karasawa *et al.* : Physics B, **241-243** (1998) 139.
2) K. Sakasai *et al.* : IEEE2003 Conference Record (CD-ROM).

原子炉：JRR-3　　装置：NRG(7R, C2-3-3-1)　　分野：中性子ラジオグラフィー（新素材）

研究テーマ:極低エネルギー中性子による高機能中性子イメージング法の開発
表題:極低エネルギー中性子を用いた高ｺﾝﾄﾗｽﾄｲﾒｰｼﾞﾝｸﾞのコンクリート研究への適用

2-4 High Contrast Imaging for Concrete study using Very Low Energy Neutrons

Y.Kawabata, T.Nakano*, U.Matsushima** and M.Hino

Research Reactor Institute, Kyoto University, Kumatori, Osaka 590-0494, Japan;
**Graduate School of Engineering, Kyoto University, Sakyo-ku, Kyoto 606-851, Japan*
***University of the Ryukyus, Nishihara, Okinawa 903-0213, Japan*

As the absorption cross-section is inversely proportional to neutron velocity, low energy neutron radiography has higher contrast than that of thermal neutron. It means that cold and very cold neutron radiographies have good sensitivity to estimate the water distribution better than that of thermal neutrons. They have been used to measure the water distribution in thin leaves, flowers and stems[1].

The role of water in concrete is also very important for the practical performance. Though the microscopic study by neutron scattering has been performed[2], the macroscopic study has not tried yet. The water distribution was measured by neutron radiography using white neutron beam at C3-1-2, JRR-3M, JAERI.

The radiography measurement system is as follows. The converter is ^{6}LiF:ZnS(Ag) and the size is $45mm^{W} \times 45mm^{H}$. The cooled CCD camera (BS-41L Bitran Co., Ltd.) has a scan area of $8.8 \times 6.6mm^{2}$ covered by 1360×1024 pixels and a dynamic range of 16bits (65,536 gray-levels per pixel). The pixel size is 6.45μm square. The camera is cooled to −5 ℃ in order to reduce electronic background.

Three types of samples which are prepared in two curing conditions are investigated. Sample size is 1cm x 2cm x 5cm. Three type of samples are

a) Paste samples : made only by cement paste, Cement(700g) + water(385g).

b) Mortal samples : made by mixed paste and sands, Cement(333g) + sand(1000g) + water(183g).

c) Concrete samples : made by mixed paste and aggregate, Cement(244g) + aggregate(1270g) + water(134g).

After samples are poured into molding form, they are cured in the air or water for 30days. The results of mortars and concretes are shown in Fig.1 and 2. The positions of aggregates and the water distributions in samples are clearly shown.

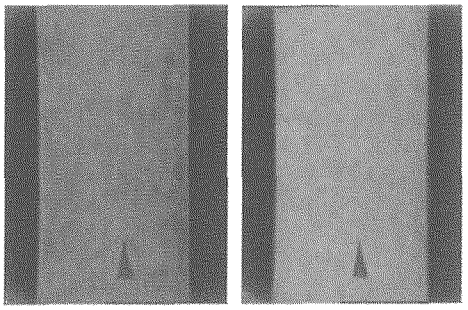

Cured in air　　Cured in water

Figure 1: Radiography images of Mortar samples

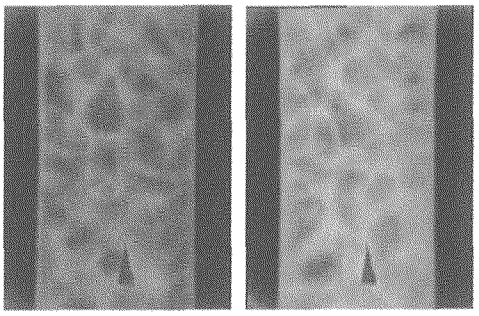

Cured in air　　Cured in water

Figure 2: Radiography images of Concrete samples

References

[1] Y.Kawabata et al., Journal of Radioanalytical and Nuclear Chemistry, in print.

[2] K. Mori et al., Proceedings of the International Symposium on Pulsed Neutron Science and Instruments (IPN 2003), KEK, October 2003, submitted.

使用施設:JRR-3M, 装置:C3-1-2, 分野 Neutron Radiography

研究テーマ：中性子光学素子の開発と中性子分光法の研究
表　題：低エネルギー単色中性子を用いたコントラスト可変画像取得法の開発

2-5

Very Low Energy Neutron Radiography with Neutron Energy Selection System for Variable Image Contrast

Y.Kawabata, T.Nakano[1], M.Hino, T.Oku[2], J.Susuki[2] and U.Matsushima[3]

Research Reactor Institute, Kyoto University, Kumatori, Osaka 590-0494
[1]*Faculty of Engineering, Kyoto University, Kyoto 606-8501*
[2]*Japan Atomic Energy research Institute, Tokai, Ibaraki 319-1195*
[3]*University of the Ryukyus, Nishihara, Okinawa 903-0213*

Neutron radiography is widely used in nondestructive tests and basic researches, for instance, mechanics, biology and so on. Many techniques for high quality images are progressing and the control of neutron energy is one of the important methods. There are two ways for this purpose. One is to use white beam and another is to use monochromatic beam.

Usually, white beam is used in neutron radiography. It gives high flux and a short exposure time. When a sample is thick, faster neutrons are used because they have higher penetration power into samples. Low energy neutrons are used when the high resolution is required.

Monochromatic neutron radiography is usually performed with a velocity selector or a monochromator. As polycrystal materials have the Bragg cut-off wavelength of about 0.4nm, the neutron total cross section changes drastically at this wavelength. The typical technique of the monochromatic neutron radiography is the comparison of the difference in the images with the neutrons of wavelength longer or shorter than the Bragg cut off. It makes clear image of some polycrystal samples.

When the characteristic wavelength of a cold neutron guide tube is longer than the Bragg cut-off, it is impossible to use this effect. Though it does not have a drastic change, the change of the absorption cross-section according to the neutron wavelength gives us the chance to guess the materials in the sample. The cross-sections of elements are well known but the sample and measurement geometry affects an image because of the neutron scattering. It is difficult to estimate the quantity of materials from an image directly when the geometry is complicated. So it is necessary to measure the neutron transmission with a simple geometry to estimate quantitatively. This is a reason to measure neutron transmission of typical step samples with the neutron radiography measurement system.

The wavelength dependence of the neutron transmission was measured for typical samples by a neutron radiography system. It is performed at NOP(C3-1-2), JRR-3M, using a velocity selector. As the geometry should be simple, a converter is set close to a plate type sample of 1cm width. The images are taken by using a monochromated beam of which the wavelength resolution is 82%. Samples were Al, Pb, Sn, Zn, Cu, Fe, Ni, polyethylene resin, stainless steel, acrylic resin, Ag, brass and Ti. Some results of attenuation coefficient are shown in Fig.1 and 2. The results would be a basic data to identify materials in a sample from a neutron radiography images [1].

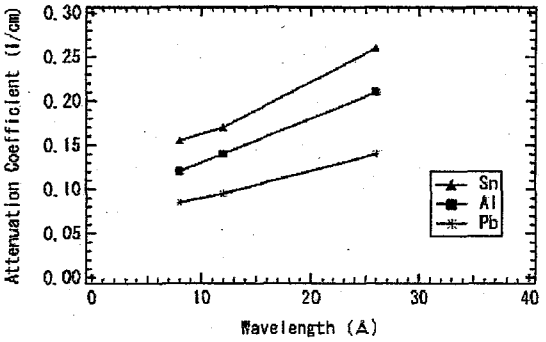

Figure 1: Fig.1 Attenuation Coefficient of Sn, Al and Pb.

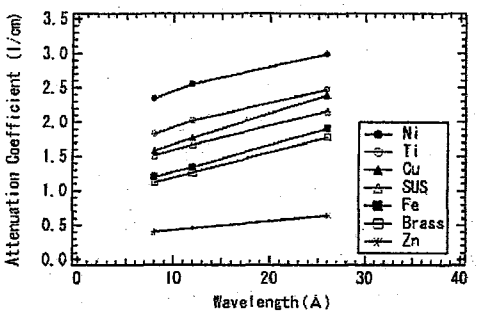

Figure 2: Fig.2 Attenuation Coefficient of Ni, Ti, Cu, stainless steel, Fe, brass and Zn.

References

1) Y.Kawabata, T.Nakano, M.Hino, T.Oku, J.Suzuki, U.Matsushima,: *Proc. 11th Asia-Pacific Conference on Non-Destructive Testing, Jeju, Korea ,2009.*

原子炉：JRR-3　　装置：NOP(C3-1-2-1)　　分野：中性子ラジオグラフィー（その他）

2-6

植物試料における水動態解析
Analysis of Water Movement in Plants

二瓶直登、飯倉寛、大矢智幸、賴泰樹、林芳武、田野井慶太朗、中西友子
N.NIHEI, H.IIKURA, T.OHYA, H,RAI, Y.HAYASHI, K.TANOI, T.M.NAKANISHI
東京大学大学院農学生命科学研究科
Graduate School of Agricultural and Life Science, the University of Tokyo

1．はじめに

水は生きている植物体の80%以上を占め、ほとんどの生化学的な生理活動は水なしには起こり得ない。 DNAの二重らせんが開くのも水があるからであり、養分吸収もイオンが水中に溶解した形で吸収される。 ミクロからマクロの現象を捉える際、最も重要な役割を果たしている植物中の化学物質は何といっても水である。 水分の動きを知る事ができれば、今までともすると静的な解析であった植物生理について、動的な立場からの解明が可能となるだろう。 我々は生きている植物中の水の動きを探るために中性子線を用い、水に特異的な像を得ることを試みてきた。 特に根については、通常見る事ができない土壌中の活動を解析することが可能となってきた。 土の中での根の動きを経時的に見るためには中性子ラジオグラフィーが非常に有用である。また、根近傍の水分分布を解析することにより、根のどの部分が水分（養分）吸収を活発に行っているのかを判別できるかもしれない。 土壌中の栄養分に対し根がどのような応答を示すのか、局所的に設置した養分に対し根の「養分屈性」というものがあるのかどうか、その際の根近傍の水分動態はどのように変化するのであろうか、未だ明確な知見は報告されていない。 そこで本研究では畑作物、特にダイズに対する肥料の種類や施肥位置、麦との混作における根系発達について、非破壊測定法である中性子ラジオグラフィー法を用いた検討を試みた。

近年、農業が環境に及ぼす影響について議論されることも多く、肥料窒素の溶脱による地下水の硝酸汚染、オゾン層破壊や地球温暖化の原因となる脱窒による亜酸化窒素の増大などが注目されている。

これらの問題を解決するために、施肥効率を上げることが必要である。 施肥効率を上げるためには、施肥範囲を局在化しつつ、できるだけ種子や根と近づけることである。 しかし、従来の速効性肥料を種子の近くに局在化した場合、土壌溶液の塩濃度が増大するために、常に根と肥料が一定の距離をおかなければならなかった。

わが国で開発された肥効調節型肥料（Controlled Availability Fertilizers,以下CAFと略）は、水溶性粒状肥料を界面活性剤およびタルク鉱物を含むポリオレフィン系樹脂で被膜し、その溶出は温度によってコントロールされる。 溶出速度の温度依存性を植物生長の温度依存性と一致させているため、作物の生育に応じて継続的に養分の供給が可能となる。 また、肥料濃度が急激に高まらないことを利用して、播種位置に全量を施肥する方法も検討されている。これらの施肥法は、肥料成分を一回の施肥で、土壌をできるだけ介さず直接作物根へ供給するために、農業生産性の向上はもとより、資源の節約や環境保全に大きく貢献することが期待できる。 デントコーンを用いたこれまでの試験では、施肥窒素利用率の向上、施肥位置での根系の促進が報告されている。しかし接触施肥法は、CAFを用いているものの局所多量施肥であるために、出芽障害や根系発達抑制などの影響を、作物の特性（耐塩性や根系発達タイプ）を考慮して体系的に検討する必要がある。 効率的な施肥法の開発には、根の広がりを把握することが必要である。 根系の調査法は堀取りにより調査が基本であり、根重などで土壌中の根系分布を間接的に測定するもので、これまで土壌中の根系分布を直接観察する方法はなかった。

研究施設：JRR-3M　装置：中性子ラジオグラフィー装置　研究分野：植物生理・生態学

表1 肥料種類と根系発達

	試験区名	施肥位置	窒素施肥量(g/unit)	肥料
肥料種類の検討	無窒素	—	—	—
	接触	種子位置より 5cm 下	0.63**	LP30
	S 接触	種子位置より 5cm 斜下	0.63**	LPS60
施肥位置の検討	全層	全層	0.21*	LP30
	接触	種子位置より 5cm 下	0.63**	LP30
	局所	種子位置より 10cm 下	0.63**	LP30
	側条1	種子位置より 10cm 下 5cm 側	0.63**	LP30
	側条2	種子位置より 10cm 下 10cm 側	0.63**	LP30
	一列	種子位置より 5cm 下に一列	0.63**	LP30
麦混作の検討	麦混播	—	—	—
	麦混播+肥料	種子位置より 5cm 斜下	0.63**	LP30

ほ場における施肥量 *3kg/10a、**9kg/10a に相当

肥効調節型肥料；施肥後直ちに肥料分が溶出を始めるリニア型と、一定期間ほとんど溶出しないで、その後溶出を始めるシグモイド型の2つグループがある。溶出速度は温度に依存し、溶出日数別（25℃水中で成分の80%が溶出する日数）に様々なタイプ（30日～360日）がある。

2．実験

供試品種はスズユタカを用いた。 試験区の設定は表1とし、豊浦標準砂（水分18%）を充填したアルミニウム製の薄い容器（200mm×250mm×5mm、厚:1mm）に移し替え、ファイトトロン内で7日間育成した。植物試料をイメージングプレート（以下 IP）に固定し、日本原子力研究所の研究炉JRR-3Mの炉室内で中性子線を2秒間（中性子束：1.5×10^{8}n/cm²/s）照射した。

3．結果

無窒素区は、主根が真下に伸び、主根から側根が左右に発達した。 接触区は施肥位置で主根の生長は停止し、種子と肥料の間で側根が発達した。 S接触区は主根の生長は肥料で停止せず、肥料をかき分けるようにして生長した。

全層区は、無窒素区と同様に根系が発達しているものもあるが、反復によっては、根系の発達が小さくなったものも見られた。 接触区は施肥位置で主根の生長は停止し、種子と肥料の間で側根が発達した。 局所区は主根の伸長が停止し、側根は肥料(LP30)と一定の距離を置いて肥料を囲むように生長した。 側条1区は、肥料近くで主根が寄り、肥料側の側根の生長は停止した。 側条2区は、主根は肥料によらず、肥料側で側根の生長が停止し、根先が細かく分かれた。 一列区は、LP局所区同様に施肥位置で主根の生長は停止し、側根が発達した。

麦混播区では、お互いを抑制するような発達は見られない。 ダイズの根に比べ小麦の根は細い。麦混播+肥料区では、等距離にある肥料に対し、ダイズでは肥料とある程度の距離をとって生長したが、麦では肥料を取り囲むように発達した。

以上のことから、ダイズにリニア型の肥効調節型肥料を局所施肥した場合、肥料と種子の距離が近すぎると主根の生長が停止し、根系の発達を阻害することが明らかとなった。 よってダイズ栽培に肥効調節型肥料を基肥に用いる場合には、種子とある程度距離をおくか、シグモイド型の肥効調節型肥料を利用する必要がある。 また、麦と混作する場合の効率的な施肥法について、活用できると考えられた。

他にも、根近傍の水分動態を解析するために最適な土壌粒子の設定を検討した。 豊浦標準砂は均一な画像（粒塊が生じない）が得られることは利点であるが、水分保持能力に欠けるために扱いづらかった。 そこで他の土壌粒子の中性子ラジオグラフィー画像を取得、また標準砂との混合土壌を検討した結果、バーミキュライトとの1:1の混合土壌が粒子の均一性、および水分保持能力ともに適合することが判明した。

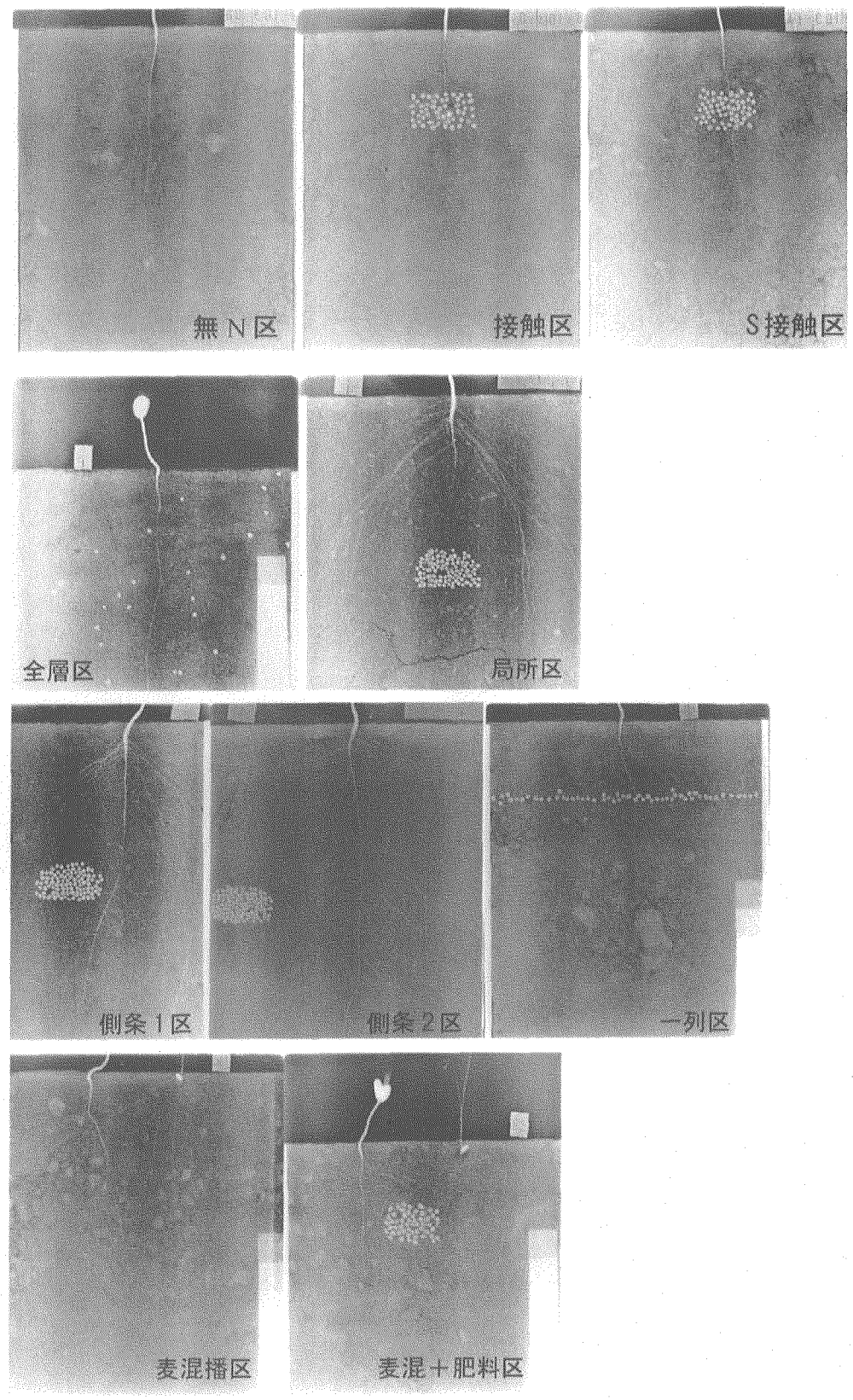
無N区
接触区
S接触区
全層区
局所区
側条1区
側条2区
一列区
麦混播区
麦混＋肥料区

土壌種類(粒径0.5mm以下)

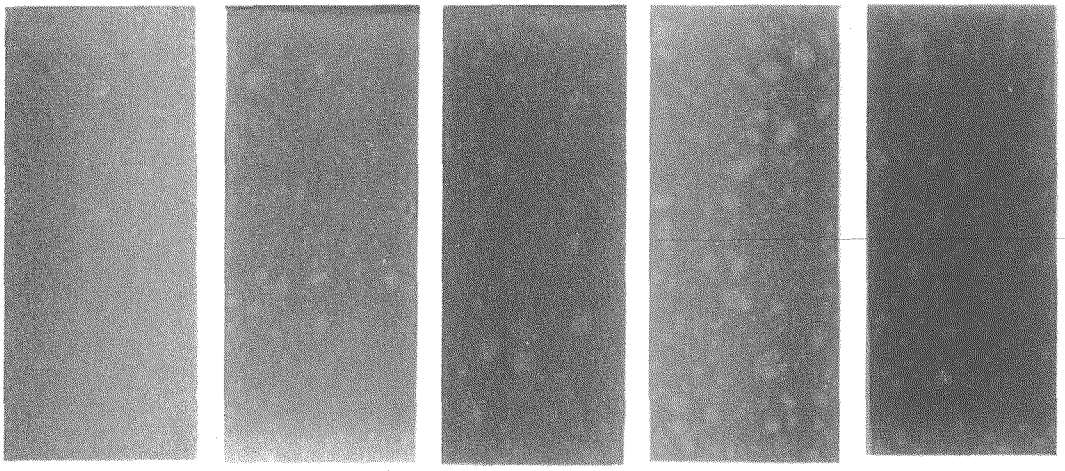

土壌水分量は13% 一箱に入る土壌の量は変わるので、水分量も多少誤差は生じる
砂(豊浦標準砂)以外は粒塊が生じた。

砂と混和(1:1)

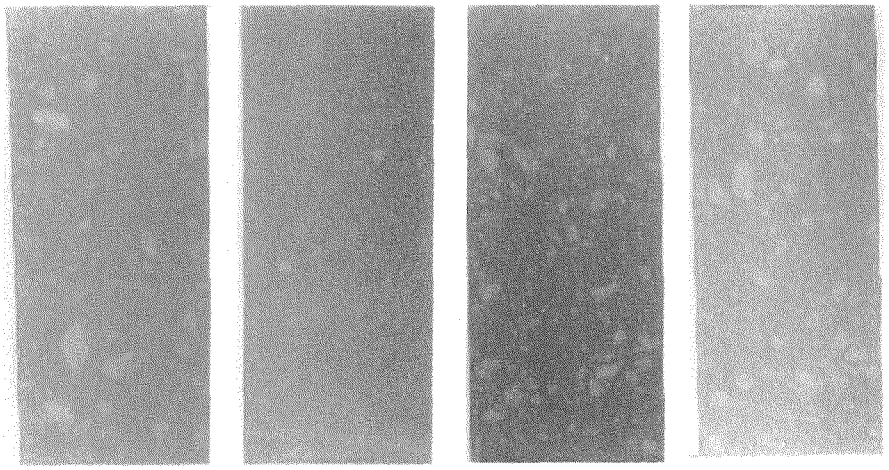

砂と混和することで、塊をなくす目的。砂と土壌を体積比1:1で混和した結論バーミキュライトとの混合は粒塊がほとんど生じなかった。

4. 今後の課題

本研究により、根系の発達を可視化することができ、肥料の種類と位置により根系の発達が異なることを明らかとした。 施肥効率のよい全量基肥施肥法を開発するには、根系発達を阻害しない肥料の種類や施肥位置の検討などが必要である。 またダイズと麦の肥料に対する根系発達が異なることから、両作物の根系発達を考慮したリビングマルチ栽培におけるダイズに効率的な施肥法の開発が必要となる。

今後の研究にこの手法を応用しながら、環境負荷軽減、省力化となる施肥法の開発に努めたいと考える。

研究テーマ：中性子の産業利用技術の開発研究
表　題：高時間分解能中性子ラジオグラフィ高速度撮像法の開発
2-7

Development and Application of Neutron Radiography Techniques with High Temporal Resolution

K. Mishima, Y. Saito and M. Matsubayashi[1]

Research Reactor Institute, Kyoto University, Osaka 590-0494
[1]*Neutron Science Research Center, JAERI, Tokai, Ibaraki 319-1195*

Introduction To make clear rapid transient phenomena, such as boiling bubbles and molten-metal-water interaction by using high frame-rate neutron radiography (HFR-NR), an imaging system requires high temporal and spatial resolutions. The limitation of resolution of the HFR-NR has restricted its applications. To overcome this limitation, it is important to seek the best combination of imaging devices such as a fluorescent converter, high-speed video camera, and image intensifier [1]. In this study, to achieve high temporal and high spatial resolution for HFR-NR, various combinations of imaging devices have been tested.

Fluorescent Converter High resolution, high sensitivity and rapid decay of scintillation are required for the fluorescent converter in the HFR-NR system. Addition of the killer material into the ZnS type scintillator causes a drop of the scintillation intensity but has potential capability of reducing scintillation decay time [2]. ^{6}LiF:ZnS(Ag, Ni) fluorescent converters of which specification are shown in Table 1, were examined to confirm the effect of killer materials by using thermal neutrons in JRR-3M in this study.

Table 1: Specification of fluorescent converters

	Ni (ppm)	Particle size (μm)	Coating weight (mg/cm^2)
JN1	0.0	10.0/ZnS(Ag):3.8	43.5
JN2	0.5	10.0/ZnS(Ag):3.8	43.5
JN3	1.0	10.0/ZnS(Ag):3.8	43.5
JN4	2.0	10.0/ZnS(Ag):3.8	43.5

Table 2: Specification of image intensifier

Image Intensifier	GIB-M2P	C6598-50MOD
Company	nac	Hamamatsu
Micro Channel Plate	Double	Single
Photo Cathode	Multialkari	GaAsP
Resolution [lp/mm]	25	35

Image intensifier The I.I. used in this study are shown in Table 2. The effects of photocathode material and the number of micro channel plates on the image quality were investigated.

High speed video camera In this study, three kinds of high-speed video cameras were tested (FASTCAM ultima-UVS, FASTCAM Super10K, and HG-100K) in this study. In the HFR-NR system, the internal shutter of the camera is disabled but the gating operation of the I.I. makes exposure time control possible to suppress moving effect for slower recording.

Experiments Experiments were performed using a rotating stainless steel disc and a rotating cadmium disc, which has several holes of various diameters to study the temporal resolution of the imaging system. Original images of the rotating cadmium disc were shown in Fig.1 a),b). As shown in these figures, the effect of killer material s could be investigated.

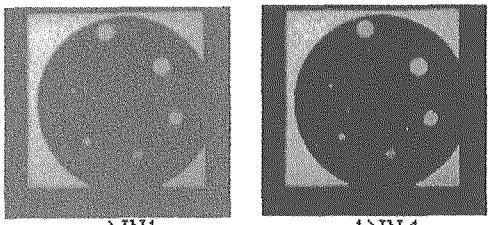

Figure 1: Original images of the rotating Cd disc.

Summary To achieve high temporal and high spatial resolution for high frame-rate NR, various combinations of imaging devices have been tested. The development of fluorescent converters to realize fast scintillation decay with killer materials has performed.

References

1) T. Hibiki, K. Mishima, K. Yoneda, S. Fujine, A. Tsuruno and M. Matsubayashi: Nucl. Instrum. Methods Phys. Res. A, **351** (1994) 423.
2) M. Matsubayashi, T. Hibiki, and K. Mishima: Nonestr. Test. Evalu., **16** (2001) 267.

原子炉：JRR-3　　装置：NRG(7R, C2-3-3-1)　　分野：中性子ラジオグラフィー（熱水力）

2-8
多色発光蛍光コンバータの中性子ラジオグラフィへの応用研究

Neutron Radiography Using Multi-Color Scintillator

持木幸一、桑子雅史、伊東　覚、菊地　秀、橋　康達

K. Mochiki, M. Kuwako, S. Itoh, S. Kikuchi and Y. Hashi

武蔵工業大学　Musashi Institute of Technology

1. 緒　論

中性子ラジオグラフィとγ線ラジオグラフィは互いに相補的な情報を得ることができる。原子炉からはこれらの放射線が同時に放出されているので、同時に透過像を得ることが期待でき、Gd系の赤色蛍光コンバータを利用して、中性子とX線（γ線）の透過像を１つの撮像系で取得する方法を開発してきた。（１）赤色と緑色発光の２層の蛍光板、赤と緑の光学フィルタ、および高感度モノクロＣＣＤカメラからなる撮像系、（２）同じ２色発光蛍光板と高感度カラーＣＣＤカメラ、そして、（３）赤色発光蛍光板と高感度モノクロＣＣＤカメラを使用し、ボロン入りプラスチック板で中性子線をカットする方法の３種類を開発してきたが、静止画の場合には、画質的には（３）の方法が優れており、そこで今回は、蛍光板の最適化を試みた。また、その方法を拡張して、中性子とγ線の同時ＣＴを試み、また、コンクリートの評価への応用研究を試みたので報告する。

2. 中性子・γ線ラジオグラフィ

2.1　蛍光コンバータ

LiF(ZnS)コンバータ、Gd系赤色と緑色の２層コンバータ、およびGd系の赤色コンバータの３種類について、中性子とγ線の透過像を取得して比較した。実験はＪＲＲ－３ｍのＴＮＲＦ２で行った。浜松ホトニクス製フルフレーム方式の冷却型モノクロＣＣＤカメラ C4880-50-24W：(画素数1008×1023）を用いた。結果を図１に示す。中性子の透過像はすべて露光時間１秒の画像を８枚とり、画像間での最小値フィルタ処理を行っている。γ線については、LiF(ZnS)コンバータは20秒、２色コンバータは５秒、および赤色コンバータは２０秒であった。図２は中性子透過像のASTM-E545 SIインジケータ部分を拡大したものであり、　LiFコンバータが解像度の点で最も優れているが、赤色コンバータも遜色ないことを示している。図３はγ線透過像のASTM-E545 BPIインジケータ部を拡大したもので、LiFコンバータは感度がほとんどなく、赤色コンバータが最も優れていることが分かった。よって、赤色コンバータを使い、以下の実験を行った。

2.2　中性子・γ線同時ＣＴ

同じ方法で中性子とγ線の投影像を１台のカメラで取得するＣＴ実験をおこなった。角度は０．５度間隔で３６０方向から、露光時間は中性子が２秒（４フレーム）、γ線が２０秒（３フレーム）で、暗電流補正やシェーディング補正、および複数のフレーム間での最小値フィルタ処理でγ線ノイズを除去した。図４（a）は中性子の、図５(a)はγ線の補正処理された投影像の１つである。また、各図の(b)は巻尺の、(c)はアルミニウム中のFe, Ti, Pb, 空孔, C, およびGd溶液の、また（ｄ）はアルミニウムに直径0.75, 1.0, 1.25, 1.5, 1.75, 2.0, 2.5, 3.0, 4.0mmの穴のあいた分解能ファントムの再構成断面図である。重畳積分法で処理してある。この結果より、まったく位置ずれの無いＣＴ像が得られることがわかった。このことより、今後元素分析などの手法を開発する予定である。

2.3　コンクリート

現在コンクリートの引張性能を向上させる目的で短繊維（鋼やポリエチレン）をコンクリート中に混入させた短繊維補強コンクリートが補修・補強材料として多く利用されており、その均一度の検査ができるかの実験を行った。図６は各種コンクリートの透過像を、図７はＣＴ像を示す。コンクリートについては、冷中性子の使用など、課題が残された。

最後になりましたが、赤色コンバータを提供していただいた、(株)東芝の日塔光一氏と小長井主税氏に感謝する次第です。

参考文献

1) Nittoh, K.: Discriminated neutron and X-ray radiography using multi-color scintillation detector, Nucl. instrument & Methods, A428 (1999).
2) 増子大輔, 持木幸一, 村田裕, 日塔光一, 小長井主税; マルチカラーシンチレータを用いた中性子・ガンマ線同時ＣＴ, 電気学会　計測研究会 (2002).

ＪＲＲ－３Ｍ　７Ｒ　中性子ラジオグラフィ装置、非破壊検査、イメージング

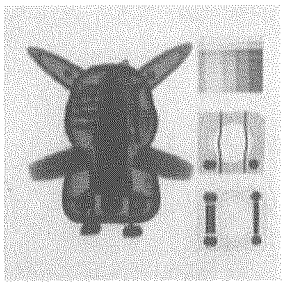

(a) LiF (ZnS) コンバータ
中性子（露光時間１秒）

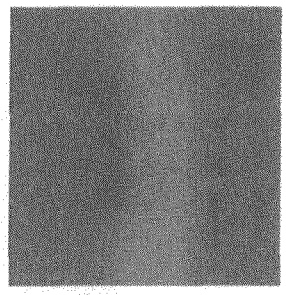

(b)LiF (ZnS) コンバータ
γ線（露光時間２０秒）

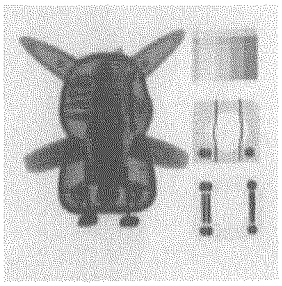

(c) ２色コンバータ
中性子（露光時間１秒）

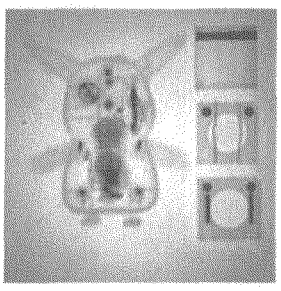

(d) ２色コンバータ
γ線（露光時間５秒）

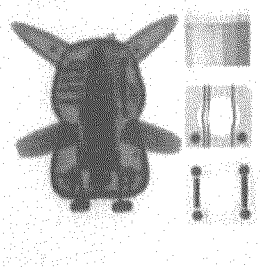

(e) 赤色コンバータ
中性子（露光時間１秒）

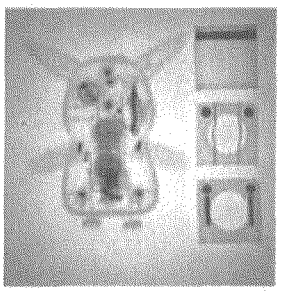

(f) 赤色コンバータ
γ線（露光時間２０秒）

図１　蛍光コンバータの比較

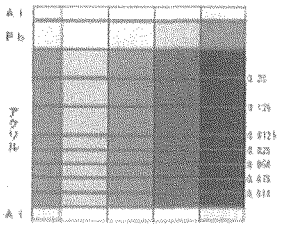

(a) ASTM-E545 SI
インジケータ

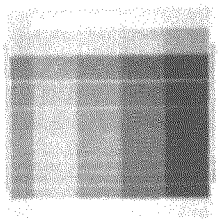

(b) LiF (ZnS)
コンバータ
（露光時間１秒）

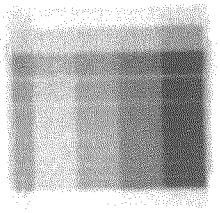

(c)２色コンバータ
（露光時間１秒）

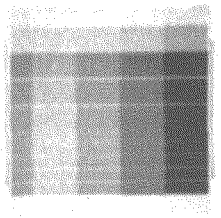

(d)赤色コンバータ
（露光時間１秒）

図２　中性子透過像の解像度比較

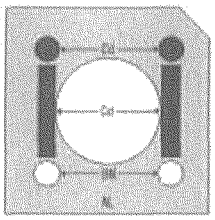

(a) ASTM-E545 BPI
インジケータ

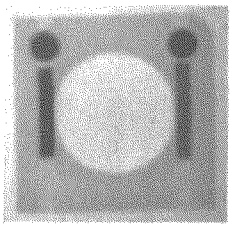

(b)２色コンバータ
（露光時間５秒）

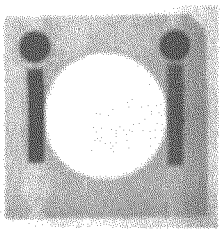

(c)赤色コンバータ
（露光時間２０秒）

図３　γ線透過像の解像度比較

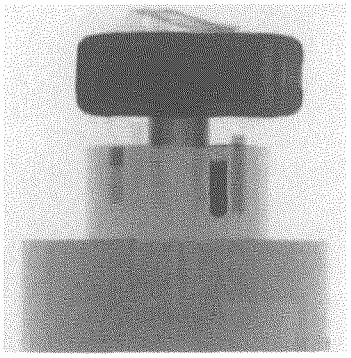

(a) 投影像

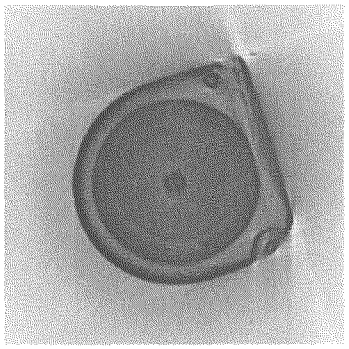

(b) メジャー部のＣＴ像

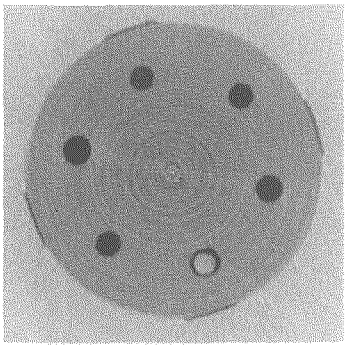

(c) 各種材料部のＣＴ像

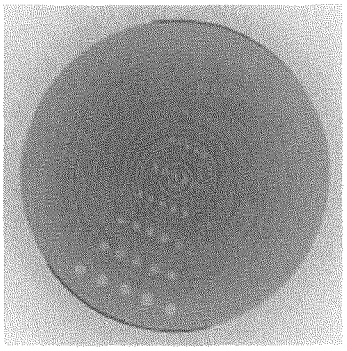

(d)Ａｌインジケータ部のＣＴ

図４　中性子ＣＴ像

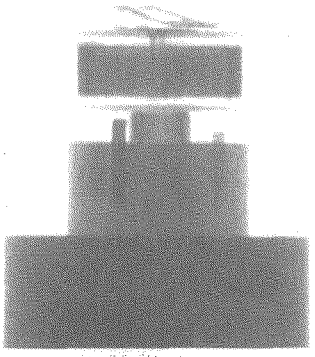

(a) 投影像

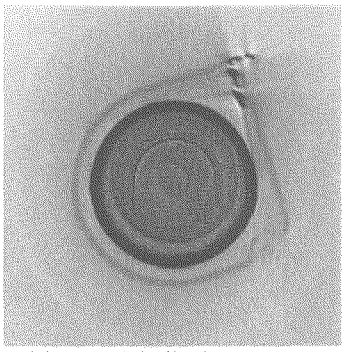

(b) メジャー部のＣＴ像

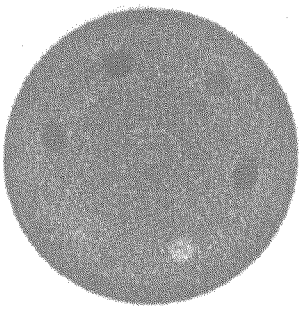

(c) 各種材料部のＣＴ像

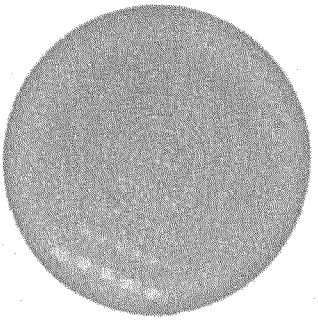

(d)Ａｌインジケータ部のＣＴ

図５　γ線ＣＴ像

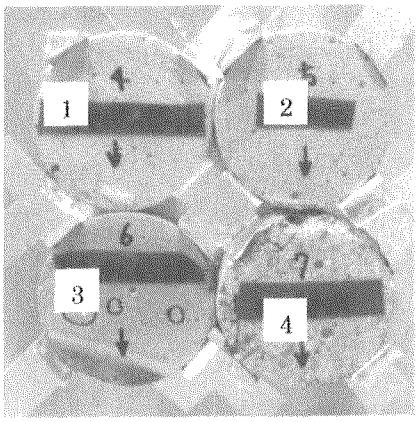

(a)コンクリート資料の写真

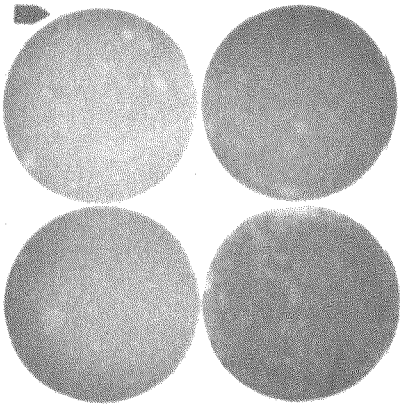

(b)中性子透過像

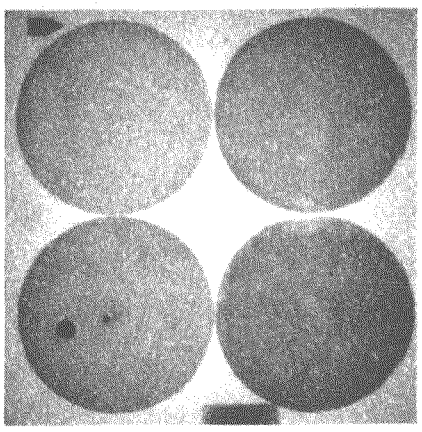

(c)γ線透過像

図６コンクリート資料の透過像

① ファイバ入り、②高靭性、③スチール入り

④ひび割れ

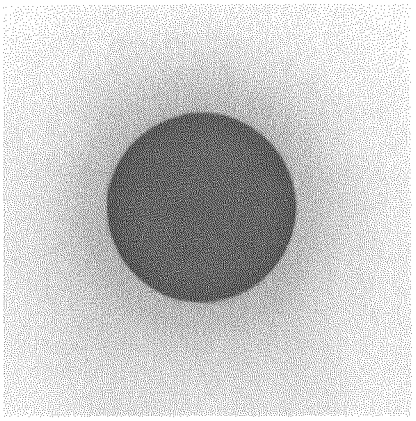

(a)中性子ＣＴ像（３番）

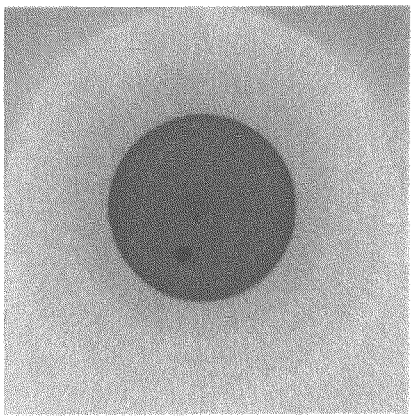

(b)γ線ＣＴ像（３番）

図７コンクリート資料のＣＴ像

試料は③のスチール入り

研究テーマ：照射後試験及びWASTEF試験に関する技術開発
表　　題：中性子ラジオグラフィによる非破壊試験法の開発
2-9

Observation of Simulated Mixed OXide Fuel Rod by Neutron Radiography

R. Yasuda, M. Nakata, M. Matsubayashi[1], A. Harada, K. Harada, Y. Nishino

JAERI, Dept. of Hot Laboratories
[1] JAERI, Neutron Science Research Center

1.Introduction

In Mixed OXide (MOX) fuels, high concentrated Pu particles in fuel pellets cause issue, which is inhomogeneous distribution of thermal stress in the fuel pellets and cladding tubes due to difference in burn up between the particles and matrix. Hence, information about the number, size, and distribution of the particles are required to evaluate integrity and reliability of the fuels. Neutron radiography (NRG) is good tool for obtaining the information about the particles because the neutron cross-section of the particle is very larger than that of the matrix. We have investigated the feasibility of advanced NRG techniques such as the neutron imaging plate (NIP) and neutron computed tomography (NCT) methods for evaluation of the Pu particle size and distribution. However, because Pu included in the MOX fuel is a fissile and poison material, usage of the MOX fuel is difficult and complicated. Hence, simulated fuel pellets controlled with neutron cross-section using ZrO_2 and Dy_2O_3 were prepared to obtain the basic data for evaluating the availability of those techniques to MOX fuels. This paper describes the outline results of examinations of the NIP and NCT techniques using the simulated fuel rod.

2.Exeperimental

ZrO_2 and Dy_2O_3 powders were prepared for making the simulated pellets. Those powders were ground and refined by a ball mill, and mixed with the weight percent of Dy_2O_3 to ZrO_2, 10.0, 5.0, 3.0, 2.0, 1.0, 0.5, 0.2, 0.1 wt.% cylinder type green pellets. The mixed powder was compression-molded with loading 1.5 ton to a pellet. The pellets were sintered under air atmosphere at 1500℃ for 4 hours. The sintered pellets were installed into a Zircaloy cladding tube with hydrides formed to simulate the irradiate one.

The NIP and NCT methods on the simulated fuel rod were performed using at the 2nd thermal neutron radiography facility in JRR-3. In the NIP method, the rod is fixed on a cassette with Al tapes and exposed with neutron beam for 4sec. In the NCT method, the 180 pieces of projections of the rod were obtained by a cooled type CCD camera in every 1° from 0 ~180°. The projections were reconstructed to tomographies by image analyses.

3. Results and Discussion

Figure 1①shows a NIP image of the simulated fuel rod. The image of the pellets becomes black with increasing the amount of adding Dy_2O_3 with the large neutron cross-section. The several black particles are observed in some pellets and are Dy_2O_3 clusters, which have not dissolved in ZrO2 matrix at the sintering process. Fig.1② shows the Photo Stimulated Luminescence (PSL) distribution along a white dotted line A on the Fig.1① . Each plateau region on the plotted line corresponds to a position of the pellet on the Fig.1①. The difference in the concentration of the Dy_2O_3 can be numerically observed among the pellets from 0.5 to 10.0 wt.% Dy_2O_3, although cannot be confirmed from 0.1 to 0.5 wt.%.

Figure 2 shows a CT image on a white dotted line in Fig.1① .In the CT image, the Dy_2O_3 particle distribution on the cross section can be observed. Little black areas on the image show that of less Dy_2O_3 concentration.

By the NCT and NIP method, thus, the 3d-distribution of the Dy_2O_3 particles can be non-distractively obtained.

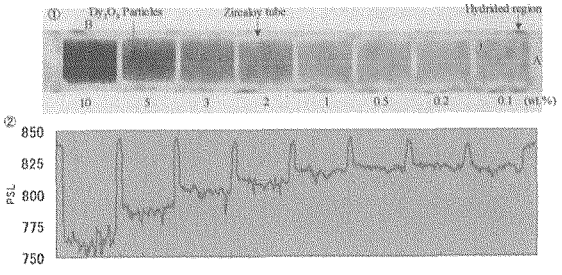

Figure 1 : ①:NIP image of simulated rod.
②:PSL distribution on the white dotted line A on the NIP image.

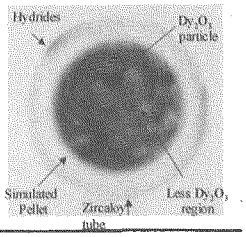

Figure 2 :
NCT image of simulated rod. Position of the cross-section is on the white dotted line B in Fig.1①.

原子炉：JRR-3　装置：NRG(7R, C2-3-3-1)　分野：中性子ラジオグラフィ(原子炉用燃料・材料)

2-10
中性子ラジオグラフィによる機械内部の熱流動現象の定量的計測
Quantitative Measurement on Thermal Hydraulic Phenomenon in Industrial Products by Neutron Radiography

竹中信幸，浅野等　（神戸大学工学部機械工学科）
Nobuyuki Takenaka and Hitoshi Asano
Dept. of Mech. Eng., Faculty of Eng., Kobe University

1．はじめに

原子力・火力に代表される発電サイクルや化学プラント，我々の生活に身近な冷凍サイクルなどでは熱輸送媒体として流体が使用されている．熱輸送効率を上げるため流体の沸騰・凝縮における蒸発潜熱が利用されるが，この場合，流体は液相と蒸気相が混在した気液二相状態で機器内を流動する．気液二相流の熱流動特性（例えば，圧力損失や熱伝達率）は流体の流量や乾き度など平均的な特性だけでなく，液相と気相の空間分布とその流動構造の影響を強く受ける．特に，実用機器では機器の構造はより複雑になる傾向にあり，気液分布が不均質になることも容易に予測できる．気液の不均質分布は，機器性能の低下に作用することが多い．例えば，蒸発流における液量の低下は伝熱面のドライアウトにつながり，炉心冷却系では炉心溶融など大事故に繋がる恐れがあり，液分布を知ることは極めて重要である．また，機器開発を進める場合も，現状の機器における気液二相流の流動構造を知り，その問題点を明らかにすることが必要とされる．

現象解明には可視化が有効であるが，前述のとおり機器構造は複雑であり，実用機器における可視化が必要であることから，可視光による可視化は極めて困難である．被写体における放射線の減衰を利用した非破壊検査法として，中性子線，X 線，γ 線そして陽子線ラジオグラフィがあるが，本研究の可視化対象は金属で製作されていることが多く，流路形状が複雑になれば，容器の壁の厚みに対して流路厚みが薄くなる．そのため，流体に対して金属での減衰が大きい X 線やγ線ラジオグラフィには不向きである．

中性子線は，工業製品でよく使用される鉄，アルミ等の金属材料を良く透過し，作動流体に含まれる水素に対する減衰が大きいことから，中性子ラジオグラフィは機器内部の流体挙動の非破壊検査法として非常に有効であるといえる．

本研究では，中性子ラジオグラフィの混相流機器設計への適用を目的とし，実用製品における気液二相流の可視化と診断，さらには，液相分布の定量計測手法の開発を進めてきたのでその成果を報告する．

2．真影法による定量計測

可視化画像の輝度 S がコンバータ上の中性子線強度に比例するとすれば，画像の輝度分布は被写体の密度 ρ，質量減衰係数 μ_m を用いて次式で表される．

$$S(x,y)=G(x,y)exp[-\rho\mu_m t(x,y)]+O(x,y) \qquad (1)$$

ここで，$O(x,y)$ はオフセットであるが，この値は機器特性のみに依存するゲイン $G(x,y)$ と異なり，被写体での散乱中性子線やコンバータが設置された暗箱内の光の散乱に起因するものであり，被写体の状態に依存する．研究対象である熱流動現象では作動流体に水素を含むことが多く，中性子線は主に散乱で減衰するため，流体が占める厚み（式(1)中 $t(x,y)$）を定量的に計測するためには，オフセット項を流動条件毎に計測する必要がある．本研究では，中性子

JRR-3M7R，実時間熱中性子ラジオグラフィ装置，熱流体工学，混相流工学

吸収体を利用して散乱中性子線を直接計測した．中性子吸収体を被写体の前面（線源側）に設置した場合，可視画像における吸収体の真影部の輝度がオフセット輝度であると言える．実験では，二次元計測への展開，できるだけ高い空間分解能かつ真影部が得られることを条件に，3 mm 幅の中性子吸収体の帯を，3mm の間隔をあけて縞状に配置したグリッドを作成した．

グリッドの構造を図１に示す．アルミニウムに幅 3 mm×深さ 3 mm の溝を削り，B_4C の粉末を充填した．グリッドを使用した場合のアクリル樹脂製ステップの撮影結果を図２に示す．図２上部で黒い縞状に見えるのが B_4C グリッドである．B_4C グリッドの真影部の輝度は上下の可視部におけるオフセット輝度であり，可視部のオフセット輝度は，その上下の吸収体真影部の輝度を内挿して求めることができる．図２中の右の図が，内挿演算で算出したオフセット輝度で補正後の画像である．なお，左の図は原画像，真中の図はモロフォロジフィルタによる CCD 素子の放射線障害によるスポットノイズ除去後の画像を表す．図２下部の輝度分布を見ると，真影法を適用することで中性子散乱によるエッジ効果はなくなり，ステップが鮮明に可視化されていることがわかる．

図３がアクリル樹脂製ステップの厚みに対する中性子線の減衰をプロットしたものであるが，高い直線性が得られていることが確認できる．

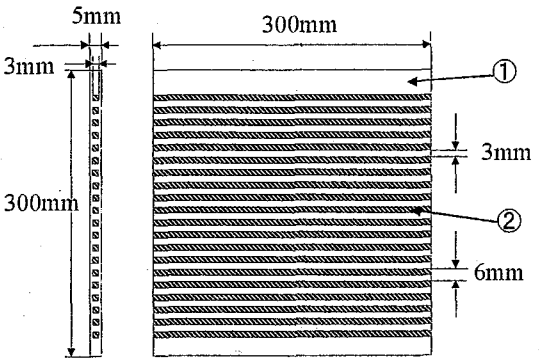

① Aluminum ② Boron Carbide
図１ B_4C グリッド

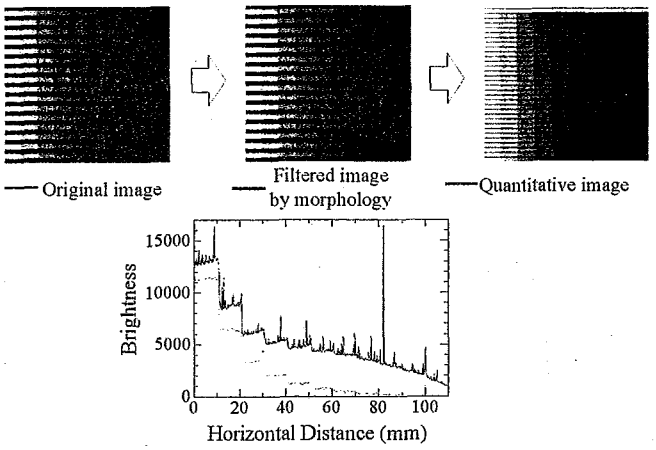

図２ アクリル樹脂製ステップの計測例

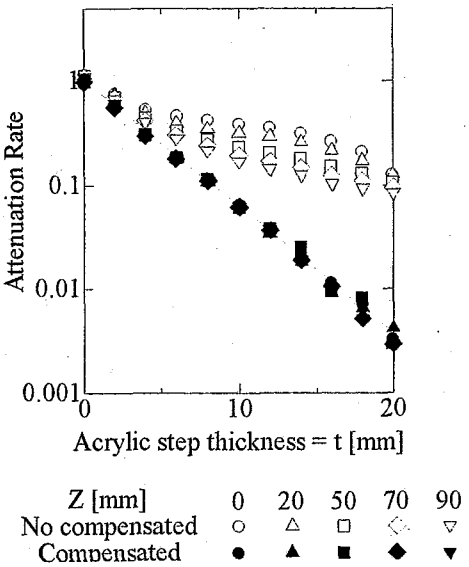

図３ アクリル樹脂製ステップでの中性子線の減衰

３．気液二相流の計測

前項２で開発された定量計測法を気液二相流計測に適用した．気液二相流計測では，気体での中性子線の減衰を無視すれば，可視化画像の輝度分布は次式で表される．

$$S_{TP}(x,y)=G(x,y)exp[-\rho_w\mu_{mw}t_w(x,y) - \{1-\alpha(x,y)\}\rho_L\mu_{mL}t_c(x,y)]+O_{TP}(x,y) \quad (2)$$

ここで，$t(x,y)$，$\alpha(x,y)$ は中性子線照射方向の厚み及び平均ボイド率をそれぞれ表し，添字，w, L, c はそれぞれ，容器，液，流路を表す．容器が空の場合（ボイド率 $\alpha(x,y)=1$），容器が液で満たされている場合（$\alpha(x,y)=0$）の輝度分布は，それぞれ

$$S_1(x,y)=G(x,y)exp[-\rho_w\mu_{mw}t_w(x,y)]+O_1(x,y) \quad (3)$$

$$S_0(x,y)=G(x,y)exp[-\rho_w\mu_{mw}t_w(x,y) - \rho_L\mu_{mL}t_c(x,y)]+O_0(x,y) \quad (4)$$

で表される．それぞれの可視化条件でのオフセット輝度が計測できれば，ボイド率もしくは液相ホールドアップの二次元分布が次式で計測可能である．

$$\alpha(x,y)=\frac{ln\left[\frac{S_{TP}(x,y)-O_{TP}(x,y)}{S_0(x,y)-O_0(x,y)}\right]}{ln\left[\frac{S_1(x,y)-O_1(x,y)}{S_0(x,y)-O_0(x,y)}\right]} \quad (5)$$

$$\{1-\alpha(x,y)\}t_c(x,y)=\frac{1}{\rho_L\mu_{mL}}ln\left\{\frac{S_1(x,y)-O_1(x,y)}{S_{TP}(x,y)-O_{TP}(x,y)}\right\} \quad (6)$$

さらに，多方向から同様に計測できればCT再構成による断面分布計測が実現される．つまり，気液二相流のボイド率もしくは液相ホールドアップの3次元分布を計測することができる．

3.1 ロッドバンドル内気液二相流の3次元計測

ロッドバンドル内空気－水二相流への適用結果を以下に示す．試験部構造を図 4 に示す．試験部は，原子炉の燃料集合体を模擬したものであり矩形容器内にアルミニウム製ロッドが千鳥状に，ロッド周りにらせん状に巻かれたワイヤーをスペーサとして設置されている．ロッドバンドルは鉛直に設置され，空気-水二相流は下部から流入し，ロッドバンドルの

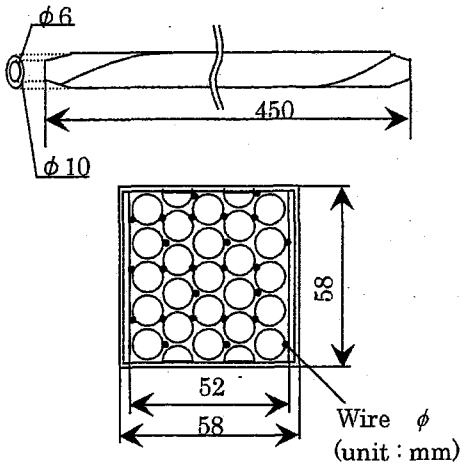

図 4 ロッドバンドル試験部

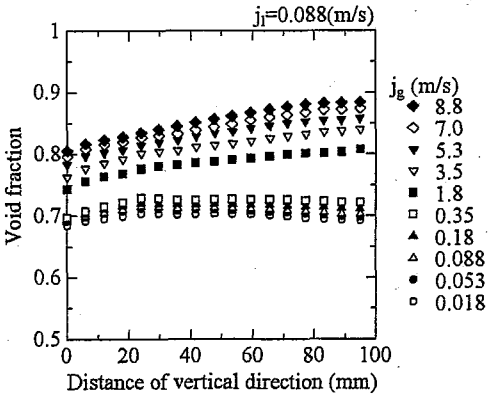

図 5 ロッドバンドル内気液二相流の断面平均ボイド率の軸方向分布

空隙を垂直上昇方向に流れ，上部より排出される．ここでは，試験部を回転させ，多方向から可視化・撮像し，CT 再構成により液相ホールドアップの 3 次元計測を行った．

図 5 は断面平均ボイド率の軸方向分布である．ボイド率は流動方向に対して上昇する傾向にあるが，これは気相が下流へ行くにしたがい断面方向に分散し，気相平均流速が低下したためと予想される．

図 6 に CT 再構成で得られた液相ホールドアップの断面分布を示す．図中，z は垂直方向の距離であり，山の高さが液相の存在割合を表す．これより，z= 0 で 4 隅に偏っていた液相が，z = 72 では分散し，ほぼ均一の断面分布が得られていることがわかる．また，液相はロッド周りに液膜を形成し，流動して

いることがはっきりと確認できる．

図 7 は，サブチャネルごとに平均ボイド率を算出し，その値を高さで表現したものである．ここでは 2 断面についてのみ計算結果が出力されているが，可視化画像では連続したデータが得られており同様の画像処理を施すことで流動方向に対し連続した，同様の断面分布データを出力することができる．これらのデータは，サブチャネル解析に対し極めて有効であると言える．

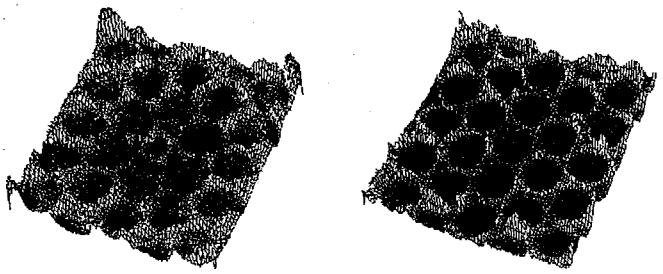

(a) Z=0mm　　(b) Z=72mm

図 6　ロッドバンドル内気液二相流の 3 次元ボイド率分布の計測例
(j_G= 8.8 m/s, j_L = 0.026 m/s)

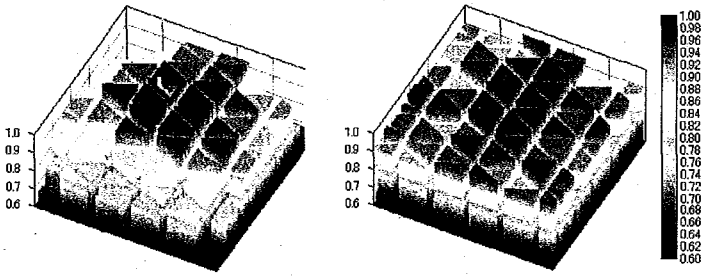

(a) Z=0mm　　(b) Z=72mm

図 7　サブチャネルボイド率分布の計測例
(j_G= 8.8 m/s, j_L = 0.026 m/s)

3.2　流動形態の特長を活かしたボイド率の断面分布計測

CT 計測を行うには多方向からの照射が必要であり，試験部の回転機構を要すると共に長い照射時間が必要である．これは試験部の放射化や多条件の計測の面から望ましくない．そこで，流動形態の特長を活かし，ボイド率の断面分布に仮定を加えることで断面分布を計測する方式を試みた．以下に 2 つの計測手法と計測結果例を示す．

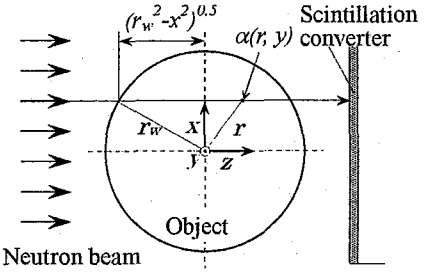

図 8　垂直管上面から見た中性子線の投影

a．軸対称分布を仮定（アーベル変換による計測）

流路形状が軸対称形である場合，流れが発達した気液二相流の流動構造も軸対称であると仮定できる．垂直管の任意の断面における上面からの模式図を図 8 に示す．ボイド率分布が軸対称であると仮定した場合，半径 r での局所の液相体積割合 $1-\alpha(r,y)$ を，位置 x において中性子線照射方向（図 8 中，z 方向）に積分すると，中性子線照射方向の液相の積分量 $\left\{1-\bar{\alpha}(x,y)\right\}_c(x,y)$ が下式で得られ，これを $I(x,y)$ と定義する．

$$\int_{(x,y)line}\{1-\alpha(x,y,z)\}dz=\left\{1-\bar{\alpha}(x,y)\right\}_c(x,y)=I(x,y) \tag{7}$$

ここで，$\left\{1-\bar{\alpha}(x,y)\right\}_c(x,y)$ は可視化画像から式(6)を用いて計測できる．

z 方向の積分をアーベル変換により r に関する積分に変換し，

$$I(x,y)=2\int_x^{r_w}\left\{1-\bar{\alpha}(x,y)\right\}\frac{rdr}{\sqrt{r^2-x^2}} \tag{8}$$

逆変換により x の積分として次式を得る．

$$\{1-\alpha(r,y)\}=\frac{1}{\pi}\int_r^{r_w}\frac{dI(x,y)}{dx}\cdot\frac{dx}{\sqrt{x^2-r^2}} \tag{9}$$

可視化画像より計測される $I(x,y)$ は，画素ごとの離散データとして得られることから，式(9)において $I(x,y)$ の x 微分に中心差分を適用し，x 積分にシンプソンの公式を適用することで，半径方向の液相体積割合の分布 $\{1-\alpha(r,y)\}$ を求めることができる．

計測対象として，内径 20 mm のアルミニウム製直円管の軸上に外径 10 mm のアルミニウム製丸棒を挿入した環状流路を有する同心二重円管を使用した．試験部形状と可視化結果の一例を，図 9(a), (b)に示す．断面平均ボイド率の軸方向一次元分布（図 10）を見ると，気相低流速条件において，スペーサ部でボイド率が低下する現象が見られた．この原因を明らかにするには，断面分布を知ることが重要である．図 11 にアーベル変換を利用して計測された半径方向分布を示す．スペーサがない部分では，半径方向分布に対する気相流速の影響は小さいが，スペーサ部ではスペーサと内壁の空隙部（厚さ 1mm）のボイド率が強い影響を受けていることがはっきりと確認された．

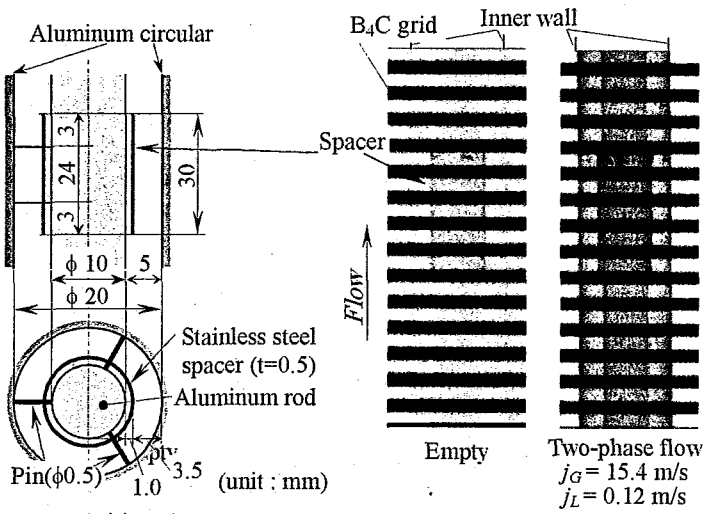

(a) 試験部　　(b) 可視化画像

図 9　環状流路を有する同心二重円管内気液二相流

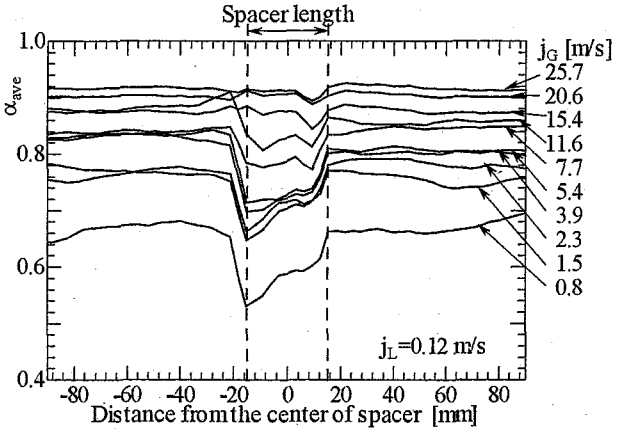

図 10　環状流路内気液二相流の断面平均ボイド率の軸方向分布

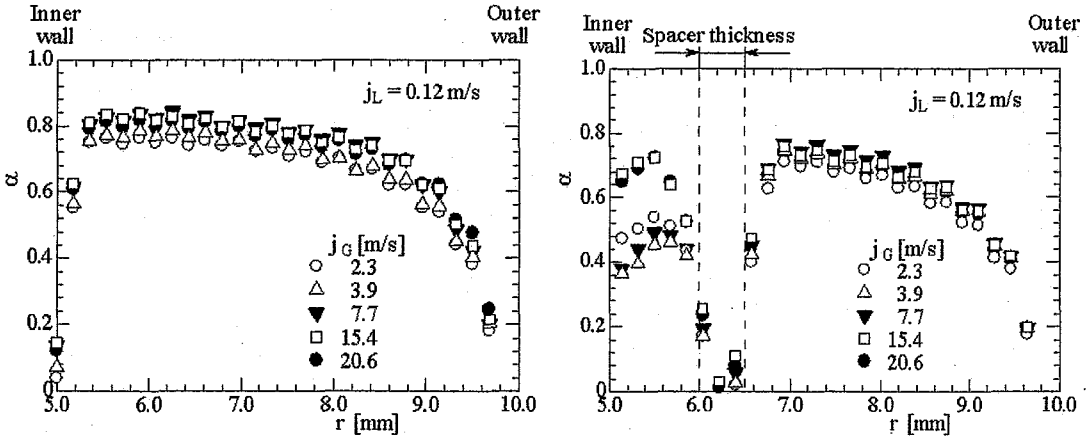

(a) スペーサなし　　(b) スペーサ部

図 11　環状流路内気液二相流の半径方向ボイド率分布

b．回転軸対象分布を仮定（CT 計測の適用）

配管内に伝熱促進体を設置する場合，流動抵抗を抑えるため，それらはらせん状に設置されている場合が多い．すなわち，視点を任意の方向に固定した場合，軸方向距離に対し流路形状が一定の回転角で回転していると捉えることができる．気液二相流が流動する場合，流れが完全に発達しておれば，気液各相の流路形状に対する相対的な相分布は，軸方向に対し維持されていると推測できる．つまり，ある方向から投影された 2 次元画像は，任意の断面に対し被写体を回転させて得た投影像を積み重ねたものと等価であると評価できる．これは，CT による断層撮影法での多方向からの投影像を積み重ねたサイノグラムに相当する．そこで，一方向からの投影により得られた結果をサイノグラムとして扱い，CT 再構成を施し断面分布を得る方法を試みた．計測対象は，ワイヤーコイルが挿入された円管を用いた．試験部形状と可視化結果の一例を，図 12 および図 13(a), (b)にそれぞれ示す．気液二相流の可視化画像では，ワイヤー付近が黒くなっており，液相が多いことがわかるが，液相分布とワイヤー位置の相関は明確には得られない．

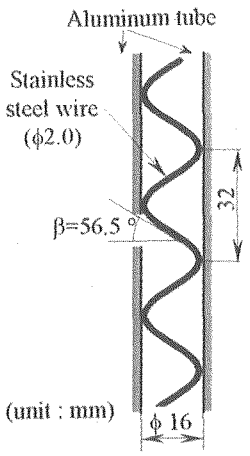

図 12　ワイヤーコイル挿入管試験部

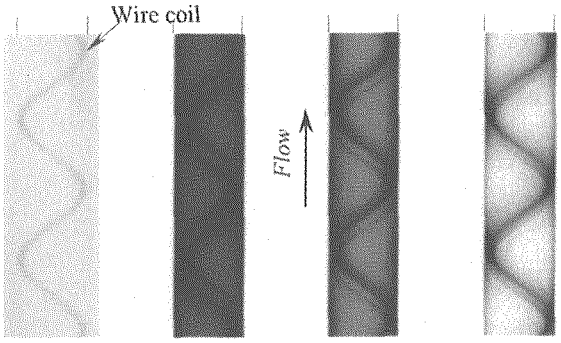

(a) Empty.　(i) j_G=2.0 m/s　(ii) j_G=10 m/s　(iii) j_G=62 m/s
(b) With gas-liquid two-phase flow (j_L=0.102 m/s).

図 13　ワイヤー挿入管内気液二相流の可視化画像

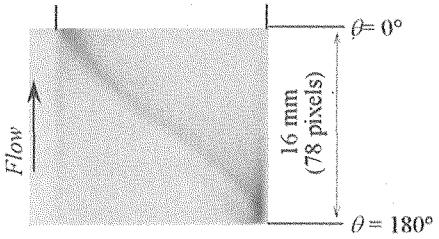

図 14　サイノグラムの一例

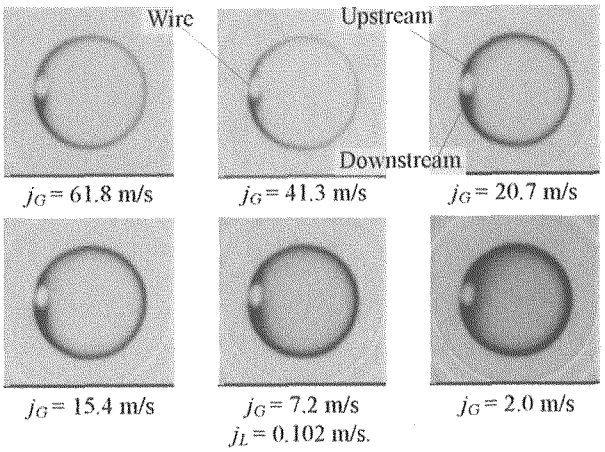

図 15　ワイヤーコイル挿入管内気液二相流ボイド率断面分布

断面平均ボイド率が一定である領域を取り出し，サイノグラム（図 14）として使用し，CT 再構成を施して断面分布を計測した．得られた結果の一例を図 15 に示す．ワイヤーが存在する部分に液は存在せずボイド率が 0 となり，ワイヤーの断面が楕円形状ではっきりと現れている．楕円の縦横の長さはワイヤーの形状から計算されたものと一致し，高い精度で計測されていることがわかる．壁面上の反時計回りの周方向分布は，流れ方向の分布に相当し，図中ワイヤーの上が上流側，下が下流側にあたる．これより，いずれの場合もワイヤー周りに液相が多く集まっているのがわかる．

3.3 プレート熱交換器内気液二相流

プレート熱交換器は波型に加工された複数の金属製伝熱板を積層した構造であり，その間の扁平流路を作動流体が流動する．個々の流路にはプレートの波形状で網目状の細かな流路が形成され，作動流体は分流・合流を繰り返しながら流動する．そのため，熱伝達率が高く，単位容積あたりの伝熱面積を大きくすることができる．しかし，流動抵抗が増大するため熱交換量を増大させるには伝熱板の枚数を増やす，つまり並行流路を増やす必要がある．作動流体が気液二相の場合，各流路への気液の分配に加え，それぞれの扁平流路での気液分布が熱交換器の性能に強く影響し，液相に偏流が生じればプレート枚数に対し能力は必ずしも比例せず著しい性能低下を招くことが予想される．偏流改善には熱交換器内における流動特性，特に液分布を明らかにすることが重要である．

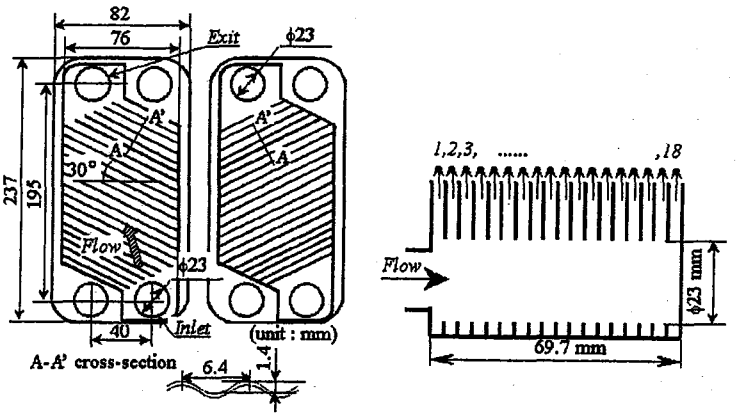

(a) プレート　　(b) 分配ヘッダー

図 16　プレート熱交換器形状

ここでは，実用製品に対する空気-水二相流動の可視化結果を示す．プレート形状を図 16 に示す．日阪製作所製BX型熱交換器を使用した．板厚0.45mmの SUS 製プレートに図 16(a)の波形状が加工され，上下反対にした 2 枚を重ねて真空ロウ付けすることで網状の流路が形成される．流路の平均水力等価直径は 3.36mm である．実験では 2 枚のプレートのみを使用した単一流路内の流動，そして 18 の並行流路を有するプレート熱交換器の流動が可視化された．

a．単一流路内気液二相流の可視化・計測

水力等価直径が 3mm 程度の細い流路が網状に構成されたプレート間を気液二相流が流動する場合，その液相分布は伝熱性能を評価する上で極めて重要である．さらに，この流路を多数並列配置した場合，流量分配を評価・予測するためには，単一流路の平均的な流動特性（圧力損失，平均ボイド率）が必要となる．そこで，単一流路内断熱二相流に対し中性子ラジオグラフィ実験を行い，SIT 管カメラによる動的挙動の観察，流動様式分類，そして冷却型 CCD カメラによるボイド率の定量計測を行った．

図 17 に SIT 管カメラによるビデオ映像（30fps）から抽出した連続画像を示す．気液各相の流量が小さい場合，気相は連続的に流れず，間欠的に流動し，流入口が液相で満たされる様子が確認された．入口部が液相で満たされたとき，熱交換器上部では気相流速が低下し，部分的に液相が逆流していた．また，流入口付近の拡大部では液相が滞留し，そのため熱交換器左側の液相割合が高くなっていた．一方，気相流速が増せば，両端に液の流れが確認できるが，気相は連続的に流動しており，液の逆流も観察されず，熱交換器内の液相分布は両端の一部を除きほぼ均一のようであった．そこで，流動様式を前者の場合を間欠流に，後者の場合を分離流に分類した．間欠流は円管内のプラグ流やスラグ流に，分離流は環状流に相当する．

図 18 に冷却型 CCD カメラのスチル画像から算出したボイド率の 2 次元分布を示す．露光時間は 4.0 秒とした．これより，気相低流速の条件では，液相が両端へ偏り，気相は中央付近を流動し，熱交換器内部では気液の混合が期待できない様子をみることができる．しかし，気相流速が見かけ流速にして

31.0m/s と増大すれば，液相の偏流は小さくなり，ほぼ均質の相分布が得られている．

得られた2次元分布から断面平均ボイド率を算出し，流動方向距離に対してプロットすると，熱交換器内の流路面積の変動によると考えられる周期的なボイド率の変動がみられたものの，絶対値として大きな変化は見られなかった（図省略）．このことからも，熱交換器内では水平方向の気液混合は期待でき

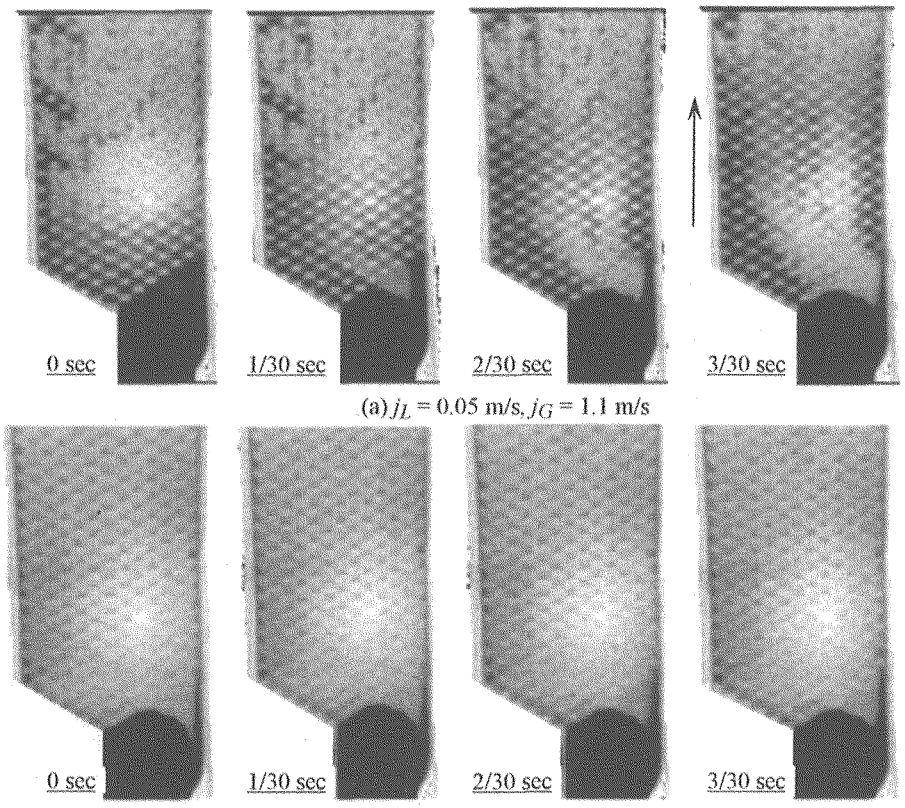

図 17　単一流路プレート熱交換器内気液相流の流動挙動
（SIT 管カメラによる連続画像）

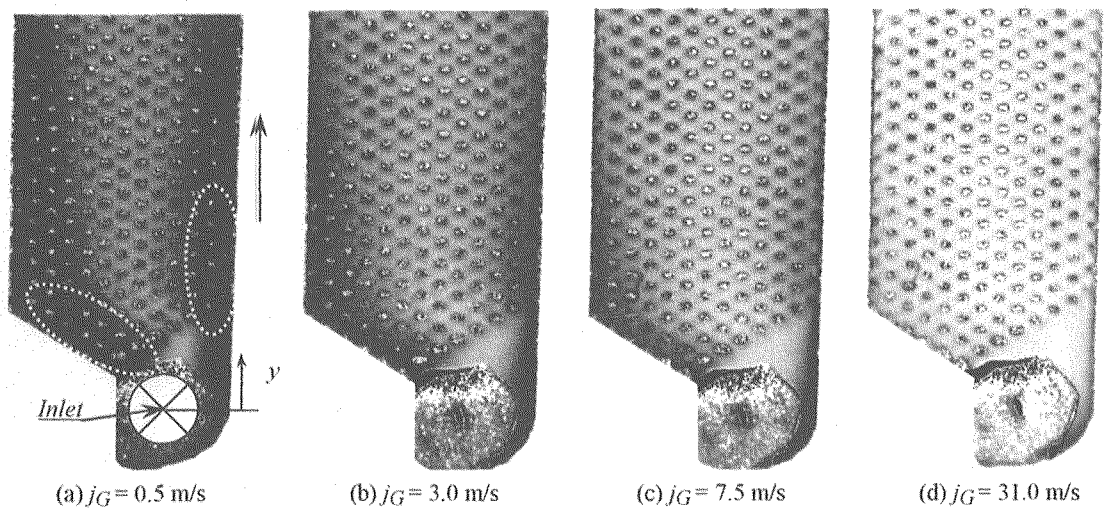

図 18　2次元ボイド率分布（冷却型 CCD カメラのスチル画像からの計測）

ないと考えられる.

そこで，単一流路内の平均ボイド率を算出し，ドリフトフラックスモデルに基づき整理した．整理結果を図 19 に示す．横軸が全容積流速（j_G+j_L），縦軸が気相平均流速（j_G/α_{AVE}）である．これより，プレート熱交換器単一流路内の平均ボイド率はドリフトフラックスモデルで整理でき，その傾向は円管内気液二相流によるものと良く一致していることが明らかとされた．すなわち，間欠流の場合，液流速の影響はほとんどみられないが，分離流の場合，円管内環状流と同様に液相流速の影響を強く受ける．

b．複数流路への流量分配

プレート熱交換器は多数の並行流路で構成されるため，作動流体が気液二相流で熱交換器に流入する場合，液相の流量分配が熱交換性能に極めて強い影響を及ぼす．流量分配はヘッダー間の差圧で決定されるため，各パスの乾き度が異なれば，乾き度の小さいパスでは液流量が大きく，乾き度が多いいパスでは液流量が小さく，各パスの差圧が同じになるように調節されるであろう．このような，液相の不均一分配は大きな性能低下に繋がる．ここでは，各パスの液相体積割合を熱交換器側面からの透過画像を元に計測し，流量分配を評価した．

図 20 に液相ホールドアップの計測結果の一例を示す．白く見えるラインが各流路を示す．これより，18 流路の液相ホールドアップが独立して計測されていることが確認できる．

入口から上方へ y = 60mm の地点で計測した各パスの平均液相ホールドアップを図 21 に示す．液相の分配特性は気液流動条件の影響を強く受け，正反対の傾向を示すことがある結果を得た．

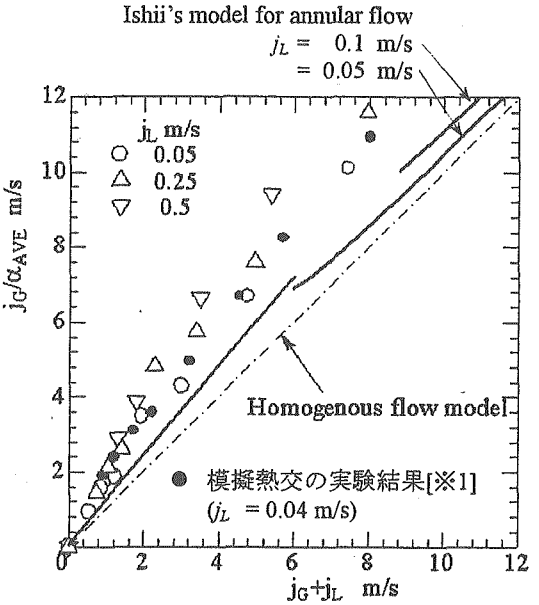

図 19 プレート熱交換器単一流路内空気-水二相流の平均ボイド率

[※1] H. Asano, et al., Experimental Thermal and Fluid Science, Vol. 28, (2003) pp.223-230.

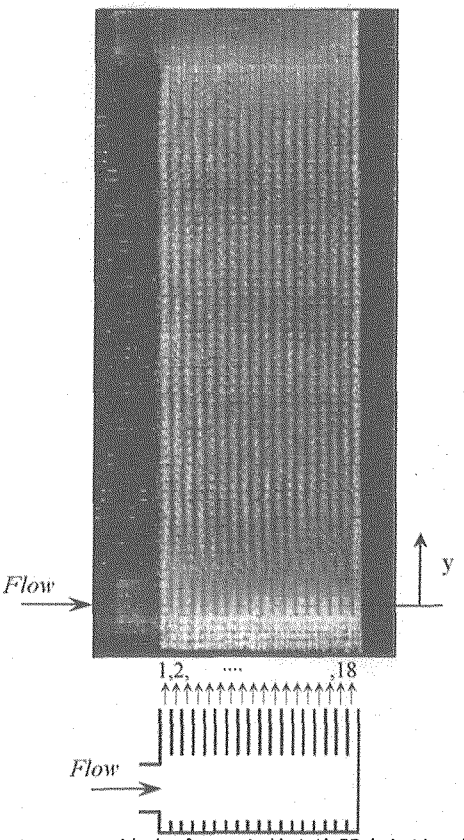

図 20 18 流路プレート熱交換器内気液二相流の液相ホールドアップ分布計測結果の一例.

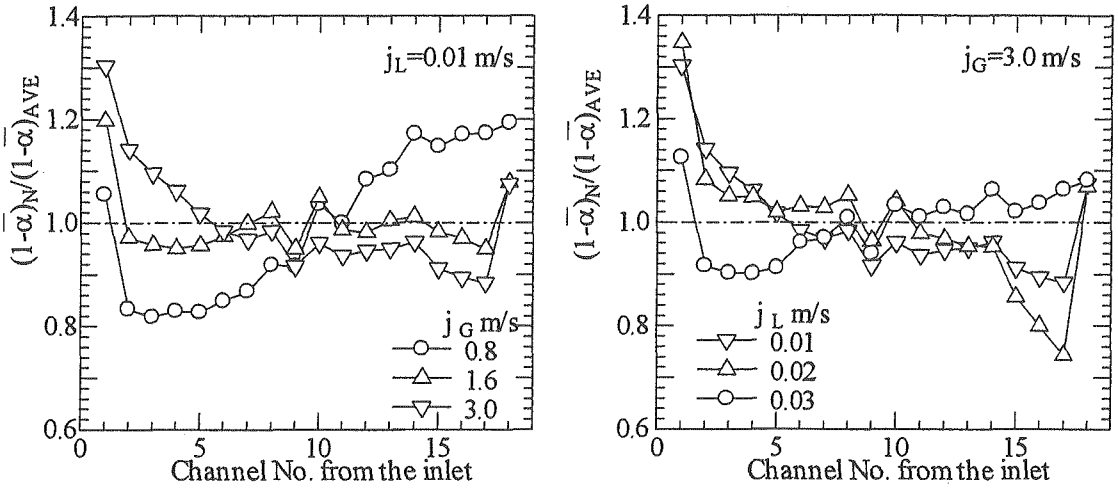

(a) 気相流量の影響　　(b) 液相流量の影響

図 21　液相ホールドアップの分布

7．シリカゲル充填層内の湿分分布の計測

シリカゲルは乾燥剤として身近な物質であるが，吸着式冷凍サイクルやデシカント空調システムの水分吸着材としても使用される．吸着冷凍サイクルの動作模式図を図 22 に示す．シリカゲル粒子が充填された吸着器は蒸発器に接続されており，粒子を冷やすことで蒸気はシリカゲル粒子表面と粒子内の微細気孔に吸着される．粒子の冷却温度は蒸発器の蒸発温度より高いが吸着に伴う凝縮潜熱を除去するため冷却が必要である．一方，凝縮器に接続されたシリカゲル容器では粒子が加熱され脱水する．バッチ処理でシリカゲル容器を切り替えることで連続運転するサイクルが構成される．吸着式冷凍サイクルは熱駆動の冷凍サイクルであるが，バッチ処理で容器接続を操作するため容器やシリカゲルの顕熱が損失となり冷凍サイクルとしての成績係数は吸収式冷凍サイクルに比べ低い．しかし，吸収冷凍機より低温で動作するため排熱利用機器として有効である．吸収式冷凍サイクルの性能改善には，シリカゲル充填層内の熱物質移動の高効率化が必要である．

本研究では，シリカゲル充填層の脱水過程における湿分分布の可視化・計測を行った．シリカゲル（主成分：SiO_2）粒子（粒径：0.25～0.71mm）は内径

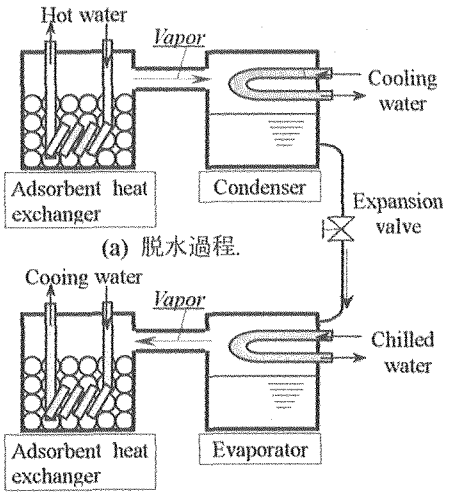

(a) 脱水過程.

(b) 吸着過程.

図22　吸着式冷凍サイクル

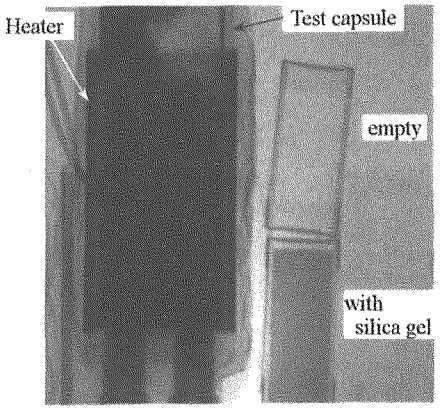

図 23　可視化原画像

36mm×肉厚 2mm×高さ 120mm のアルミ製円筒容器に充填され，予め蒸気を通すことで水分を吸着させた．試験部表面に設置されたシリコンラバーヒーターで容器が加熱され，脱水された蒸気は円筒容器上部から排出され，蒸気取出口に接続されたコンデンサで凝縮し，回収された．

試験部の可視化原画像を図 23 に示す．画像右側の 2 つの容器は，シリカゲル粒子の中性子線減衰特性計測用のサンプル容器であり，上は空で，下の容器には十分脱水させたシリカゲル粒子が充填されて

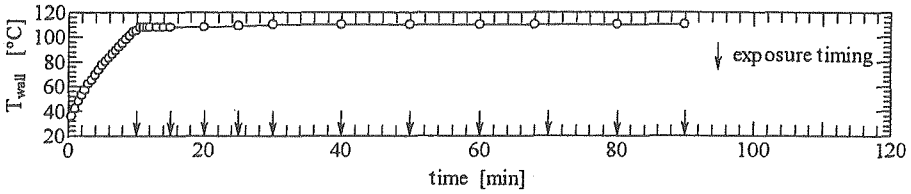

図24　容器壁温の時間変化と撮像のタイミング

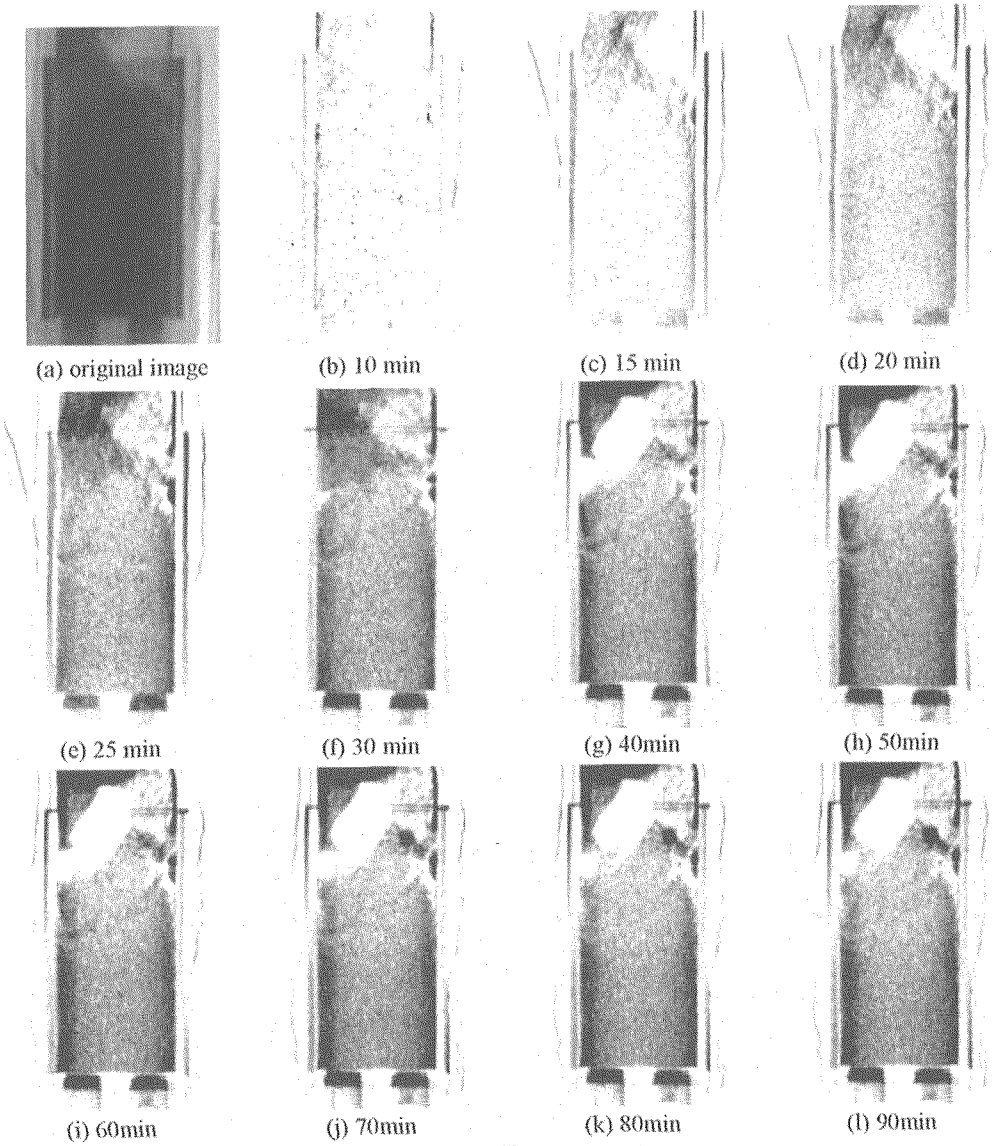

図25　脱水量の2次元分布

いる．この画像からシリカゲル粒子の減衰係数を求めた結果，0.121 cm^2/g であった．因みに，シリカゲル粒子層のかさ密度は1.170 g/cm^3，空隙率は0.63であった．

脱水過程における容器壁温の時間変化と撮像のタイミングを図24に示す．実験開始10分後に壁温は110℃に達し，その後は壁温一定の条件で容器は加熱された．

実験開始前の画像との割り算で中性子減衰の変化量を求め，脱水量分布を計測した．得られた結果をグレースケールで表し，図25に示す．黒い部分ほど脱水量が大きいことを示す．

実験開始15分後には，壁面近くと層の表面で脱水が行われている．層の表面で早く脱水が行われるのは，実験開始時，容器上部の相対湿度が低いためと考えられる．脱水は時間経過と共に順調に進行するが，40分後に白く変化する領域が出現する．これは，この部分で吸着が行われていることを意味する．この部分はヒーター設置面の境界にあり充填層の表面近くである．この領域と加熱面の間には十分に粒子が充填されておらず，粒子の加熱が不十分であり，さらに脱水の進行に伴い雰囲気の湿度が増大したため吸着に転じたものと推察される．

8．おわりに

混相流機器や熱利用機器における熱流動現象の解明を目的として，中性子ラジオグラフィによる実用製品内の流動挙動の観察，気液二相流のボイド率の定量計測法の開発を進めてきた．定量計測手法については，真影法が有効であり，中性子吸収体グリッドを用いて二次元計測が可能であることを示した．多方向からの撮像が可能であれば，CT計測法により三次元データが出力される．また，ボイド率分布が軸対称である，もしくは回転軸対称である，との仮定を利用すれば一方向からの透過画像をもとに断面分布を計測可能であることが示された．

今後，定量計測法の検証を進めると共に，流体振動式ヒートパイプ，ロッドバンドル内気液二相流，気液二相流の細管分岐特性，等の混相流機器への応用展開を進めていく予定である．

成果の公表

1. N. Takenaka and H. Asano, "Quantitative Void Fraction Measurement Method by Neutron Radiography and Some Applications, Proc. 3rd European-Japan Two-Phase Flow Meeting, (2003).
2. N. Takenaka, Y. Tagami and H. Asano, "Measurement Uncertainty of Gas-Liquid Two-Phase Flow by Neutron Radiography", The 7th World Conference on Neutron Radiography, (2002).
3. N. Takenaka, S. Kawano and A. Matsumoto, "Void Fraction Distribution of Gas-Liquid Two-Phase Flow in a Rod Bundle by Neutron Radiography", Proc. 5th Int. Conf. on Multiphase Flow on CD-Rom,(2004) Paper No.472.
4. N. Takenaka and H. Asano, "Quantitative CT-Reconstruction of Void Fraction Distributions in Two-Phase Flow by Neutron Radiography", 5th International Topical Meeting on Neutron Radiography, (2004).
5. H. Asano, N. Takenaka, T. Fujii, E. Nakamatsu, Y. Tagami and K. Takeshima, "Image Processing Methods to Obtain Symmetrical Distribution from Projection Image", Applied Radiation and Isotopes, 61 (2004), pp.625-630.
6. H. Asano, N. Takenaka, T. Fujii, H. Hayashi and T. Wakabayashi, "Visualization and Void Fraction Measurement of Gas-liquid Two-phase Flow in a Commercial Plate Heat Exchanger by Thermal Neutron Radiography", The 7th World Conference on Neutron Radiography, (2002).
7. H. Asano, N. Takenaka, T. Fujii and T. Wakabayashi, "Adiabatic Gas-Liquid Two-Phase Flow Characteristics in a Commercial Plate Heat Exchanger", Proc. 5th Int. Conf. on Multiphase Flow on CD-Rom,(2004) Paper No.172.
8. H. Asano, N. Takenaka, T. Wakabayashi and T. Fujii, "Visualization and Void Fraction Distribution of Downward Gas-Liquid Two-Phase Flow in a Plate Heat Exchanger by Neutron Radiography", 5th International Topical Meeting on Neutron Radiography, (2004).
9. H. Asano, T. Nakajima, N. Takenaka and T. Fujii, "Visualization of Hygroscopic Water Distribution in an Adsorbent Bed by Neutron Radiography", 5th International Topical Meeting on Neutron Radiography, (2004).

研究テーマ：中性子ラジオグラフィによる沸騰流のボイド率計測
表　題　：中性子トモグラフィによる超高熱流束負荷時の沸騰流 3D 計測
2-11

3D Measurement of Void Distribution of Boiling Flow in a Tight-Lattice Rod Bundle by Neutron Tomography

Masatoshi Kureta, Hidesada Tamai

Dept. of Nuclear Energy System, Japan Atomic Energy Research Institute, Japan

1. Purpose of the Experimental Study

Study on void fraction in tight-lattice rod bundles is indispensable for R&D of the Reduced-Moderation Water Reactor (RMWR)[1]. 3D void distribution of boiling flow in a seven-rod tight-lattice bundle was measured by neutron tomography in order to investigate the boiling transition and to verify the numerical analysis codes.

2. Neutron Tomography Experiment

2.1 Neutron tomography (Neutron radiography 3D CT)

Neutron tomography system for measurement of void distribution was developed based on the neutron radiography (NR) and computed tomography (CT) techniques[2]. The experimental system was installed into the research reactor, JRR-3. Void fraction was calculated using parallel processing technique. CT value was reconstructed by the FBP method with Shepp&Logan filter. Spatial resolution was 0.1–0.2mm. Measurement error was estimated within +/-5%.

2.2 Experiment

Void measurement experiment was conducted using a seven-rod bundle test section with diameter of 12mm, gap between tubes of 1mm and heated length of 0.89m. Pure water flowed between stainless tubes which were uniformly heated by the DC power supply. Experimental condition is shown in Table 1. NR images were recorded by 180 steps (1°) in the radial direction.

Table 1: Experimental condition

Flow	Uniformly Heated, Vertical Upward, Boiling
Pressure	In: Max.0.33MPa, Exit: Atmospheric Pressure
Temperature	Inlet Temperature = 85-90 °C
Mass Velocity	139 - 462 kg/m^{2}s
Elevation	0.86 m
Heat Flux	19.6 – 117.6 kW/m^2

2.3 Result

Figure 1 shows the measured void distribution with the tubes and flow shroud. White and dark areas between tubes indicate high and low void fraction regions, respectively. It was found from the experiments that water tends to remain between tubes and vapor tends to gather from the peripheral to the center.

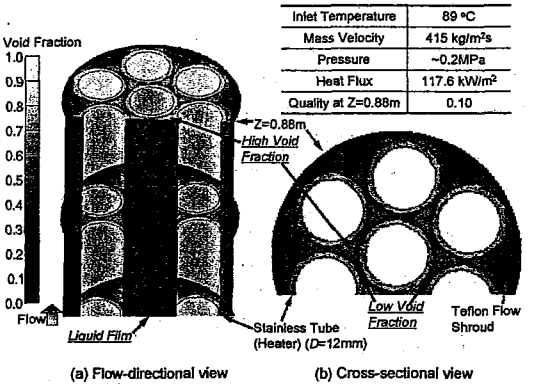

Figure 1 : Void distribution of boiling flow measured by neutron tomography.

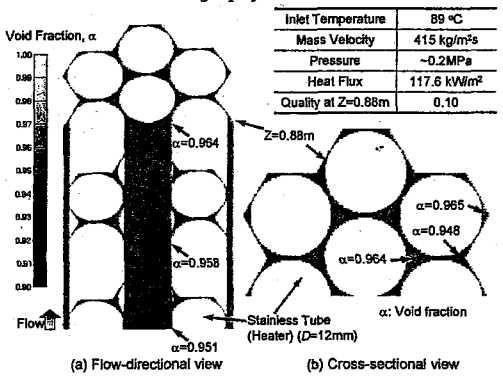

Figure 2 : Subchannel analysis of the experiment by the COBRA-TF code.

3. Discussion

To evaluate the extensibility of the subchannel analysis code, COBRA-TF, to the tight-lattice rod bundle, prediction by the code was compared with the measured data. Figure 2 shows the prediction by the code. It was found from the comparison between Fig.1 and Fig. 2 that trend of the void distribution calculation was similar but the code was overestimated the void fraction.

It is because the effect of the narrow gap is not taken into account in the code. That is, applicability of the constitutive models in the code which is originally developed for a tube becomes low for a tight triangular configuration.

4. Summary

Void distribution of boiling flow in a tight-lattice bundle was measured by neutron tomography.

Followings were made clear:

(1) Water remains between tubes and vapor gathers into the center.

(2) Subchannel analysis code, COBRA-TF, overestimates the void fraction in the tight-lattice bundle.

References

1. T. Okubo, *et al.*, CD-ROM of GENES4/ANP2003, No. 1145, Kyoto, Japan, 2003.
2. M. Kureta, J. of Jet Flow Eng., Vol.20, 2, pp. 24-31, 2003 (in Japanese).

原子炉：JRR-3　装置：NRG(7R、C2-3-3-1) 分野：中性子ラジオグラフィー（熱水力）

研究テーマ：中性子ラジオグラフィによる沸騰流のボイド率計測
表　題　：中性子ラジオグラフィによる沸騰流のボイド率計測
2-12

Measurement of Vapor Behavior in Tight-lattice Bundles by Neutron Radiography

Masatoshi Kureta and Hajime Akimoto

Japan Atomic Energy Research Institute, Tokai, Ibaraki, JAPAN 319-1195

Three-dimensional (3D) and instantaneous void fraction distributions in tight-lattice bundles were measured by neutron radiography (NR) in order to make clear the flow behavior and to verify the advanced fine-mesh numerical analysis codes for the R&D of the Reduced-Moderation Water Reactors (RMWR) which are water-cooed breeder reactors.

Void fraction is calculated using two neutron radiography measurement systems, (1) neutron radiography 3D computed tomography (neutron tomography) and (2) high-frame-rate neutron radiography (HFR-NR) which were developed by authors. 3D time-averaged void fraction distribution is evaluated with the spatial resolution of 0.1-0.2mm using neutron tomography and consecutive changing of 2D vapor behavior is observed quantitatively with time step of 1ms using HFR-NR. Experiments were conducted in the research reactor JRR-3. 7-rod bundle test section with heated length of 0.89m ("7-rod test section") and 14-rod bundle test section with heated length of 0.24m ("14-rod test section") were used. Schematic view of the test sections were shown in Fig. 1. Void fraction is measured under atmospheric pressure and similar inlet condition to the designed RMWR core. Rods (tubes) are fixed with gap of 1.0mm/1.3mm, and are uniformly heated. Water flows upward between rods in the flow shroud.

In this paper, void fraction and vapor behavior in tight-lattice bundles is focused and discussed based on the results obtained by the NR experiments. Figures 2 and 3 show the half-cut view of 3D void distribution and consecutive images of instantaneous void fraction in a 14-rod test section, respectively. It was found from the result of Fig. 2 that "Void drift phenomenon", vapor accumulates to the central or wide space, and high void fraction spots are appeared between rods at low quality region. And, it was observed by the HFR-NR experiments as shown in Fig. 3 that big vapor bubbles flow upward frequently not only in central flow space but in peripheral space of the channel.

The present study was conducted with the governmental funding from Publicly Invited Research Projects for Development of Innovative Nuclear Technologies by the Ministry of Education, Culture, Sports, Science and Technology (MEXT).

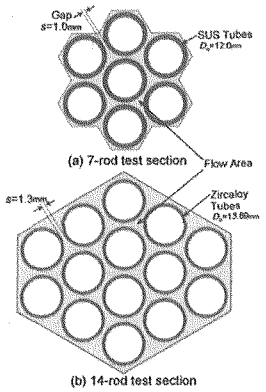

Figure 1: Test sections.

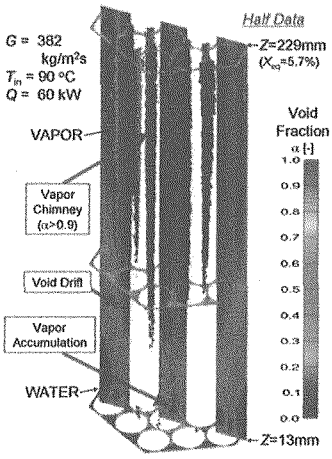

Figure 2: 3D void distribution.

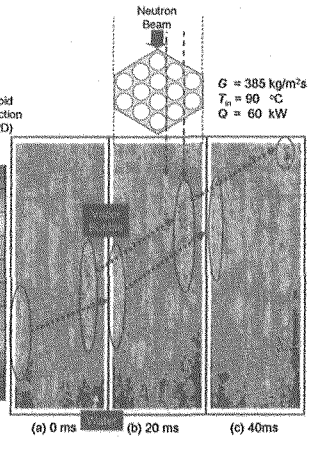

Figure 3: Consecutive images of void fraction.

原子炉：JRR-3　装置：NRG(7R、C2-3-3-1) 分野：中性子ラジオグラフィー（熱水力）

研究テーマ：中性子ラジオグラフィによる生体組織の画像解析
表　題：中性子ラジオグラフィによる生体組織の画像解析
2-13

Preliminary Bone Imaging Study Using Neutron Computed Tomography

T. Takeda, Y. Tsuchiya, M. Matsubayashi[1], Jin Wu, Thet Lwin and A. Yoneyama[2]

Graduate School of Comprehensive Human Sciences, University of Tsukuba, Tsukuba, Ibaraki 305-8575
[1] Tokai Establishment, JAERI, Tokai, Ibaraki 319-1195
[2] Advanced Research Laboratory, Hitachi, Ltd., Hatoyama, Saitama 350-0395

The osteoporosis is a risk factor for fracture in older person. Since bone strength depends on quantity and quality of trabecular bone, non-destructive inner observation of bone provides a useful information for investigation of osteoporosis. Inner trabecular bone has been observed by an micro X-ray CT using synchrotron radiation, although, the inner soft tissue was not visible. Neutron radiography can sensitively detect minute changes of water content in tissues due to the large neutron attenuation for water[1)]. Therefore, there is a possibility to detect the inner soft tissue structure of bone by neutron radiography. In this study, neutron computed tomography (CT) was applied to observe the inner bone structures for the basic medical research.

Neutron CT was performed at the thermal neutron radiography facility (TNRF-2). The sample was a rabbit's thighbone that was fixed by 10% formalin solution. A cooled CCD camera (C4880, Hamamatsu photonics. K. K.) with a fluorescence neutron converter of ^{6}LiF-ZnS(Ag) was used for taking projection images. The operation temperature of the CCD was 223K. The pixel number of the CCD was 1000 × 1080 and the area of the visual view was set about 50mm × 50mm by an optical lens. Thus, the spatial resolution was 50 × 50 μm per pixel. The distance between the center of the sample stage and the fluorescence neutron converter was set at 20 mm. The projection images were taken for one degree step up to 180 degrees. Exposure time was 3 seconds for every projection. The CT images were reconstructed using filtered back projection (FBP) method with Shepp and Logan filter.

Figure 1 shows a projection image of the rabbit's thighbone. Neutron transmission was more acquired in the bone than in the inner bone marrow area. The reconstructed CT images are shown in Fig. 2. The bone and bone marrow were depicted in different CT value. The projection and CT images seemed to reflect the different moisture for bone structure.

This study showed that neutron CT has an ability to depict the different soft tissue density, and it might be possible to estimate the amount of moisture in the bone.

[Figure]

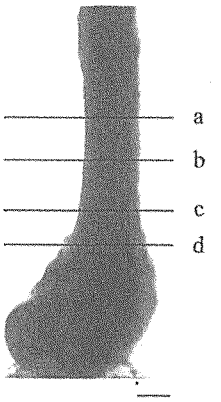

Figure 1: Projection image of the rabbit's thighbone. Bar = 5 mm.

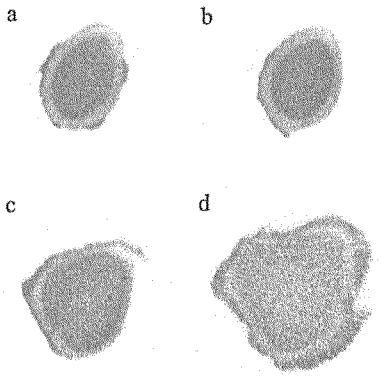

Figure 2: Neutron CT images of rabbit's thighbone.

References

1) Y. Tsuchiya, M. Matsubayashi, T. Takeda, Thet Thet Lwin, Jin Wu, A. Yoneyama, A. Matsumura, T. Hori and Y. Itai: Jpn. J. Appl. Phys. **42** (2003) 7151.

原子炉：JRR-3　　装置：NRG(7R, C2-3-3-1)　　分野：中性子ラジオグラフィー（医学）

研究テーマ：中性子産業利用技術の開発研究
表　題：中性子ラジオグラフィを用いた水素吸蔵合金中の水素濃度分布観察
2-14

Observation of hydrogen distribution in hydrogen–absorbing–alloys by using neutron–radiography technique

M. Matsubayashi, T. Ebisawa[1)], K. Kubo[2)], H. Arashima[2)], and H. Itoh[2)]

Neutron Science Research Center, JAERI, Tokai, Ibaraki 319-1195
[1]Machinery Research Laboratory Yokohama branch, The Japan Steel Works, Ltd., Yokohama, Kanagawa 236-0004
[2]Muroran Research Laboratory, The Japan Steel Works, Ltd., Muroran, Hokkaido 051-8505

Introduction

Recently, research and development of fuel cells is actively conducted because fuel cells are regarded as one of promising clean energies. To avoid degradation of the performance of fuel cells, hydrogen gas of a high degree of purity should be utilized. As resources of hydrogen of a high degree of purity to fuel cells, hydrogen–absorbing alloys which can store hydrogen gas in high concentration and under low pressure, are proposed. In this study, hydrogen distribution in hydrogen–absorbing alloys and alloy particles with which are filled ultra-slim hydrogen–absorbing–alloy tanks were obtained by using neutron computed tomography (CT) technique. The high–resolution–static neutron radiography system[1)] in JRR-3M was utilized for capturing projection images.

Hydrogen storing alloy

Even in the case that low concentration of hydrogen such as 500 ~ 600 ppm was injected into TiCrV alloy and TiCrMo alloy unlike with Mg–based alloys[2)], hydrogen was observed to distribute homogeneously in the alloys, and to be diffused in the alloys relatively quickly.

Ultra-slim hydrogen storing alloy tank

As for ultra-slim hydrogen–absorbing–alloy tanks filled with alloy particles, the once–hydrogenated sample and the 30–times–hydrogenation–repeated sample were compared with each other. In the vicinity of the hydrogen–gas–injection hole, comparatively homogeneous distribution was observed for the once–hydrogenated sample as shown in Fig. 1. The darker portion in the image indicates higher concentration of hydrogen gas. Meanwhile, hydrogen distribution in low concentration was observed for the 30–times–hydrogenation–repeated sample in the vicinity of the hydrogen–gas–injection hole and at the bottom of the tank, due to the repetition of hydrogen injection–and–discharge, or due to the swelling–and–shrinkage of alloy particles, or movement of alloy particles. In addition, it was confirmed that outer wall was bulged after hydrogenation by the actual measurement and that the distribution of bulge correlated well with the hydrogen distribution.

The experimental results are expected to be fed back to the manufacturing technique of tank. In the future, mechanism of hydrogen process for this alloy series and design technique of tank would be established.

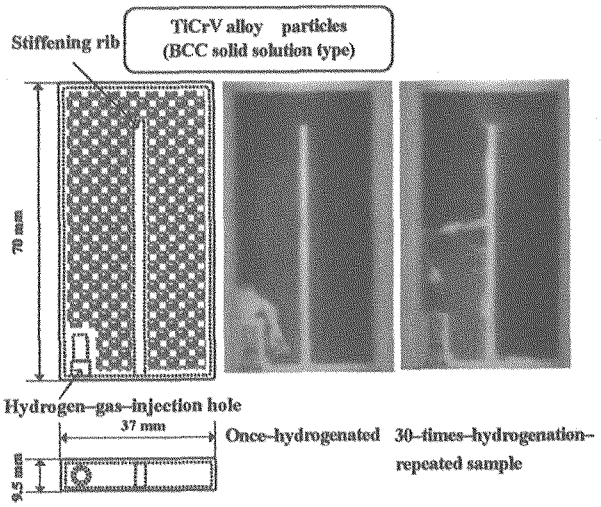

Figure 1: Schematic drawing of the Ultra-slim hydrogen absorbing alloy tank and projection images.

References:

1) M. Matsubayashi, *et al.*, :Nuclear Technology **132** (2000) 309-324.
2) H. Sakaguchi, *et al.*, :J. Alloys and Compounds **354** (2003) 208-215.

原子炉：JRR-3　装置：NRG(7R)　分野：中性子ラジオグラフィ（その他）

This is a blank page.

3. 即発ガンマ線分析

3. Prompt Gamma-ray Analysis

This is a blank page.

研究テーマ：中性子産業利用技術の開発研究
表　題：大豆植物中のホウ素の即発γ線ドップラー広がり法による追跡
3-1

A Research on Boron in Soybean Plants using Doppler Broadening of Prompt γ-Ray

Y. Sakai, M. K. Kubo[1], H. Matsue[2] and C. Yonezawa[2]

Daido Institute of Technology, Nagoya 457-8530, Japan
[1]*International Christian University, Tokyo 181-8585, Japan*
[2]*Japan Atomic Energy Research Institute, Ibaraki 319-1195, Japan*

We revealed that the prompt γ-ray analysis (PGA) can be applied to physico-chemical characterization of materials containing and/or surrounding boron species by probing the Doppler broadened line shape of 478-keV γ-ray emitted from ^{7*}Li which is produced in the ^{10}B(n,α)^{7*}Li reaction[1]. The energetic ^{7*}Li ion loses the kinetic energy through the interaction with atoms which the moving ion encounters in medium. It was proved experimentally and theoretically that the velocity v(t) decreases with time t;

$v(t) = v_0 exp(-Dt)$,

where v_0 is the initial velocity (4.8 x 10^6 ms^{-1}) and D is called " degradation constant ". At the first approximation, the degradation constant D for a compound or a mixture is obtained from a weighted sum of degradation constants of the constituent elements. From analytical-scientific viewpoints, D is expected to reflect the elemental composition and the average density of a material where ^{7*}Li ions move and lose their kinetic energy.

It is well known that boron is one of the essential micronutrients for plants. However, the biochemical function of boron in plant life has not been yet understood sufficiently, although a number of investigations have been done so far. In most of such researches, physiological and/or biochemical changes occurring when plants are deprived of boron have been experimentally studied, which should, however, be indirect functions but not those for normal " live " plants.

In the present article, we report on the boron dynamics in soybeans at the various stages of growing by applying the Doppler broadening method. It should be emphasized that by this non-destructive method boron species in " live " soybeans were examined in-situ, resulting in an important clue to clarify the biological functions in plants.

Commercially available soybean seeds were purchased. Prompt γ-ray measurement was carried out for the dry seed with no treatment (Sample A). The seeds were germinated on sheets of wetted tissue paper after immersing in water overnight. One of the swelling seeds with a bourgeon after 3 days (Sample B) was submitted to the measurement. Another one was grown to a greenish sprout after 7 days and used as a target sample (Sample C). Another swelling seed was transferred onto a pot of soil. It grew up to a young plant of ca. 30 cm height with many green leaves after 40 days, one of which was taken as Sample D. All the samples were picked up and sealed in a polyethylene bag immediately before the measurements. Harvested seeds (Sample E), which were obtained after air-drying the mature soybean plant with crops inside a room for about two months, were also submitted to the measurement.

The measurements were performed for several hours using the PGA system installed at the neutron-beam guide of JRR-3M by Yonezawa et al.[2]. The line shapes of the Doppler broadened spectra depend greatly on the degradation constant D, from which we evaluated the D values by a fitting procedure proposed by Kubo and Sakai[3] previously. The measured prompt γ-ray spectra at 478 keV of ^{7*}Li for the soybean samples are shown in Figure 1. The degradation constants D obtained from the line-shape analysis are 1.46, 1.26, 1.27, 1.74, and 1.47 in a unit of 10^{12} s^{-1} for the samples of A, B, C, D, and E, respectively. For a comparison, it had better cite the D values reported in our previous paper[1]; 1.48 and 1.22 in a unit of 10^{12} s^{-1} for polycrystalline boric acid (H_3BO_3) and aqueous solution of H_3BO_3, respectively.

The D values for both the dry seeds for planting (Sample A) and the dry seeds harvested (Sample E) are close to each other, implying that the boron species in the harvested soybean seeds

原子炉：JRR-3　　装置：PGA(T1-4-1,C2-3-2-2)　　分野：即発γ線分析実験（農・水産物）

was recycled to that of the starting seeds. These values are also very close to that for polycrystalline boric acid. This result suggests that boron in dry soybean seeds is in the physicochemical form of solid H_3BO_3 or that close to it.

As been obviously distinguished in Figure 1, the line shapes of the swelling seed (Sample B) and the sprout (Sample C) are substantially different from those of the dry seeds (Sample A and E). The fitted D vales for both the samples are found to be close to each other and close to that an aqueous solution of boric acid, leading to that the boron species in the swelling seed and the sprout should be dissolved in water.

The D value obtained for the fresh green leaves of young soybean plant (Sample D) was relatively high as described above. It is, however, very difficult or almost impossible to ascribe such a high D value of 1.74 x 10^{12} s^{-1} to boron in some organic medium or polycrystalline boric acid, because the high value forces us to speculate that boron might be surrounded with atoms having high atomic-numbers and/or with a high density. This finding seems mysterious but very interesting, which stimulates our academic and practical curiosity greatly and leads us to furthermore research.

Our work does not provide information on sufficient biological functions of boron. However, it is safely mentioned that the Doppler broadening method should be a new and powerful tool for non-destructive characterization of boron species in biological samples.

Details of the present report will be soon published elsewhere[4].

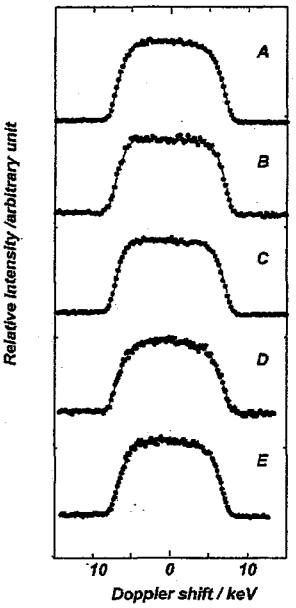

Figure 1: Spectral line-shapes of prompt γ-ray of 478 keV of ^{7*}Li measured for the following samples of soy-bean plant:. A; Dry seeds (no treatment after purchased) (0 day ,i.e., before planting), B; Swelling seeds with a small bourgeon (3 days), C; Sprout (7 days), D; Leaves of the young plant (40 days), E; Dry seeds (153 days, harvested)

References

1) Y. Sakai, C. Yonezawa, M. Magara, H. Sawahata, Y. Ito : Nuclear Instrum. Methods, Phys. Res.**A353** (1994) 699.
2) C. Yonezawa, A. K. Haji Wood, M. Hoshi, Y. Ito, E. Tachikawa : Nuclear Instrum. Methods, Phys. Res.**A329** (1993) 207.
3) M. K. Kubo, Y. Sakai :J. Nucl. Radiochem. Sci. **1** (2000) 83.
4) Y. Sakai, M. K. Kubo, H. Matsue, C. Yonezawa : J. Radioanal. Nucl. Chem.:in press (2004).

研究テーマ：リアルタイム非破壊超微量元素分析法の開発

表　　題：多重即発ガンマ線分析装置のバックグラウンド測定

3-2

多重即発ガンマ線分析装置のバックグラウンド測定

藤　暢輔、大島真澄、小泉光生、長　明彦、木村　敦、後藤　淳
日本原子力研究所　物質科学研究部　原子核科学研究グループ

多重即発ガンマ線分析装置が JRR-3M の冷中性子ビームラインに設置され、クローバー型 Ge 検出器、コアキシャル型 Ge 検出器、BGO 検出器（コンプトンサプレッサー）を用いた実験が開始された。クローバー型 Ge 検出器は、電気的に独立した 4 つの結晶からなり、3×3inch の NaI 検出器に対して 120%の効率を持つ。また、コアキシャル型 Ge 検出器の相対効率は 35%である。多重即発ガンマ線分析では、即発ガンマ線の同時計数測定を行うため、イベントレートはガンマ線のシングル測定における検出効率の 2 乗となる。そのため、統計エラーを低減するためには検出器を測定試料に近接して設置して立体角を大きくすることにより検出効率を上げる必要がある。冷中性子ビームラインは鉛、LiF、ボロンカーバイト、ボロン入りゴム、によって遮蔽されているが、検出器を試料に近接して設置させているために、これらの遮蔽材からのガンマ線が検出器に入りバックグラウンドを増加させる。また、テフロン製の試料ホルダーを取り囲んで検出器が設置されるために、ホルダーからのガンマ線もバックグラウンドとなる。バックグラウンドは検出限界を悪化させるため、その低減のためにバックグラウンドのソースを特定する必要がある。

ルームバックグラウンドの確認のために、中性子ビームを止めた状態で測定を行った。ルームバックグラウンドとしては、コンクリート等に含まれる ^{40}K とルームバックグラウンドの中性子等と Pb との反応によるガンマ線のピークが観測された。空の試料ホルダーを測定位置に設置し、中性子ビームを通すと、バックグラウンドの増加が認められ、テフロンに含まれる F のガンマ線とビームラインに存在する空気中の N のガンマ線ピークが見出された（図 1）。イベントレートはルームバックグラウンドが約 15cps であったのに対し、中性子ビームを出した場合には約 70cps であった。試料を測定する場合のイベントレートは 10kcps 以上を想定しており、この程度のバックグラウンドは、測定に殆ど影響ないと考えられる。また、ビームラインの空気を He で置換し N からのバックグラウンドを減少させる予定である。

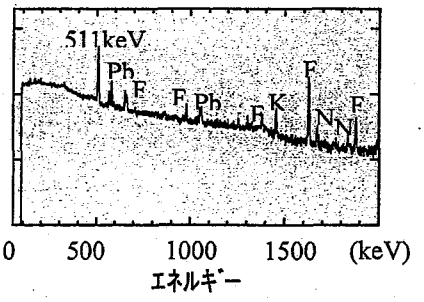

図 1 中性子ビームを出した時のバックグラウンドスペクトル

原子炉：JRR-3　　装置：多重即発ガンマ線分析装置　　分野：即発γ線放射化分析（その他）

研究テーマ：中性子産業利用技術の開発研究
表　題：中性子インビームメスバウアー分光装置の開発
3-3

Development of Neutron In-beam Mössbauer Spectrometer

M. K. Kubo, Y. Kobayashi[1], Y. Yamada[2], Y. Sakai[3], H. Shoji[4], C. Yonezawa[5], H. Matsue[5]

Department of Chemistry, International Christrian University, Tokyo 181-8585
[1]*Applied Nuclear Physics Laboratory, RIKEN, Wako, Saitama 351-1098*
[2]*Department of Chemistry, Science University of Tokyo, Shinjuku, Tokyo 162-8061*
[3]*Daido Institute of Technology, Minami-ku, Nagoya 457-8530*
[4]*Graduate School of Science, Tokyo Metropolitan University, Hachioji,Tokyo 192-0039*
[5] *Japan Atomic Energy Research Institute, Tokai, Ibaraki 319-1195*

Emission Mössbauer spectroscopy is a sensitive tool for investigation of trace amount of chemical species formed after radioactive decay and nuclear reactions. Among various nuclear excitation methods, thermal neutron capture has its uniqueness in the aspect that the neutron has no charge and gives less radiation damage to the material along its passage compared with charged particles especially when only γ-rays are emitted during de-excitation after the nuclear reaction. Chemical form change following a neutron capture reaction had attracted a lot of interest, but there have been a few works[1)] utilizing the advantage of the emission Mössbauer spectroscopy. We have been investigating the chemical and physical behaviors of implanted radioactive nuclei in various materials, e.g., ^{57}Mn in graphite and $KMnO_4$[2)] by using a parallel plate avalanche counter (PPAC)[3)]. The high efficiency and signal-to-noise ratio (S/N) of the PPAC prompted us to start a new emission Mössbauer study aiming at the detailed *in situ* spectroscopic study on chemical and physical behaviors of the trace species produced via neutron capture reactions. Our first goal is to establish a stable system for emission Mössbauer spectroscopy of ^{57}Fe arising from the neutron capture reaction ^{56}Fe(n,γ)^{57}Fe.

After a preliminary feasibility study, electrons originating from prompt γ-rays were suspected to the main part of the noise. The PPAC is an electron detector which detects the conversion electrons after Mössbauer excitation and also Compton scattered electrons of prompt γ-rays after nuclear reactions hitting the inside of the detector, since the detector has not been equipped with an electron energy discriminator. In order to obtain good S/N we treated the inner part of the PPAC with enamel coating. After this treatment and the change of the counter gas from 2-methylpropane to perfluoropropane lead to an improvement of S/N about 50% in an off-line radioisotope source experiment.

At the PGA sample station we installed a detection setup. A stainless foil sample of 25μm thick was placed at the target position of the PGA system facing to the neutron beam with 45 degrees and also to the PPAC. The measurement was conducted at room temperature. The spectrum (Fig. 1) showed one singlet peak similar to the normal absorption one and no significant changes were observed in physical or chemical state of iron in stainless steel caused by the nuclear reaction. A metallic iron was also examined (Fig. 2).

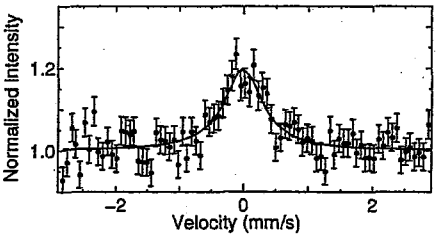

Figure 1: A neutron in-beam Mössbauer spectrum of stainless steel.

Although the only large four peaks were clearly seen due to insufficient statistics, the spectrum consisted of a sextet line as seen in normal absorption spectroscopy. In this study the first step of construction of a neutron in-beam Mössbauer spcetrometer has been achieved. Temperature variation in measurement will be the next stage.

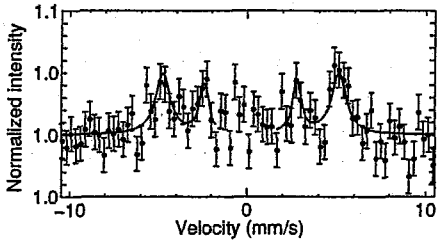

Figure 2: A neutron in-beam Mössbauer spectrum of metallic iron.

References

1) W. G. Berger *et al.*, *Phys. Lett.*, **24A**, 466 (1967). W. G. Berger, *Z. Phys.*, **225**, 139 (1969). G. Czjzek and W. G. Berger, *Phys. Rev.*, **B1**, 957 (1970).
2) Y. Kobayashi *et al.*, *Eur.Phys. J.* **A 13**, 243 (2002). Y. Kobayashi *et al.*, *J. Radioanal. Nucl. Chem.*, **255**, 403 (2003).
3) T. Saito *et al.*, *J. Radioanal. Nucl. Chem.*,**255**, 519 (2003).

原子炉：JRR-3　　装置：PGA(T1-4-1,C2-3-2-2)　　分野：即発γ線分析実験（その他）

研究テーマ：多重ガンマ線分析の分析化学への応用
標　　題：多重ガンマ線分析による高感度多元素同時定量

3-4

多重ガンマ線放射化分析を用いたルビー・サファイアの分析

Trace elements in Ruby and Sapphire samples from Vietnam using multiparameter coincidence method

初川雄一、トランヴァン　リュエン、藤暢輔、木村敦、大島真澄

我々はガンマ線の同時測定と中性子放射化分析法を組み合わせることにより新たな高感度元素分析法開発し、これにより高感度な多元素、非破壊、同時定量が可能になり、環境試料、地球科学試料、考古学試料など多岐の分野への応用を行ってきた。本研究では、これを用いてベトナム産の鉱物試料ルビー、サファイア中の極微量元素分析を行い地球化学的知見が得られたのでこれを報告する。ルビー、サファイアはともに鉱物学的にはコランダムと呼ばれる酸化アルミニウム（Al_2O_3）を主成分とする六方晶系結晶で硬度９とダイアモンドに次ぐ硬さを示す。ルビーはクロムの混入により赤色になったコランダムのことをいい、大理石、片麻岩など高温で変成作用を受けた岩石中に産することが多い。サファイアはチタンや鉄のために青色になったコランダムで変成岩中、玄武岩中および気成鉱床中に生じる。測定試料はベトナムから産出したものでルビーはベトナム北部の Lucyen 産、サファイアは南部の Thuong Xuan 産の試料の分析を行った。試料は超音波洗浄したのちにポリエチレン袋あるいは石英管に封入し、標準岩石 JB-1a, JP-1, JA-1 および標準試料溶液より調整し、ろ紙上に滴下し乾燥させた標準試料とともに原子炉において中性子照射を行った。中性子照射は原研研究炉 JRR－３を用い、短時間、中時間、長時間照射によりそれぞれ適当な半減期を持つ核種を Ge 検出器によるシングルガンマ線測定および、GEMINI-II による多重ガンマ線測定を行い合計４５元素の定量に成功した。得られた元素濃度比などから地質学的考察を加えた。一例として本研究で得られた希土類元素のパターンを図に示す。Eu においてルビーとサファイアが異なる傾向を示していることがわかる。この傾向はルビーとサファイアの生成環境の違いに由来するものと思われる。

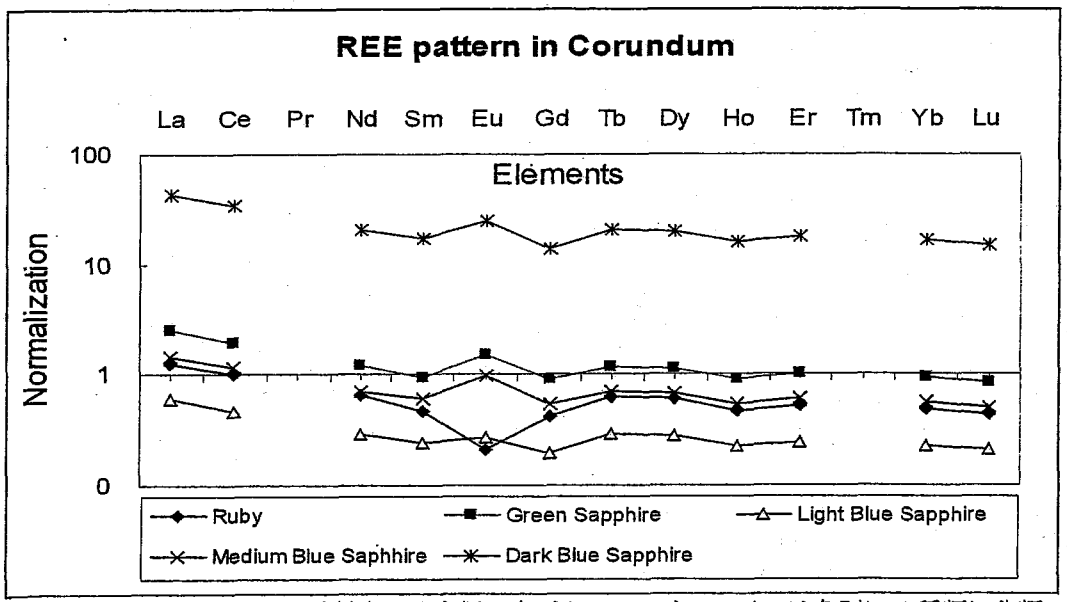

図　ルビー、サファイア試料中の希土類元素パターン。サファイアは色別に４種類に分類してある。

原子炉：JRR-3

研究テーマ：核物理・核化学的手法を用いた原子核科学の研究
表　題：多重ガンマ線検出法を用いた米に含まれるカドミウムの分析

3-5

Cadmium Analysis in Rice by Multiple Gamma-ray Detection Method

Y. Toh, M. Oshima, M. Koizumi, A. Osa, A. Kimura, J. Goto, Y. Hatsukawa
Department of Material Science, JAERI, Tokai, Ibaraki 319-1195

Maximum level for cadmium of the rice in Japan is specified to 1.0 ppm. Based on the risk assessment of cadmium in Joint FAO/WHO Expert Committee on Food Additives (JECFA), the provisional tolerable weekly intake for cadmium 0.7ug/kg.bw was set up provisionally in 1988. The discussion based on the provisional tolerable 0.4ppm has been performed in Codex Committee on Food Additives and Contaminants (CCFAC)[1-3].

The issue on cadmium concerns all foods, and especially, rice is the most important staple food in Japan and is the major crop in the Japanese agriculture. The dietary intake of rice accounts for a quarter of total daily food intake on an energy basis; and rice represents 30% of total agricultural production. Since about 50% of this is brought about from rice, the amount of ingestion will be greatly dependent on the cadmium concentration of rice. Therefore, the measurement of cadmium concentration is important for the Japanese health.

Instrumental Neutron Activation Analysis (INAA) cannot be used for the determination and quantification of cadmium. Therefore, Prompt Gamma Neutron Activation Analysis (PGA) is suitable for measurement of cadmium. When cadmium is measured by PGA, Hydrogen is the disturbance element. Since the prompt gamma ray of hydrogen is 2223keV, the prompt gamma ray of cadmium are covered by low-energy tail due to the Compton scattering and a detection limit is reduced. Although the influence from hydrogen can be reduced by using ashesed samples, this procedure needs the long time and effort. Cadmium mainly emits the prompt gamma ray of 558 and 651 keV. By applying the multiple gamma ray detection method to PGA, the influence from nuclei which emits only one prompt gamma ray coincidently can be reduced. The detection limit of cadmium contained in the rice by Prompt Gamma Neutron Activation Analysis using the Multiple Gamma ray detection method (MPGA) was estimated[4]. The quantification of Cd contained in rice performed by MPGA at the C-2 port of Japan Research Reactor No.3 Modified (JRR-3M) in Japan Atomic Energy Research Institute (see Fig.1).

Taking account of Compton gamma rays of hydrogen, it is presumed that one can quantify cadmium contents in rice to 0.05 ppm or less by the MPGA measurement for 10 minutes if the detector system have about 10% absolute efficiency for prompt gamma rays of cadmium. About 10^4 samples of the rice may be measured for three months, and the more detailed pollution inspection may be attained.

This study is supported by Industrial Technology Research Grant Program in 03A52003c from New Energy and Industrial Technology Development Organization (NEDO) of Japan.

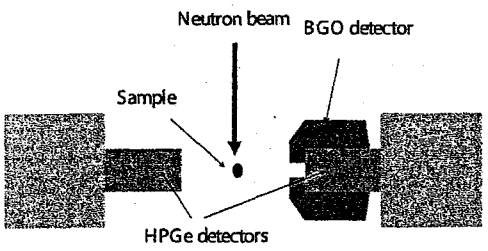

Figure 1: A schematic drawing of gamma ray detectors used in the measurement for cadmium in rice.

References

1) Report of the 36th session of the CODEX committee on food additives and contaminants, (Rotterdam, The Netherlands 22 - 26 March 2004).
2) Thirty-third Report of the Joint FAO/WHO Expert Committee on Food Additives World Health Organization Technical Report Series, (1989) p. 776.
3) Report of the 35th session of the CODEX committee on food additives and contaminants, (Arusha, Tanzania 17-21 March 2003).
4) Y.Toh, M. Oshima, Y. Hatsukawa, M. Koizumi, A. Osa, A. Kimura, J. Goto: J. of Nucl. Radiochem. Sci, Vol4 (2003) p. 197.

原子炉：JRR-3　　装置：PGA(T1-4-1,C2-3-2-2)　　分野：即発γ線分析実験（農・水産物）

3-6

隕石試料の即発ガンマ線分析(III)

Prompt gamma-ray analysis of meteorite samples

海老原充、大浦泰嗣、唐牛譲、白井直樹、本橋健晴、岡本千里
M. Ebihara, Y. Oura, Y. Karouji, N. Shirai, T. Hotohashi, C. Okamoto
東京都立大学大学院理学研究科
Graduate School od Science, Tokyo Metropolitan University

1. はじめに

平成13年度から15年度の間、標記課題で原研施設を利用した共同研究を行った。これまで同じ研究課題で(I)と(II)を行った。(I)では隕石試料を粉末にし、その一部を用いて即発γ線分析(以下 PGA と略記する)によりその元素組成を求める実験を行った。その結果、PGA は隕石の全岩組成(特に、主成分元素組成)を求める手段として、大変優れていることを実証した。続く(II)では隕石試料を粉末にせず、そのままの状態で分析することを試みた。PGA は非破壊分析法として大きな利点をもっているので、隕石の様な試料には最適の手法であることを確認した。(I)、(II)のそれぞれの研究において、所定の目的を果たすと当時に、それによる研究成果を公表することができた。

以上の経過を基に、「隕石試料の即発γ線分析(III)」を実施した。3 年の研究期間に行った研究は2つに分類できる。1つはこれまでの経験を生かして、各種隕石試料の非破壊分析を行ったことで、ほとんどの場合が粉末試料か、或いは塊状であっても、中性子のビーム径(2cm x 2cm)以内に収まる程度の試料で、比較法により定量をおこなった。もう一つは、隕石中の特定元素の存在度と存在状態を知ることを目的にして行った研究で、従来の研究を発展させた、新しい試みである。本報告では、このうちの2番目の課題を中心にまとめる。

本報告では、隕石中に微量に存在するホウ素と塩素の存在度について述べる。これらの元素は PGA で比較的感度よくはかれるので、これまでの非破壊全岩分析によっても定量値を求めてきたものである。このうちホウ素に関しては、特に隕石試料等の固体岩石試料に適用するにあたっては他に適当な分析法が無いことから、PGA のデータは非常に重要である。ホウ素と塩素の隕石中での存在度は ppm の桁で、微量元素に分類される。また宇宙化学的には比較的揮発性の高い元素であるが、ホウ素に関してはこれまで十分信頼できるデータがあまり報告されてこなかったので、その宇宙化学的挙動に関しては不明な点が多い。本研究でホウ素の存在度を取りあげたのはそのような事情が背景にある。

隕石中のホウ素の含有量に関しては、汚染の問題が深刻である。汚染の原因は必ずしも特定されておらず、落下後すぐ回収される、いわゆるfallに分類される隕石でも、試料によってはかなり深刻なホウ素の汚染があると報告されており、恐らく落下回収後の不適切な取り扱いのためだろうと考えられている。地球落下後に生じる汚染としてよく知られている例は、南極隕石におけるハロゲンの汚染である。本研究でハロゲン元素の塩素を取りあげて、ホウ素と共にその存在度を求めたのは、そのような事情からである。研究の目的は、日本の誇るべき研究試料である南極隕石がどのくらい研究試料としての価値があるかを見積ることであり、仮にホウ素の汚染があったとしたら、それを取り除くことができるかどうか、塩素との

研究施設名と装置
JRR-3M (PGA)

研究分野
宇宙化学

関係はあるか、という点を明らかにすることである。

2. 実験

2. 1 全岩分析

炭素質コンドライト隕石 22 試料、オーディナリコンドライト質隕石 12 試料の非破壊分析を行い、ホウ素と塩素の定量値を求めた。試料 0.1~1g を FEP フィルムの袋に封入し、JRR-3M の冷中性子、および熱中性子ビームを用いて、数時間の間照射した。

2. 2 溶出実験。

溶出実験には、これまでのデータを参考にして3つの隕石を選んで用いた(Yamato (Y) 79428 , Y 790461、Allan Hills (ALH) 77011)。これらの試料に関しても全岩分析を行った後に、水とアセトンを用いて溶出操作を行った。溶出駅の分析も試みたが満足すべきデータが得られなかったために、溶出操作の前後での値から、溶出された分を推定した。そのために誤差が大きくなり、溶出部分を直接はかるべく、今後改良する課題として残された。

3. 結果と考察

3.1 炭素質コンドライト隕石中のホウ素と塩素

分析データを Table 1 に示す。この結果と文献値から、対応するグループの南極隕石、非南極隕石の値を比較すると、南極隕石における塩素の定量値は系統的に高いことが分かった。これにたいしてホウ素では CO グループでは同様のことがいえる反面、CM グルーでは南極ー非南極間で誤差の範囲内で一致した含有量を示した。南極隕石間では、塩素とホウ素の含有量の間には相関が認められなかった。

非南極炭素質コンドライト隕石においては、ホウ素と硫黄の含有量の間に相関が認められた、これは両元素の凝縮温度が似ており、母天体形成過程やその前の気相ー固相間での元素の凝縮過程で似た挙動をとったためであると推定される。これに対して、南極炭素質コンドライト隕石では、その S/Si 比と B/Si 比が相関せず、B/Si 比が非南極隕石の値よりも大きいことが明らかになった。これは南極炭素質コンドライト隕石がホウ素に汚染されているためであると解される。

3. 2 普通コンドライト隕石中のホウ素と塩素

普通隕石に対するデータを Table 2 に示す。南極普通コンドライト隕石中の塩素含有量は同じグループの非南極隕石の塩素含有量より系統的に高い値が得られ、以前得られた結果を再確認する結果となった。同様に、ホウ素の含有量についても同じ傾向が認められたが、南極ー非南極間での差が小さく、約半分の隕石では、濃度の上で両グループ間で差が認められなかった。炭素質隕石の場合と対照的に、普通コンドライト隕石では塩素とホウ素の間に明らかな相関が認められた。このことは、南極隕石は両元素とも落下後に汚染されていることを示唆するものである。

3. 3 化学溶出実験における南極普通コンドライト隕石のホウ素と塩素の溶出挙動

ALH 77011では水とアセトンによる溶出によってその質量が 18%減少し、塩素は約 50%減少した。これは恐らく、ハライトのような基から隕石中に存在していた鉱物やアカガネ石のような風化によって生成した物質が選択的に溶出した結果、そのような大幅な質量の減少につながったのであろうと考えられる。これは、この隕石が分析した中で最も高い塩素含有量(1950ppm)を示すこととの符合するところである。同隕石は2.73ppm と高いホウ素含有量を有するが、水とアセトンの溶出の結果、ほとんどホウ素の溶出は認められなかった。このことは、両元素とも南極隕石が落下した後で付け加わったものと考えられるが、ホウ素と塩素は隕石試料中で異なる鉱物相に存在しているものと考えられる。ホウ素と塩素は共通の汚染物質を介して隕石に付着したか、別々の物質により持ち込まれたか、2つの可能性が考えられる。前者の方がより考えやすいが、この場合、ホウ素と塩素は隕石表面に付着した後、両元素の化学的性質の違いに応じて、異なる鉱物相に拡散して行ったものと推測される。ホウ素と塩素は恐らく海由来で、揮発性の高い物質として南極の内陸部まで運ばれたのであろう。

研究成果(発表論文)

(共同研究の期間 (2001~2004) に PGA を用いて得られた成果を報告したもの)

1. M. Ebihara and Y. Oura (2001) Applicability of prompt gamma-ray analysis to the initial analysis of the extraterrestrial materials for chemical composition. Earth Planet. Sci. 53, 1039-1045.

2. A. Yamaguchi, R. N. Clayton, T. K. Mayeda, M. Ebihara, Y. Oura, Y. N. Miura, H. Haramura, K. Misawa, H. Kojima and K. Nagao (2002) A new source of basaltic meteorites inferred from Northwest Africa 011. Science 296, 334-336.
3. Y. Oura, M. Ebihara, S. Yoneda and N. Nakamura (2002) Chemical composition of the Kobe meteorite; Neutron-induced prompt gamma ray analysis study. Geochem. J. 35, 295-307.
4. Y. Oura, N. Shirai and M. Ebihara (2003) Chemical composition of Yamato (Y) 000593 and 000749: Neutron-induced prompt gamma-ray analysis study. Antarctic Meteor. Res. 16, 80-93.
5. M. Ebihara and Y. Oura (2003) Non-destructive analysis of unknown samples named 1G and 2G by using nuclear analytical methods. ISAS Report SP No. 15, 9-17.
6. 白井直樹、海老原充 (2004) 火星隕石 Yamato 980459 の化学組成と火星地殻の希土類元素存在度. 月刊地球 26, 599-606.
7. 唐牛譲、海老原充(2004)月隕石Yamato 981031 の化学組成の特徴. 月刊地球 26, 625-631.

Table 1. PGA data for Cl and B abundances in in Antarctic carbonaceous chondrites

Meteorite	Type	Weight [g]	Cl [ppm]*	B [ppm]*
LEW90500,25	CM2	0.4041	461±69	0.566±0.192
Y791198,77	CM2	0.3798	89±48	1.39±0.20
Y793321,67	CM2	0.4509	732±13	0.839±0.068
ALH77003,86	CO3	0.5940	273±37	0.781±0.51
Y791717,88	CO3	0.2249	378±12	1.64±0.09
Y81020,73	CO3	0.3850	399±11	1.12±0.08
Y82050,74	CO3	0.3996	769±14	2.13±0.08
Y82094,90	CO3	0.9371	417±7	0.154±0.027
Y86751.56	CV3	0.5439	385±39	1.13±0.16
ALH85002,32	CK4	0.2779	227±57	0.48±0.24
DAV92300,14	CK4	0.4466	260±35	1.15±0.27
EET99430,13	CK4	0.5151	753±30	2.84±0.25
LEW86258,15	CK4	0.2432	183±39	1.45±0.32
PCA82500,41	CK4	0.6566	540±31	1.05±0.22
PCA91470,13	CK4	0.5699	295±19	0.75±0.16
EET83311,14	CK5	0.1679	313±28	1.38±0.31
EET87507,21	CK5	0.2342	412±34	1.42±0.31
EET87860,19	CK5-6	0.3217	296±51	0.78±0.21
LEW87009,20	CK6	0.2086	135±45	2.92±0.38
A881595,65	CR2	0.1798	1470±70	6.28±0.57
EET92042,24	CR2	0.1727	165±29	1.33±0.29
PAT91546,6	CH3	0.1576	94±31	0.23±0.35

*Errors accompanied are due to counting statistics (1σ).

Table 2. PGA data for Cl and B abundances in Antarctic ordinary chondrites

Meteorite	Type	Weight [g]	Cl [ppm]*	B [ppm]*
Y791429,94	L3	0.2374	326±14	1.21±0.09
ALH77011,85	L3.5	0.0786	1950±30	2.73±0.14
ALH77252.71	L3/L6	0.3228	211±10	0.856±0.075
ALH77304,71	LL3	0.1858	282±13	1.36±0.08
Y790461,95	H3	0.2307	662±17	1.13±0.10
Y791428,81	H3	0.3476	703±18	1.34±0.08
Y74155,101	H4	0.3036	327±35	1.14±0.17
Y74155,102	H4	0.4353	298±27	0.93±0.13
Y74155,103	H4	0.5759	168±22	0.78±0.11
Y74014,102	H6	0.3555	294±30	1.00±0.15
Y74014,103	H6	0.2767	302±33	1.00±0.17
PCA91241,6	R3.8	0.2151	369±30	1.68±0.26

*Errors accompanied are due to counting statistics (1σ).

3-7

固体環境試料および地球化学的試料の即発ガンマ線分析（Ⅲ）

Neutron-induced prompt gamma-ray analysis of solid environmental samples and geochemical samples

松尾基之・久野章仁・片岡正樹[1]・田中佑人・清宮貴美子[1]・高橋　統
M. Matsuo, A. Kuno, M. Kataoka[1], Y. Tanaka, K. Seimiya[1], O. Takahashi

東京大学大学院総合文化研究科広域科学専攻
[1]東京大学大学院理学系研究科化学専攻
Graduate School of Arts and Sciences, The University of Tokyo
[1]Graduate School of Science, The University of Tokyo

1．はじめに

固体環境試料や地球化学的試料中に含有される元素を定量し、その分布を明らかにすることは、試料自体の形成過程を知る上でも、試料の置かれた環境を理解する上でも重要な課題と考えられる。中性子誘起即発γ線分析法(PGA)は、通常の機器中性子放射化分析法(INAA)と同様に、多元素同時定量分析が可能なため、多くの元素の分布を総合的に判断するのに適した分析法と言える。さらにＰＧＡは、ＩＮＡＡでは分析が困難な H, B, S, Si 等の軽元素や Cd 等の有害元素の定量が可能である、試料の誘導放射能が低く同分析法で使用した試料を他の分析法で再使用することが可能である、といった特長を持つ優れた分析法である。本研究では、同法を用いることにより、次に掲げる試料について種々の環境化学的、地球化学的な検討を行ったので、それぞれの試料ごとに研究内容およびその結果を報告する。

2．谷津干潟底質中の元素及び化学状態の垂直分布

【序】　干潟は多くの生物の生活の場であると同時に環境浄化作用を持っており、周辺の水の汚れを除去し、綺麗な水を海へ流し出すことでも知られている。このような干潟の底質中で、どのような物質移動及び化学変化が起こっているかを明らかにすることは、環境評価の上で重要な情報を与える。本研究ではフィールドとしてラムサール条約登録地である谷津干潟を選び、中性子誘起即発γ線分析(PGA)、及び機器中性子放射化分析(INAA)を用い、30 数元素の定量を行った。また、底質中では嫌気性の微生物である硫酸還元菌が硫酸イオンを還元し、硫化水素を発生させていることが知られている。その際に底質中の鉄イオンと反応し、硫化鉄や Pyrite(FeS_2)が生成している。このことから、メスバウアー分光法で底質中の鉄の化学状態を測定することにより、これらの鉄の硫化物の分布を明らかにすることを試みた。

【実験】　試料は東京湾奥に位置する谷津干潟の底質を垂直方向に採取した。採取には内径 11cm の HR 型不撹乱柱状採泥器を用い、得られた約 50cm のコアを現地で 3cm ごとに分別し、N_2 中に封入した。得られた試料は N_2 を用いた加圧濾過により間隙水を取り除き、メスバウアー測定に用いた。またその後、風乾し、めのう乳鉢で粉砕した。その中から約 200～400mg を精秤し、錠剤成形器を用いて約 100 kgf cm^{-2}の圧力で５分程度置き、直径 10mm、厚さ約１mm のペレットに成形した。これを、中性子ビームのサイズである 20mm 四方以内に収まるように、厚さ 12μm の

研究施設と装置名
ＪＲＲ－３M、即発γ線分析装置

研究分野
環境化学、地球化学、分析化学

FEP フィルムに封入し、テフロン製の専用ホルダーに固定した上で、日本原子力研究所 JRR-3M の冷中性子ビームガイド、または熱中性子ビームガイドに設置した即発γ線分析装置にセットし、He 雰囲気中で 3600 秒間（冷中性子）または 9000 秒間（熱中性子）即発γ線を測定した。測定したγ線スペクトルは通常のγ線スペクトル解析プログラム(Gamma Studio)でピークサーチとピーク面積の計算を行った。各ピークについて得られた計数率は、中性子束の変動を補正するために、24 時間に 1 回、一定の Ti の板(Ti flux monitor)を測定して得られる 342keV と 1381keV のピークの計数率の平均値で割り、比較標準試料について報告されている Ti flux monitor の計数率で規格化した分析感度を用いて各元素の含有量を計算した。

INAA 法に関しては、日本原子力研究所 JRR-4 にて照射を行い、大学開放研のγ線スペクトロメーターにて測定を行った。

【結果及び考察】 PGA, INAA 法により、30 数元素の垂直分布を得ることができた。谷津干潟底質中の重金属元素の多くは他の東京湾に流入する河川の底質に比べ濃度が低く、汚染が少ない場所であるということがわかった。一例として、図 1 に Cd および Cr の垂直分布を示す。Cd はいずれの深さにおいても、検出限界である 0.5ppm を下回っていた。また、Cr は日本の土壌の平均濃度である 50ppm 程度であった。

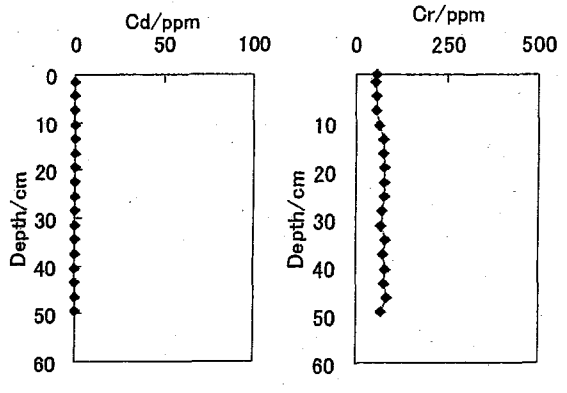

図 1．谷津干潟底質中の Cd と Cr の垂直分布

これらの元素の垂直分布は、汚染の激しい都市内部河川においては、H や S と同様に中層部で高い濃度を示し、水酸化物や硫化物の形で存在している可能性が示唆された。谷津干潟においては、H および S の垂直分布は図 2 に示すとおり、中層部で高い濃度を示すにもかかわらず、Cd や Cr が低濃度で且つ深さ方向に変化がなかった。このことにより、これらの元素の分布が、人為汚染の影響を受けていないことが再確認された。

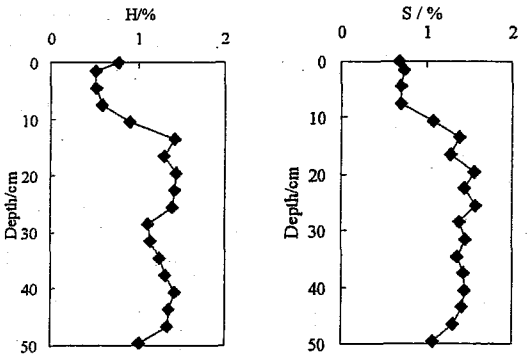

図 2．谷津干潟底質中の H と S の垂直分布

また、得られた元素を垂直分布の特徴に従って、いくつかのグループに分けることができた。表層部から深層部に行くに従って減少する元素としては Na, Ca 等があった。Na は底質の母岩を構成する鉱物中に含まれており、深層部に行くほど溶脱が進んでいるものと解釈された。また、Sc, La 等の微量金属の一部は深層部に行くに従って増加する傾向が見られた。底質深層部では粒径が細かく、底質の表面積が広くなっており、それらの元素の吸着がより多く起こっていると思われた。

メスバウアー分光法を用いた鉄の状態分析により得られた Pyrite の垂直分布を、硫酸還元菌の垂直分布とともに図 3 に示す。Pyrite および硫酸還元菌は、いずれも中層部に多く存在する傾向が見られ、よく似た垂直分布を示した。このことから、Pyrite の生成には硫酸還元菌が強く関与していることが示唆された。また、Pyrite の増加に伴い Fe^{3+}が急激に減少していることがわかった。これは 20cm 付近を境にして底質中は著しく還元的

になっており、主に Fe^{3+}が硫酸還元菌によって Pyrite になり底質中に固定されたものであると解釈された。

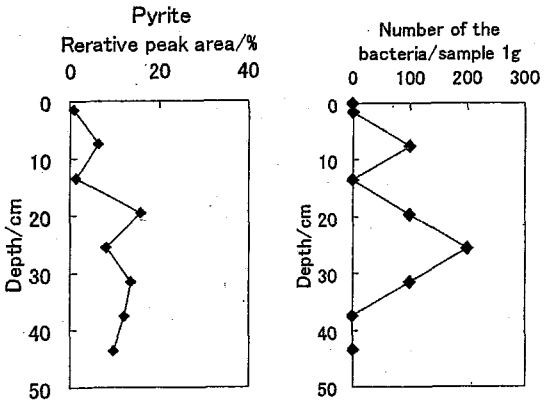

図３．谷津干潟底質中の Pyrite と硫酸還元菌の垂直分布

３．荒川底質中の元素及び化学状態の垂直分布

【序】　荒川は東京湾にそそぎ込む一級河川であり、中・下流域では人口の集中している地域を横断している。このような都市の中を流れる河川は人間活動による汚染が起こっていると考えられ、河川底質にはその汚染が記録されていると考えられる。そこで本研究では、PGA 及び INAA を用いて 30 数元素の定量を行い、それらの垂直分布を調べた。また、河口域底質中では海水起源の硫酸イオンが還元され、悪臭を持つ硫化水素が発生し問題となっている。そこで、底質中で硫化物を生成すると考えられる Fe, Mn についてメスバウアー分光法、XAFS (X 線吸収微細構造)法をそれぞれ用いて、深さごとに化学状態分析を行い、底質中での硫化物の分布を調べた。

【実験】　試料はアクリルパイプを用いて垂直方向に約 50cm のコアとして採取した後、現地で 3cm ごとに切り分け、変質を防ぐために窒素ガス中に封入した。得られた試料は４気圧の窒素を用いて加圧濾過を行い、間隙水を取り除き、メスバウアー分光法を用いて Fe の化学状態分析を、また XAFS 法を用いて Mn の化学状態分析を行った。試料はその後、風乾し PGA, INAA 測定に用いた。PGA, INAA 法は日本原子力研究所 JRR-3M, JRR-4 でそれぞれ行った。また、XAFS 法の測定は高エネルギー加速器研究機構(KEK)の放射光実験施設において Lytle 型検出器を用いた蛍光法で行った。

【結果及び考察】　得られた底質は表層部では泥質であり粒径が細かく、中層から深層にかけては砂質であり、粒径が大きかった。我々はこれまでに東京湾内に位置する干潟や都市の内部河川底質について研究を行ってきたが、それらの地点では粒径が中層から深層部で細かくなる傾向があり、荒川の底質は粒径の分布が他の地点と大きく異なっていた。元素分析の結果、Al, Ti 等の垂直分布は他の地点と同様の傾向を示したが、希土類元素の一部は他の地点とは逆に、深くなるに従って減少する傾向が見られた。これらの元素は粒径が細かいほど表面積が大きくなることで吸着しやすくなり、粒径の分布と相関があるものと考えられた。また、Cr は汚染の少ない谷津干潟と比較すると高濃度で存在していた。メスバウアー分光法を用いた鉄の状態分析の結果、ここでも Pyrite は中層部に多く存在する傾向が見られた。このことから粒径や塩分濃度等の環境因子や人為的な負荷の影響によらず、Pyrite は中層部で極大をとる傾向が見られることがわかり、様々な環境の汽水域で鉄が底質中から発生した硫化水素をトラップしているということがわかった。また、XAFS 法を用いた Mn の状態分析から底質の表層部に MnS が多く含まれている傾向が見られた。

４．遠洋深海性層状チャート中の元素の定量及び状態分析

【序】　生物史上複数の大量絶滅が知られており、その原因の一つとして地球全体にわたる酸素欠乏事件が挙げられている。元素は各々の酸化還元電位によって化学状態を変化させるが遠洋深海で起こるこれらの反応は局所的な現象ではなく、全地球的な海洋環境を反映したものであると考えられる。従って遠洋深海で堆積した層状チャートの分析から年代を追って地球規模での酸化還元状態の変化を見ることが可能である。酸化還元環境の変動については多くの研究がなされているが、単一の指標のみでは変化の程度を明らかに

することは不十分である。そこで本研究ではMn、Fe、U、Sを分析対象とした。最も酸化的な条件下ではMnとFeは沈殿し、UとSは溶解しているが、徐々に還元的になるにつれてMnの溶解、Feの溶解、Uの沈殿、Sの沈殿が順に起こると考えられる。このような複数の元素の酸化還元電位の差を利用して段階的な酸化還元状態の変化を推定した。

【実験】 美濃帯犬山地域で採取したジュラ紀及び三畳紀の遠洋深海性層状チャートを試料とし、年代順に重なる層毎にスタンプミル及びめのう乳鉢を用いて紛体にしたのち測定を行った。対象元素の定量分析のために日本原子力研究所JRR-3MにてPGA法を、同JRR-4にてINAA法を用いた。さらにFeはメスバウアー分光法、Mnは高エネルギー加速器研究機構においてXAFS法を用いてLytle型検出器を使用した蛍光法で状態分析を行った。

【結果及び考察】 ここで便宜上、酸化還元状態を段階別に名称をつける。Mn^{4+}が沈殿している最も酸化的な状態をLevel 1、次に酸化的な、Mn^{4+}は溶解し、Fe^{3+}が沈殿する状態をLevel 2、Fe^{3+}が溶解し、Fe^{2+}/total Fe比が増加する状態をLevel 3とする。三畳紀とジュラ紀の境界の前後では、メスバウアー分光法及びINAA法よりLevel 2であることがわかった。しかし境界付近において、前後の層に比べFe^{2+}/total Fe比が約2倍、赤鉄鉱の比率が約1/3となり、より還元的なLevel 3と考えられる部位が見られた。この層より時代を遡った三畳紀側に隣接した層ではMn含有量の一時的な増加が見られ(前後の層の含有量に比べ2~3倍)、Mnの沈殿が起きた最も酸化的な状況であると考えられた。またXAFS法の結果からこの層のMnの化学形態はMnO_2であることがわかり、酸化的条件での沈殿形態と一致した。従ってMn含有量の増加は酸化還元状態の変化によるものと考えられた。これはLevel 1に相当する。ジュラ紀前期試料にて見られたMnは$MnCO_3$に近い化学形態であり、MnO_2と区別ができた。以上の結果から三畳紀とジュラ紀の境界付近ではLevel 2からLevel 1、Level 3、Level 2へと変遷していることがわかった。

また、本研究で用いた試料はUやSの濃度は極めて低く、古生代/中生代境界(P/T境界)で見られたような非常に還元的な環境ではなかったことが分かった。このことは、上記のMnとFeによる評価と矛盾しないものである。このように複数の元素の状態変化の情報を組み合わせる事で酸化還元状態の程度を評価することができた。

5. 成果の公表

学術誌

1. "A study of environmental analysis of urban river sediments using activation analysis", Y. Tanaka, A. Kuno and M. Matsuo, J. Radioanal. Nucl. Chem., Articles, 255(2), 239-243 (2003)
2. "A study on vertical distribution of elements and their chemical states in Yatsu Tideland sediments", M. Kataoka, A. Kuno and M. Matsuo, J. Radioanal. Nucl. Chem., Articles, 255(2), 283-286 (2003)
3. "Moessbauer spectroscopic study on characterization of iron in the Permian to Triassic deep-sea chert from Japan", M. Matsuo, K. Kubo and Y. Isozaki, Hyperfine Interact. (C), 5, 435-438 (2003)

学位論文

4. "河川底質中に含まれる多元素の定量データの多変量解析を用いた環境評価"、高橋統、東京大学教養学部広域科学科 卒業論文I (2001年11月)
5. "底質中の元素とその化学状態に着目した都市河川環境分析"、田中佑人、東京大学大学院総合文化研究科広域科学専攻 修士論文 (2002年2月)
6. "遠洋深海性層状チャート中の元素の定量及び状態分析"、清宮貴美子、東京大学大学院理学系研究科化学専攻 修士論文 (2002年2月)
7. "河口域底質に含まれる多元素の濃度及び化学状態の垂直分布に関する研究"、高橋統、東京大学大学院総合文化研究科広域科学専攻 修士論文 (2004年1月)

学会発表

8. "Moessbauer spectroscopic study on characterization of iron in the Permian to Triassic deep-sea chert from Japan", M. Matsuo, K. Kubo and Y. Isozaki, International Conference on the Applications of the Moessbauer Effect (ICAME 2001), (Sep. 2001)
9. "底質中元素とその化学状態に着目した都市河川及び干潟の環境分析"、松尾基之・田中佑人・片岡正樹・久野章仁、第5回分析化学東京シンポジウム (2001年9月)
10. "都市河川および干潟底質中の元素の分布と化学状態を用いた環境分析"、松尾基之・田中佑人・片岡正樹・久野章仁、日本化学会第80秋季年会 (2001年9月)
11. "遠洋深海性層状チャート中の微量元素の酸化還元状態による古環境の評価"、清宮貴美子・松尾基之・磯崎行雄、日本地球化学会年会 (2001年10月)
12. "A study of environmental analysis of urban river sediments using activation analysis", Y. Tanaka, A. Kuno and M. Matsuo, 2001 Asia-Pacific Symposium on Radiochemistry (APSORC 2001), (Oct. 2001)
13. "A study on vertical distribution of elements and their chemical states in Yatsu Tideland sediments", M. Kataoka, A. Kuno and M. Matsuo, 2001 Asia-Pacific Symposium on Radiochemistry (APSORC 2001), (Oct. 2001)
14. "谷津干潟底質中の元素の化学状態と硫酸還元菌の関係"、片岡正樹・松尾基之・杉森賢司、日本分析化学会第50年会 (2001年11月)
15. "遠洋深海性層状チャート中の元素の定量及び状態分析：古海洋の環境変動の推定"、清宮貴美子・松尾基之・磯崎行雄、日本分析化学会第50年会 (2001年11月)
16. "干潟および河口域底質中における重金属の化学状態に関する研究"、片岡正樹・田中佑人・久野章仁・松尾基之、日本分析化学会第51年会 (2002年9月)
17. "荒川底質中の元素及び化学状態の垂直分布"、片岡正樹・松尾基之、第46回放射化学討論会 (2002日本放射化学会年会) (2002年9月)
18. "底質中元素とその化学状態に着目した河口域及び干潟の環境分析"、松尾基之・片岡正樹・高橋統・久野章仁、東京コンファレンス (2003年9月)
19. "干潟および河口域底質中の重金属硫化物の垂直分布"、片岡正樹・松尾基之、日本分析化学会第52年会 (2003年9月)
20. "河口域底質中に含まれる多元素の濃度及び化学状態の垂直分布"、高橋　統・片岡正樹・久野章仁・松尾基之、日本分析化学会第52年会 (2003年9月)
21. "河口域および干潟底質中の重金属の化学状態"、片岡正樹・松尾基之、第47回放射化学討論会 (2003日本放射化学会年会) (2003年10月)
22. "河口域底質中の元素の垂直分布"、高橋　統・久野章仁・杉森賢司・松尾基之、第47回放射化学討論会 (2003日本放射化学会年会) (2003年10月)

3-8

宇宙化学的試料中の即発γ線分析

Neutron induced prompt gamma-ray analysus for cosmochemical samples

尾嵜 大真、澤幡 浩之、川手 稔
Hiromasa Ozaki, Hiroyuki Sawahata, Minoru Kawate

東京大学 原子力研究総合センター
Research Center for Nuclear Science and Technology, University of Tokyo

岩石や隕石などの化学組成を用いたさまざまな宇宙・地球化学的な議論においてその主成分であるケイ素や硫黄は指標元素として用いられており、これまでは蛍光X線分析法や化学的な湿式分析法などにより主に分析されてきた。しかし、これらの分析法は操作が煩雑であったり、グラムオーダーの試料量を必要とする上、微量元素のほとんどが分析できない。隕石などの宇宙化学的試料の多くは実際に分析に利用できる量が限られており、少ない試料量から多くの情報を得ることが強く求められる。その点においては非破壊中性子放射化分析(INAA)法は少量での多元素同時分析が可能であり、宇宙化学ではUCLA のグループなどによって多くの隕石の分析が行われている。即発γ線分析(PGA)法はINAA 法と同様に少量の試料量で多元素同時分析が可能な上に、INAA 法では分析困難なケイ素や硫黄の分析も可能であり、INAA 法と組み合わせることによってほぼすべての主成分元素の分析を行える相補的な分析法である。本研究ではINAA 法やRNAA 法などとPGA 法を組み合わせて宇宙化学的試料の分析を行い、その成因などについて議論することを目標とした。

本研究では限られた試料量の隕石を同じ試料を用いてINAA 法・PGA 法両法で分析することをまず検討した。通常、試料の包装材にはPGA 法でFEP、INAA 法ではポリエチレンが用いられている。これはPGA 法において水素の感度が高く、ポリエチレンを包装材に用いるとバックグラウンドが増加してしまうことなどから水素を含まないFEP を採用している。しかし、PGA 法で分析した試料の包装しなおすことは、低いとは言え残留放射能もあることを考慮すると避けたいところである。INAA 法でFEP を包装材として用いるのは長時間照射による硬化など困難であると考えられ、両法で同じ包装材を用いるとすればポリエチレンになるであろう。ここで、PGA 法でポリエチレンを包装材として用いた場合に考えられるデメリットを推測すると

・水素の分析が不可能になる
・水素のγ線によるバックグラウンドの上昇に伴うS/N 比の低下
・大量の水素による中性子の熱中性子化に伴う感度の減少

があげられる。このうち、水素の分析は本研究の対象試料の多くで含有量が低くもともと分析困難であることや目的上必ずしも必要でないことから無視し、そのほかの二点について検討した。

まず、水素の即発γ腺によるバックグラウンドの増加だが、図1に包装材にポリエチレン、FEP を用いた場合のAllende 隕石の即発γ線スペクトルを示す。図からも明らかなように2223keV の水素の即発γ線によるコンプトンプラトーのためおよそ2000keV より高エネルギー側で5倍程度

研究施設・装置
JRR-3 PGA 装置

研究分野
宇宙・地球化学

の上昇が認められるが、このエネルギー範囲に定量に用いるγ線はなく実際の分析には影響はない。さらに2000keVより低エネルギー側でも2倍程度上昇しているが、実際のピーク分析への影響はほとんどなかった。すなわち、水素の即発γ線によるバックグラウンドの上昇は実際の分析にはほとんど影響はないものであった。

次に包装材の違いによる感度比として図2に示す。この影響は冷中性子の熱中性子化に起因すると考えられることから冷中性子ビーム時のみに感度の減少が予測されたが、熱中性子ビーム時の結果もともに示す。図からも明らかなように熱中性子ビームのときに限らず、冷中性子ビームのときにも感度の差はほとんど誤差の範囲内であり、減少は認められなかった。したがって、本研究の目的においてPGA法で試料の包装材にポリエチレンを用いることは問題はないことが示された。

これらの結果を踏まえ、課題名にある宇宙物質だけに限らず、多くの岩石試料などの分析をINAA法と組み合わせて行い、上記の基礎的な検討結果とともに公表に向けて吟味中である。

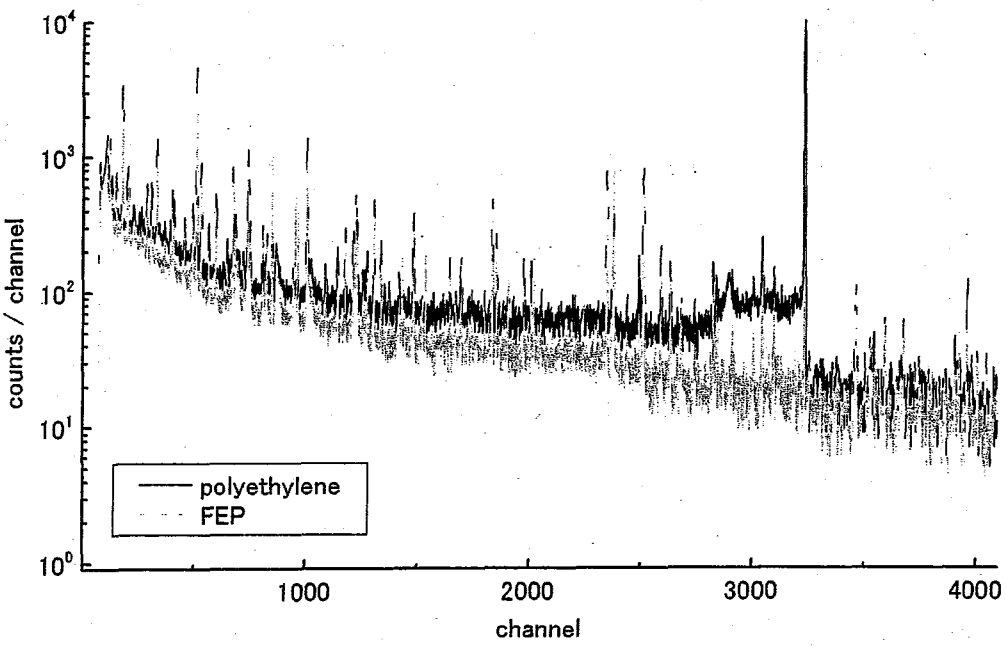

図1 Allende隕石の即発γ線スペクトル(～3000keV)

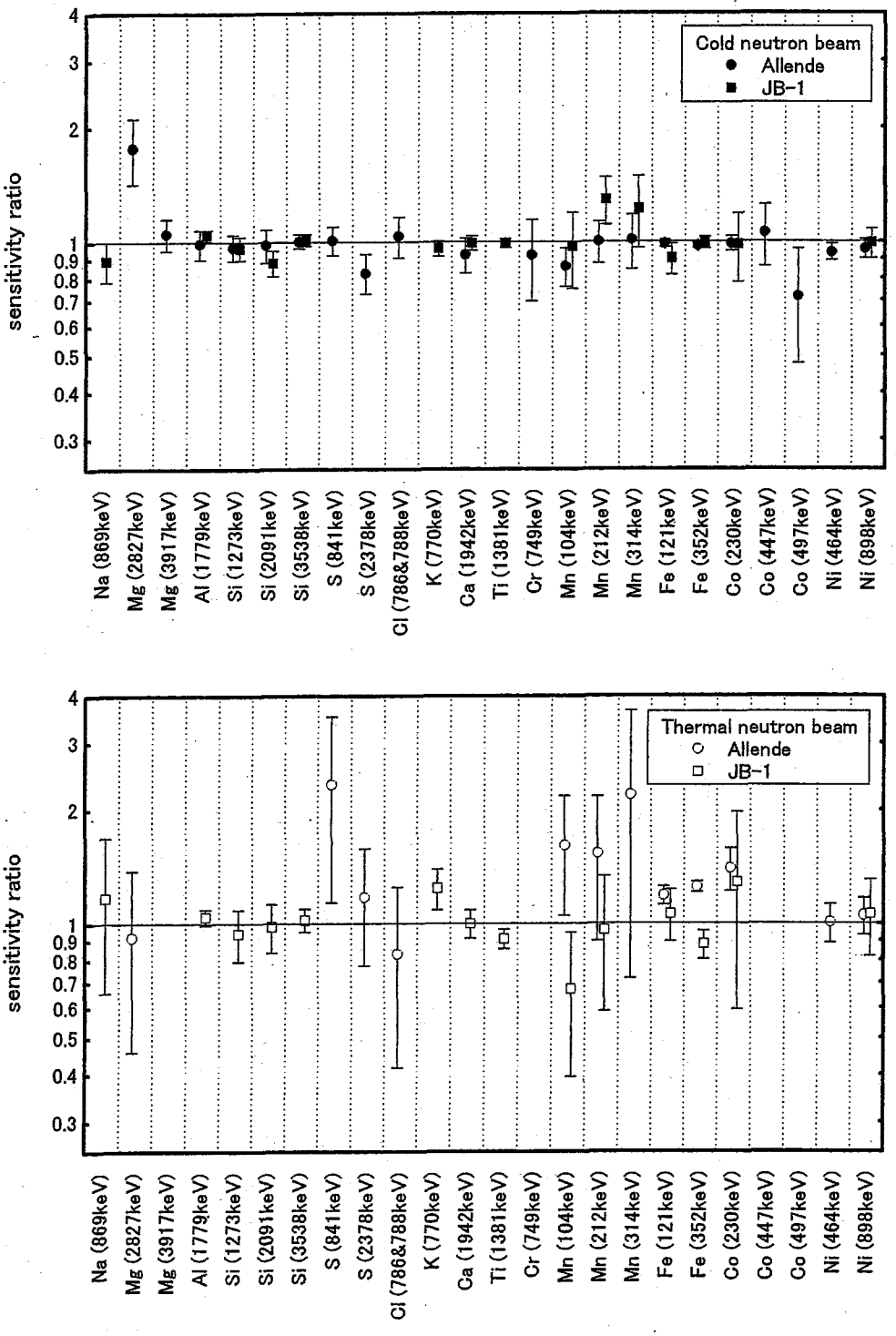

図2 包装材にポリエチレン・FEPを用いたときの感度の比(ポリエチレン/FEP)

3-9

火山岩試料の即発γ線分析（II）

Neutron-induced prompt γ-ray analysis for volcanic rocks (II)

福岡孝昭[1]・長谷中利昭[2]・佐野貴司[3]・新生裕尚[4]・伊藤靖浩[1]

[1]立正大学地球環境科学部，[2]熊本大学理学部，[3]富士常葉大学環境防災学部，[4]東京経済大学経営学部

Takaaki FUKUOKA[1], Toshiaki HASENAKA[2], Takashi SANO[3], Hironao SHINJO[4] and Yasuhiro ITO[1]

[1]Faculty of Geo-Environmental Science, Rissho University, [2]Faculty of Science, Kumamoto University,
[3]College of Environment and Disaster Research, Fuji Tokoha University,
[4]Fadulty of Business Administration, Tokyo Keizai University

1．はじめに

日本の多くの火山のように、島弧火山の岩石中のホウ素含有量は高い。これは、ホウ素を多量に含む深海底堆積物が、プレートのもぐり込みにともない、海溝からマントル中に入り、マグマが生じる時に混入するためと説明されている。しかしこの混入のメカニズムは必ずしも明らかでない。本研究では、このメカニズムを解明するため、海溝の堆積物と島弧火山の岩石試料について、ホウ素含有量を求めるとともに、高圧実験を含むモデル実験で地下深部でのホウ素の挙動を明かにする。海溝に沿ったあるいは直交する火山の試料について、ホウ素含有量を求め水平方向の変化も明らかにする。

また、世界の火山について、どのタイプの火山か不明な火山について、その火山岩中のホウ素含有量を測定して、タイプを明かにする。

本報告では、一連の研究に関連した過去３年間に行われた研究のうち、①海底堆積物のホウ素含有量研究と、②メキシコ火山帯の火山岩のホウ素含有量の研究について報告する。

2．海底堆積物のホウ素含有量の研究

西太平洋下オントンジャワ海台上部は1000m以上の堆積物から構成されている。海洋堆積物の深さに対するホウ素含有量の違いを調べるため、オントンジャワ海台から採取した38個の堆積物の分析を行った。分析の結果、ホウ素含有量には水素含有量と強い正の相関が見られた（図１）。 分析試料の大部分は石灰岩であったが、チャー トが含まれるとホウ素含有量が高くなるという結果も得られた。

3．メキシコ火山帯の火山岩のホウ素含有量

メキシコ火山帯中央部のセグメントからは噴出位置、年代が異なる火山岩を選んで、微量元素、同位体の特徴を明らかにした上で（長谷中、ベルマ、2003；Verma and Hasenaka, 2004）即発ガンマ線分析でホウ素等の微量元素の分析を行った（Hasenaka et al., 2004）。初生マグマ中のホウ素の含有量を推定したところ地域差が大きく、海溝に近い火山から噴出したマグマは非常に幅広い変化幅を示すが、海溝から遠くなると全て低い値を示す（図２）。このことから海洋プレート（堆積物、変質玄武岩）によって 運ばれてくるホウ素の大部分が海溝に近い位置で放出されてしまうことが推察される。メキシコの火山岩も典型的な島弧火山岩に比べると、初生マグマへの海洋堆積物、変質海洋岩の寄与が著しく低いことが推定された（図３）。沈み込むココス・プレートの年代が若くてまだ熱いので、メキシコ火山帯下の熱構造は他の島弧に比べてより高温を示すかもしれない。そうだとすれば、海洋堆積物、

JRR-3M，即発γ線分析装置

即発γ線放射化分析（地球化学・宇宙化学）

変質海洋岩に含まれるホウ素は流体相と共に非常に浅い深度で放出されてしまい、火山が出現する地下100kmに達した時には、もう海洋プレートにはほとんどホウ素が残っていないことになる。ホウ素から見た場合、メキシコでは非常に特殊な沈み込みを観察しているのかも知れないことが明かになった。

4．まとめ

ここでは即発γ線分析に強いホウ素を中心とした研究結果2件を報告した。他に火山岩中の塩素の分析もPGAではじめた。

今後、ホウ素以外の元素分析も含め、研究をさらに発展させたい。

5．成果の公表

学会誌

1．Sano T., H. Naruse, T. Hasenaka and T. Fukuoka, Boron contents of Leg 192 sediments. In Fitton, J.G., Mahoney, J.J., Wallace, P.J., and Saunders, A.D. (Eds.), Proceedings of the Ocean Drilling Program, Scientific Results,192, [Online]. Available from World Wide Web: http://www-odp.tamu.edu/publications/192_SR/102/102.htm, (2004).

2． Verma, S.P. and Hasenaka, T., Sr, Nd, and Pb isotopic and trace element geochemical constraints for a veined mantle source of magmas in the Michoacan-Guanajuato volcanic field, west-central Mexican Volcanic Belt. Geochem. J. 38, p. 43-65 (2004).

学会発表

1．Sano T., T. Hasenaka and T. Fukuoka, Constraints on sediment-derived fluid in mantle wedge beneath Northeast Japan arc: comparison between element contents in Japan Trench sediments and those in Iwate lavas, State of the Arc (SOTA) 2003 meeting, 2003年8月.

2．Hasenaka, T., Aguirre-Diaz, G., Sano, T., Fukuoka, T., Boron contents in lavas from the central part of the Mexican Volcanic Belt: temporal and spatial variation of subduction component input to the source mantle. Geological Society of America, Penrose Conference, 2004年1月.

3．長谷中利昭，ベルマ，スレンドラ P.：メキシコ火山帯中央部、ミチョアカンーグアナフアト火山地域で活動したマグマのSr, Nd, Pb同位体組成--脈状で不均質な起源マントルモデルへの制限．日本火山学会，2003年10月.

4．佐野貴司，福岡孝昭，長谷中利昭，即発ガンマ線分析による火山岩中塩素の定量，日本地球化学会2002年度年会，2002年9月.

5．加藤瞳，長谷中利昭，三好雅也，佐野貴司，福岡孝昭：九州北部火山岩類のホウ素含有量．日本火山学会，2003年10月.

6．三好雅也，長谷中利昭，佐野貴司：阿蘇火山西部におけるカルデラ形成後の火山活動ー微量元素化学組成と温度推定ー．日本火山学会，2003年10月.

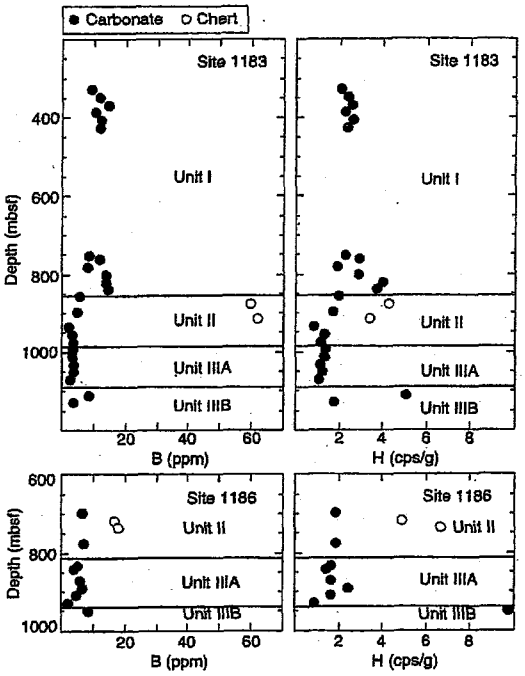

図１．オントンジャワ海台の海洋堆積物の
ホウ素と水素含有量

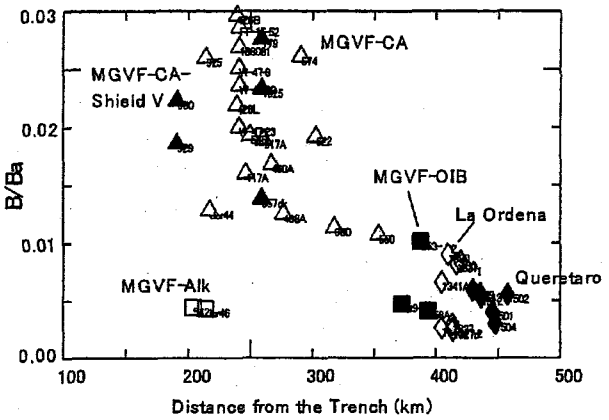

図２．メキシコ火山帯中央部火山、火山岩試料の
B/Ba 比と海溝からの距離の関係

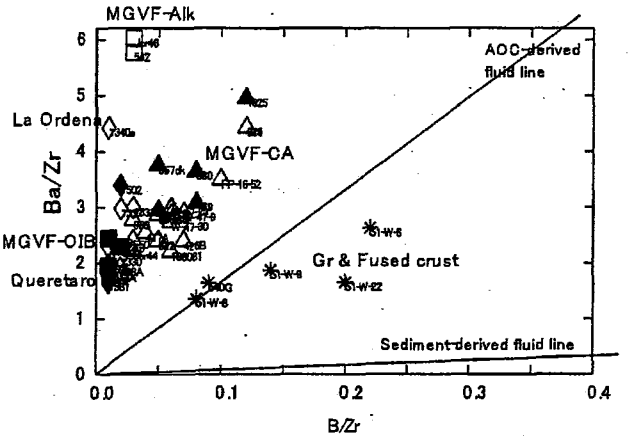

図３．メキシコ火山帯中央部火山、火山岩試料の
B/Zr 対 Ba/Zr 関係

This is a blank page.

4. 放射化分析

4. Neutron Activition Analysis

This is a blank page.

研究テーマ：分散型小型炉に関する研究
表　　題：中性子検出用 TL シートの放射化特性
4-1

中性子検出用 TL シートの放射化特性

小田野直光、大西世紀、近内亜紀子、石田紀久[1]
海上技術安全研究所、東京都三鷹市新川 6-38-1
[1]所日本原子力研究所、茨城県那珂郡東海村白方白根 2-4

日本原子力研究所では、分散型エネルギー源として、小型軽水炉をエネルギー需要地近傍に立地し、熱や電力を供給するシステム及びそれに適した小型軽水炉の概念検討を実施している。海上技術安全研究所では、日本原子力研究所と共同で、分散エネルギー源に適した小型軽水炉の概念検討を実施しており、放射線安全性の評価や放射線検出・計装系の検討を実施している。本研究は、原子炉施設等からの放射線の漏洩を迅速かつ精度よく検出するための技術として、放射線の二次元分布を熱蛍光線量計素子によって検出する方法の中性子に対する適用性について検討したものである。

中性子の原子炉施設等からの漏洩箇所を迅速に検知するための手法として、中性子に感度を有する線量計素子の開発を、海上技術安全研究所で開発した薄シート型人体組織等価二次元線量計素子(1)をベースにして実施した。開発した中性子線量計素子では、熱中性子による $^{6}Li(n,\alpha)^{3}H$ 反応を利用する。天然の LiF の Li の同位体存在比は ^{6}Li が 7.59 atom%で ^{7}Li が 92.4 atom%であるが、^{6}Li を濃縮した ^{6}LiF を使用することで、線量計素子の中性子に対する感度を上げることが可能である。本研究では、^{6}Li を 94.7%まで濃縮した ^{6}LiF と熱蛍光体 LiF:Mg,Cu,P を混合し、シート状に成型した。製作した中性子に感度を有するシート線量計素子の中性子線量計としての適用性を調べるため、日本原子力研究所 JRR-4 炉の気送管照射設備（熱中性子束 $1.4\times10^{12}n/cm^2/sec$ 及び高速中性子束 $4.5\times10^{13}n/cm^2/sec$）で 1cm 角のシート線量計素子を 60 秒間照射し、放射化特性を評価した。その結果、照射後の試料表面の線量率は 300～600μSv/h であり、また、短半減期核種からのガンマ線、ベータ線であり、実際の線量計の使用環境を考えた場合には、線量の読み取り及び読み取り時の取扱に支障はないことを確認した。

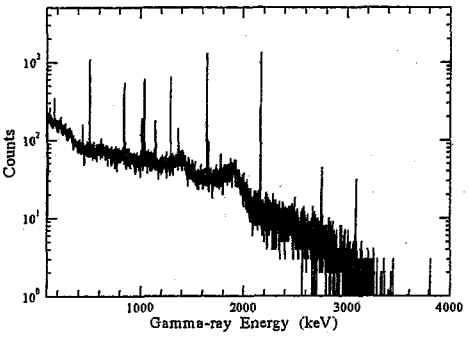

日本原子力研究所研究炉 JRR-4 気送管照射設備を用いた放射化特性評価の例

謝辞
本研究の一部は、原子力委員会の評価に基づき、文部科学省原子力試験により実施されたものである。

参考文献
1) N.Nariyama, et al: AIP Aphys2003 Proceedings (2004).
2) A.Konnai, et al: KEK Proceesings, to be published (2004).

原子炉：JRR-4　　装　置：気送管　　分　野：放射化分析（工業材料）

研究テーマ：関東地方における浮遊粒子状物質中の金属成分濃度の把握

表　　題：関東における大気エアロゾルのキャラクタリゼーション（第21報）

表 4-2

放射化分析による関東における大気エアロゾルの金属成分濃度の把握

内藤季和

千葉県環境研究センター

関東地方環境対策推進本部大気環境部会浮遊粒子状物質調査会議

関東地方の19地点において夏期と冬期に分けて粒子状物質の調査を実施した。夏期調査は平成14年7月29日～8月2日に冬期調査は平成14年12月2日～12月6日に関東甲信静の1都9県3市で実施した。粒子状物質は3段に組替えたAndersen Low Volumeサンプラーにより，粒径2.1～11μm（粗大粒子），2.1μm未満（微小粒子）に分級捕集し，秤量後，水溶性成分，炭素成分，多環芳香族炭化水素（PAHs），金属成分（放射化分析）を分析した。

この試料について、日本原子力研究所の東海研究所JRR-3での熱中性子放射化分析（短寿命核種）により、バナジウム、アルミニウム、マンガン、塩素、ナトリウム、カルシウム、臭素、チタン及びマグネシウムの9元素を定量した。銅とカリウムについても定量を試みたが、検量線のバラツキが大きいため不採用とした。これら成分の季節的・地点的な特徴について考察した。

平成11年度からの3年間では，バナジウムは微小粒子側に偏在し，夏期の東京湾臨海部で濃度が高い傾向を示した。粗大粒子側に偏在するアルミニウム，カルシウム，チタンは土壌起源と考えられ，沿岸部から内陸部で濃度が高く，比較的季節差は少なかった。マンガンは粒径による偏りや季節的な濃度差は少なく，地域的には臨海部で高めであった。塩素は夏期にはナトリウム，マグネシウムと同様に粗大粒子側に偏在し，海塩起源の特徴を示している。一方，各年度の冬期では，微小粒子側で濃度が上昇し，都市部で高く，北関東地域などで低い濃度分布を示した。銅は特異的･局地的に高い濃度が出現しているが，総じて，粒径による偏り，季節的な濃度差は少ない。臭素は冬期で微小粒子側に偏在する傾向が強く，濃度も高いが，年度による濃度分布に違いがみられた。

この金属成分等のデータにより発生源寄与の推定を行った。粗大粒子では，道路粉じんと海塩粒子は地点によるバラツキが大きく，自動車は地点差が認められたが夏期で2～27%，冬期で12～29%の寄与率であった。

微小粒子では夏期には，二次粒子22～53%，自動車13～61%であり，二次粒子の寄与率が高く，冬期では自動車34～65%，二次粒子22～46%と，例年同様の寄与率であった。廃棄物焼却については発生源データを見直した影響があり，夏期・冬期で2～15%の寄与が計算され，実状に近づいた結果と考えられる。過去6年間の微小粒子の発生源寄与は，二次生成，自動車の寄与率とも夏期で年度毎の変動が大きい。一方，冬期の自動車からの寄与率は40%前後で推移していた。また，ほとんどの例で夏期,冬期とも微小粒子の約8割の寄与分が説明された。

原子炉：ＪＲＲ－３　　装置：ＰＮ－３　　分野：放射化分析（環境科学）

研究テーマ：地層中における微量元素の挙動に関する研究
表　　題：新潟県のウラン濃集地域における微量元素の挙動

4-3

新潟県中東地域のウラン濃集帯試料の化学組成

上岡　晃
産業技術総合研究所，深部地質環境研究センター

はじめに　高レベル廃棄物中に含まれる核種の地層中での移行を予測するためには，ウラン，トリウム，希土類元素などナチュラルアナログとして有用な元素の地層中における溶解・沈着等の挙動の実態を把握し，それらを支配する要因を解明することが重要である．本研究では，実際のフィールドで採取された試料中の各種元素の移動・濃集に関する基礎的データを収集することを目的として，新潟県下のウラン濃集帯である中東地区において系統的に採取された試料につき，化学分析を行った．さらに，ウラン濃度の高い試料を含む一部試料については粒度分離を行ったうえで化学分析を行った．

試料および分析法　中東地区は，基盤の岩船花崗岩（白亜紀後期）上に新第三紀の釜杭層（アルコーズ質砂岩）および下関層（泥岩，下部はベントナイト層）が存在する．試料は地表の露頭において，下関層の泥岩から釜杭層の砂岩にかけて深さ方向に約 2.5mの範囲で各層準から採取した．化学分析は，機器中性子放射化法により行った．中性子照射は日本原子力研究所 JRR-4，Tパイプで1時間行った．

試料のバルク化学組成　ウラン濃度は，泥岩層やベントナイト層上部では 10ppm 以下であるが，ベントナイト層下部のリン酸塩鉱物に富む層から砂岩層にかけて，数 10ppm から最大 300ppm と高濃度であった．トリウムは各層準による濃度の差は小さい．希土類元素存在度パターンにおいて，セリウムは上位の泥岩層で大きな正異常を示し，ベントナイト層では負異常が顕著である．希土類元素濃度（セリウム以外）は負のセリウム異常がある方が高い傾向を示す．これは酸化的条件下では希土類元素のうちセリウムのみが3価から難溶性の4価へ酸化されるため，溶脱したところでは正異常が，沈着・濃集したところでは負異常が生じたものと考えられる．

粒度別化学組成　砂質ベントナイト層，リン酸塩鉱物層，砂岩層（ウラン濃集帯：下図）の3試料につき，粒径2mm 以下の部分を 2μm 以下，2-16μm，16-63μm，63-250μm，250 μm-1mm，1-2mm の 6 種の粒度フラクション（それぞれ CLAY，SS，S，M，L，LL とする）に分離して化学組成を求めた．いずれも細粒の SS，CLAY でウラン，トリウム，希土類元素の濃度が高い．特に CLAY はMの2～4倍程度濃集している．ハフニウムはSで濃度が高く，砕屑性のジルコンの存在を示唆する．CLAY へのウランおよび希土類元素の濃集は，リン酸塩鉱物層で最も顕著であり，ウランや希土類元素とリン酸塩鉱物との高い親和性を示唆する．

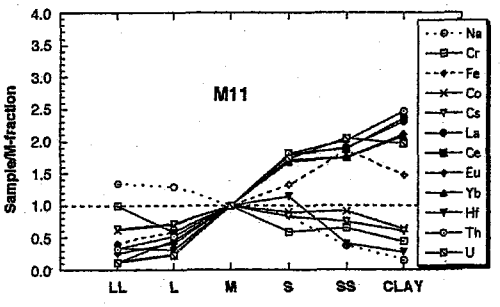

原子炉：ＪＲＲ－４　　装置：Tパイプ　　分野：放射化分析（地球化学・宇宙化学）

研究テーマ：放射化分析技術開発
表　　題：中性子放射化分析のためのポリイミドフイルムの開発

4-4

中性子放射化分析のためのポリイミドフイルムの開発

本木良蔵
研究炉利用課

JRR-3やJRR-4で数時間照射し、中性子放射化分析する場合、ガラス転移温度113℃のPEN-4フイルムを試料包装に使用している。このPEN-4フイルム袋の生産中止が予定されていることから、新たな試料包装材の開発が必要となった。新試料包装材には
1)加熱融着が可能である。
2)PEN-4フイルムと同等以上の耐放射線性と耐熱性を有する。
3)耐薬品性を有し、多量の不純物を含まない等の条件が必要となる。PEN-4フイルム（75～25μm）の真空中におけるγ線による破断伸び半減線量は42～12MGyである。[1)]PEN-4と同等以上の耐放射線性を有する有機材料には、ポリイミド樹脂やポリビフエニルエーテル樹脂等がある。これらの中で、加熱融着できる入手可能な樹脂はA社製のポリイミドX-RNがある。このX-RNは空気・表面酸化の条件で、破断伸び半減線量は30MGyであり[2)]PEN-4と同等の耐放射線性を有している。ガラス転移温度についてはPEN-4より高い287℃である。

以上の品質からX-RNは実用性が高いと考え、加熱融着や中性子放射化分析による不純物の分析にについて実験をおこなった。

（１）加熱融着技術の開発

X-RNのガラス転移温度はPEN-4より高い。この様な高融点樹脂フイルム用のシーラは市販されていない。そこで、低融点の樹脂フイルムの封入に使用されているシーラを改良した。石崎電気KK製シーラ(NL-201JC-3)を用い、加熱部のテフロンシートをX-S(厚さ25μm、耐熱寿命290℃で2×10^4hr)に、押付部のシリコンゴムをポリイミド樹脂であるベスペルSP-1(熱変形温度360℃)に交換した。この改良したシーラでは、厚さ25μmのX-RNを袋状に加熱融着可能である。融着部はPEN-4以上に剪断されにくく、水を沸騰させた試験では、漏洩することはなかった。

（２）中性子放射化分析

X-RNの製造に使用される触媒や添加物をPEN-4と同様なものと仮定し、また数時間の照射では、数時間以上の半減期の核種が核種同定と定量の対象になることからNa、K、Cr、Zn、Co、Br、Sbを比較標準元素とした。JRR-4で3時間照射し、中性子放射化分析した結果を示す。

表1　X-RNとPEN-4の不純物濃度比較

元素	X-RN (μg/g)	PEN-4 (μg/g)
Na	17	2.4
K	ND	1.9
Cr	0.96	ND
Zn	ND	ND
Co	0.44	0.20
Br	4.9	0.40
Sb	0.14	0.91

ND:検出限界以下

X-RNはNaとBrの濃度がPEN-4より高いが、特に多量の不純物は含まれていない。また、その他のγ線スペクトルにLa-140が確認された。

(3)まとめ

X-RNはPEN-4より耐熱性に優れ、同等の耐薬品性を有する。耐放射線性の比較やシーラの改良により、PEN-4に替わり、原子炉での照射に使用できると考える。但し、NaとBrの濃度が高く、この元素の定量には注意を要する。また、実用には照射時間と安全性との関係確認が必要である。

参考文献

1)有金 賢次、信田 重夫他"原子炉照射用プラスチックキャプセルの開発"JAERI-M 92-078(1992.6)
2)瀬口 忠男 "耐放射線性有機材料"、放射線と産業、(66)、6(1995)

原子炉：ＪＲＲ－４　　装置：ＴＢ　　分野：放射化分析（工業材料）

研究テーマ:ラジオアイソトープ技術者の養成
表　　題 :実習　放射化分析

4-5

貝殻中の銅・ナトリウムの放射化分析

上沖　寛
国際原子力総合技術センター（RI・放射線研修班）

本研究は、ＲＩ技術者の養成を目的とする研修コースの中で実習教科として行うものである。本報告では、平成15年度の研究炉をもちいた成果として、国内原子力技術および放射線利用に関係する人材養成を行った基礎課程における実習教科としての放射化分析について報告する。

原子力の基礎として中性子核反応の理論や応用を理解させることは重要である。放射化分析の実際を経験させることはこれらの知識の理解を深めるのに大変重要であり、結果としてガンマ線スペクトル解析による放射能測定法および非密封ＲＩの安全取扱法を習得させることになる。

平成15年度は基礎課程で3回の放射化分析実習を行った。分析試料は海水産の大アサリであり、炭酸カルシウムをマトリックスにして微量元素を含有する。分析目的核種は、放射化生成核種のガンマ線スペクトルで主成分となるﾅﾄﾘｳﾑ24、放射化生成物が 陽電子壊変を伴い陽電子消滅ピークを主要放射線ピークとする銅64である。照射条件は研究炉の気送管で2分間照射とし、ナトリウムと銅の標準試料と共に大アサリ貝殻の照射を3回行った。

銅の分析：

銅64の陽電子消滅放射線は、他の放射化生成核種からの高エネルギーガンマ線や宇宙線が物質にもたらす電子対生成による放射線と同一放射線であるから、銅64の分析には化学分離を必要とした。簡単な銅の化学分離法として金属亜鉛により銅イオンを還元させて銅の沈殿分離を行った。この化学分離の操作は、30分間の所用時間で0.1ppm Cu 濃度に対して5%の精度で分析された。本実習は、生成核種を同定および定量することにより核反応の理解を深め、ＲＩ実験における放射線被ばくに対する工夫、除染、サーベイ等、一連の安全取扱いの基礎を習得させるものとして有効であった。

本実験による研修生の被ばく線量は、線源が10^6Bq位に対し最大1μSv程度であった。

原子炉：JRR−3M、JRR−4　　装置：気送管　　分野：放射化分析（環境）

研究テーマ：中性子放射化分析法の環境影響元素・物質研究に対する新利用法と高度化技法の開発
表　　題：金属元素類（重金属元素等）の同位対比測定法の開発による土壌中の挙動解明

4-6

^{114}Cd, ^{64}Znによる土壌有機物中重金属の標識化

櫻井泰弘、木方展治
農業環境技術研究所

環境中の無機元素（Cd, Se, Zn, Cu等）の動態解明や影響評価に資するために、野外での　使用が可能である安定同位体(SI)による環境物質の標識化法と中性子放射化分析による安定　同位体の高精度測定法を開発する。今年度は土壌中での水移動に伴う重金属の動態を計測するために、重金属SI(^{114}Cd, ^{64}Zn)で標識化した水溶性有機物(フルボ酸: FA)の土壌中での安定性をカラム実験で検討する。

1）土壌有機物(フルボ酸)の標識化

堆肥を連用した淡色黒ボク土壌から抽出したフルボ酸を陽イオン交換樹脂(Amberlite CG 120)でH型に精製後、^{114}Cd, ^{64}Znで標識化した。

2）土壌カラム実験

黒ボク土３種（A, B, C)、灰色低地土１種（D）の風乾細土(表2）をクロマト管に5.0 g充填し、SI標識化フルボ酸の水溶液(フルボ酸濃度2500 mg / L)を10 mLづつ添加し、土壌通過液中のフルボ酸をXAD-7樹脂に吸着、溶離し、中性子放射化分析によりSI濃度を定量した。放射化分析はろ紙に吸着させた試料液を日本原子力研究所研究炉JRR-3M,4で、熱中性子束を600秒間照射し、２時間～１日間冷却後、Ge検出器と波高分析器で放射性核種(^{115}Cd, ^{65}Zn)のγ線スペクトルを計測した。ブランク値、検量線値の測定も全て同一の放射化条件を用い、実験は全て２連で行った。^{114}Cd, ^{64}Znは濃度認証済みの酸化物を所定の濃度に希釈して使用した。その結果、イオン交換水を土壌カラムに通液し、自然賦存する^{115}Cd, ^{65}Znのバックグラウンド値を測定した結果、全ての土壌で両元素ともに同一測定条件では放射化分析の検出限界値以下であった。標識化したフルボ酸中の^{115}Cd濃度は2.9 mg/L,^{65}Zn濃度は3.2 mg/Lであった。また、XAD-7樹脂によるフルボ酸の回収率は89～93 %であり、同一の実験条件によるCd^{2+}, Zn^{2+}のフリーイオンの樹脂への吸着量は検出限界値以下であった。標識化SIの土壌カラム通過率は52～86%で砂質土壌、腐植含量の高い土壌で吸着が少ない傾向であった。土壌カラム通過液と通過液をXAD-7樹脂で吸着・溶離した液中の^{115}Cd, ^{65}Zn濃度を比較し、土壌中での^{115}Cd, ^{65}Znとフルボ酸との解離率を測定した結果、^{115}Cdは3～7%, ^{65}Znは0～4%であった(図1)。XAD樹脂への吸着・溶離処理による損失量は約9%であり、土壌カラム通過による解離は供試土壌の全てで、極めて少なく、^{115}Cd, ^{65}Zn標識化フルボ酸は有機態Cd, Znの土壌中トレーサとして利用可能であると考えられた。

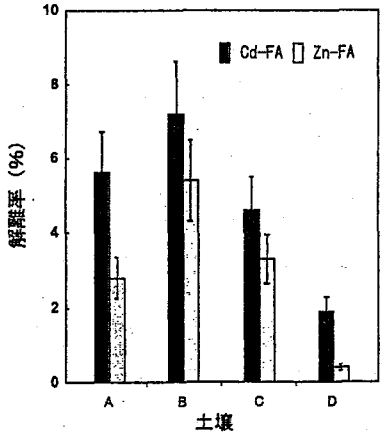

図1 土壌カラム通過によるSI標識化フルボ酸の解離率

原子炉：JRR-3M,4　　装置：気送管　　分野：放射化分析（農・水産物）

研究テーマ：微量有害化学物質の分析方法、環境汚染実態の把握に関する研究
表　　題：大気微小粒子(PM2.5)中の微量元素の放射化分析

4-7

大気微小粒子(PM2.5)中の微量元素の放射化分析

Neutron activation analysis of trace elements in atmospheric fine particle (PM2.5)

鎌滝裕輝、安藤晴夫（東京都環境科学研究所）
山崎正夫（東京都立産業技術研究所）

Hiroki KAMATAKI, Haruo ANDOU
(Tokyo Metropolitan Research Institute for Environmental Protection)
Masao YAMAZAKI (Tokyo Metropolitan Industrial Technology Research Institute)

１．はじめに

近年PM2.5(大気微小粒子のうち粒径が2.5μm以下のもの）の重量濃度測定が環境省のマニュアルに沿って測定されるようになってきた。しかし、PM2.5に含まれている元素成分についての知見は少ない。また、PM2.5の削減対策には、その起源を予測するための成分を把握することが不可欠である。そこで、PM2.5中の元素成分を放射化分析法によって測定を行い、都内の沿道、一般環境（住居地）における元素成分のレベルや経月変化などの特性について検討した。

２．試料採取

採取試料は、都内の沿道4地点と一般環境4地点では、2002年1月から2002年3月の毎月1回行ったものを利用した。また、沿道1地点と工業地域1地点では、2002年1月から2002年7月の毎月1回行ったものを利用した。装置はFRM2000採取装置等（PM10インパクタカット後にPM2.5インパクタカットを装着した装置）を用いて数日間連続してPM2.5を捕集した。

３．放射化分析

ろ紙の前処理は、サポートリング付きテフロンフィルタをカッター盤に安置し、カッターで均等に2分の1に切断して折りたたみ、ポリ袋に二重に封じ込み放射化分析用試料とした。このとき、分析に不要なサポートリングは除去した。分析は放射化分析法（長寿命核種）により行い、Zn, Fe, Cr, Sb, Se, Ag, Ce, Co, Cs, Yb, Scの11元素成分が定量できた。また、検出された成分はRb, Ni, As, Mo, Cd, Br, Sr, Baの8成分あったが定量下限値未満であった。原子炉（JRR-3）の照射孔特性は、照射設備PN-1、照射領域：重水反射体、冷却方式：N_2ガス、照射時間：20分、照射方式：気送管、熱中性子束：5.2×10^{17} ($m^{-2}\cdot s^{-1}$)、カドミ比：23である。

４．結果及び考察

図1に沿道と一般環境のPM2.5の2002年1-3月の濃度レベルを示す。沿道の方が一般環境に対して、1.4-1.8倍となっていた。PM2.5と同様に沿道の方が高い成分は、Zn, Cr(図2)であった。これに対して逆転していた成分はSe(図3)であり、それぞれの特徴があった。図4に工業地域と沿道におけるPM2.5の元素成分の経月変化を示す。1-7月の経月変化はPM2.5ではほぼ同レベル、同じ変化であった。成分では、ScはPM2.5の変化と同様であった(図5)。Sb, Ceでは沿道の方が常に高い状況を示した(図6)。Se, Agの変化は工業地域が常に高い状況を示した(図7)。また、Coは全く異なる変化を示した(図8)。

沿道の各成分の変化の相関性から次の（PM2.5, Fe, Se, Ag)、(Zn, Cr, Sb, Ce, Sc, Cs)及び（Co, Yb）の3グループに分けられた。

一般環境のPM2.5の起源は沿道、工業地域からのそれぞれの影響が各成分の濃度レベルと変化によって見分けることが可能であることがわかった。今後の課題として、さらに時間分解能を高めた試料採取により精度の高い起源解明が望まれる。

原子炉：JRR-3　装置：PN-1（気送管）　分野：放射化分析(環境)

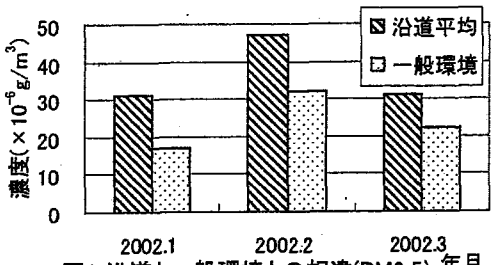

図1 沿道と一般環境との相違(PM2.5)

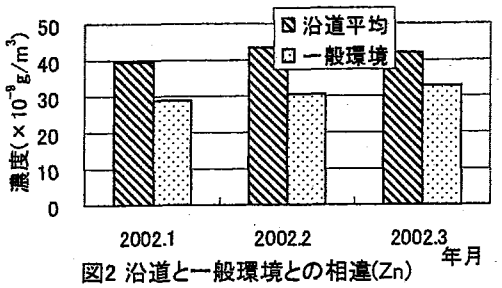

図2 沿道と一般環境との相違(Zn)

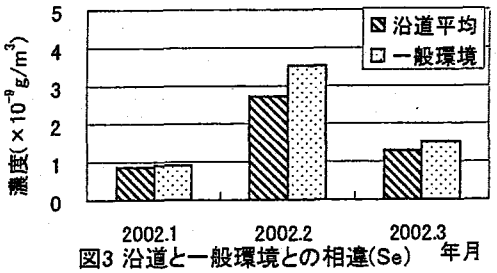

図3 沿道と一般環境との相違(Se)

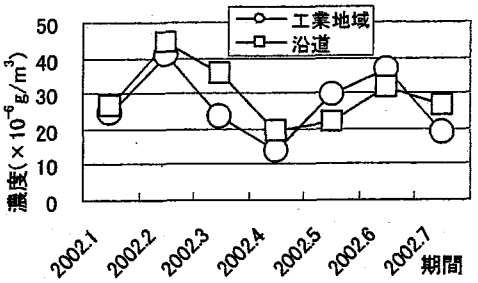

図4 経月変化(PM2.5)

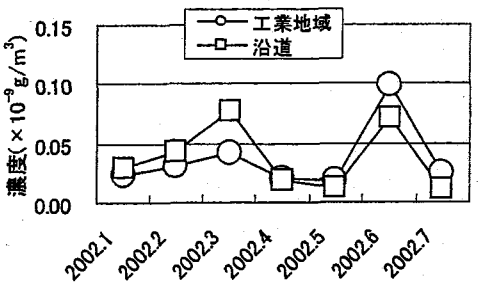

図5 経月変化(Sc)

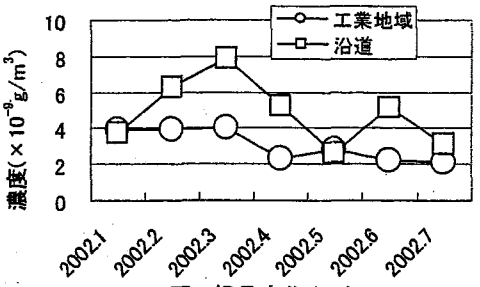

図6 経月変化(Sb)

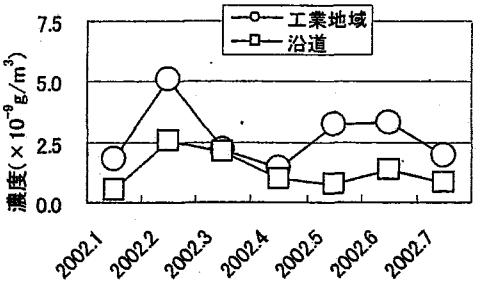

図7 経月変化(Se)

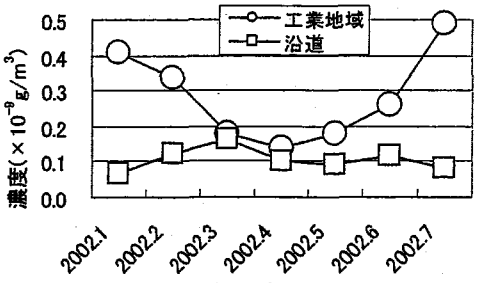

図8 経月変化(Co)

成果の公表

所内報告

1．鎌滝裕輝，大気微小粒子状物質(PM2.5)中無機成分の分析，東京都環境科学研究所年報 ***2003***, 40-48(2003).

口頭発表

1．鎌滝裕輝，白井清嗣，PM2.5の元素成分について，第44回大気環境学会年会講演要旨集，287(2003).

2．鎌滝裕輝，味村昭，早福正孝，PM2.5の元素成分について（2），第45回大気環境学会年会講演要旨集，608(2004).

研究テーマ：中性子放射化分析法の環境影響元素・物質研究に対する新利用法と高度化技法の開発
（フッ素等肥料起源陰イオン元素の表流水－土壌浸透水－地下水系での動態）

4-8

肥料中フッ素の放射化分析手法の開発

木方展治、藤原英司
独立行政法人農業環境技術研究所

1．はじめに

フッ素は平成 11 年に歯状班の原因になるなどの有害作用があるため、人の健康に係わる水質の環境基準項目（0.8mgL^{-1} 以下）に指定された。一方で、適度な濃度のフッ素は虫歯予防に効果があるとして水道水への添加が実施されている国も多く、健康や環境に関わる重要な元素として注目されている。リン酸肥料中には、高濃度のフッ素が含まれており、農業と環境中のフッ素の関係を整理する必要が出てきている。肥料中のフッ素の分析は、湿式分解試料を蒸留した後、イオン電極法で測定する方法が従来行われてきたが、温度管理を厳密にしなければならないことや、分解に多くの時間を要すること等の問題がある。固体のまま分析できる放射化分析法は、試料調整の手間が少なく、その際の汚染、損失も受けにくい分析法である。フッ素の唯一の自然に存在する同位元素 ^{19}F から(n, γ)反応で生ずる半減期 11 秒の ^{20}F を利用する、フッ素の放射化分析法について検討を行った結果を報告する。

2．実験方法

リン酸を含む化学肥料 10～20mg を不純物のアルミらに低アルミニウム含量のカプセルに入れて、日本原子力研究所の JRR3 研究用原子炉の短寿命核種用照射孔(PN3)で気送管照射し、気送されてくる放射化試料を Ge 半導体検出器にマルチチャンネルアナライザを装着したγ線スペクトロメトリに導入し、カプセルのまま 1633keV のγ線を測定した。また標準土壌も同様に測定した。

3．結果および考察

肥料中フッ素の照射・測定には10秒照射、7秒冷却、20 秒測定の条件が適していた。ほとんどアルミニウムおよび塩素の妨害は見られず、ピークの形状はガウス分布に従った（図１、図２）。化成肥料では従来法に概ね一致した分析値が得られた（図３）。標準土壌（NCSDC73320)の放射化によるフッ素の分析値は、2097±494mgkg^{-1} (n=2)であり、保証値の 2240±175mgkg^{-1} の範囲内に入った。

上記の結果は、化成肥料中のフッ素分析に短寿命核種を利用した放射化分析法が使用できることを示しており、一部土壌に対してもこの方法が適用できる可能性を示唆している。

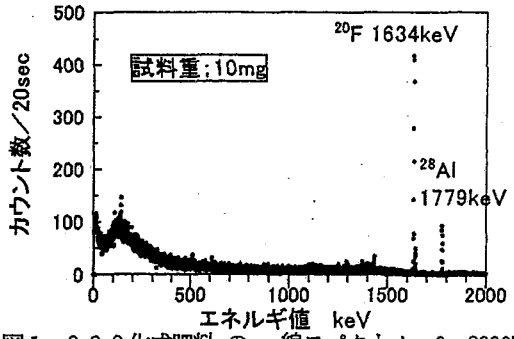

図１ 8-8-8 化成肥料 のγ線スペクトル 0－2000keV

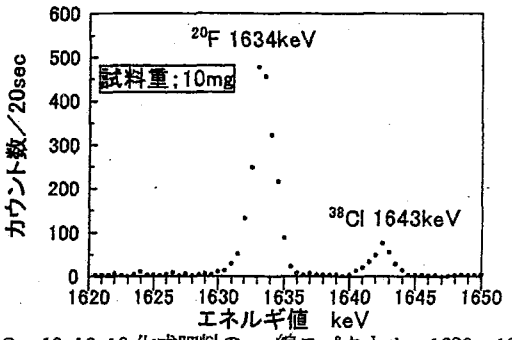

図２ 10-10-10 化成肥料のγ線スペクトル 1620－1650keV

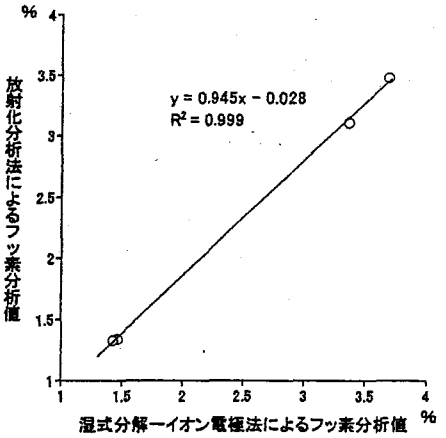

図３ 化成肥料のフッ素分析値の比較

参考文献

第 41 回理工学における同位元素・放射線研究発表会要旨集(2004), p. 159

原子炉：JRR-3　　装置：気送管(PN-3)　　分野：放射化分析（環境、農・水産物）

研究テーマ：放射化分析による家畜・家禽における土壌摂取量の推定
表　　題：家畜・家禽の糞中の土壌特有元素の定量
4-9

家畜・家禽の糞中の土壌特有元素の定量

西村宏一、木方展治[1]、宮本　進
独立行政法人農業・生物系特定産業技術研究機構畜産草地研究所　茨城県つくば市池の台２
１：独立行政法人農業環境技術研究所　茨城県つくば市観音台３－１－３

豚および鶏の一般的な飼養法では家畜が土壌と隔離されている。最近増加してきた自然飼育法や有機農法では、豚や家禽が土壌と接触する機会が多く、土壌に含まれる有害な化学物質も家畜の体内へ取り込まれる恐れがある。これらの解明のために、家畜の土壌摂取量を調べる必要がある。土壌特有の元素であるスカンジウム（Sc）について家畜糞中の含量を、放射化分析で定量し、家畜における土壌摂取量を推定する。

鶏における土壌の摂取量を調べるため、鶏を用いて屋内・屋外飼養実験を行った。白色レグホーン系のデカルブ種の雛を、屋内、屋外飼養区とも 15 羽ずつ供試し、約６ヶ月間群飼で飼育した。屋内区は通常の鶏舎内に設けた。屋外飼養区は黒色土（園芸用庭土）を約 10cm の厚さに敷いた園芸用ネットハウス内に設けた。ハウスの広さは 5.4 × 5.4 mで、中に 0.9 × 1.8 mのプレハブハウスを庇陰小屋として設置した。両区とも飼料は飽食させ、供試鶏の体重と採食量を２週間毎に秤量するとともに、中雛期に採糞した。屋内区および屋外区に分けて飼養した供試鶏から得られた糞を乾燥し、妨害元素（^{24}Na、^{56}Mn 等）の影響を避けるために１ヶ月以上クーリングを行った後に、試料中の Sc（^{46}Sc、0.889MeV）の測定を行った。

その結果、Sc の検量線（0.02 ～ 5 μg）は良好で、20 分間の照射で微量レベルの Sc を定量できることが明らかとなった（図１）。鶏に給与された飼料中の Sc 濃度は 0.04 μg/g であり、屋内飼養区の鶏の糞では 0.07 μg/g、屋外飼養区では 0.33 μg/g であった。また、上記のデータおよび供試土壌のデータ（Sc 25 μg/g）から計算した各試料中の土壌存在量は、飼料中で 1.5mg/g、屋内飼養区の糞で 2.8mg/g で、鶏体内における飼料の消化を反映し、約２倍となった。一般に家畜に摂取された飼料は、消化されて固形物が減少するが、Sc は吸収されないので、結果的に糞中の Sc 濃度は高まる。屋外飼養区の糞では 14.0mg/g であり、土壌存在量のうち飼料由来のものが約 20%、屋外飼養による土壌摂取由来のものが 80%と推定された。

現在、この課題に関する実験を継続して実施しており、鶏の成育時期および飼養条件の違い等による土壌摂取量の検討を進める予定である。

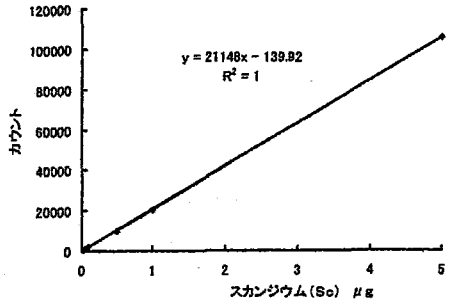

図１　Ｓｃの検量線

表１　試料中の Sc 量と土壌の存在量

	Sc(μg/g)	土壌の存在量(mg/g)
飼料（乾燥物）	０．０４	１．５
糞（屋内区）（乾燥物）	０．０７	２．８
糞（屋外区）（乾燥物）	０．３３	１４．０

原子炉：JRR-3M　　装　置：気送管　　分　野：放射化分析（農・水産物）

研究テーマ：広域環境モニタリング試料の微量元素分析
表　　題：広域環境モニタリング試料の微量元素分析

4-10

広域環境モニタリング試料の微量元素分析（4）

宮本 ユタカ，齋藤 陽子，間柄 正明，桜井 聡，臼田 重和
原研，環境科学研究部，環境技術開発グループ

はじめに

大気に放出された極微量の放射性核種や大気汚染物質の挙動，分布などを評価するために，これらの直接的な輸送媒体である大気浮遊塵の量や組成についてモニタリングすることは重要である。大気浮遊じんの物質輸送経路は大気の流れによって決まるが，輸送途中にさらされる環境条件，例えば降雨などによって大気浮遊じんの組成は異なってくるので，環境条件による影響を考慮することが必要である。原研東海研究所内には防砂・防塩害のために松が数多く植林されているが，大強度陽子加速器施設の建設工事に伴い，防砂林の一部が伐採された。このような工事が大気浮遊じんに対する防砂林の影響を調べるのには絶好の機会であるととらえて，防砂林伐採前後の期間に捕集した大気浮遊じんを元素分析した。防砂林の伐採前後で生じた元素組成の変動について比較検討した結果を報告する。

実験方法

原研東海研 CLEAR 施設周辺にハイボリュームエアーダストサンプラー[平均流量：120 m^3/h]を設置し，大気浮遊塵を石英ガラス繊維製のフィルター上に捕集した。捕集は2001年5月14日から開始し，天候の変化に応じて2～6日ごとにフィルターを交換した。原研保健物理部環境放射線管理課の協力を得て，原研東海研敷地内（捕集場所から約400 m 北）の気象観測塔で連続観測されている湿度，風速，降水量などの1時間毎の平均値を入手し，それを捕集時の気象観測データとした。

捕集したフィルターから 15 mm×15 mm の試料を切り取り，ポリ袋に二重封入して照射試料とした。比較標準試料として日本地質調査所（現産業技術総合研究所）発行の4種類の標準岩石試料を用いた。これに加えて試薬から調製した溶液を石英フィルターに染み込ませたものも標準試料として使った。中性子照射は原研 JRR-3M の圧気輸送管 PN-3 あるいは PN-2 で行った。照射時間はそれぞれ10秒間と10分間であった。中性子照射後，適当な冷却時間をおいて高純度 Ge 半導体検出器でγ線スペクトロメトリーを行い標準試料との比較法で元素定量を行った。

結果と考察

伐採前後における元素組成変動を検討するため，捕集した181試料を以下の3つの期間に分類し，元素組成の変動を比較検討した。**期間1**．伐採作業実施前：2001年5月～2002年6月末（80試料）。**期間2**．伐採作業中：2002年7月～2003年3月（53試料）。**期間3**．伐採作業終了後：2003年4月～2003年11月（48試料）。

分類した捕集期間によって捕集大気体積あたりの大気浮遊じん量（μg/m^3）の最頻値に違いは認められず，この捕集場所では大気浮遊じん量は伐採に影響されないことが分かった。Sc について捕集大気体積に対する元素濃度の度数分布を図1に示す。図には示していないが Al も Sc と同様の分布傾向を示した。Al，Sc ともに期間2の最頻値（図中、矢印）だけ期間1や期間3の値よりも少し高い方へ移動する傾向を示したが，伐採作業前後で濃度にほとんど変動がない点では大気浮遊じん量の度数分布と同様である。一般的には大気浮遊じんの重量組成の大半を土壌粒子が占めているので，大気浮遊じん量の度数分布はほぼ土壌粒子量の度数分布とも言える。Al や Sc は土壌粒子に多く含まれている元素なので，これらの元素濃度の分布は大気浮遊じん量の度数分布と類似する結果を示したと考えられる。

注目元素が地殻（土壌）起源であるかを調べるために，Fe に対する注目元素の濃度比を地殻におけるその元素の対 Fe 濃度比と比べる方法がよく用いられている。捕集した試料では Cl，As，Zn，Sb の4元素の対 Fe 濃度比が地殻[1]のものより10倍以上高い値を示していた。これはこれらの元素が地殻（土壌）以外に別の起源から多く供給されていることを示している。Cl の供給源については捕集場所の近隣に海が存在していることから海塩起源であると考えられる。残りの3つの元素について濃度の相関関係を調べてみると，Zn は Sb や As と濃度の相関関係が強かった（それぞれの相関係数は 0.81 および 0.91。図2参照）が，Sb と As では相関関係が弱かった（相関係数は 0.67）。また捕集試料の濃度分布は，Zn/Sb 濃度比や Zn/As 濃度比の分布では，最頻値がそれぞれ 16，0.6 で高濃度側に分布が広がる形となった。国立環境研究所が調製した環境標準試料，NIES No.8「自動車排出粒子」の保証値[2]から Zn/Sb 濃度比および Zn/As 濃度比を計算するとそれぞ

原子炉：JRR-3M　装置：照射設備（PN-2, PN-3）　利用分野：放射化分析（環境）

れ173，400である。また，米国NISTが調製したばい煙標準試料NIST-SRM-1633A (Coal Fly Ash)[3]ではZn/Sb濃度比およびZn/As濃度比はそれぞれ32，1.5である。試料の濃度比から判断すれば，この2つの濃度比はばい煙標準試料の値に近いので，Zn，As，Sbは自動車の排出粒子起源のものよりもばい煙起源のものが多く含まれていると推定される。Sb濃度の変動について、Sb濃度の度数分布を作成して調べてみると、期間1（伐採作業前）ではSb濃度の度数分布の最頻値が0.0025 μg/m³であったが期間3（伐採作業後）では0.0015 μg/m³と工事前の60%になった。Sb濃度が減少した理由ついては伐採による影響も含めて検討中である。

防砂林は海砂が運ばれてくるのを防ぐだけでなく，海洋からの海塩に対しても同様の目的で植林されていることが多い。Clは海塩の主成分元素なので，INAAで測定したCl濃度が海塩成分の濃度を代表するものとして考えた。伐採期間で分類した大気浮遊じん中のCl濃度の度数分布は期間1（伐採作業前）の最頻値は0.5 μg/m³であったのに対して，伐採作業が進むにつれて期間2では1.0 μg/m³，期間3では1.75 μg/m³と増加した。大気浮遊じんを捕集した時の気象条件を揃えるため、大気浮遊じんを捕集している時の平均相対湿度が70～80%の範囲内となる試料を選び出して比較すると、3つの期間とも北東風の平均風速が2.5 ～ 3 m/sでその風向の出現頻度が15～20%であった。すなわち、選び出した試料は3つの期間において平均相対湿度，風向の出現頻度，平均風速が類似した気象条件であった。これらの試料について，各期間毎にCl濃度の度数分布を作成した結果を図3に示す。期間1，2，3それぞれのCl濃度の最頻値は0.5 μg/m³, 1.5 μg/m³, 1.5 μg/m³であった。期間1から期間2の間での伐採，すなわち防砂林が伐採され始めると、大気中のCl濃度（海塩粒子濃度）が3倍高くなっていた。もしCl濃度の増加が全て防砂林によるものであると仮定するならば，海岸側の防砂林（約500m長）は捕集した地点の大気浮遊じん中のCl（海塩粒子）濃度を約1/3に低くする効果があると言える。

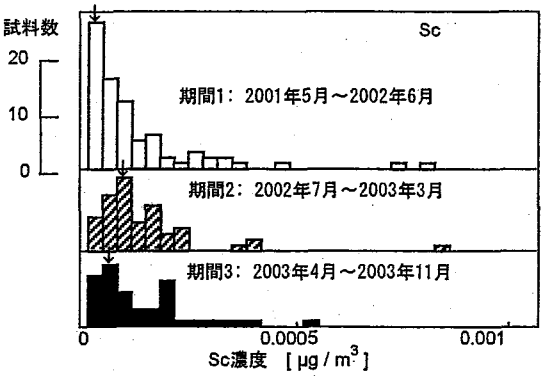

図1 大気浮遊じんのSc濃度の度数分布図。図中の矢印は最も試料数が多い濃度の部分を示す。

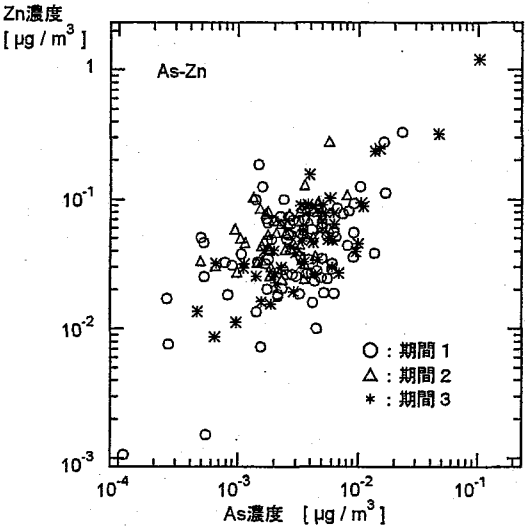

図2 大気浮遊じんのAs濃度とZn濃度の関係（相関係数：0.91）

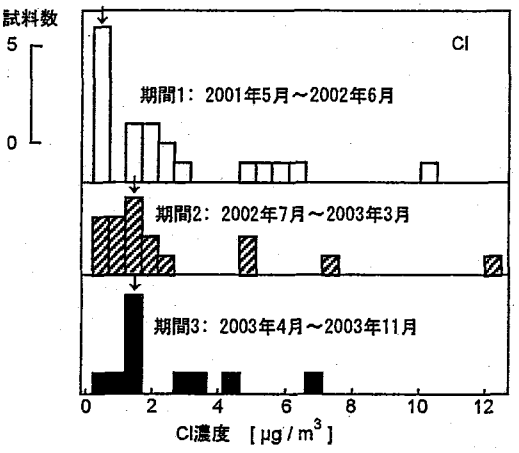

図3 相対湿度が70-80%となる試料について集計した大気浮遊じんのCl濃度の度数分布図。図中の矢印は最も試料数が多い濃度の部分を示す。

参考文献

1) B.Mason, "Principles of Geochemistry", John Wiley & Sons, Inc., New York (1966).
2) 国立環境研究所ホームページ (http://www.nies.go.jp/labo/crm/vehicle.htm)，「環境標準試料 NIES No.8 自動車排出粒子」.
3) E.S.Gladney et al.,"Compilation of elemental concentration data for NBS clinical, biological, geological and environmental standard reference materials", NBS/S P-260/111 (1987).

4-11

微生物による重金属元素集積機構の物理化学的解析

Physico-chemical analysis of biosorption by microorganisms

宮崎医科大学医学部化学、精神医学
中島　暉、植田勇人

Akira Nakajima, Yuto Ueda
Department of Chemistry, Department of Psychiatry, Miyazaki Medical College

1. はじめに

微生物のなかには、特定の重金属元素をその体内に集積するものが存在する。これまでの研究で、緑藻類、放線菌、細菌などが、銅、カドミウム、モリブデン、金、ウラン、トリウムなどに対して、優れた集積能を示すことが明らかになっているが、この集積の大部分は、代謝と無関係に細胞の物質と結合しており、生物吸着(Biosorption)と呼ばれている。生物吸着は主に細胞外部に重金属を蓄積し、しかも蓄積容量が大きいことから、水圏中有用金属資源の回収及び環境中有害重金属元素の制御の視点から、近年、活発に研究されている。

本研究では、重金属集積能の高い細菌を用い、中性子放射化分析により、該菌による希土類元素生物吸着解析を行ったので報告する。

2. 実験方法

(1) 微生物の培養：東京大学分子細胞生物学研究所 IAM カルチャーコレクション(IAM)及び広島大学大学院先端物質科学研究科生命分子機能化学講座(HUT)より分譲された微生物菌株を 3 日間培養後、遠心分離法またはろ過法で集菌し、後の実験に用いた。培地は、肉エキス 3 g/l, ペプトン 5 g/l, 塩化ナトリウム 5 g/l (細菌)；酵母エキス 4 g/l, 麦芽エキス 10 g/l, グルコース 4 g/l, pH 7.1 (放線菌)；酵母エキス 4 g/l, 麦芽エキス 10 g/l, グルコース 4 g/l, pH 5.7 (糸状菌・酵母)を用いた。

(2) 希土類金属イオン吸着実験：前培養した微生物菌体 20 mg（乾重量として）を 40μM の希土類金属イオンを含む溶液 40 ml に懸濁し、金属イオンを取り込ませた。試験した希土類金属イオンの全てが pH 6 以上で沈殿を生じたことから、溶液の pH は 5 に調整した。希土類金属塩として、硝酸塩を用いた。なお、硝酸塩を入手できなかった Tm 及び天然の同位体が存在しない Pm は実験を行わなかった。遠心集菌後、菌体を凍結乾燥し、中性子放射化分析法により菌体中の金属量を求めた。また、原液及びろ液は、ろ紙に滲みこませ乾燥後、中性子放射化分析を行った。微生物菌体粉末又はろ紙を日本原子力研究所 JRR－4 炉気送管（3.5 MW、中性子束 3.2×10^{13} n・cm^{-2}・sec^{-1}）で熱中性子を 1 分間照射し、冷却後、波高分析器でγ線を計測した。中性子放射化断面積が大きく、放射性核種の生成量が多い Eu については、低出力条件（100 kW、中性子束 9.14×10^{11} n・cm^{-2}・sec^{-1}）で照射を行い、γ線を計測した。分析に用いた核種、半減期及びγ線を表 1 に示す。中性子照射した微生物菌体のγ線スペクトルを図 1 に示す。

3. 結果・考察

(1) 微生物による希土類生物吸着

細菌 *Arthrobacter nicotianae* (IAM 12342)を用いて，種の希土類金属イオンの吸着を調べた。表 2 に結果を示す。希土類金属吸着量は、470~510 μmol/g 程度と金属の種類によって大差がなかった。これは、希土類元素間の化学的類似性の高さを反映している。該菌体による Eu の吸着は、Langmuir の吸着等温式に従うことも明らかになった。該菌体は、銅を 603 μmol/g 吸着できることから[1]、希土類金属吸着量は銅吸着量よりやや小さい値を示した。Palmieri らは、褐色藻類 *Sargassum fluitans* による La の吸着を調べ、硫酸塩で 530 μmol/g 吸着することを示しており、われわれの結果は、これと同程度であった[2]。

文献

[1] 中島暉：第 10 回東京大学原子力研究総合センターシンポジウムプロシーディング　p403 (2001).

[2] M. C. Palmieri et al. : Hydrometallurgy, **67**, 31 (2002).

研究施設・装置:JRR-4 (気送管)　　研究分野：放射化分析

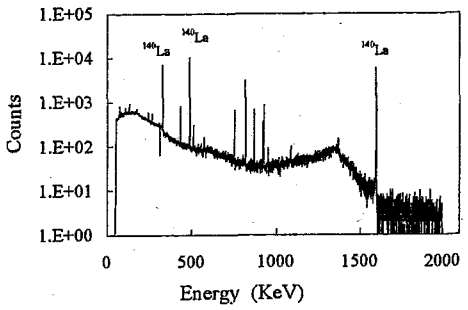

図 1. La を吸着した *Arthrobacter* 菌体のγ線スペクトル（出力 3.5 MW、4 時間冷却）

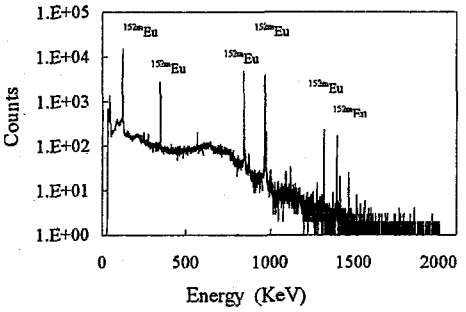

図 2. Eu を吸着した *Arthrobacter* 菌体のγ線スペクトル（出力 100 kW、2 日冷却）

表 1. 中性子放射化分析に用いた元素の生成核種、半減期、γ線

元素	母核	存在比 (%)	核反応と生成核種	放射化断面積 (barn)	半減期		γ線
La	^{139}La	99.911	(n,γ) ^{140}La	8.2	40.27	h	328.6, 486.8, 1595.4
Ce	^{140}Ce	88.48	(n,γ) ^{141}Ce	29	32.5	d	145.4
Pr	^{141}Pr	100	(n,γ) ^{142}Pr	12	19.14	h	1575.5
Nd	^{146}Nd	17.22	(n,γ) ^{147}Nd	10	11.3	d	91.4, 531.0
Sm	^{152}Sm	26.72	(n,γ) ^{153}Sm	210	47.1	h	69.6, 103.2, 172.9,
Eu	^{151}Eu	47.82	(n,γ) ^{152m}Eu	3100	9.3	h	121.8, 344.2, 841.6, 963.5, 1315.0, 1388.9
Gd	^{158}Gd	24.87	(n,γ) ^{159}Gd	3.5	18.5	h	363.5
Tb	^{159}Tb	100	(n,γ) ^{159}Tb	46	73	d	87.0, 197.2, 298.6, 879.4, 965.8, 1177.6
Dy	^{164}Dy	28.18	(n,γ) ^{165}Dy	951	5.93	d	94.6, 279.5, 361.7, 545.7, 633.1, 715.2,
Ho	^{165}Ho	100	(n,γ) ^{166}Ho	64	26.7	h	80.6, 1378.1, 1580.5
Er	^{170}Er	14.88	(n,γ) ^{171}Er	9	7.5	h	111.6, 124.0, 295.8, 308.1, 796.0
Tm	^{169}Tm	100	(n,γ) ^{170}Tm	127	130	d	84.4
Yb	^{176}Yb	12.73	(n,γ) ^{177}Yb	7	1.9	h	121.6, 138.3, 150.3, 1079.8, 1240.9
Lu	^{176}Lu	2.59	(n,γ) ^{177}Lu	4000	6.7	d	113.0, 208.4

表 2. *Arthrobacter nicotianae* に吸着された希土類金属量

Metal	La	Ce	Pr	Nd	Sm	Eu	Gd	Tb	Dy	Ho	Er	Yb	Lu
Metal in cells (μmol/g)	476	494	459	480	505	507	480	482	470	464	474	531	500

微生物菌体（5 mg）を各金属イオン 40 ml に懸濁し、1 時間接触後、ろ過した。

4-12

環境試料中の有機態フッ素(EOF)の放射化分析法に関する検討

INAA for the Determination of Extractable Organofluorine (EOF) in Environmental Samples

愛媛大学農学部　河野公栄、松田宗明、脇本忠明

Masahide Kawano, Tadaaki Wakimoto, Muneaki Matsuda

Faculty of Agriculture, Ehime University

はじめに

有機ハロゲン[Extractable organohalogens: EOX (EOCl, EOBr, EOI)]は環境中で安定で残留性が強く生態系を通じて高次生物に次第に濃縮され、しかもPCBs, DDTsさらにダイオキシン類を例として挙げる事ができるように毒性影響が大きいことから環境汚染物質として注目され、人間活動に近い都市域から遠隔の地である極域など地球的規模の汚染が次第に解明されつつある。しかしながら近年、上記、塩素、臭素、ヨウ素化合物に加え、有機フッ素化合物に関する環境汚染が注目されている。フッ素は炭素との共有結合が他のハロゲン元素に比べ強く環境中で極めて安定で容易に分解されずしかも生物に及ぼす毒性影響も大きいことが知られている。欧米の研究者による有機フッ素化合物汚染に関する検討で生物種によっては有機塩素化合物に匹敵する体内蓄積濃度が明らかにされている。今後、世界的に見て有機フッ素化合物に関する環境汚染に関する調査・研究が進展するものと考えられる。そこで本研究課題では、本研究分野での先駆的研究を展開すべく放射化分析によって有機フッ素化合物を総体としてとらえる Extractable Organofluorine (EOF)分析法を検討し、従来から取り組んでいるEOCl, EOBr, EOIに加えてEOFを分析するための全有機態ハロゲン分析法を確立するための基礎的な分析条件の検討を行った。なお、EOCl, EOBrおよびEOI分析に用いている機器中性子放射化による手法をEOF分析に適用する際の最適分析条件について検討を試みた。

分析条件の検討

自然界に存在する^{19}Fから中性子照射によって生成する^{20}Fは極めて短寿命であるため照射後直ちに計測する必要があり JRR-4 気送管・短寿命照射装置を用い測定条件を検討した。

JRR-4での3.5MW運転時と100KW運転時の誘導放射能について比較したところ、低出力運転時のカウント数が理論値通り低く、従って低レベルの試料に対して高感度分析を行うには中性子フラックス数が大きい高出力運転が望ましいことが明らかとなった。

試料封入容器及び照射用容器に測定を妨害する元素の存在は認められなかった。標準溶液としてフッ化アンモニウム水溶液を超純水を用い調製し、妨害元素の有無を検討したところ、妨害元素及びフッ素は検出限界以下であった。

試料を収納した照射用容器を窒素ガスで気送し、中性子照射を行い照射試料を再び窒素ガスで気送して試料を回収し直ちに開封し、γ線スペクトロメーターで計測する一連の分析作業のうち、中性子照射後からγ線測定までの所要時間は90秒程度であった。照射終了直後に補正した計数値は、フッ素61.29μgの場合、35652±955 であった。フッ素量と中性子照射による生成放射能の間に定量的な直線関係が見られ、検量線は40.23～160.92μgで

研究施設・装置

JRR-4、気送管、γ線スペクトロメーター

研究分野

環境化学、放射化分析

関係を示した(図1)。なお、容器、溶媒からのバックグラウンドの寄与は低いが、短半減期であるため精度よく測定するために試料中にフッ素量として5 ～10μg以上の存在量が必要である。

有機フッ素化合物として perfluorobiphenyl のヘキサン溶液(フッ素量として 61.29μg)を調製しフッ化アンモニウム標準溶液で測定した結果(8回測定)、理論値の 95.7%(RSD 2.68%)で、良好な精度で測定可能であることが示唆された。

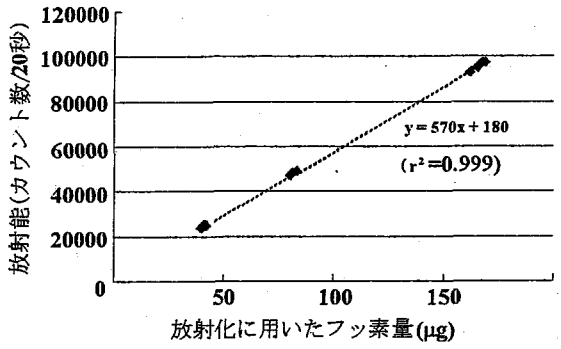

図1 フッ素量と生成放射能の関係(検量線)

図2は、フッ素 81.2μg を繰り返し測定した場合の誘導放射能の変動を示している。変動の幅は小さく問題ないと考えられるが、試料と共に標準溶液も照射して中性子束の変動に起因する測定誤差を小さくすることとした。

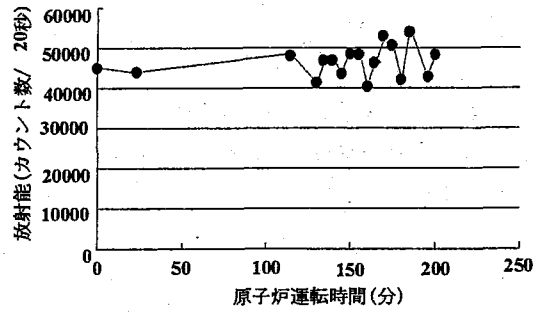

図2 誘導される ^{20}F の原子炉運転時間による変動 (19F 81.2μg の場合)

表1 Perfluorobiphenyl を用いた生成放

供試量	生成放射能レベル	
61.29μg	36355 34175 36619 35460	35652±955*1
122.58μg	65452 68818 69071 69082	68106±1536*2

*1 及び*2: フッ素として 59.29μg(理論値の 96.7%)及び 116.1μg(理論値の 94.7%)である。

本分析法では有機フッ素化合物を測定対象として考えている。先に有機フッ素化合物を用いて放射化の定量性について検討し良好な結果を得たが(図 1)、検量線の低い濃度と高い濃度域での perfluorobiphenyl の放射化の変動について検討した。その結果を表1に示しているが、再現性の良い定量的な測定値が得られた。

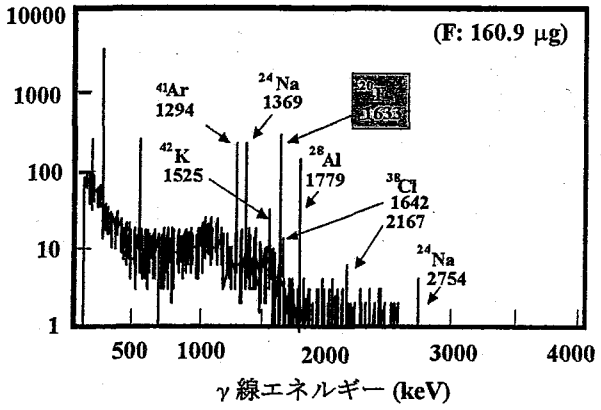

図3 フッ化アンモニウム標準溶液のγ線スペクトル

フッ化アンモニウムは市販試薬(特級)を用いたが妨害元素の存在が懸念される故、スペクトル上で妨害するピークの有無について検討した。図3に標準溶液のγ線スペ

クトルを示す。フッ素以外に、カリウム、アルゴン、ナトリウム、アルミニウム、塩素、ナトリウムに由来するピークが確認された。このうちアルゴンは試料容器の雰囲気の窒素置換を行う際に混入する気体に由来し、またアルミニウムはポリエチレン製試料容器に由来することが考えられる。その他のカリウム、ナトリウム、塩素等は標準品として用いているフッ化アンモニウムの試薬中に不純物として含まれているものである。フッ素の定量の際に、塩素 1642keV 及びフッ素 1633keV の間のγ線エネルギー領域のピークが妨害することが考えられるが、図4に示すように両者間に妨害するピークは存在しなかった。

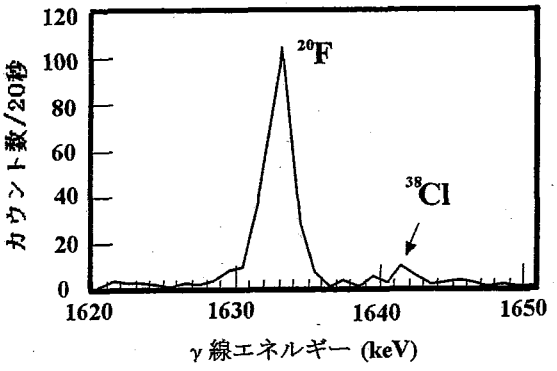

図4 ^{20}F 1633keV に隣接する塩素同位体 ^{38}Cl 1642keV 付近のγ線スペクトルの詳細

表2 中性子放射化分析条件

中性子原及び照射条件	
日本原子力研究所: JRR-4 気送管照射装置	
照射条件	中性子フラックス 3.5 x 10^{13} n/cm^2・秒
	照射時間 30 秒
γ線測定	
γ線測定器: CANBERRA	
	Detector Model GX2018
	Cryostat Model 7500SL
測定条件	照射直後、直ちに測定
	計測核種 ^{20}F 1633keV

以上の検討結果に基づき、表2のように放射化分析条件を設定した。

フッ素は短半減期であるため、放射化後、迅速な分析が必要である。検討事項の項ですでに述べたが、本法の最低検出量は5～ 10μg程度であり、従って試料量10g用いた場合、最低検出濃度は 1ppm である。今日、多種類の有機フッ素化合物が製造・使用されており環境試料中の有機態フッ素濃度として検出可能と考えられる。

成果の公表

1)河野公栄、環境試料中の有機態ハロゲン、放射化分析ハンドブック、伊藤泰男・海老原充・松尾基之監修編集、日本アイソトープ協会、丸善、p100、2004年

2)M. Kawano, J. Falandysz, T.Wakimoto: Instrumental neutron activation analysis of extractable organohalogens (EOX) in Antarctic marine organisms. Journal of Radioanalytical and Nuclear Chemistry, 255, No.2, 235-237 (2003).

3)Mitsuaki Matsui, Yuji Kashima, Masahide Kawano, Muneaki Matsuda, Kazunori Ambe, Tadaaki Wakimoto, Rikuo Doi, Dioxin-like potencies and extractable organohalogens (EOX) in medical, municipal and domestic waste incinerator ashes in Japan. Chemosphere, 53, 971-980 (2003).

4)Mitsuaki Matsui, Yuji Kashima, Masahide Kawano, Muneaki Matsuda, Tadaaki Wakimoto, Rikuo Doi, Estrogenicity in crude and fractionated extracts of medical waste incinerator ashes. Organohalogen Compounds, 56, 61-64 (2002).

4-13

地圏環境における元素分布・循環の研究
—多試料・多元素分析による愛知県東部の地圏化学環境評価の試み—
Geoenvironmental assessment of Aichi Prefecture by INAA multi-elements analysis for a large number of stream sediments

田中　剛(TANAKA Tsuyoshi)[1)]・南　雅代(MINAMI Masayo)[1)]・山本鋼志(YAMAMOTO Koshi)[1)]・浅原良浩(ASAHARA Yoshihiro)[1)]・三村耕一(MIMURA Koichi)[1)]・仙田量子(SENDA Ryouko)[2)]・柴田信之介(SHIBATA Shin-nosuke)[1)]・武邊勝道(TAKEBE Masamichi)[1)]・田中万也(TANAKA Kazuya)[1)]・林　隆正(HAYASHI Takamasa)[1)]・小島　久(KOJIMA Hisashi)[3)]

1) 名古屋大学大学院環境学研究科地球環境科学専攻,　464-8602　名古屋市千種区不老町
Graduate School of Environmental Studies, Nagoya University, Chikusa, Nagoya 464-8602, Japan
2) 名古屋大学大学院理学研究科地球惑星理学専攻,　464-8602　名古屋市千種区不老町
Graduate School of Sciences, Nagoya University, Chikusa, Nagoya 464-8602, Japan
3) 名古屋大学アイソトープ総合センター,　464-8601　名古屋市千種区不老町
Radioisotope Center, Nagoya University, Chikusa, Nagoya 464-8601, Japan

Abstract

Geochemical map is a useful tool for geoenvironmental assessment. Major elements tend to express the geological background. The analyses suggest that the stream sediments from areas with sedimentary rock basement are more enriched in SiO_2 than those from areas with granitic basement. Samples from the area in the granitic basement are characterized by enrichment of Na, K, and Ca. The relative abundance of these elements differs in the respective granitic bodies. This difference reflects the difference of abundance and chemical composition of plagioclase and potassium feldspar in stream sediments. A large granitic body named Inagawa-granite distributes widely in the mapping area. According to the geological and petrologial studies, the Inagawa granite is subdivided into I ~ IV types (Nakai, 1976). A new subdivision has emerged from the Ca-K-Na diagram based on chemical composition of stream sediments. This suggests that geochemical map may be more useful as supporting data for geological mapping Minor elements, on the other hand, are expected to reflect artificial activities effectively. 27 trace elements, Sc, Cr, Co, Ni, Zn, As, Br, Rb, Sr, Zr, Sb, Cs, Ba, La, Ce, Nd, Sm, Eu, Tb, Yb, Lu, Hf, Ta, W, Au, Th and U were analysed for 1500 stream sediments by INAA, being supported by JAERI Program #3137. The stream sediment contains a varieties of minerals hardly dissolving in acid. The non-destructive INAA is the reliable method for analysis. The precision and accuracy for analysis is better than +/-3~5%. The data reproducibility for multiple sampling at the same site is about 10%. A big amount of samples, more than 100mg, was used for analysis to avoid chemical heterogeneity. The following discussions, however, are based on the elemental variations bigger than 30% to several tens time.

Cobalt and zinc are rich in the eastern and western parts, where the sedimentary rocks and volcanics are distributed. These distributions are correlated well with those of Fe and Mg. High concentration of these elements are observed sporadically in the area without any relation to the basement geology. Scandium and hafnium distributions are correlated well with those of Ca and Fe. These areas correspond to the geology of the Obara granite and of mafic part of the Inagawa granite. Cesium distribution is reversely correlated with above elements. La distribution looks like that of Ce. The distribution differs from that of Yb. The distribution of Sm does not show intermediate one between La and Yb. Several groups of independent magmatic differentiation must be there.

Arsenic and Gold can be determined by INAA with reagent standards. Arsenic distributes with Au and Sb at Tsugu area, the eastern part of the study area. This suggests the origin of the elements related with geothermal activity. Au is also observed without any correlation of As and Sb at several parts in granite area. Arsenic is observed at the northwestern part of the study area without any correlation with Au. The different combinations of these elements indicate different origins at each location.

研究施設と装置名：JRR-3気送管、JRR-4気送管・Tパイプ・Sパイプ
研　究　分　野：中性子利用分析・放射化分析、地球化学、環境化学

1. はじめに

人為汚染と資源元素の濃集は、どちらも通常は分散している元素が異常に濃集することを問題とする点において、似たような結果にみえる。しかし、自然界の所作によって濃集した資源元素からは、地球化学的あるいは鉱物学的諸法則に基づいた元素挙動が読みとれる。一方、人為汚染は、その当初は、地球化学的に意味のとれない元素分布をみせる。元素の濃集機構の研究に沢山の研究と経験を積み重ねてきた地球化学者が、人為汚染の評価に食い込む大きな隙は、元素濃集に鉱床学的あるいは地球化学的諸法則の匂いを嗅げるか否かに存在するのではなかろうか。以下に、中性子放射化分析の特性である多試料・多元素分析を用いた地球化学図による地圏環境評価の試みを報告する。

2. 地球化学図による地圏環境評価

地球化学図は、鉱床探査ツールのひとつであった。しかし、ここでは環境を意識してより広い意味をもたせるよう以下のように定義する。すべての地圏環境情報は、中学校で学ぶ理科の科目、物理、化学、生物、地学、の4分野に集約・分類される。例えば、高低・距離・方向など物理情報は、地形図として表され、樹木などの生物情報は植生図として、岩相や断層など地学情報は地質図として、それぞれまとめられる。では地圏の化学情報はどのように表現されるのだろうか？　その地圏の化学情報を図化したものが、地球化学図であると定義しよう。

地球化学図はもともと探鉱を目的としたものであったから、特定の元素群を目標として、その作成地域も限定されていた。一方、イギリス、ドイツやポーランドなど欧米の環境先進国では、30以上の元素について、全国土をカバーする環境評価を目的とした地球化学図が作られている。最近公表されたウエールズ地方のヒ素の地球化学図（Breward et al., 2000）の作成には川床堆積物約19000試料中の34元素を蛍光X線分析法で分析した結果が用いられている。ウエールズの地球化学図では、地域分布のほか、岩相別分布や、地質時代別分布がわかるようになっている。また、一部の地域では土壌や河川水も分析され、それらとの対比やAs^{3+}とAs^{5+}の安定条件、さらにはAs-Co-Mn の相互関係から、ヒ素の起源と地圏環境での挙動が詳細に検討されている。イギリスでは、南東部を除く北部地域でもこのスケールの地球化学図が完成している。また、国際地球化学・宇宙科学協会（International Association of Geochemistry and Cosmochemistry）は全地球をカバーする地球化学図の品質管理をめざして活発な活動を続けている（Darnley et al., 1995）。

日本における研究は、残念ながら数える程しか無い。椎川ほか（1984）の秋田県の地球化学図や伊藤ほか（1991）による北関東の地球化学図などが主なものである。研究が少ない理由として、地圏の環境を面的に評価しようと思えば、たくさんの試料の多くの元素を分析しなければならず、そのハードルが大きかったからであろう。しかし、蛍光X線分析やICP-MS分析の普及も進み、その気さえあれば現在、ことは容易である。二つ目の理由は、地球化学調査は単純労働で、量子力学を解析手段に用いつつある最先端？の研究からみれば、19世紀の復活と映る事ではなかろうか？　上記ウエールズの地球化学図の解析には、地表水や土壌のデーターも取り込み、多様な溶液化学／結晶学が駆使されていることを見てほしい。最先端の地球化学の理論なくして、地球化学図は解析できないのである。

3. 試料と分析法

何を試料とすればその地域（面）の元素存在度を的確に表現できるかについては、試料採集のし易さとも関連してさまざまな考えがある。本研究では、川床堆積物（stream sediment）を用いた。これはイギリスやドイツの地球化学図と同じで、図1に示すように小さな沢ごとにその出口で川砂を集め、それが、その集水域の化学組成を代表するとみなすのである。通常のINAA分析には数100 mg程度の少量の試料しか用いられないので、現場で180 μ mの篩を通し、代表性を高める。毎年同じ場所で試料を採集したり、篩の目の荒さを変えたり、実際の露岩を分析するなどして、川床堆積物試料の代表性を検討した。アクセサリー鉱物に由来する元素は30%をこえる変動を示すこともあるが、通常は10%以内の変化におさまる。この変動は大きいように見えるが、図2以降に示す地域変化より遥かに小さく、解析の障害とはならない。試料採集の手順は、田中ほか（2001）に準じて行った。4名の採集作業員（学生やアルバイト）が、職員の運転する車に乗り、2名が1組になって作業を行う。1組の班が1日に採集できるのは約10試料である。

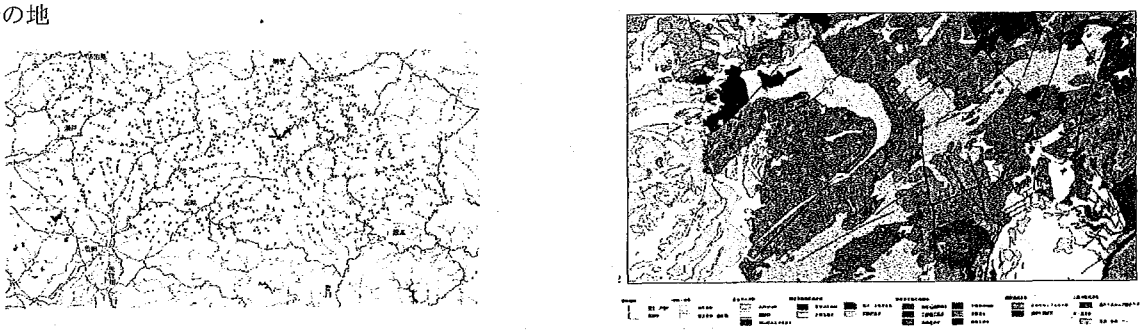

図1. 本研究で用いた愛知県東部の河川堆積物採集地点（左）と同地域の地質図（地質調査所 豊橋図幅, 1987）

川は5万分の1地形図に示されている部分を表し、試料の多くはそこに流れ込む枝川で採集された。

分析には、多くの試料の多くの元素が容易に分析できる方法が選ばれる。試料の不均質性と地点代表性から考え、±3%以上の分析精度は必要ないといえる。筆者らは、主要化学成分は蛍光X線分析（山本ほか, 1998）、微量成分は、中性子放射化分析（田中ほか, 1988）を用いた。試料の酸分解過程がないのが強みである。分析データは、試料産状データとともに緯度／経度値に従って、“エクセル”上にファイルされる。

4. 解析と解釈

地球化学図の一般的な解釈例は「天然資源と人為汚染を見分ける地球化学図」(田中,2003)を参照して頂きたいが、ここでは本報告にのせられた図に簡単な注釈をつける。この図は、1600余の数値を処理して得られた図であるから、図の周辺部分や細かい境界の形には正確でない部分が含まれることを承知していただきたい。

図2にアルミニウム、カルシウムとナトリウムの分布図を示す。地図の中央部分に濃度の高い地域が、西部（左側）に濃度の低い地域が分布する。図1の地質図に対比すると、濃度の高い部分が花崗岩の分布に、低い部分が新第三紀層・第四紀層と領家変成岩の分布に良く合うことがわかる。元素の組み合わせとその分布から、これらの元素が花崗岩にたくさん含まれる長石という鉱物に由来する事が推察される。

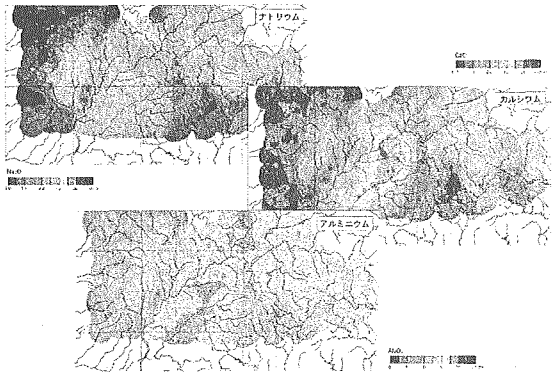

図2. 図1と同一地域のアルミニウム、カルシウムおよびナトリウムの地球化学図。

図3に鉄、マグネシウムとマンガンの分布図を示す。これらの濃度が高い部分は比較的小さな面積で分布する。鉄の分布を地質図に対比すると、図の中央から東側の分布は、マグネシウムの分布にも一致し、領家帯中の苦鉄質岩や設楽火山岩類の安山岩および玄武岩の分布に対応する事がわかる。一方、図の西部にスポット状に分布する高濃度鉄の分布は、マグネシウムではなくマンガンの分布に良く合うが、対応する地質がみあたらない。はてこの違いは？　衛星写真と見比べると、西部にみられる高い鉄の分布は、そのいくつかがゴルフ場の位置に対応することがわかる。元素組み合わせの違いは、両地域における鉄の起源の違いを示している。

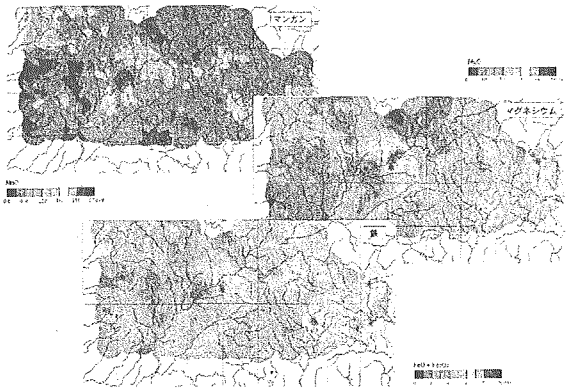

図3. 図1と同一地域の鉄、マグネシウムおよびマンガンの地球化学図。

図4にランタン、サマリウムとイッテルビウムの分布図を示す。これらの元素はⅢb族の希土類元素に属する。希土類元素はそれぞれの元素に単離され、多くの工業素材に使われる。この地域では、希土類（ランタニド）14元素は地殻と似た割合で含まれる事から、人為的な付加は無いと言えよう。自然界での希土類元素の変動幅は主要化学成分より大きく、岩石成因研究の指標として重用される。存在度は花崗岩の分布する地域に多いが、山本ほか(1998)でも述べられているように、同一花崗岩体の中でも大きな違いがあり、花崗岩形成の空間的差異が読み取れる。

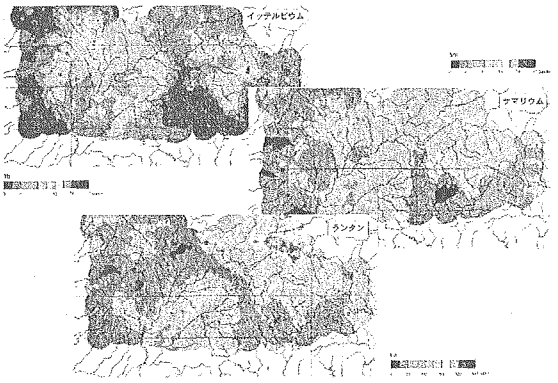

図4. 図1と同一地域のランタン、サマリウムおよびイッテルビウムの地球化学図。

図5にスカンジウム、セシウムとハフニウムの分布図を示す。これらの元素はいずれも自然界に数十ppmしか存在しない稀元素であるが、INAAでの分析感度は高い。スカンジウムは一般的に花崗岩より玄武岩に多く含まれる元素であるが、図の中央部の花崗岩分布地域に例外的に多い事は、この花崗岩

が、玄武岩質の包有物を多く含む事と関係がある。セシウムはスカンジウムと相反する分布を示し、図

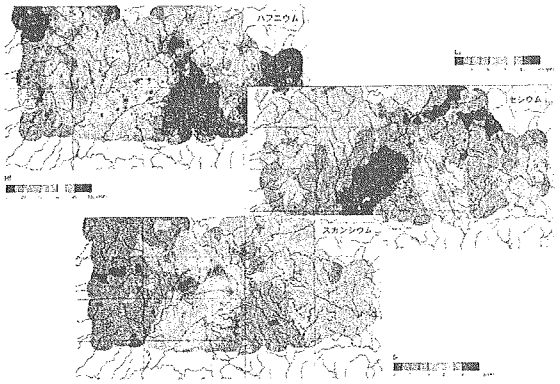

図5. 図1と同一地域のスカンジウム、セシウムおよびハフニウムの地球化学図

図6にクロム、コバルトと亜鉛の分布を示す。これらの元素は金属資源としても重要な元素である。いずれも、西部の第四紀層や新第三紀層の分布する地域での濃度が高いところに共通点があるが、細かな分布パターンは3元素の間でそれぞれ異なる。それぞれのスポット毎の元素の起源の違いが表れているものと考えられる。

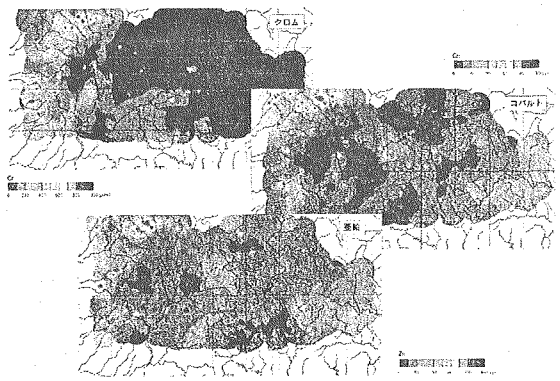

図6. 図1と同一地域のクロム、コバルトおよび亜鉛の地球化学図

5. 評価と今後の展開

地球化学図が元素の起源を判断する基本情報として役立つことが判明した。評価に関わる重要なことは、単純に元素濃度の高い低いではなく、他の元素との関連とその地球化学的／鉱床学的解析が元素の由来を判断する基本になることである。精度の良い解析のためには一見無駄に見える多数の元素数が必要である。また、地質試料には酸分解が困難なジルコンなどのアクセサリー鉱物が含まれる。それらの点から、酸分解を必要としない非破壊中性子放射化分析の結果の信頼度はとても高いことがわかった。今後、分析された値がその試料を代表している事がより強く求められよう。その点で、従来とは異なった発想で、大量の試料を分析に供し得ることが重要と考えられる。また、これまでのINAAでは

の北西端にセシウム濃度の高い地域がみられる。

図７に金、ヒ素とトリウムの分布を示す。人間に好まれる元素と嫌われる元素を並べた。いずれの元素も自然界には極微量にしか存在しないが、中性子放射化分析で精度良く定量できる。図の東（右）方の金の多い所は、武田信玄の時代から有名な、津具の金山（現在は廃坑）周辺である。熱水性鉱床では金とヒ素とアンチモンが良い相関を示すと言われるとおり、ここでも3元素は極めて高い相関をもって分布する。戸上ほか（1997）はこれら元素の相関と地質構造から大峠付近の地下にも金の存在を予想している。加えてもう一つ、この図では鉱山直下のずりの影響をうけた川床堆積物が分析されており、当然1000ppb近い金とヒ素が検出されている。しかしヒ素は、少なくとも近年金の採掘がなされた形跡のない鉱山北方や大峠周辺の至る所に分布し、鉱山直下より高い濃度を示す地点さえ存在する。この地域に広く分布するヒ素は、金の鉱兆であると同時に、採鉱に関係していない自然界のバックグラウンドとはいえないだろうか。

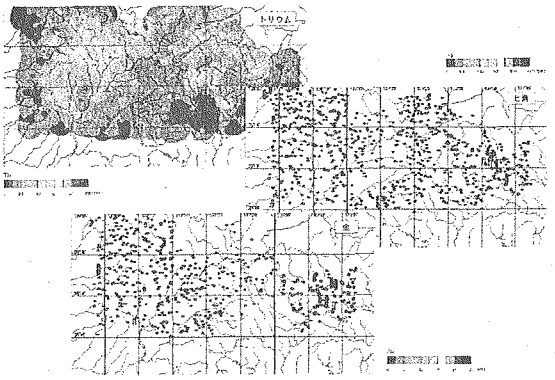

図7. 図1と同一地域の金、ヒ素およびトリウムの地球化学図

分析が困難であった元素の新しいINAA分析手法に依る分析法のルーチン化が望まれる。

バックグラウンドレベルはその地域の地質に依存する。自然のバックグラウンドを正しく評価するためには様々な地質の地域を調べることが必要である。環境評価にとどまらず、地形図や地質図のような国土基本情報の一つとしても、地球化学図の整備が望まれる。 図７では、金とヒ素の関係が明らかとなった。しかし、調査地域の北西部では、金の異

常が見られないヒ素の異常地域が見られる。次期の展開として、金やヒ素の分析感度が高い中性子放射化分析の特性を利用して、地質に依るヒ素の挙動を、もちろん多元素の挙動と関連付けながら、解明をすすめたい。

参考文献

Breward et al. (2000) Regional geochemistry of Wales and part of west-central England: stream sediment and soil. pp.156, British Geological Survey Pub.

Darnley et al. (1995) A global geochemical database for environmental and resource management. IGCP project 259 final report, pp. 122, UNESCO Pub.

今井 登ほか (2001) 国内外の地球化学図と日本全国をカバーする地球化学図プロジェクト.地質ニュース 558号, 9-17.

伊藤司郎ほか (1991) 地球化学アトラス- 北関東, pp.35, 地質調査所出版物.

椎川 誠ほか (1984) 秋田県の地球化学図, pp. 29, 秋田大学教育学部.

田中 剛ほか (1988) 放射化分析用放射線自動計測・解析システムの開発と標準岩石試料の分析。地質調査所月報 39巻, 537-557

田中 剛ほか (2001) 地学野外実習としての地球化学図作成.地質ニュース 558号, 41-47.

田中 剛 (2003) 天然資源と人為汚染を見分ける地球化学図. "資源環境地質学" 資源地質学会刊, 373-378.

戸上 薫ほか (1997) 愛知県北東部津具地域の元素濃度分布とその規定要因.資源地質 47巻, 305-318.

山本鋼志ほか (1998) 愛知県豊田市北東部の領家花崗岩地域の地球化学図.地質雑, 104巻, 688-704.

本研究に関連した成果の印刷公表

Hayashi, T., Tanimizu, M. and Tanaka, T. (2004) Origin of negative Ce anomalies in Barberton sedimentary rocks, deduced from La-Ce and Sm-Nd isotope systematics. Precambrian Res. (in press).

Shimizu, O., Tanaka, T. and Senda, R. (2004) Isotopic measurements of Re, Os, Ir and Ru by quadrupole negative thermal ionization mass spectrometry. Jour. Mass Spectrom. Soc. Japan. vol.52, 189-195.

Yamamoto, K., Itoh, N., Matsumoto, T., Tanaka, T. and Adachi, M. (2004) Geochemistry of Precambrian carbonate intercalated in pillows and its host basalt: Implications for the REE compositions of circa 3.4 Ga seawater. Precambrian Res. (in press).

Wakaki, S. and Tanaka, T. (2004) Single mineral Rb-Sr isochron dating applied to the Nohi Rhyolite and quarts porphyry dyke, central Japan. Geochemical Jour. vol.38, (in press).

Tanimizu, M., Hayashi, T. and Tanaka, T. (2004) Development of Ce isotope analysis for Cosmochemistry using the dynamic multicollector technique. Jour. Mass Spectrom. Soc. Japan. vol. 52, 177-181.

浅原真理・田中 剛 (2004) 水による鉱物の風化:結晶構造規制.ぶんせき, 7号, 389-392.

田中 剛 (2003) 地圏環境評価を目的とする多試料多元素分析 放射化分析研究会編 "放射化分析概論" pp.231, 東京大学出版会 (分担執筆)

田中 剛 (2003)天然資源と人為汚染を見分ける地球化学図. "資源環境地質学- 地球史と環境汚染を読む- " 資源地質学会刊, 373-378. (項目執筆)

Tanimizu, M. and Tanaka, T. (2002) Coupled Ce-Nd isotope systematics and REE differentiation of the moon. Geochim. Cosmochim. Acta. vol.66, 4007-4014.

Kim, K. H., Tanaka, T., Suzuki, K., Nagao, K. and Park E. J. (2002) Evidences of the presence of old continental basement in Cheju volcanic Island, South Kores revealed by radiogenic ages and Nd-Sr isotopes of granitic rocks. Geochemical Jour. vol 36, 421-441.

柴田信之介・田中 剛・南 雅代・仙田量子・武邊勝道・加地拓哉・近藤正史・織田周平・林隆 正・西澤邦秀・小島 久 (2001) 名古屋大学アイソトープ総合センターに設置されたγ線自動測定・解析システムによる地質試料の中性子放射化分析手順と分析精度.名古屋大学博物館報告17号, 15-32.

Kojima, S., Ahmad, T., Tanaka, T., Bagati, T. N., Mishra, M., Kumar, R., Islam, R. and Khanna, P. (2001) Early Cretaceous radiolarians from the Indus suture zone, Ladakh, northern India. Proceedings of the Seventh Radiolarian Symposium. News of Osaka Micropaleontologists, Special Volume, No.12, 257-270.

柴田信之介・田中 剛・南 雅代・仙田量子・武邊勝道・加地拓哉・近藤正史・織田周平・林隆 正・西澤邦秀・小島 久 (2001) 地圏環境における元素分布・循環の研究 —原子炉中性子照射, 郵送, γ線計測による多資料・多元素分析システムの確立- 平成12年度原研施設利用共同研究成果報告書 no.40, 118-136. 東京大学原子力研究総合センター.

武邊勝道・山本鋼志・田中 剛・浅原良浩・三村耕一・谷水雅治・近藤正史・柴田信之介 (2001) 地球化学図作成を目的とする河川堆積物の多試料多元素分析 (2) —海洋堆積物のPorcellanite化作用に伴う化学元素の分別.立教大学原子炉利用共同研究成果報告書(平成11年度)26号, 32-40. 東京大学原子力研究総合センター.

田中 剛・山本鋼志・浅原良浩 (2001) 地球化学図による地圏環境評価手法の研究.岩谷直治記念財団研究報告書, Vol.24, 43-45.

高木真理・田中 剛・浅原良浩・青木和弘・天野健治 (2001) ストロンチウム同位体の挙動から見た岩石の化学風化：釜石鉱山の地下水による水-岩石反応の研究.地球化学35巻, 61-72.

田中 剛・川辺岩夫・山本鋼志・三村耕一・浅原良浩・南 雅代 (2001) 地学野外実習としての地球化学図作成.地質ニュース558号, 41-47.

冨樫茂子・今井　登・奥山康子・田中　剛・岡井貴司・狛　武・村田泰章・青山秀喜（2001）日本列島の“クラーク数”若い島弧の上部地殻の元素存在度.地質ニュース558号, 25-32.

本研究に関連した成果の国際会議での発表

Tanaka, T., Minami, M., Shibata, S., Yanai, K. and Shiraishi K. (2004) Precambrian Antarctic Meteorite "Phantasia". 14th V. M. Goldschmidt Conference, June 5-11, 2004 Copenhagen（口頭）

Ahmad, T., Tanaka T., Sachan, H.K., Gouzu, C., Hyodo, H., Itaya, T., Asahara, Y. and Mukherjee, B.K. (2003) Geochemical and isotopic constraints on the protolith of ultra high pressure eclogitic rocks from the Tso-Mortari crystallines, Ladakh Himalaya, India. 13th V.M. Goldschmidt Conference, Sept. 7-12, 2003 Kurashiki (口頭)

Asahara, M.T. and Tanaka, T. (2003) The rock-forming plagioclase controles water-rock interractions: On the view of strontium isotope ratio. 13th V.M. Goldschmidt Conference, Sept. 7-12, 2003 Kurashiki (ポスター)

Asahara, Y., Ishiguro, H., Tanaka, T., Yamamoto, K., Mimura, K., Minami, M., Yoshida, H.D. and Yogo, S. (2003) New attempt to geochemical mapping of Sr isotope in Aichi Prefecture, central part of Japan. 13th V.M. Goldschmidt Conference, Sept. 7-12, 2003 Kurashiki (ポスター)

Hayashi, T., Tanimizu, M. and Tanaka, T. (2003) Ce and Nd isotopic geochemistry of Barberton Greenstone Belt, South Africa: Constraint on early Archeam mantle and origin of Ce anomaly. 13th V.M. Goldschmidt Conference, Sept. 7-12, 2003 Kurashiki (口頭)

Senda, R. and Tanaka T. (2003) More radiogenic Os in continental-side ultramafic rocks of Japanese Islands. 13th V.M. Goldschmidt Conference, Sept. 7-12, 2003 Kurashiki (口頭)

Tanaka, T., Yamamoto, K., Minami, M., Mimura, K., Asahara, Y., Yoshida, H., Yogo, S. and Inayoshi, M. (2003) Geochemical map of Aichi Prefecture, central part of Japan-Minor elements. 13th V.M. Goldschmidt Conference, Sept. 7-12, 2003 Kurashiki (ポスター)

Wakaki, S. and Tanaka, T. (2003) Single mineral Rb-Sr isochron dating. 13th V.M. Goldschmidt Conference, Sept. 7-12, 2003 Kurashiki (口頭)

Yamamoto, K., Tanaka T., Minami, M., Mimura, K., Asahara, Y., Yoshida, H., Yogo, S. and Inayoshi, M. (2003) Geochemical map of Aichi Prefecture, central part of Japan-Major elements. 13th V.M. Goldschmidt Conference, Sept. 7-12, 2003 Kurashiki (ポスター)

Ahmad, T., Harris, N.B.W., Tanaka, T., Bickle, M.J., Chapman, H., Khanna, P.P. and Bunbury, J. (2003) Nd-, Sr-isotopic and geochemical constrains on the source characteristics and petrogenesis of the arc volvanics from the Shyok Suture Zone, Ladakh, India. HIMPROBE workshop at Indian Institute of Technology, Roorkee 17~18 th Oct. 2003 (口頭)

Tanaka, T.(2002) Review on geochenical map projects in Japan. FOREGS and IUGS/IAGC Meeting, April 22-25, 2002 Svincice Czech Republic (口頭)

Tanaka, T., Senda, R., Shibata, S., Minami, M. and Tanimizu, M. (2002) Isotope diluted neutron activation analysis (ID-NAA) for quantitative analysis of PGEs and Re.12th V.M. Goldschmidt Conference, Aug. 18-23, 2002 Davos （口頭）

Senda, R., Kachi, T. and Tanaka, T. (2002) Sr, Nd and Os isotopic systematics of Nikubuchi Ultramafic Rocks in Central Shikoku, Japan. 12th V.M. Goldschmidt Conference, Aug. 18-23, 2002 Davos （ポスター）

Shibata, S. and Tanaka, T. (2002) Experimental study for the dissolution of rare earth elements in water-rock interaction. 12th V.M. Goldschmidt Conference, Aug. 18-23, 2002 Davos （ポスター）

Tanaka, T. (2002) REE in minerals seems be ready soluble in water: A deduction from experimental studies. Invited Lecture at Institute of Geochemistry, Guiyang, China, Oct. 31, 2002

Tanaka, T. (2002) 138La-138Ce isotope systematics in geochemistry: A trial to find 5.67 Ga pre-solar fragment in meteorite. Invited Lecture at Institute of Geochemistry, Guiyang, China, Oct. 31, 2002

Takagi, M., Tanaka, T. and Asahara, Y. (2001) Crystal structure control in elemental dissolution: Evidence from ^{87}Rb-^{87}Sr isotope systematics. 11th V.M. Goldschmidt Conference, May 20-24, 2001 Roanoke, Virginia （口頭）

4-14

宇宙化学的試料中の白金族元素の中性子放射化分析

Neutron activation analysus for platinum group elements in cosmochemical samples

尾嵜 大真、澤幡 浩之、川手 稔
Hiromasa Ozaki, Hiroyuki Sawahata, Minoru Kawate

東京大学 原子力研究総合センター
Research Center for Nuclear Science and Technology, University of Tokyo

白金族元素のほとんどは宇宙・地球化学的に難揮発性親鉄元素と分類される。これらの元素は高温であった原始太陽系星雲ガスから最初に凝縮・固化して、固体微粒子となり、惑星などに集積していったものと考えられている。その後に地球などの惑星で起こったような大規模な変成作用を経験していない始原的な物質であるコンドライトには固体微粒子として集積したときの白金族元素の相対存在度が保持されているものと考えられ、コンドライトの分類ごとに精確な白金族元素の相対存在度を求めることは難揮発性親鉄元素が凝縮・固化した凝縮過程最初期の情報を得るのに有効な方法と言える。

近年、白金族元素の分析は負イオン化質量分析法やICP質量分析法などの多くの手法により試みられているが、こと含有量を求めることに関しては感度など多くの点において放射化分析法は他の手法より秀でていると思われ、本研究では主たる手法として用いていく。最終的な目標は白金族元素の相対存在度などを基にコンドライトやその基となった固体物質の形成過程の解釈を試みることで、コンドライトの白金族元素の RNAA 法による分析を主に行っていくが、主成分元素や他の親鉄元素などの分析値も必要となっていくことから非破壊(INAA)法および即発γ線分析(PGA)法も用いていくこととした。

まずは原研共同利用施設内で長期間にわたる化学分離操作が可能である施設を探すことが必要となった。現状の共同利用施設のうち短期間の化学分離操作はJRR-1実験室やJRR-4実験室などにて可能であるが、長期間にわたる実験は24時間の空調運転が行われていないため不可能である。したがって、JRR-3M運転期間中という制限はあるが24時間の空調運転をおこなっているJRR-3M共同利用実験室1で実験を行うこととした。ただし、原子炉付随施設であるためJRR-3M以外(たとえばJRR-4)で照射した試料は持ち込めない。そのため、中性子照射もJRR-3Mで行うこととした。

本研究の代表者はこれまでにもコンドライト中の白金族元素のRNAAを行ってきたが、その中性子照射はJRR-4 T孔で行ってきた。今回は実験室の制限からJRR-3 HR孔での照射となった。JRR-3 HR孔はJRR-4 T孔と比較して二倍ほど熱中性子束が高く、照射時間を短くできる。これによりPtを定量する際に利用する ^{199}Auへの ^{197}Auの二重中性子捕獲反応の影響を減少されることが予測され、Ptの分析誤差が低く抑えられることが期待された。実際のAuからPtへの影響はJRR-4 T孔12時間(6時間/日×2日)の場合とJRR-3 HR孔6時間照射においてそれぞれ5.97ngPt/ngAu、8.97ngPt/ngAuであった。コンドライトではたとえばAllende隕石でPtが1.25ppm、

研究施設・装置
JRR-3 気送管、HR-1 JRR-4 気送管、T-パイプ

研究分野
宇宙・地球化学

Au が 144ppb 含まれており、Au からの寄与は Pt からの生成量と同程度で、Au の影響の補正による Pt の分析誤差に与える影響は JRR-4 T 孔と JRR-3M HR 孔とで大きくは変わらなかった。ただし、HR 孔の照射カプセルは内容積が小さく同時に分析可能な試料数が 4 個程度に限定されてしまう。今後、精力的に分析を行うためには JRR-4 T 孔と同程度(標準試料3個と試料10個)の試料をひとつのカプセルに同梱できるようになることが望まれる。

本研究ではまず提供元の異なる二種類の Allende 隕石について分析を行った。その結果を表1、図1に文献値とともに示す。本研究の分析結果は文献値ともよく一致しており、二種類の Allende 隕石の値も非常によく一致している。Allende 隕石は凝縮過程において最初に凝縮・固化して白金族元素などの難揮発性親鉄元素が濃縮した refractory metal nugget を多く含むことが知られており、この refractory metal nuggetの偏在化によって白金族元素の分析結果は試料ごとに大きくばらつくことが指摘されている。図表から本研究で用いたもの、Smithsonian 博物館から配布されたものと国立科学博物館の米田氏から提供されたもの間、さらには文献値との間にも違いは認められず、均一な良い試料であることが示された。また PGA 法および INAA 法によるその他の微量元素および主成分元素についても同様の結果が得られた。

ここまでの結果により、PGA、INAA、白金族元素の RNAA によるコンドライトの一連の分析手法が確立された。本研究は 2 年間で新しい種類のコンドライトである CH コンドライトの分析を行うことを目標としていたが、現実的に JRR-3M 共同利用実験室1を使用できるまでに時間がかかったこと、最終年度である平成 15 年度後半の JRR-3M の運転が大きく変更されたこと、などから CH コンドライトの分析までは行えなかった。しかし、原研の共同利用施設内で長期間にわたる化学分離を行う放射化分析を可能としたことはひとつの成果と考える。

表1 Allende 隕石の分析結果

Ru / ppb	Pd / ppb	Re / ppb	Os / ppb	Ir / ppb	Pt / ppb	Au / ppb
Smithsonian Intitution, split 6 position 26						
1054 ± 17	716 ± 25	63.7 ± 1.3	942 ± 29	823 ± 19	1319 ± 28	127 ± 2
National Science Museum						
1039 ± 15	798 ± 22	63.2 ± 1.3	869 ± 27	789 ± 18	1449 ± 31	117 ± 2
literature (Kallemeyn and Wasson, 1988)						
1030	705	65	825	760	1250	144

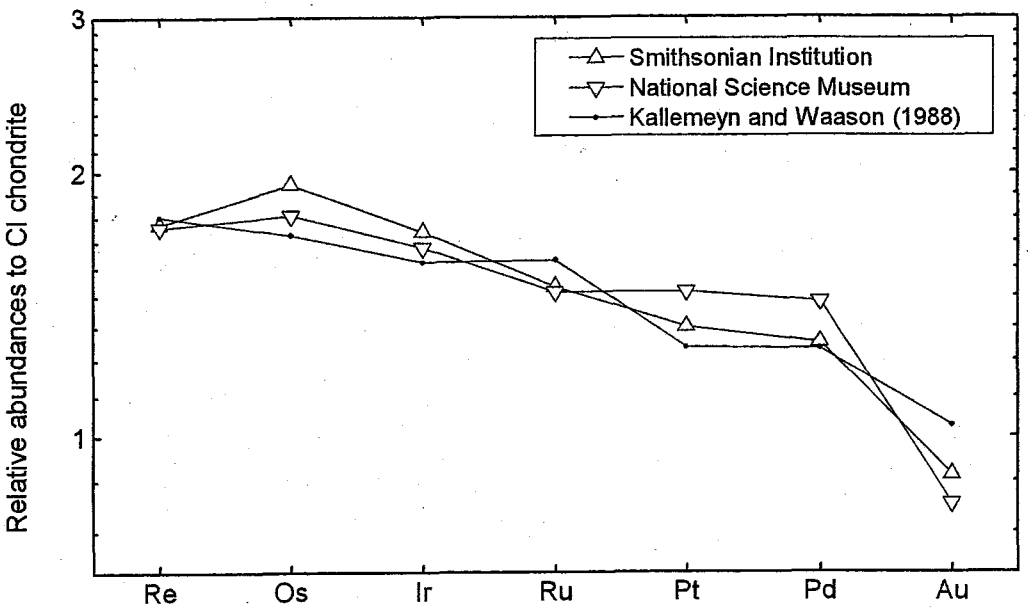

図1 CIコンドライトで企画化したAllende 隕石の白金族元素存在度パターン

4-15
中性子放射化分析による宇宙・火山起源物質の研究（III）

Geochemical studies on cosmic and volcanic matters by instrumental neutron activation analysis (III)

福岡孝昭[1]・野上謙一[2]・田澤雄二[3]・横田裕子[4]・佐野貴司[5]・中井弥生[1]
[1]立正大学地球環境科学部，[2]独協医科大学，[3]京都大学理学部，
[4]青山学院大学理工学部，[5]富士常葉大学環境防災学部
Takaaki FUKUOKA[1], Kenichi NOGAMI[2], Yuji TAZAWA[3], Yuko YOKOTA[4], Takashi SANO[5] and Yayoi NAKAI[1]
[1]Faculty of Geo-Environmental Science, Rissho University, [2]Dokkyo University, School of Medicine,
[3]Faculty of Science, Kyoto University, [4]College of Science and Engineering, Aoyamagakuin University,
[5]College of Environment and Disaster Research, Fuji Tokoha University

1．はじめに

本研究の最終目標は、南極を中心とした宇宙塵・隕石の起源を推定するとともに、落下頻度を求めることにある。南極氷床には火山灰層が存在している。これらの給源火山を明らかにすることにより、火山灰の年代を明らかにできる。この年代から氷の年代を求め、宇宙塵・隕石の落下頻度を求めるための時間軸として利用する。南極氷中には世界各地の巨大噴火による火山灰が含まれているはずで、巨大噴火による火山灰の微量元素組成のファイルを作り、氷中の火山灰層のそれとの対比により氷床の年代を求める。

これまでの研究で、宇宙塵等のμgオーダーの微小試料の放射化分析法の手順はほぼ確立した。しかし、宇宙物質としての判定基準になるAu, Ir 等親鉄元素用の適当な標準試料がまだない。これら金属元素の合金等を作製する。親石元素用標準試料も不足しているので地質調査所の岩石標準試料 JB-1, JR-2 粉末からガラスを作製する。南極氷中の非溶融宇宙塵はもろくこわれやすいので、高純度の試料の保持体（ポリエチレン等）の開発も必要である。南極氷床・表層雪中より回収した宇宙塵試料及び深海底堆積物から回収した宇宙塵が分析対象である。

ここでは、これら一連の研究に関連して過去３年間に行われた研究のうち、南極氷床から採取された非熔融型の宇宙塵の化学組成に関する研究を報告する。

2．試料と実験

第37次観測隊によって採取されたドームFuji基地の生活水造水槽の沈殿物から集めた非熔融型宇宙塵３試料（F97AG記号）と第38次観測隊によりやまと山脈クワガタヌナターク地区の裸氷から集めた非熔融型宇宙塵10試料（K5100記号）１粒ずつについて20元素を中性子放射化分析で求めた。

試料とJB-1ガラス片（親石元素分析用標準試料）を一粒ずつ、約3×3mm大の高純度ポリエチレンフィルム袋中に融封し、JRR-3M炉のPN-3（～2×10^{13} n/cm^{2}s）で10分間熱中性子照射し、ポリエチレン袋ごとγ線測定を行い、Al, Mg, Ca, Na, Ti, Mn, Vの分析を行った。その後同一試料についてポリエチレン袋を除去し、Al-Au合金線（IRMM-530, Auの標準試料）、Pt線（NISTのSRM-680a, Irの標準試料）のチップとともに、１粒づつ高純度石英容器に

JRR-4, Sパイプ；JRR-3M, PN-3, HR-1, 2　　宇宙・地球化学試料の放射化分析

入れ、JRR-3M 炉の HR 照射孔（1×10^{14}n/cm^{2}s）で98時間熱中性子照射を行った。3日間冷却後、石英容器から取り出し、2回繰り返しγ線測定を行い、Cr, Fe, Sc, La, Ce, Sm, Eu, Yb, Lu, Co, Au, Ir, Os 等の分析を行った。

3．結果と考察

分析結果を Table 1 に示した。また C1 コンドライト隕石の値で規格化したものを元素の揮発性の順（右に行く程高い）に Fig.1 にプロットした。どの試料からも親鉄元素である Au, Ir, Os 等が含まれており、全て宇宙起源であることが明かである。さらに、親石元素は F97AG013, K5100-30 を除き、ほぼコンドライト的である（C 1 で規格化した値がほぼ1）。親鉄元素は Os, Ir が大きく枯渇しているのが特長である。この原因についても現在考察中である。

4．まとめ

本報告では南極氷床中が採取された非熔融型宇宙塵の分析例を示した。まだこのような微小な試料一粒ずつの分析法は完成したわけではなく、理想的な標準試料(特に親鉄元素用)はまだ得られていない。微小試料の簡便な取扱い法についてもさらに改善の予定である。

5．成果の公表

学会誌

1. Tazawa, Y. and Fukuoka, T., Fe-Ni-Oxide Spherules with/without Ni-Fe-rich and Fe-Al-rich Silicate Cores, and Chondritic Spherules from Deep Sea Sediments, Acta Scientiarum Naturalium Musei Moraviae Occidentalis Třebíč, Czek Repablik, 41, 107-121, (2003) (Proceedings of the IXth International Symposium on Moldavites, Tektites and Impact Processes, Františkovy Lázně, Sept. 23-26, 2002). ISSN0231-603X.

学会発表

1. Fukushi, Y., Tazawa, Y., Fukuoka, T., Saito, Y. and Yada, T., Chemical composition of individual micrometeorites collected from Antarctic ice, 28th Symposium on Antarctic Meteorites, 2004 年 6 月.
2. Tazawa, Y., Fukuoka, T., Saito, Y., Sakurai, H., Suzuki, Y. and Noguchi, T., Unmelted chondritic micrometeorites from Antarctic Ice revealed by INAA, International Symposium: Evolution of Solar System Materials: A New Perspective from Antarctic Meteorites. 2003 年 9 月.
3. Tazawa, Y., INAA and AMS investigations of fused samples collected from surroundings of Akaogi-bay, Amami-Oshima Island, International Symposium on Impact Events in Japan, southeast Asia and Pacific Rim. 2003 年 11 月.

Table.1. INAA Results of Unmelted Antarctic Micrometeorites

Sample		F97AG00(	F97AG01:	K5100027	K5100030	K5100031	K5100033	K5100035	K5100040	K5100041	K5100042	K5100043	K5100044	Range of	CI	Std.
Weight	μg	1.9	0.5/0.1	1.7	3.8	6.8	4.8	2.1	1.2	1.2	1.5	3.7	2.4	% Error		
Elements																
Na	%	0.77	0.13	0.45	0.42	0.45	1.22	0.58	0.50	0.77	0.69	0.01	0.23	1-12	0.50	2.07
Mg	%	15.0	21.0	16.2	15.3	7.61	15.4	10.8	9.36	11.2	14.6	20.0	9.31	5-11	9.89	4.67
Al	%	1.52	2.89	2.14	0.92	1.96	1.16	1.58	2.06	2.04	2.07	0.046	1.16	1-10	0.868	7.69
Ca	%	1.70	3.70	1.13	0.49	0.78	0.97	0.89	-	-	1.39	-	-	24-40	0.928	6.61
Sc	ppm	15.1	0.896	8.31	14.0	31.8	8.64	10.7	10.9	16.4	14.6	2.40	3.82	<1.3	5.82	28.9
Ti	%	-	0.36	0.20	0.27	0.23	-	0.16	0.11	-	-	0.10	0.09	12-46	0.0436	0.603
V	ppm	86.3	153	97.8	126	62.1	72.4	95.6	100	118	97.8	9.89	72.2	4-21	56.5	207
Cr	ppm	4370	2090	4090	6480	3710	3410	4260	4070	4060	5570	778	1750	<0.3	2660	414
Mn	%	0.28	0.58	0.29	0.36	0.20	0.36	0.21	0.23	0.11	0.28	0.33	0.17	1-3	0.199	0.12
La	ppm	-	2.6	0.86	-	0.59	0.33	0.43	-	2.2	0.64	-	1.1	14-44	0.235	38.8
Ce	ppm	4.5	1.2	2.9	6.0	3.7	1.2	2.1	2.5	4.3	5.3	0.5	1.4	2-47	0.603	63
Sm	ppm	0.320	-	0.231	-	0.689	0.156	0.227	0.415	0.386	0.358	-	0.067	1-3	0.147	5.02
Eu	ppm	-	-	0.20	-	0.25	0.15	0.20	0.21	-	0.22	0.029	-	14-44	0.056	1.59
Yb	ppm	0.15	-	0.14	-	0.38	0.13	0.13	-	0.29	0.20	-	-	12-50	0.163	2.4
Lu	ppm	0.048	0.044	0.045	0.032	0.113	0.030	0.033	0.031	0.063	0.090		0.012	6-34	0.0243	0.37
Fe	%	26.2	11.25	30.3	10.9	26.8	16.9	27.8	24.9	42.4	33.2	18.3	9.57	<0.4	19.04	6.3
Co	ppm	531	76.0	416	15.3	162	107	293	175	336	471	17.4	147	<0.5	502	39.1
Au	ppb	80	170	60	-	110	49	110	47	180	450	-	110	1-15	140	*0.1(%)
Ir	ppb	5.21	-	9.08	29.8	21.3	2.37	9.14	5.74	9.44	11.25	-	3.56	1-4	481	"10
Os	ppb	3.2	-	5.9	*11.5	8.7	-	3.0	1.7	3.9	3.9	-	1.1	6-27	486	*11.5

Note 1) Numbers except for the Weight's row (μ g) are elemental abundances in respective units denoted in the second column. Those in boldfaces are the standard (JB-1 values except those with * (Au: IRMM-530) and " (Ir: SRM-682a). 2) Those replaced with "-" indicate "not detected elements" or "those with experimental errors larger than 50%". 3) *: Os were estimated firstly for K5100030 (11.5 ppb) by using the ratio of neutron activation cross-sections for $Ir^{191}(n,\gamma)Ir^{192}$ and $Os^{190}(n,\gamma)Os^{191}$, and that of isotopic abundances of the respective nuclides. 4 Numbers in the column CI are the CI average values from Anders & Grevesse (1989).

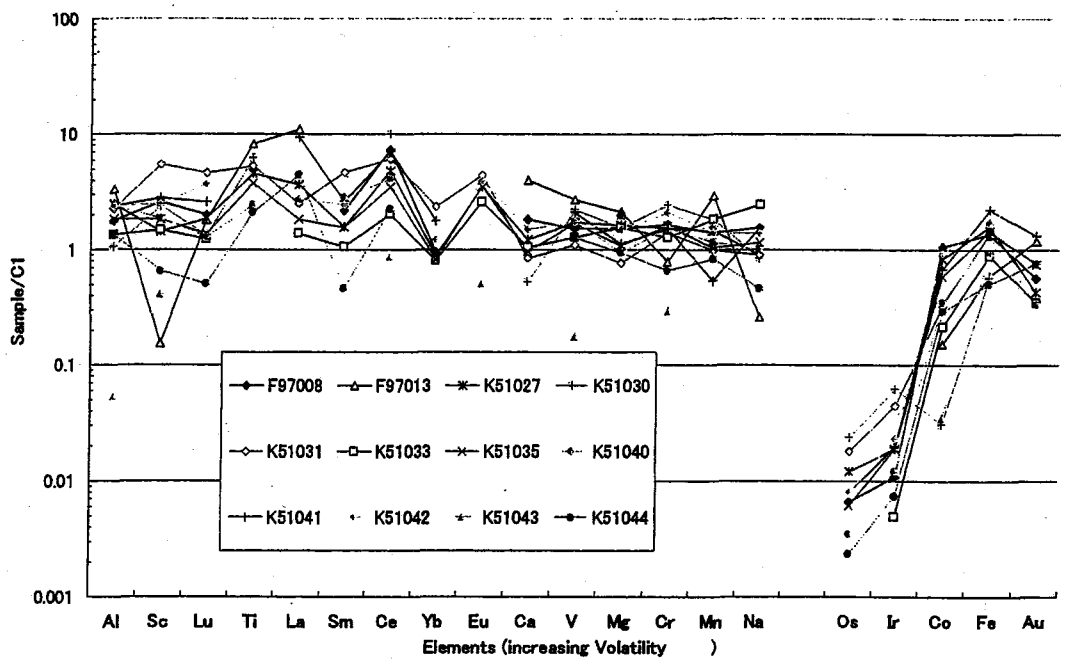

Fig. 1 Abundances of Elements normalized to C1

4-16

植物の葉等の季節変化等による特定元素の取り込み（Ⅱ）

Intake of specific element to plant leaves caused by seasonal variationAct

笠原　茂、増子　捷二、大西　俊之、関　興一
Shigeru Kasahara, Syouji Masuko, Toshiyuki Ohnishi, Koh-ichi seki
1）北海道大学ｱｲｿﾄｰﾌﾟ総合ｾﾝﾀｰ
Centyral Institute of Isotope Science、Hokkaido University

1．はじめに

リョウブ*Clethradeae*という科は、リョウブ属Clethaだけの科で、この科の植物は他の植物より一桁以上高いコバルト元素を特異的に集積することが報告されている[1]。リョウブ、クマイザサ、ユキザサ、ヤマモミジの葉に含まれる主な元素濃度、リョウブの葉に分布するコバルトの分布[2]、およびリョウブの枝、葉、総状果序における放射線の分布[3]、[4]は報告している。今回、金属元素がリョウブの枝にも葉と同様に集積するかどうか、および、季節変化によって葉に集積する量がどのようになるかを中性子照射で放射化して検討した。本報は、

a) リョウブの枝に含まれる亜鉛、セシウム、コバルトの量と分布を検討した。
b) リョウブの葉を季節ごとに採取して、葉に含まれる金属元素の量を検討した。

2．方法

1）リョウブの枝に含まれる亜鉛、セシウム、コバルトの量と分布

北海道大学植物園に生育しているリョウブの枝を採取し、以下の方法で測定を行った。

a) 枝採取後に、輪切り（写真１）直径２cm、厚さ１mm、板（写真２）横２cm、縦１cm,厚さ１mmに加工し、乾燥後重量を測定した。
b) ポリエチレン袋に枝を封入した。
c) 日本原子力研究所（ＪＲＲ－４）Ｔパイプ、で、中性子束密度６×１０^{13}n/cm^{2}sの条件で４０分間の中性子照射を行った。
d) 試料は１．５ヶ月間冷却後、ピュアゲルマ半導体検出装置により核種分析を行った。
e) 試料は１．５年間冷却後、イメージングプレート（Imaging Plate、以下「IP」）に露光して、バイオ・イメージングアナライザー（富士フィルムKK,BAS-5000）でIPを読み取り放射線の分布図を作成した。写真３、写真４に示す。

2）季節ごとの、リョウブの葉に含まれる金属元素の量

北海道大学植物園に生育しているリョウブの葉を６月、７月、１０月、１１月毎に採取し、以下の方法で測定を行った。

a) 葉採取後に、蒸留水で洗浄し、６０度で６時間乾燥し、重量を測定した。
b) ポリエチレン袋に葉を封入した。
c) 日本原子力研究所（ＪＲＲ－４）Ｔパイプ、で、中性子束密度６×１０^{13}n/cm^{2}sの条件で４０分間の中性子照射を行った。
d) 試料は１ヶ月間冷却後、ピュアゲルマ半導体検出装置により核種分析を行った。

写真１ リョウブの枝（輪切り）

JRR-４T-パイプ　放射化分析（環境）

写真２　リョウブの枝（板）

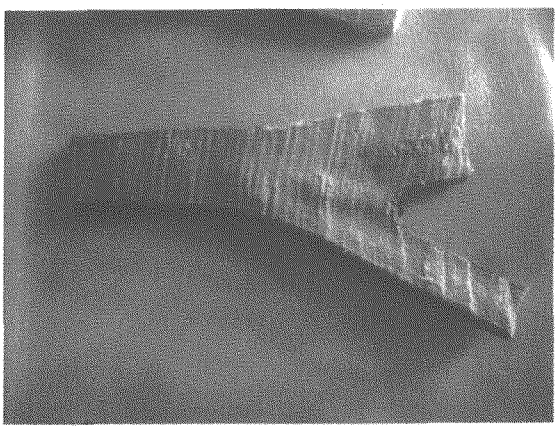

写真３　放射線画像（輪切り）

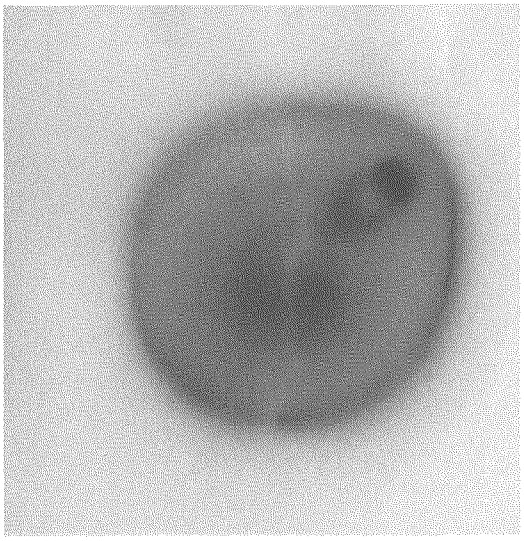

写真４　放射線画像（板）

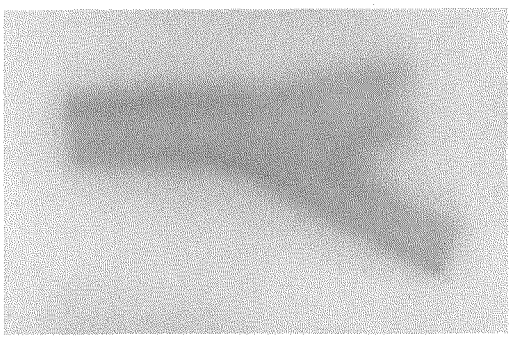

図1　亜鉛含有量

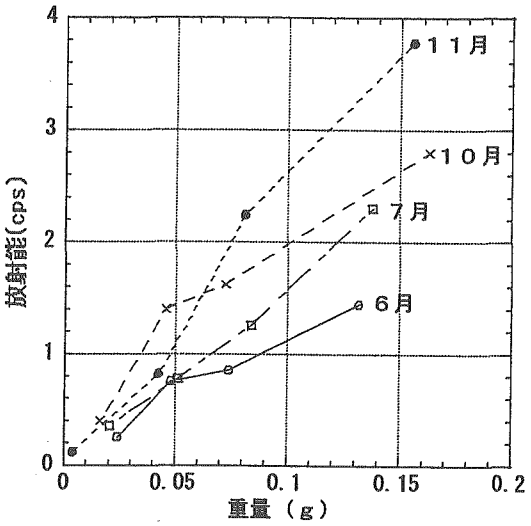

図２　コバルト含有量

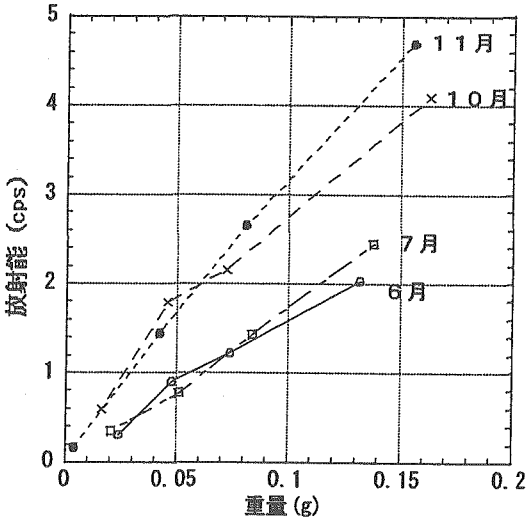

3）結果と考察

方法１）リョウブの枝に含まれる亜鉛、セシウム、コバルトの量と分布からは、枝の乾燥重量当たりで亜鉛：２６．３μg/g、セシウム：４．３μg/g、コバルト：０．９μg/gが得られた。これらの値は、環境標準試料（リョウブ標準試料の保証値（葉の乾燥重量当たり

で亜鉛：３４０±２０μg/g、セシウムは参考値：１．２μg/g、コバルト：２３±３μg/g、））との比較から、亜鉛は葉の方に１３倍程多く、セシウムは枝の方に３倍程多く、コバルトは葉の方に２５倍程多くなっていることが分かった。枝に含まれている亜鉛、セシウム、コバルト等の分布状態は、デジタルカメラで撮影した写真１リョウブ枝（輪切り）とイメージングプレートに露光して得た放射線画像写真３放射線画像（輪切り）を比較することで枝の外樹皮に多く、それより内部は少ないことが分かった。また、特に中心から右上４５度方向に見える節の部分に多く分布することが分かった。また、写真２リョウブの枝（板）と写真４放射線画像（板）を比較することで外樹皮が多く、中心部は少ないことが同様に確認できた。

方法２）季節ごとの、リョウブの葉に含まれる金属元素の量は、特に亜鉛、コバルトに注目した。葉を採取する季節は、６月、７月、１０月、１１月とし、葉の成長（乾燥重量）と含有量を放射線の量で比較した。その結果から、同月に採取した葉への亜鉛、コバルトの含有量（放射能）は、単位重量当たり一定であることが分かった。６月、７月、１０月、１１月と季節が深まるにつれての葉への亜鉛、コバルトの含有量（放射能）は、単位重量当たり増加することが分かった。また、リョウブの葉をそのまま、葉の状態でエタノール抽出すると葉に含まれている亜鉛、セシウム、コバルトは抽出液にそれぞれ、３０～６０%、８～１２%、２～４%含まれることが分かった。この結果を踏まえて、リョウブの葉に分布しているコバルトの定性、形態について解明していく予定である。

謝辞

この実験にあたり、貴重な試料を提供して頂いた、北海道大学北方生物圏フィールド科学センター植物園簾内技術専門職員、大野技術専門職員および試料調整等の技術指導して頂いた、大学共同利用開放研究室の澤幡氏、川手氏に厚くお礼申しあげます。

「微量元素」（山県　登　著）増子捷二、笠原茂、「原研施設利用共同研究成果報告書」平成９年度、71-76増子捷二、笠原茂、大西俊之「原研施設利用共同研究成果報告書」平成１２年度、140-1444）大西俊之他, Proceedings of the Third Workshop on Environmental Radioactivity, 163(2002)

4-17

人の爪試料中のセレンの放射化分析

Neutron Activation Analysis of Selenium in Human Toe-nail

関　李紀、大野智司、薄井利英
筑波大学　化学系
R. SEKI, S. Oono, T. Usui

研究目的

セレンは生体内に微量存在し、健康を保つために欠くことのできない必須元素として注目されている。

当初は毒性が多く報告されていたが、最近は発ガン抑止効果が認められ、セレンを含むサプルメントが市販されている。米国などでは健康や種々のガンなどの関係を明らかにするために多くの分析がなされている。

特に、ミズーリー大学のグループは人の足の爪の放射化分析を用いて行い、住んでいる地域とガン死亡率などとの間に負の相関関係があると報告している。この他に以前から土壌中のセレン濃度が高いことが知られているアメリカのサウスダコタ、逆に低いことが知られているニュージーランドで、居住者の足の爪を測定し住んでいる地域によって足の爪のセレン濃度に違いがあることが示されている。この結果を日本で比較するためには、日本におけるバックグランドを知る必要がある。

本研究では、日本国内の各地において健康な人の足の爪を集め、中性子放射化分析で日本人のレベルを求めることを目的とした。比較のために、日本以外居住する人およびセレンを日常的に扱っている研究者の試料も分析した。

通常、セレンの放射化分析は半減期の長い ^{75}Se を測定する方法が行われているが、日本原子力研究所の JRR-3 の気送管では半減期の短い核種の測定に適したシステムが装備されており、バックグランドも非常に低く抑えることができるので、本研究ではこのシステムの有用性も調べた。

表　1　試料提供者内訳

	総数(人)	男性(人)	女性(人)
全員	299	193	106
20歳未満	38	24	14
20歳以上30歳未満	103	69	34
30歳以上40歳未満	47	39	8
40歳以上50歳未満	37	20	17
50歳以上60歳未満	29	14	15
60歳以上	36	21	15
青森	15	9	6
福島	6	3	3
茨城	72	54	18
北関東（埼玉・栃木・群馬）	61	29	32
南関東（東京・千葉・神奈川）	32	21	11
東海(愛知・静岡)	11	8	3
北陸(石川)	9	6	3
関西(大阪・兵庫)	11	9	2
九州(長崎・熊本・福岡)	31	19	12

研究施設：JRR-3
研究分野：環境科学、放射化分析

実験方法

分析試料：日本全国の放射化学研究者、環境放射能研究者を中心として、その家族など本研究に協力された約300人と北京、台湾で集められた足の爪を用いた。

試料の洗浄：約50mg以上の足の爪をアセトン、超純水（Mili-Q system）で超音波洗浄した後、24時間凍結乾燥した。

標準試料：原子吸光用の1000ppm標準溶液を希釈し、精秤して作成した。

放射化分析：用いた反応は$^{76}Se(n,\gamma)^{77m}Se$で、$^{76}Se$の同位体存在度は9.37%、熱中性子放射化断面積は22bで、生成した^{77m}Seの半減期は17.36秒で161.9keV（53.2%）のγ線を測定した（日本アイソトープ協会のアイソトープ手帳（10th edition））。日本原子力研究所の原子炉JRR-3の気送管PN-3で、20秒照射した後、8秒後にGe検出器で30秒間測定した。PN-3の熱中性子束は$1.5\times10^{13}n/cm^2/sec$である。

比較標準物質：NBS1566（Oyster tissue）を用いた。

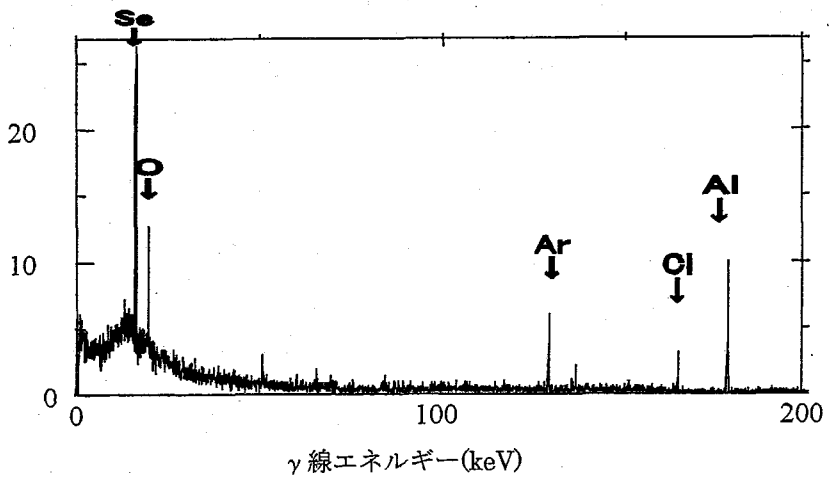

図1　人の足の爪の中性子照射後のγ線スペクトル

研究結果

足の爪試料を20秒照射した後、8秒後の代表的なγ線スペクトルは図1のようになり、妨害となるγ線はほとんどないことがわかった。検出限界は爪の重量として30mg程度で、セレン含有量が少ないために検出限界となる試料はなく、爪の量が不足しているために検出限界以下となる場合があった。

比較標準物質のNBS 1566のセレン濃度は文献値2.1±0.5μg/gに対し、2.2±0.2μg/gとなり、よく一致した。

測定結果を全体と男女別、年齢別、居住している地域別に分類して表2に示した。またこの結果の分布を図2に示した。全データはほぼ正規分布となり、全試料の平均は0.95±0.17 ppmで、男性より女性のほうが一般に高い傾向があり、平均値で比較すると、男性0.91 ppmに対して女性が0.93 ppmとなり、この傾向はカナダでのデータと一致する。年齢別分布を見ると、年齢に対して大きな変化はなく、成長と共に体内濃度が変動する種類の元素ではないことが分かった。しかし、平均値は20歳以下では0.90 ppm、20歳代で0.92、30から40歳代で0.94と増加し、60歳以上では0.85 ppmと減少している。これはセレンの体内での役割や、代謝に関連していると考えられる。

足の爪の中のセレン濃度は地域によって多少差があるが、大きく外れる地域は見られず、本研究で分析した試料全体を1つの集団と考えて、他の地域と比較することとする。

また、本研究では、日本以外の国として、中国の北京在住および、台湾在住の人から足の爪試料を集めることができた。その結果、北京では試料数が男性12、女性2となり、そのセレン濃度の平均は0.49±0.15ppmであった。台湾では男性6、女性2で平均0.68±0.17ppmであった。

この他に実験で気体状のセレンを扱っている研究室の研究者の足の爪も入手したので、その分析も行った。その結果、同じ研究室内の居住者は平均

3.5±2.6ppmで、隣接する研究室のメンバーは0.76±0.08ppmとなり、セレンの摂取は非常に狭い範囲に限られていることが分かった。また当該研究室の実験者で、研究室から離れて1年を経過している研究者の足の爪を分析したところ 1.0±0.1ppm と通常のレベルであった。爪の再生時間は数ヶ月から半年とされているので、順調に回復していることもわかった。

これまでに報告されている諸外国の足の爪中のセレン濃度と今回得られた結果を表3にまとめた。カナダの4地域についてMorrisらの論文[1]によれば、地域差が認められるとしている。しかし、今回の研究から国内における地域差も同程度に得られたが、明確に地域差が認められるほどデータの精度は得られていないと考えている。しかし、日本と北京、台湾の差は明らかであり、その差はその地域の土壌中のセレンなどの環境因子を反映しているか、食習慣の違いを反映しているかどうかは不明であるが、地域、国などによって大きく変動するものであることがわかった。

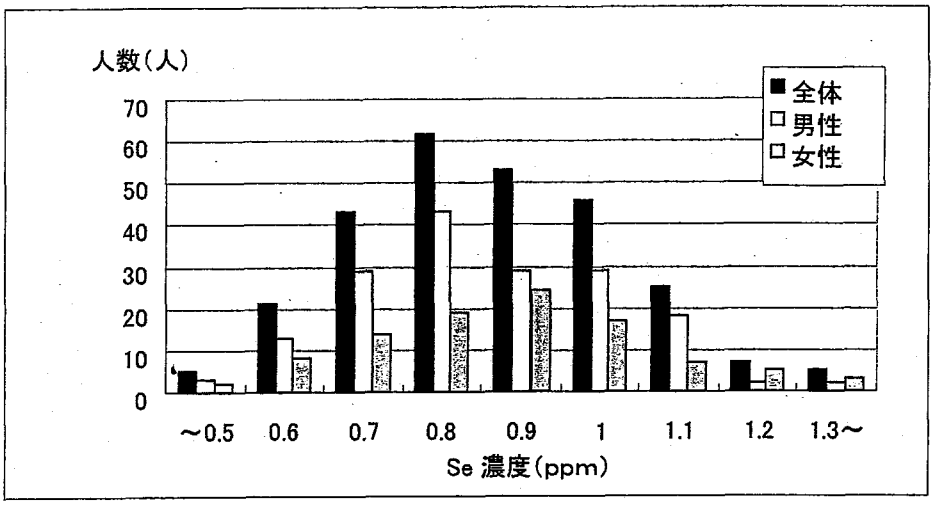

図2 足の爪のセレンの男女別濃度分布

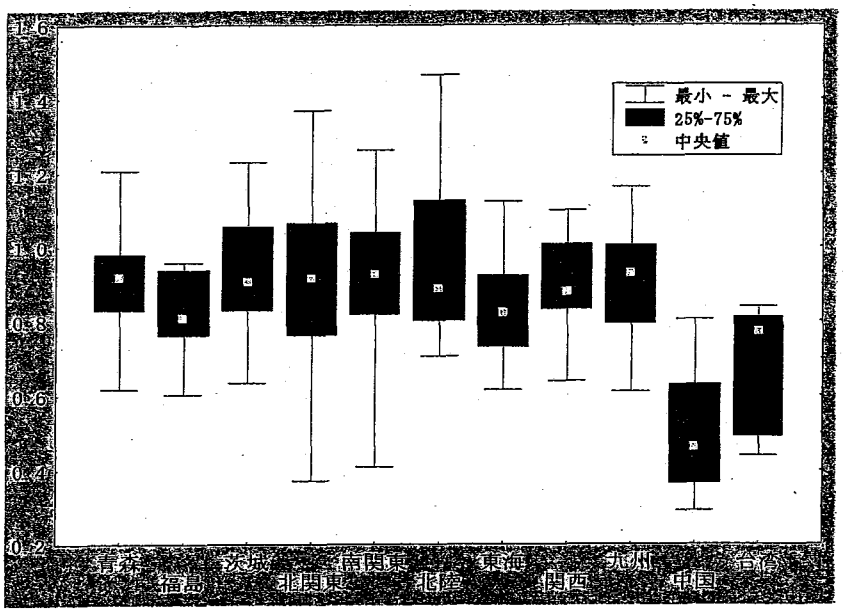

図3 足爪中のセレン濃度の地域別分布

表2 分析した足の爪中のセレン濃度（ppm）

	平均値	幾何平均	中央値	最小値	最大値	標準偏差	分散
全体	0.915	0.899	0.909	0.371	1.465	0.168	0.028
男性	0.905	0.891	0.891	0.409	1.228	0.159	0.025
女性	0.931	0.913	0.932	0.371	1.465	0.181	0.033
20以下	0.902	0.885	0.879	0.574	1.261	0.174	0.030
20代	0.918	0.901	0.925	0.371	1.278	0.165	0.027
30代	0.941	0.918	0.949	0.409	1.465	0.199	0.040
40代	0.941	0.926	0.909	0.597	1.368	0.173	0.030
50代	0.922	0.911	0.932	0.682	1.285	0.147	0.022
60以上	0.846	0.838	0.852	0.603	1.055	0.115	0.013
青森	0.915	0.906	0.919	0.616	1.206	0.128	0.016
福島	0.813	0.804	0.808	0.603	0.958	0.129	0.017
茨城	0.930	0.918	0.906	0.634	1.228	0.149	0.022
北関東	0.911	0.887	0.915	0.371	1.368	0.202	0.041
南関東	0.924	0.904	0.927	0.409	1.261	0.179	0.032
北陸	0.977	0.956	0.887	0.707	1.465	0.219	0.048
東海	0.837	0.823	0.823	0.616	1.122	0.161	0.026
関西	0.897	0.887	0.880	0.640	1.099	0.135	0.018
九州	0.911	0.901	0.931	0.611	1.161	0.136	0.019

表3 各国における爪試料中のセレン濃度（ppm）

	n	Se(ppm)			
Vancouver	167	0.97	±	0.18	ref.1
Edmonton	168	0.95	±	0.14	ref.1
Toronto	182	0.94	±	0.13	ref.1
Montreal	164	0.90	±	0.13	ref.1
Boston	9	0.74	±	0.13	ref.2
South Dakota	12	1.11	±	0.37	ref.2
Georgia	24	0.90	±	0.24	ref.2
New Zealand	14	0.26	±	0.09	ref.2
Sao Paulo	10	0.49	±	0.01	ref.3
Hawaii	285	0.98	±	0.10	ref.4
Japan	299	0.92	±	0.17	this work
Beijing	15	0.49	±	0.15	this work
Taiwan	8	0.67	±	0.17	this work

成果の公表

2003 日本放射化学会年会「人の足の爪の中のセレンの放射化分析」関　李紀、薄井利英、松広岳司、大野智司

2004 日本放射化学会年会発表予定「人の足爪試料中のセレンの放射化分析」大野智司、関　李紀

文献

１）J. S. Morris, T. Rohan, C. L. Soskolone, M. Lain, T. l. Spate, C. k. Baskett, M. M. Mason, T. A. Nichpls: Selenium status and cancer mortality in subject residing in four Canadian provinces. *J. Radioanl. Nucl. Chem.*, 249, (2001) 421-427

２）J.S. Morris, W. C. Willett, M. Stampfer: Utilization of Toenails as Dietary Selenium, *Trans. Am. Nucl. Soc.* (1983) 44, 25-26

３）A. R. Aguir, M. Saiki: Determination of trace elements in human nail clippings by neutron activation analysis. *J. Radioanl. Nucl. Chem.*, 249, (2001) 413-416

４）M. M. Mason, J. s. morris, V. l. Spate, C. K. Baskett, T. A. Nichols, T. l. Horsman, L. Le Marchand, L. N. Kolonel, S. Yukimoto: Comparison of whole blood, plasma and nails as monitors for the dietary intake of selenium, *J. Radioanl. Nucl. Chem.*, 236, (1998) 29-34

5)NBS 1566 成績表

4-18

中性子放射化分析法による環境試料中の微量元素の分析

Neutron activation analysis of trace elements in environmental samples

相沢省一（群馬大学工学部）

S. Aizawa (Faculty of Engineering, Gunma Univ.)

1. はじめに

金属鉱山からの鉱石採掘やその精錬過程によって環境中に放出された重金属元素による河川の水質汚濁現象は昭和30年代から40年代にかけて日本各地で見られ、大きな社会問題となった。しかし昭和46年（1971年）に施行された「水質汚濁防止法」などを契機に重金属元素による水質汚濁は減少し、最近では環境問題で騒がれることも無くなった。しかし鉱山跡の鉱屑堆積場からは降雨などによって現在でも重金属元素が溶出し、河川を汚染させている場合がある。そのため河川水の重金属汚染をモニタリングすることは今日でも重要なことである。今回、河川中に生息するトビケラ中の重金属元素を定量することで、河川の重金属汚染を明らかにできるか否かを検討した。

淡水系の代表的な水生昆虫であるトビケラは、体内に特定の重金属を濃縮するという性質を持つと言われている。トビケラは藻類をエサとしており、幼虫で3～4cmほどに成長する。世界中のどこにでも生息し、川底の小石の下に巣を作り、幼虫は1年間通して採取可能である。河川水中の重金属元素濃度とトビケラ中の重金属元素含量との間に何らかの関連を導き出すことができれば、汚染の影響をより顕著に示すことが可能になる。重金属汚染環境指標生物としてのトビケラの有用性を明らかにすることを目的に、トビケラ中の微量重金属元素を中性子放射化分析法で定量した。

2. 実験

群馬県桐生市近郊を流れる桐生川と、かつて足尾周辺からの銅公害で有名な渡良瀬川の2河川からトビケラ(約30匹)を年間通して1ヶ月に約2回ずつ採取した。サンプリング地点はいずれも桐生市内で、渡良瀬川は相川橋付近、桐生川は群大工学部周辺の天神橋付近で採取した。トビケラは採取した後、イオン交換水で洗浄し、冷凍庫内で保存した。12時間かけて凍結乾燥後、メノウ製乳鉢で粉末化し、分析用試料とした。

試料への中性子照射及びガンマ線の測定は以下に示す条件で行なった。照射試料は群馬大学工学部内のR.I.実験室に持ち帰り、キャンベラ社製(Genie2000)及びセイコーEG&G社製(Maestro)マルチチャンネルアナライザーでガンマ線測定及びスペクトル解析を行なった。ろ紙に定量目的元素を一定量しみ込ませたものを基準に定量し、同時に照射した標準試料（JLk-1：湖底堆積物）で値の正確さをチェックした。Table 1には定量に用いた核種とそのγ線エネルギー値を示した。

Sm-153からLa-140までは中寿命測定、Ce-141

JRR-4 ガンマ線スペクトロメトリー

環境試料放射化分析

以下は長寿命測定で計測した。

試料質量：約 0.1g/個
（ポリエチレンで三重にシール）
照射日：2003 年 11 月 28 日、同 12 月 18 日
2004 年 1 月 23 日
原子炉：原研 JRR-4
照射設備： T パイプ
出力：3.5MW
照射時間： 10 分

	中寿命	長寿命
冷却時間	3-4d	30-40 日
計測時間	1-2 h	12-24h

Table 1 定量に用いた核種とそのγ線エネルギー値

核種	keV
Sm-153	103.2
As-76	559.2
Na-23	1368.4
K-42	1524.7
La-140	1595.4
Ce-141	145.4
Pa-233	311.8
Cr-51	320.0
Eu-152	344.2
Ba-131	496.4
Cs-134	795.8
Sc-46	889.4
Rb-86	1076.6
Fe-59	1098.6
Zn-65	1115.4
Co-60	1173.1
Fe-59	1291.5
Co-60	1332.4

3. 結果及び考察

Table 2 及び Table 3 に渡良瀬川及び桐生川から採取したトビケラ中の元素含量の定量値を示した。両表の下部に記載した平均含量を比較すると、Na や K 含量は両河川でほぼ同程度の値であり、Fe は 20%ほど桐生川よりも渡良瀬川の方が高い。しかし桐生川よりも渡良瀬川で Zn や Cr、Co、Th などは約 2 倍高く、As は約 3 弱倍高い。原子吸光分析法で求めたトビケラ中の Cu 含量は桐生川（平均 Cu 含量：34μg/g）に比較して渡良瀬川（平均 Cu 含量：260μg/g）で約 9 倍高いが、両河川で生息するトビケラ中のこれら重金属元素含量の差異は明らかに渡良瀬川の上流でかつて稼動していた足尾銅山に起因するものと見なすことができる。なおこれら重金属元素含量は季節変動している傾向が標から見られる。Fig.1 は両河川から採取したトビケラ中の As 含量を縦軸に、横軸に採取日をとってプロットし、元素含量の季節変動を調べた結果である。元素によって差異はあるものの、他の重金属元素も冬季に比較して夏季から秋季に含量が多くなる傾向が見られ、季節変動が確認できる。しかも桐生川に比較して渡良瀬川で季節変動が大きい傾向が認められる。これは夏場になると気温が上昇することと、台風や雨により河川の流量が増加することによって、上流から鉱屑中の重金属成分がより多く溶出するためと考えられる。

4. 結論

- 桐生川に比べて、渡良瀬川では生息するトビケラ中の重金属元素含量が高い。これは渡良瀬川では足尾周辺からの重金属元素の汚染が現在もなお認められことを示し、トビケラが汚染環境指標生物としての有用性であることを示唆している。
- トビケラ中の重金属元素含量には季節変動が見られ、夏季から秋季に含量が増加し、冬場になると減少していく傾向にあることが確認された。環境モニタリングとしてトビケラを用いるにはこの季節変動因子を考慮し、河

Table 2 渡良瀬川から採取したトビケラの元素含量(μg/g)

試料No.	採取日	Na	K	Rb	Cs	Ba	Fe	Cr	Zn	Co	As	Th	Sc	La	Ce	Sm	Eu
W-01	2002年4月14日	5280	17100	20.8	4.0	120	5560	15.2	276	13.6	9.3	1.2	1.9	3.3	7.3	0.71	0.14
W-02	2002年5月22日	4330	13700	13.6	0.86	92	3990	10.4	215	9.1	6.0	0.75	1.4	2.1	4.6	0.46	0.085
W-03	2002年6月19日	8100	21400	30.5	2.0	197	10800	26.2	436	19.1	17.5	1.8	3.6	5.7	12.2	1.20	0.26
W-04	2002年7月19日	6640	17300	30.3	2.2	181	6790	12.3	204	10.8	12.6	2.0	2.5	5.4	11.3	1.20	0.25
W-05	2002年7月31日	5160	16900	25.5	1.4	142	5610	6.7	208	17.7	10.9	1.3	2.0	3.5	7.8	0.74	0.15
W-06	2002年8月15日	4840	13700	23.8	1.3	129	6570	12.3	199	9.4	8.3	1.2	2.3	3.2	7.0	0.68	0.15
W-7	2002年8月31日	6310	18200	19.7	1.5	162	8290	13.3	237	14.6	10.7	2.5	2.9	4.5	9.3	0.95	0.22
W-8	2002年9月20日	5460	14500	11.8	0.81	123	4750	5.4	159	5.9	6.6	0.72	1.7	2.3	4.9	0.51	0.12
W-9	2002年9月30日	4950	13200	15.6	0.88	103	4130	6.8	164	5.2	6.0	0.77	1.4	2.1	4.5	0.45	0.096
W-10	2002年10月17日	6640	19300	32.3	2.3	204	9470	23.5	190	13.2	13.7	1.96	3.3	5.8	11.9	1.20	0.25
W-11	2002年10月30日	6900	19100	29.8	2.2	200	9150	12.5	208	13.6	16.5	2.0	3.2	5.6	11.6	1.15	0.24
W-12	2002年11月18日	5480	18900	17.2	1.1	157	4250	3.7	189	10.2	12.0	1.0	1.4	2.8	5.8	0.56	0.11
W-13	2002年11月29日	5570	17000	20.3	1.1	118	4680	12.4	207	8.6	13.1	1.0	1.5	2.7	5.6	0.60	0.091
W-14	2002年12月16日	5150	16900	16.6	1.2	97	4100	6.9	187	9.0	12.4	0.86	1.4	2.5	5.3	0.52	0.10
W-15	2002年12月31日	5380	14000	16.2	0.95	106	4020	6.6	122	8.7	8.6	0.76	1.3	2.1	4.3	0.43	0.11
W-16	2003年1月16日	5440	14400	14.5	0.63	106	2700	5.2	157	6.8	6.1	0.54	0.89	1.5	2.9	0.29	0.085
W-17	2003年1月31日	5570	12600	13.5	0.59	55.7	3410	7.7	154	8.3	4.7	0.43	1.3	1.3	2.8	0.27	0.077
W-18	2003年2月7日	5760	23400	13.6	0.61	97	2410	6.3	149	8.5	5.0	0.4	0.72	1.4	2.2	0.25	0.056
平均		5720	16800	20.3	1.4	133	5600	10.7	203	10.7	10.0	1.2	1.9	3.2	6.7	0.68	0.14
標準偏差		890	2990	6.8	0.85	42	2430	6.1	68	3.9	3.9	0.62	0.85	1.5	3.3	0.33	0.069

Table 3 桐生川から採取したトビケラの元素含量(μg/g)

試料No.	採取日	Na	K	Rb	Cs	Ba	Fe	Cr	Zn	Co	As	Th	Sc	La	Ce	Sm	Eu
K-1	2002年4月14日	2510	9540	4.6	0.25	52	1010	1.6	71	1.4	1.8	0.13	0.41	0.50	0.70	0.12	0.025
K-2	2002年5月22日	3570	15000	8.5	0.57	125	3000	5.5	109	3.3	3.8	0.43	1.2	1.4	3.0	0.33	0.086
K-3	2002年6月19日	6410	19800	13.1	0.85	232	3550	5.5	162	5.1	3.2	0.54	1.4	1.8	3.8	0.41	0.10
K-4	2002年7月19日	7980	24500	22.8	1.9	187	7210	12.3	157	8.6	4.0	1.3	3.0	4.1	8.6	0.99	0.27
K-5	2002年7月31日	6450	21000	27.2	1.7	262	7960	13.3	142	9.1	5.4	1.2	3.2	4.2	8.7	0.98	0.26
K-6	2002年8月15日	4540	16100	17.7	1.4	196	6440	9.8	111	5.9	4.7	0.8	2.8	2.9	6.2	0.69	0.19
K-7	2002年8月31日	5940	18800	15.4	1.3	262	6350	8.6	123	5.5	3.7	0.87	2.2	2.6	5.3	0.63	0.16
K-8	2002年9月20日	5690	15600	10.5	0.74	180	3440	4.7	120	2.8	2.0	0.43	1.2	1.5	3.0	0.39	0.091
K-9	2002年9月30日	7220	21000	14.8	1.3	284	7380	9.6	130	5.0	3.9	0.91	2.4	2.9	6.1	0.63	0.16
K-10	2002年10月17日	7520	23200	21.6	1.5	212	10600	14.8	142	6.9	4.2	1.1	3.5	3.4	7.2	0.79	0.23
K-11	2002年10月30日	6480	22500	17.2	1.1	225	6940	8.8	130	5.1	4.3	0.76	2.2	2.4	5.0	0.52	0.14
K-12	2002年11月18日	5600	20100	11.1	0.55	170	2870	4.0	105	3.4	5.3	0.34	0.93	1.1	2.2	0.25	0.054
K-13	2002年11月29日	5700	21000	11.1	1.3	176	4160	5.6	114	3.7	4.2	0.48	1.4	1.3	2.2	0.28	0.089
K-14	2002年12月16日	5760	19500	8.0	0.86	134	2850	4.2	101	2.9	3.6	0.43	0.88	1.1	2.2	0.30	0.058
K-15	2002年12月31日	5220	19100	7.6	0.62	134	3040	3.6	100	3.4	3.3	0.29	0.94	0.85	1.7	0.21	0.062
K-16	2003年1月16日	4620	17900	6.4	0.43	108	1600	2.5	89	2.3	3.0	0.24	0.53	0.76	1.4	0.15	0.041
K-17	2003年1月31日	5150	17000	7.6	0.45	95	2350	2.5	94	2.2	2.6	0.23	0.63	0.67	1.4	0.15	0.043
K-18	2003年2月7日	5600	16300	5.7	0.43	77	2500	2.7	103	2.2	2.3	0.20	0.71	0.63	1.3	0.14	0.036
平均		5660	18800	12.8	0.96	173	4630	6.6	117	4.4	3.6	0.59	1.6	1.9	3.9	0.44	0.12
標準偏差		1340	3530	6.4	0.49	67	2640	4.0	24	2.2	1.0	0.36	1.0	1.2	2.6	0.28	0.079

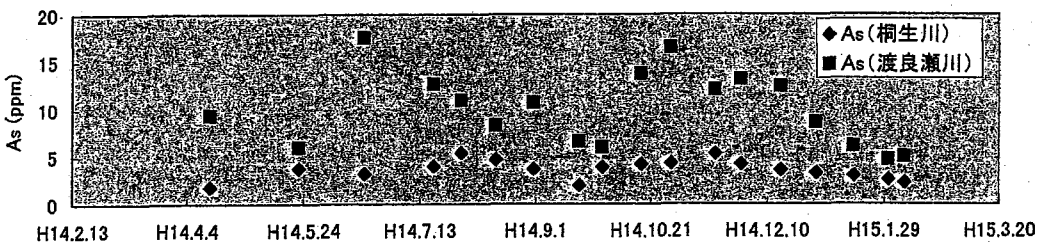

Fig.1 渡良瀬川及び桐生川から採取したトビケラ中のAs含量の季節変動

川間の重金属元素含量の差異を比較する際には同季節に採取したトビケラ試料を分析することが必要である。

成果の公表

無し

4-19

環境水の重金属汚染指標としてのメダカの有効性に関する研究

Study on availability of Medaka (*Oryzias latipes*) as an metal contamination indicator in waters

熊本大学理学部　百島　則幸
N. Momoshima (Faculty of Science, Kumamoto University)
熊本大学大学院自然科学研究科　豊嶋　孝浩、松下　力示
T. Toyoshima, R. Matsushita (Graduate School of Science and Technology, Kumamoto University)

1．はじめに

環境水の重金属汚染を評価するために指標生物を利用することにはいくつかの利点が挙げられる。まず、水中の重金属は生物濃縮されるので生物中の重金属濃度を分析する方が一般的に高感度である。水中濃度が時間変動するような場合でもある程度の時間平均として濃度を評価できる。すなわち生物が重金属に対して代謝時間に関連した体内濃度を持つ場合、変動する河川水の重金属濃度は時間平均されて体内濃度に反映されると考えられる。河川の水質を月平均あるいは季節平均として評価したい場合指標生物の利用は有効と言える。

環境試料の分析には様々な分析法が用いられるが、これらの多くは比較標準試料に含まれる元素しか定量できない。生物を環境指標として用いる場合、より多くの元素を定量することが望ましい。k_0放射化分析法は近年ヨーロッパを中心に盛んに用いられている分析法のひとつであり、目的元素ごとの比較標準試料を必要とせず多元素を同時に分析できるという利点を持っており、多数の未知元素分析が必要な環境科学の分野での利用が期待されている。

本研究ではメダカ（*Oryzias latipes*）に含まれる元素を河川水における汚染の環境指標として利用の可能性を調べた。メダカは東北以南の広い範囲に分布しており平野部を中心とする河川の下流域に生息していることから、比較的水質汚染に強い魚類の一種であると考えられている。また成魚になっても4cm程度であるため放射化分析において丸ごと一匹の分析が可能である。メダカのサンプリングは熊本県に河口がある第一級3河川（菊池川、白川、緑川）の水系で行った。白川水系ではメダカと同時にカダヤシ（*Gambusia affinis*）をサンプリングした。カダヤシは北アメリカニュージャージー州からメキシコを原産地とする小型淡水魚で、形態や生息域、食餌など生態的地位がメダカと似通った外来種である。本研究ではk_0放射化分析法によりメダカ及びカダヤシを分析し、陸水系の環境指標としての適応性を検討するとともに3河川間における元素濃度を比較した。

2. 実験

2.1. サンプリングと前処理

メダカ、カダヤシ試料は熊本県内の3河川（菊池川、白川、緑川）で毎月1回採取した。この3河川はそれぞれ違う水源（菊池川：阿蘇外輪山北西部菊池渓谷、白川:阿蘇カルデラ内部南郷谷及び阿蘇谷、緑川：熊本県中央部九州山地）を持っている。緑川は2001年7月から、白川と菊池川は2002年

4 月から採取を開始した。菊池川、緑川ではメダカのみ、白川ではメダカとカダヤシが採取できた。採取した試料は 1 時間以上イオン交換水中で泳がせた。このときイオン交換水は２～3 回交換した。試料をイオン交換水中から取り出し表面をイオン交換水で洗い流し、ろ紙で包んでシリカゲルの入ったデシケーター内で 5 日間以上放置し、乾燥試料を得た。乾燥試料はそれぞれ石英管あるいはポリエチレン袋に封入し、照射用キャプセル (PE) に詰めた。またキャプセルには石英管、ポリエチレンに封入した Au と Zr も詰めた。

2.2. 照射

照射は日本原子力研究所の原子炉 JRR-4 で低出力 (100kW あるいは 350kW) 及びフルパワー (3.5MW) で行った。低出力照射試料はポリエチレン袋に、フルパワー照射試料は石英管に封入した。照射日時と照射条件を表１に示す。

表１ 試料の照射日時と照射条件

日時	照射条件
2001 年 12 月	100kW 1h、100kW 2h
2002 年 6 月	100kW 1h、100kW 5h
2002 年 12 月	100kW 1h、100kW 5h、350kW 6h
2003 年 7 月	350kW 1h、3.5MW 3h

2.3. 測定及び解析

照射後東京大学原子力研究総合センター大学開放研究室の高純度ゲルマニウム半導体測定システムで測定した。解析支援ソフト「SAMPO90」、「KAYZERO/SOLCOI」を用いて解析した。

3. 結果と考察

3.1. k_0法の精度の検討

k_0 法の精度を確かめるために原子吸光用標準溶液をろ紙に染みこませたものと産業技術総合研究所地質調査総合センター（旧地質調査所）の岩石標準試料 JG-1 と JB-1 を低出力で照射した。標準溶液をろ紙に染みこませた試料は±20%以内で、岩石標準試料は±10%以内の精度で定量されたことから、k_0 法では概ね±20%以内で定量できることがわかった。

3.2. 検出される元素数と妨害核種

高濃度で試料に含まれ核反応断面積が大きい核種は、γ線測定において妨害を与える場合がある。環境試料では生成した Na-24 が測定時に妨害を与える場合が多いので、本研究では Na-24 の生成を低く押さえるため低出力照射を行った。低出力照射のもう一つの利点は安定した中性子フラックスが得られることである。低出力照射で定量された元素は 9 元素 (Na、K、Sc、Mn、Fe、Co、Zn、Br、Sr) であった。定量元素数が少なかった原因は、メダカ一匹が持つ情報を得るために基本的に一試料一個体としたため、供試料重量が不足したことと、低出力照射のために生成核種量が少なかったことが挙げられる。生物指標してメダカを利用するにはもっと多くの元素が定量される方が望ましい。そこでフルパワー3.5MW で 3 時間照射を行ったところ 16 元素が定量できることがわかった (Na、K、Ca、Sc、Cr、Fe、Co、Zn、As、Se、Br、Rb、Sr、Ba、Ce、Sm)。また、350kW で 1 時間照射の条件では 3 元素 (Na、K、Mn) が定量されたことから、合わせて 17 元素の定量が行えた。

3.2. 元素数の濃度範囲と河川間の比較

各元素の濃度範囲を図１に示す。平均濃度は、

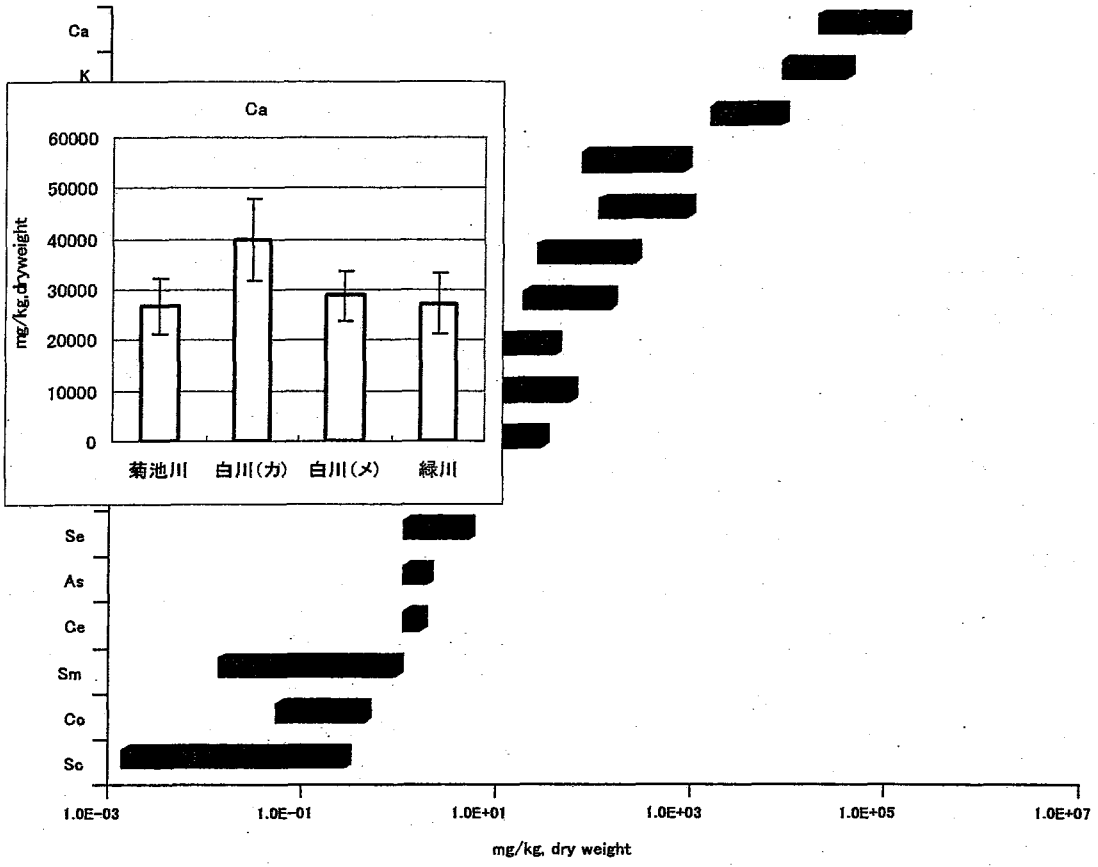

図２　Ca 濃度の比較、菊池川と緑川はメダカ
白川（カ）：カダヤシ、白川（メ）：メダカ

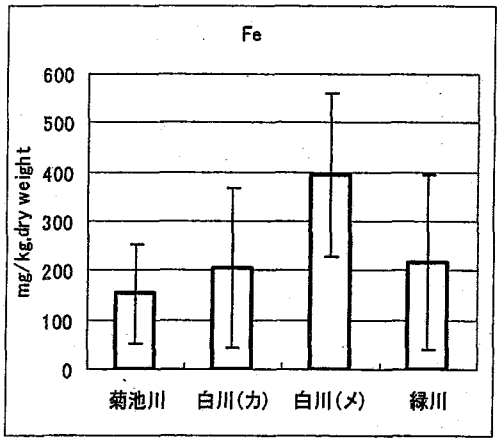

図３　Fe 濃度の比較、菊池川と緑川はメダカ
白川（カ）：カダヤシ、白川（メ）：メダカ

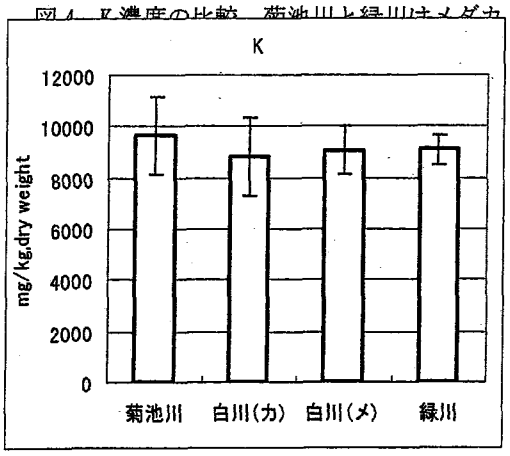

図４　K 濃度の比較、菊池川と緑川はメダカ
、白川（カ）：カダヤシ、白川（メ）：メダカ

Ca ＞ K ＞ Na ＞ Fe ＞ Zn ＞ Sr ＞ Mn ＞ Ba ＞ Rb ＞ Br ＞ Cr ＞ Se ＞ As ＞ Ce＞ Sm ＞ Co ＞ Sc の順であり、10^{-2}mg/kg－10^{4}mg/kg の範囲であった。

このように多元素を分析できるという点においてk_0放射化分析法は極めて有効である。

次に、各元素について河川間及びメダカとカダヤシの種間の差の有無についてｔ検定を行った。検定の結果、1）メダカとカダヤシの種間に違いがある、2）河川間での違いがある、また3）ほとんど差がない元素に分類することが出来た。白川のカダヤシとメダカの Ca 濃度には有意差があることが明らかになった（図2）。同様なことが Na と Br にも認められた。河川間の差がメダカの Fe 濃度に観察された（図3）。同様の傾向は Sc、Co、Zn、Se に認められた。種間および河川間に違いが認められなかった元素には K（図4）、Rb、Sr がある。

4．まとめ

k_0放射化分析法は環境試料分析に極めて有効であることが明らかになった。熊本県内の3河川系に生育するメダカに含まれる元素濃度には、有意に河川間で異なる値を示すものがあり、河川水の元素濃度とメダカの元素濃度の関係を暗示する結果が得られた。今後は、有意差が認められた元素の河川水中濃度の測定とメダカの餌と食餌行動の関係解析が必要となる。

5．成果の公表

学会発表

1） 豊嶋孝浩、百島則幸、k_0放射化分析法による環境試料の測定、第5回環境放射能研究会(2004).

2） 松下力示、百島則幸、熊本県に生息するメダカのk_0標準化放射化分析、平成14年度京都大学原子炉実験所専門研究会（2002).

3） 豊嶋孝浩、松下力示、百島則幸、熊本県に生息するメダカのk_0標準化放射化分析（2）平成15年度京都大学原子炉専門研究会（2003).

4） 松下 力示、百島 則幸、放射分析法によるメダカの分析、第39回放射線影響懇話会（2002).

5） 松下力示、百島則幸、k_0標準化放射化分析法を用いたメダカの分析、第46回放射化学討論会（2002).

6） 松下力示、豊嶋孝浩、百島則幸、メダカの多元素分析 −k_0法による放射化分析−、日本原子力学会九州支部、第21回研究発表講演会(2002).

4-20

植物試料の元素分析（II）
Analysis of the Elements in Plants (II)

飯倉寛、大矢智幸、林芳武、田野井慶太朗、中西友子
H.IIKURA, T.OHYA, Y.HAYASHI, K.TANOI, T.M.NAKANISHI
東京大学大学院農学生命科学研究科
Graduate School of Agricultural and Life Science, the University of Tokyo

1．はじめに

食の安全を図るため、現在、作物中の重金属蓄積を中心に元素濃度、特に可食部における特定元素の濃縮度に関して再検討が行われており、かつて公害問題発生時に設定された重金属の環境濃度基準ならびに細部データの見直しが必要な事態となってきている。

日本での公害病第一号と認定されたイタイイタイ病は神通川流域の Cd 汚染が主要因であることは有名であり、予防対策として流通される玄米中の Cd 含量を 1.0 ppm 未満に抑える制限がなされたのは昭和45年である。 近年、FAO/WHO 食品規格委員会合同の CODEX 委員会において農作物中の Cd 含量に 0.2 ppm 未満という基準設定が提案され、世界的な注目をあびている。 日本は Ni-Cd 電池に代表されるように世界有数の Cd 消費・生産国であり、特に鉱山下流域には高 Cd 汚染土壌が多く存在している中、農作物の可食部に含まれる Cd 含量を抑えるために様々な対応を迫られているのが現状である。

可食部の Cd 含量を抑えるため、「食の安全」を確保するため、土壌から植物（作物）中に移行される Cd の挙動を調べる事が重要である。 必須元素ではない Cd が植物体中でどのように流動するのであろうか。 また、土壌に含まれる Cd のうち植物が吸ってしまう Cd の形態（可給態 Cd）についても未だはっきりとした見解は得られていない。 他にも、Cd 吸着・蓄積により、植物がどのような応答をするのかも不明な点が多い。 Cd が存在することにより生じる必須元素の植物体中含量の増減を調べ、Cd と他元素との相関解析を行うことは、植物中の Cd 含量を抑えることに繋がると考えられた。 また、これらの応答に関して品種間差異について考察することも重要な要素である。

そこで、Cd 汚染土壌で生育させた作物中の各組織における元素濃度が経時的にどのように増減しているのかを放射化分析法を用いて調べた。 試料にはダイズを用い、おおすず・サチユタカ・納豆小粒・タチナガハ・スズユタカの 5 品種を用いた。

2．実験

試料のダイズは発芽させた後、ワグネルポット 1/5000 (a) に Cd 汚染土壌（黒ボク土）を 3 kg 入れ、2 本挿しで生育を行った。 植物体試料は開花期、子実肥大期、成熟期の 3 ステージにおいてサンプリングを行い、葉・茎・莢・種子に切り分けた。 根は植物根表面から完全に土壌粒子を排除することが困難な為、測定試料には加えなかった。 サンプリングした各組織試料は 60 度で 2 日以上乾燥させ、乾燥重量を測定した後、ミキサーにより粉砕し、粉末試料とした。 50～70 mg の粉末試料を高純度ポリエチレン袋に二重に封入し、放射化分析に供した。

放射化分析は、日本原子力研究所東海研究所の研究炉 JRR-3M で行った。 使用した設備は放射化分析用照射設備（PN-3）であり、熱中性子線束約 1.9×10^{13} n/cm^2・sec で 5 秒間照射した。 照射後の試料を 2 分間冷却した後、Pure Ge 検出器（キャンベラ製 GX1519）を用いて元素分析を行った。（測定時間は 150 秒間）

ピーク分析には SEIKO EG&G 社製 Spectrum navigator 2ED を用いた。 また、各元素の定量には 1014 (^{27}Mg)、1525 (^{42}K)、1809 (^{56}Mn)、3084 (^{45}Ca) keV を採用した。 なお、濾紙に各元素を一定量マウントしたものを標準試料として調製し、同様の条件下でγ線スペクトロメトリを行った。

研究施設：JRR-3M　装置：放射化分析装置　研究分野：植物生理学

植物試料中の Cd 含量の定量は、試料調整法は上記と同様に行い、照射時間を 20 min とし、^{115}Cd の 492keV および 528keV のピークを用いて測定したが、今回用いた 50～70 mg の植物試料からは十分なピークが得られなかったため、粉末試料を濃硝酸により酸分解し、濃縮後、ICP-AES による Cd 定量も同時に行った。

3. 結果

開花期・子実肥大期・成熟期の各ステージにおいて組織ごとにサンプリングし、定量分析を行った。右図では子実肥大期における各元素含量を示す。

まず、Mg 濃度は非汚染土壌（Soil A）と Cd 汚染土壌（Soil B）のそれぞれにおいて生育させた植物体組織中で、ほとんど濃度差異は現れなかった。 濃度は 2500～10000 ppm の値を示し、部位別には莢≧茎＞葉＞種子の順に高い濃度であった。 若干葉における Mg 濃度が Cd 汚染区において減少しているようにも思われた。 Ca 濃度は部位による濃度差が最も大きく、種子中は約 1500 ppm であるのに対し、茎や葉では 15000～20000 ppm もの濃度を示していた。しかしながら、Cd 汚染の影響は全く認められなかった。 また同様に K も Cd 汚染の影響はほとんど受けていなかった。 Mn は Soil A に比べ Soil B で生育させた植物体中の濃度が減少しており、その効果は主に葉において顕著に現れていた。

植物体中の Cd 濃度は Soil B で生育させた植物体中には茎＞葉＞種子＞莢の順に多く、スズユタカの茎では 1 ppm 近い濃度を示した。 品種間差異も他元素に比べ最も大きいと考えられ、種子や莢ではスズユタカ＞タチナガハ＞おおすず＞サチユタカ＞納豆小粒の順に多く Cd が蓄積していた。 今回用いた Cd 汚染土壌（Soil B）は実際に現在農作物を育成している土壌を用いたものである。 この土壌ではスズユタカ、タチナガハ、おおすずの 3 種の種子中（可食部）Cd 濃度は CODEX 委員会が提案する 0.2 ppm 基準値を上回っており、これらの品種を生育させる為には今後非汚染土壌による客土など、何らかの対応が必要となってくるであろう。

今回の測定では前述したように放射化分析法による Cd の検出は困難であった。Cd 含量は最大でも 1 ppm 以下であり、放射化分析用サンプルとして調整した 50-70 mg の試料中の Cd 絶対量は 50-70 ng 以下であったことが想定された。 従って、放射化分析法による Cd の検出感度は 50 ng 以下であることが実験結果からも推定された。 測定試料の重量を増やせば Cd の検出が可能であるとも考えられるが、Cd は通常の放射化分析法よりも即発γ線分析法を用いた方がより高感度に検出できることから、今後は即発γ線分析も併用しての測定を試みている。

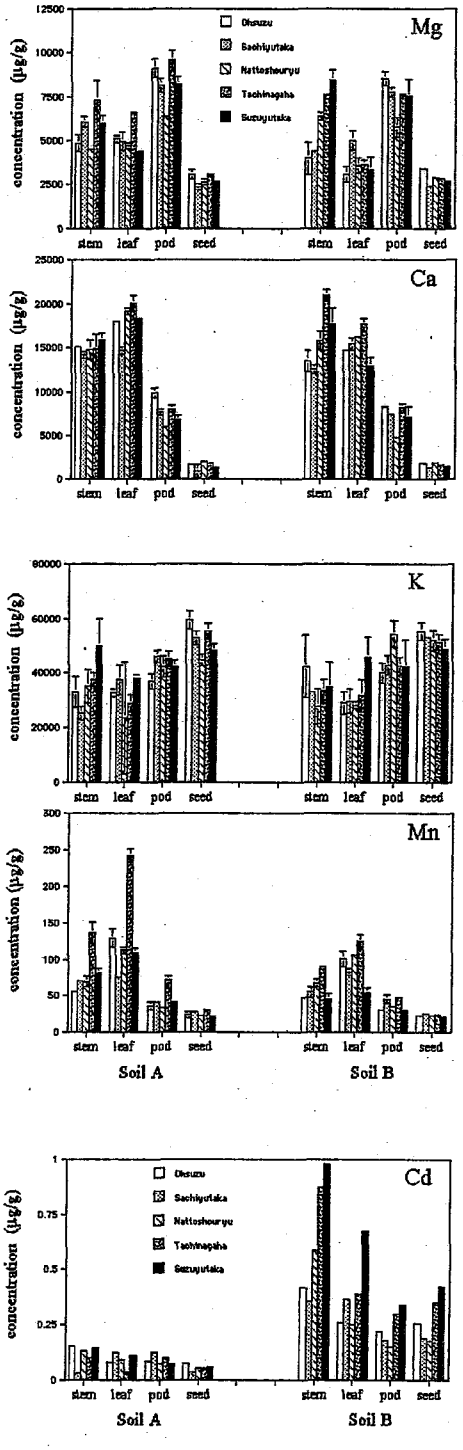

Soil A: 非汚染土壌　Soil B: Cd 汚染土壌
品種は左から、おおすず、サチユタカ、納豆小粒、タチナガハ、スズユタカ

Cd と相関のある元素として現在報告されているものとしては、正の相関があるとされるZn、負の相関があるとされるMnおよびCaがある。 今回の測定結果から、CdとMnの負の相関は顕著に現れていると考えられた。 Cdが植物体中に多く取り込まれることによりMn含量が減少、特に葉におけるMn減少が顕著であり、光合成機能の低下を引き起こし、生育不順につながったと考えられた。 また、Caは負の相関が想定されていたが、今回の結果からは特にCd蓄積の影響を受けているとは考えられなかった。 しかしながら、別に行った水耕実験から、水耕液中のCa濃度を増加させていくことにより、Cd障害の緩和作用が認められたことから（data not shown）CdとCaの相関は、Cd蓄積度の大小ではなく、Cd感受性・耐性に関わるのではないかと考えている。 これまでCdとMgとの相関については特に報告はなされておらず、葉におけるMgの若干の減少傾向は新しい知見として着目すべき点ではないかと考えられた。 またCaと同様に水耕実験において水耕液中のMg濃度を増加させていくことにより、Cd障害の緩和効果が認められたことから、CdとMgとの関わりについても今後研究を進めていく予定である。

4．おわりに

現在頻用されている元素分析手法は原子吸光法やICP-AES, ICP-MS等であるが、植物中の重金属を定量するにあたり、主に三つの理由で上記手法よりも放射化分析法の方が適していると思われた。 一つは、非破壊で他元素同時定量を行えること。 通例元素分析を行う場合、試料を酸分解し溶液濃度として定量を行うが、測定元素のコンタミネーションの可能性や微量元素定量の為の濃縮作業など、正確な定量を行うために様々な注意点や手間が生じる。比べて放射化分析法は試料をそのまま測定でき、濃度ではなく絶対量測定のため、超微量に含まれる元素を定量するためには試料の量を増やすだけでよい。二つ目は、試料中に含まれる目的元素以外の元素含有量の影響を受けないで定量できることであろう。生体試料中にはCa、KやMgが乾燥重量濃度として数千～数万ppmのオーダーで存在している。 これら多量含有元素と共に存在する数ppmオーダーの微量重金属を定量するにあたり、吸光法などは目的元素ピークが多量含有元素のピークに埋もれてしまい、正確な定量値が得られない場合がある。 比べて放射化分析法は複数の固有γ線スペクトルを持つ元素が多く、今回の報告でも多量に存在するCa, Mgおよびのピークが他の測定元素の定量に与える影響を考えなくても良い点は非常に有用であると言えよう。

5．成果の公表

Cadmium Effect on an Elemental Profile in the Edible Part of Soybean Plants Revealed by INAA.

H. Iikura, M. Katsu, Y. Takase, S. Yoshida, T. Ohya and T. M. Nakanishi

Journal of Radioanalytical and Nuclear Chemistry (JRNC). 2004, in press.

4-21
大気・海洋試料の放射化分析

Activation analysis of atmospheric and marine samples

永井尚生、松村　宏, 多田　亘（日本大学文理学部）
H.Nagai, H.Matsumura, W.Tada
College of Humanities and Sciences, Nihon University

1．はじめに

本研究の目的は大気エアロゾル中に含まれるFe,Al,Na,Ca,Mg などを中性子放射化分析により定量することであるが、大気中に生成する宇宙線生成核種 ^{7}Be(53d)および ^{10}Be(1.5×10^{6}y)の分布および地球表層における移動についての研究の一部であり、これらの微量成分の分析からは、エアロゾルの起源（大陸・海洋）についての情報を得るためである。

^{7}Be･^{10}Be は地球大気における宇宙線生成核種の中でも ^{14}C･^{3}H と共に濃度が最も高い核種のグループに分類され、高度分布・緯度分布・時間変化（季節変化、永年変動）を示す。これらの核種の地表・海面付近の分布及びフラックスは、大気中の移動の挙動に大きく支配される。^{14}C のように酸化され CO_2 として速やかに拡散し、ほぼ均一な分布を示す核種に対し、^{7}Be,^{10}Be は生成後酸化されエアロゾルとして（吸着して）大気中を移動するので、その分布は不均一であり、大気の動きに支配される。地表・海面付近の大気中の濃度分布は、これらの核種の大部分が、成層圏および対流圏上部で生成するので、特に垂直方向の大気の動きに支配されると考えられる。また、大気中から地表・海面へのフラックスに対しては雨水の影響が大きい。このように ^{7}Be,^{10}Be の分布及びフラックスは、多くの要因に支配されるため、年代測定などへの応用は簡単ではないが、物質移動についての情報が得られる可能性を持っている。これまでに主に太平洋における船舶上の観測データから、海洋直上の ^{7}Be,^{10}Be の分布は、赤道付近0-10°において極小値、南北両半球において、赤道に対してほぼ対称に20-30°付近で極大値、40-50°付近で極小値を示すという緯度分布が得られている。しかしながら船舶を利用する場合は時間変化（季節変化、永年変動）を観測することは困難であり、陸上で観測せざるを得ない。その場合、一度地表の土壌などに降下し、一定時間経過した後、壊変により ^{7}Be が減少し、相対的に ^{10}Be 濃度が高く ^{10}Be/^{7}Be の高い土壌粒子が再浮遊して、大気上層から移動してきたエアロゾルと混在して観測することになり、真の季節変化を観察することができない。そこでこのような土壌粒子の再浮遊の影響を元素分析から見積もることを試みた。

2．実験

1）試料

a)日本大学文理学部 5 号館屋上(東京都世田谷区、35.7° N 139.6° E)及び八丈島灯台(東京都八丈町、33.1° N 139.9° E)において、2002年1月からハイボリュームエアサンプラー(紀本電子工業製 AS-810)を用いてロ紙(Whatman41)上に大気エアロゾルを捕集した。試料採取は約1週間連続して行い、積算流量は日本大学(NA)で2000ー3000m^{3}、八丈島灯台(HA)で4000ー6000m^{3}であった。

b) 東京大学海洋研究所白鳳丸 KH03-1 航海（Leg 2-5, 2003/6-9、東部太平洋［ハワイーペルーータヒチー東京］）において、ハイボリュームエアサンプラー(紀本電子工業製 AS-1400)をアッパーデッキに設置し、ロ紙(Whatman41)上に大気エアロゾルを捕集した。試料採取時間は1ー3日、積算流量は1500ー4500m^{3}であった。

これらの試料は、まず非破壊で ^{7}Be(Eγ:477.6keV)、^{210}Pb(Eγ:46.5keV)のγ線測定を行った後、^{10}Be の加速器質量分析及び放射化分析に用いた。

2）放射化分析

東京及び八丈島の試料は1x1cm、KH03-1の試料は2x2cm のサイズにロ紙を切り取った、また標準試料として、同一のサイズのロ紙上に各元素の濃度既知の溶液を滴下し乾燥させたものを調製し、それぞれポリエチレン袋に二重封入し、JRR4 (3.5MW) 気

JRR4　気送管、地球科学試料放射化分析

送管において、１分間及び２分間照射を行った。照射時には Au をフラックスモニターとして全カプセルに同封した。照射した試料は照射後直ちに２台の Ge 検出器を用いて非破壊で 50 秒及び 300 秒測定を行った。

３．結果と考察

１）気送管中性子フラックスの安定性

Au フラックスモニターの測定結果から算出した気送管中性子フラックスの安定性を表１に示す。２日間で１０回ずつ照射を行ったが、両日とも午前中（1/22#1,2 および 1/23#1,2,3）の安定性が悪く、最大 19%平均値より低く見積もられた。それ以外の照射における中性子フラックスの安定性は良く、それぞれフラックスの変動は約 2%以内であった。また両日の平均値には約 4%の差があった。

２）海塩成分

３種類の未知試料のうち KH03-１および八丈島試料については海塩成分が主であることが予想される。図１に Na と Cl,Mg,Ca の相関を示す。Na と Cl の関係において、KH03-１試料は海水の組成と一致し、八丈島試料もかなり良い一致を示すが、東京試料は Na,Cl 濃度が低く Cl が過剰であった。KH03-１試料については、Mg,Ca についても海水の組成と一致したが、日大試料はどちらも過剰が認められた。

表１　JRR4 気送管における中性子フラックス（相対値、2004.1.22-23）

Irradiation No.	Relative neutron flux	Average /(Deviation)
2004.1.22 , 2min		
1	0.808 ± 0.015	(-19%)
2	0.921 ± 0.020	(-8%)
3	1.005 ± 0.023	1.000 ± 0.015
4	0.996 ± 0.025	
5	0.980 ± 0.028	
6	1.017 ± 0.031	
7	0.980 ± 0.032	
8	1.014 ± 0.034	
9	0.996 ± 0.035	
10	1.013 ± 0.037	
2004.1.23, 1min		
1	0.881 ± 0.036	(-8%)
2	0.913 ± 0.037	(-5%)
3	0.883 ± 0.036	(-8%)
4	0.983 ± 0.040	0.962 ± 0.020
5	0.980 ± 0.040	
6	0.988 ± 0.040	
7	0.958 ± 0.028	
8	0.954 ± 0.039	
9	0.948 ± 0.039	
10	1.000 ± 0.041	

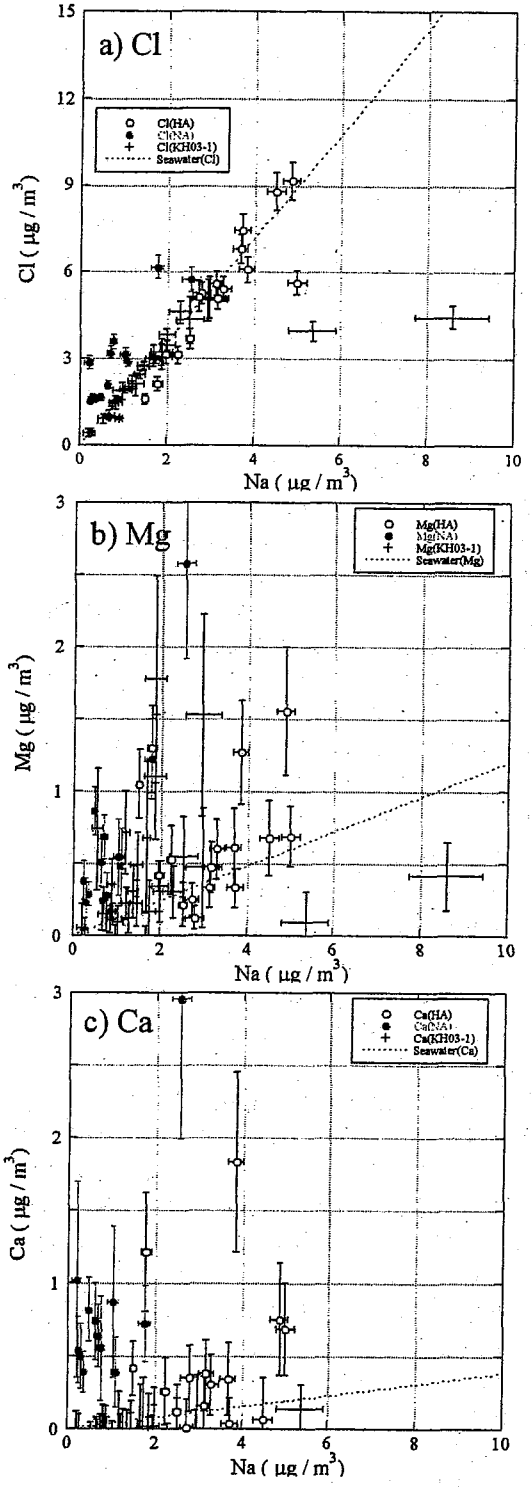

図１　大気試料（○八丈島、● 日大、＋KH03-1）における Na と a) Cl, b) Mg, c) Ca の相関

3）土壌粒子の寄与

土壌粒子の影響については、図2に示す Al と海塩成分の補正を行った Mg,Ca の相関から検討を行った。まず KH03-1試料は全ての試料において Al は検出限界以下であり、土壌粒子の寄与は認められなかった。八丈島試料は少数の試料を除いて Al, Mg,Ca は低濃度であり、土壌粒子の寄与は小さいと思われる。日大試料の大部分と一部の八丈島試料はは Al, 海塩補正 Mg,Ca 濃度から、土壌粒子の寄与が認められるが、Mg,Ca 共に日本列島の地殻の平均組成あるいは黄土堆積物の組成と比較して、過剰が認められた。この原因として、図1の東京試料において示されている Cl の過剰のように、都市における人為起源の寄与が考えられる。また、他の可能性として、Al の分析が不適切で、分析値は過小に算出されたことも考えられる。

4）土壌粒子の寄与

2002年における、八丈島及び東京で観察された大気中の ^{7}Be,^{10}Be 濃度と $^{10}Be/^{7}Be$ を図3に示す。、同じ時期の大気中 Al 濃度および海塩成分補正後の Mg,Ca 濃度を図4に示す。3月から6月にかけて ^{7}Be,^{10}Be 濃度、$^{10}Be/^{7}Be$ の全てに高い値となっている。これは生成速度が大で、滞留時間が長い成層圏エアロゾルの特徴を有しており、この時期に成層圏と対流圏間の大気の交換が盛んであることによるものである。一方この時期 Al,Mg,Ca 濃度もピークを示しており、土壌粒子の再浮遊の影響が大であることも考えられる。しかしながら再浮遊の影響を受けない ^{7}Be 濃度が高いこともあり、現段階では定量的な取り扱いには至ってはいない。再浮遊の影響を補正するためには、$^{10}Be/^{7}Be$ の値が低く一定している時期（例えば7−8月）における、八丈島と東京の差から見積もる方が有効であると思われる

4．今後の予定

今回の Al,Mg,Ca の分析結果においては、精度があまり良くなかった。これはブランクの補正が大きいことによるものであり、分析条件を検討する必要があると思われる。また、今回の分析試料以降に採取した試料について分析を行うと共に今回の分析試料のうち、必要な試料について再度分析を行い、土壌粒子の再浮遊の補正に必要なデータを得ることを試みる予定である。

［成果の公表］

Ⅰ．学会誌等

1. 永井尚生、山形武靖、山根尚子、大島　淳，"八丈島における ^{7}Be・^{10}Be の観測"（"Observation of ^{7}Be and ^{10}Be in Hachijo Island"), Proceedings of the Fourth Workshop on Environmental Radioactivity, 119-122 (2003)
2. H. Nagai, T.Yamagata, C. Saito and H. Matsuzaki, "Beryllium isotopes observed in Hachijo Island", Geochimica et Cosmochimica Acta, 67, A318 (2003)

Ⅱ．口頭発表

1. 永井尚生，"地球表層における誘導放射性核種の分布"，シンポジウム「海洋環境における放射能研究の現状と未来」，千葉　(2003.3)
2. 山形武靖、齊藤慶太、齊藤敬、永井尚生，"大気中の ^{7}Be、^{10}Be 濃度と同位体比の季節変動"，第5回環境放射能研究会、筑波 (2004.3)

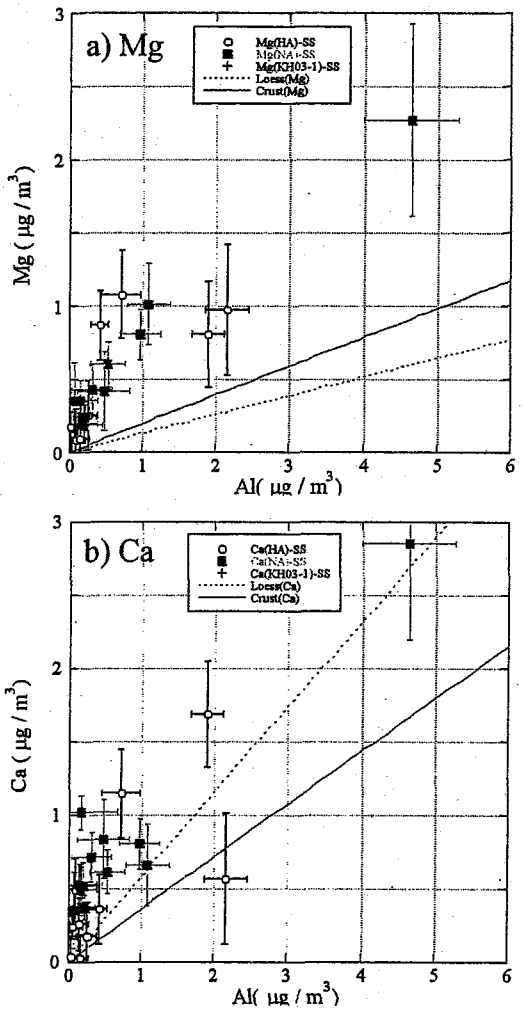

図２　大気試料（○八丈島、■日大、＋KH03-1）
における Al と海塩成分補正後の a) Mg, b)
Ca との相関

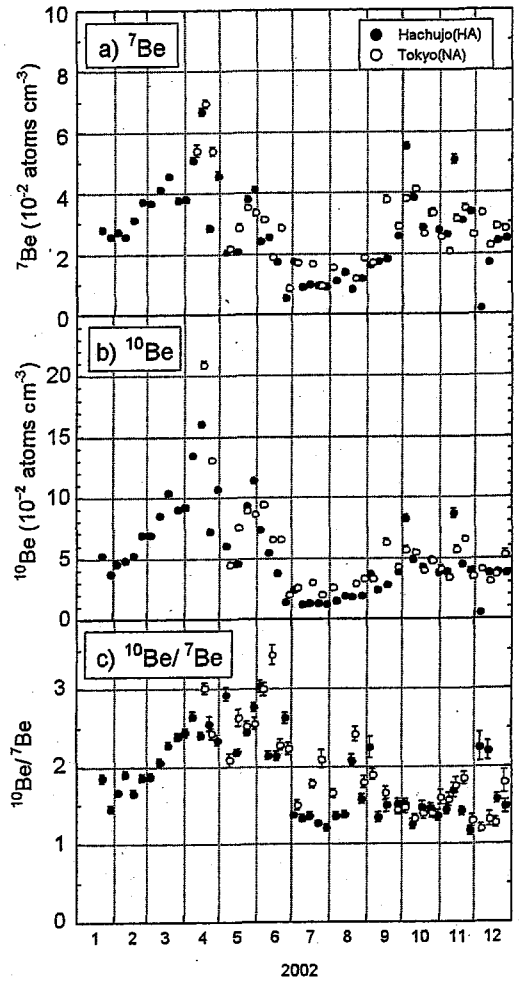

図3　2002年1月から2002年12月まで、八丈島（●）及び東京（○）で観察された大気中、a)^{7}Be濃度、b)^{10}Be濃度、c)^{10}Be/ ^{7}Be

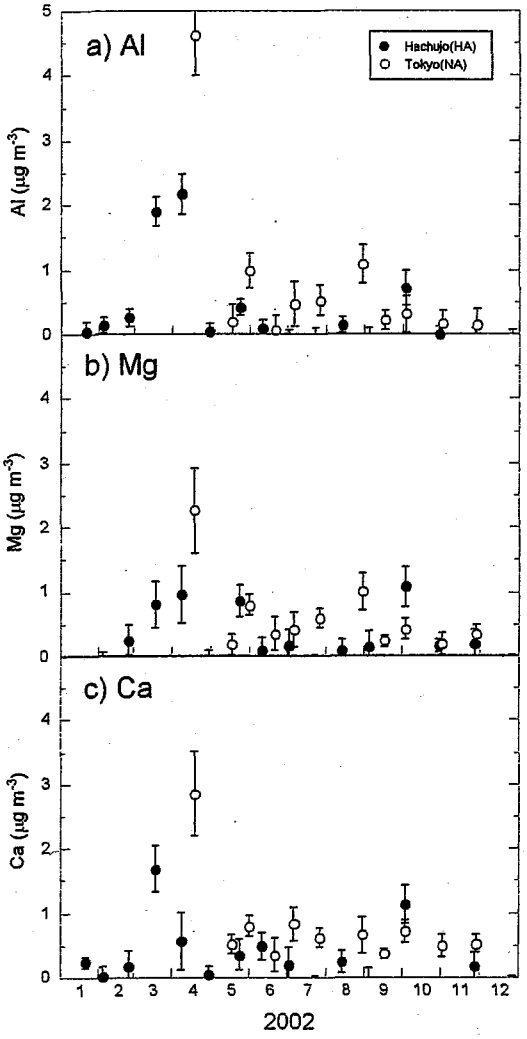

図4　2002年1月から2002年12月まで、八丈島（●）及び東京（○）で観察された大気中、a) Al濃度、b) Mg(海塩補正)濃度、c)Ca(海塩補正)濃度

4-22

中国南部のエルハイ湖とインドのサンバール湖で採取された堆積物コア試料の放射化分析

Neutron Activation Analysis of sediment core samples of Lake Erhai in southern China and a salt lake in India

豊田和弘・篠塚良嗣・三浦雅洋・森保友樹
(北海道大学・大学院地球環境科学研究科)
Kazuhiro Toyoda, Yoshitsugu Shinozuka, Masahiro Miura, Yuki Moriyasu
(Graduate school of Environmental Earth Science, Hokkaido Univ.)

【研究目的と報告試料の振替】本研究の目的は、ユーラシア大陸の中でモンスーンの影響の大きい地域の湖中央部で採取された、時間的に連続した堆積物コア試料を時間高分解能に無機分析することで、ここ数万年間の古環境変動、特にモンスーンに支配される気候変動についての情報を得るものである。本申請のタイトルにある、中国南部エルハイ湖とのインドのサンバール湖のコア試料についてはそれぞれ約１００試料ほど分析をおこなった。これらの試料データの検討会（国際日本文化研究センター主宰）は、豊田の米国での在外研究中に開催されたために、豊田はこれらの研究会での情報交換に参加することができなかった。そのため、現時点ではそれらのコア試料の分析値と花粉分析や年代測定値との比較による考察が十分になされてない。

一方、ヒマラヤ山脈南斜面のカトマンズ盆地で採取された全長２００m 以上のラビバーワンコアについてはこれまで年２回ほど九州大で研究会があり、情報交換を行ってきた。さらに、2004 年９月にも地質学会と地球化学会で共同研究者と会い、検討を行う事になっている。ラビバーワンコアについては既に約五百試料について放射化分析をおこなってきた。また学位修得を目的とした院生の研究テーマとして、モンスーンの影響の大きい中部日本の琵琶湖のコアについてもさらに細かい間隔で計六百試料について分析を行った。そこで、タイトルにあるエルハイ湖とサンバール湖のコア試料の研究成果については次回報告するとして、今回はネパールのカトマンズ盆地の掘削コア試料（過去７０万年分）解析と琵琶湖のコア解析（過去４万年分と過去８千年分）で得られた成果について報告する。

【分析法と本研究のテーマ】非破壊中性子放射化分析で長寿命核種を測定するために、当初は試料 100m g を高純度石英管に入れて封入していた。これらの試料を標準岩石とともにＪＲＲ4のＴ孔などで 100 分間ほど照射し、一カ月間冷却した後、日本原研の大学開放研の管理区域にて、化学実験室のドラフト内で試料を包装しなおした上で、ガンマ線計測器で１試料約３０００秒間測定していた。しかし、最近は試料をポリエチレンで３重に封入して並べた状態で、ＪＲＲ4のT孔などで水に浸けた状態で２０分間照射して冷却後、1試料約６０００秒間測定するようになってきた。定量した元素は Ce、Yb、Th、Hf、Sc、Co、Ta、Eu、Fe である。

JRR-4 、Tパイプ、γ線スペクトロメトリー、堆積物コア試料の放射化分析

これまでの一連の本研究の目的の一つは「花崗岩質の後背地を持つ湖で掘削された堆積物コア試料中の Th/Sc 比は過去の降水量の変動や地震などのイベントの指標になる」という作業仮説を検証する事である。Sc は粘土鉱物等に普遍的に含まれて水に不溶な元素である。一方、Th は花崗岩などに含まれるモナザイトやジルコンなどの風化残留性の重鉱物などに濃縮している。琵琶湖の１４００m掘削コア中のTh/Sc比の変動は、氷河期—間氷期のサイクルと同調しており（Toyoda, 2003)、過去４万年のピストンコア試料を粒度別に分離した試料の分析から、風成塵の寄与の変動よりも粒度の粗い重鉱物の寄与の変動によるという結果が得られている（shinozuka and Toyoda, 投稿準備中:データが複雑なので本報告書では記載を省略する)。ここでは詳しく気候変動のわかっている琵琶湖の過去４万年と、７０万年もの環境変動を記憶したカトマンズのコアについて、Th/Sc 比の変動と堆積環境の対応関係について検討した成果を報告する。

日本周辺で採取されたコア試料を用いて古環境変動を研究する上で、一番問題となるのは試料の年代測定値であり、年代が確定した広域火山灰層の存在が一番頼りになる。過去二百万年のもの間、日本に広く降下した火山灰はもちろんほとんどが日本の火山から噴出されたものだ。その例外としては韓国鬱陵島と朝鮮半島北部白頭山起源の火山灰がそれぞれ中央日本と北日本の広い範囲に降下した事が知られている。これらは大陸系のアルカリ岩質の火山から噴出されたため、その火山灰は日本の島弧火山のものとは全く異なる化学組成を持つ。タンタルやトリウムなどに著しく富み、スカンジウムなどが乏しいという特徴を持つ。従って、Ta/Sc 比を測定する事により、肉眼では判別できないようなわずかなアルカリ岩質の火山灰の混入を検出する事ができるはずである。広域火山灰近畿地方を中心に広く分布する U-Oki という記号で記載されるアルカリ岩質の広域火山灰は炭素１４年代で約９３００年程前（年稿暦年代では１万６５０年前）に鬱陵島から噴出したものとされている。しかし日本海のコアからは６０００千年前から２万３千年前には U-Oki を含めて３層の鬱陵島起源の火山灰が発見されて、どれが U-Oki に対比されるかという事が問題になっている（堂満ほか、２００２)。特に、その年代は最終氷河期の終焉の時期に近く、日本海へ対馬暖流が流入する時期とも近いため、それらの対比は学術的に大変重要である。そこで、琵琶湖のピストンコアで検証してみた。

【結果と考察】

❶ 琵琶湖ピストンコア中の Ta/Sc 比

１９９５年に琵琶湖中央部で採取された、４万年分のピストンコアから分取した約４００試料中の Ta/Sc 比を図１に、同じく１９９５年に琵琶湖中央部やや南の地点で採取された８千年分のピストンコアから分取した約１００試料中の Ta/Sc 比を図２に示した。琵琶湖中央部には２５０mの粘土層が切れ目なく堆積しており、過去４３万年間の堆積環境を記録している。この２つのコア試料中の Ta/Sc 比の値はほとんどは 0.05—0.12 の範囲に収まったが、例外は３層あることが図１からわかる。試料と童子に定量した標準岩石 JB-1a 中のタンタルの値の変動係数（１σ）は７%前後であることから、これらの異常値は測定値の誤差によるものとは考えられ

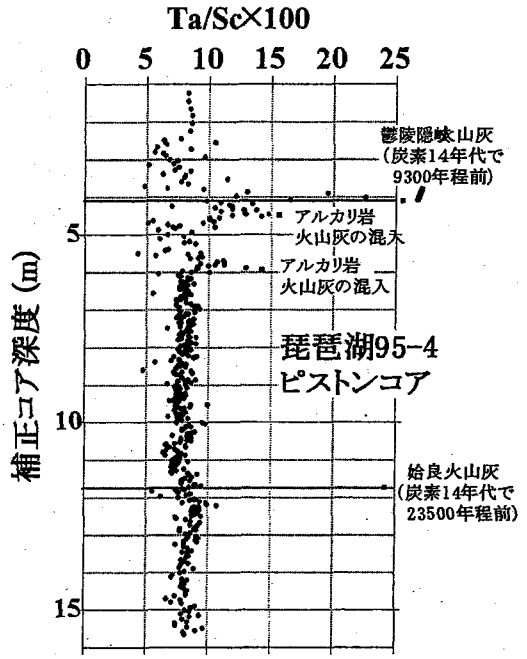

図1. 琵琶湖95—4ピストンコア試料中の
タンタル／スカンジウム比の垂直分布

ず、これら３層にはアルカリ岩質の混入があったものと結論できる。３層の一番上の層は鬱陵隠岐火山灰（U-Oki）と鑑定された層の直上で、この火山灰の一部が生物による撹乱で混入したためと考えられる。後の２つは鬱陵隠岐火山灰よりも数百年前と、三千年から四千年ほど前に、鬱陵隠岐火山から噴出した火山灰の混入が検出されたものと考えている。水月湖の年稿堆積物ピストンコアにもアルカリ岩質火山灰の混入によるものと考えられる Ta/Sc 比の高まりが同時期にいくつか得られており、それらの結果を学術雑誌「第四紀研究」に投稿準備中である。

❷琵琶湖ピストンコア中の Th/Sc 比

図１ではタンタル/Sc 比を示した４万年分のピストンコアについて、ここではそのコア中のトリウム/Sc 比の変動を見やすくするために、図３には補正コア深度１m－８m の Th/Sc 比の垂直

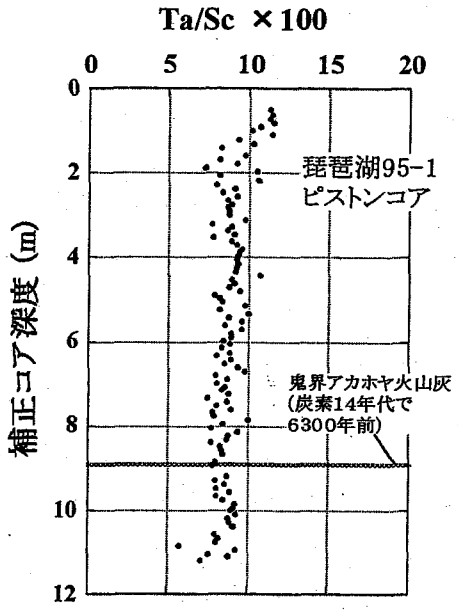

図2. 琵琶湖95—1ピストンコア試料中の
タンタル／スカンジウム比の垂直分布

分布を、図４にはその下部の補正コア深度８m－１６m の Th/Sc 比の垂直分布というように上下に

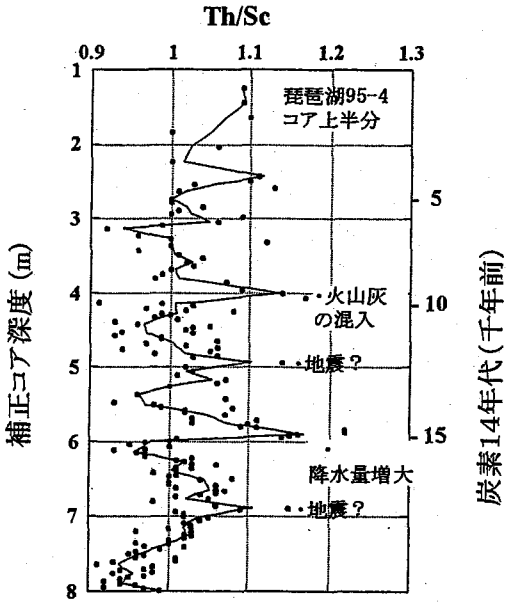

図3. 琵琶湖95—4コア上半分中の
トリウム／スカンジウム比の垂直分布

２つに分けて示した。日本では急激な温暖化に伴い洪水の頻度の急増が推測される。降水量の

急増に伴い、琵琶湖中央部までのトリウムに富んだ重鉱物の移送量が増えて、そのような環境変動のあった時代の堆積物には Th/Sc 比の高まりが記憶されるはずである。果たして、図３と図４中の Th/Sc 比の垂直分布において、約九千五百年前、約一万五千年前、約二万五千年前（いずれも炭素１４年代値で）などの Th/Sc 比のピークは最終氷期から後氷期への移行（ヤンガートリアスの終焉）、ベーリング・アレレード温暖期の始まり、ダンスガード・オシュガーサイクルによる急激な温暖化の時期に対応しているように思える。ただし、約九千五百年前の Th/Sc 比のピークは鬱陵隠岐火山灰の混入による可能性も高い。

Th/Sc 比の値が高くなるもう一つの原因として、地震により生じたタービダイトにより、斜面にたまっていた重鉱物が一気に湖中央部に輸送されたという機構も考えられる。その場合には１試料だけぽつんと Th/Sc 比が高くなると考えられる。そのような試料については他の化学成分からも乱泥流起源である証拠を探している。

さらに図５には１９９５年に琵琶湖中央南部の地点で採取された８千年分のピストンコアのトリウム/Sc 比の垂直分布を示した。図５の垂直分布で明瞭にわかるのは最近数百年間で Th/Sc 比が急激に増加している事である。安土桃山時代になると琵琶湖周辺の農村にも市場経済が訪れ、農民も貨幣を得るために夜なべ仕事に励むようになる。油は大変高価だったので、夜の明かりを得るために琵琶湖周辺の花崗岩質の山林の松林の根元を掘り起こし、松明として使用した。そのため琵琶湖周辺の山林はほとんどはげ山になってしまったと歴史書にある。そのために土壌流出が著しくなり、この数百年の間に重鉱物の混入量が急増して、それが近年の Th/Sc 比の急激な増大として表れたと考えている。なお、現時点ではこの 95-1 コアから５cm 毎に分取した測定試料をまだ３つおきにしか放射化分析をしていないので、切れ目なく約四百試料を分析した 95-4 コアのようには、Th/Sc 比の微細な変動の原因を考察する事は出来ない。

❸カトマンズ盆地の掘削コア

ネパール国のカトマンズ盆地で採取された全長約２００m 長のラビバーワンコアの層序と Th/Sc 比の変動を図６に示した。この湖の堆積盆

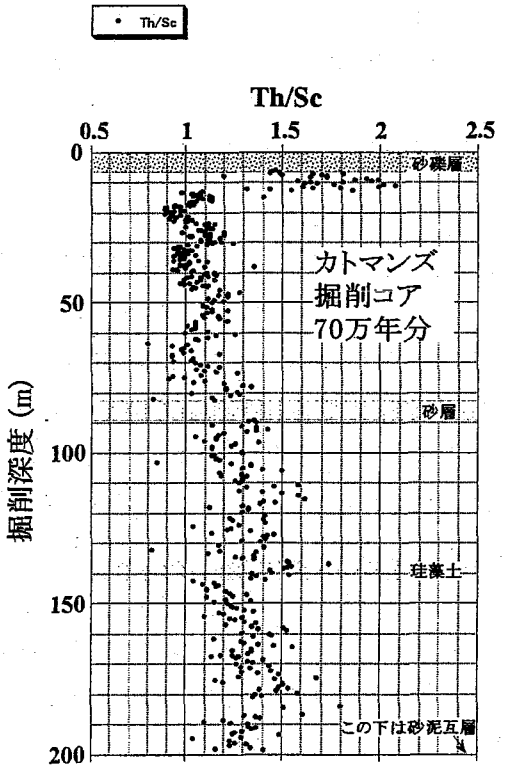

図6. ネパール国カトマンズ盆地ラビバーワン掘削コア中のトリウム／スカンジウム比の垂直分布

は７０万年以上前から発達を始め巨大な湖を形成したが、二十数万年前に突如干上がった。が、暫くすると再び新しく深い湖が生じた。恐く周囲の地殻変動で水の流出口ができたのが、すぐ

にふさがったのだろうか。一万五千年程前にはこの湖も埋まって現在の掘削地点は陸上であり隣にはネパールの首都カトマンズの町がある。図６を見ると、掘削深度１０m 付近に極めて Th/Sc 比の高い値が分布しているが、これらの試料は、湖中央部の粘土質試料ではなく湖周辺部の砂質試料だからである。これ以外の試料は粘土質の部分のみを分取してある。

深度１０m－４０m については５cm 長の試料を３つおきに分取した試料について、４０m 以深は１０個おきに試料を分析した。なお、この４０m までの測定値については前回の報告書で既に記載しており、今回は新たに４０m－２００m を分析している。この合計約４８０試料中の Th/Sc 比の変動を見やすくするために、図７には掘削深度１０m－９０m の新しい湖の Th/Sc 比の垂直分布と花粉分析による気候変動の対応関係を、図８にはその下部の掘削深度９０m－２００m の Th/Sc 比の垂直分布と花粉分析による気候変動の対応関係を示した。ただし花粉分析のデータもまだ確定したものではない。図７と図８から Th/Sc 比の変動と気候の寒暖は一部を除いてよい対応関係があるようにみえる。また、このコアの周辺から採取した約２０個の試料の化学分析値とも比較考察をおこない、これまで得られた結果はとりあえずこの秋に、ネパール地質学会の学術雑誌で組まれるこのコアの特集号に、データ報告を主として投稿する事にしている。

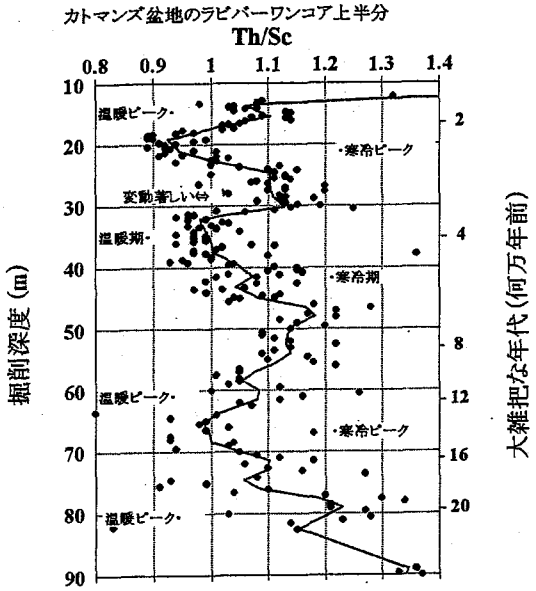

図7. カトマンズ掘削コアの上半分中の Th/Sc 比の変動と古気候の寒暖変化との対応関係

【今後の方針】カトマンズ盆地のラビバーワンコアの粘土層は２００m で試料は５cm ごとに分取しているので、試料の数は全部で４０００個近くになる。これまでのおおよその結果を基に、今度はどの時代の試料について優先的に高い時間分解能で各項目について分析するべきかを共同研究者と検討して、研究をさらに進めていく

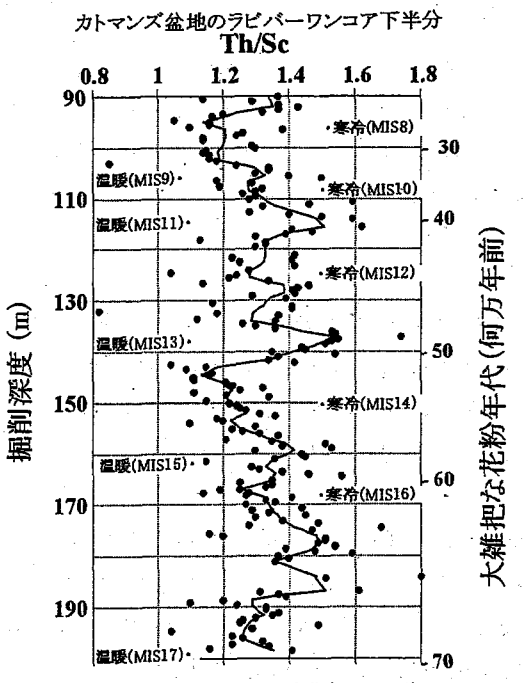

図8. カトマンズ掘削コアの下半分中の Th/Sc 比の変動と古気候の寒暖変化との対応関係

予定である。ということで、平成１６年度には原研施設利用共同研究課題「ネパールのカトマンズ盆地で採取された堆積物コア試料の放射化分析」として申請させていただいた。

中国南部のエルハイ湖の同一コア中の花粉分析などのデータも学術雑誌に掲載されはじめている。これらの研究者と連絡を取って、中国南部のエルハイ湖とインドのサンバール湖で採取された堆積物コア試料の放射化分析もこれまでの予備的なデータについて考察を行い、さらに高い時間分解能で放射化分析を行い、その成果を学術雑誌に投稿できるようにしていきたい。

【成果の報告】

2003 Kazuhiro Toyoda, Chemical composition of a drilled core of Lake Biwa in Japan and its implication for the source changes during the past 430,000 years. Quaternary International 105, 57-69

2004 Kazuhiro Toyoda and Yoshitsugu Shinozuka, Validation on arsenic as a proxy for lake level change during the past 40,000 years in Lake Biwa, Japan (in press).

Kazuhiro Toyoda and Hiroki Haraguchi, Water-depth related chemical component in oxic sediment of Lake Biwa, Japan. Geochimica et Cosmochimica Acta に投稿中。

Yoshitsugu Shinozuka and Kazuhiro Toyoda, Geochemical records in delivery and accumulation of heavy minerals in sediments of Lake Biwa in Japan and the implications for climatic and tectonic changes. Chemical Geology に投稿中。

5. ＲＩの製造

5.Production of Radio Isotopes

This is a blank page.

研究テーマ：RIの製造・利用に関する開発
表　　題：がん治療用イットリア微小球の放射化

5-1

がん治療用イットリア微小球の放射化

○反田孝美[1]、木暮広人[1]、小林勝利[1]、小久保正[2]、川下将一[2]、
清水秦博[3]、澤田良樹[3]、斎藤 誠[3]、川嵜一博[4]、井上好明[4]
[1]日本原子力研究所
[2]京都大学
[3]株式会社シミズテック
[4]高周波熱錬株式会社

肝臓がんの治療法の一つとして、^{90}Yを含有した放射性ガラス微小球[1]を用いる内照射療法が諸外国で行われている。これは、肝臓がんに連なる動脈にカテーテル経由で放射性ガラス微小球を注入することにより、肝臓がんを養っている毛細血管を塞栓させると同時に^{90}Y（半減期2.67日）からのベータ線（最大エネルギー2.28MeV)を直接照射してがん細胞を死滅する治療方法である。この放射性ガラス微小球は、イットリア（Y_2O_3）の含有率が約40 W%のガラス微小球（粒径　20～30μm）を放射化したものである。これに代るイットリア含有率100 w%のイットリア微小球を京都大学が開発した。このイットリア微小球の有効性を研究するため、原研と京都大学医学部は協力研究「血管内小線源の安全性と有効性に関する研究」の下で、原研が原子炉照射による放射化技術の開発を行った。

イットリウム(Y)は^{89}Y同位体の天然存在比が100%で、原子炉照射により(n，γ）核反応を起こし^{90}Yになる。

イットリア微小球をそのまま原子炉照射すると一部がプラズマ焼結したように固まる。これを防ぐため、今回開発した気密性アルミニウムインナーカプセルにイットリア微小球（200mg）と水（200μl）のスラリーを封入してJRR-3水力照射設備で照射した。

照射後のイットリア微小球は、キャピンテック製放射能校正器で^{90}Yの放射能を測定した。この測定値は同じ試料を放射能測定用双子型伝導微小熱量計[2]で測定して得た放射能を基準に求めた校正係数で補正した。

今回の照射において、気密性アルミインナーカプセルの気密が保たれ、イットリア微小球の焼結が観られなかった。得られた放射能は照射直後において2時間照射で11 MBq/mg(Y_2O_3)、17時間照射で87 MBq/mg(Y_2O_3)であった。

2時間照射した放射化イットリア微小球はアクリル製注入カプセルに30mg分取し、京都大学に輸送し、抗腫瘍効果を観る動物実験に用いた。

イットリア微小球

イットリア微小球は京都大学、(株)ネツレンと（株）シミズテックが共同研究で開発したPlasma Beeads Y_2O_3（粒径分布20～30μm）を用いた。Y_2O_3の純度は99.9%以上である。顕微鏡写真を図1に示す。

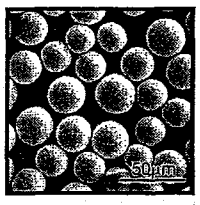

図1　イットリア微小球の電子顕微鏡写真

気密性アルミニウムインナーカプセル

イットリア微小球水添加スラリーを石英アンプルに封入して照射すると水の放射線分解で生じた水素と酸素がアンプル開封時に爆発的に燃焼して危険である。これを避けるため図2に示す気密性アルミニウムインナーカプセルを新たに開発した。

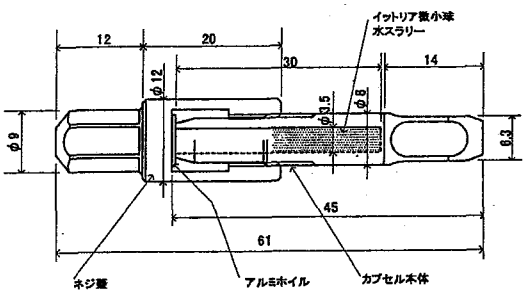

図２　気密性アルミニウム
インナーカプセル

このカプセルにイットリア微小球と水を封入し、100℃の加熱試験を行い重量減少の少なかったものを照射に用いた

原子炉照射

気密性アルミニウムインナーカプセルをアルミニウムホイルで包み、標準のアルミニウム製圧接キャプセルにヘリウム置換封入して照射キャプセルとした。

照射は JRR-3 水力照射設備（熱中性子束 $9.6\times10^{17}m^{-2}\cdot s^{-1}$、速熱中性子束 $1.7\times10^{16}m^{-2}\cdot s^{-1}$）で行った。

カプセルの気密性と放射化微小球の回収

原子炉照射後の照射キャプセルを開封し、取り出した気密性アルミニウムインナーカプセルの重量を測定し、重量変化で気密性能を観た。表１に示すように重量変化がほとんど無く、ネジ蓋開封時に内部が加圧になっている兆候も観られなかった。

内部のイットリア微小球水スラリーはエッペンドルフ 200μl コンビチップ [3]で吸い上げ V バイアルに回収、水洗した。この一部を分取し、イットリア微小球スラリー1μl に含まれるイットリア微小球重量（2.5～2.7mg）を求めた。この値を用いて放射能測定試料、動物実験用試料の分取を行った

イットリア微小球の回収率は 90 %以上であった。

表１　気密性アルミインナー
カプセルの気密性能

100℃加熱試験		照射後	
加熱時間 h	重量変化量 mg	照射時間 h	重量変化量 mg
2	-1.4	2.0	+1.5
40	-23	17.0	-1.8

放射能測定

放射化イットリア微小球水スラリーを既定のガラス瓶に分取し、これをキャピンテック社製の RI キャリブレータ CRC-15R(Cal.No. 48×10)で測定し、得た測定値に校正係数 0.69 を掛け放射能を求めた。この校正係数は放射能測定用双子型伝導微小熱量計 [3]で ^{90}Y の放射線による発熱量(5.55μW/mCi)を測定して得た放射能を基準とした。

表２　イットリア微小球分の放射能

照射時間 h	照射直後の放射能 MBq/mg(Y_2O_3)
2	11
17	87

まとめ

気密性アルミニウムインナーカプセルに水を添加したイットリア微小球を封入して JRR-3 水力照射設備で照射し、問題なくイットリア微小球を放射化出来た。また、0.5mg 単位の精度で正確に分取できた。

放射能校正器 CRC-15R でイットリア微小球水スラリーを直接測定し簡便に放射能を求めることができた。

これらの技術により実用放射能 170GBq の取扱いの可能性が示唆された。

参考文献

1) TheraSohere® MDS Nordion Inc., Kanata, Ontario, Canada
2) 源河次雄、他：RADIOISOTOPES, 37, 155-158(1988)
3) エッペンドルフ電動分注システム EDOS522

6. 原子炉材料照射試験

6. Irradiation Test of Reactor Materials

This is a blank page.

研究テーマ：燃料の安全性に関する研究
表　　題：シビアアクシデント時における燃料からの短半減期放射性物質の放出

6-1

シビアアクシデント時における燃料からの短半減期放射性物質の放出

工藤保、日高昭秀[1]、更田豊志
原研・燃料安全研究室
[1]原子力安全委員会事務局

原子炉シビアアクシデント時の放射性物質の放出機構解明とソースタームの予測制度向上を目的として、燃料からの放射性物質放出を調べる VEGA 計画[1]を実施している。本報告では、研究炉を用いた成果の一部として短半減期核種の放出に着目したVEGA-6実験の結果について報告する。

56GWd/tU まで照射された高燃焼度 BWR 燃料（被覆管付き、ペレット重量約 13g）を JRR-3 にて線出力密度 0.68kW/m で 26 日間再照射した。その燃料を大気圧、水蒸気雰囲気下で 2773K まで昇温した。燃料から放出された放射性物質は、キャリアガスによって後段へ運ばれ、エアロゾル状のものはフィルタまでに、ガス状のものは冷却活性炭にそれぞれ捕集される。

燃料のγ線強度の経時変化から求めた Cs-137 の放出量の初期インベントリに対する割合(放出割合)の履歴を燃料温度とともに図1に示す。Cs は約 1600K から放出が始まり、昇温終了時にはほぼ全量が放出された。試験燃料に対する実験前後のγ線測定から評価した核種別最終放出割合をγ線強度の測定誤差とともに表1に示す。JRR-3 で再照射することにより、再照射を行わない従来の VEGA 実験では測定できなかった I-131、Te-132、Ba-140、Ru-103、La-140 の最終放出割合を評価した。

燃料に対する昇温実験中のγ線測定では高周波等の影響により Cs 以外の核種は検出できなかったが、加熱炉下流側のフィルタに捕集された短半減期核種を検出できた。フィルタで測定した I-131 のγ線強度の最大値に対する相対γ線強度の履歴を図1に示す。Cs と I は、ともに粒子状のものが捕集されており、相対γ線強度は概ね同じ履歴となった。また、図示していないが、Te と Ba の相対γ線強度も Cs とほとんど同じ履歴を示した。このことは、I、Te、Ba の燃料からの放出割合履歴は Cs とほぼ相似であることを示唆している。Cs の放出割合履歴とフィルタでの相対γ線強度履歴から相対捕集効率を求め、それが I、Te、Ba に対しても適用できると仮定してフィルタにおける I、Te、Ba の相対γ線強度履歴及び最終放出割合から放出割合履歴を評価した。次に燃料からの放出速度を定量化するために、結晶粒内の拡散を律速過程と仮定した Booth モデル[2]を用いて見かけの拡散係数を算出した。結果を図2に示す。揮発性の Cs、I、Te の拡散係数は近接しており、中揮発性である Ba の拡散係数は Cs 等のそれに比べて約 1/10 であった。

参考文献

1) 日高他, JAERI-Res. 2001-055 (2001).
2) Booth, et al., CRDC-721(1957).

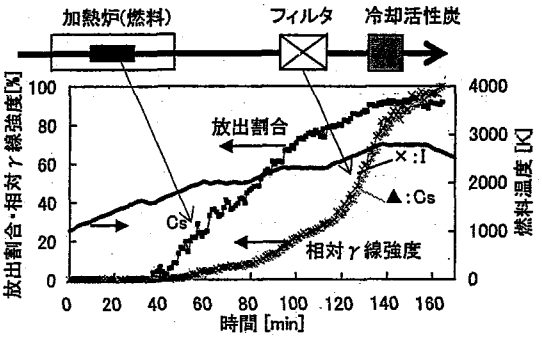

図1　Cs の放出割合及びフィルタにおける Cs と I の相対γ線強度

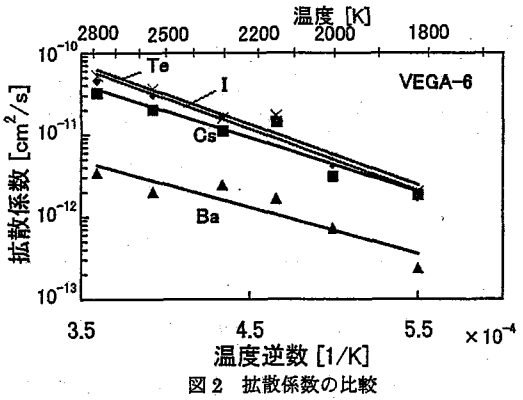

図2　拡散係数の比較

表1　VEGA-6 における最終放出割合

核種（半減期）	^{137}Cs (30y)	^{131}I (8d)	^{132}Te (3d)	^{140}Ba (13d)	^{106}Ru (1y)	^{103}Ru (39d)	^{140}La (2d)
放出割合[%](測定誤差[%]	93(0.03)	97(5)	98(3)	49(3)	14(2)	16(2)	3(2)

原子炉：JRR-3　　装　置：DR-1 孔　　分　野：原子炉燃料・材料（軽水炉）

研究テーマ: 核融合炉用 固体増殖材からのトリチウム放出
表　　題: 酸化リチウム焼結体からのトリチウム放出：細孔内の吸着・脱離挙動

6-2

酸化リチウム焼結体からのトリチウム放出　：細孔内の吸着・脱離挙動

Tritium release from neutron-irradiated Li2O: Desorption kinetics in micropore

谷藤隆昭　　實川資朗
所属　　日本原子力研究所　物質科学部

1.緒言： これまでに種々の気孔率をもつ酸化リチウム焼結体からのトリチウム放出挙動を調べてきた。かさ密度71％ＴＤから86％ＴＤの焼結体ではトリチウム放出挙動の気孔率依存性はなく、この気孔率の範囲ではトリチウム放出はトラップサイトからの脱離が律速であることを明らかにしてきた。今回、焼結体の細孔内壁への前吸着させたトリチウムの放出挙動を等温加熱実験により調べた。

2.実験： 細孔への前吸着　かさ密度81％Ｔ.Ｄ（開気孔率は約16％、閉気孔率3％、平均Grain sizeは11ミクロン）の酸化リチウム焼結体を JRR-4,T-パイプで10分間、照射した。原子炉照射後の石英アンプルはそのまま、アンプル（内容積、約0.5ｃｃ）ごと密封状態で電気炉内に入れて 360Ｃで4時間熱処理を行い、焼結多孔体の細孔内壁にHTOとして吸着させた。

放出実験　電気炉の炉冷後、石英アンプルから前吸着を施した試料を分取し、 583Ｋから683Ｋの温度範囲で等温加熱を行なった。等温加熱により、前吸着トリチウムは細孔内壁での吸着・脱離を繰り返しながら焼結体の表面まで移行してくる。このトリチウムをアンモニア・ガスでスイープし、計数ガスとしてメタンガスを加えてガスフロー・カウンターに導き測定した。

3.結果： 熱処理によりトラップ・サイトから逃れたトリチウムは焼結多孔体の細孔内壁に均一に HTOの化学形で吸着しているものと考えられる。等温加熱によるトリチウム放出速度の時間依存性の測定を行った。トリチウム放出率Ｆと焼鈍時間ｔは図1に示すように　log(1-F)　vs $t^{0.5}$　のプロットにより直線関係が得られた。トリチウムの細孔からの脱離挙動は Avrami式　$(1-F)=\exp(Kt^n)$　のｎ=0.5に従う。トリチウムの残存割合（1-Ｆ）が焼鈍時間ｔの平方根に比例することは、細孔からの脱離移行がランダム・ウオークに従うこと示唆し、細孔内での吸着・脱離を伴うポア拡散が律速過程とみなされる。平均ポア滞在時間τは図 1の傾きより次式により評価したτ $=1/(\text{Slope})^{1/0.5}$ 。平均ポア滞在時間τの温度依存性を図2に示す。これよりマイクロポアからの脱離移行の活性化エネルギーは 184kJ/molと評価された。

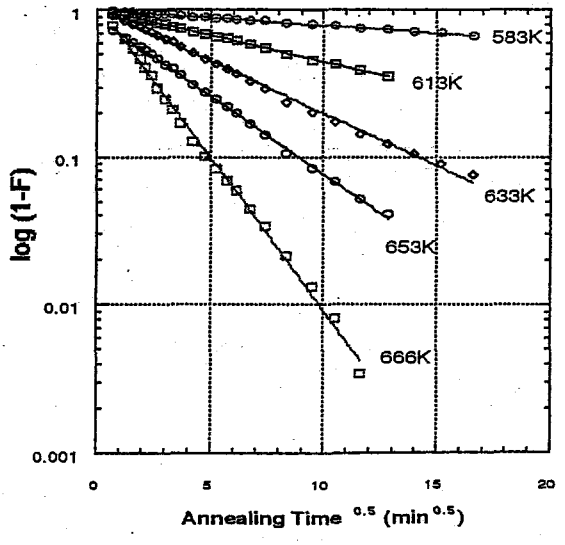

図1 残存トリチウムの割合 vs（焼鈍時間）$^{0.5}$

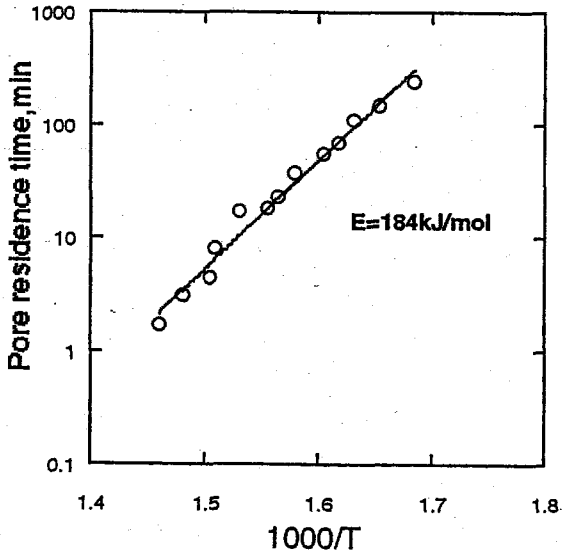

図2 平均ポア滞在時間 vs 絶対温度の逆数

原子炉　ＪＲＲ-4　　装置: T-パイプ　　分野: 原子炉燃料・材料（核融合炉）

7. その他

7. Others

This is a blank page.

7-1

熱中性子照射によるボロン分布観察法の材料学への応用（II）

Application of boron distribution observation method to material science by thermal neutron irradiation (II)

東京大学大学院工学系研究科マテリアル工学専攻　　朝倉健太郎、柴田浩司

Department of Materials Science, Faculty of Engineering, The Univ. of Tokyo
K.Asakura and K.Shibata

Ⅰ．研究の目的と意義

Ⅰ－1．研究の目的

ボロン（以下B）は極微量でも鉄鋼の性質を向上させることが知られており、非常に多くの鋼で利用されている。さらに今後ますます重要となる環境問題、資源・エネルギー問題に対処できる鋼としてB添加鋼の重要性の認識が高まっている。

著者らは立教大学原子炉において熱中性子とボロン10の反応を利用したα線トラックエッチング（以下、ATEと略）法について実験を進めてきたが、平成11年度をもって閉鎖された。その後、日本原子力研究所において幾多の困難に出会いながらも、ATE法を利用できるシステムを立ち上げた。結果についてはすでに報告しているので文献を参照されたい。この3年間は、各種鋼中Bの状態分布について研究を進めてきた。主として以下の2テーマについて報告する。

Ⅱ．研究成果

研究1：低炭素鋼におけるBの挙動に及ぼすMoの影響

1．緒言

Bは、ごく微量の添加で鉄鋼材料の特性に大きな影響を及ぼすことが知られている。鉄鋼材料中のBに関する研究は非常に多くなされており、またその結果から多くの知見が得られているが、未だ不明な点も残っている。その一つがBと他元素の相互作用である。

とくに鋼の焼入れ性は極微量のB添加で著しく向上するがそのメカニズムについては諸説あり、未だ定説はない。焼入れ性に及ぼすBの影響は、Grange[1]や上野ら[2-3]によって詳しく調べられ多くの知見が得られている。例えば上野ら[2]によると、B鋼の焼入れ性がオーステナイト化温度にともない変化するのは、加熱温度によって固溶B量が変化するためであり、固溶B量が変化しなければ、B鋼の焼入れ性はオーステナイト化温度にも、オーステナイト粒度にも依存しない。上野[4]は、また、1999年にまとめたフォーラム報告書「鉄鋼材料の組織と特性に及ぼすボロンの影響」において、Mo-B間には相互作用が認められ、BによってMoの効果は倍加すると指摘し、Bの偏析と析出挙動に関する研究の中で残された課題の1つに、このB-Mo間の相互作用の解明をあげている。

Asahi[5]は、0.15C-1.0～1.5Mn鋼の焼入れ性に及ぼすBとMoの影響について調べ、①焼入性はB量の増加により増大するが、最適B量を超えると減少する、②Moの添加は$M_{23}(CB)_6$の析出を遅らせるため、固溶Bの多くは結晶粒界に沿って偏析する、③高温からの冷却中に、Bは非平衡偏析によりオーステナイト粒界に沿って偏析するため、$M_{23}(CB)_6$の析出が容易に生じることを明らかにしている。しかし、広い範囲の熱処理条件、組成において、Bの偏析、析出挙動、およびそれらに対するMoの影響を明らかにする必要がある。

そこで本研究では、日本鉄鋼協会「鉄鋼材料における微量ボロンの挙動解明と利用促進」研究会の共通試料を用いて、Bの偏析および析出挙動に及ぼすMoの影響を調べ、MoとBの相互作用についての理解を深めることを目的として研究を行うことにした。Bの挙動は主としてATE法を用いて調べた。

2．実験方法

1）供試鋼と熱処理

供試鋼の組成は以下のとおり。基本組成は0.05C-0.25Si-3Mn-0.01Ti-0.0015Nであり、A～E鋼はBを単独に1～42ppm添加、F～J鋼は0.5Mo+（1～42ppm）Bを複合添加している。

熱処理条件は1250℃×1hの加熱後に熱間圧延で16mm厚に圧延し、その後均質化処理として1250℃×1

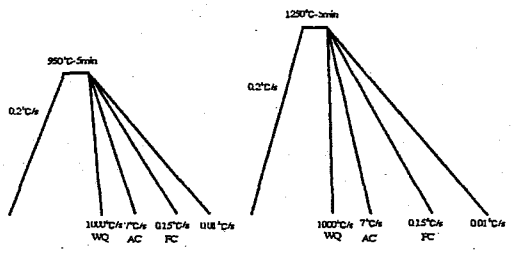

Fig.1 Heat pattern of cooling after austenitizing at 950℃ and 1250℃.

研究施設：原子力研究所、装置：研究炉JRR-4（医療用照射）、研究分野：ボロンの分布観察

h 加熱後空冷した。

2）連続冷却時のBの挙動

上記熱処理後、さらに 1250℃×5min および 950℃×5min で均質化処理した後、以下の各種速度で冷却し、冷却速度の違いにおける組織および ATE 像を調べた。ヒートパターンを Fig. 1 に示す。

加熱速度は各供試鋼ともに 0.2℃/s で、850℃～600℃間の平均冷却速度は、水冷時およそ 1000℃/ s 、空冷時 7℃/ s 、炉冷時 0.15℃/ s であった。上記炉冷より冷却を遅くした 0.01℃/s 冷却についても調べた。

3）等温保持時のBの挙動

BおよびMo 添加が偏析、析出に及ぼす影響を詳細に調べるために、A 鋼(1ppmB)、F 鋼(1ppm+0.5Mo)を用いて等温保持実験を行った。

2 台の電気炉を用意し、1 台目の電気炉は 1250℃のオーステナイト化温度に加熱しておき、2 台目の電気炉を 1000℃から 600℃の間の温度に 100℃刻みで設定した。試料に Pt－Rh 熱電対をスポット溶接し、1250℃でオーステナイト化して 5min 保持後に 2 台目の電気炉に試料を入れ、試料の温度をモニターしながら、設定温度になってから 10～1000s 保持して水冷した。2 台目の電気炉に移すまでの温度低下は約 100℃であった。1250℃の炉から試験片を取り出して 2 台目の電気炉にいれて所定の温度になるまでの平均冷却速度は、1.4～2.6℃/s の範囲であった。その後、ATE 法によってBの粒界偏析及び析出状態を調べた。

4）ＡＴＥ法による観察

各供試鋼を 5mm×10mm×1mm（厚さ）に切出し、鏡面研磨した。観察面に工業用硝酸セルロースフィルム（推奨フィルム[6]）を、酢酸メチルを用いて貼り付けた。その後、日本原子力研究所 JRR-4 において中性子照射を行い、照射後のフィルムを 30℃の NaOH 水溶液（2.5N）で 40min のエッチングを施した。さらにフィルム表面のカールを除去するため、100℃、30min のプレス加熱を加えた。その後さらに観察面にカーボン蒸着を施した後、ATE 像を光学顕微鏡で観察した。

3．実験結果

3.1 ATE 像による連続冷却時のBの挙動の観察

(1) 水冷材のおけるATE 像

950℃から水冷したときの ATE 像の結果を以下に示す。1～10ppm のB単独添加鋼では、粒界偏析が見られる。22ppmB 鋼では粒界偏析と粒界析出、42ppmB 鋼では粒内析出、粒界偏析が認められる。

一方、B と同時に 0.5%の Mo を複合添加した鋼（以下Mo 添加鋼と略）では、B 量が 1ppm の場合（F 鋼）の場合、粒界偏析、析出は認められず、5～22ppm までは粒界偏析だけが観察される。B 量が 42ppm になると、粒界偏析とともに粒界析出が見られるようになる。Mo 添加によって粒界偏析、粒界析出、粒内析出の進行が遅れる。

1250℃から水冷したときの ATE 像は、950℃から水冷したときに比べて、1250℃から水冷した場合の大きな違いはB単独添加鋼およびMo 添加鋼において、ほう化物の析出が抑制されて粒界析出、粒内析出がほとんど見られない。

(2) 炉冷材における ATE 像

950℃から炉冷したときのATE 像を Fig.2 に示す。B単独添加鋼では、1ppmB 鋼で粒界偏析と粒界析出が見られる。5～42ppmB 鋼では粒界析出と粒内析出だけで粒界偏析は見られない。B 量が増えるにしたがってほう化物密度が高くなる傾向が認められる。Mo 添加鋼では、1ppmB 鋼から 22ppmB 鋼まで粒界偏析と粒界析出が見られ、42ppmB 鋼ではほとんど粒界析出だけになる。すなわち、B 単独添加鋼では、5ppm 以上のB添加でBの粒界偏析が認められ無くなるが、Mo 添加鋼では 22ppm まで粒界偏析が観察される。また、Mo 添加鋼では、B 単独添加鋼とくらべ全体にボライドの析出量が少ない。

1250℃から炉冷したときのATE 像を Fig.3 に示す。B単独添加鋼では、1ppmB 鋼では粒界偏析と粒界析出が観察される。5ppmB 鋼では粒界偏析は認められず粒界析出だけとなる。10ppmB 以上では、粒界析出が認められ粒内析出も生じる。42ppmB では、Fig.5(e)に示すように、粒界近傍に PFZ(precipitation free zone)が観察される。

Mo 添加鋼では、1ppm から 42ppmB 添加にわたって、粒界偏析と粒界析出となり、粒内析出はほとんど認められない。Fig.3 において、B 単独添加鋼の粒内の像に比べ、Mo 添加鋼の粒内の像が著しく平滑である。このことは、Mo 添加鋼では、ボライドの粒内析出が著しく生じにくくなっていることを示すものと思われる。

(3) 空冷材のおける ATE 像

ATE 像は省略するが、空冷材における B の挙動は以下のようである。950℃から空冷したときのATE 像は、B単独添加鋼においては、1～5ppmB 鋼では粒界偏析と粒界析出、10～42ppmB 鋼では粒界析出と粒内析出が見られる。Mo 添加鋼も析出物量は少ないが同様であった。

1250℃からの空冷材においても、B単独添加鋼、Mo 鋼ともに 1ppm～42pmpB で、粒界析出と粒内析出が観察される。

(4) 0.01℃/ s 冷却における ATE 像

きわめて遅い冷却速度 0.01℃/s においては、B単独添加鋼では、22ppmB 添加まで粒界偏析と粒界析出、42ppmB では粒界析出と粒内析出であった。Mo 添加鋼では 1～42ppmB の広範囲において粒界偏析と粒界析出が認められた。

3.2 ボライドのATE像とTEM像の比較

塊状ないしは点状にほう化物が凝集すると、焼入れ性向上に不都合であることはUenoら[7]によっても指摘されている。本研究では、Bの挙動を主としてATM像によって観察している。従来から、ATM像の感度は高いが、位置分解能が低いことが指摘されている。しかし、ATM像の分解能に関する具体的データはほとんど報告されていない。

そこで、B添加量がもっとも多いE鋼（42ppmB）の1250℃炉冷材を用いて、抽出レプリカをTEMで観察し、ボライドの同定とともにATE像と寸法の比較をおこなった。

Fig.4に示すようにオーステナイト結晶粒界に200～250nmのほう化物が沿うように観察される。また粒内には100nmの微細析出物が観察される。ほう化物を電子線回折によって解析した一例をFig4の右上に示す。ほう化物の多くは正四面体あるいは長四角形の形態をしたものが多く、解析の結果は$Fe_{23}(CB)_6$であったが、BNも観察できた。BNは$Fe_{23}(CB)_6$に比べて粗粒であった。Fig.3(e)のATE像による塊状ほう化物は15～20μmの大きさで観察される。この像が1個のほう化物の像であると仮定すると、ATE像のほう化物は60～100倍に拡大されて観察されることが分かる。

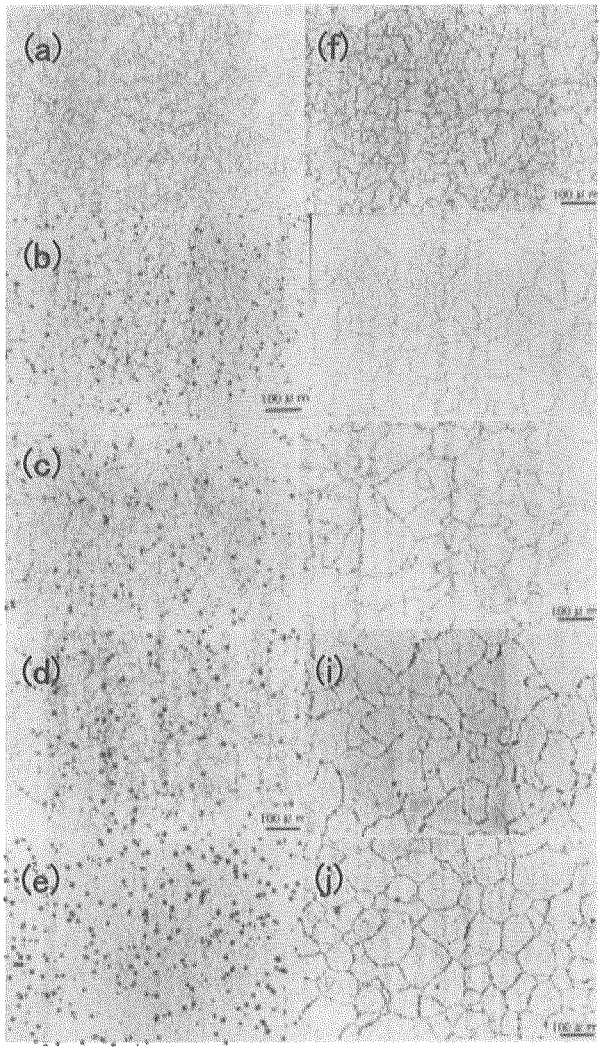

(a)1ppmB (b)5ppmB (c)10ppmB (d)22ppmB (e)42ppmB (f)1ppmB+0.5Mo
(g)5ppmB+0.5Mo (h)10ppmB+0.5Mo (i)22ppmB+0.5Mo (j)42ppmB+0.5Mo

Fig.2 ATE images of steels cooled at 0.15℃/s from 950℃.

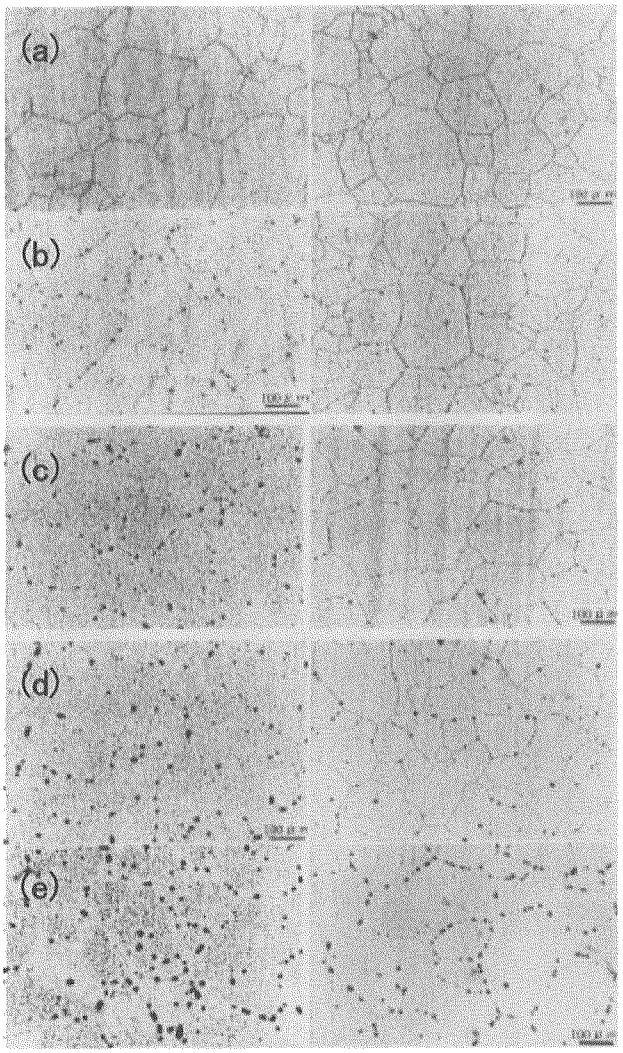

(a)1ppmB (b)5ppmB (c)10ppmB (d)22ppmB (e)42ppmB (f)1ppmB+0.5Mo
(g)5ppmB+0.5Mo (h)10ppmB+0.5Mo (i)22ppmB+0.5Mo (j)42ppmB+0.5Mo

Fig.3 ATE images of steel scooled at 0.15℃/s after heating at 1250℃.

従って、半径1μmのボライドにおいては、間隔がおよそ100μmより広くあいていないと、ATE像では2つの析出物として観察できないことになる。

4. 考 察

(1) 偏析・析出図

前章で述べたATE像の観察結果をまとめると、冷却速度、B量を変化させたときのBの偏析およびボライドの析出状態は、Fig.5～Fig.8のようになる。

図中の記号は、以下のようである。×は偏析も析出も認められない場合、○はオーステナイト粒界への偏析(segregation)、□は粒界偏析＋粒界析出、△は粒界析出、◇は粒界析出と＋粒内析出、◎は粒内析出、▽は粒界偏析＋粒内析出を表す。

粒界偏析だけが生じる領域は、高い冷却速度の低B側にのみ存在し、それより冷却速度が遅くなっても、またB量が増えても、粒界析出あるいは粒内析出が生じる。Uenoら[7]はBの偏析は100℃/sの急速冷却時でも生ると指摘している。しかし著者らによる実験ではさらに冷却速度の速いおよそ1000℃/sにおいても、オーステナイト粒界へのB偏析が認められた。土生ら[8]やSimcoeら[9]による研究をはじめ多くのこれまでの研究から、Bは10ppm程度の極微量の添加で焼入れ性を大きく向上させることが分かっている。これはBがオーステナイト

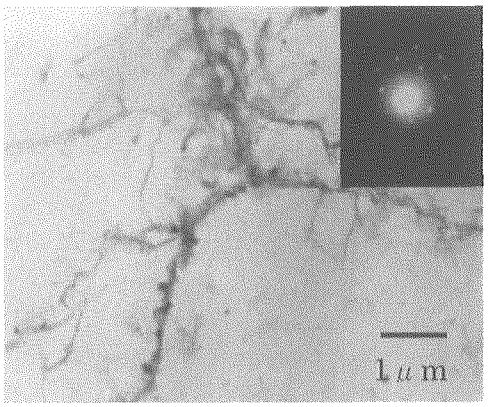

Fig.4 Precipitations of ferrite grain boundary in specimen E(1250℃→FC, 0.15℃/s) observed by extraction replica method.

Table 2 Microstructures of chemically etched specimens observed under optical microscope. Specimens were cooled at 0.15℃/s from 1250℃.
( ): small amount

steel	microstructure	steel	microstructure
A	bainite	F	bainite
B	bainite+(α)	G	bainite
C	bainite+ α	H	bainite
D	bainite+ α	I	bainite
E	bainite+ α	J	bainite

粒界に偏析し、そこからのフェライトの核生成を遅らせるためとされている。従ってBを有効に利用するためには、粒界偏析だけが生じる領域を把握することが重要である。

粒界偏析が生じるか生じないかに注目すると、もっとも少ないB量でもっとも速い冷却速度の場合を除いて、図中に示すような曲線を描くことができる。これらの曲線の左側（低B側）が、粒界析出が生じる領域、右側が粒界偏析の生じない領域である。これらの曲線はCの字の形をして、粒界偏析が生じない領域は、およそ1～10℃/sの冷却速度でもっとも低B側位置し、冷却速度がそれより速くなるほど、また遅くなるほど高B側に位置している。

Bの粒界偏析の生じない領域は、ボライドの粒界析出、粒内析出がかなり進んでいる領域に対応していて、曲線の位置は、粒界析出がかなり進んだ状態の出現に対応している。何故、中間の冷却速度で粒界析出がかなり進んだ状態が出現しやすいのだろうか。Yamaguchi ら[10]は、IF鋼において、炉冷の場合より空冷の場合のほうに粒界析出が顕著に認められることを観察し、その理由を、主にBの非平衡偏析機構に起因して冷却中の結晶粒界周辺のB濃度が中間の冷却速度においてもっとも高くなるためと考察している。詳細は今後検討されなければならない点と考えられる。

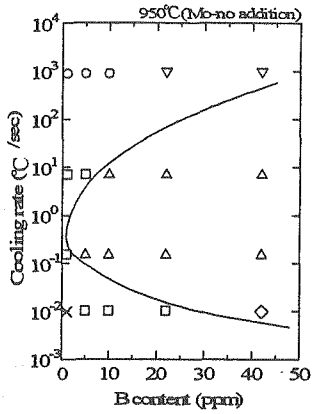

Fig.5 Effect of B content and cooling rate on the behavior of segregation and precipitation of B in no Mo steels during cooling from at 950℃. In Figs. 6, 7, 8 and 9, the meanings of symbols are as below. (×:no segregation and no precipitation, ○:grain boundary segregation, □: grain boundary segregation + itergranular precipitation, △: intergranular precipitation, ◇: intergranular precipitation + intragranular precipitation, ◎: intragranular precipitation, ▽: ingrain boundary segregation + intrgranular precipitation)

もし、Bを粒界にのみ存在させたかったら、上述のようにB量、冷却速度のせまい領域だけしか利用できない。しかし、析出が生じていても同時に粒界偏析していれば、フェライトの生成を抑えることができる。Table 2は、1250℃から0.15℃/s（炉冷）で冷却した試料を化学腐食して光学顕微鏡組織を観察した結果である。Fig.8、Fig.10と合わせて見ると、ボライドが生じていてもこの冷却速度でフェライトの生成が押さえられていることが分かる。

以下に、Fig.5からFig.8の結果から加熱温度とMo添加の影響について考察する。

（2）偏析・析出図に及ぼす加熱温度の影響

Fig.5とFig.6を比較して、B単独添加鋼において加熱温度の影響をみると、粒界偏析の見られない領域の形、位置は両加熱温度でほとんど同じのようにみえる。ただ、1000℃/s冷却の場合を1250℃加熱の場合と、950℃加熱の場合を比較すると、1250℃加熱の場合のほうが、広いB組成範囲で粒界偏だけが観察されるのに対して、950℃加熱の場合、Bが多くなると粒内析出も共存するようになる。とくに42ppm鋼の場合、950℃加熱のほうがボライドの析出がより速く進行していることがよく分か

る。しかし、冷却速度が遅い場合には、Fig.5 と Fig.6、Fig.2 と Fig.3 を比較すると分かるように、1250℃加熱のほうが、粒界析出、粒内析出の進行がはやく生じる。他方、Mo 添加鋼について加熱温度の影響を見ると、Fig.7 と Fig.8 における粒界偏析の見られない領域の形、位置が、両加熱温度で異なっている。およそ 1℃/s の冷却速度付近では、1250℃加熱のほうが少ない B 量で粒界偏析が生じない領域になってしまうが、それより低い冷却速度では、1250℃加熱のほうが、粒界偏析領域が広くなっている。高冷却速度域では、加熱温度による差は小さいように見受けられる。

以上述べたように、B の偏析、析出挙動は、加熱温度によって影響をうける。とくに、Mo 添加鋼での影響は小さくない。したがって、焼入れ性も加熱温度の影響を受けることが推察されるが、組織に対する影響の詳細、加熱温度による影響がどのような理由によって生じるかについての検討は、今後の課題である。

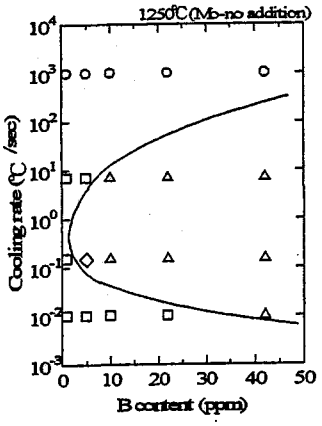

Fig.6 Effect of B content and cooling rate on the behavior of segregation and precipitation of B in no Mo steels during cooling from at 1250℃.

(3) 偏析・析出図に及ぼす Mo 添加の影響

Fig.5 と Fig.7 の比較、Fig.6 と Fig.8 を比較すると、950℃加熱、1250℃加熱いずれにおいても、Mo 添加により、粒界偏析領域が広がることが分かる。Asahi[5] は、Mo は $M_{23}(CB)_6$ の析出を遅らせ、固溶 B の多くを結晶粒界に偏析させるとしている。そのように考えると Fig.5 から Fig.8 に示される Mo の影響は理解することができる。従って、本研究で用いた鋼においても、Mo には Asahi が主張するような効果があるものと考えられる。しかし、Mo にはその他の効果はないのであろうか。Figs.8 と Fig.9 は、B の挙動に及ぼす Mo の影響をさらに詳しく見るために行った等温保持実験の結果である。すなわち、A 鋼、F 鋼を 1250℃に加熱し、それ以下のいくつかの温度まで下げて等温保持したとき

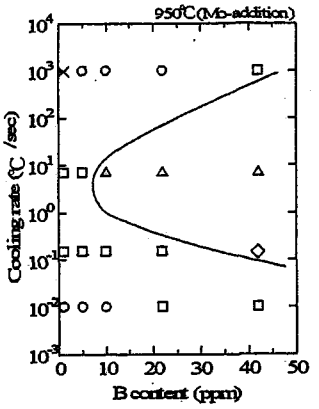

Fig.7 Effect of B content and cooling rate on the behavior of segregation and precipitation of B in Mo steels during cooling from 950℃.

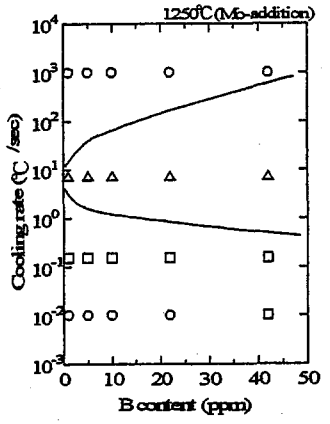

Fig.8 Effect of B content and cooling rate on the behavior of segregation and precipitation of B in Mo steels during cooling from 1250℃.

の、保持温度、保持時間と偏析挙動の関係を示している。図中の曲線は、偏析開始曲線である。

これらの結果から、Mo には 900℃以上の温度での B の偏析を押さえる効果もあるように見受けられる。A 鋼および F 鋼を 900℃で 100s 等温保持後、水冷したときの ATE 像を Fig.10 に示す。A 鋼では粒界偏析が観察されるが、F 鋼ではボライドはもとより粒界偏析も認められない。

これらの結果は、B 量が 1ppm と非常に低い鋼の結果であるため、B 量の多い鋼で同じような効果が認められるかどうか、現在実験を進めている。

4．結　論

Nを Tiによって十分に固定した低炭素 3%Mn 鋼を用いて、主として ATE 法で B の偏析および析出挙動とそれらに及ぼす Mo の影響、加熱温度の影響を調べ、以下の結果を得た。

1) 1000℃/s の冷却速度でも、冷却時オーステナイト粒界への B 偏析が生じる。

2) 連続冷却によって生じる偏析・析出挙動を、縦軸冷却速度、横軸 B 量にとって整理すると、偏析が生じる領域と生じない領域との境界が C 曲線状となる。

3) この C 曲線の位置は、おおよそ粒界析出が進行して粒界偏析が見られなくところに一致する。

4) Mo 添加によりほう化物の析出が抑制される。

5) 低 B 鋼で、Mo 添加により、900℃付近でのオーステナイト粒界への B の偏析開始が遅れることが認められた。

6) B の偏析、析出挙動は加熱温度の影響を受ける。この影響は、とくに Mo 添加鋼で大きい。

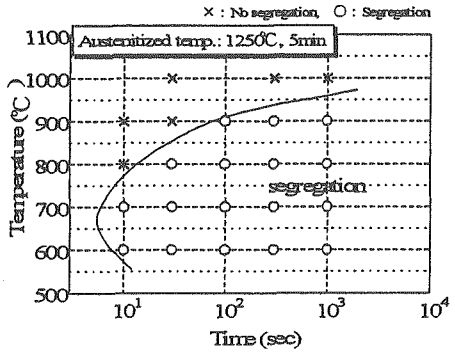

Fig.9　Time-Temperature-Segregation diagram obtained by isothermal holding of Steel A (1ppmB).

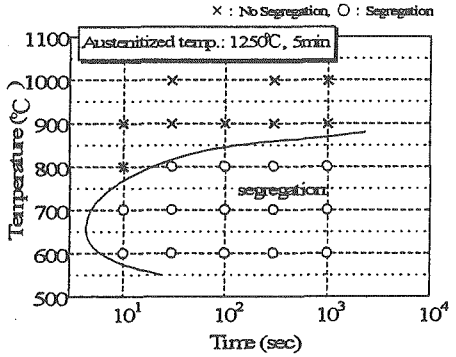

Fig.10　Time-Temperature-Segregation diagram obtained by isothermal holding of Steel F (1ppmB+0.5Mo).

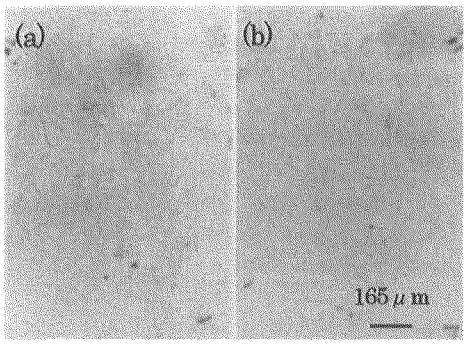

Fig.11　ATE images of Steels A and F held for 100s at 950℃ and water quenched.

参考文献

1) R.A.Grange and J.B.Mitchell: Trans. Am. Soc.Met., 53(1961), pp.157-185

2) 上野正勝、伊藤亀太郎：鉄と鋼、74,(1988), pp.2337-2344

3) 上野正勝、伊藤亀太郎：鉄と鋼、74,(1988), pp.910-917

4) 上野正勝：鉄鋼材料の組織と特性に及ぼすボロンの影響、日本鉄鋼協会・材料の組織と特性部会、（1999 年）、pp.65-77

5) H.Asahi: ISIJ International, 42,(2002), pp.1150-1155

6) 朝倉健太郎、柴田浩司、原澤　進、澤幡浩之、川手　稔：鉄と鋼、89(2003), pp.375-380

7) M.Ueno and T.Inoue: Trans. ISIJ, 13 (1973) pp.210-217

8) 土生隆一、宮田政祐、関野昌蔵、合田　進：鉄と鋼、60,(1974), pp.1470-1482

9) C.R.Simcoe, ARElsea, and G.K.Mannig: J. of Metals, (1955), pp.193-200

10) 山口和之、柴田浩司、朝倉健太郎、小関敏彦：鋼中微量ボロンの挙動と性質への影響、日本鉄鋼協会（2003）、pp.147-151

研究2：インコロイ 908 の高温強度と SAGBO に及ぼす B の影響

1．緒言

応力下粒界酸化 (Stress Accelerated Grain Boundary Oxidation: 以下 SAGBO と略) は一部の Ni 基、Fe-Ni 基合金などで見られる現象で、粒界に沿った酸化が生じ脆化、割れにいたる。SAGBO はこれらの合金の熱処理や熱間加工の際に生じるため、利用が制約されている。インコロイ 908 合金は Fe-Ni 基であり、温度、引張応力、酸素分圧の状況により SAGBO を起こす。国際核融合実験炉 ITER における CICC（Cable in Conduit Conductor）作製の際も、Nb_3Sn の生成とインコロイ 908 合金の時効処理を兼ねた熱処理時に SAGBO が発生

し問題となっている（908合金は、コンジットと呼ばれるNb_3Snワイヤーを包むパイプ材として用いられる。このパイプ内に液体ヘリウムなどの冷媒を通す）。

Morra[1]によって指摘されたインコロイ908合金のSAGBO発生条件をTable 1に示す。この処理において、Table 1に示された温度条件はNb_3Snの生成温度と重なるため避けることができない。また、熱処理に先立つ圧縮や曲げ加工による残留応力が最大500MPaに達するため、引張応力条件も満たされてしまう。よってSAGBOを発生させないためには酸素分圧をTable 1の条件以下にする必要がある。

Table 1 SAGBO condition of Incoloy 908 alloy.

Temperature	823～1073K (550～800K)
tensile stress	> 200MPa
oxygen partial pressure	> 1.33×10^{-2}Pa

酸素分圧1.33×10^{-2}Paという数値は、1気圧では0.13ppmにあたり、大気と同組成の気体ならば全圧5.0×10^{-4}Torrに相当し、超高純度Arガス（O_2：0.1ppm未満）や油拡散ポンプによる排気（到達圧力1×10^{-4}程度）によって比較的容
易に達成できる。しかし、加熱によりコンジット材のインコロイ908合金や超伝導体のNb_3Snなどから酸素や油分などのガスが発生するため、インコロイ908合金表面で局部的に酸素分圧がSAGBO発生条件を満たしてしまう。

Fe-Ni基合金の耐酸化性およびB添加による延性の向上に関してはいくつかの研究があるものの、いずれもBの効果を明確にしていない。いずれもBがSAGBO抑制に効果があるという根拠に欠けている。そこで著者らはインコロイ908合金においてSAGBOが、合金の成分調整により抑制することができれば、インコロイ908合金の応用範囲も広がり、他のオーステナイト系低熱膨張率合金開発の参考にもなり、有用であると考えた。

2．実験方法

2.1 試料と熱処理条件

基本的な組成はTable.2に示すように、インコロイ908合金とほぼ同じである。基本組成は0.13C-48Ni-3.9Cr-1.5Ti-2.9Nb (mass%)である。B量を10ppm未満(T1)、80ppm(T2)、150ppm(T3)、230ppm(T4)と変化させた。試料は1150℃～1125℃にて3～4回に分けて鍛造し、最終形状を110mm×460mm×40mmにした。

980℃、1h空冷の溶体化後、クリープ試験片に加工した。試験片の形状は丸棒試験片で平行部長さ30mm、φ6mmである。

Table 2 Chemical composition (mass %) of the alloys used.

	C	Ni	Cr	Nb	B	Fe
T1	0.012	47.0	3.76	2.89	<0.001	Bal
T2	0.014	48.2	3.87	2.85	0.008	Bal
T3	0.014	48.6	3.85	2.90	0.015	Bal
T4	0.010	48.4	4.06	2.84	0.023	Bal

other :0.08Si, 0.04Mn, <0.005P, <0.0005S, 1.5Ti, 0.8Al

2.2 定荷重引張試験

各試料の耐SAGBO特性を調べるため、大気中（酸素分圧2.1×10^4Pa）および低真空中（酸素分圧2.8×10^{-2}Pa）において定荷重引張試験を行い、時間と伸びの関係を測定した。また、大気中および低真空中においてクリープ破断試験を行い、クリープ破断に対するボロンの影響を調べた。試験片を750℃および650℃まで昇温した後、応力500MPaを付加した。

2.3 B分布観察と組織観察

各試料のB分布状態をα線トラックエッチング（ATE）法、により調べた。ATE法の長所はBの高感度（添加量1ppm未満のBを識別）測定が可能である。

試料は所定の熱処理後、約10（横）×10（縦）×1（厚さ）mmの大きさに切り出した。観察面（10×10mm）は鍛造材のT方向に垂直に採取した。またクリープ破断材については、試験片を輪切りにし、観察した。中性子照射は立教大学TRIGA Mark-II（100kW）および日本原子力研究所JRR-4（3.5MW）の原子炉を用いた。

破断面をSEM(S-4200, 15keV)によって観察し、延性－脆性破面率を算出した。

3．実験結果

3.1 結晶粒径

各試料の結晶粒径を求めた結果をTable 3に示す。平均結晶粒径がもっとも大きかったのはT2で84μm、もっとも小さかったのはT3で65μmであった。

Table 3 Average austenitic grain size of each alloy.

alloy	crystal grain diameter
T1	72μm
T2	84μm
T3	65μm
T4	80μm

3.2 定荷重引張試験

3.2.1 単式クリープ試験機による結果

T1（B量がもっとも少ない：<10ppm）について大気中、650～700℃クリープ試験による温度、引張応力条件およびクリープ破断時間の関係をTable 4に示す。インコロイ908合金に相当するT1は、ITERの熱処理[2]と

して実際に採用されている650℃、240h（500Mpa）の引張応力下では破断しなかった。したがって真空中のクリープ試験では、これらの結果よりさらに長くなることが予想されるため当初750℃、500Mpaで試験した。

3.2.2 両てこ式クリープ試験機による結果

(1) 750℃クリープ試験

大気中における各試料の時間ー伸び曲線をFig. 1に示す。大気中で破断時間がもっとも長かったのがT2、ついでT1であり、B量の多いT3、T4は短時間で破断した。

Table 4. Relation among temperature, tensile stress and creep ruptured time in air.

Alloy	Temperature (℃)	Tensile stress (Mpa)	Rupture Time
T1	650	300	>240h
T1	650	500	>240h
T1	700	500	4.4h
T1	750	500	14.1min

これはB量の多い試料の場合、時効硬化が比較的長時間側で生じることに起因していると考えられる。破断伸びはT1、T2が5〜6%、T3、T4が約3%程度ときわめて小さい。破断した試験片をSEM観察すると、大気中の実験ではすべての試料で脆性破面が見られ、局所的に延性破面が観察された。

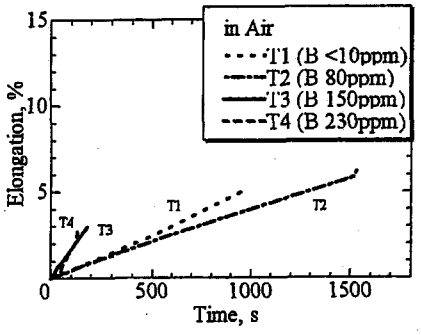

Fig.1 Creep curves of the alloys in air at 750℃.

低真空中における各試料の時間ー伸び曲線をFig. 2に示す。破断時間がもっとも長かったのがT2、ついでT3であったが、T2の破断時間はT3に比べると3倍以上の強度差を示した。破断伸びは両試料とも30%程度あった。他方、破断絞りは、B量が多いほど大きかった。また破断時間はB量が少ないT1およびB量が多いT4とT2を比較すると、T2は著しく長寿命であった。

(2) 650℃クリープ試験

大気中における各試料のクリープ曲線をFig.3に示す。T1およびT4は破断時間が短く、伸びも小さい。これに対してT2およびT3の破断時間、クリープ伸びはともに改善される。クリープ伸びはT2が約5%、T3が2%と低い値であった。定常クリープ速度は、T3が最も小さな値を示した。

低真空中（10^{-4}Torr＝2.8×10^{-2}Pa）での試験結果をFig.4に示す。Fig.3と比べると、すべての試料において破断時間は長くなっており、Bを添加したT2〜T4の破断時間、破断伸びはT1に比べて大きく、とくにT2の試

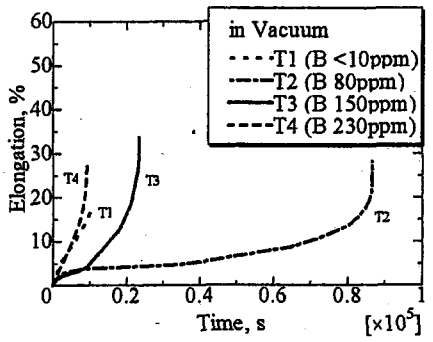

Fig.2 Creep curves of the alloys in vacuum at 750℃.

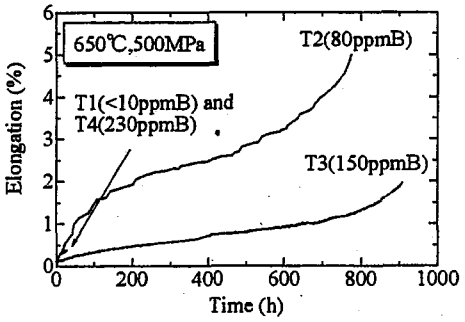

Fig.3 Creep curves of the alloys in vacuum at 650℃.

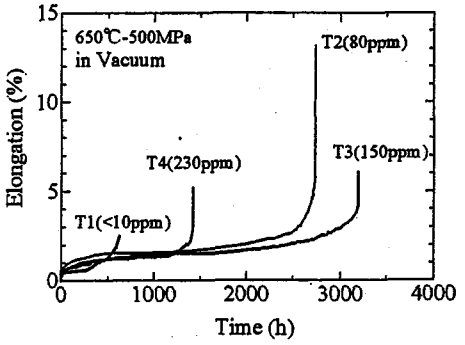

Fig.4 Creep curves of the alloys in vacuum at 650℃.

料においては顕著であり、T3 に比べると 2 倍の破断伸びを示す。

3.4 粒界脆性破面率

クリープ試験片の破断面を SEM 観察した結果、大気中では、どの試料にも粒界破面が観察される。これらは粒界に沿って酸化が生じて粒界が脆化し、割れに至った SAGBO 割れと思われる。

低真空中では大気中と比較すると、擬へき開破面のように見える破面や延性破面も観察されるようになる。他方、一部には Fig. 7 (c)に見られるような SAGBO 割れによって生じたと思われる粒界破面も観察され、この程度の低真空中では SAGBO が抑制できないことがわかる。

クリープ破壊後の SEM 破面から粒界脆性破面率を求めた結果を Fig.5 に示す。これらの結果からわかるように、各試料において粒界脆性破面の比率が大きい。とくに大気中の試験結果においては顕著である。

Fig.6 に示した低真空中におけるクリープ破断時間の優位順は T3(150ppm)>T2 (80pppm) >T4(230ppm) >T1(>10ppm)である。クリープ破断時間と脆性破面の比率を比べると、クリープ破断時間の短かった T1 および T4 の脆性破面の比率が多かった。またクリープ伸びは T2>T3>T4>T1 の順である。

低真空中における試験結果では T4 を除いて、粒界脆性破面率は約 6～20%減少した。T2 および T3 では約 20 %低下するが、T4 の脆性破面率はあまり低下しない。

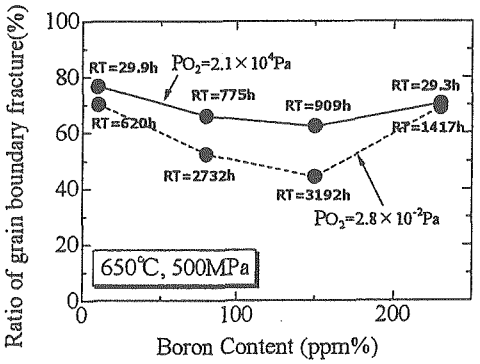

Fig.5 Ratio of grain boundary fracture after creep rupture.

3.5 ATE 法によるほう化物の観察

(1) 単純加熱材

980℃、1h 空冷材（溶体化処理まま）における各試料の ATE 像を Fig.6 に示す。T1 (＜10ppm) および T2(80ppm)の試料には鮮明な ATE 像は観察できなかったが、T2 ではわずかに球形のほう化物が観察できる。T3 (150ppm) では、オーステナイト結晶粒界への B の偏析、そして球状ほう化物と一部に棒状のほう化物が認められた。また T4(230ppm)でも同じように B のオーステナイト結晶粒界への偏析と、棒状のほう化物が多く認められた。

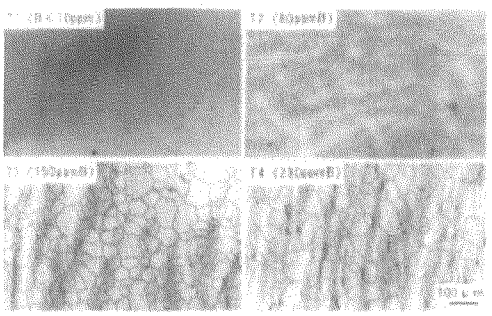

(a)<10ppmB (b)80ppm (c)150ppm (d)230ppm

Fig.6 ATE images of the alloys after the solution treatment at 980℃ for 1h.

980℃、1h 空冷後、650℃で 40 h 加熱した後の ATE 像を Fig.7 に示す。溶体化処理ままの ATE 像に比べると T1 および T2 において、弱いコントラストであるが ATE 像が観察できるようになった。しかし、T1 では球状ほう化物はほとんど観察できなかった。また T2 の球状ほう化物は、密度がわずかに高くなった。T3 および T4 では、溶体化処理まま状態に比べて、微細なほう化物が多数観察できるようになる。

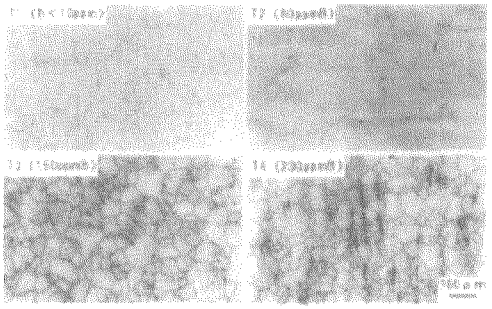

(a)<10ppmB (b)80ppm (c)150ppm (d)230ppm

Fig.7 ATE images of the alloys heated at 650℃ for 40h after the solution treatment at 980℃ for 1h.

(2) クリープ破断材

650℃においてクリープ試験した後、破断部から約 10mm 離れた平行部から試料を採取し、ATE 像を観察した。大気中において試験したクリープ破断材の ATE 像を Fig.8 に示す。

クリープ破断時間は T1 が 29.9 h、T4 が 29.3 h であった。クリープ破断材 (Fig.12) と単純加熱材 650℃、40 h の ATE 像 (Fig.11) は、クリープ破断材の熱履歴の方が単純加熱材に比べて約 10 h 短いが、ATE 像は大きく異なった。クリープ破断の T1 には、単純加熱材で

観察されなかった球状ほう化物が観察され、T4では微細ほう化物が消失していた。またT2のオーステナイト結晶粒界にはBが鮮明に偏析しており、球状ほう化物も凝集化している。これは応力500MPaの影響であると考えられる。したがって、本合金系では応力下でオーステナイト結晶粒界へのBの偏析およびほう化物の凝集が促進するといえる。

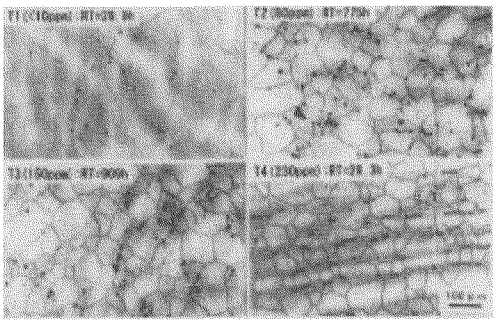

(a)<10ppmB (29.9h) (b)80ppm (775h)
(c)150ppm (909h) (d)230ppm (29.3h)

Fig.8 ATE images of the alloys creep-fractured at 650℃ in air.

一方、B量の多いT4 (230ppm) のクリープ破断時間がT2(80ppm)、T3 (150ppm) に比べて著しく短いが、この理由として、ほう化物が棒状に析出することが関係していることが推察される。

低真空中において試験したクリープ破断材のATE像をFig.9に示す。ATE像の大きな相違はT1を除いて認められ

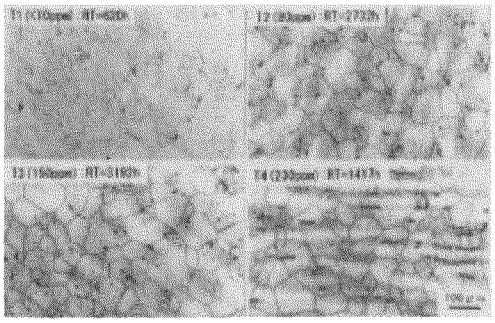

(a)<10ppmB (620h) (b)80ppm (2732h)
(c)150ppm (3192h) (d)230ppm (1417h)

Fig.9 ATE images of the alloys creep-fractured at 650℃ in vacuum.

4. 考察

津田ら[9]は、Fe-36%Ni合金において0～150ppmの範囲でB添加して、大気中及びArガス中で1250℃の引張試験を行い、絞り値から熱間加工性を評価し、B添加が表層付近の粒界酸化を抑制し絞り値の改善に寄与するとしている。Bによる粒界酸化抑制のメカニズムについては、酸素は表層から内部へ粒界拡散するのに対し、Bは粒界を通って表層に向けて拡散し、酸素を捕縛することにより、酸素の粒界拡散を阻止し、粒界脆化を防止するとしている。しかし彼らの結果をみると、B添加による絞り値の上昇は大気中だけではなく、Arガス中でも生じており、大気中での絞り値の上昇は、Ar中の上昇と大差がない。したがって、B添加による絞り値の改善は、酸化抑制とは関係のない材料強度の上昇によることも考えられる。

超合金のSAGBO割れのメカニズムに関して、Carpenterら[4]は、き裂先端においてNbの酸化が生じることによると報告しているが、詳細は明らかとなっていない。Nazmyらは[5]、IN706合金(0.02C-0.08Mn-16.0Cr-41.4Ni-1.7Ti-0.18Al-2.8Nb-Fe)を母材として、これに157ppmBを添加した試料を溶製し、705℃においてさまざまな歪み速度で引張試験を行っている。その結果、Bを添加した鋼の延性が増加した。B無添加とB添加材の延性伸びについて比較すると、(a)低歪み速度の方がB添加の影響が大きく、(b)高温になるほどB添加の影響が大きいことから、BがSAGBOを抑制したものと結論している。しかし、彼らは大気中の実験しか行っておらず、B添加による延性向上が、SAGBO抑制によるものとは判断できないものと考えられる。

前章で述べた実験結果から、大気中と低真空中における各合金の破断時間と定常クリープ速度を求めFigs.10, 11に示す。各合金のクリープ破断時間は、B添加の影響、雰囲気の影響いずれにおいても、定常クリープ速度に対応しているように思われる。通常、定常クリープ状態は、変形による加工硬化と、転位の上昇運動、交差すべりなどによる回復が平衡することによって生じる。しかし、酸化が生じる場合、上記加工硬化、回復に加えて酸化による弱化の3者間のバランスによって、見かけ上定常クリープ状態が生じると考えられる。この場合、酸化による弱化が生じない場合に比べ定常クリープ速度は上昇する。Fig.11における大気中と低真空中での定常クリープ速度の差は、この酸化による弱化に起因するものと考えられる。

Fig.5で示されるように、大気中でクリープ破断した試料は低真空中に比べ多くの粒界で脆性破壊しており、著しく破断伸びが小さいので、SAGBOが生じているものと考えられる。B添加により粒界破面率が低下し破断伸びが向上するので、B添加によりSAGBOが抑制されたためかどうかは明らかでない。酸化とは関係ないB添加による材料強化効果による可能性もある。BによるSAGBO抑制効果と材料強化効果の大きさを明確にするには、完全にSAGBOが生じないような高真空中での実験データが必要である。しかし、高真空中でのデータ採取が間に合わなかったので、以下、低真空中における実験結果を用いてB添加による破断伸び向上の理由を考察

する。

低真空中においても、すべての合金で粒界破面が認められるが、粒界破面率は大気中より低下する。しかし、粒界破面率の低下はBを添加していないT1では小さく、80ppm～150ppmのBを添加したT2、T3では大きく、

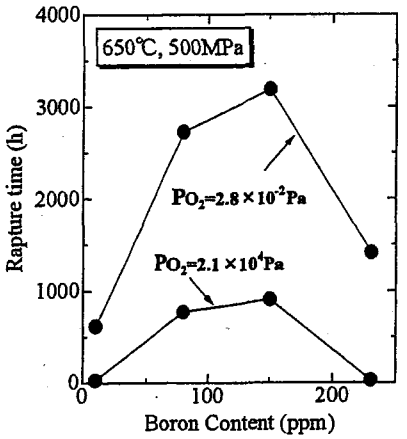

Fig.10 Rupture time of each alloy in air and vacuum.

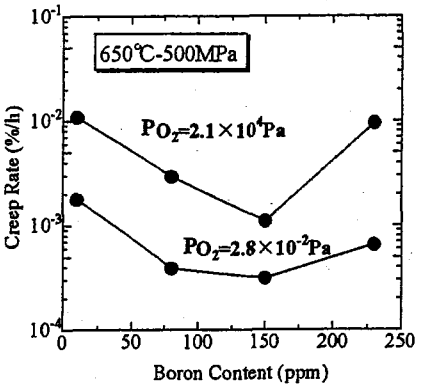

Fig. 11 Relation between minimum creep rate and amount of B.

破断寿命も大幅に増加する。このことから、Bを添加しないと真空度が十分でないため低真空ではSAGBO抑制効果が小さいが、B添加によりSAGBOがより大きく抑制されるものと考えられる。

B添加量が多いT4（230ppmB）では、低真空中でもクリープ破断寿命は著しく低下する。この理由は、TEMによりT4では粗大析出物（$M_{23}C_6$）が粒界に沿って析出していることが観察され、またATEによってもT2およびT3は微細な球状ほう化物、T4では板状または塊状の粗大ほう化物が観察されたことから、大気中、低真空中いずれにおいても、T4のクリープ破断寿命および破断伸びがT2およびT3に比べて小さいのは、このような粒界析出物によって粒界脆化が生じるためと考えられる。

4．結　言

本研究を通して、以下のことが明らかになった。

(1) Incoloy 908合金に80-150ppmBを添加することにより大気中、低真空中での破断伸び、破断時間が改善された。

(2) 大気中でクリープ破断した試料は低真空中に比べ多くの粒界で脆性破壊しており、著しく破断伸びが小さいので、SAGBOが生じているものと考えられる。

(3) 低真空中においても、すべての合金で粒界破面が認められるが、粒界破面率は大気中より低下する。

(4) 低真空では真空度が十分でないため、B無添加材においてはSAGBO抑制効果が小さい。しかし、Bを添加するとSAGBOがより大きく抑制され、クリープ破断寿命が延びる。

(5) B添加によって酸化とは関係ない材料強度が上がり破断寿命が向上する効果の存在を否定することはできない。この効果がどの程度のものかを明らかにするには、もっと高い真空中でのデータを採取する必要がある。

参考文献

1) M.M.Morra, R.G.Ballinger, and I.S.Hwang:Metall. Trans, A,23A(1992),3177

2) Y. Tsuchiya et al., Residual Stress of a Jacket Material for ITER Superconducting Coil, Physica B, 241-243, 1264 (1998).

3) 津田正臣，根本力男：鉄と鋼，80（1994），729

4) W. Carpenter, B.S.-J. Kang, and K.M. Chang: Superalloys 718, 625, 706 and Various Derivatives, (1997), 679.

5) Nazmey : M. Nazmy, M. Staubli and C. Noseda: Superalloys 718, 625, 706 and Various Derivatives, (1997), 419.

Ⅲ. 結果の公表

1) 朝倉健太郎、柴田浩司、澤幡浩之、川手　稔、原澤　進、：原研炉を用いたα線トラックエッチング法による鋼中ボロンの状態分析観察システムの確立）、鉄と鋼, 89 (2003), 369-374

2) 朝倉健太郎、柴田浩司、原澤　進、澤幡浩之、川手　稔：α線トラックエッチング法における推奨フィルムの探索、鉄と鋼, 89 (2003), 375-380

3) Emad EL-KASHIF, Kentaro ASAKURA and Koji SHIBATA: Effects of Nitrogen in 9Cr-3W-3Co Ferritic Heat Resistant Steels Containing Boron, ISIJ Intern. 42(2002), 1468-1476

4) Emad EL-KASHIF, Kentaro ASAKURA and Koji SHIBATA: Effect of Cooling Rate after Recrystallization on P and B Segregation along Grain Boundary in IF Steels, ISIJ Intern. 43(2003), 2007-2014
5) Emad EL-KASHIF, Kentaro ASAKURA and Koji SHIBATA: Role of Boron in Preventing Intergranular Fracture in Steels: International Forum for the Properties and Application of IF Steels, IF STEELS, 2003, ISIJ, (2003),188-191
6) 朝倉健太郎、柴田浩司：低炭素鋼における B の挙動に及ぼす Mo の影響：鉄鋼材料における微量ボロンの挙動解明と利用促進研究会、日本鉄鋼協会、(2003),25-33
7) Emad EL-KASHIF, Kentaro ASAKURA and Koji SHIBATA : Effects of Nitrogen in 9Cr-3W-3Co Ferritic Heat Resistant Steels Containing Boron、鉄鋼材料における微量ボロンの挙動解明と利用促進研究会、日本鉄鋼協会、(2003),114-121
8) 山口和之、柴田浩司、朝倉健太郎、小関敏彦：鉄鋼材料における微量ボロンの挙動解明と利用促進研究会、日本鉄鋼協会、(2003),147-151
9) Emad EL-KASHIF, Kentaro ASAKURA and Koji SHIBATA : Effects of Boron on the Grain Growth in Ultra High Purity 18%Cr Ferritic Stainless Steel, 鉄鋼材料における微量ボロンの挙動解明と利用促進研究会、日本鉄鋼協会、(2003),152-158
10) Emad EL-KASHIF, Kentaro ASAKURA and Koji SHIBATA : Effect of Cooling Rate after Recrystallization on P and B Segregation along Grain Boundary in IF Steels, 鉄鋼材料における微量ボロンの挙動解明と利用促進研究会、日本鉄鋼協会、(2003),159-166
11)朝倉健太郎、柴田浩司：インコロイ 908 の高温強度と SAGBO に及ぼす B の効果、鉄鋼材料における微量ボロンの挙動解明と利用促進研究会、日本鉄鋼協会、(2003),181-188

Ⅳ. 今後の方針

原研炉を用いての ATE 法の手法は前述したように、ほぼ確立した。

そこで今後については以下の研究について遂行する。

(1) 溶接構造用鋼の成分を基本に C, Nb, B を変化させた鋼を真空溶解で作製し、インゴットを 15mmまで圧延後、12mm□×70mm試験片を作製する。その後、高周波加熱により溶接熱影響部相当の熱サイクル（加熱ピーク 1400℃×１～10ｓ，冷却速度 1～10℃/ｓ）を付与しacicular フェライトを含む溶接部組織を再現する。その断面（12mm□）上で組織観察を行うとともに、それに対応するボロンの存在位置の調査研究を行う。また、ベイナイト変態に関しては、等温変態（600℃～350℃）の各ステージのサンプルを作成し、B の状態分布挙動の調査を行う。

具体的には溶接構造用鋼に「硝酸セルロースフィルム」を貼付し、中性子照射する。1 回の照射で約 20－30 個をポリエチレンの袋に封入し、6 時間×2 日照射する。72～96 時間以上の冷却後、硝酸セルロースフィルムをはく離し 2.5N の水酸化ナトリウムでエッチング処理を行い、ATE 像を写真撮影する。

(2) これまでは鉄鋼材料におけるボロン分布観察を主として行ってきたが、今後は Cu および Cu 合金(Cu-Ni-Si-0.02B)を用いての研究も併せて遂行する。高周波加熱溶解炉で純銅中に B 量を 25ppm、50ppm、100ppm 添加し、種々の熱処理における B 分布について調査研究を行う。

(3) これまで照射設備としてはJRR-4 の「医療用中性子照射ビーム設備（カドミ比 2.5）」を用いてきたが、カドミ比の大きい JRR-3 の「放射化分析用照射設備(PN-3、カドミ比 290)」を用いて ATE 分解能向上に関する研究についても行う。最大の課題は硝酸セルロースフィルムの試料からの剥離という問題があるので、この点についてクリアする予定である。

謝辞

本研究の中性子照射に関する一部は東京大学原子力研究総合センター（東海研究所）の澤幡浩之氏と川手 稔氏の協力によった。ここに感謝の意を表します。

5)河野公栄、Jerzy Falandysz、脇本忠明、南極海洋生態系を構成する生物種に蓄積する残留性有機塩素化合物と有機態ハロゲン、第11回環境化学討論会、講演要旨集、486-487、神奈川、2002年6月3ー5日.
6)河野公栄、Jerzy Falandysz, 脇本忠明、中性子放射化分析法による南極生物中の有機態ハロゲン(EOX)の定量、第39回理工学における同位元素・放射線研究発表会、要旨集 p166, 東京、2002年7月3ー5日
7)河野公栄、Jerzy Falandysz, 脇本忠明、南極昭和基地付近で捕獲したウェッデルアザラシにおける有機態ハロゲン(EOX)の機器中性子放射化分析、2002 日本放射化学会年会・第46回放射化学討論会、要旨集 p121、北海道、2002年9月23ー25日.
8)河野公栄、河野裕美、Jerzy Falandysz, 脇本忠明、Neutron activation analysis of extractable organohalogens (EOX) in wildlife. -Accumulation in brown booby (*Sula leucogaster*) from Nakanokamishima Island, South Ryukyu, Japan. 機器中性子放射化分析法による野生生物に蓄積する有機態ハロゲンの定量、第11回 東京大学原子力研究総合センターシンポジウム、講演要旨集、p336-339、東京、2002年10月7,8日.
9)河野公栄、脇本忠明、河野裕美、Jerzy Falandysz、脇本忠明、環境科学における機器中性子放射化分析法の応用 --野生鳥類に蓄積する有機態ハロゲン(EOX)-、原総センターNEWS No.87、東京大学原子力研究総合センターニュース Dec. 2002
(http://www.rcnst.u-tokyo.ac.jp/)
10)河野公栄、脇本忠明、機器中性子放射化分析法による有機態フッ素(EOF)分析条件の検討、第40回理工学における同位元素・放射線研究発表会、要旨集 p154、東京、2003年7月9-11日
11)河野公栄、中津 尊、脇本忠明、松山周辺域で採取した魚類における有機態フッ素(EOF)の機器中性子放射化分析、2003 年日本放射化学会年会・第47回放射化学討論会、p115、泉佐野市、2003年10月1〜3日
12)河野公栄、松井三明、鹿島勇治、松田宗明、中性子放射化分析の環境化学研究への利用 -廃棄物焼却灰中の有機態ハロゲン(EOX)-、放射化分析研究会 平成15年度研究会、日本原子力研究所東海研究所、平成16年3月26日

7-2

高線量γ線により生成する石英過酸化ラジカル中心と先第四紀年代測定への応用

Peroxy radical center in quartz produced by high γ-ray dose and its application to pre-Quaternary dating

福地 龍郎[1]・西村剛志[1]・伊藤泰男[2]
1 山口大学理学部化学地球科学科，2 東京大学原子力研究総合センター
Tatsuro FUKUCHI[1], Takehi NISHIMURA[1] and Yasuo ITO[2]
1 Department of Chemistry & Earth Sciences, Faculty of Science, Yamaguchi University
2 Research Center for Nuclear Science & Technology, University of Tokyo

There are mainly two types of lattice defect center in quartz, vacancy-associated and impurity types. As for the vacancy-associated type centers, E' center derived from oxygen vacancies, peroxy radical center (PRC) derived from oxygen interstitials and non-bridging oxygen hole center (NBOHC) derived from non-bridging oxygen are well known. These centers are detectable as ESR (electron spin resonance) signals and mainly applicable to Quaternary dating. Many researchers had so far considered that the PRC could not be produced in crystalline quartz but in amorphous silica glass by γ-ray irradiation. Thus we have examined in detail the behavior of the PRC by high γ-irradiation and have discussed whether or not the PRC is applicable to pre-Quaternary dating. We used five natural quartz samples extracted from Cretaceous and Tertiary granitic rocks named the Aio, Hofu, Murotsu, Towa and Tamagawa granites in Yamaguchi prefecture. The radiometric ages of these granitic rocks have been determined by Rb-Sr or K-Ar dating. The E' center irregularly increased after high γ-irradiation, whereas the PRC almost proportionally increased with irradiation dose. As for the reason why the PRCs obtained from natural quartz grains in those granites increase by γ-irradiation, amorphous parts in natural crystalline quartz may be attributed to the production of the PRC. As a result of ESR dating of those quartz samples using the PRCs, all ESR ages obtained are consistent with the radiometric ages within the range of measurement errors. This result indicates that the PRC is applicable to pre-Quaternary dating.

【はじめに】

石英中には幾種類もの格子欠陥（点欠陥）が存在し，自然放射線により励起した不対電子を捕獲している．この様な格子欠陥に捕獲された不対電子は，電子スピン共鳴（ESR）装置を用いることによりESR信号として検出される．石英から検出されるESR信号の空孔型中心には，石英中の酸素イオンの抜けた空孔に電子が1個獲得された格子欠陥であるE'中心（g=2.0011）[1-3]の他，格子間酸素に正孔（ホール）が捕獲されている過酸化ラジカル中心（peroxy radcal center，PRC）や非架橋酸素に正孔が捕獲されたNBOHC（non-bridging oxygen hole center）が知られている[3-5]．PRCは結晶異方性のため，最大・中間・最小のg値（g_1=2.027，g_2=2.0085，g_3=2.0020）[6]を持つ．石英中のESR信号強度は自然放射線の下で時間と共に増大して行くので，ESR信号強度と自然放射線量との比例関係を利用することにより石英の年代値を決定できる．同様の性質は石英以外の鉱物にも認められ，主に第四紀の年代測定として利用

研究施設・装置：JRR-3M（PN-2），JRR-4（S-パイプ），コバルト60ガンマ線照射施設，ESR装置
研究分野：地球物性学，地球年代学

されている．一方，ESR 信号が先第四紀の年代測定に適用された例も幾つか知られている [7-9] が，γ線照射による効果を無視するなど，得られた結果の信憑性については問題がある．そこで本研究では，高線量γ線照射による ESR 信号の挙動を調べ，ESR 年代測定法を第四紀年代測定から先第四紀年代測定へ適用することが可能かどうかについて考察する．

【高線量γ線照射実験】

石英粒子（昭和化学株式会社製）に日本原子力研究所高崎研究所の ^{60}Co 線源を利用して線量率約 22kGy/h で約 90～1800kGy の高線量γ線照射を行い，照射前後の ESR 信号を測定した結果を Fig.1 に示す．ESR 測定は， Bruker 製の EPR 装置 E500 －CW を用い，室温において，掃引磁場 336.5±5mT，マイクロ波出力 1mW，変調磁場 100kHz0.05mT，掃引時間 20.97sec で行い，50 回積算したスペクトルを測定結果とした．γ線照射に伴い，E'中心と PRC の信号強度が増大して行くのが分かる．これまで，PRC はγ線照射によってはほとんど増大しないと考えられてきた [7-8] ので，今回得られた結果はこれまでの定説を覆すものであり，今後 PRC を年代測定に利用する上で非常に重要なデータである．

【粒子線照射結果との比較】

高線量γ線照射と中性子線照射による効果を比較するために，中性子束の異なる日本原子力研究所の原子炉 JRR-3M（PN-2）と JRR-4（S パイプ）で照射した石英試料の ESR スペクトルを Figs.2 及び 3 に示す。JRR-3M における熱中性子束は 5.0×10^{13} (n/cm^2·s)，速中性子束は 1.0×10^{11} (n/cm^2·s) で，JRR-4 における熱中性子束は 5.0×10^{13} (n/cm^2·s)，速中性子束は 5.5×10^{12} (n/cm^2·s) である。ESR 測定は，日本電子製 ESR 装置 JEOL RE-2X を用い，室温において，掃引磁場 336.5±5mT，マイクロ波出力 1mW，変調磁場 100kHz0.05mT，掃引

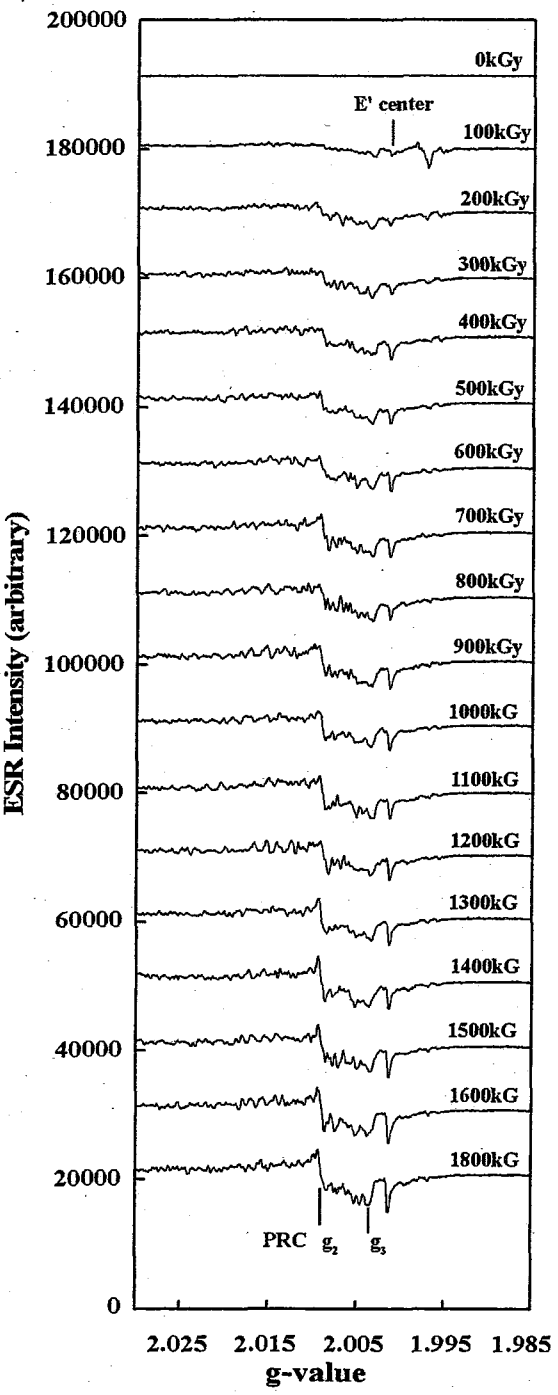

Fig.1 ESR spectra obtained from quartz grains irradiated by γ-rays with a ^{60}Co source.

時間 8min.で行い，3 回積算したスペクトルを測定結果とした．なお，同一の試料で ESR 信号を比較した結果，日本電子製と Bruker 製の ESR 装置で若干の S/N 比の違いは認められるが，スペクトルの形状にはほとんど違いは見られなかった．

JRR-4に比べて，速中性子束が熱中性子束よりも 2 桁小さいJRR-3Mでの照射では，E'中心及びPRCの生成が一応認められるが，E'中心の生成の方がより顕著である（Fig.2）．これに対して，JRR-4（S パイプ）において，熱中性子束をほぼ同一にして，速中性子束を JRR-3M よりも 1 桁大きくした照射では，PRC がほとんど増大しないのに対し，E'中心に著しい増大が認められた（Fig.3）．また，これらの信号の他に，g =2.0051 で鋭いピークを持つ未知の ESR 信号も検出されている（Fig.3）。この未知の信号は，速中性子束が高い場合のみ検出され，熱中性子捕獲により放出されるγ線やβ線，β反跳によってはほとんど生成されないことが分かっている[10-11]。

一方，石英粒子表面にホウ酸（boric B-10 acid）を吸着させ，JRR-4 において Fig.3 と同じ条件下で中性子照射を行い，^{10}B と熱中性子の反応 [$^{10}B(n,\alpha)^{7}Li$)]により発生するα線（1.47MeV）照射の効果を調べた結果を Fig.4 に示す。α線照射により，E'中心や未知の信号（g =2.0051）はさらに増大し，照射効果は速中性子よりもずっと大きいが，PRC はほとんど増大しないことが分かる。

以上の結果に加えて，熱中性子捕獲による放射化の際にはγ線が大量に発生することを考慮すると，石英結晶から検出される PRC は粒子線ではなく，主にγ線により生成すると考えられる．

【先第四紀年代測定】

高線量γ線照射により生成する PRC が，先第四紀年代測定に適用可能であるかどうかを調べるために，山口県内に分布する年代が既知の花崗岩（秋穂・防府・室津・東和・田万川の各花崗岩）から石英粒子を抽出し，高線量γ線を照射した．Fig.5

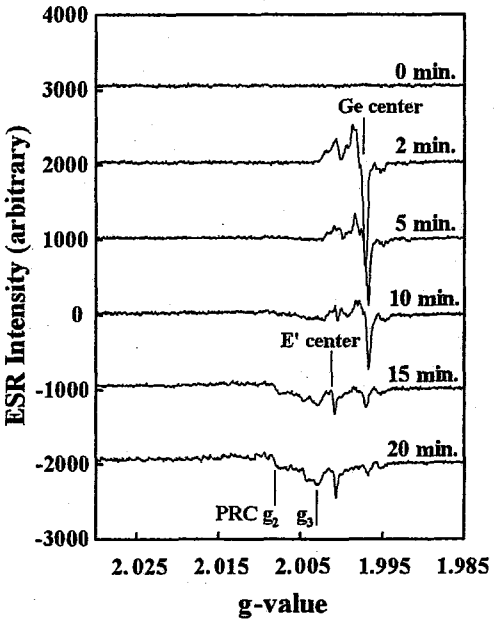

Fig.2 ESR spectra obtained from quartz grains irradiated by neutrons at JRR-3M

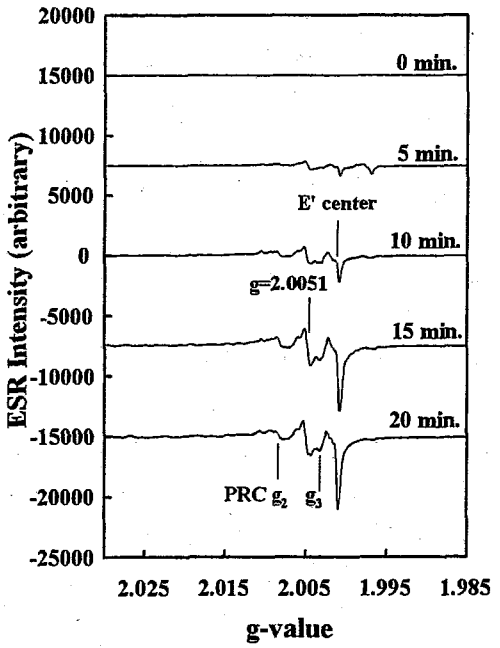

Fig.3 ESR spectra obtained from quartz grains irradiated by neutrons at JRR-4.

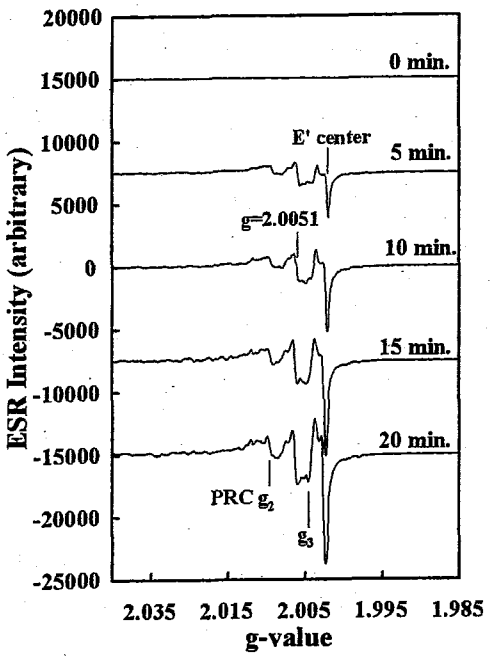

Fig.4 ESR spectra obtained from quartz grains coated with boric B-10 acid irradiated by neutrons at JRR-4

は，秋穂花崗岩から抽出した石英粒子から得られる ESR 信号のγ線照射による変化を示す．図からも明らかなように，人工γ線照射により PRC は規則的に増大して行く．PRC の g_2 における強度を測り，各照射線量から得られる強度データを最小二乗法により飽和曲線に回帰し，飽和曲線の強度がゼロになる点まで曲線を外挿すると，総被曝線量（E_D）が得られる．一方，各花崗岩試料中の ^{238}U，^{232}Th，K_2O の濃度を産業技術総合研究所のICP-MS（横川電気製PMS-200）及びICP-AES（日本Jarrell Ash製IRIS - Advantage）を用いて定量し，Adamiec and Aitken（1998）[12] の換算表を用いて年間線量率（D）を計算し，最後に総被曝線量を年間線量率で割ること（E_D /D）により，ESR 年代値が得られる（Table 1）．PRC から得られる ESR 年代値と放射年代値を比較すると，両者は全試料とも誤差範囲内で一致していることが分かる．

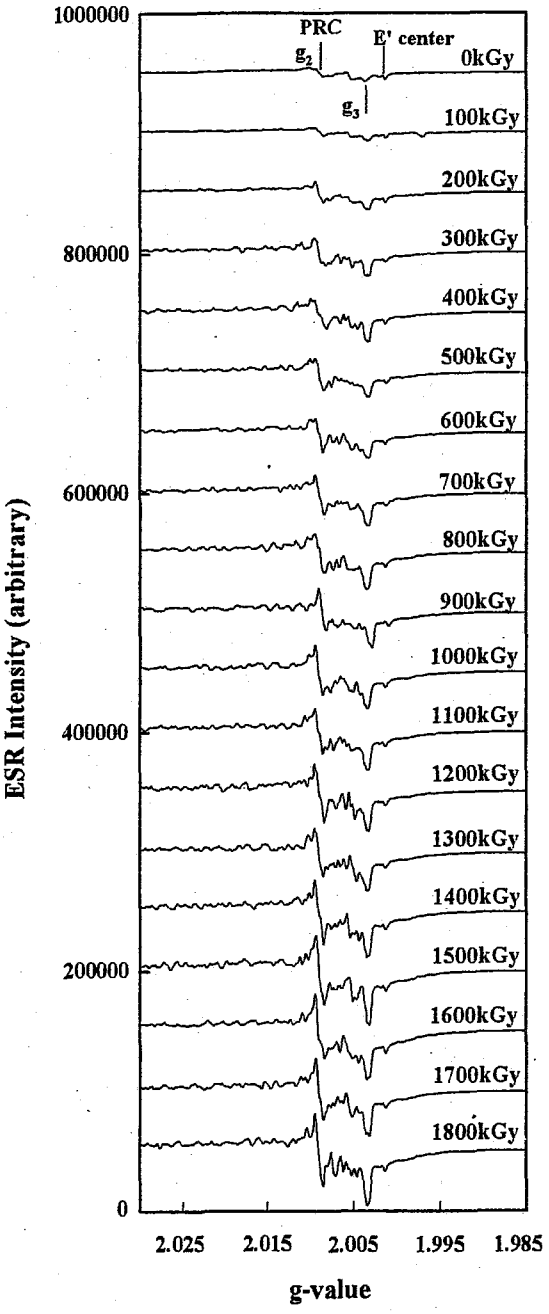

Fig. 5 ESR spectra obtained from quartz grains in the Aio granite distributed in Yamaguchi Prefecture irradiated by γ-rays with a ^{60}Co source.

【考察】

人工石英結晶を解析したWeeks (1956) [13] 以来，PRCはγ線照射ではほとんど生成されないと考えられていたが，今回の高線量γ線照射によってPRCがγ線照射に対して規則的に増大することが明らかとなった．これまでの研究によると，変形石英のように結晶内部に亜結晶粒界（subgrain boundary）が多く存在する石英からは強いPRCが検出されることが知られている [14]．こうした亜結晶粒界や通常の結晶成長の過程でできる結晶粒界，流体包有物の気泡が抜けた空洞部分などにはアモルファス領域が多く存在するので，石英結晶中のPRCはこの様なアモルファス領域で大量に生成している考えられる．

一方，天然石英の内部には微量の ^{238}U や ^{232}Th が含まれており（Table 2），これらの元素から放出されるα線やα反跳によってもアモルファス領域が生成する可能性が指摘されている [8]．しかし，^{238}U や ^{232}Th の含有量が多く，α線による損傷効果がより大きいと考えられる室津花崗岩や東和花崗岩よりも，α線の損傷効果がより小さいと考えられる秋穂花崗岩や防府花崗岩の方が，PRCはより高いγ線感度を示している（Fig.6）．この結果は，石英内部のアモルファス領域の生成にはα線がそれ程大きく寄与している訳ではないことを示している．

【結論】

本研究の結論として以下の項目が挙げられる．

1)石英結晶中のPRCは，高線量γ線照射によって主に生成され，中性子線やα線による生成効果は低いことが明らかとなった．

2)年代既知の花崗岩中に含まれる石英粒子のPRCから得られるESR年代値と放射年代値は誤差範囲内で一致し，PRCは白亜紀～古第三紀の年代測定に適用できる可能性がある．

3)石英結晶中にPRCが生成するメカニズムとしては，結晶粒界や空洞部分などのアモルファス領域の存在が関係していると推定される．

Table 1 Comparison between ESR and radiometric ages obtained from granitic rocks in Yamaguchi.

Name of granite	ESR age (Ma)	Radiometric age (Ma)
Aio	84.5±19.3	91.6±4.0 [15] 83 [17]
Hofu	72.7±30.2	95 [17]
Murotsu	91.5±30.8	96.1±4.9 [16] 92.0±3.9 [16]
Towa	107.2±58.9	95.5±4.3 [16] 84 [17]
Tamagawa	53.0±48.4	39.3±4.6 [18] 32.8±1.3 [19]

15) Rb-Sr (whole rock: Wakisaka, 1982), 16) Rb-Sr (whole rock: Shigeno & Yamaguchi, 1976), 17) K-Ar (biotite: Kono & Ueda, 1966), 18) Rb-Sr (biotite-whole rock: Seki, 1978), 19) FT (zircon: Murakami, 1985)

Table 2 Concentrations of ^{238}U and ^{232}Th inside quartz grains and annual doses (D) contributed by α -rays.

Name of granite	^{238}U (ppm)	^{232}Th (ppm)	D (mGy/y)
Aio	0.105	0.193	2.9×10^{-5}
Hofu	0.102	0.157	2.7×10^{-5}
Murotsu	0.269	2.608	1.8×10^{-4}
Towa	0.526	11.538	6.9×10^{-4}
Tamagawa	0.168	0.411	5.3×10^{-5}

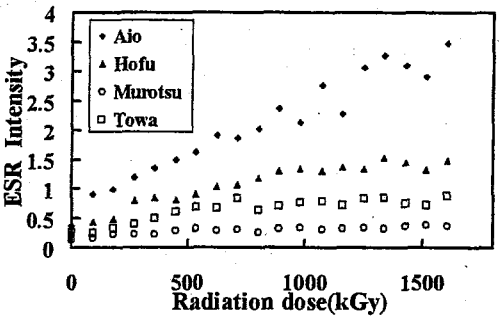

Fig.6 Comparison of radiation sensitivity of PRCs obtained from the age-known granitic rocks in Yamaguchi.

【謝辞】

本研究を進めるに当たり，中性子照射，γ線照射及び線量計測で種々のご協力頂いた開放研究室の澤幡浩之氏，川手　稔氏，大工原和子氏，原研高崎研究所の羽田徳之氏，ESR 測定でお世話になった原研東海研究所の正木信行氏，ICP 分析でお世話になった産業技術総合研究所の今井登氏，年間線量率換算表についてご教示頂いた北海道教育大学の鴈沢好博氏に深く感謝致します。本研究では科学研究費補助金基盤研究 C(2)(No.13640462：研究代表者 福地龍郎）の一部を使用した。

引用文献

1) D. W. McMorris (1970) *Nature* **226**, 146-148.

2) K. L. Yip & W. B. Fowler (1975) *Phys. Rev.* **B 11**, 2327-2338.

3) D. L. Griscom (1979) *Proc. 33rd Freq. Contr. Symp.*, 98-109.

4) M. Stapelbroek, D. L. Griscom, E. J. Friebele & G. H. Sigel Jr.(1979) *J. Non-Cryst.Solids* **32**, 313-325.

5) E. J. Friebele, D. L. Griscom & M. Stapelbroek (1979) *Phys. Rev. Lett.***42**, 1346-1349.

6) D. L. Griscom (1989) *Phys. Rev.* **B40**, 4224-4227.

7) E. G. Garrison, R. A. Rowlett, D. L. Cowan & L. V. Holroyd (1981) *Nature* **290**, 44-45.

8) A. L. Odom & W. J. Rink (1989) *Geology* **17**, 55-58.

9) R. Grün (1989) *Nature* **338**, 543-544.

10)福地龍郎（1999）原子炉利用による研究成果集(平成 9 年度), JAERI-Review 99-007, 487-491.

11)福地龍郎（2001）原研施設利用共同研究成果報告書（平成 12 年度）通巻 40 号，68-71.

12) G. Adamiec & M. Aitken (1998) *Ancient TL* **16**, 37-50.

13) R.A. Weeks (1956) *J. Appl. Phys.* **27**, 1376-1381.

14) T. Fukuchi (1996) *Appl. Radiat. Isot.* **47**, 1509- 1521.

15)脇坂安彦(1982)日本地質学会第 89 年学術大会講演要旨, 408.

16)茂野博・山口勝(1976)地質学雑誌 **82**, 687－698.

17)河野義礼・植田良夫(1966)岩石鉱物鉱床学会誌 **56**, 191－211.

18) T. Seki (1978) *Mem. Fac. Sci. Kyoto Univ.*,[*Geol. & Minel.*] **45**, 71－110.

19) 村上允英(1985)地質学雑誌 **91**(10), 723－742.

成果の公表

1) T. Fukuchi & N. Imai (2001) ESR and ICP analyses of the DPRI 500m drilling core samples penetrating through the Nojima fault, Japan. *The Island Arc* **10**, 465-478.

2) T. Fukuchi, H. Mie, S. Okubo & N. Imai (2002) Assessment of fault activity by ESR dating of fault gouge using surface E' center in quartz produced with clay mineralization: The case of the Atotsugawa Fault in Japan. *Advances in ESR Applications* **18**, 145-151.

3) T. Fukuchi & T. Nishimura (2002) Decay characteristics of vacancy-associated ESR centers in quartz by UV-irradiation: A physical basis for absolute dating of planetary sediments. *Advances in ESR Applications* **18**, 171-176.

4) 福地龍郎・西村剛志 (2001) 石英格子欠陥中心の UV 照射による減衰特性：堆積年代測定のための基礎(Qm-008),地球惑星科学関連学会合同大会要旨集.

5) 西村剛志・福地龍郎・今井登 (2002) 石英過酸化ラジカル中心の先第四紀年代測定への適用可能性(Q037-004),地球惑星科学関連学会合同大会要旨集.

6) 西村剛志・福地龍郎・今井登 (2002) 石英過酸化ラジカル中心の高線量 γ 線照射による挙動と年代測定への応用，第 39 回理工学における同位元素・放射線研究発表会要旨集(3a-Ⅱ-5)，118，日本アイソトープ協会.

7) 西村剛志・福地龍郎・今井登 (2002) 石英過酸化ラジカル中心の先第四紀年代測定への応用，第 19 回 ESR 応用計測研究発表会講演要旨集(ESR 応用計測 19 巻)，8，ESR 応用計測研究会.

研究テーマ：フィッション・トラック熱年代解析による中国タリム盆地クチャガス田の熱史
表題：クチャガス田のアパタイト・フィッション・トラック年代

7-3

クチャガス田のアパタイト・フィッション・トラック年代

荒木俊貴[1]、李京昌[1]、渡辺公一郎[1]、大平寛人[2]
[1]*九州大学工学研究院地球資源システム工学部門*
[2]*島根大学総合理工学部地球資源環境学科*

中国タリム盆地北部に位置するクチャガス田はアジアの中でも最大級のガス田である。この研究の目的は、クチャ沈降帯が位置するタリム盆地北縁に露出している古生代から第四紀までの地層の構造運動をフィッション・トラック(FT)法を用いて明らかにし、石油熟成度について考察することである。我々はタリム盆地の北縁に位置するコルラからアクスーまでの道を基点に大きく分けて５つのルートで露頭岩石のサンプリングおよび堆積層の観察を行った。今回はクチャ川沿いにて採取した砂岩について、アパタイトのＦＴ年代を測定したので報告する。

年代測定結果を第１表に示した。Fish Canyon Tuff の測定から得られたゼータ値は 354 となった。測定粒子数が少なく誤差が大きい試料も含まれるが、二畳紀から新第三紀までの試料のＦＴ年代は 26.1～77.4Ma の間の値となった。二畳紀層下部の試料から白亜紀層下部の試料のＦＴ年代は 54.5～61.5Ma となり、実際の堆積年代よりもかなり若い値を示した。この結果はこれらの岩石が Annealing zone までの温度上昇を被ったことを示している。対して新第三紀、古第三紀の試料のＦＴ年代は実際の堆積年代と調和的な値をとっている。また、他に特徴的な事として、ジュラ紀、白亜紀の試料のＦＴ年代が他の試料よりも比較的古い値を示した事があげられる。引き続き、トラック長測定を行い、熱史について考察を行いたい。

apatite-FT年代測定結果

Sample name	Layer name		No. of Crystal	ρs(Ns) (10^5cm)	ρi(Ni) (10^5cm)	P(x^2) (%)	ρd(Nd) (10^5cm)	Age (Ma)
ku18	N1j	新第三紀下部	25	3.416(329)	16.352(1575)	36.5	6.9682(4891)	26.1±2.0
ku16	E2-3s	古第三紀中部	24	3.654(622)	12.47(2123)	0.0	6.9682(4891)	49.2±7.1
ku14	K1bs	白亜紀下部	24	6.363(1073)	14.238(2401)	0.0	6.969(4798)	61.5±5.4
ku12	K1y	白亜紀下部	23	9.199(1289)	15.751(2207)	0.0	6.9686(4891)	71.3±4.8
ku11	J1a	ジュラ紀下部	23	7.303(1155)	11.609(1836)	0.0	6.9685(4891)	77.4±4.7
ku10	T3t	三畳紀上部	23	5.853(819)	16.724(2340)	0.0	6.9679(4891)	43.7±4.7
ku8	T3t	三畳紀上部	23	3.654(622)	12.47(2123)	0.0	6.9682(4891)	49.2±7.1
ku1	T3h	三畳紀上部	24	3.208(619)	10.392(2005)	0.0	6.9679(4891)	43.4±3.5
ku5	T1eh	三畳紀下部	8	3.547(209)	11.404(672)	0.01	6.9682(4891)	50.6±5.8
ku2	P1x	二畳紀下部	24	3.455(757)	7.85(1720)	0.0	6.968(4798)	54.5±3.8

第１表. アパタイトのFT年代

原子炉：JRR-4　　装置：気送管　　分野：その他（フィッション・トラック）

研究テーマ：フィッショントラック法による環境試料中の核物質検出
表　　題：フィッショントラック法の保障措置環境試料パーティクル分析への応用

7-4

フィッショントラック法の保障措置環境試料パーティクル分析への応用

井口一成，李致圭，伊奈川潤，鈴木大輔[1]，福山裕康，桜井聡，
臼田重和，江坂木の実，小野寺貴史，江坂文孝[1]，渡部和男[1]，間柄正明

日本原子力研究所　環境科学研究部　環境技術開発研究グループ
[1]日本原子力研究所　環境科学研究部　分析科学研究グループ

日本原子力研究所(原研)は2003年1月に、未申告原子力活動検知を目的とした保障措置環境試料分析のためのIAEAのネットワーク分析所として認証された。保障措置環境試料分析法の一つに、個々の粒子中に含まれる核物質の分析ができ、過去の原子力活動をも検知できるパーティクル分析がある。原研では、粒径1 μm以下の粒子の分析にも対応できるフィッショントラック(FT)法を応用した分析技術の開発を進めている。この方法では、FT法により核物質を含む粒子を検出し、表面電離質量分析法(TIMS)により同位体比を測定する。今回はこの分析法により環境試料中の核物質の検出および同位体比測定を行ったので、その結果について報告する。

原子力関連施設内から拭き取りにより採取した試料(スワイプ試料)から、吸引法[1]により、ポリカーボネートメンブランフィルター(直径25 mm, 細孔径0.1 μm, Advantec)に核物質含有粒子を捕集した。そのフィルムを1,2ジクロロエタンとジクロロメタン混合液に溶解した。良く撹拌した後、ガラス板上に伸ばして再固化させ、粒子を含んだフィルム(検出器)を作製した。JRR-4にて熱中性子(中性子束: 8×10^{14} cm^{-2})を検出器に照射した後、NaOH溶液(55℃, 6 M)で化学エッチングを行うことでFTを可視化した。デジタル顕微鏡(VHX100, Keyence)により、FTの観察をすることで核物質含有粒子の検出をした。粒子検出後、図1に示すように同位体比測定用試料を作製した。窒素レーザにより、1粒子を含むフィルム片(50×50 μm)を切り出し、タングステン針を用いて、TIMSフィラメント上に置いた。更に、ジクロロエタンを滴下することで、フィルム片をフィラメント上に固定した。同位体比測定は表面電離型質量分析装置(TRITON, Thermo electron)により行った。図2はその環境試料のTIMS測定結果を示す。点線は天然ウランの^{235}Uの存在比(7.253×10^{-3})を示し、測定値は天然ウランの値と誤差の範囲内で一致することがわかる。このことから、本法は環境試料中の核物質含有粒子の検出および同位体比測定に有効な分析法であることが示された。

参考文献

1) K. T. Esaka *et al.*, Jpn. J. Appl. Phys., 43(2004) 915

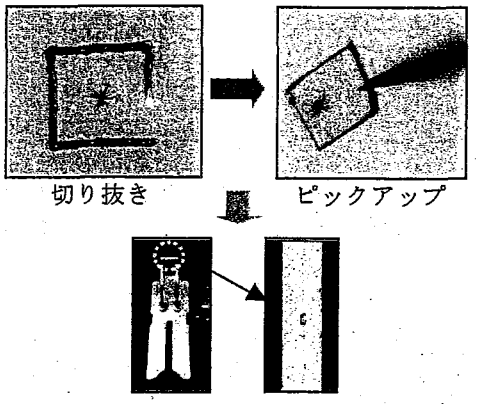

図1 TIMS測定用試料作製

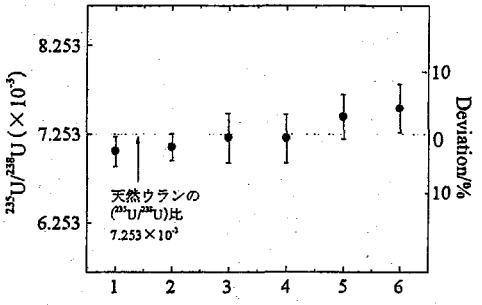

図2 同位体比測定結果

7-5
α線トラックエッチング法を利用した鉄鋼材料中のBの解析

Analysis of Morphology of Boron in Steel by using α-Ray Track Etching Method

千葉工業大学 Chiba Institute of Technology
為広 博 Hiroshi TAMEHIRO
千葉工業大学 Chiba Institute of Technology
斉藤秀雄 Hideo SAITO
千葉工業大学(元大学院生) Chiba Institute of Technology
高野貴光 Takamitu TAKANO

Ⅰ. 研究成果

研究課題-Ⅰ TMCP鋼の組織・特性におよぼすBとNb, Mo複合添加の効果

1. はじめに

TMCP鋼において、微量Bを有効に活用し強度・靭性バランスの向上をはかるには、B単独添加ではほとんど効果がなく微量Nbもしくは Moとの複合添加が極めて有効であることが知られている[1~5]。一般に、TMCPにおける圧延後の冷却速度は、直接焼入れを除いてそれほど大きくないので、その組織はベイナイト単相あるいはフェライトとベイナイト、マルテンサイトの混合組織となる。複合添加の場合、かなり遅い冷却速度(空冷以下)でもBが有効に働き、焼入性を増大(γ-α変態を抑制)させる。その結果、ベイナイトまたはマルテンサイト生成量は増加し、強度が向上する。さらに、複合添加では圧延中のオーステナイト未再結晶化温度が単独添加に比べて著しく上昇し、結晶粒の微細化が達成される。

本研究では、Nb-B、Mo-B複合添加による機械的性質の改善、γ-α変態の抑制機構についてレビューした。また、微量Bのもう1つの利用法としてフェライト-マルテンサイト2相組織化に対する微量B添加の効果についても検討した。

2. Nb-BおよびMo-B複合添加の効果(レビュー)

2.1 強度・靭性と組織

図1に途中水冷停止型TMCPを行った極低炭素鋼の引張強さ、靭性におよぼすNb-B、Mo-B複合添加の典型的な効果を示した。冷却速度が中程度の20℃/sの場合、C-Mn鋼への微量B添加は強度向上にほとんど寄与せず、むしろ靭性を劣化させる傾向にある。これに対してNb-BまたはMo-B複合添加すると、強度・靭性バランスは単独添加に比べて大幅に向上する。とくに微量Nb添加の効果は著しく、合金コスト削減の面からもその効果は絶大である。光学顕微鏡組織はB、NbおよびMo単独添加の場合、ポリゴナルフェライト主体の組織でベイナイト生成量は少ない(図2)。一方、複合添加の場合、ベイナイト単相組織(ベイニティクフェライト+微細なMA-constituentの混合組織)となり、組織中に延伸化した旧オーステナイト粒界が明瞭に観察される。これは複合添加によってγ-α変態やオーステナイト再結晶が抑制されたことを示唆する。このような複合添加の効果は、0.07%Ti-B添加においても認められるが、0.08%V-B添加では小さい[2]。ただし、Ti添加の場合、強度はNb-B複合添加と同程度に向上するが、靭性劣化が大きい。

したがって、途中水冷停止型TMCPのように冷却速度が直接焼入れほど大きくないとき、微量B添加によってγ-α変態を抑制し、かつ結晶粒を微細化して微細なベイナイト組織に基づく強度・靭性バランスの向上をはかるためには、Nb-MoまたはMo-B複合添加が不可欠と考えられる。

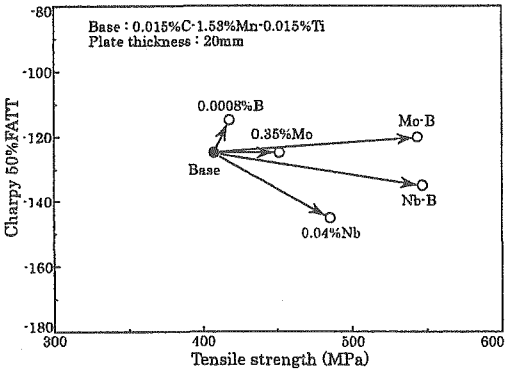

Fig.1 Relationship between strength and toughness of TMCP plates[4].

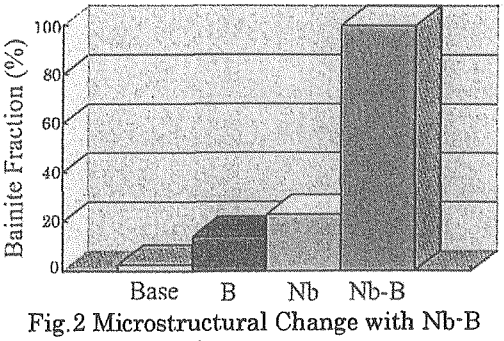

Fig.2 Microstructural Change with Nb-B addition[2].

2.2 γ-α変態温度とB分布

図3に添加元素によるγ-α変態温度の変化を示す。変態温度はB、Nbあるいは Ti単独添加によって数10℃程度低下するが、Nb-B、Ti-B複合添加ではベース鋼に比較して150℃も低下する。その結果、ポリゴナルフェライトは生成せずベイナイト型変態特性を示す。これはB添加による焼入性増大効果の大きさに起因すると思われる。図4にα線トラックエッチング（ATE）法で観察したB鋼とMo-B鋼におけるB分布を示す。B鋼では、旧オーステナイト粒界に粗大な析出物状のB(電子線回折により borocarbide Fe23(CB)6と同定、boride はなし)が多数認められる。このB析出物は、フェライト域ではなく変態前のオーステナイト域で析出することが確認されている[4]。一方、Nb-B複合添加鋼ではB析出物は観察されず、B原子は延伸化した旧未再結晶オーステナイト粒界や粒内の格子欠陥に分布(偏析)している。Bの存在形態はNb-BおよびTi-B鋼においてもMo-B鋼と同様であった。B添加により焼入性が向上するのは、B原子が旧オーステナイト粒界をはじめとする格子欠陥に偏析した状態であり、粗大なB析出物が生成すると焼入性が著しく低下することが知られている。したがって、Nb-BおよびMo-B複合添加により焼入性が増大する理由は、B析出物(Fe23(CB)6)の生成が抑制されるためと推定できる。

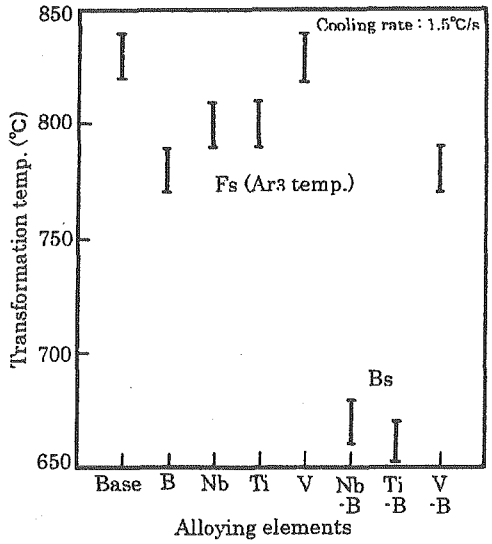

Fig.3 Change in γ-α transformation temperature of TMCP plate with alloying element[2].

2.3 熱間加工中のオーステナイト未再結晶化温度

図5に添加元素によるオーステナイト未再結晶化温度の変化を示す。単独添加では B、Ti、Nbの順に再結晶抑制能力が強い。注目すべきことはBが再結晶抑制能力を有すことで、そのオーステナイト未再結晶化温度は約870℃である。その機構については明らかでないが、B原子と転位や空孔との相互作用、B原子による粒界移動の低下に基づくと思われる。Nb-B、Ti-B 複合添加によって未再結晶化温度は単独添加に比べてさらに上昇する。これは、Nb、Ti添加によって、Fe23(CB)6の生成が抑制され、固溶B量が増加するためと考えられる。

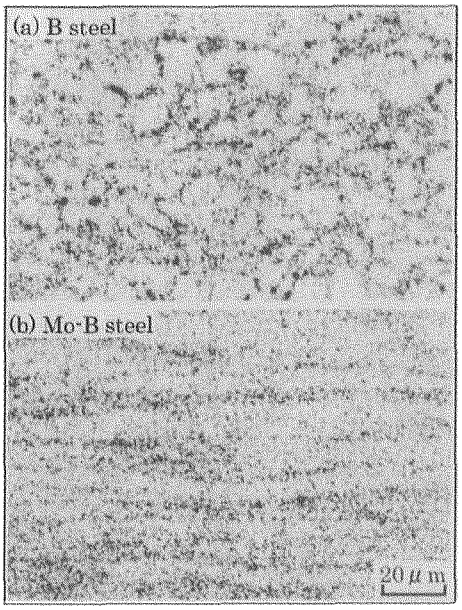

Fig.4 Distribution of boron in TMCP plates observed by ATE method[4].

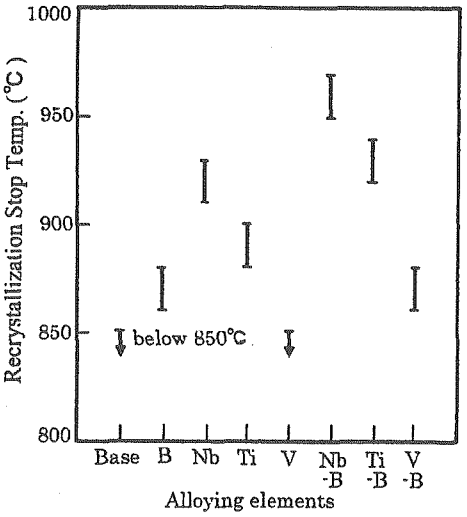

Fig.5 Change in recrystallization stop temperature of TMCP plate with alloying element[2].

2.4 Nb-B,Mo-B複合添加による焼入性向上の機構

上述の実験結果から、Nb-BおよびMo-B複合添加によってB添加TMCP鋼の焼入性が向上(γ

-α変態温度が低下）する原因は、Fe23(CB)6の生成抑制にあると考えられる。そこでFe23(CB)6生成抑制機構について考える。Nb-B、Mo-B複合添加による焼入性向上に、オーステナイト組織の未再結晶化のような加工は必ずしも必要でなく、熱処理時にもこの効果は認められている[2]。しかし、オーステナイト域加熱でNb、Moが十分に固溶していることが必須である。したがって、圧延前の低温加熱は、結晶粒の微細化以上に焼入性の低下を招く。図6にTMCP鋼(0.03%C-1.5%Mn-0.02%Ti-0.0012%B)の機械的性質、組織におよぼすNb量の影響を示す。Nb量が増加するにつれて、ベイナイト分率は増加し約0.015%Nbでほぼ100%となる。強度も約0.02%Nbで飽和する傾向を示す。スラブ加熱時(1200℃)に固溶するNb量はこの値よりも大きいが、固溶Nbの大部分は圧延時に歪誘起析出してオーステナイト未再結晶化などを通じて結晶粒の微細化に寄与すると考えられる。図7は図6に相当するTMCP鋼のB分布を示したものである。Nb添加量が増加するとFe23(CB)6は減少し、ベイナイト分率が100%となる約0.014%Nbでは、Fe23(CB)6は認められない。このことから、Fe23(CB)6の抑制には、変態前のオーステナイト中に一定量の固溶Nbが必要であることがわかる。この固溶Nb量は、鋼の炭素量やTMCP条件、とくに冷却速度に依存することがわかっている。したがって、炭素量の増加は、Fe23(CB)6を生成しやすくするので、Nb-B複合添加鋼の焼入性を低下させる。低～極低炭素化は、TMCP鋼において微量Bによる焼入性を利用する上で、極めて重要な要素である。冷却速度は大きいほど焼入性増大にとって望ましいが、炭素量、固溶Nb量が適当であればかなり小さい冷却速度でもB添加による焼入性向上効果は得られるものと思われる。すなわち、Fe23(CB)6の抑制の観点からすると、冷却速度、炭素量、固溶Nb、Mo量などは等価な効果を有する。

Fe23(CB)6生成の律速過程はC原子の拡散速度であり、固溶Nb、MoによってFe23(CB)6生成が抑制される理由はC原子の拡散速度が低下するためと考えられる。船越らによるC原子の拡散係数の測定結果によると、0.1%C鋼への0.05%Nb、0.10%Tiおよび0.5%Mo添加は、900℃以下で原子の拡散を遅延する傾向があり、この傾向はNb、TiがMoよりも強い。実際、炭化物形成元素であるNb、Mo原子はNb-C、Mo-Cクラスターを形成することが確認されているが[4]、これはC拡散速度の低下に寄与するものと考えられる。

以上のことから、微量BとCとの相互作用が強いNb、MoさらにTiなどの複合添加はC原子の拡散を遅らせ、Fe23(CB)6生成を抑制して、B添加による焼入性を相乗的に向上させるものと考えられる。

3. フェライト-マルテンサイト2相組織化におよぼすMo-B複合添加の効果

Mo-B複合添加によるγ-α変態温度の低下と結晶粒の微細化効果を利用して、低冷却速度(空冷)

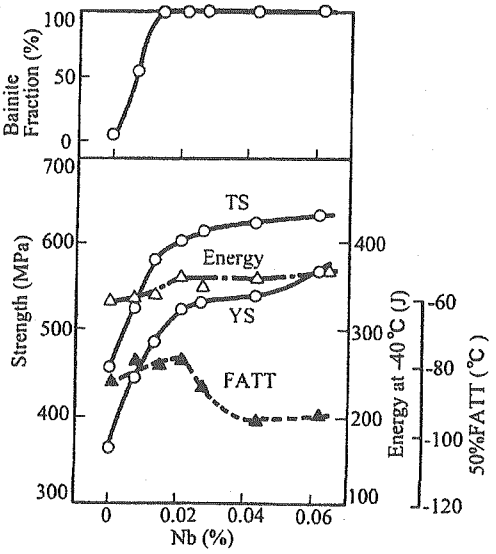

Fig.6 Effect of Nb content on mechanical properties and microstructure of TMCP plate[2].

における組織のフェライト-マルテンサイト2相組織化について検討した。図8および図9にそれぞれMo鋼、Mo-B複合添加鋼の機械的性質におよぼす圧延終了温度の影響、鋼板のミクロ組織を示す。加熱温度は、結晶粒微細化のため1000℃の低温とした。Mo-B複合添加鋼はMo鋼に比べて、強度が高く降伏比が低い。また低温靭性にも優れている。Mo鋼の組織は、圧延終了温度約750℃においてもγ-α域で圧延された加工フェライトと粗大なベイナイト、MA-constituentの混合組織である。一方、Mo-B複合添加鋼の組織は、微細な加工フェライトと微細に分散したMA-constituentの混合組織であり、約750℃の圧延温度ではフェライトは加工されていない。この組織的な相違は、Mo-B複合添加鋼の圧延再結晶温度やγ-α変態温度がMo鋼に比べて低いことに起因すると考えられる。なお、ATEの結果、Mo-B鋼では、650℃程度の低温圧延においても粗大なB析出物は認められなかった(Fig.10)。

したがって、Mo-B複合添加は2相域圧延(空冷)するような場合においても、微細なフェライトと微細なMA-constituentの混合組織の形成に有効であると考えられる。

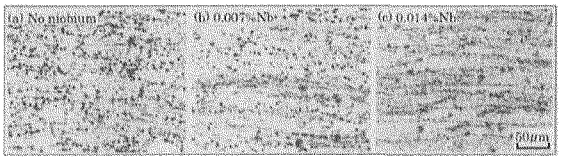

Fig7 Change in boron distribution of TMCP plate observed by ATE method with niobium content[2].

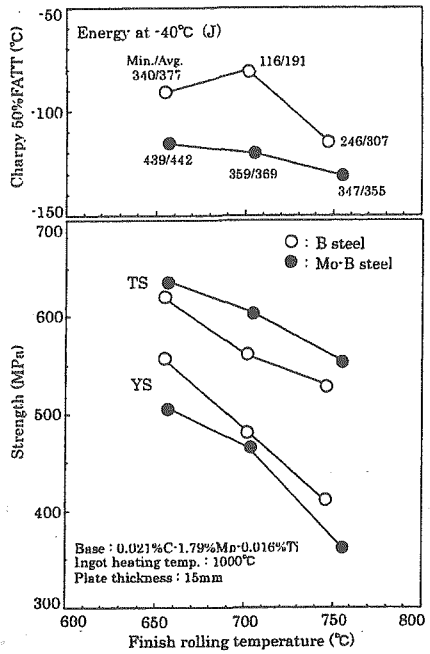

Fig.8 Effect of finish rolling temperature on mechanical properties of air-rolled Mo and Mo-B plates.

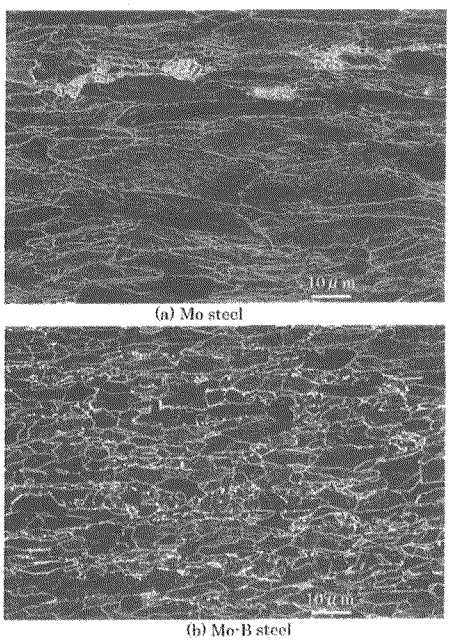

Fig.9 SEM microstructure of air-rolled Mo and Mo-B plates (FRT : approximately 700℃).

4. 結論

TMCP 鋼の強度・靭性バランスの向上をはかるには、極低炭素化に加えて微量 B と Nb もしくは Mo との複合添加が極めて有効である。強靭化は

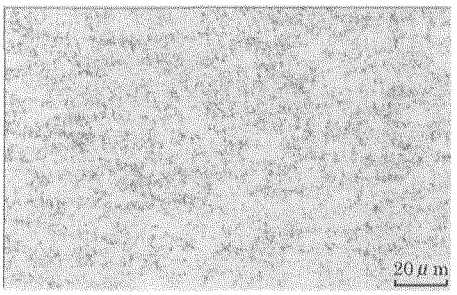

Fig.10 Boron distribution of Mo-B plate (FRT : approximately 700℃)

微細な極低炭素ベイナイト組織に起因する。極低炭素化と B と Nb または Mo 複合添加によって粗大な Fe23(CB)6 の形成が抑制され、旧オーステナイト粒界への B 偏析が安定して維持される結果、γ-α変態が著しく抑制されるだけでなく、熱間圧延中のオーステナイト再結晶が遅延し結晶粒微細化が達成される。Nb, Mo は C 拡散を遅らせて Fe23(CB)6 生成を抑制するものと考えられる。したがって、効果に差異はあるが、Ti など他の炭化物形成元素も同様の効果を有するものと思われる。

さらに微量 B と Mo んお複合添加は、低温圧延(2 相域圧延)による組織の微細フェライト-マルテンサイト 2 相化に対しても効果を有することがわかった。

参考文献

1) 鉄鋼材料の組織と特性に及ぼすボロンの影響：日本鉄鋼協会 (1999).
2) H.Tamehiro, M.Murata, R.Habu and M.Nagumo : Trans. ISIJ, 27(1987), p.120.
3) H.Tamehiro, M.Murata, R.Habu and M.Nagumo : Trans. ISIJ, 27(1987), p.130.
4) 原 卓也, 植森龍治, 為広 博：CAMP-ISIJ, 11(1998)-1140.
5) 原 卓也, 朝日 均, 植森龍治, 為広 博：CAMP-ISIJ, 15(2002)-605.
6) 船越, 上田, 瀬山：[田中智夫, 榎並禎一：鉄と鋼, 58(1972), p.1775] で言及.

研究課題-2 構造用鋼の液相拡散接合

1. はじめに

近年、材料の接合技術において精度・性能の高度化あるいは高能率化の観点から拡散接合が注目を集めている。液相拡散接合は通常の溶接法に比べ加熱温度が低いため母材の材質変化が小さく、熱影響部の劣化が少ないなどの利点を有する。そのため、液相拡散接合を鋼管および条材などの接合に適用することが検討されている。しかし、液相拡散接合過程を律速する等温凝固過程における融点降下元素Bの母材への拡散挙動については明らかでない点が多い。

本研究では、Ni-Si-B 系のインサート金属を用いて接合応力、熱影響部のオーステナイト粒径を変化させて液相拡散接合を行った。1200℃の等温凝固過程を観察するとともに、ATE 法から得られたB分布よりB濃度を測定し、B拡散係数を求め、液相拡散接合機構について考察した。

2. 実験方法

被接合試料として引張強さ 500MPa 級構造用鋼から機械加工した丸棒試験片(10mm ϕ × 50mm)を、インサート金属には 3%Si-3.5%B 系アモルファス Ni 合金(MBF-30:厚さ 50 μm)を使用した。また熱影響部におけるB原子の粒界拡散の寄与割合を明らかにするため、微量 Ti を添加し熱影響部のオーステナイト粒を微細化した鋼も作製した。鋼の化学組成を Table 1 に示す。液相拡散接合は窒素雰囲気において接合温度 1200℃、昇温速度 20℃/s、冷却速度 100℃/s で行い、保持時間、接合圧力はそれぞれ 0s～2500s、1~10MPa の範囲に変化させた。実験方法と装置を Fig.1 に示した。

得られた接合部の断面組織を光学顕微鏡にて観察し、各保持時間における液相幅(h)の厚みを測定した。さらに、α線トラックエッチング(ATE)法によって得られたB分布像を光学顕微鏡で拡大観察してB原子数の測定を行い、式(1)の薄膜拡散源に対する解をもとに実測拡散係数(D)の算出を行った。また、Fick の第二法則に基づく差分式によりプログラム「Form1」を作成し、実測拡散係数を用いBの理論数値計算を行った。

$$D = \frac{x^2}{4t \ln C_o / C} \qquad \cdots \qquad (1)$$

D:拡散係数、x:拡散距離、t:時間、C_o:初期濃度、C:濃度

Table 1 Chemical compositions of steel (wt%, *ppm)

Steel	C	Si	Mn	P*	S*	Ti	N*
Base steel	0.1	0.25	1.43	50	20		44
Ti-steel						0.013	

3. 実験結果

電解腐食によって現出した接合部の例として、ベース鋼(接合応力 1MPa、400s 保持)の光学顕微鏡写真を Fig.2 に示す。図中の A 部は母材熱影響部である。平坦な白色部(B 部)はインサート金属の Ni 富化域で加熱時に溶融しなかった部分である。さらに、その内部に灰色部が観察され、この領域は加熱時に溶融した液相部(C 部)と考えられる。その固液界面は平坦でなく波状である。液相部では、B は母材側にほとんど拡散せず、Ni-Si-B 濃度が高いと思われる。

保持時間の平方根と接合応力による液相幅変化の関係を Fig. 3 に示す。全ての試料において、保持時間の延長にしたがって液相幅は直線的に減少してくことがわかる。また 1MPa の時は等温凝固終了時間が 2500s に対し 5MPa では 250s、10MPa では 60s と接合圧力の増加にともない、等温凝固の終了時間が短時間に移行していった。

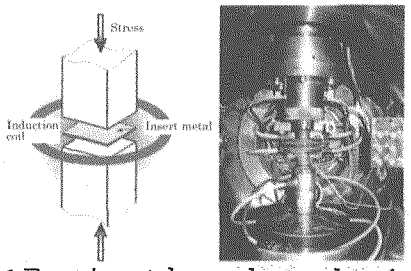

Fig.1 Experimental procedure and equipment.

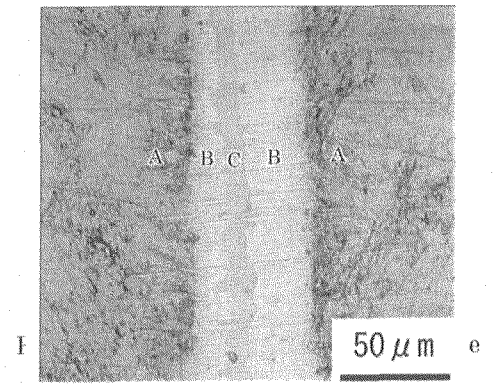

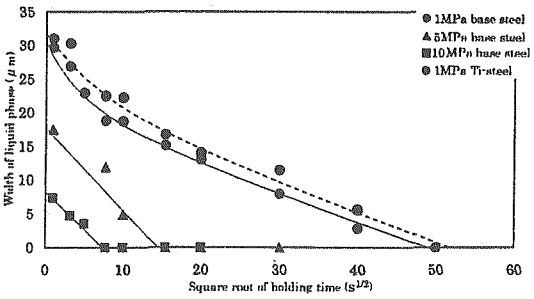

Fig.3 Change in width of liquid phase with holding time.

この理由は、昇温過程において溶融したインサート金属が接合応力により母材外部により多く排出されるためと考えられる。接合応力 1MPa の場合、液相幅は Ti 添加鋼と Ti 無添加のベース鋼おいて大きな差異は見られなかった。液相幅は保持時間の短い 1s～100s 付近まで急激に減少するがが、それ以降は少し勾配が緩やかになる傾向が見られた。

ATE 像により得られた B 分布の拡大写真例(接合応力 1MPa、100s 保持のベース鋼)を Fig.4 に示す。会合部の極近傍では、B 濃度が高く、B 分布の測定は不可能であった。そのため、拡大写真から測定可能な部分を選択して B 分布を測定した。図中の各黒点が B 原子の位置を示している。黒点が線状に並んで分布する領域は旧オーステナイト粒界と考えられる。B 分布の測定は粒界および粒内に単位枠を描き、その中に存在する B 個数をカウントした。

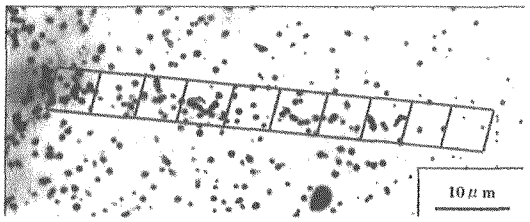

Fig.4 Example of boron distribution in HAZ revealed by ATE method.

Fig.5 に保持時間の平方根と接合応力による粒界・粒内の拡散係数の変化を示す。すべての試料において保持時間 100s まで、粒界・粒内の拡散係数は保持時間の延長とともに減少したが、保持時間 100s 以上では、拡散係数はおよそ 1~7 x 10^{-10}m²/s の範囲でほぼ一定となった。この拡散係数の値は多結晶における文献値とほぼ一致する。短時間側で拡散係数が大きくなった理由の一つとして、B 濃度勾配の影響が考えられる。粒界、粒内あるいは接合応力による拡散係数に明瞭な違いは認められなかった。しかし、旧オーステナイト粒径の小さい Ti 添加鋼(粒径~100μm)では、短時間側で拡散係数がベース鋼(粒径~300μm)に比較して大きくなった。高温の接合温度(1200℃)では、一般に粒内と粒界の拡散結晶数の差が小さいと考えられるため、この理由がオーステナイト粒径の違いに起因するかどうか明らかでない。

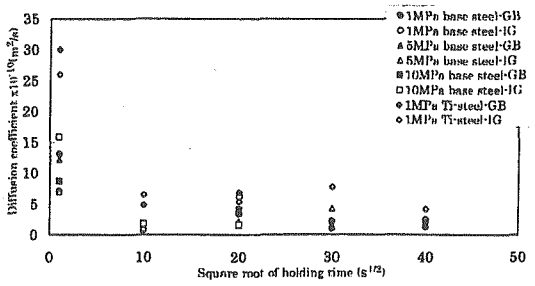

Fig.5 Change in diffusion coefficient of boron with holding time.

拡散係数計算プログラムに初期液相幅(Wi)ともっとも一致する実測拡散係数(D)を入力した場合における時間経過による B の拡散距離と濃度の関係を Fig.6(a)~6(d)に示した。Fig.6(a)、6(b)は接合応力 1MPa、保持時間 1～1600s におけるベース鋼および Ti 添加鋼、また Fig.6(c)、6(d)は接合応力 5MPa および 10MPa、保持時間 1～900s におけるベース鋼における結果である。

接合応力 1MPa の Ti 添加鋼およびベース鋼において、B 濃度の変化に差は見られなかった。しかし、1MPa、5MPa および 10MPa のベース鋼では、接合応力の増加にともなって B 濃度が全体的に低下していることがわかる。保持時間 900s のとき、会合部から 500μm 位置においても B 濃度は、接合応力の増加により減少していた。また B 濃度の均一化は接合応力の高い条件ほど短時間に進行している。これは、接合応力の増加にともない、等温凝固過程が短時間で終了し成分均一化過程に速く移行したことを示唆する。接合応力 1MPa のベース鋼および Ti 添加鋼を比較すると、B 拡散に相違は認められない。したがって等温凝固過程は、オーステナイト粒径の大きさに依存せず、接合応力にのみ影響されると考えられる。接合応力の増加により溶融インサート金属の排出量が増加するためである。

4. 結論

Ni-Si-B 系のインサート金属を用いた液相拡散接合において 1,200℃における等温凝固過程を観察し、母材への B 原子の拡散挙動および B の拡散係数について検討した。その結果、以下のことが明らかになった。

(1)初期液相幅は接合応力が大きいほど小さい。これは接合応力が増加すると、溶融インサート金属の外部への排出量が多くなるためである。また液相幅は保持時間の延長にともなって、約 100s まで急激に減少するが、それ以降は緩やかに減少する傾向が見られた。

(2)接合応力の増加にともなって、全体的 B 濃度分布が低下し、成分均一化過程が速く進行していた。

(3)オーステナイト粒の微細化、接合応力の増加による B の拡散距離に変化は見られなかった。B の拡散が影響されないのは、接合温度が 1200℃と高温のためと考えられる。

(4)すべての試料とも粒界と粒内において実測拡散係数に違いは見られなかった。保持時間が長い場合、実測拡散係数の値はおよそ 1~7x10^{-10}m²/s でほぼ一定となった。しかし保持時間が短い場合(100s 以下)、実測拡散係数は大きくなった(1~3x10^{-9}m²/s)。これは B の拡散係数が温度だけではなく濃度にも依存するためと考えられる。

(5)数値計算プログラムを用いて凝固終了時間を計算の結果、1200℃における鋼中 B の拡散係数 1~2x10^{-10}m²/s がもっとも実測値と一致した。

参考文献

1. Pall G. Shewmon : "Diffusion in Solid", 2nd edition, 1989.
2. W. F. Gale and E. R Wallach : "Micro-structural Development in Transient Liquid-Phase Bonding" Metall. Trans, 22A(1991), 2451
3. 中尾、西本、篠崎、堀：溶接学会論文集, 6(1988), 519.
4. 中尾、西本、篠崎：溶接学会論文集, 7(1989), 213.
5. 西本、篠崎:溶接学会論文集 14-2(1996), 731.
6. 西本、篠崎:溶接学会論文集 15-2(1997), 321.

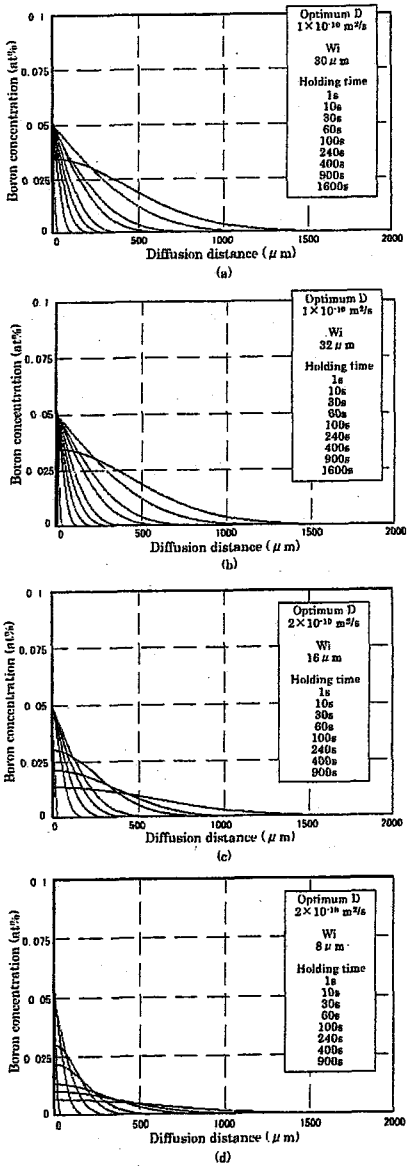

Fig.6 Calculation results of boron distributions.

Ⅱ．今後の方針

研究課題-1については、Mo-B複合添加による2相域圧延による組織の微細フェライト-マルテンサイト2相化を中心に16年度も継続して検討する。また、研究課題-2については当初の成果が得られたので、15年度で完了とする。

Ⅲ．成果の公表

1) 為広 博、原 卓也、植森龍治：「TMCP鋼の組織・特性におよぼすBとNb, Mo複合添加の効果」，鋼中微量ボロンの挙動と性質への影響，平成15年10月，日本鉄鋼協会，pp.54-57.
2) 高野貴光，斉藤秀雄，為広 博，篠原康浩，長谷川泰士：「構造用鋼の液相拡散接合」，同上，pp.189-191.
3) 斉藤秀雄，為広 博，森藤文雄：「熱中性子照射によって結晶粒界に偏析したMo-Bの定量的解析の一例」，同上，pp.209-212.
4) T.Hara, H.Asahi, R.Uemori and H.Tamehiro："Role of Combined Addition of Niobium and Boron and of Molybdenum and Boron on Hardenability in Low Carbon Steels", ISIJ Int., Vol.44(2004), No.8, pp.1431-1440.

謝　辞

本報告書の発刊にあたり、多くの皆様から多大なご協力を頂きました。編集に際し、ご協力頂いた、東京大学物性研究所吉沢英樹氏、東京大学原子力研究総合センター中沢正治氏、研究炉部長桜井文雄氏、JRR-4管理課加島洋一氏に深く感謝致します。

付　録

Appendix

This is a blank page.

付 録

原研研究炉の利用設備一覧

1．ＪＲＲ－３

1）実験設備

実 験 孔	実 験 装 置
１Ｇ	高分解能粉末中性子回折装置（ＨＲＰＤ）
１Ｇ－Ａ	生体高分子用中性子解析装置（ＢＩＸ－Ⅲ）
１Ｇ－Ｂ	生体高分子用中性子解析装置（ＢＩＸ—Ⅳ）
２Ｇ	三軸型中性子分光器（ＴＡＳ－１）
３Ｇ	中性子トポグラフィ及び精密光学実験装置（ＰＮＯ）
４Ｇ	汎用三軸型中性子分光器（ＧＰＴＡＳ）
５Ｇ	偏極中性子散乱装置（ＰＯＮＴＡ）
６Ｇ	東北大学中性子散乱分光器（ＴＯＰＡＮ）
７Ｒ	中性子ラジオグラフィ装置（ＴＮＲＦ）
Ｔ１－１	中性子偏極回折装置（ＨＱＲ）
Ｔ１－２	単結晶中性子回折装置（ＫＳＤ）
Ｔ１－３	粉末中性子回折装置（ＫＰＤ） （ＨＥＲＭＥＳ）
Ｔ１－４－１	即発ガンマ線分析装置（ＰＧＡ）
Ｔ１－４－１Ａ	化学反応実験装置（ＬＣＥ）
Ｔ１－４－２	多重即発ガンマ線分析装置（ＭＰＧＡ）
Ｔ１－４－３	ＴＯＦ型中性子反射率計（ＴＯＦ）
Ｔ１－４－４	中性子ラウエ回折装置（ＬＡＵＥ）
Ｔ２－１	残留応力測定中性子回折装置（ＲＥＳＡ）
Ｔ２－２	中性子４軸回折装置（ＦＯＮＤＥＲ）
Ｔ２－３	中性子ＩＰ付生体物質中性子回折計（ＢＩＸ－Ⅱ）
Ｔ２－４	高分解能三軸型中性子分光器（ＴＡＳ－２）
Ｃ１－１	高エネルギー分解能三軸型中性子分光器（ＨＥＲ）
Ｃ１－２	二次元位置測定小角散乱装置（ＳＡＮＳ－Ｕ）
Ｃ１－３	超高分解能後方散乱装置（ＵＬＳ）
Ｃ２－１	冷中性子散乱実験デバイス開発装置（ＬＴＡＳ）
Ｃ２－２	中性子反射率計
Ｃ２－３－１	中性子スピンエコー分光器（ＮＳＥ）
Ｃ２－３－２－１	多重即発ガンマ線分析装置（ＭＰＧＡ）
Ｃ２－３－２－２	即発ガンマ線分析装置（ＰＧＡ）
Ｃ２－３－３－１	冷中性子ラジオグラフィ（ＣＮＲＦ）
Ｃ２－３－３－２	パルス中性子機器開発装置（ＣＨＯＰ）
Ｃ２－３－３－３	ＴＯＦ型中性子反射率計（ＴＯＦ）
Ｃ２－３－３－４	中性子ラウエ回折装置(ＬＡＵＥ)
Ｃ３－１－１	高分解能パルス冷中性子分光器（ＡＧＮＥＳ）
Ｃ３－１－２－１	中性子光学システム評価装置（ＮＯＰ）
Ｃ３－１－２－２	多層膜中性子干渉計／反射率計（ＭＩＮＥ）
Ｃ３－２	中性子小角散乱装置（ＳＡＮＳ－Ｊ）

2）照射設備

水力照射設備	HR－1，2
気送照射設備	PN－1，2
放射化分析用照射設備	PN－3
均一照射設備	SI－1
回転照射設備	DR－1
垂直照射設備	VT－1，RG－1～4 BR－1～4，SH－1

2．JRR－4

1）実験設備

プール
中性子ビーム設備
散乱実験設備
冷却水循環ループ
医療照射設備（BNCT）
即発ガンマ線分析装置

2）照射設備

簡易照射筒	Tパイプ（水力）
	Sパイプ
	Dパイプ
	Nパイプ
気送管照射設備	PN

国際単位系（SI）と換算表

表1　SI基本単位および補助単位

量	名称	記号
長さ	メートル	m
質量	キログラム	kg
時間	秒	s
電流	アンペア	A
熱力学温度	ケルビン	K
物質量	モル	mol
光度	カンデラ	cd
平面角	ラジアン	rad
立体角	ステラジアン	sr

表2　SIと併用される単位

名称	記号
分，時，日	min，h，d
度，分，秒	°，′，″
リットル	l，L
トン	t
電子ボルト	eV
原子質量単位	u

1 eV=1.60218×10^{-19}J

1 u=1.66054×10^{-27}kg

表5　SI接頭語

倍数	接頭語	記号
10^{18}	エクサ	E
10^{15}	ペタ	P
10^{12}	テラ	T
10^{9}	ギガ	G
10^{6}	メガ	M
10^{3}	キロ	k
10^{2}	ヘクト	h
10^{1}	デカ	da
10^{-1}	デシ	d
10^{-2}	センチ	c
10^{-3}	ミリ	m
10^{-6}	マイクロ	μ
10^{-9}	ナノ	n
10^{-12}	ピコ	p
10^{-15}	フェムト	f
10^{-18}	アト	a

表3　固有の名称をもつSI組立単位

量	名称	記号	他のSI単位による表現
周波数	ヘルツ	Hz	s^{-1}
力	ニュートン	N	m·kg/s^2
圧力，応力	パスカル	Pa	N/m^2
エネルギー,仕事,熱量	ジュール	J	N·m
工率，放射束	ワット	W	J/s
電気量，電荷	クーロン	C	A·s
電位，電圧，起電力	ボルト	V	W/A
静電容量	ファラド	F	C/V
電気抵抗	オーム	Ω	V/A
コンダクタンス	ジーメンス	S	A/V
磁束	ウェーバ	Wb	V·s
磁束密度	テスラ	T	Wb/m^2
インダクタンス	ヘンリー	H	Wb/A
セルシウス温度	セルシウス度	℃	
光束	ルーメン	lm	cd·sr
照度	ルクス	lx	lm/m^2
放射能	ベクレル	Bq	s^{-1}
吸収線量	グレイ	Gy	J/kg
線量等量	シーベルト	Sv	J/kg

表4　SIと共に暫定的に維持される単位

名称	記号
オングストローム	Å
バーン	b
バール	bar
ガル	Gal
キュリー	Ci
レントゲン	R
ラド	rad
レム	rem

1 Å=0.1nm=10^{-10}m

1 b=100fm^2=10^{-28}m^2

1 bar=0.1MPa=10^5Pa

1 Gal=1cm/s^2=10^{-2}m/s^2

1 Ci=3.7×10^{10}Bq

1 R=2.58×10^{-4}C/kg

1 rad=1cGy=10^{-2}Gy

1 rem=1cSv=10^{-2}Sv

(注)

1．表1－5は「国際単位系」第5版，国際度量衡局 1985年刊行による。ただし，1 eVおよび1 uの値はCODATAの1986年推奨値によった。

2．表4には海里，ノット，アール，ヘクタールも含まれているが日常の単位なのでここでは省略した。

3．barは，JISでは流体の圧力を表わす場合に限り表2のカテゴリーに分類されている。

4．EC閣僚理事会指令ではbar，barnおよび「血圧の単位」mmHgを表2のカテゴリーに入れている。

換　算　表

力	N(=10^5dyn)	kgf	lbf
	1	0.101972	0.224809
	9.80665	1	2.20462
	4.44822	0.453592	1

粘　度　1 Pa·s(N·s/m^2)=10 P(ポアズ)(g/(cm·s))

動粘度　1m^2/s=10^4St(ストークス)(cm^2/s)

圧力	MPa(=10bar)	kgf/cm^2	atm	mmHg(Torr)	lbf/in^2(psi)
	1	10.1972	9.86923	7.50062×10^3	145.038
	0.0980665	1	0.967841	735.559	14.2233
	0.101325	1.03323	1	760	14.6959
	1.33322×10^{-4}	1.35951×10^{-3}	1.31579×10^{-3}	1	1.93368×10^{-2}
	6.89476×10^{-3}	7.03070×10^{-2}	6.80460×10^{-2}	51.7149	1

エネルギー・仕事・熱量	J(=10^7 erg)	kgf·m	kW·h	cal(計量法)	Btu	ft·lbf	eV
	1	0.101972	2.77778×10^{-7}	0.238889	9.47813×10^{-4}	0.737562	6.24150×10^{18}
	9.80665	1	2.72407×10^{-6}	2.34270	9.29487×10^{-3}	7.23301	6.12082×10^{19}
	3.6×10^6	3.67098×10^5	1	8.59999×10^5	3412.13	2.65522×10^6	2.24694×10^{25}
	4.18605	0.426858	1.16279×10^{-6}	1	3.96759×10^{-3}	3.08747	2.61272×10^{19}
	1055.06	107.586	2.93072×10^{-4}	252.042	1	778.172	6.58515×10^{21}
	1.35582	0.138255	3.76616×10^{-7}	0.323890	1.28506×10^{-3}	1	8.46233×10^{18}
	1.60218×10^{-19}	1.63377×10^{-20}	4.45050×10^{-26}	3.82743×10^{-20}	1.51857×10^{-22}	1.18171×10^{-19}	1

1 cal= 4.18605J（計量法）

= 4.184J（熱化学）

= 4.1855J（15℃）

= 4.1868J（国際蒸気表）

仕事率　1 PS(仏馬力)

= 75 kgf·m/s

= 735.499W

放射能	Bq	Ci
	1	2.70270×10^{-11}
	3.7×10^{10}	1

吸収線量	Gy	rad
	1	100
	0.01	1

照射線量	C/kg	R
	1	3876
	2.58×10^{-4}	1

線量当量	Sv	rem
	1	100
	0.01	1

（86年12月26日現在）

研究炉利用における研究成果集（平成15年度）